SPACE RESEARCH IN UKRAINE

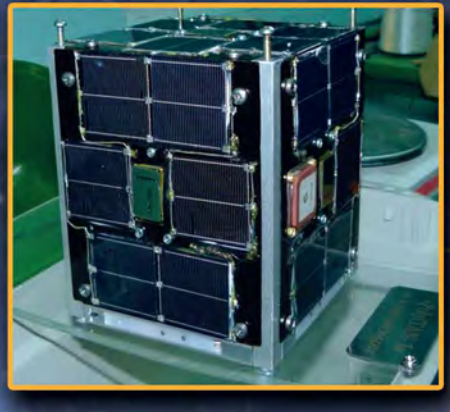

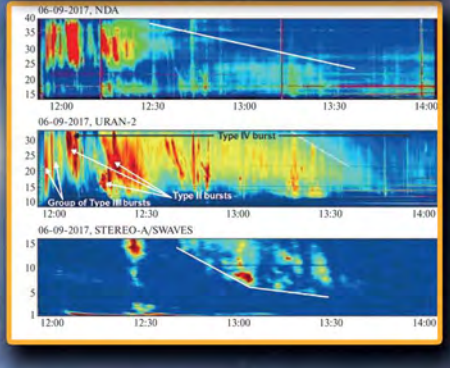

2022–2024

NATIONAL ACADEMY OF SCIENCES OF UKRAINE

SPACE RESEARCH IN UKRAINE 2022–2024

Report to COSPAR

The Report Prepared by the Space Research Institute of NAS of Ukraine and SSA of Ukraine

Scientific Editor O. FEDOROV

KYIV • AKADEMPERIODYKA • 2024

https://doi.org/10.15407/akademperiodyka.507.172
UDC 001.891(15)"2022/2024"
S78

SRI NASU-SSAU
Space Research Institute
of National Academy of Sciences of Ukraine
and State Space Agency of Ukraine
Ukraine
03680, Kyiv 187
40, Glushkov Ave., bilding 4/1
http://www.ikd.kiev.ua

NASU
National Academy of Sciences of Ukraine
Ukraine
01601, Kyiv 30
54, Volodymyrska St.
http://www.nas.gov.ua

Layout is funded within the framework of the Targeted Complex Program «Creation and Development of Scientific Publishing Complex of the National Academy of Sciences of Ukraine»

The edition is funded within the framework of the Nationwide Target Research and Engineering Space Program of Ukraine

Space research in Ukraine. 2022—2024 / Ed. O. Fedorov. — Kyiv: Akademperiodyka, 2024. — 172 p.
S78
ISBN 978-966-360-507-4

Report to COSPAR summarizes the results of space research performed during the years 2022—2024. This edition presents the current state of Ukrainian space science in the following areas: Space Astronomy and Astrophysics, Earth observation and Near-Earth Space Research, Life Sciences, Space Technologies and Materials Sciences. A number of papers are dedicated to the creation of scientific instruments for perspective space missions. Considerable attention paid to applied research of space monitoring of the Earth. The collection can be useful for a wide range of readers, interested in space research.

UDC 001.891(15)"2022/2024"

ISBN 978-966-360-507-4

CONTENTS

FOREWORD

The publication represents the main results of research and development in exploration and utilization of space, performed by leading Ukrainian institutions in 2022—2024. The collection is the report of Ukraine to COSPAR prepared by the decision of the Ukrainian National Committee of COSPAR and the Space Research Council of National Academy of Sciences. The publication covers the period 2021—2023 and follows a structure similar to those of previous periods. At the same time, behind the presented scientific reviews of this collection there is an unprecedented situation of wartime and critical conditions in which Ukrainian scientists worked. Among the authors of the articles are scientists from Kharkov, Odessa, Lviv, Dnipro, Kyiv, Poltava and our foreign colleagues. All the mentioned Ukrainian scientific centers were targets of Russian shelling, and many of our colleagues suffered or died as a result of aggression.

Reading the reports of Kharkiv scientists, it should be imagined demolishing the buildings of one of the best universities of Ukraine; It is also worth imagining how Kharkiv astronomers are restoring their observatory, which was under the temporary occupation of russian invaders and was used as a barracks. Our main space industrial center in the city of Dnipro works both for defense and in the interests of science, despite the numerous shelling of кussian aggressors.

A significant part of the review articles focused on *space information technology and the use of Earth observation satellite data.* The focus of the Ukrainian scientists was on the study of the consequences of the hostilities, the contamination of the land and sea surface, the degradation of the land cover, the assessment of damage and the economic consequences of the Russian aggression. Particular attention was paid to the impact of the destruction of the Kakhov hydroelectric plant in southern part of Ukraine.

One of the sections of the collection dedicate to the fundamental and applied research of *near-Earth space,* specifically to the features of acoustic-gravity waves in the Earth's atmosphere, studies of physical processes in the ionosphere over Ukraine, physical effects in the atmosphere and geospace environment. Scientific basis for advanced energy emissions monitoring satellite project developed in work on the effect of power lines electromagnetic emission to the space.

Space astronomy and astrophysics section includes review of large international team dedicated to achievements in the development of low-frequency broadband antennas for receiving the radiation of space objects at extremely low frequencies and testing of their prototypes in real conditions, determining the parameters of the ionized gas inside and outside the supernova remnant Cassiopeia A. Authors used the low-frequency antenna arrays of the GURT, NenuFAR and URAN-2 radio telescopes as interferometers in the ultra-wide frequency band, and present the study of the properties of solar bursts due to their simultaneous observations by ground-based radio telescopes and the Parker Solar Probe (PSP) spacecraft at perihelion, the analysis of ionospheric effects on the results of radio observations at very low frequencies; preparation and creation of low-frequency radio-astronomical elements, which are proposed to be placed on the far side of the Moon for the study of cosmic objects in the Universe.

Ukrainian Space biologists continue intensive research for future manned missions. In the collection three directions of research are presented. The first deals with role of plant cell signaling systems in adaptation to microgravity. Another article descried the stage of research dedicated to neurotoxicity risk assessment of planetary dust. Advanced life support systems might be interested in results of the research of the ways preventing human health disorders associated with spaceflight.

The section of *Space Technologies and Materials Sciences* as well oriented on future space missions. The review of our main space center — Yuzhnoye State Design Office — dedicated to research activities on Moon exploration. Developments of modern tools for welding in space (including Moon) and some other technologies presents Paton Electric Welding Institute. Teams of engineers and scientists propose conceptual designs for advanced orbital platforms and systems that are expected to be the focus of future space projects.

Ukrainian space science was going through a difficult period of war, extremely limited funding and brain drain. But it is also a time for the adoption of new conceptual approaches, a new model for space activities. One of the most important tools for establishing a new quality of Ukrainian space research is the decisive strengthening of international cooperation. Participation in COSPAR is an important part of this effort.

ULTRALOW FREQUENCY BROADBAND RADIO ASTRONOMY: TECHNOLOGY AND ASTROPHYSICS

A. Stanislavsky[1], A. Konovalenko[1], V. Zakharenko[1, 2], I. Bubnov[1], P. Tokarsky[1], S. Yerin[1, 2], L. Stanislavsky[1], P. Zarka[3, 4], C. Viou[4], A. Loh[3, 4], N. Kalinichenko[1], A. Brazhenko[5], R. Vashchishin[5], A. Frantsuzenko[5]

[1] Institute of Radio Astronomy of the NAS of Ukraine
[2] V.N. Karazin Kharkiv National University
[3] LESIA, Observatoire de Paris, CNRS, Université PSL, Sorbonne Université, Université Paris Cité, CNRS
[4] Observatoire Radioastronomique de Nançay (ORN), Obs. Paris, CNRS
[5] Poltava Gravimetrical Observatory of Institute of Geophysics of the NAS of Ukraine

Introducon

Achievements in the development of low-frequency radio astronomy depend heavily on the investigation and application of new advances in antenna technology, analog and digital electronics, computer systems and technologies [1]. Together, their application creates new and, not by chance, unique opportunities in the study of very complex astrophysical processes occurring in cosmic space, which were previously difficult to investigate due to the insufficient capabilities of previous technical means. This important headway makes it possible to significantly enrich knowledge about the Universe with new results of fundamental importance. It should be noted that in the decameter and meter ranges of radio waves (frequencies 3—30 MHz and 30—300 MHz, respectively), the Universe looks completely different from the way mankind has seen it in optics, and then also in high-frequency radio astronomy. And it is clear what the reason is. In the low-frequency radiation of the Universe, many types of so-called non-thermal sources of radio emission are dominant, while in optics the main mechanism of radiation is thermal. The study of such unusual, and in some ways even exotic, astrophysical objects and phenomena with non-thermal radiation require ultra-broadband, very stable, flexible in applications radio astronomical elements and instruments for experiments, and this is almost impossible without the use of the latest technologies, implementations and observation methods.

In this report we present recent development of low-frequency broadband antennas for receiving the radiation of space objects at extremely low frequencies and testing of their prototypes in real conditions, determining the parameters of the ionized gas inside and outside the supernova remnant Cassiopeia A using the low-frequency antenna arrays of the GURT, NenuFAR and URAN-2 radio telescopes as interferometers in the ultra-wide frequency band (8—80 MHz), the study of the properties of solar bursts due to their simultaneous observations by ground-based radio telescopes and the Parker Solar Probe (PSP) spacecraft at perihelion, the analysis of ionospheric effects on the results of radio observations at very low frequencies; preparation and creation of low-frequency radio-astronomical elements, which are proposed to be placed on the far side of the Moon for the study of cosmic objects in the Universe.

Potential of new technologies and equipment in ground-based observations

The antenna systems of modern radio telescopes are excellent examples of the quality and efficiency of a superb scientific installation. Such gigantic and expensive structures are not an end in themselves for work of radio astronomers. The main goal here has always been and is significant discoveries for understanding the nature of space [2]. Thanks to these devices, it is possible to establish the characteristic properties of cosmic objects at great distances with high spatial resolution. Cutting-edge research conducted at the Institute of Radio Astronomy of the National Academy of Sciences of Ukraine in the early 2000s showed the undeniable advantages of small-sized active dipoles and antenna arrays made from them for use in low-frequency radio astronomy. Based on these works, a number of criteria for finding the effectiveness of such dipoles in radio observations were proposed. Many years of experience in operating active dipoles with the GURT ground-based radio telescope confirmed their reliability and scientific performance. Such dipoles, having small dimensions, provide optimal «radio astronomical sensitivity», which is determined, first of all, by the negligible contribution of the amplifier temperature to the noise temperature of the active dipole. In the case of a no-noise amplifier, the noise temperature of the active dipole is equal to the antenna temperature obtained from the reception of radio emission from the Galaxy (so-called Galactic background).

Active Antenna Models and their verification

The theory of an active receiving antenna for applications in radio astronomical observations and the method of determining its parameters were developed in detail in papers [3—8]. Such an active antenna has a cross-shaped design consisting of two identical mutually orthogonal symmetric dipoles of a complex shape fixed on a common holder. Identical low-noise amplifiers (LNA) are connected to the terminals of the dipoles, from the outputs of which the received signals carried by electromagnetic waves of two mutually orthogonal linear polarizations are recorded. The same design of dipoles is currently used in the GURT antenna array. Thus, the functional scheme of the active antenna consists of a dipole and a LNA, which can be represented by a linear 2-port network. The electrical parameters of the LNA are given by the scattering matrix, and the noise parameters are given by the covariance matrix of the spectral densities of the noise waves. To find the sensitivity of the active antenna, the total (or system) noise temperature at its output is calculated. It is determined by the sum of the external and internal noise temperatures, respectively, at the output of the active antenna. In this case, the external noise temperature is determined by the reception of Galactic and extragalactic radiation by the antenna, which is characterized by the brightness temperature of the sky. The sources of the own noise temperature at the output of the active antenna are heat losses in the dipole material and the underlying soil, as well as electronic noise of the LNA. The value of Sky Noise Dominance (SND) describes the excess of the external temperature over the internal and characterizes the quality of the active antenna. The larger it is, the weaker signals such an antenna can receive. This is very important for successful low-frequency observations in radio astronomy.

As a result, a suitable numerical model of this antenna has been suggested, which made it possible to calculate its impedance and energy parameters, as well as directivity characteristics [6—8]. In this way the software program known as NEC-4 was used for wire antenna calculations. Unlike similar ones, this software product correctly finds the parameters of antennas that are close to the soil surface and even cross it. Based on the simulation results, the impedance, the efficiency and the effective area of the antenna under study were calculated in a wide frequency range, from 4 MHz to 80 MHz. Since the radio astronomy antenna has to receive wideband signals, it is desirable to have a fairly flat amplitude-frequency characteristic over the entire range of its usage. This is achieved through LNAs. In addition to the appropriate amplification of received signals in the entire frequency range of the antenna, this device gives the matching of the dipole with the complex resistance of the cable through which these signals are sent to the receiver. Using this antenna model, the electrical and noise parameters of the active antenna array that is built from such antennas were calculated. The analysis includes also finding its directional patterns of the subarray of the GURT radio telescope in the frequency range of 8—80 MHz. In the studies, special attention was paid to its sensitivity, which was defined in the generally accepted terms of the system equivalent flux density (SEFD). This value indicates the efficiency of the antenna for radio astronomy observations without taking into account the frequency and time signal accumulation in the receiver used. A lot of effort was also spent on evaluating the external influence on the characteristics of the GURT array and its elements, in particular, the influence of seasonal variations of soil parameters that occur due to cyclical changes in weather conditions. Based on the research, recommendations were made regarding their consideration during radio astronomical observations.

The simulation results were verified by measurements of real active antennas of various configurations and showed a complete coincidence of their properties with the results of calculations using the proposed models [5]. For this stage, the device «Oglyad-103» was used, which allowed us to accurately measure the frequency dependence of both impedance and efficiency of the dipole, as well as for different heights of its location above

Fig. 1. Active antenna for radio observations at 4—70 MHz. It is cross-shaped and consists of two identical mutually orthogonal symmetric dipoles of a complex shape, mounted on a common holder. The active antenna has also two identical LNAs, each of which is connected to the terminals of the corresponding dipole, from the outputs of which received signals transmitted by electromagnetic waves of two mutually orthogonal linear polarizations are recorded. Such a dipole is identical in shape to any GURT dipole, but all its dimensions have been increased

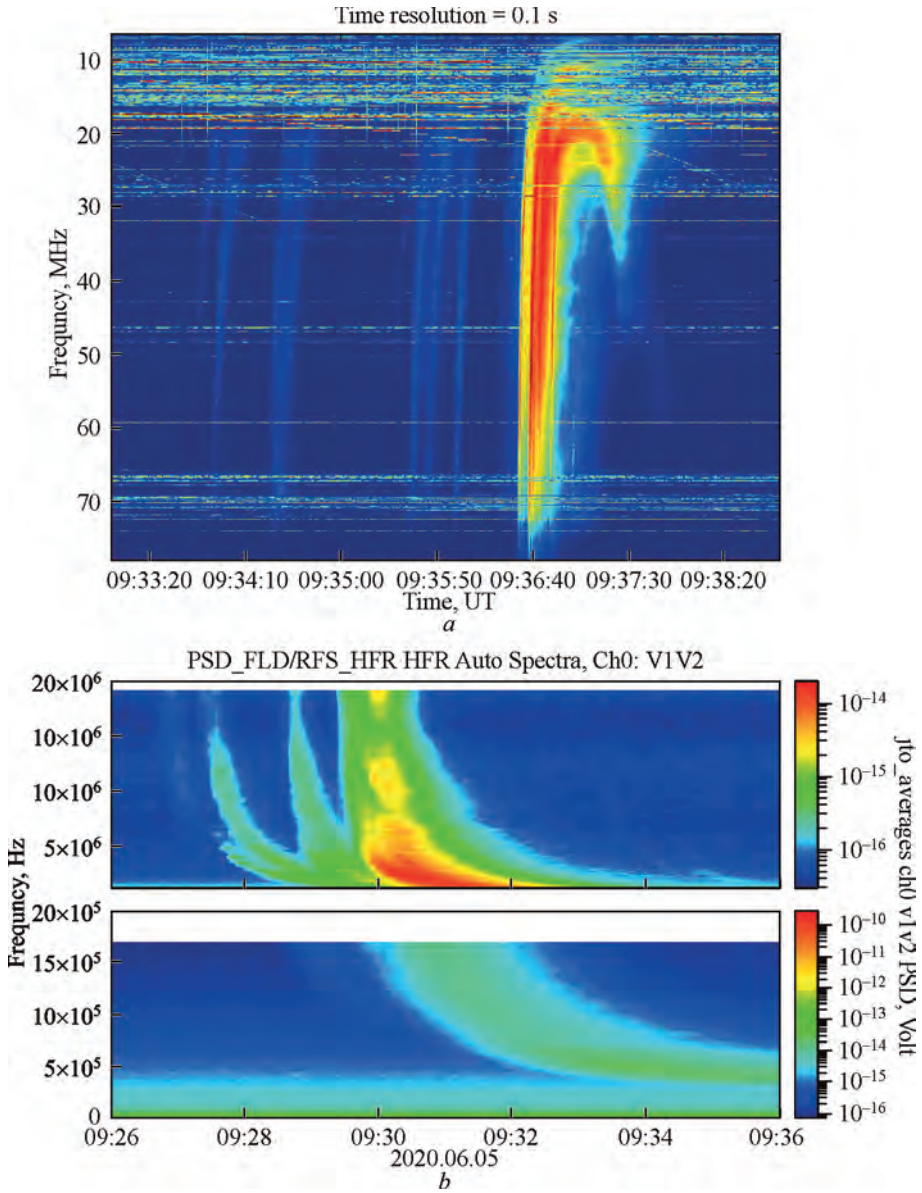

Fig. 2. Solar Type U+III bursts from radio observations on June 5, 2020 with different records: (a) GURT; (b) Parker Solar Probe, where the top picture was obtained with the high frequency receiver, whereas the bottom picture manifests the low frequency receiver spectrum

the soil surface. The tests of active dipoles were conducted at different times of the year from 2019 to 2021 on the territory of the Radio Astronomical Observatory named after S.Ya. Braude, which is located 80 km from the city of Kharkiv (Fig. 1). These measurements have shown that the excess is more than 6 dB in the specified frequency range. In other words, the contribution of the amplifier temperature to the noise temperature of the active dipole is no more than 25% [2]. Such a summary turns out to be quite sufficient for the successful use of such antennas in low-frequency radio astronomy.

At the next stage, the created technologies of active antennas and elements were applied to radio astronomical observations in order to check their full effectiveness for real astrophysical research. For this purpose, several essentially different observations were conducted [9—16].

Ground-based support of PSP mission

The Sun is one of the most intense natural sources of radio waves in our solar system. During solar activity, its character has a wide variety. Solar radio emission is studied in radio astronomy from kHz to GHz by various means both on Earth and in space. The antennas we produced made it possible to conduct broadband observations of the Sun at low frequencies, starting from the ionospheric cutoff frequency up to 80 MHz with record sensitivity and high frequency-time resolution [10, 11]. It should be noted that at frequencies below 20 MHz there are no radio telescopes in the world that could match the capabilities of the GURT. This result was achieved in large part due to our contribution to the development of antenna technique and its application. One of significant achievements was the radio observation of the Sun on June 5, 2020 in the

frequency band from 6 MHz to 66 MHz. The solar activity was caused by NOAA's bipolar active region AR12765. Bipolar magnetic fields on the Sun are interesting primarily because they are responsible for U-shaped solar radio bursts, which arise as a result of the movement of electron beams in the solar plasma along magnetic field lines. The U-shaped nature of the spectrum of radio bursts indicates the fact that at the beginning the electron beam moves from the Sun to the Earth (the plasma frequency decreases), and then the bipolar magnetic field of the active region on the Sun returns it back to the Sun (the plasma frequency increases). We managed to successfully receive such a burst on June 5, 2020, using a prototype of the ultra-low-frequency radio astronomical antenna element (Fig. 1) planned for the use for the antenna array in a future lunar radio observatory, as well as with the help of the GURT subarray [12]. On the other hand, this burst was also observed by NASA's newest PSP spacecraft, which was launched on August 12, 2018. Its goal is to fly closer to the Sun than any previous spacecraft. The ground support of this spacecraft is very important for the interpretation of the radio observations carried out on board. On June 5, 2020, the space vehicle was at perihelion with respect to the Sun. This gave us the opportunity to conduct joint ground-space studies of solar radiation from kHz to 80 MHz [13]. It should be pointed out that this case is not the first example of successful ground support of spacecraft, including PSP, in our research. The absence of sunspots from the PSP's side contributed to the propagation of radio waves from the dense loop of the Sun in the NOAA sunspot AR12765 to regions with low density, through which the radio instruments of this spacecraft detected the radiation of behind-limb sources of solar bursts in the frequency range from 19.2 MHz and below. The radio spectra obtained by the GURT and the PSP are drawn in Fig. 2. This important result is difficult to imagine without observations from ground-based radio astronomy instruments, which were created thanks to our substantial contribution [14].

Radio observations of ionospheric cutoff

In order to check the quality of the prototype of the ultra-low-frequency radio astronomical antenna element for a future lunar radio observatory (Fig. 1), we performed a special study of solar Type III bursts on May 22, 2021 near the ionospheric cutoff together with the simultaneous use of our modern HF equipment of coherent sounding of the ionosphere, which is located near the town of Zmiiv (Kharkiv region) [10]. In this case, the critical frequencies F2 of the ionosphere layer were measured by two independent methods, active with the help of this ionosonde and passive, by receiving solar bursts up to their ionosphere cutoff frequency. On that day, a moderate storm of solar Type III bursts with varying intensity was observed. Our radio astronomy observations were conducted from 09:20 to 17:00 UT, and the ionosonde soundings lasted from 07:00 to 17:00 UT. Eleven powerful solar bursts were selected during the day of radio observations. Since the Sun was moving across the sky over time, the position of sources of solar radio bursts had a different angle of inclination to the zenith, which was taken into account. On the other hand, due to the ionospheric cutoff, the bursts had frequency cutoff on the dynamic spectrum of their recordings. Thus, it was possible to establish the critical frequencies of the F2 ionospheric layer during May 22, 2021, from radio astronomical records. Their values have shown a good agreement with the ionosonde data [11], as well as the good quality of the antenna prototype itself. With this experiment, we proved that the produced antenna can be used as an additional device in ultra-low-frequency observations together with the GURT subarray. It can receive radio emissions from space at lower frequencies than those available for the GURT. This provides useful information in the support of cosmic missions.

Free-free absorption of radio emission from Cassiopeia A and its properties

In addition to researching the Sun and ionosphere properties, we also applied our technical and methodological developments to the observations of more distant space objects. One of the intense radio sources in our galaxy at decameter waves is the supernova remnant Cassiopeia A, which is located at a distance of 11000 light years from the Earth. The low-frequency observations used a two-element correlation interferometer built from two subarrays of the GURT radio telescope, which received radio emission from Cassiopeia A and Cygnus A one after another in each session in 2019. Observations lasted four months. In this case, the radio galaxy Cygnus A served as the calibration source. The interferometric responses from both radio sources are presented in Fig. 3. We first have studied the integral spectrum of this source in the frequency range of 12—78 MHz with a step of 1 MHz [26]. Thanks to the long-term observations, it was established that in the epoch of 2019, the peak of the radio flux density spectrum of Cassiopeia A is 31743 ± 1894 Jy at a frequency of 22 ± 0.5 MHz. Next, a model was built that takes into account the influence of thermal absorption of the synchrotron radiation source of this remnant due to the ionized gas inside and outside Cassiopeia A. If this model is fitted with the spectrum of observations of the radio source, then the model parameters show the properties of the absorbing regions of the remnant. These quantities include the emission measure, the electron temperature, and an average number of ion charges. Based on the results of this analysis, inside Cassiopeia A, the emission measure is 37.36 parsec cm^{-6}, the temperature is 100 K, and the average number of ion charges is about 2.55, which is in good agreement with the results of studies performed in other frequency ranges. In addition, we managed to find the density and mass of the inner region (unshocked ejecta) of Cassiopeia A, which have values of 15.3 cm^{-3} and 2.61 ± ± 0.31 $M_{\odot}$ (the mass of the Sun), respectively, which are also consistent with known research results for Cassiopeia A obtained by other technical means.

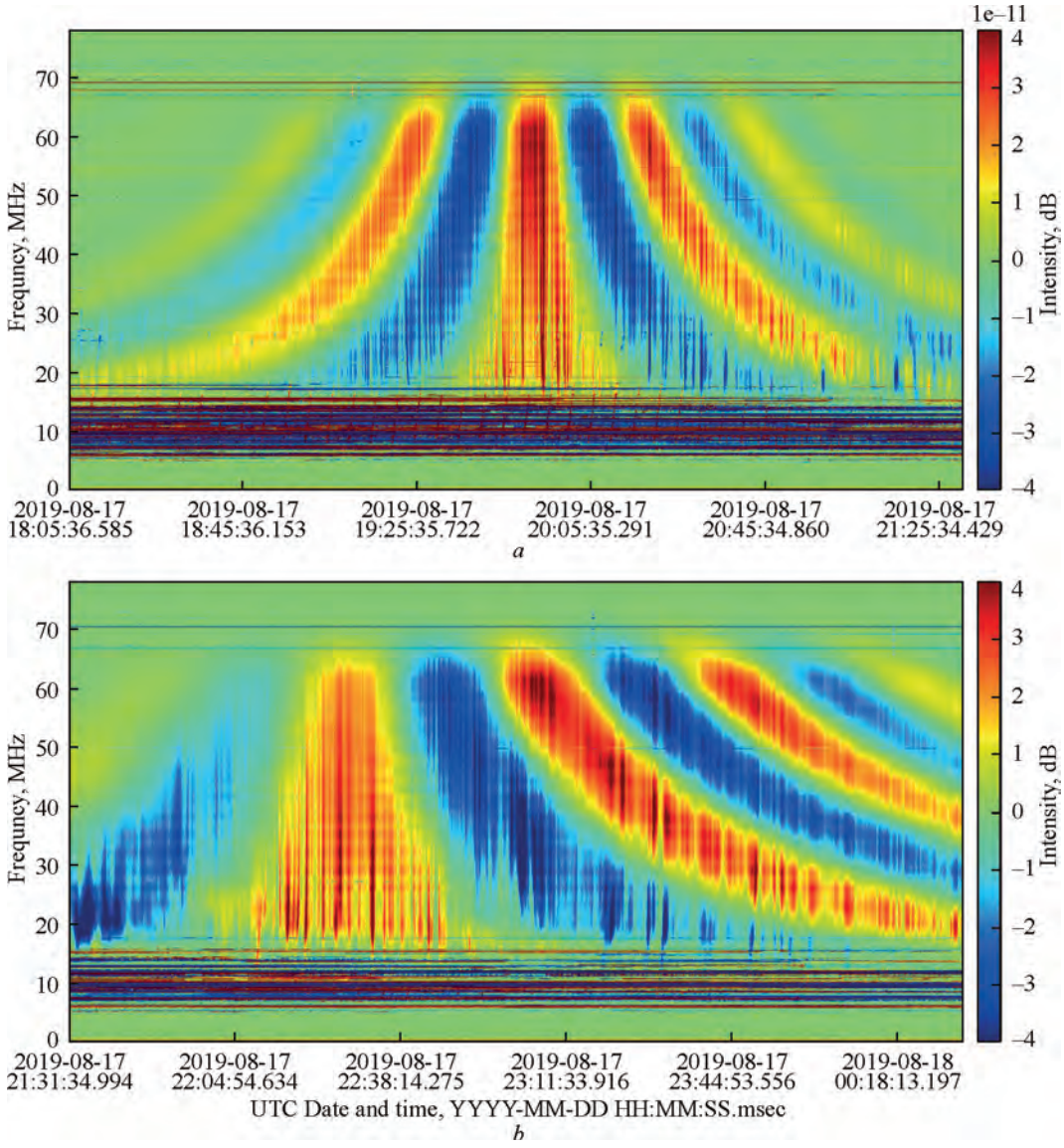

Fig. 3. Dynamic cross-spectra of the interferometric response of Cyg A (a) and Cas A (b) from observations by two GURT subarrays on August 17, 2019

The experience of improving active receiving antennas for radio astronomy, made by us, turned out to be useful not only for Ukrainian radio astronomy, but it was also applied by our French colleagues during the construction of the NenuFAR low-frequency radio telescope in Nançay [7]. Following the examples of the Ukrainian technology development, French radio astronomers used active antennas of a similar type with analog control of targeting sources of cosmic radio emission within the framework of individual phased mini-arrays. This made it possible to use this radio astronomical system effectively and fully adaptable for observations in the frequency range 20—80 MHz. Now we are actively participating in observations at this radio telescope. An excellent example of this collaboration is the observation of the pulsar PSR B0950 + 08 [9]. This interesting object is characterized by high variability. Such observations were made simultaneously on two radio telescopes, NenuFAR (55 MHz) and the Westerbork Synthesis Radio Telescope (1.4 GHz). This work shows that the variability of the pulsar is probably related to the change in time of the properties of the interstellar medium along the line of sight to this pulsar, namely due to the fluctuating size of the decorrelation bandwidth of diffractive scintillation, which makes an important contribution to the observed variability of each pulse.

Multi-antenna probing with the radio telescopes URAN-2 and NenuFAR

The Russian invasion and occupation in February 2022 caused enormous damage to the GURT and UTR-2 radio telescopes. They were disabled. New observations of Cassiopeia A at 8—66 MHz have been fulfilled with other radio telescopes such as NenuFAR in France and URAN-2 in Ukraine [16]. From their sub-arrays we implemented a two-element correlation interferometer for each radio telescope. Their interferometric responses are shown

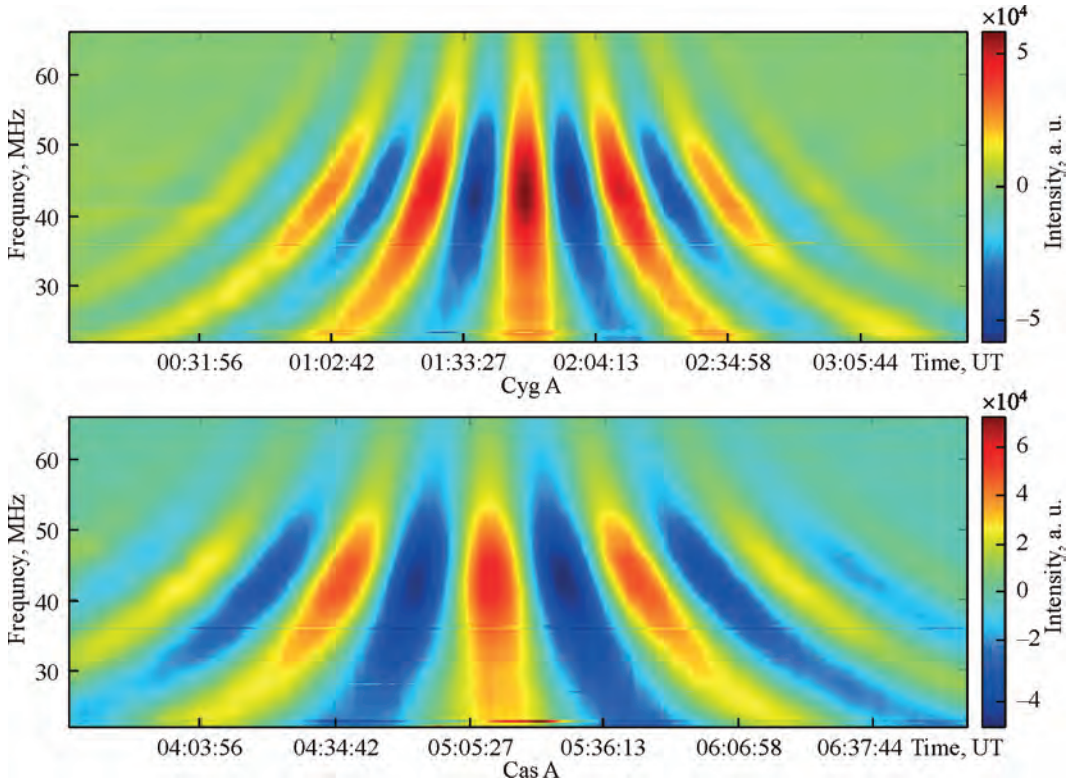

Fig. 4. Interferometric responses obtained from the observations on June 24, 2023 with two mini-arrays of NenuFAR. The color-coded intensity decline of this figure towards lower frequencies is explained by the amplitude-frequency response of this antenna system that includes preamplifiers, filters and others. But this does not affect the spectral results, since a ratio of measurements for Cas A and Cyg A is used

in Fig. 4 and Fig. 5, respectively. Because of intensive radio frequency interference (RFI) the NenuFAR records were not available below 21 MHz. Therefore, we used radio observations with the URAN-2 at 8—40 MHz and concatenated two data parts: from 8MHz to 21 MHz, using the radio records of URAN-2; and the frequency range of 21—66 MHz obtained with NenuFAR. The observations were carried out in the summer of 2023. In this epoch the spectral peak of Cassiopeia A had the flux density of radio emission 29 880 ± 2980 Jy at 21.5 ± 0.2MHz. The most parameters of absorbing regions inside and outside Cassiopeia A were close ones resulted from the observations of 2019 with the GURT [15]. Nevertheless, we have established that the spectral peak moves in the direction of lower frequencies over time. Such changes can be connected with the evolution of emission measure outside Cassiopeia A and indicate the interaction between the supernova remnant and its environment. This important result was obtained for the first time.

Conclusion remarks

Despite the difficult times and the devastating consequences of Russian aggression for Ukrainian radio astronomy, as well as difficult working conditions, we continued our scientific research in low-frequency radio astronomy. Thanks to hard work, we managed not only to obtain new experimental results from pre-war observations, but also to restore the damaged GURT radio telescope for further observations. Already on October 12, 2023, we conducted the first observations on the first restored section of the GURT radio telescope. Field works on restoration began after August 23, when a solar power plant was installed at the Radio Astronomical Observatory named after S.Ya. Braude. Already on September 7, the voltage from it was supplied to the infrastructure of GURT. Due to the fighting in the nearby territory, the antenna system of the GURT sections suffered the most; more than 50% of their technical devices were damaged. The first subarray resumed operation on September 28, 2023. Currently, the next section of the GURT was also restored. We are conducting measurements from the Sun and Cassiopeia A with the GURT, NenuFAR and URAN-2 radio telescopes. They will also perform the ground-based support of cosmic missions again.

Acknowledgment

The authors thank the National Academy of Sciences of Ukraine for the partial support under Contract No. 0123U102426. Stanislavsky Lev acknowledges the support of young researchers due to Contract No. 0123U103014 from the National Academy of Sciences of Ukraine. Zakharenko Vyacheslav is grateful for the financial support of the Europlanet 2024 RI project funded by the European Union's Horizon 2020 Research and Innovation Program

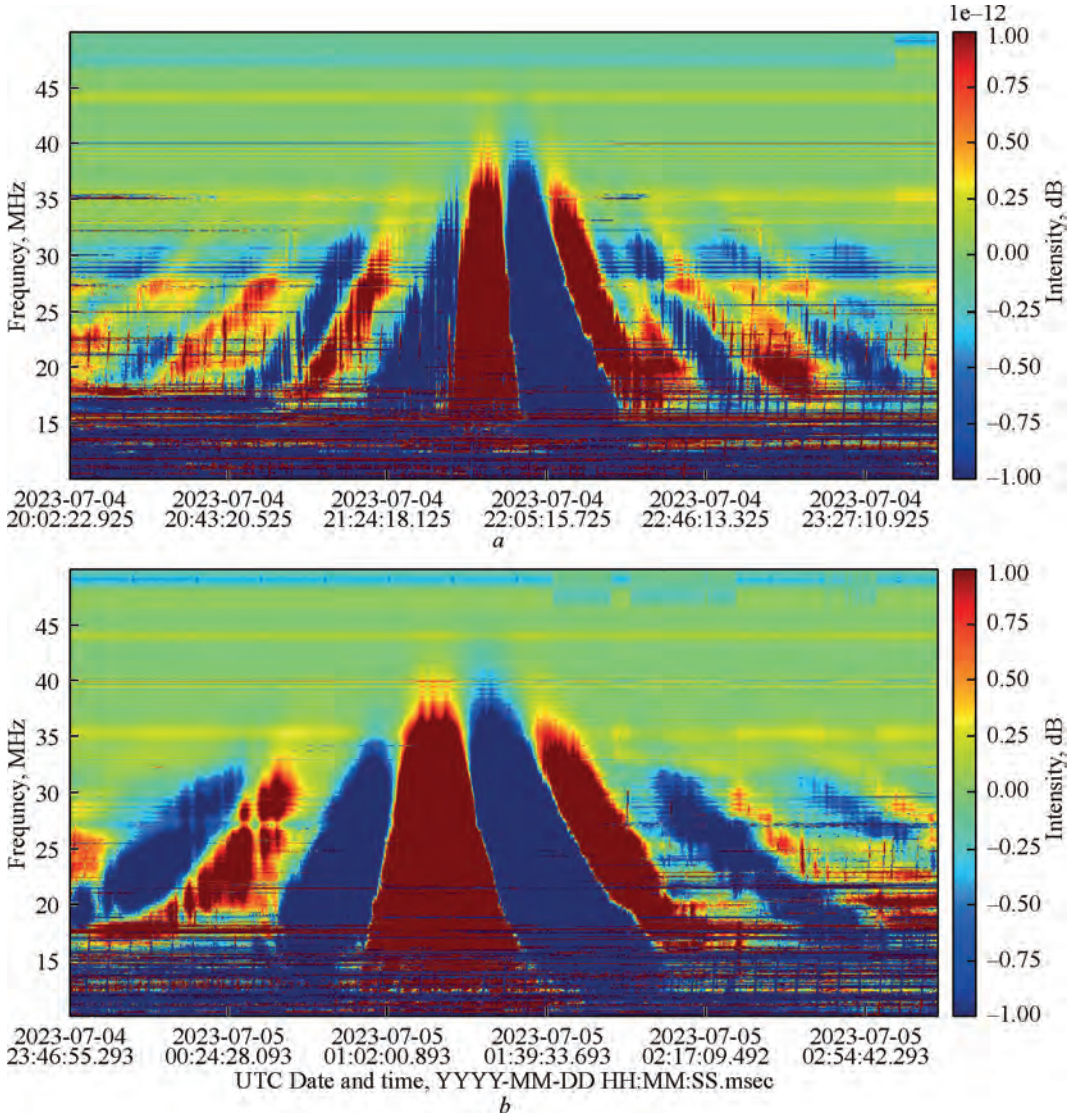

Fig. 5. Dynamic cross-spectra of the interferometric response of Cyg A (a) and Cas A (b) from observations by two URAN-2 subarrays on July 4-5, 2023

(grant agreement No. 871149). The FIELDS experiment on the Parker Solar Probe spacecraft was designed and developed under NASA contract NNN06AA01C. PSP/FIELDS data are publicly available at http://fields.ssl.berkeley.edu/data/. The data were obtained using the NenuFAR radio-telescope. The development of NenuFAR has been supported by personnel and funding from: Station de Radioastronomie de Nançay, CNRS-INSU, Observatoire de Paris-PSL, Université d'Orléans, Observatoire des Sciences de l'Univers en région Centre, Région Centre-Val de Loire, DIM-ACAV and DIM-ACAV+ of Région Ile de France, Agence Nationale de la Recherche.

REFERENCES

1. Konovalenko O.O., Zakharenko V.V., Lytvynenko L.M., Ulyanov O.M., Sidorchuk M.A., Stepkin S.V., Shepelev V.A., Zarka P., Rucker H.O., Lecacheux A., Panchenko M., Bruck Yu.M., Tokarsky P.L., Bubnov I.M., Yerin S.M., Koliadin V.L., Melnik V.M., Kalinichenko M.M., Stanislavsky O., Dorovskyy V.V., Khristenko O.D., Shevchenko V.V., Belov O.S., Gridin A.O., Antonov O.V., Bovkun V. P., Reznichenko O.M., Bortsov V.M., Kvasov G.V., Ostapchenko L.M., Shevchuk M.V., Shevchenko V.A., Yatskiv Ya.S., Vavilova I.B., Braude I.S., Shkuratov Y.G., Ryabov V.B., Pidgorny G.I., Tymoshevsky A.G., Lytvynenko O.O., Galanin V.V., Ryabov M.I., Brazhenko A.I., Vashchishin R.V., Frantsuzenko A.V., Koshovyy V.V., Ivantyshyn O.L., Lozinsky A.B., Kharchenko B.S., Vasylieva I.Y., Kravtsov I.P., Vasylkivsky Y.V., Litvinenko G.V., Mukha D.V., Vasylenko N.V., Shevtsova A.I., Miroshnichenko A.P., Kuhai N.V., Sobolev Ya.M., Tsvyk N.O. The founder of the decameter radio astronomy in Ukraine Academician of NAS of Ukraine Semen Yakovych Braude is 110 years old: history of creation and development of the national experimental base for the last half century. *Radio Physics and Radio Astronomy*. 2021. Vol. 26, No. 1. P. 005—073. https://doi.org/10.15407/rpra26.01.005

2. Bubnov I.N., Konovalenko A.A., Tokarsky P.L., Korolev A.M., Yerin S. N., Stanislavsky L.A. Creation and approval of low-frequency radioastronomic antennas for the research of Universe objects on the far-side of the Moon. *Radio Physics and Radio Astronomy*. 2021. Vol. 26, No. 3. P. 197—210. https://doi.org/10.15407/rpra26.03.197

3. Tokarsky P. Parameters of a short dipole antenna placed over a two-layer lunar soil. *Journal of Astronomical Instrumentation*. 2023. Vol. 12, Iss. 2, id. 2350001. https://doi.org/10.1142/S2251171723500010

4. Tokarsky P. Power Parameters of a Dipole Antenna Placed over a Two-Layer Dielectric Medium. *2022 IEEE 2nd Ukrainian Microwave Week (UkrMW)*, Kharkiv, Ukraine, November 14—18. P. 269—272. https://doi.org/10.1109/UkrMW58013.2022.10036958

5. Yerin S., Konovalenko A., Tokarsky P., Bubnov I., Zakharenko V., Ulyanov O., Kvasov G., Dorovskyy V., Melnik V., Kalinichenko M., Stanislavsky A., Shevchuk M., Shevtsova A., Kharlanova V., Vasylkivskyi Y., Kravtsov I., Reznichenko A., Bortsov V., Lisachenko V., Sydorchuk M., Stepkin S., Shepelev V., Khristenko A., Belov A., Myasoyed A., Mukha D., Zarka P., Rucker H., Panchenko M., Denis L., Coffre A., Charier D., Girard J. Phased subarray of the low-frequency radio telescope GURT as a standalone instrument for radio astronomy studies. *2020 IEEE Ukrainian Microwave Week (UkrMW)*, Kharkiv, Ukraine, September 21—25. P. 130—134. https://doi.org/10.1109/UkrMW49653.2020.9252788

6. Tokarsky P., Konovalenko A., Kalinichenko M., Yerin S. Impact of Ground Parameters on Performances of an Active Phased Array Element of the Low-Frequency Radio Telescope GURT. *Journal of Astronomical Instrumentation*. 2020. Vol. 9, Iss. 4, id. 2050015. https://doi.org/10.1142/s2251171720500154

7. Zarka P., Denis L., Tagger M., Girard J., Coffre A., Dumez-Viou C., Taffoureau C., Charrier D., Bondonneau L., Briand C., Casoli F., Cecconi B., Cognard I., Corbel S., Dallier R., Ferrari C., Grießmeier J.-M., Loh A., Martin L., Pommier M., Semelin B., Tasse C., Theureau G., Tremou E., Hellbourg G., Konovalenko A., Koopmans L., Tokarsky P., Ulyanov O., Vermeulen R., Zakharenko V., and other members of the NenuFAR-France team. The low-frequency radio telescope NenuFAR. *URSI GASS 2020*, Rome, Italy, 29 August — 5 September 2020, J01—02. https://tinyurl.com/ycocd5ly

8. Tokarsky P. Antenna Analytical Representation by a Two-Port Network. *International Journal of Antennas and Propagation*. 2020. Vol. 2020, Article ID 2609747. https://doi.org/10.1155/2020/2609747

9. Bilous A.V., Grießmeier J.M., Pennucci T., Wu Z., Bondonneau L., Kondratiev V., van Leeuwen J., Maan Y., Connor L., Oostrum L.C., Petroff E., Verbiest J.P.W., Vohl D., McKee J.W., Shaifullah G., Theureau G., Ulyanov O.M., Cecconi B., Coolen A.H., Corbel S., Damstra S., Dénes H., Girard J.N., Hut B., Ivashina M., Konovalenko O.O., Kutkin A., Loose G.M., Mulder H., Ruiter M., Smits R., Tokarsky P.L., Vermaas1 N.J., Zakharenko V.V., Zarka P., Ziemke J. Dual-frequency single-pulse study of PSR B0950 + 08. *Astronomy & Astrophysics*. 2022. Vol. 658, A143. https://doi.org/10.1051/0004-6361/202142242

10. Stanislavsky L.A., Bubnov I.N., Yerin S.N., Zalizovski A.V., Lisachenko V.M. The critical frequency of the ionospheric F2-layer as obtained from ionosonde data and observations of solar radio bursts. *Radio Physics and Radio Astronomy*. 2022. Vol. 27, No. 3. P. 203—212 (2022). https://doi.org/10.15407/rpra27.03.203

11. Stanislavsky A.A., Bubnov I.N., Koval A.A., Stanislavsky L.A., Yerin S.N., Zalizovski A.V., Lisachenko V.M., Konovalenko O.O., Kalinichenko M.M. Validation of F2-layer critical frequency variations in the ionosphere with radio observations of solar bursts. *Journal of Atmospheric and Solar-Terrestrial Physics*. 2023. Vol. 245, id. 106056. https://doi.org/10.1016/j.jastp.2023.106056

12. Stanislavsky L.A., Bubnov I.N., Konovalenko A.A., Tokarsky P.L., Yerin S.N. The first detection of the solar U+III association with an antenna prototype for the future lunar observatory. *Research in Astronomy and Astrophysics*. 2021. Vol. 8, id. 187. https://doi.org/10.1088/1674-4527/21/8/187

13. Bubnov I.N., Stanislavsky L.A., Yerin S.N. Simultaneous observations of solar radio bursts with Ukrainian radiotelescopes and by Parker Solar Probe during its encounter. *Proceedings of 13th Workshop*, Primorsko, Bulgaria, 13—17 September 2021. P. 14—19. https://doi.org/10.31401/WS.2021.proc

14. Stanislavsky A.A., Bubnov I.N., Koval A.A., Yerin S.N. Parker Solar Probe detects solar radio bursts related with a behind-the-limb active region. *Astronomy & Astrophysics*. 2022. Vol. 657, A21. https://doi.org/10.1051/0004-6361/202141984

15. Stanislavsky L.A., Bubnov I.N., Konovalenko A.A., Stanislavsky A.A., Yerin S.N. Free–free absorption parameters of Cassiopeia A from low-frequency interferometric observations. *Astronomy & Astrophysics*. 2023. Vol. 670, A157. https://doi.org/10.1051/0004-6361/202245271

16. Stanislavsky L.A., Bubnov I.N., Stanislavsky A.A., Zarka Ph., Loh A., Viou C., Konovalenko A.A., Brazhenko A.I., Frantsuzenko A.V. Multi-antenna probing of absorbing regions inside and outside Cassiopeia A, *Astronomy & Astrophysics*. 2024. Vol. 683, A7. https://doi.org/https://doi.org/10.1051/0004-6361/202348356

FEATURES OF ACOUSTIC-GRAVITY WAVES IN THE EARTH'S ATMOSPHERE

O. Cheremnykh, A. Fedorenko, D. Vlasov, V. Lashkin, E. Kryuchkov, Yu. Klymenko, I. Zhuk, S. Cheremnykh

Space Research Institute of the NAS of Ukraine and the State Space Agency of Ukraine

The results of the research of acoustic-gravity waves (AGWs) in the Earth's atmosphere, obtained by the researchers of the Space Research Institute of NAS of Ukraine and SSA of Ukraine during 2021—2023 years, are presented. The work was carried out mainly in the following directions: 1) development of theoretical models of AGW taking into account the properties of the real atmosphere, including vertical non-isothermality, effects of dissipation as well as atmospheric rotation; 2) search and study of new types of wave disturbances in the atmosphere; 3) data analysis of satellite measurements of wave atmospheric disturbances; 4) verification of theoretical models based on measurements from space vehicles.

Among different types of wave disturbances, that can occur in the Earth's atmosphere under the influence of various energy sources, the acoustic-gravity waves are of particular interest. This interest is due to the important contribution that these waves occur to the dynamics and energetics of planetary atmospheres, providing an effective redistribution of the energy of local disturbances on a global scale. The waves of this type can be generated by various natural and anthropogenic sources located at different heights of the atmosphere. AGWs are associated with influences "from above" if their sources are in the upper atmosphere. For example, it can be precipitation of charged particles in high latitudes, ionospheric currents, motion of the solar terminator [1—3]. Influences on the atmosphere and ionosphere "from below" are realized by using AGW caused by a surface or lithospheric sources [4, 5].

The linear theory of AGW allows the existence of a continuous spectrum of freely propagating waves in the atmosphere, consisting of acoustic and gravitational regions, as well as horizontally propagating evanescent wave modes [6, 7]. The evanescent waves can be generated in those regions of the atmosphere where there are significant vertical temperature gradients [7].

Seasonal features of global distribution of acoustic-gravity waves in the Earth's thermosphere

According to data of satellite measurements, the spatial distribution of AGW in the Earth's thermosphere was studied in [8]. It was found that large-amplitude AGWs in the polar regions of both Earth's hemispheres are systematically observed. Based on the analysis of the measurements on the Dynamics Explorer 2 satellite, a connection between the spatial distribution of AGWs and the auroral oval was revealed. Seasonal regularities of the distribution of the wave field over the Antarctic and the Arctic have been established on the basis of a lot of experimental data. It was shown that during the night in the summer months, the extent of the disturbed areas was significantly greater than in the winter. In particular, at night over the Antarctic in December-February and over the Arctic in June-August, the disturbed AGW region can extend even to low geomagnetic latitudes [8]. In the winter months, the activity of polar AGWs is mainly limited to the high geomagnetic latitudes. In spring and autumn, the localization of wave activity boundaries becomes more unclear in geomagnetic latitude. A comparative analysis of the features of AGW in the polar thermosphere of both hemispheres was carried out for polar day and polar night conditions in [8].

The features of the spatial distribution of AGW for the southern and the northern hemispheres of the Earth are presented in Fig. 1 for different seasons and levels of geomagnetic activity. In geomagnetic coordinates (invariant latitude and magnetic local time), the boundaries are shown when the amplitude of polar AGWs is approximately equal to the background level. These borders show a pronounced spatial connection with the auroral oval in the daytime sector, actually filling the oval from the inside. However, in the night sector, the area of increased wave activity can extend even to 10—20° geomagnetic latitude. Seasonal features of the distribution of AGW for the northern hemisphere are shown in Fig. 2. It can be seen, that if the polar cap is illuminated by the Sun, the wave activity can extend far beyond the auroral oval, sometimes reaching low geomagnetic latitudes.

The southern hemisphere is characterized by a pattern of distribution of wave activity that is generally symmetrical to the northern hemisphere, but there are some peculiarities [8]. The obtained results regarding the spatial distribution of AGW indicate the connection of these waves with wind circulation in the polar thermosphere. It has been suggested that the observed seasonal features of the AGW distribution are related precisely to rearrangement of the polar wind circulation when the Sun's illumination changes.

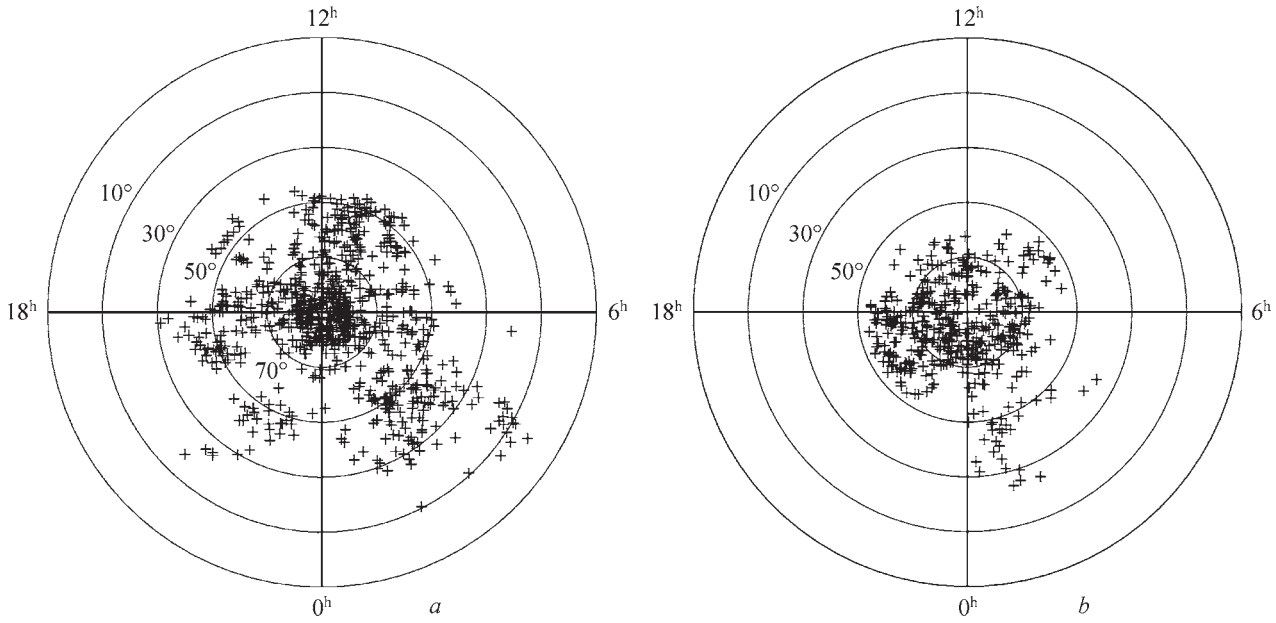

Fig. 1. Distribution of activity of polar AGWs for northern (a) and southern (b) hemispheres in geomagnetic coordinates [8]

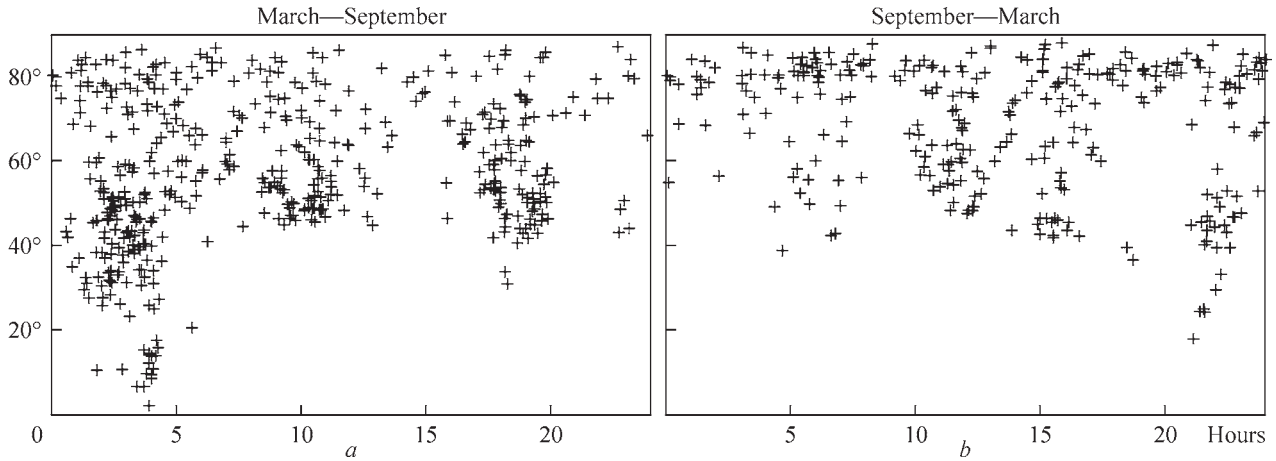

Fig. 2. Distribution of AGW in polar regions depending on conditions of illumination by the Sun in northern hemisphere: *a* — spring-summer-autumn; *b* — autumn-winter-spring [8]

Evanescent wave modes in isothermal atmosphere

Unlike freely propagating AGWs, evanescent waves propagate only horizontally [9—11]. In the vertical direction, the energy density of such waves should decrease up and down from the propagation level. In the Sun's atmosphere, favorable conditions for the realization of evanescent modes occur at the boundary between the photosphere and the convective zone, as well as between the chromosphere and the corona [9, 11]. The most famous evanescent waves are the horizontal Lamb wave and the vertical Brunt — Väisälä oscillations [10]. In hydrodynamics and the physics of the atmosphere and the Sun, the *f*-mode is also well known [10]. Experimental observations of the *f*-mode on the Sun are used to diagnose the peculiarities of the structure and the dynamics of the Sun [11]. In the Earth's atmosphere, the evanescent waves are observed near the mesopause heights [12].

The new types of the evanescent modes (γ-mode and the family of previously known pseudo-modes) were discovered in the frames of our research. It is shown that each evanescent mode can be matched with a pseudo-mode, which coincides with the direct mode in terms of dispersion, but differs in polarization and amplitude dependence on the height [13]. The discovery of the γ-mode made it possible to combine the known evanescent acoustic-gravity modes into a system of the main evanescent modes of the isothermal atmosphere. The location of the dispersion curves of the main evanescent modes of the atmosphere on the frequency-horizontal wave vector $\omega(k_x)$ spectral plane is shown in Fig. 3 [10, 13]. The shaded

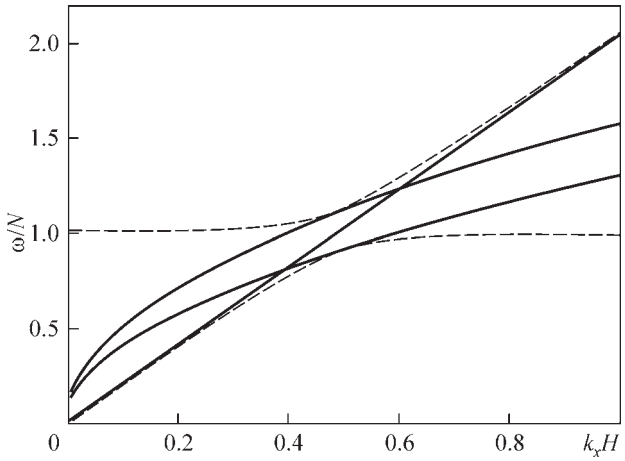

Fig. 3. Dispersion dependences of main evanescent wave modes of isothermal atmosphere: $\omega = \sqrt{k_x g}$ and $\omega = \sqrt{k_x g(\gamma - 1)}$ (upper and lower solid curves, respectively), $\omega = N$ (horizontal line), $\omega = k_x c_s$ (sloping line) [10, 13]. Here H is atmosphere scale height, N is Brunt — Väisälä frequency (BV) and c_s is speed of sound

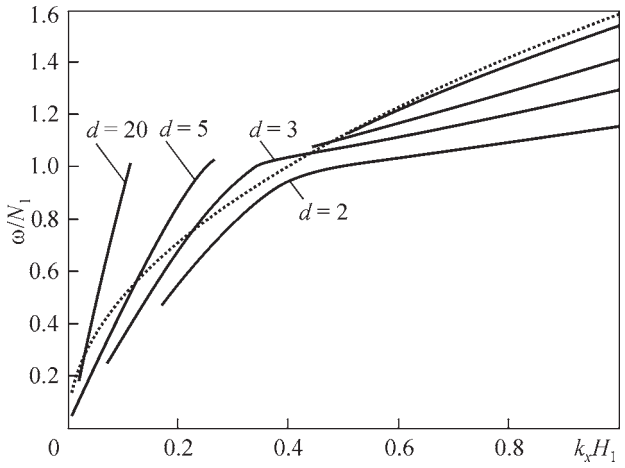

Fig. 4. Dispersion dependences $\omega(k_x)$ for waves at boundary of two isothermal media at different values of parameter $d = T_2/T_1$. Here, H_1 and N_1 are atmosphere scale height and BV frequency in lower half-space with temperature T_1

curves indicate the gravitational and the acoustic regions of freely propagating AGWs. The dispersion dependence $\omega^2 = k_x g(\gamma - 1)$, which corresponds to γ- and γ_p-modes, closes with the gravitational region of freely propagating AGWs at the same value $k_x = 1/2H$ (H is the atmosphere scale height), at which the curve $\omega^2 = k_x g$ (dispersion of f- and f_p-modes) closes with the acoustic region (Fig. 3).

Waves at the boundary of two isothermal media

The peculiarities of the propagation of evanescent acoustic-gravity waves at the boundary of two isothermal half-spaces with different temperatures have been studied in [14]. In the model of an infinite isothermal atmosphere, it is not possible to ensure simultaneous upward and downward energy decay for horizontally propagating waves from the level of propagation. The simplest model of the atmosphere, where such a condition can be fulfilled, is two isothermal half-spaces with different temperatures. Taking into account the boundary conditions simultaneously with the condition of decreasing wave energy density up and down from the interface of the media leads to the dispersion dependences shown in Fig. 4. Here T_1 and T_2 is the temperature in the lower and upper half-space, respectively. A notable feature of the dispersion curves in Fig. 4 are cut-offs, the location of which coincides with the boundaries of the regions of free propagation of waves on the spectral plane $\omega(k_x)$. The reason for these cut-offs is due to the fact that the temperatures of the media are different in the lower and upper half-spaces, and, therefore, the evanescent regions in the two half-spaces do not coincide. The waves at the boundary exist only in the region of overlap of these two evanescent regions, so the spectral diagram shows cut-offs of the dispersion curves.

At large values of the parameter $d = T_2/T_1$ and at $k_x H_1 > 0.5$, the dispersion dependence is approached to the pure f-mode dispersion $\omega^2 = k_x g$ (thin solid curve). At large d and small k_x values, the dispersion dependences $\omega(k_x)$ are close to the linear, which is the characteristic of acoustic type waves. When $d > 4$, the spectrum of the evanescent waves at the boundary of the medium splits into two branches, separated by the discontinuity region. In the discontinuity region, the waves satisfy the boundary condition, but they cannot simultaneously decrease in energy up and down [14].

Continuous spectrum of evanescent acoustic-gravity waves in atmosphere

A new mathematical method has been developed in [15] for the study of evanescent acoustic-gravity waves in the atmosphere of the Earth and the Sun. Using this method, it is shown that the spectrum of evanescent AGWs in an isothermal atmosphere consists of infinite number of modes that fill the entire area, forbidden for free propagation of waves on the frequency-horizontal wave vector diagnostic diagram. These solutions were found by imposing the additional spatial relationship on the components of the perturbed velocity vector of the elementary volume of the medium. Based on the analysis of the system of the hydrodynamic equations, it is shown that it is appropriate to use characteristic parameter α to describe the evanescent spectrum [15]. At different fixed real values of parameter α, "forbidden" for free propagation, the region is filled with curves, is shown in Fig. 5.

Evanescent wave modes in non-isothermal atmosphere

The possibility of the existence of evanescent modes in a non-isothermal atmosphere with a continuous altitudinal temperature profile was investigated in [16]. It is shown that two evanescent wave modes can be realized in a non-isothermal atmosphere: the f-mode with a dispersion that coincides with the isothermal case, and the γ-mode with

a dispersion, modified by the height dependence of the temperature. The condition of the simultaneous decrease of the energy density in the upward and the downward direction is fulfilled for the *f*-mode at the heights of local temperature minima. At the same time, the characteristic wavelength of the *f*-mode is $\lambda_x = 4\pi H_0$, where H_0 is the atmosphere scale height in the minimum temperature. These disturbances can be observed, for example, at the heights of the Earth's mesopause with characteristic lengths $\lambda_x \approx 75$ km and period $T_f \approx 235$ c. A similar energetic condition for the existence of γ-modes is satisfied at the heights of local temperature maxima. Accordingly, altitude intervals favorable for the existence of these modes can be identified in the atmosphere, as shown in Fig. 6.

Acoustic-gravity waves in quasi-isothermal atmosphere with random vertical temperature profile

In the real atmosphere, the temperature profile is very complex and time-varying function of the vertical coordinate and, generally speaking, cannot be reduced to any deterministic form. In addition, the altitudinal temperature profile significantly depends on latitude, time of day, solar and geomagnetic activity, etc. Nevertheless, above ~200 km, the atmosphere can be considered quasi-isothermal, and the model of a quasi-isothermal atmosphere can be used to describe the wave disturbances.

We focused on the study of AGW within the framework of a model of a quasi-isothermal atmosphere with a noise disturbance of the vertical temperature profile. A stochastic equation in the Bourret approximation was obtained to describe the AGW. It was shown that in this equation, the poles of the average Green's function determine the generalized dispersion relation of the AGW. Two separate cases are considered: random inhomogeneities in the form of white noise (δ-correlated in space) and the opposite case of a δ-like noise spectrum. For both cases, the instability of acoustic-gravity waves was detected and the corresponding increments of instability were determined [17].

Propagation of AGW in spatially inhomogeneous atmospheric flows

The presence of spatially inhomogeneous wind flows in an atmosphere leads to modification of AGW properties. As a result of the interaction of waves with non-homogeneous flows, it is possible to change their spectrum, the appearance of prevailing propagation azimuths, selective amplification or attenuation of the amplitudes of various spectral harmonics. In [18, 19], we investigated the features of the propagation of AGW in a spatially inhomogeneous wind flow under the assumption that flow speed slowly changes in the horizontal direction. The system of hydrodynamic equations was used for the analysis, which takes into account the wind flow with horizontal spatial heterogeneity. The analytical expression was obtained that describes the changes in the amplitude of waves in a

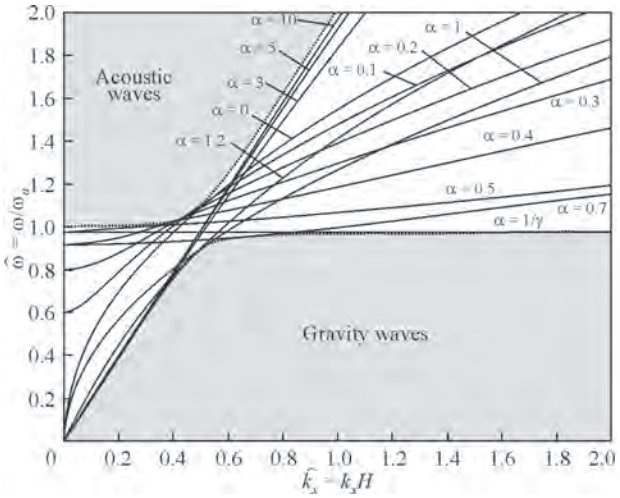

Fig. 5. Dispersion dependences of evanescent waves at different values of parameter α > 0 [15]. Here $\hat{k}_x = k_x H$, $\hat{\omega} = \omega/\omega_a$, where ω_a is acoustic cutoff frequency

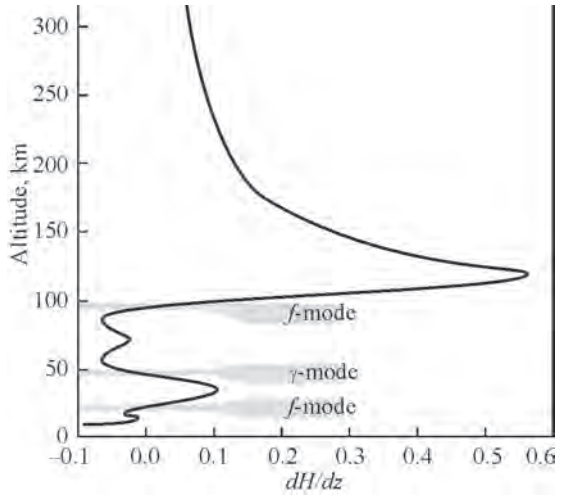

Fig. 6. Altitude dependence *dH / dz* and hypothetical areas of existence of *f*- and γ-modes at heights of local extremes of temperature (*dH / dz* = 0) in Earth's atmosphere [16]

medium moving at a non-uniform speed. The amplitude change in the accompanying and headwind is shown in Figs. 7, *a*, 7, *b* for three values of fixed frequencies and the initial value of the wavelength λ_{xo}. The initial wavelengths are chosen as follows: for a fair wind λ_{xo} = 230 km (increases with increasing wind speed), for a headwind λ_{xo} = 1500 km (decreases with increasing wind speed). It can be seen that the dependence of the amplitude on the speed of the oncoming wind is weakly dependent on the initial frequency (Fig. 7, *a*). In the accompanying wind, which is increasing in magnitude, the AGW rapidly fades (Fig. 7, *b*).

Analysis of measurements on the Dynamics Explorer 2 satellite indicates a close connection between atmospheric wave disturbances in the polar thermosphere and the wind circulation. According to satellite data, large-amplitude

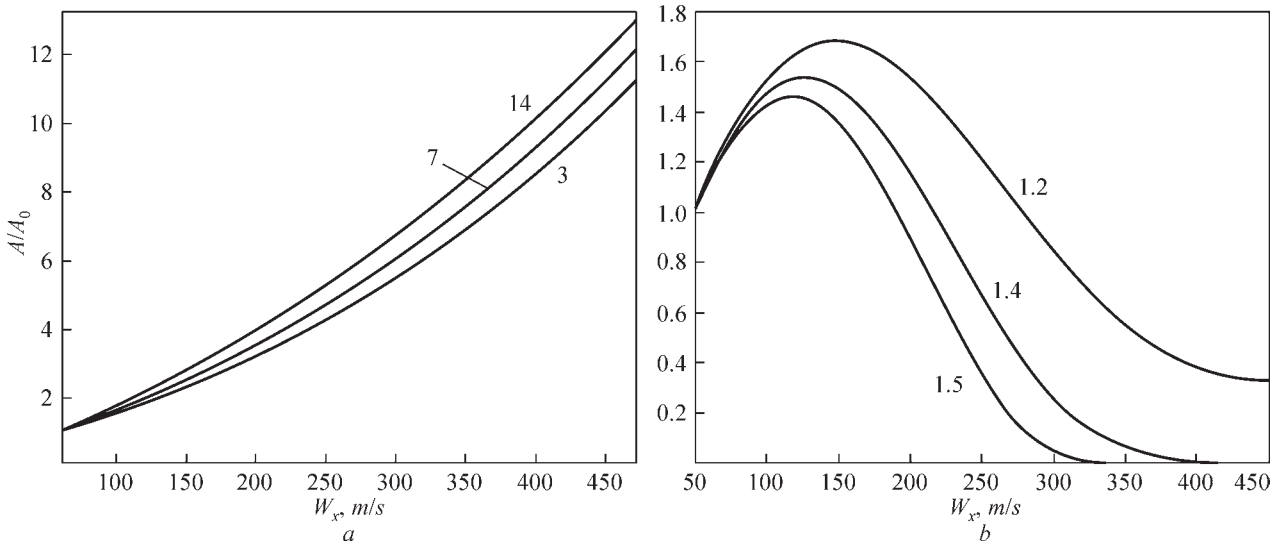

Fig. 7. Dependence of AGW amplitude on wind speed: *a* — headwind (from top to bottom N/ω_0 = 14, 7, 3 at λ_{xo} = 1500 km); *b* — fair wind (from top to bottom N/ω_0 = 1.2, 1.4, 1.5 at λ_{xo} = 230 km). Amplitude is normalized to amplitude A_0 of background level of AGW, which corresponds to background wind W_{xo} ≈50 m/s

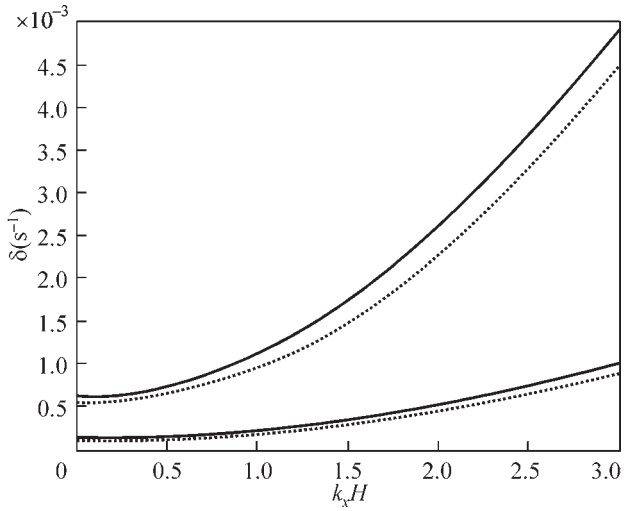

Fig. 8. Decrement of attenuation of gravitational (solid curves) and acoustic branches of AGW (dotted curves): $\nu = 2 \cdot 10^5$ m^2/s (lower curves) and $\nu = 1 \cdot 10^6$ m^2/s (upper curves), $k_zH = 1$ [21]

acoustic-gravity waves are systematically observed in the regions of powerful wind systems [18, 19]. The theoretical results obtained allow us to explain the peculiarities of the formation of the wave field in the polar thermosphere as a result of wind filtering of the spectrum of primary waves generated by various sources.

Dissipation of AGW due to atmospheric viscosity and thermal conductivity

For an analysis of AGW in the atmosphere with dissipation, the system of hydrodynamic equations is usually adjusted with components that take into account viscosity and thermal conductivity [20]. Unlike previous works, when considering the dissipation of AGW in the atmosphere, we took into account new components in the Navier-Stokes and the heat transfer equations. These components describe the transfer of momentum and energy by waves due to the background density gradient, in addition to the usually considered velocity gradient [21]. From the modified system of equations, the local dispersion equation of AGW in the atmosphere with attenuation is obtained. Since the coefficient of kinematic viscosity ν in the atmosphere changes with height, this dispersion equation is valid in the local approximation within thin layers, where the value of ν can be approximately considered constant. An expression for the decrement of wave attenuation δ is obtained. The value of δ for the acoustic and gravitational branches of the AGW at $k_zH = 1$ (k_z is the vertical component of the wave vector) and two characteristic values of the viscosity coefficient $\nu = 2 \cdot 10^5$ m^2/s and $\nu = 1 \cdot 10^6$ m^2/s in the thermosphere are shown in Fig. 8. The value of δ increases as expected with an increase in the viscosity coefficient and decreases in the horizontal wavelength.

Evanescent acoustic-gravity waves in the atmosphere taking into account effect of Earth's rotation

he influence of the Earth's rotation on the spectrum of evanescent wave modes becomes notable in the range of low frequencies comparable with the rotation frequency. The general analysis of the dispersive properties of waves in a rotating atmosphere is rather complicated. It is known that the dependence of the vertical component of the Earth's rotation frequency on the horizontal coordinate determines the existence of Rossby waves [23]. In [24], we considered the influence of atmospheric rotation on the spectrum of AGW in high-latitude regions, where only the vertical component of the Earth's rotation frequency can be taken into account. The waves with a length small compared to the Earth's radius were studied. For the analysis, the well-known equations of the dynamics of an ideal gas were used, which are written in a coordinate

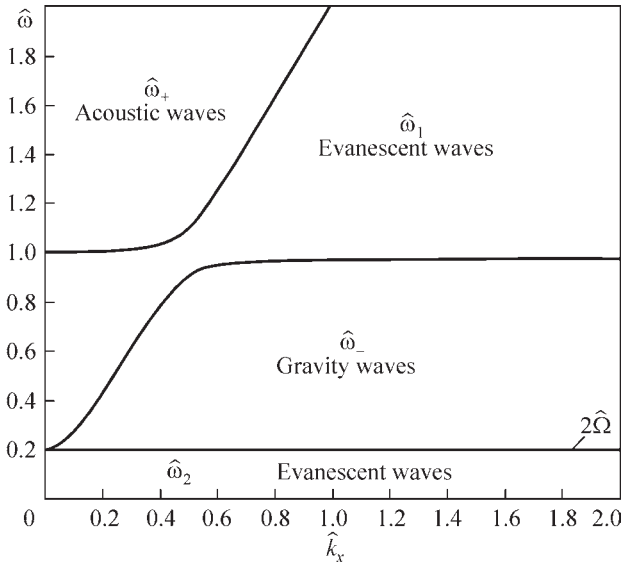

Fig. 9. Spectral diagram of AGW with consideration of Earth's rotation for high-latitude regions of atmosphere [24]. Here $\hat{k}_x = k_x H \quad \hat{\omega} = \omega / N$

system that rotates together with the Earth's atmosphere with constant angular velocity.

The obtained results are conveniently explained using the diagnostic diagram shown in Fig. 9 [24]. The spectrum of acoustic-gravity waves presented in this figure consists of acoustic and gravitational regions, as well as two regions of evanescent waves with a continuous spectrum. One region of evanescent waves (with frequencies $\hat{\omega}_1$), studied in [15], is located between the regions of freely propagating acoustic and gravitational waves and contains a continuous set of frequencies above the frequency 2Ω (Coriolis parameter). The second region of evanescent waves (with frequencies $\hat{\omega}_2$) is realized due to the rotation of the Earth's atmosphere and was discovered for the first time in [24]. This region lies below the frequency 2Ω, which at all wavelengths is the lower limit of the region of gravitational waves. It is shown that the obtained solutions for certain values of the parameter α [15] pass into the known evanescent modes.

Conclusions

The main results of studies of acoustic-gravity waves in the upper atmosphere of the Earth, obtained during 2021—2023, are presented. Seasonal patterns of the global distribution of acoustic-gravity waves in the upper atmosphere according to satellite measurements have been in [8] established. The possibility of realizing evanescent wave modes at the boundary of two isothermal media with different temperatures is considered [14]. The new method of studying the continuous evanescent spectrum of acoustic-gravity waves in the Earth's atmosphere has been developed [15]. Evanescent acoustic-gravity modes in a non-isothermal atmosphere with a continuous altitudinal temperature profile are considered [16]. Increments of instability of acoustic-gravity waves in a quasi-isothermal atmosphere with a random vertical temperature profile are found in [17]. The peculiarities of the interaction of acoustic-gravity waves with spatially heterogeneous atmospheric flows have been studied [18, 19]. The effect of acoustic-gravity wave attenuation in the atmosphere was studied on the basis of the modified Navier-Stokes and the heat transfer equations [21]. It was shown that the rotation of the atmosphere leads to a modification of the continuous spectrum of evanescent AGWs with frequencies greater than the Coriolis parameter [24].

REFERENCES

1. Bespalova A.V., Fedorenko A.K., Cheremnykh O.K., Zhuk I.T. Satellite observations of wave disturbances caused by moving solar terminator. *J. Atmos. Solar*. Terr. Phys. 2016. V. 140. P. 79—85. https://doi.org/10.1016/j.jastp.2016.02.012.

2. Hajkovicz L.A. Auroral electrojet effect on the global occurrence pattern of large scale travelling ionospheric disturbances. *Planet. Space. Sci.* 1991. V. 39. P. 1189—1196.

3. Somsikov V.M. Solar terminator and dynamics of the atmosphere, Nauka, Alma-Ata, 1983.

4. Rapoport Yu.G., Gotynyan O.E., Ivchenko V.M., Kozak L.V., Parrot M. Effect of acoustic-gravity wave of the lithospheric origin on the ionospheric F region before earthquakes. *Phys. and Chem. Earth*. 2004. V. 29. P. 607—616.

5. Sauli P., Boska J. Tropospheric events and possible related gravity wave activity effects on the ionosphere. *J. Atmos. Solar. Terr. Phys.* 2001. 63, No. 9. P. 945—950. https://doi.org/10.1016/S1364-6826(00)00205-4.

6. Cheremnykh O.K., Fedorenko A.K., Kryuchkov E.I., Selivanov Y.A. Evanescent acoustic-gravity modes in the isothermal atmosphere: systematization, applications to the Earth's and Solar atmospheres. *Ann. Geophys.* 2019. V. 37. P. 405—415. https://doi.org/10.5194/angeo-37-405-2019.

7. Waltercheid R.L., Hecht J.H. A reexamination of evanescent acoustic-gravity waves: Special properties and aeronomical significance. *J. Geophys. Res.* 2005. 108 (D11). 4340. https://doi.org/10.1029/2002JD002421.

8. Vlasov D.I., Fedorenko A.K., Kryuchkov E.I., Cheremnykh O.K., Zhuk I.T. Seasonal Features of the Spatial Distribution of Atmospheric Gravity Waves in the Earth's Polar Thermosphere. *Kinematics and Physics of Celestial Bodies.* 2022. V. 38, N. 2. P. 73—82. https://doi.org/10.3103/ S0884591322020076.

9. Cheremnykh O.K., Fedorenko A.K., Kryuchkov E.I., Selivanov Y. A. Evanescent acoustic-gravity modes in the isothermal atmosphere: systematization, applications to the Earth's and Solar atmospheres. Ann. Geophys. 2019. 37. P. 405—415. https://doi.org/10.5194/angeo-37-405-2019

10. Waltercheid R.L., Hecht J.H. A reexamination of evanescent acoustic-gravity waves: Special properties and aeronomical significance. *J. Geophys. Res.* 2005. 108 (D11). 4340. https://doi.org/10.1029/2002JD002421

11. Rosental C.S., Gough D.O. The Solar f-mode as interfacial mode at the chromosphere-corona transition. *The Astrophysical Journal.* 1994. V. 423. P. 488—495. https://doi.org/10.1086//173826

12. Simkhada D.B., Snively J.B., Taylor M.J., Franke S.J. Analysis and modeling of ducted and avanescent gravity waves observed in the Havaiian airglow. *Ann. Geophys*. 2009. V. 27. P. 3213—3224.

13. Fedorenko A.K., Klymenko Yu.O., Cheremnykh O.K., Kryuchkov E.I., Zhuk I.T. Specific acoustic-gravity wave modes in isothermal atmosphere. *Space Sci. and Technol.* 2023. V. 29 (2). P. 45—53. https://doi.org/ 0.15407/knit2023.02.045

14. Fedorenko A.K., Kryuchkov E.I., Cheremnykh O.K., Melnychuk S.V., Zhuk I.T. Properties of acoustic-gravity waves at the boundary of two isothermal media. *Kinematics and Physics of Celestial Bodies*. 2022. V. 38 (6). P. 340—350. https://doi.org/10.3103/S0884591322060022

15. Cheremnykh O.K., Fedorenko A.K., Selivanov Y.A., Cheremnykh S.O. Continuous spectrum of evanescent acoustic-gravity waves in an isothermal atmosphere. *Mon. Notic. Roy. Astron. Soc.* 2021. V. 503. P. 5545—5553. https://doi.org/10.1093/mnras/st.ab845

16. Cheremnykh O.K., Fedorenko A.K., Vlasov D.I., Melnychuk S.V. Evanescent acoustic-gravity wave modes in the nonisothermal atmosphere. *Kinematics and Physics of Celestial Bodies*. 2021. V. 37(4). P. 3—17. https://doi.org/10.3103/S0884591321040024.

17. Lashkin V.M., Cheremnykh O.K. Acoustic-gravity waves in quasi-isothermal atmospheres with a random vertical temperature profile. *Wave Motion*. 2023. V. 119, No. 6, 103140.

18. Fedorenko A.K., Kryuchkov E.I., Cheremnykh O.K., Zhuk I.T. Wave disturbances of the atmosphere in a spatially inhomogeneous flow. *Space Sci. and Technol.* 2022. V. 28 (6). P. 25—33. https://doi.org/10.15407/knit2022.06.025.

19. Fedorenko A. K., Kryuchkov E. I., Cheremnykh O. K., Zhuk I. T. Acoustic-Gravity Wave Spectrum Filtering in the Horizontally Inhomogeneous Atmospheric Flow. *Kinematics and Physics of Celestial Bodies.* 2023. V. 39. P. 217—224. https://doi.org/10.3103/S0884591323040049

20. Vadas S.L., Fritts M.J. Thermospheric responses to gravity waves: Influences of increasing viscosity and thermal diffusivity. *J. Geophys. Res.* 2005. 110 (D15103).

21. Fedorenko A.K., Kryuchkov E.I., Cheremnykh O.K., Selivanov Y.A. Dissipation of acoustic-gravity waves in the Earth's thermosphere. *J. Atmos. Terr. Phys.* 2021. V. 212. 105488. https://doi.org/10.1016/ j.jastp.2020.105488

22. Cheremnykh O.K., Fedorenko A.K., Kryuchkov E.I., Vlasov D.I., Zhuk I.T. Attenuation of Evanescent Acoustic-Gravitational Modes in the Earth's Thermosphere. *Kinematics and Physics of Celestial Bodies.* 2021. V. 37. P. 221—229. https://doi.org/10.3103/S0884591321050044

23. Rossby C.-G. Planetary flow patterns in the atmosphere. *Quart. J. Royal Meteorological Society*. 1940. V. 66. P. 68—87.

24. Cheremnykh O., Kaladze T., Selivanov Y., Cheremnykh S. Evanescent acoustic-gravity waves in a rotating stratified atmosphere. *Advances in Space Research.* 2022. V. 69, No. 3. P. 1272—1280. https://doi.org/ 10.1016/j.asr.2021.10.050

STUDY OF ATMOSPHERIC WAVE DISTURBANCES BASED ON NETWORK OF VLF RADIO STATIONS

A. Fedorenko, O. Cheremnykh, A. Voitsekhovska, E. Kryuchkov, Yu. Klymenko, I. Zhuk, S. Cheremnykh

Space Research Institute of the NAS of Ukraine and the State Space Agency of Ukraine

Introduction

The propagation of acoustic-gravity waves (AGWs) in the atmosphere is registered by various experimental methods in the form of quasi-periodic parameter fluctuations with periods ranging from ~5 min up to about a few hours. According to satellite measurements, such wave disturbances are systematically observed in the Earth's upper atmosphere [1—3]. To study the disturbances in the stratosphere and the mesosphere, remote ground methods are mainly used, including the ground network of VLF radio stations. During the reporting period, the researchers of the Space Research Institute have investigated the wave disturbances in the mid-latitudes of the atmosphere based on the measurements of the VLF radio signal amplitudes. This report briefly presents the main results obtained by the authors in this research direction.

The interaction of the VLF radio waves with the ionosphere is mainly determined by electron concentration at the wave reflection level, the height distribution of the electron concentration and the frequency of electron collisions with neutral particles [5]. The reflection of the VLF waves from the upper wall of the Earth-ionosphere waveguide occurs during the daytime at an altitude of ~70—74 km (the D-region of the ionosphere) and at nighttime at altitudes of ~85—90 km (the lower E-region of the ionosphere) [4, 5]. The propagation of the disturbances in the neutral atmosphere at these altitudes leads to the changes in the geometry of the waveguide and in the reflection coefficients of the radio waves. This is accompanied by the corresponding fluctuations of the amplitudes and the phases of VLF radio signals at the reception point. Such fluctuations with the periods of tens of minutes, corresponding to the periods of atmospheric AGWs, are usually clearly visible in measurements at a nighttime, as well as at the solar terminator [6, 7]. Therefore, there is a hypothetical possibility to determine the properties of the atmospheric wave disturbances at the reflection heights by the measuring the characteristics of the VLF radio waves. The worldwide network of VLF radio stations makes it possible to systematically study of the distribution of the wave activity in the lower ionosphere and the mesosphere on a global scale. The importance of such research is also due to the fact that the indicated atmospheric heights are difficult to study for other experimental methods. The data of VLF radio stations measurements can be used to solve a number of scientific problems, in particular, in the study of impacts "from below" on the ionosphere.

Fluctuations of VLF radio wave amplitudes depending on reflection height changes

Two main approaches are traditionally used to the theoretical study of the propagation of VLF radio waves in the Earth-ionosphere waveguide: mode theory [8] and "wave-hop theory" [9, 10]. The mode theory studies the properties of the waveguide along its entire length from the transmitter to the receiver. This method is effectively used to the study of the ionosphere response to the solar X-ray bursts, during which the properties of the waveguide change approximately equally throughout the illuminated region of the ionosphere [11]. When studying AGWs, it is necessary, if possible, to localize disturbances on the path to search a hypothetical connection with possible sources. Therefore, for such the tasks, it is advisable to choose relatively short paths up to ~2000 km, for which the approximation of the geometric optics can be used. In this approximation, the signal amplitude at the reception point is considered as a superposition of a ground wave and several sky waves reflected from the ionosphere (the wave-hop theory) [9, 10].

In the geometrical optics approximation and in the absence of the VLF disturbances, the wave is reflected at some effective height h, which is determined by the equilibrium concentrations of the electrons and the neutral particles. For approximate calculations, the amplitude at the reception point can be considered as an interference of a ground wave with the amplitude A_g and two ionospheric waves with amplitudes A_1 and A_2, which reflected from the ionosphere one and two times, respectively [10]. The propagation of VLF radio waves in the Earth-ionosphere waveguide is schematically shown in Fig. 1. The amplitude of the received signal is determined by adding vectors $\vec{A}_1$, $\vec{A}_2$ and $\vec{A}_g$.

In the approximation of the geometric optics, the expression was obtained that connecting the small relative changes in the amplitudes of the radio waves with the fluctuations in the effective level of their reflection [6]:

$$\Delta A / \bar{A} \approx K \Delta h. \qquad (1)$$

Here, Δh is the vertical displacement in the level reflection of the radio waves, K is the "transmission" coefficient, which depends on the length of the path, the radio signal frequency and the ratio between the

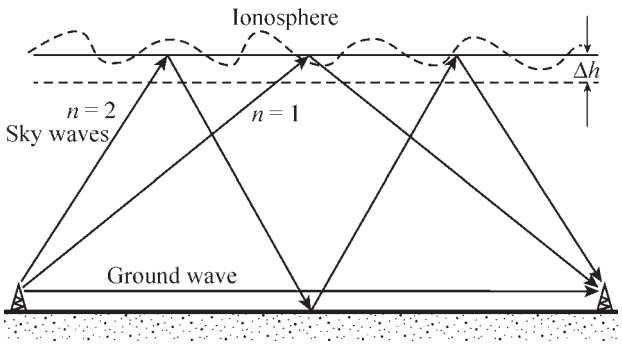

Fig. 1. Schematic representation of VLF radio waves propagation in the Earth-ionosphere waveguide

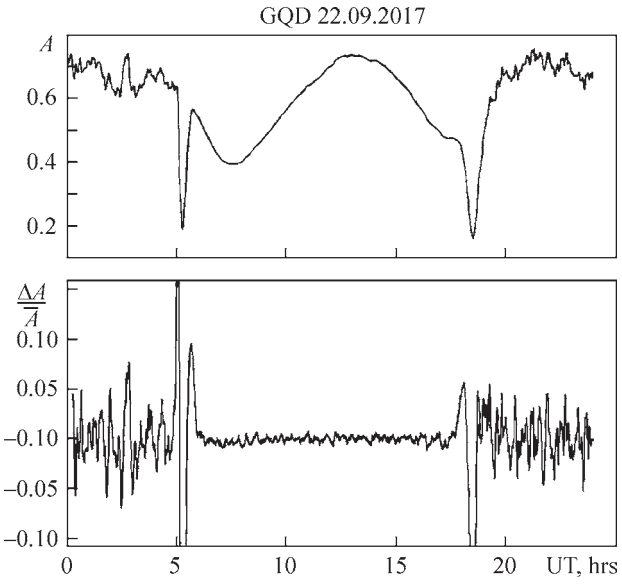

Fig. 2. Diurnal course of amplitude of VLF radio signal on GQD-A118 path: above is amplitude in volts; below is fluctuations of $\Delta A / \bar{A}$. The data was taken from site: https://sidstation.loudet.org/data was used

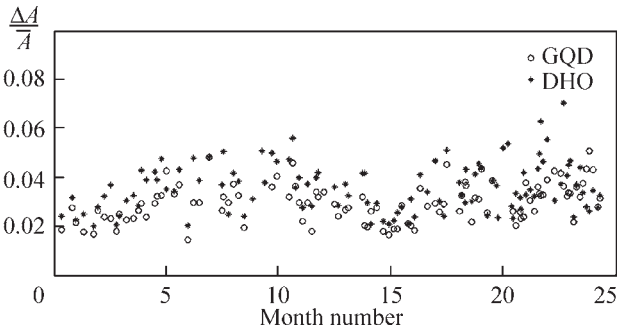

Fig. 3. Fluctuations of amplitudes $\Delta A / \bar{A}$ in evening hours (UT = 20—24^h) on DHO38-A118 path and GQD-A118 path during 2013—2014. Horizontal axis shows number of month starting from January 2013 [6]

amplitudes of the ground and the ionosphere waves. The amplitude of the received radio signal is presented in the form $A = \bar{A} + + \Delta A$, where $\bar{A}$ is the average undisturbed value, and ΔA is the wave disturbance. It is shown, that, when considering AGWs, it is advisable to consider the relative fluctuations of the amplitudes of VLF radio waves $\Delta A / \bar{A}$ [6]. It allows us to exclude a number of factors of a technical nature, for example, the differences in the methods of signal reception on different paths, as well as of a physical nature, in particular, the large-scale amplitude trends.

Diurnal changes in radio signal amplitudes

The fluctuations of the radio wave amplitudes were studied based on the measurements at three mid-latitude VLF stations: in Germany (DHO38, $f = 23.4$ kHz), Great Britain (GQD, $f = 22.1$ kHz) and Italy (ICV, $f = 20.74$ kHz) with a reception point in France (A 118). An example of the daily course of the amplitude of the VLF signal on the GQD-A118 path and of the relative amplitude fluctuations after excluding the daily trend are shown in Fig. 2. The sharp changes in the diurnal course of the amplitude of the radio waves in the morning and in the evening are associated with a change in the height of the wave reflection depending on the sunlight conditions. As can be seen from the figure, the amplitude fluctuations are much larger at night than during the day. However, the observed significant fluctuations in the amplitudes of the radio waves at the night do not necessarily mean large amplitudes of AGWs in the atmosphere. They can be due to the daily course of the function K, which at nighttime has significantly greater values than during the daytime [6]. The establishing a connection between the amplitudes of VLF fluctuations of the radio waves and the amplitudes of the AGWs was one of the main tasks of our research.

Seasonal features of radio wave amplitude fluctuations

The results of the observations of the amplitude fluctuations of the VLF radio signals were summarized for different seasons during 2013—2014 years on two European paths DHO-A118 and GQD-A118 [6]. Magnitudes of $\Delta A / \bar{A}$, averaged over the evening hours (UT = 20—24^h), shown in Fig. 3. For the DHO-A118 path, the relative fluctuations are 2—6%, with average value of ~3.5% and a minimum level of ~2%, which probably reflects a certain background level of AGW amplitudes in the mesosphere. For the GQD-A118 path, the average level of the amplitude fluctuations is slightly lower (~3%), and the minimum level is <2%. As can be seen from Fig. 3, the amplitude fluctuations are observed in different seasons with a tendency to increase the amplitudes in the summer on both paths. The observed excess of the summer values in $\Delta A / \bar{A}$ does not mean that AGW amplitudes are larger in the summer. The reason may be that the effective level of reflection of h in the summer is systematically higher than in the winter. Due to, this value of K and, accordingly, the observed values of $\Delta A / \bar{A}$ will also be larger.

Influence of AGW propagation on height of radio wave reflection

Using the expression (1), the changes in the reflection heights were calculated based on the fluctuations of the radio signal amplitudes on the several paths. Average values of fluctuations $\Delta A / \bar{A}$ and Dh, according to the measurements on three mid-latitude radio-paths during August 4, 2017 — August 6, 2017, are summarized in Table. 1 [6]. It can be seen that $\Delta A / \bar{A}$ at nighttime significantly exceed daytime values, on all considered paths. However, at the same time, the value of Δh are close in magnitude on different paths during the day and at the night. On average, the periodic fluctuations in the height of the radio waves reflection are in the interval $\Delta h \approx 0.2$—0.4 km.

According to the observations of the amplitudes of the VLF radio signals, it was found that the values of Δh are close on different paths. This shows that the value of Δh probably reflects the real fluctuations of the neutral atmosphere. This prompted us to more carefully investigate the possible relationship between the atmospheric concentration fluctuations and the values of Δh. Within the framework of certain simplifying assumptions, the expression was obtained that relates the fluctuations of the neutral atmosphere concentration to the height reflection of radio waves [12]:

$$\frac{\Delta N_n(h)}{N_{n0}(h)} = \frac{\Delta h}{H}\left(1 + \frac{dH}{dz}\right). \quad (2)$$

Here, H is the atmosphere scale height, $N_{n0}(h)$ and $\Delta N_n(h)$ defines the equilibrium concentration of the neutral atmosphere and the change in the concentration due to the AGW propagation at height h. Expression (2) relates the amplitude of AGW (in relative fluctuations of the neutral concentration) with the displacement in the reflection level on average of the radio waves Δh. For the characteristic heights of the radio waves reflection during the daytime (below the mesopause), we have $dH / dz \approx -0.08$. At the nighttime, the reflection of radio waves occurs near the mesopause ($dH / dz \approx 0$) or slightly higher ($dH / dz \approx 0.1$). These values shown in Table 1, here Δh = 200—400 m correspond to the fluctuations $\Delta N_n / N_{n0} \approx 3$—6% in the neutral concentration which is the characteristic of AGWs.

In the AGW theory, the relative fluctuations in the atmosphere concentration are related with vertical displacements of elemental volume of the medium Δz_n [13]:

Table 1

Fluctuations of amplitudes and reflection level of radio waves on three mid-latitude paths during August 4, 2017 — August 6, 2017 [6]

Radio path	Night		Day	
	$\Delta A / \bar{A}$, %	Dh, km	$\Delta A / \bar{A}$, %	Δh, km
GQD-A118	2—3	0.3—0.4	0.4—0.5	0.2—0.3
ICV-A118	5—7	0.2—0.4	1—2	0.2—0.3
DHO-A118	2—4	0.2—0.4	0.5—1	0.15—0.3

$$\frac{\Delta N_n}{N_{n0}} \approx \left(\frac{\gamma - 1}{\gamma} + \frac{dH}{dz}\right)\frac{\Delta z_n}{H}. \quad (3)$$

Therefore, with the help of (2) and (3), it is possible to relate the vertical displacement of the volume of the atmospheric gas in the AGW with value of Δh:

$$\Delta z_n = \frac{\gamma(1 + dH / dz)}{\gamma - 1 + \gamma dH / dz}\Delta h. \quad (4)$$

From formula (4) it follows that at displacements Δh = = 200—400 m of reflection level, we get displacement Δz_n = = 0.7—1.4 km of the neutral atmosphere volume. According to the AGW observations using the EISCAT radar [14], the waves with periods of 30—40 min prevail at the heights of the mesopause, while the vertical velocity amplitudes are ~2.5 m/s. In the assumption of a monochromatic wave, it holds to $V_z = i\,\omega\Delta z$, where V_z is the vertical speed of the particles, and ω is the wave frequency. Then, for the waves observed by the EISCAT radar, the estimates are given Δz_n = 710—950 m, which is in good agreement with the results obtained by using (4).

Expressions (1), (2) and (4) relate the observed changes in the amplitudes of VLF radio waves with the fluctuations in the concentration of the neutral atmosphere. With the help of these equations, the relationship between the fluctuations of the radio signals amplitudes and the neutral density at the reflection heights can be written in the form:

$$\frac{\Delta A}{\bar{A}} = \alpha\frac{\Delta N_n}{N_{0n}}. \quad (5)$$

Here, "transmission" coefficient $\alpha = HK / (1 + dH / dz)$ is determined by atmospheric parameters and function K, which depends on the length of the path and the frequency of the radio waves. Equation (1)—(5) make it possible to determine the properties of AGW at the heights of the mesosphere by observing the amplitudes of VLF radio waves.

Observation of wave disturbances from the solar terminator

The solar terminator is a global source of various types of atmospheric disturbances, including the acoustic-gravity waves [15]. To study the disturbances on the terminator, we used the data from the VLF transmitter of the radio waves at the station in Great Britain (GQD, f = 22.1 kHz) with a reception point in France (A118), which are presented on website: https://sidstation.loudet.org/data. The processing of the data measurements of the amplitudes of VLF radio waves at the terminator is complicated by sharp changes in the amplitude caused by the changes in atmospheric sunlight conditions [6, 16]. During the passage of the solar terminator, a sharp decrease in the signal amplitude is systematically observed in the morning and in the evening (Fig. 2). During automatic data processing using standard methods of the spectral analysis, such amplitude jumps give non-physical spectral harmonics. In this regard, in order to search for atmospheric waves from the terminator,

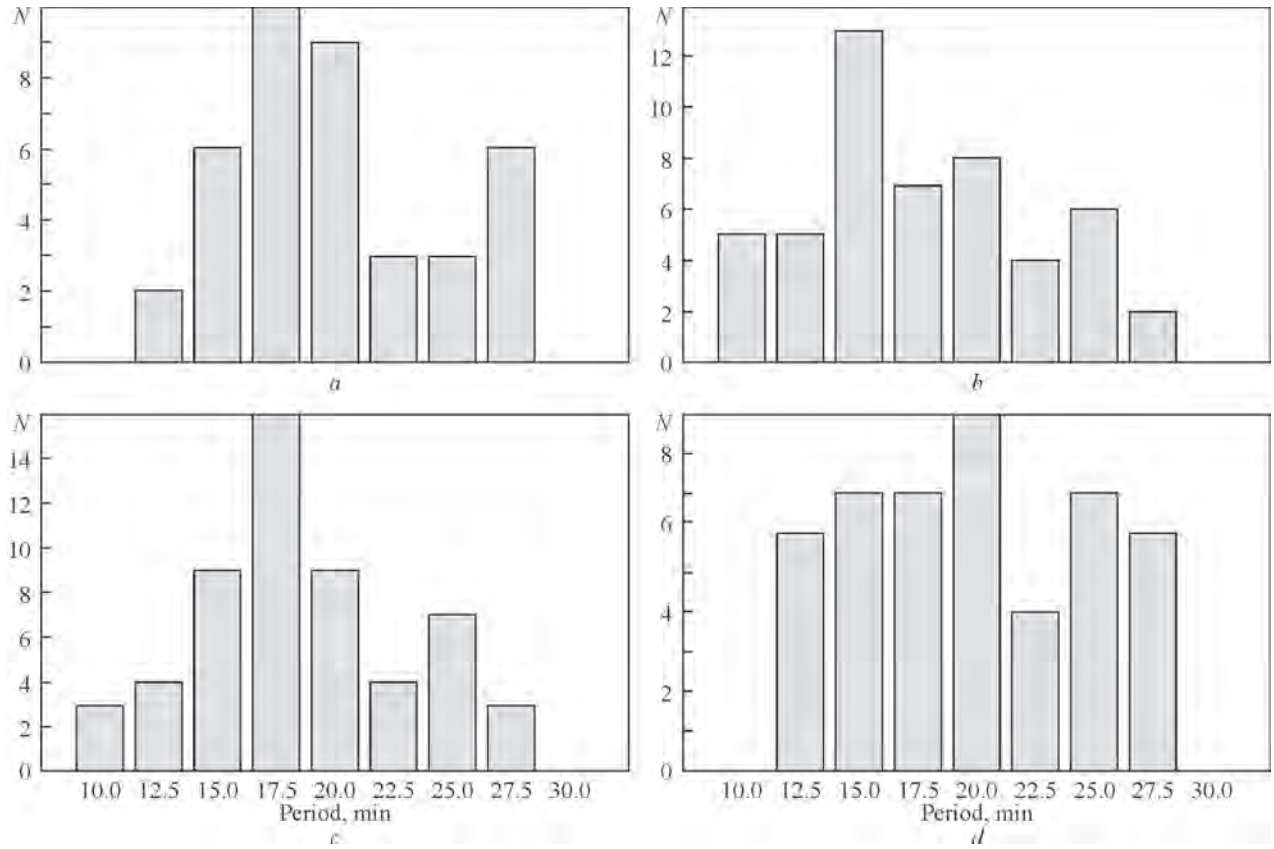

Fig. 4. Distribution of periods of wave disturbances on the terminator with amplitudes $\Delta A / \bar{A} > 0.03$ on the GQD-A118 path in evening time: April (a), June (b), October (c) and February (d) [17]

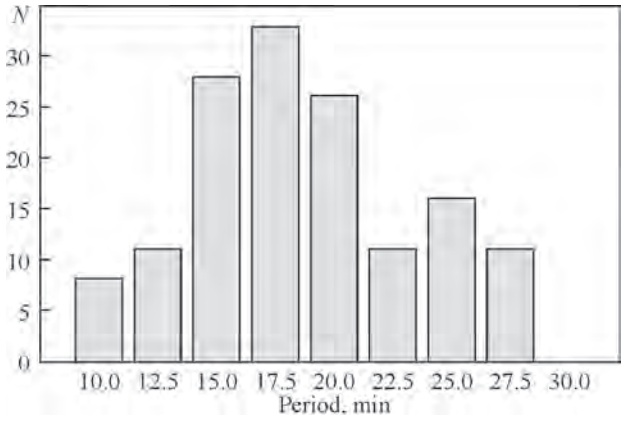

Fig. 5. Distribution of wave disturbances periods at the terminator, summarized for three months [17]

we considered evening sections of data after the passage of the terminator lasting several hours. At the same time, we excluded the moment of passing the terminator, assuming that the wave activity develops after it.

When studying AGWs, there is a need to separate the wave fluctuations from the large-scale trends. To obtain curve $\bar{A}$, which describes the undisturbed amplitude, the moving average method with the window size of 1 h is applied. The data of the radio signal amplitude measurements on the GQD-A118 path over 4 months (April, June, October 2020 and February 2021) were analyzed. The magnitude of amplitude fluctuations $\Delta A / \bar{A}$ in different months is 3—10%. At the same time, the large values of $\Delta A / \bar{A}$ do not necessarily mean the large amplitudes of AGW, but may be the result of changes in the conditions in the atmosphere and the height of the radio waves reflection [6].

After passing the evening terminator, the predominance of fluctuations of $\Delta A / \bar{A}$ was noticed with periods of 15—20 min. At the same time, the maximum wave activity develops mainly 1.5—2.5 hours after the terminator. In June, the wave activity from the terminator is expected to develop later in a local time than in the other months considered. In Fig. 4 we show the period distribution histograms of number N of observed wave events with amplitudes $\Delta A / \bar{A} > 0.03$ for four months in different seasons [17]. The wave fluctuations with periods of 15—20 min are noticeable for three of the four considered months (except February). In Fig. 5 we show the period distribution of the number of the wave events summarized for three months (April, June and October).

On histogram Fig. 5, it is clear that the distribution of AGW periods are more clearly manifested due to the increase in the number of the wave events. It is most likely that the prevailing wave mode on the terminator with a period of 15—20 min corresponds to the condition of synchronism with the source. In February, the superposition of fluctuations of several scales is more often observed without a

pronounced predominance of this mode. The conditions for observing the main AGW modes at the terminator should depend on the season and on the orientation of the path relative to the terminator line. To study these features, further statistical studies of disturbances on the terminator for different seasons with the involvement of measurement data on other radio paths are required.

Determination of AGW characteristic on the terminator

Near the equator, the speed of terminator VT exceeds the speed of sound near the Earth's surface (~300 m/s), but it is less than the speed of the sound in the upper atmosphere (~700—900 m/s at average solar activity). At atmospheric altitudes where the terminator is supersonic (below 150—180 km), it can generate both infrasonic and internal gravity waves [15]. Due to the Earth's rotation, the wave fronts generated by the terminator should move approximately from the west to the east. The horizontal speed of the terminator decreases in the direction from the equator to the poles approximately according to law $V_x(\varphi) = V_x(0)\cos\varphi$, where φ is the latitude, and $V_x(0)$ is the speed of the terminator at the equator. The considered GQD–A118 path is mid-latitude with the location of the GQD transmitter (54.91° N; 3.28° W) and the A118 receiver (43.46° N; 1.33° W). In the approximation of geometric optics, the main contribution to the amplitude fluctuations of the radio waves is given by the first ionospheric harmonic, which is reflected from the ionosphere exactly in the middle between the transmitter and the receiver [10]. On the GQD-A118 path, the latitude of this point is about 49°, that is the horizontal component of the terminator's speed in the middle of the path $V_{Tx} \approx$ $\approx$ 300 m/s, which is close to the speed of the sound. That is, on the considered radio path, the phase horizontal speed of the waves that are synchronized with the terminator is $U_x = \omega k_x = V_{Tx} \approx 300$ m/s, where ω is frequency, k_x is the horizontal component of the wave vector. In the assumption of synchronism with the terminator, for AGW with periods of 15—20 min the horizontal wavelengths should be equal to $\lambda_x = U_x T \approx 270$—360 km.

The propagation of the acoustic-gravity waves causes periodic fluctuations of atmospheric parameters: the density, the temperature, pressure, and the speed of particles. The observed fluctuations of VLF radio wave amplitudes $\Delta A / \bar{A}$ only indirectly reflect the distribution of AGW at the heights of the mesosphere, where these radio waves are reflected. It can be assumed that periods of fluctuations $\Delta A / \bar{A}$ coincide with the periods of AGW. However, the information on the spectral and amplitude characteristics of AGWs from such measurements remains unknown. In the general case of values of $\Delta A / \bar{A}$ are related to AGW amplitudes by equation (5), which is determined to a greater extent by the features of the radio path than by the physical properties of the waves themselves in the atmosphere. Having determined the value of K for the selected path, based on measurements of fluctuations $\Delta A / \bar{A}$, it is possible to calculate the amplitude of AGWs in fluctuations of the concentration of neutral particles $\Delta N / N_0$. Dependence of K from the effective level of radio wave reflection for the path GQD-A118 was analyzed in [6]. Value of V_z can be estimated using formula (3) assuming that $U_x \approx c_s$ and $V_x \approx V_z (T / T_B)$ for sufficiently long periods of AGWs, in comparison with the period of Brunt–Väisälä. In the monochromatic wave assumption $V_z = i\,\omega\Delta z$, then expression (3) follows $|\Delta N / N_0| \approx k|V_z|$, where the coefficient k depends on the period of the wave. The approximate values of AGW characteristics at the evening terminator, calculated for two periods T = 15 min and T = 20 min, are given in Table 2.

Conclusions

It is developed the methodology, which makes it possible to determine the characteristics of the acoustic-gravity waves based on the measurements of the amplitudes of VLF radio signals on paths <2000 km long. The proposed technique was tested on the measurements of amplitudes of VLF radio waves on several European radio paths. The fluctuations in the amplitudes of VLF radio waves in different seasons during 2013—2014 were studied with the use of these measurements. The peculiarities of the amplitude fluctuations in daytime and nighttime conditions were analyzed. It was obtained that the values of Δh in the day and the night conditions, as well as on different paths, are close amount to 250—400 m at the night and 200—300 m during the day. Using these results, the AGW amplitudes in the relative fluctuations of the concentration of the neutral particles were calculated (3—6%) with the volume of vertical displacement (0.7—1.4 km) during the propagation of AGW, which is consistent with the theoretical ideas. The perturbation from the solar terminator was investigated based on the data of amplitude measurements of VLF radio signals. It was established that the evening terminator for different seasons is dominated by the waves in the range of 15—20 min. The obtained results indicate the predominance of the wave harmonics on the solar terminator, corresponding to the condition of synchronism with the source.

Table 2

Characteristics of AGW on the evening terminator

AGW period, min	Coefficient k, s/m	Concentration fluctuations $\Delta N / N_0$	Vertical velocity of particles V_z, m/s	Horizontal velocity of particles V_x, m/s	Vertical volume displacement Δz, km
15	$1.6 \cdot 10^{-2}$	0.12—0.14	7.5—8.8	22.5—26.4	1.1—1.3
20	$2.1 \cdot 10^{-2}$	0.12—0.14	5.7—6.7	22.8—26.8	1.1—1.3

REFERENCES

1. Fedorenko A.K., Bespalova A.V., Cheremnykh O.K., Kryuchkov E.I. A dominant acoustic-gravity mode in the polar thermosphere. *Ann. Geophys*. 2015. V. 33. P. 101—108. https://doi.org/10.5194/angeo-33-101-2015

2. Innis J.L., Conde M. Characterization of acoustic-gravity waves in the upper thermosphere using Dynamics Explorer 2 Wind and Temperature Spectrometer (WATS) and Neutral Atmosphere Composition Spectrometer (NACS) data. *J. Geophys. Res*. 2002. V. 107, NA12.

3. Johnson F.S. et al. Gravity waves near 300 km over the polar caps. *J. Geophys. Res.* 1995. V. 100. P. 23993—24002.

4. Bezrodny et al. Fluctuations of Superlong Radio Waves in the Earth-Ionosphere Waveguide. Nauka, Moscow, 1984. 144 p.

5. Wait J.R., Spies K.P. Characteristics of the Earth-ionosphere waveguide for VLF radio waves. National Bureau of Standards, Technical Note, No. 300, 1964.

6. Fedorenko A.K., Kryuchkov E.I., Cheremnykh O.K., Voitsekhovska A.D., Rapoport Yu.G., Klymenko Yu.O. Analysis of acoustic-gravity waves in the mesosphere using VLF radio signalmeasurements. *J. Atmos.Terr. Phys*. 2021. 219. 105649. https://doi.org/10.1016/j.jastp.2021.105649

7. Nina A., Cadež V.M. Detection of acoustic-gravity waves in lower ionosphere by VLF radio waves. *Geophys. Res. Lett*. 2013. V. 40 (18). P. 4803—4807. https://doi.org10.1002/grl.50931

8. Ferguson J.A., Snyder F.P. Approximate VLF/LF mode conversion model. Technical Document, 400. Naval Ocean Systems Center, San Diego, California, USA, 1980.

9. Berry L.A. Wave Hop Theory of Long Distance Propagation of Low-Frequency Radio Waves. *Radio Science Journal of Research*. 1964. 68D (12). P. 1275—1284.

10. Yoshida Y. et al. On the generation mechanism of terminator times in subionospheric VLF/ELF propagation and its possible application to seismogenic effects. *Nat. Hazards Earth Syst. Sci*. 2008. V. 8. P. 129—134.

11. Kolarski A., Grubor D. Comparative Analysis of VLF Signal Variation along Trajectory Induced by X-ray Solar Flares. *J. Astrophys. Astr*. 2015. V. 36 (4). P. 565—579.

12. Fedorenko A.K., Kryuchkov E.I., Cheremnykh O.K., Voitsekhovska A.D., Klymenko Yu.O. Recover of acoustic-gravity wave properties revealed from measurements of VLF radio wave amplitudes. arXiv: 2011.05084v1 [physics.ao-ph] 10 Nov 2020. https://doi.org/10.48550/arXiv.2011.05084

13. Makhlouf U.R. et al. On the importance of the purely gravitationally induced density, pressure and temperature variations in gravity waves: Their application to airglow observation. *J. Geophys. Res.* 1990. V. 95. P. 4103—4111.

14. Mitchell N.J., Howells V.St. C. Vertical velocities associated with gravity waves measured in the mesosphere and lower thermosphere with the EISCAT VHF radar. *Ann. Geophysicae*. 1998. V. 16. P. 1367—1379.

15. Somsikov V.M., Ganguly B. On the mechanism of formation of atmospheric inhomogeneties in the solar terminator region. *J. Atmos. Sol. Terr. Phys*. 1995. 57. P. 75—83.

16. Yoshida Y. et al. On the generation mechanism of terminator times in subionospheric VLF/ELF propagation and its possible application to seismogenic effects. *Nat. Hazards Earth Syst. Sci*. 2008. V. 8. P. 129—134.

17. Cheremnykh O., Fedorenko A., Voitsekhovska A., Selivanov Y., Ballai I., Verth G., Fedun V. Atmospheric waves disturbances from the solar terminator according to the VLF radio stations data. *Advances in Space Research*. 2023. V. 72, Is. 11. P. 4825—4835. https://doi.org/10.1016/j.asr.2023.08.036

PHYSICAL EFFECTS IN THE ATMOSPHERE AND GEOSPACE ENVIRONMENT UNDER QUIET AND DISTURBED CONDITIONS

L. Chernogor
V.N. Karazin Kharkiv National University

The purpose of this paper is to report the results of experimental, theoretical studies and simulation of physical processes acting in the atmosphere and geospace, conducted during 2021—2023.

The observations were made with the remote radio sensing instrumentation located at the Radiophysical Observatory (49°38′N, 36°20′E), with the magnetometer located at the KhNU V. N. Karazin Magnetometric Observatory (49°38′N, 36°56′E), and with the multi-frequency multiple-path radio system located at the Kharbin engineering university (People's Republic of China) (45.78°N, 126.68°E). Data from the INTERMAGNET network and GNSS recordings were also used.

Effects of solar eclipses (SEs)

SE on 5—6 January 2019. Paper [1] deals with the variations in the Doppler spectra and in the relative amplitudes of the signals observed at oblique incidence over the China during the partial SE and on reference days. The partial SE was found to be associated with broadening of the Doppler spectrum, up to ±1.5 Hz, alternating sign Doppler-shift variations, up to ±0.5 Hz, in the main ray, and quasi-sinusoidal Doppler-shift changes. The relative amplitude of electron density N disturbances in the 15 min period of atmospheric gravity wave (AGW) field and in the 4—5 min period of infrasound wave field was estimated to be 1.6—2.4% and 0.2—0.3%, respectively.

SE on 21 June 2020. The results of the of temporal variations in the total electron content (TEC) in the vertical column of the ionosphere caused by the SE are described in [2, 3]. The eclipse was unique in that it was observed in equatorial and subtropical latitudes near the summer solstice and had an annular character. For most time dependences of the TEC $NV(t)$, the magnitude of the ΔNV depression was increased with growth coverage of the Sun's disk. The differences in this dependence can be explained by the peculiarities of the ionosphere in the equatorial belt of the Earth. The largest depression in TEC could be 4 TECU at $M_{max} \approx -0.643$. The relative variations in the electron density N were — 19%. The eclipse was accompanied by Doppler spectrum diffuseness resulting from an increase in the number of rays, the temporal variations in the Doppler shift were observed to be bi-polar, asymmetrical, and anomalously small, with extreme Doppler shift magnitudes varying from –11 to –40 mHz and from 22 to 56 mHz [4]. The duration of processes with negative Doppler shifts varied from 50 to 80 min, and the duration of processes with positive Doppler shifts changed from 30 to 80 min. The Doppler shift exhibited 4—18-min period quasi-sinusoidal variations with 20—10-mHz amplitudes.

SE on 10 June 2021. In [5], the observational data of solar limb flickering during the SE that took place near the city of Kharkiv have been analyzed, and the statistical parameters governing air convection were estimated. Blanketing of the solar disk by clouds appreciably suppressed atmospheric convection. In [6], observation results of the thermal (temperature) effect of the SE in the atmospheric surface layer, as well as the intercomparison of the thermal effects observed during eight eclipses that occurred in the same area during 1999—2021. A decrease in the temperature amounted to about 1°C. The response of the ionosphere to the SE is described in [7—11]. The temporal variations in the Doppler shift observed with vertical and oblique sounding have been determined to be, as a whole, similar [7]. Over the oblique radio paths, the number of rays was greater. The SE was accompanied by an enhancement in wave activity in the atmosphere and ionosphere. No less than three wave trains were observed. The values of the periods (~5—12 min) and the relative amplitudes of electron density perturbations ($\delta N \approx 0.3$—0.6%) give evidence that the wave disturbances were caused by AGWs. It was established in [8], that the SE was accompanied by an increase in wave activity in the ionosphere. The wave trains observed near the ionospheric $F2$ peak height showed periods of 5 min and 14 min and the 0.6% and 1.25% relative amplitudes of the oscillations in the electron density, respectively. At 240 km, the relative amplitude of the waves with 14-min period increased by 3%. The 14-min period pertains to AGWs, and the 5-min period to waves of electromagnetic nature. A sharp and considerable increase (from 380 to 560 km) in the virtual height was detected around the instant of greatest eclipse. A weak (equal to or less than 3.3%) decrease in N that lagged behind the maximum magnitude of the SE by about 12.5 min was revealed. In [10, 11], the results of observations of variations in TEC in the ionosphere at high latitudes, where the greatest eclipse was observed, are presented. The effects from the SE were distinctly observed at all eleven receivers and for all GPS satellites that were utilized. On average, a decrease in TEC was established to track changes in illumination of the ionosphere. In the course of 60 to 100 min after the SE, TEC was decreasing, attaining a minimum, and then it returned virtually to the initial value. A decrease in TEC attained a

maximum value of ~1—5.1 TECU, while, on average, it was found to be 2.7 ± 1.6 TECU or 35 ± 18%. The maximum in TEC lagged behind the maximum magnitude of the SE by 5—35 min. The relative amplitude of oscillations with periods within the range of 5—19 min was 1—12%. The results of a global analysis of temporal variations in the geomagnetic field are presented in [12, 13]. The SE was determined to be associated with an aperiodic decrease in the *X* component by 31—36 nT to 2—3 nT. The amplitude of quasi-sinusoidal variations with periods 40 ± 2 min decreased from 4.8 nT to 0.4 nT with distance from the area of the SE. Relative changes in atmospheric wave pressure were estimated to be 1—2%.

SE on 25 October 2022. In [14] the results of observations of the critical frequency, ionospheric *F*2 peak electron density and peak height of the ionosphere over Kharkiv during a partial SE are presented. The SE was accompanied by a plasma flow from the plasmasphere to the ionosphere.

Effects from Geospace Storms

Back in the 1970s—1980s L. F. Chernogor substantiated that a geospace storm (GS) is synergistically coupling magnetic, ionospheric, atmospheric, and electric storms. It has been confirmed that the consequences of solar storms manifest themselves in all subsystems of the SIMMIAE system [15—27]. Papers [15, 16] provide an overview of the current state of knowledge about the relationship between solar-terrestrial processes, manifestations of GS and variations in atmospheric-space weather. A classification of GSs based on Akasofu's epsilon parameter has been advanced. Six types of GS have been introduced, and a GS index has been suggested. A classification of ionospheric storms (ISs) and disturbances based on the magnitude of variations in the peak electron density of the *F*2 layer has been suggested. An ionospheric index characterizing the intensity of negative and positive ISs has been suggested. A classification of ISs and disturbances based on the magnitude of variations in the lower-ionosphere electron density has been proposed. Six types of the positive IS have been introduced. The appropriate ionospheric index has been suggested. The physics-based model of the evolution of each group of ISs and disturbances has been determined. The linkages among magnetic, ionospheric, atmospheric, and electric storms have been shown. The main statistical characteristics of the geomagnetic storms (153 storms in all) over Solar Cycle 24 are presented in [17]. GS effects are also discussed in the monograph [18]. Paper [19] is devoted to the storm of September 25, 2016. The processes that took place during the GS on December 21—24, 2016 are described in [20, 21]. The effects of the storm on March 21—23, 2017 are presented in [22, 23]. Paper [24] analyzes the variations in the levels of the Earth's magnetic field and its fluctuations in the range of periods of 1—1000 s that accompanied X-class solar flare on 6, 7, and 10 September 2017. Variations in the Doppler spectra and amplitudes of HF signals and ionospheric parameters over China during the IS that took place on August 26, 2018 are described in [25]. Features of the GS effects on August 5—6, 2019 and on September 2, 2019 are described in [26, 27].

Large Celestial Bodies Falling Effects

Effects in the atmosphere and geospace caused by the impact of large (more than 1 m) meteoroids are described in [28—38].

Chelyabinsk meteoroid. A number of physical effects of this meteoroid are described in [28]. The purpose of the paper was to obtain more precise height-time dependences of radiation intensity and mass of the Chelyabinsk meteoroid during the fall, to determine the size of the bolide and to build a model of destruction with an estimate of the parameters of fragment distribution by mass.

Lipetsk meteoroid. The meteoroid entered the Earth's atmosphere on June 21, 2018 at 01:16:20 UT. In the monograph [37], a comprehensive analysis of the main processes in the EAIM system that accompanied the fall of the Lipetsk meteoroid was carried out.

Kamchatka meteoroid. New effects of this meteoroid have been studied in [29, 31, 32]. In [29], using data from a number of magnetic stations, a global analysis of temporal variations in the geomagnetic field components was carried out on the day the Kamchatka meteoroid fell (December 18, 2018) and on reference days. The passage of the Kamchatka meteoroid through the magnetosphere and atmosphere was accompanied by variations mainly in the *H* geomagnetic field component. The magnetic effect from the magnetosphere was observed to occur twice, 51 min and 28 min prior to the meteoroid explosion, the amplitude of the disturbances in the geomagnetic field did not exceed 0.2—1 nT, and the durations were observed to be approximately 20 min and 10 min, respectively. Changing in sign peaks in the level of the *H* component were observed to lag behind the meteoroid explosion by 8 min to 13 min for distances from 1.004 Mm to 4.247 Mm. The theoretical models for the magnetic effects observed are presented and theoretical estimates are performed. In [31], the results of GPS observations of the Kamchatka meteoroid ionospheric effects were analyzed and compared with the results of the ground-based oblique incidence sounding of the ionosphere. The time delays of the ionospheric response to the meteoroid explosion have been determined, the horizontal velocities of disturbances have been estimated to be 504—520 m/s, their periods to be 11—18 min, durations 22—35 min, wavelengths 333—530 km, and the relative amplitudes of disturbances in *N* 3—4%. In [32] it was established that the Kamchatka meteoroid entering the atmosphere was accompanied by the generation of a transient resonance electromagnetic signal in the 25—35 mHz band observable in the vicinity of the meteoroid explosion and in the magnetically conjugate region. The 0.2—0.8-nT amplitude oscillations were observed to occur over a 7 min interval. A mechanism for this effect has been put forward.

Yushu meteoroid. Theoretical analysis of a large number of physical effects in all subsystems of the EAIM system was carried out in [30, 33, 34]. In [30], an assessment of mechanical, optical and gas-dynamic effects was performed. The initial kinetic energy of the celestial body was estimated to be about 40 TJ. Thermodynamic and plasma effects, as well as turbulence effects, were estimated in [33]. Magnetic, electric, electromagnetic, ionospheric, and seismic effects, as well as the effects of AGWs, were studied in [34].

Kyiv meteoroid. The analysis results of the entire set of physical effects in all subsystems of the EAIM system are presented in [35, 36, 38]. In [35], a comprehensive analysis and assessment of mechanical, optical and gas-dynamic effects was carried out. In [36], a comprehensive modeling of thermal, turbulent and plasma processes in all geospheres was performed. Magnetic, electric, electromagnetic, ionospheric, and seismic effects, as well as the effects of AGWs, are estimated in [38].

Effects of earthquakes (EQs)

Papers [39—42] are devoted to a detailed study of the manifestations of seismic effects. In [39], using ionospheric TEC maps for the Northern Hemisphere, except for the polar region, the ionospheric effects of powerful seismic events were considered for the winter seasons of 2012—2018. It was shown that the seismic-ionospheric effect is planetary, which is superimposed by local effects above the sources of individual EQs. In [40], changes in pressure and temperature of the atmospheric surface layer and ionospheric TEC were analyzed at an arbitrary distance from the sources of strong EQs. It has been established that surface pressure is reduced for approximately 5 days before the EQ and increased for 5 days after it. Air temperature changes in antiphase. The TEC values increase sharply 2—5 days before the EQ. Typical deviation values are up to 2 hPa, up to 0.3 K, 3—4%. Degassing of the earth's interior is a primary factor in these global effects. The data collected during the submarine magnitude 6.0 EQ that occurred off the East coast of Honshu, Japan, on April 11, 2019, have been analyzed with the specific objectives of determining the ionospheric response to the EQ and identifying possible mechanisms for the transport of the disturbances at 845—2,260 km great-circle distances between the epicenter and the propagation path midpoints [41]. Analysis showed that after the EQ the Doppler spectra exhibit essential broadening, the Doppler shift along the main ray undergoes alternating sign Doppler variations, as well as quasi-sinusoidal variations with 3—5 and 10—20-min periods pertaining to the infrasound and AGW frequency bands. The relative amplitudes of disturbances in N were estimated to be ~1% and 2—19% in the fields of infrasound and AGW, respectively. Multi-fractal properties of the geomagnetic field time variations caused by the EQ took place on January 24, 2020 in Turkey were investigated [42].

Effects from High-Power HF Radio Emissions

In [43], the results of experimental studies of aperiodic and quasi-sinusoidal disturbances in the ionosphere, observed under the action of powerful radio emission from the SURA facility on the ionospheric plasma under quiet and magnetically disturbed conditions, are presented. Aperiodic disturbances recorded at a distance of ~960 km, with a time delay of ~25 min, are associated with the generation of a shock wave disturbance related to AGW. Quasi-sinusoidal 12—15-min disturbances had a period equal to the heating cycle period. In other cases, the period of disturbances was equal to the period of natural oscillations of air in the atmosphere. The speed of quasi-sinusoidal disturbances was 300—400 m/s. The effects of artificial generation of plasma turbulence, the combined action of the solar terminator and powerful radio emission, as well as resonance effects associated with the impact on the ionosphere of a radio wave with a frequency equal to the fourth harmonic of the electron gyrofrequency, were discovered. In [44], the analysis results of the features of large-scale disturbances generation in the ionosphere under the influence of monopulse and periodic radio emission from a heating facility are presented. It has been established that during the period of minimum solar activity, recorded disturbances in the ionosphere at a distance of about 960 km from the heating facility can occur at an effective power of 25 MW. The periodic mode of the heater was accompanied by the generation of quasi-sinusoidal disturbances in N with the relative amplitude of ~1% and a period close to the Brunt — Väisälä period.

Effects of rocket launches and spacecraft flights

A special feature of our research is the search for the effects that rocket launches (RLs) have at a significant (~1,000—10,000 km) distance from a space vehicle path [45—47]. Of special interest are the magneto-ionospheric effects from RLs and the manifestation features of these effects observed during GSs. Approximately 5,000 observations of RL effects taken by us over the 1970—2023 time interval have been analyzed. RLs are shown to be associated with the generation and/or amplification of wave disturbances in the ionosphere and in the geomagnetic field in a wide period range of 5—10 min to 2—3 hr. It has been verified that the ionospheric response to a RL significantly depends on the space weather state. The IS effects can couple synergistically with the effects from RLs and flights by enhancing each other. The IS effects significantly complicate the detection of the effects from RLs and flights. Two types of disturbance with speeds of 2—3 km/s and 400—800 m/s have been revealed. Such speeds are characteristic of slow MHD waves and AGWs, respectively. The relative amplitude of disturbances in N reached 0.05—0.07 and the value of its quasiperiod approximately 0.5—3 hr. In [45], the results of observations of ionospheric processes during the solar cycle 24 that accompanied RLs against the background of ISs are described. The number of the Soyuz RLs is 81, and

of the Proton RLs is 53. In [46], the object of the study is a reduction in the ionospheric *F*-region electron density (ionospheric «hole») arising under the action of a rocket jet. It has been proven that rockets with masses of hundreds of tons are capable of forming «holes» of scale sizes of many hundreds kilometers and of reducing the ionospheric *F*-region *N* by a factor of larger than 2. The results of the analysis of ionospheric effects from the Soyuz and Proton rockets launched from the Baikonur cosmodrome during solar cycle 24 are described in [47]. A few groups of the apparent horizontal speeds of disturbance propagation have been confirmed to exist (~100—200 m/s; 390 ± 23 m/s; 0.97 ± 0.10 km/s; 1.28 ± 0.13 km/s; 1.68 ± 0.13 km/s; 2.07 ± ± 0.13 km/s, as well as ~8 km/s).

Effects of explosive volcanic eruptions

The effects in all subsystems of the EAIM system caused by the catastrophic eruption of the Tonga volcano on January 15, 2022 are described in [48—54]. The purpose of papers [48, 49] is to thoroughly analyze and model the main physical processes that accompanied the volcanic explosion within the EAIM system on January 15, 2022. The study attempts, for the first time, to comprehensively model or estimate the magnitude of the main effects arising in the solid Earth, the troposphere, the ionosphere, and in the magnetosphere. The effects include a rich assortment of waves: Lamb, sound, seismic, tsunami, infrasonic, and AGWs, which propagated on a global scale, with the blast wave launching secondary tsunamis and seismic waves. The powerful waves nonlinearly distorted their profiles and suffered nonlinear attenuation, while the electrical processes in the troposphere caused perturbations in the global electric circuit enhancing the strength of the ionospheric electric fields by one to two orders of magnitude that led to the emergence of secondary processes in the magnetosphere and radiation belts. The volcanic explosion excited all resonators in the EAIM system, perturbing their parameters. The magnetic effect has been estimated of the submarine volcanic explosion and eruption (~100—1,000 nT), the tsunami (~0.1 nT), of the volcanic plume (~1—10 nT), and in the ionosphere due to the ionospheric «hole» ($\Delta B \sim 0.1$—10 nT) and an external current in the atmospheric wave field ($\Delta B \sim 0.1$—1 nT). The magnetospheric effects were caused by electromagnetic emissions in the ~10—100 kHz band generated by lightning in the volcanic plume, which triggered the precipitation of energetic radiation belt particles into the ionosphere. Paper [50] describes the analysis results of global bay disturbances in the geomagnetic field observed after the explosion of the Tonga volcano. The magnitude of the effect varied from ~10 to ~60 nT. The greatest disturbances occurred in the *Y* component. The propagation speed of bay disturbances was close to the speed of the blast wave. It is substantiated that bay disturbances are closely related to the occurrence of an ionospheric «hole» under the action of a blast wave from the volcano. It has been established in [51], that on the day of the volcano explosion, approximately after 04:21, there were significant variations in the level of all geomagnetic field components. The shortest time delay was 6 min. At the same time, quasi-sinusoidal variations of the geomagnetic field with a period of 4—4.5 min and an amplitude of ~2 nT were caused by acoustic resonance in the field of a standing acoustic wave generated by the volcano explosion. In addition, six groups of possible disturbances stimulated by the volcano explosion were found. It was found that the disturbances were transported at speeds close to 4, 1.5, 1 km/s and 500, 313, and 200 m/s. Such velocities are characteristic of slow MHD waves, a blast wave, an AGW, a Lamb wave, and an ionospheric wave from tsunami. In [52, 53], aperiodic and quasi-sinusoidal disturbances in the ionosphere caused by the explosion of the Tonga volcano were analyzed in a wide range of distances (from ~0.1 to ~5 Mm) from the source of disturbances using TEC temporal variations. Four groups of disturbances have been detected, each of which had different time delays with respect to the moment of the volcano explosion. The first group of speeds included the disturbances traveling with a speed close to 1,000 m/s and having an *N*-shaped profile. This disturbance was generated by a blast wave. In the second group, the speed varied in the 336 m/s to 500 m/s range, within which the speeds of AGWs are found. The speeds in the third group exhibited variability within the 260—318 m/s limits, within which the Lamb wave propagates. The speed in the fourth group was estimated to be 190—220 m/s, which is a characteristic speed of the tsunami that was caused directly by the volcano explosion. The period of quasi-sinusoidal perturbations varied from ~10 min to 20 min, while their amplitudes were from 0.5 TECU to 1 TECU. The modules of the absolute and relative magnitudes of aperiodic disturbances, «holes», showing a tendency for decreasing with increasing distance from the explosion epicenter, from ~10 TECU to 2 TECU and from 37% to 7%, respectively [54]. The «hole» time delay and its duration exhibited an increase with distance from the volcano to the observational sensors, from 35 min to 100 min and from ~30—40 min to 120—150 min, respectively. Estimates showed that the horizontal size of the «hole» did not exceed 10 Mm, and the time delay of its appearance reached 122 min. The vertical component of the perturbation velocity was estimated to be 36—72 m/s, while the horizontal component to be 2.2 km/s. The ionospheric «hole» persisted for 120—200 min. A mechanism for generating the ionospheric «hole» has been proposed, which is based on both the electric and non-electric processes.

Effects of typhoons

The effects of typhoons are studied in [55—59]. The results of a theoretical analysis of the entire variety of physical effects caused in the EAIM system by powerful tropical cyclones and typhoons are described in [55]. The premise has been validated that a tropical cyclone (TC, typhoon, hurricane), one of the most powerful large-scale formations systematically arising in the atmosphere, is an element of the ocean–atmosphere–ionosphere–magnetosphere system.

Observations of the ionospheric response to the impact of a number of unique typhoons made using multifrequency multiple path oblique incidence ionospheric sounding have confirmed the definitive role that the internal gravity waves and infrasound play in producing atmospheric–ionospheric disturbances. The purpose of the [56] paper was to describe the observations of the variations in the parameters of HF radio waves propagating through the ionosphere when the action of the super typhoon Hagibis on 6—13 October 2019 occurred. The ionosphere underwent the greatest impact on those days when the supertyphoon had maximum energy, on 8, 10, and especially 9 October 2019, and when it was found to be in an ~2,500—3,000 km distance range from the propagation path midpoints. Under the action of wave processes, the height of the reflection region was observed to oscillate within the ±(30—90 km) limits. The amplitude of the quasi-sinusoidal variations in the ionospheric *F*-region *N* was estimated to be 10—12% for periods of ~20 min, and 30—60% for periods of ~60—120 min. We have acquired HF Doppler measurements and studied the dynamics of the ionosphere in the ~100—300 km altitude range during the 1—10 September 2019 period of typhoon activity [57]. The response of the ionosphere to the Typhoon Lingling was detected along three adjacent radio-wave propagation paths where chaotic and quasi-sinusoidal variations in the Doppler shift and a significant (from −1 to 1 Hz or greater) Doppler spectrum broadening were observed to occur. The Doppler spectrum chaotic variations are due to plasma turbulence generated by typhoons in the ionosphere, and the Doppler shift quasi-sinusoidal variations along the main ray are due to infrasound and AGW launched by the typhoons. The relative amplitude of quasi-sinusoidal variations in *N* in the field of the infrasound wave reached several percent, and in the field of the AGW attained from ten to a few tens of percent. The effects of the Typhoon Faxai during 9/10 and 10/11 September 2019 nights were accompanied by a 27% decrease in *N* in the ionospheric *E* and *F* regions. At the closest approach of the Typhoon Faxai to the ionosonde during 8/9 September 2019 night, when it had the largest energy, a 56% increase was detected in *N* of the ionospheric *F* region. During the super typhoon Lekima event of 4—12 August 2019 the ionospheric response was observed [58]. The action of the typhoon was often accompanied by up to ±1.5 Hz broadening of the Doppler spectra, 10—30 dBV variations in the signal amplitude, and quasi-sinusoidal variations in the Doppler shift with 0.10 to 0.40 Hz amplitudes and periods of 20—30 to 70—80 min. The AGW generated by the typhoon gave rise to quasi-sinusoidal variations in *N* with relative amplitudes of ~3—19%. Doppler measurements at oblique propagation paths captured the response in the ionosphere to the activity of the super typhoon, Typhoon Kong-Rey, from 30 September to 6 October 2018 [59]. The amplitudes, *fDa*, of the Doppler shift variations were observed to noticeably increase (factor of ~2—3) on 1—2 and 5—6 October 2018, while the 20—120 min periods, *T*, of the Doppler shift variations suggest that the wavelike disturbances in the ionosphere are caused by AGW. The periods and amplitudes of quasi-sinusoidal variations in the Doppler shift, which have been determined for all propagation paths, may be used to estimate the amplitudes, δNa, of quasi-sinusoidal variations in *N*. The periods *T* are found to change within the 15—120 min limits, and the Doppler shift amplitudes show variability within the 0.05—0.4 Hz and $\delta Na \approx 0.4$—6%.

Effects from Natural and Great Man-Made Disasters in the Atmosphere and Geospace

Papers [60—65] describe the physical effects and ecological consequences of natural and great man-made disasters of space and terrestrial origin. It has been demonstrated that during such disasters, disturbances cover not only the Earth's surface and the atmospheric surface layer, but also the upper atmosphere and even the magnetosphere, i.e., the entire EAIM system. The main physical effects in the atmosphere and geospace that accompanied the powerful explosion in Beirut on August 4, 2020 are described in [60, 61]. In [60], a comprehensive analysis of the main physical processes that accompanied the explosion was carried out. The results of radiophysical and magnetometric observations of processes in the lower ionosphere and geomagnetic field that accompanied a powerful explosion in Beirut are described in [61]. An increase of up to 5.3° in the phase of the ionospheric wave and an increase of 3.3% in the signal amplitude caused by change in *N* of approximately 3% were detected. The propagation speed of the disturbances is estimated to be about 3 km/s. The changes in the character of variations in the geomagnetic field level occurring in 5 min and in 79 min after the explosion were revealed. The propagation speeds can be estimated to be tens of km/s and greater, as well as 490 m/s. The MHD waves have the greater speed, and the AGW have the smaller one. In [62], employing the cylindrical model of a thermic in the atmosphere, its dynamics has been studied in the case of the continuous supply of heat. The analytical solutions to the set of equations governing the temporal dependences of the velocity of a parcel of the heated air and the position of the upper bound of the thermic, as well as the excess temperature in the heated parcel have been obtained. Papers [63—65] are devoted to the ecological consequences of large-scale forest fires.

Conclusions

In 2021—2023 at the beginning of the 25th solar activity cycle, experimental studies of disturbances in the atmosphere and geospace that accompanied the impact on the medium of powerful sources of energy release (solar eclipses, geospace storms, falls and explosions of large celestial bodies, typhoons, the catastrophic eruption of the Tonga volcano, earthquakes, powerful impacts of radio emissions, rocket launches, great disasters, etc.), were carried out. Theoretical models of physical processes acting in the atmosphere and geospace caused by the influence of powerful sources of energy release have been developed or advanced.

REFERENCES

1. Chernogor L.F., Garmash K.P., Guo Q., Rozumenko V.T., Zheng Y. Ionospheric effects of the 5—6 January 2019 eclipse over the People's Republic of China: results from oblique sounding. *Ann. Geophys*. 2022. Vol. 40. P. 585—603.

2. Чорногор Л.Ф., Милованов Ю.Б., Дорохов В.Л., Поднос В.А., Цимбал А.М., Шевелев М.Б. Варіації повного електронного вмісту в екваторіальній іоносфері, викликані сонячним затемненням 21 червня 2020 р. *Вісник ХНУ імені В.Н. Каразіна. Серія «Радіофізика та електроніка»*. 2022. Вип. 36. *С*. 49—65.

3. Chernogor L.F., Mylovanov Yu.B. Global Variations of the Total Electron Content in the Equatorial Ionosphere during the Annular Solar Eclipse of June 21, 2020. *Kinematics and Physics of Celestial Bodies*. 2023. Vol. 39, No. 4. P. 181—203.

4. Chernogor L.F., Garmash K.P., Guo Q., Luo Y., Rozumenko V.T., Zheng Y. Some Features of the Ionospheric Radio Wave Characteristics Over China Observed During the Solar Eclipse of 21 June 2020. *Radio Science*. 2022. Vol. 57, Is. 10. id:e2022RS007492.

5. Chernogor L.F. Convection Effect in the Surface Atmosphere of Solar Eclipses of March 20, 2015, and June 10, 2021. *Kinematics and Physics of Celestial Bodies*. 2021. Vol. 37, No. 6. P. 284—292.

6. Chernogor L.F. Thermal Effect in Surface Atmosphere of the Solar Eclipse on June 10, 2021. *Kinematics and Physics of Celestial Bodies*. 2021. Vol. 37, No. 6. P. 293—299.

7. Чорногор Л.Ф., Гармаш К.П., Жданко Є.Г., Леус С.Г., Luo Y. Особливості іоносферних ефектів часткового сонячного затемнення над Харковом 10 червня 2021 р. *Радіофізика і радіоастрономія.* 2021. 26, № 4. С. 326—343.

8. Чорногор Л.Ф., Милованова Л.І., Милованов Ю.Б., Цимбал А.М., Luo Y. Ефекти сонячного затемнення 10 червня 2021 р. в іоносфері над Харковом. *Вісник Харківського національного університету імені В. Н. Каразіна. Серія «Радіофізика та електроніка»*. 2021. Вип. 35. С. 64—83.

9. Chernogor L.F., Garmash K.P. Ionospheric Processes during the Partial Solar Eclipse above Kharkiv on June 10, 2021. *Kinematics and Physics of Celestial Bodies*. 2022. Vol. 38, No. 2. P. 61—72.

10. Чорногор Л.Ф., Милованов Ю.Б., Luo Y. Ефекти сонячного затемнення 10 червня 2021 р. в іоносфері високих широт: результати GPS-спостережень. *Радіофізика і радіоастрономія.* 2022. 27, № 2. С. 93—109.

11. Chernogor L.F., Milovanov Yu.B. Ionospheric Effects of the June 10, 2021, Solar Eclipse in the Arctic. *Kinematics and Physics of Celestial Bodies*. 2022. 38, No. 4. P. 197—209.

12. Chernogor L.F. Geomagnetic Effect of the Solar Eclipse of June 10, 2021. *Kinematics and Physics of Celestial Bodies*. 2022. 38, No. 1. P. 11—24.

13. Чорногор Л.Ф., Голуб М.Ю., Luo Y., Цимбал А.М., Шевелев М.Б. Варіації геомагнітного поля, що супроводжували сонячне затемнення 10 червня 2021 р. *Вісник Харківського національного університету імені В. Н. Каразіна. Серія «Радіофізика та електроніка»*. 2021. Вип. 34. С. 63—78.

14. Emelyanov L.Ya., Bogomaz O.V., Chernogor L.F., Domnin I.F. Response of the mid-latitude ionosphere to the solar eclipse on 25 October 2022: Results of F2-layer vertical sounding. *Advances in Space Research*. 2024. 73, Is. 5. P. 2338—2354.

15. *Чорногор Л. Ф. Фізика геокосмічних бур.* Космічна наука і технологія. 2021. 27, № 1. С. 3—77.

16. Черногор Л.Ф. Физические эффекты геокосмических бурь. Часть 1. *Журнал проблем эволюции открытых систем.* 2021. 23, № 3—4. С. 58—87; Часть 2. *Журнал проблем эволюции открытых систем.* 2022. 24, № 1—2. ***С***. 4—54.

17. Chernogor L.F. Statistical Characteristics of Geomagnetic Storms in the 24th Cycle of Solar Activity. *Kinematics and Physics of Celestial Bodies*. 2021. 37, No. 4. P. 193—199.

18. Bogomaz O.V., Chernogor L.F., Barabash V.V., Katsko S.V. Aperiodic and wave disturbances in the ionosphere: the results of vertical sounding. Dallas, USA: Primedia eLaunch LLC, 2021. 160 p.

19. Emelyanov L.Ya., Katsko S.V., Lyashenko M.V., Chernogor L.F. Ionosphere response to geospace storm on 25 September 2016 over Kharkiv (Ukraine). *Advances in Space Research*. 2023. 71, Is. 8. P. 3323—3345.

20. Katsko S.V., Emelyanov L.Ya., Chernogor L.F. Features of the Ionospheric Storm on December 21—24, 2016. *Kinematics and Physics of Celestial Bodies*. 2021. 37, No. 2. P. 85—95.

21. Luo Y., Chernogor L.F. Characteristic Features of the Magnetic and Ionospheric Storms on December 21—24, 2016. *Kinematics and Physics of Celestial Bodies*. 2022. 38, No. 5. P. 262—278.

22. Luo Y., Chernogor L.F., Garmash K.P. Magneto-Ionospheric Effects of the Geospace Storm of March 21—23, 2017. *Kinematics and Physics of Celestial Bodies*. 2022. 38, No. 4. P. 210—229.

23. Чорногор Л.Ф., Гармаш К.П., Леус С.Г., Luo Y., Поднос В.А., Цимбал А.М., Шевелев М.Б. Спектральний склад флуктуацій геомагнітного поля впродовж геокосмічних бур 21—23 березня 2017 р. *Вісник ХНУ імені В.Н. Каразіна. Серія «Радіофізика та електроніка»*. 2022. Вип. 36. С. 30—48.

24. Luo Y., Chernogor L., Garmash K. The Geomagnetic Response to the X-class Solar Flares of September 2017. *Advances in Space Research*. 2023. 72, Is. 11. P. 4911—4922.

25. Chernogor L.F., Garmash K.P., Guo Q., Zheng Y. Effects of the Strong Ionospheric Storm of August 26, 2018: Results of Multipath Radiophysical Monitoring. *Geomagnetism and Aeronomy*. 2021. 61, No. 1. P. 73—91.

26. Luo Y., Guo Q., Zheng Y., Гармаш К.П., Чорногор Л.Ф., Шульга С.М. Ефекти геокосмічної бурі 5—6 серпня 2019 р. *Космічна наука і технологія.* 2021. 27, № 2 (129). С. 45—69.

27. Luo Y., Chernogor L.F., Garmash K.P., Guo Q., Rozumenko V.T., Zheng Yu. Dynamic processes in the magnetic field and in the ionosphere during the 30 August — 2 September, 2019 geospace storm. *Annales Geophysicae*. 2021. 39, Is. 4. P. 657—685.

28. Chernogor L.F., Mylovanov Yu.B. Dynamic Falling of the Chelyabinsk Meteoroid: Sizes, Radiation, and Destruction. *Kinematics and Physics of Celestial Bodies*. 2021. 37, No. 5. P. 241—262.

29. Chernogor L.F. Kamchatka Meteoroid Effects in the Geomagnetic Field. *Kinematics and Physics of Celestial Bodies*. 2022. 38, No. 1. P. 25—48.

30. Chernogor L.F. Physical Effects of the Yushu Meteoroid: 1. *Kinematics and Physics of Celestial Bodies*. 2022. 38, No. 3. P. 132—147.

31. Luo Y., Chernogor L.F. Ionospheric Effects of the Kamchatka Meteoroid: Results of GPS Observations. *Kinematics and Physics of Celestial Bodies*. 2023. 39, No. 2. P. 71—77.

32. Luo Y., Chernogor L.F. Resonance Electromagnetic Effect of the Kamchatka Meteoroid. *Kinematics and Physics of Celestial Bodies*. 2023. 39, No. 1. P. 1—9.

33. Chernogor L.F. Physical Effects of the Yushu Meteoroid: 2. *Kinematics and Physics of Celestial Bodies*. 2023. 39, No. 3. P. 123—136.
34. Chernogor L.F. Physical Effects of the Yushu Meteoroid: 3. *Kinematics and Physics of Celestial Bodies*. 2023. 39, No. 3. P. 137—153.
35. Chernogor L.F. Physical Effects from the Kyiv Meteoroid: Part 1. *Kinematics and Physics of Celestial Bodies*. 2023. 39, No. 5. P. 261—279.
36. Chernogor L.F. Physical Effects from the Kyiv Meteoroid: Part 2. *Kinematics and Physics of Celestial Bodies*. 2023. 39, No. 6. P. 313—324.
37. Чорногор Л.Ф. Фізичні ефекти Липецького метеороїда. Харків: ХНУ імені В.Н. Каразіна, 2023. 152 с.
38. Chernogor L.F. Physical Effects of the Kyiv Meteoroid: 3. *Kinematics and Physics of Celestial Bodies*. 2024. 40, No. 1. P. 24—39.
39. Захаров І.Г., Чорногор Л.Ф. Глобальні та локальні ефекти сейсмічної активності в іоносфері. *Косм. наука і технол.* 2022. 28, № 6. С. 12—24.
40. Захаров І.Г., Чорногор Л.Ф. Вплив глобальної сейсмічної активності на параметри іоносфери та приземної атмосфери. *Радіофізика і радіоастрономія.* 2023. 28, No 2. С. 130—142.
41. Chernogor L.F., Garmash K.P., Guo Q., Rozumenko V.T., Zheng Y. Perturbations in the characteristics of ionospheric HF radio waves during the April 11, 2019, earthquake in Japan: Results from oblique sounding. *Advances in Space Research*. 2023. 72, Is. 5. P. 1688—1702.
42. Chernogor L.F., Lazorenko O.V., Onishchenko A.A. Fractal and multi-fractal analyses of the geomagnetic field variations caused by the earthquake on January 24, 2020 in Turkey. *Journal of Natural Science and Technologies*. 2022. 1, Is. 1. P. 52—55.
43. Chernogor L.F., Frolov V.L. Features of Large-Scale Disturbances Induced in the Ionosphere by Powerful Decameter Radiation during Moderate Magnetic Storms. *Geomagnetism and Aeronomy*. 2021. 61, No. 5. P. 721—742.
44. Чорногор Л.Ф., Жданко Є.Г., Luo Y. Особливості генерації великомасштабних збурень в іоносфері під дією моноімпульсного та періодичного радіовипромінювання нагрівного стенда. Радіофізика і радіоастрономія. 2022. 27, № 3. С. 188—202.
45. Luo Y., Чорногор Л.Ф., Жданко Є.Г. Іоносферні ефекти ракет, що стартують на фоні геокосмічних бур. *Космічна наука і технологія.* 2022. 28, № 3 (136). С. 62—85.
46. Чорногор Л.Ф. Великомасштабні зниження концентрації електронів у F-області іоносфери вздовж траєкторії стартуючої ракети. *Радіофізика і радіоастрономія.* 2022. 27. № 1. С. 26—37.
47. Luo Y., Chernogor L.F., Zhdanko Y.H. Geospace Perturbations that Accompanied Rocket Launches from the Baikonur Cosmodrome. *Kinematics and Physics of Celestial Bodies*. 2022. 38, No. 6. P. 287—299.
48. Чорногор Л.Ф. Фізичні ефекти у системі Земля — атмосфера — іоносфера — магнітосфера, викликані потужним вибухом вулкана Тонга 15 січня 2022 р. *Космічна наука і технологія.* 2023. 29, № 2. С. 54—77.
49. Chernogor L.F. Physical effects from the powerful Tonga volcanic eruption of January 15, 2022, in the Earth–atmosphere–ionosphere–magnetosphere system. *Journal of Atmospheric and Solar-Terrestrial Physics*. 2023. 253. id:106157.
50. Chernogor L.F., Holub M.Yu. Bay-Shaped Variations in the Geomagnetic Field that Accompanied the Catastrophic Explosion of the Tonga Volcano on January 15, 2022. *Kinematics and Physics of Celestial Bodies*. 2023. 39, No. 5. P. 247—260.
51. Чорногор Л.Ф. Глобальні варіації геомагнітного поля, викликані вибухом вулкану Тонга 15 січня 2022 р. *Космічна наука і технологія.* 2023. 29, № 4 (143). С. 78—105.
52. Чорногор Л.Ф. Варіації повного електронного вмісту в іоносфері, викликані вибухом вулкану Тонга 15 січня 2022 року. *Космічна наука і технологія.* 2023. 29, № 3 (142). С. 67—87.
53. Чорногор Л.Ф., Милованов Ю.Б. Іоносферні збурення у ближній зоні, викликані експлозивним виверженням вулкана Тонга 15 січня 2022 р. *Радіофізика і радіоастрономія.* 2023. 28. № 3. ***С***. 212—223.
54. Chernogor L.F., Mylovanov Yu.B. Electron Density Reduction Caused by the Tonga Volcano Eruption on January 15, 2022. *Kinemat. Phys. Celest. Bodies*. 2023. 39, Is. 4. P. 204—216.
55. Chernogor L.F. A Tropical Cyclone or Typhoon as an Element of the Earth — Atmosphere — Ionosphere — Magnetosphere System: Theory, Simulations, and Observations. *Remote Sensing*. 2023. 15. id:4919.
56. Chernogor L.F., Garmash K.P., Guo Q., Rozumenko V.T., Zheng Y., Luo Y. Supertyphoon Hagibis action in the ionosphere on 6—13 October 2019: Results from multi-frequency multiple path sounding at oblique incidence. *Advances in Space Research*. 2021. 67, Is. 8. P. 2439—2469.
57. Chernogor L.F., Garmash K.P., Guo Q., Rozumenko V.T., Zheng Y., Luo Y. Disturbances in the ionosphere that accompanied typhoon activity in the vicinity of China in September 2019. *Radio Science*. 2022. 57. id:e2022RS007431.
58. Zheng Y., Chernogor L.F., Garmash K.P., Guo Q., Rozumenko V.T., Luo Y. Disturbances in the ionosphere and distortion of radio wave characteristics that accompanied the super typhoon Lekima event of 4—12 August 2019. *Journal of Geophysical Research: Space Physics*. 2022. 127. id: e2022JA030553.
59. Chernogor L.F., Garmash K.P., Guo Q., Rozumenko V.T., Zheng Y. Effects of the super-powerful tropospheric western Pacific phenomenon of September–October 2018 on the ionosphere over China: results from oblique sounding // Annales Geophysicae. 2023. Vol. 41, Is. 1. P. 173—195.
60. Chernogor L.F. Physical Effects in the Atmosphere and Geospace due to Ground-Based Events as Exemplified by the Explosion in the City of Beirut on August 4, 2020. Theoretical Modeling Results. *Kinematics and Physics of Celestial Bodies*. 2021. 37, No. 3. P. 121—134.
61. Chernogor L.F., Garmash K.P. Physical Effects in the Atmosphere and Geospace Accompanying the Surface Explosion in the City of Beirut on August 4, 2020: Observational Data. *Kinematics and Physics of Celestial Bodies*. 2021. 37, No. 4. P. 183—192.
62. Чорногор Л.Ф. Динаміка підйому терміків у атмосфері при безперервному підводі тепла: приклади практичного застосування. *Фізика атмосфери та геокосмосу.* 2021. 2, № 1. С. 5—12.
63. Чорногор Л.Ф., Некос А.Н., Тітенко А.В., Чорногор Л.Л. Екологічні наслідки горіння лісових масивів у північній півкулі в 2020 р.: результати моделювання та кількісних розрахунків. *Вісник Харківського національного університету імені В.Н. Каразіна. Серія «Екологія».* 2021. 25. С. 42—54.
64. Chernogor L., Nekos A., Titenko G., Chernogor L. Ecological consequences of the large forests fires in the Northern hemisphere during 2020. In: Sustainable development of natural and economic systems: theory, methodology, and practice. Poland: Bilostok, 2022. P. 259—276.
65. Чорногор Л.Ф., Некос А.Н., Тітенко Г.В., Чорногор Л.Л. Моделювання параметрів великомасштабних лісових пожеж. *Вісник Харківського національного університету імені В.Н. Каразіна. Серія «Екологія».* 2022. № 26. С. 43—54.

THE POWER LINES ELECTROMAGNETIC EMISSION TO THE SPACE

G. Lizunov [1], V. Korepanov [2], O. Piankova [1], V. Pronenko [2]

[1] Space Research Institute of the NAS of Ukraine and State Space Agency of Ukraine
[2] Lviv Center of Space Research Institute of the NAS of Ukraine and State Space Agency of Ukraine

Introduction

The Earth's electromagnetic environment is influenced not only by natural processes but also by human activities, including terrestrial radio transmitters, power plants, power lines, and industrial facilities. These sources of electromagnetic energy generate various space plasma effects, such as the precipitation of energetic particles from the Earth's radiation belts, deviations in ionosphere parameters, and many more. The continuous increase in electric power production has led to a persistent growth of industrial pressure on the near space, whose environmental impact is difficult to predict. Therefore, it is important to study changes in the electromagnetic profile of our planet caused by both natural and artificial factors, particularly those associated with the expanding production of electric power.

Observation of electromagnetic emissions produced by terrestrial sources in space has been ongoing since the launch of the first satellites. However, our understanding of issues related to space electromagnetic pollution remains limited. Due to technical constraints, such as sensor sensitivity and onboard system noise, satellite observations primarily capture slowly fluctuating electric and magnetic fields with frequencies below a few hertz (in the satellite reference frame), or relatively high-frequency radio emissions in the kilohertz range and above. It is only recently that diagnostic capabilities have extended to the extremely low frequency (ELF) range, encompassing frequencies from units of hertz to kilohertz. This extension has led to the discovery of stable space plasma oscillations, including Schumann resonances at central frequencies such as 7.8 Hz, 14.3 Hz, 20.8 Hz, 27.3 Hz, 33.8 Hz, and power line emissions (PLE) at industrial frequencies of 50/60 Hz [1—8]. The last type of electromagnetic emission is the most common form of ELF radio waves traveling from the Earth into space due to anthropogenic activity.

This article comprises the following main sections: Section 2 presents the results of the PLE observations obtained at the Chibis-M satellite mission; Section 3 focuses on the development of the theory regarding the generation and propagation of this emission.

Observation of the power line emission by the Chibis-M satellite

Microsatellite (MS) Chibis-M was launched on 24 January 2012 (decayed on 15 October 2014) into a 500 km circular orbit with 52° inclination. Its mass is about 40 kg, where one-third is a scientific instrumentation. The dimensions of the Chibis-M housing are 0.26 · 0.26 · 0.54 m, including the service and scientific instrumentation, as well as outside-mounted solar panels.

The MS has three-axis orientation and stabilization. The main scientific objective of Chibis-M is the theoretical model verification for the atmospheric gamma ray bursts, i.e., short, few millisecond pulses of intense radiation in the gamma ray range, particularly associated with the processes in deep space, e.g., supernova explosions. It requires the study of the accompanying electromagnetic (EM) processes such as plasma waves produced by lightning discharges in very low frequency (VLF) band. For this purpose, the combined wave probe with a very sensitive electric and magnetic sensor set, developed previously for the VARIANT experiment, was included as a part of the scientific payload [9]. The magnetic sensors provide measurements of three magnetic field components in the frequency range of 1—40,000 Hz with a noise spectral density of 10—0.02 pT/ $Hz^{0.5}$ (in the band 1—100 Hz, the noise is 10—0.1 pT/ $Hz^{0.5}$). Due to Chibis-M's compactness, the magnetic field sensors were placed too close to the service instrumentation and solar panels, where the operational currents of the service instrumentation create strong interference depending on the MS operation cycle. The last factor limited the magnetic sensor sensitivity threshold to 100—10 pT/ $Hz^{0.5}$ in the band 1—100 Hz. The electric field sensor had a measuring base of 0.42 m for the measurement of one electric field component, which is orthogonal to the orbital plane. The frequency range of the sensor is 0.1—40,000 Hz with the peak noise 0.8—0.04 (μV/m)/$Hz^{0.5}$ (in the band 1—100 Hz the noise is 0.2—0.04 (μV/m)/ $Hz^{0.5}$). As opposed to the magnetic sensors where interference considerably exceeds the noise, fortunately, the electric field interference at all MS operation conditions was close to the basic noise of the electric sensor, especially in our band of interest (1—100 Hz). Additionally, the onboard electronics did not use or generate the 50/60 Hz signals. This is because only electric field data was used for our study.

The signals from EM sensors were digitized at a fixed sampling rate 78,125/2n Hz (n = 0, 1, 2, 3) with a 16-bit resolution because the main task of the magnetic wave complex was the registration of EM signals related to plasma waves produced by lightning. Sometimes for scanning signals in the ELF range, the data were digitized at sampling rate 325.5208334 Hz with 24 bits resolution. So, the wave complex worked mainly at high sampling rates

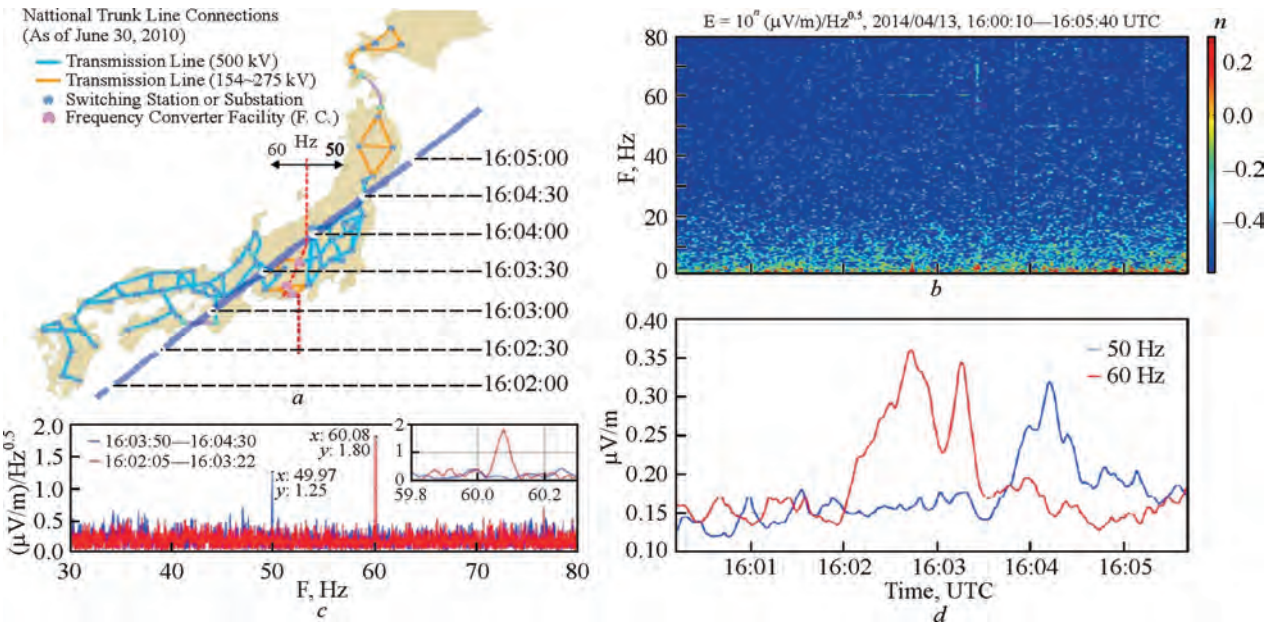

Fig. 1. Power line emission 50/60 Hz observed over Japan. See text for details

and much less at minimal value (upper frequency limit is 140 Hz with antialiasing filtering).

The typical case of PLE observation is shown in Fig. 1 (orbit 12406, 13 April 2014, 16:00:10—16:05:40 UTC, local nighttime, altitude about 413 km). Hereinafter a nightside of the orbits is marked in blue. At this moment Chibis-M was over Japan, where it crossed, at first, over 60 Hz and then over 50 Hz power lines; see Fig. 1, *a* (the power grid map is taken from http://www.fepc.or.jp/english/library/electricity_eview_japan/). The first signal maximum of 60 Hz and averaged amplitude 0.36 μV/m was registered near the branched power lines of Shikoku and the western part of Honshu Islands; see dynamic Fourier spectrum in Fig. 1, *b* and averaged absolute value of 50/60 Hz signals in Fig. 1, *d*. (At digital averaging procedure the PLE signals were extracted by the Butterworth first-order band-pass filter of bandwidth 1 Hz and resonant frequency 50/60 Hz; then the signal absolute value data were treated with a low-pass filter of first-order and cutoff frequency 0.03 Hz.) The second maximum of 60 Hz signal appeared after crossing over the power line cluster near Nagoya. The 50 Hz signal maximum 0.32 μV/m was detected after the Chibis-M passage over the boundary between 60 and 50 Hz electrical networks. It corresponds to the dense 50 Hz power line grids placed about 100 km to the north of Tokyo. The signal fast Fourier transform (FFT) spectra for the separate time intervals, which correspond to the time intervals of 50/60 Hz harmonic detection, are shown in Fig. 1, *c*.

The example of PLE detection during local daytime is shown in Fig. 2 for the Chibis-M flight over North America (orbit 12496, 19 April 2014, 11:16:14—11:27:38 UTC, altitude 417 km). The power line grid at voltage ≥ 345 kV is shown in Fig. 2, *a*. There are numerous power lines under 345 kV in Canada and U.S. which are not shown here (the map is taken from http://www.electricity.ca/media/pdfs/economic/canada_us_affairs/CEA_Enhancing_2010_final.pdf). During this time MS was in sunlight. Hereinafter a dayside of the orbits is marked in orange if MS is over the Earth's nightside and in yellow if MS is over the Earth's dayside. Chibis-M crossed the terminator at about 11:22:30 and entered in the local daytime. From the dynamic spectrum, Fig. 2, *b*, and averaged amplitude of 60 Hz signal, Fig. 2, *d*, it is seen that (1) faint 60 Hz signal (about 0.3 μV/m) appeared after 11:20:00 over power grid in North Dakota; (2) few signal maximums (about 0.6—0.7 μV/m) at time interval 11:23:00—11:25:30 related to MS location over a dense grid in Indiana, Ohio, and West Virginia states; and (3) absolute signal maximum (about 1.1 μV/m) over a single power line in Virginia and North Carolina. The signal absence over power lines in British Columbia despite the local nighttime and low interference on board Chibis-M (~0.2 μV/m) should be noted. FFT signal at time interval 11:20:10—11:27:00 is shown in Fig. 2, *c*.

All the parts of the orbits where PLE 50/60 Hz was detected are shown in Fig. 3. The detected PLE is basically following the world map of the power line's location and their operational frequency distribution, e.g., http://www.itoworld.com/map/4?lon=-10.98775&lat=-14.20775&zoom=2. Nevertheless, as it is seen from the map in Fig. 3, some parts of the orbits, where PLE 50/60 Hz was recorded, are far from intensive power line locations, especially when Chibis-M was over oceans. This fact unambiguously says about the possibility of extra far PLE propagation in the Earth's ionosphere. Two cases of such a detection are shown further in Fig. 4 (see also Fig. 3).

In the first case MS was over Maldives (orbit 13841, 14 July 2014, 17:08:20—17:09:41 UTC, altitude 376 km), Fig. 4, *a*. The distance between the orbit trace on the Earth's surface to Sri Lanka or India power line grids is over 1300 km. Another case is shown in Fig. 4, *c* when Chibis-M

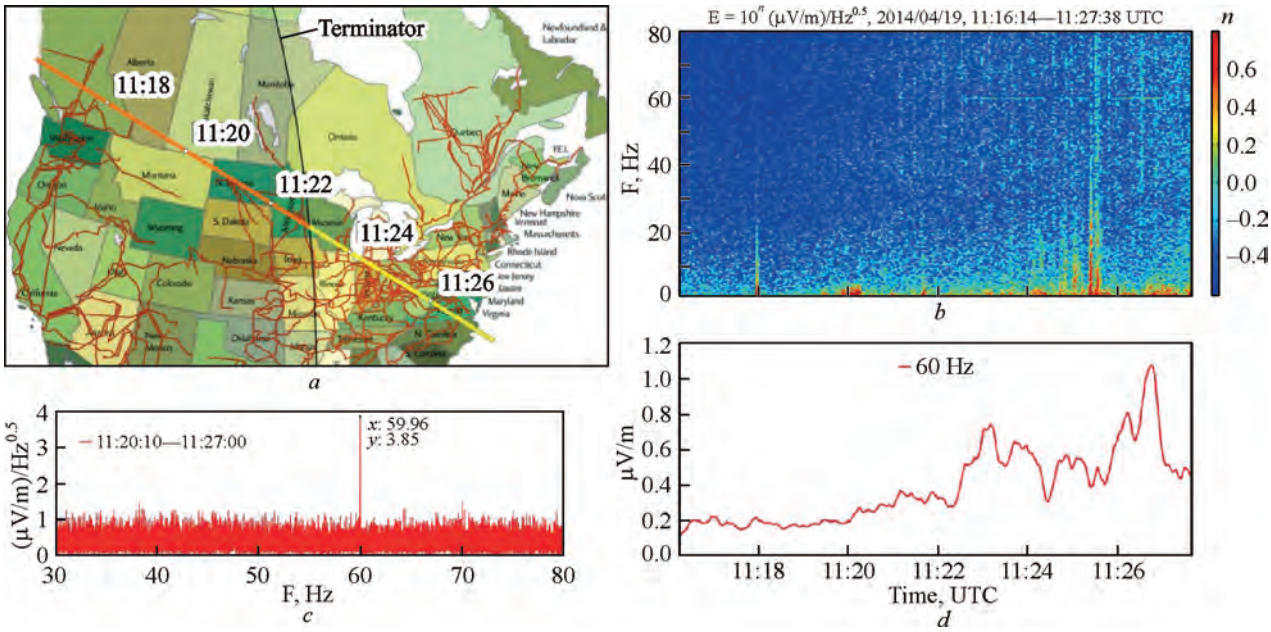

Fig. 2. Power line emission 60 Hz observed over Canada and U.S. See text for details

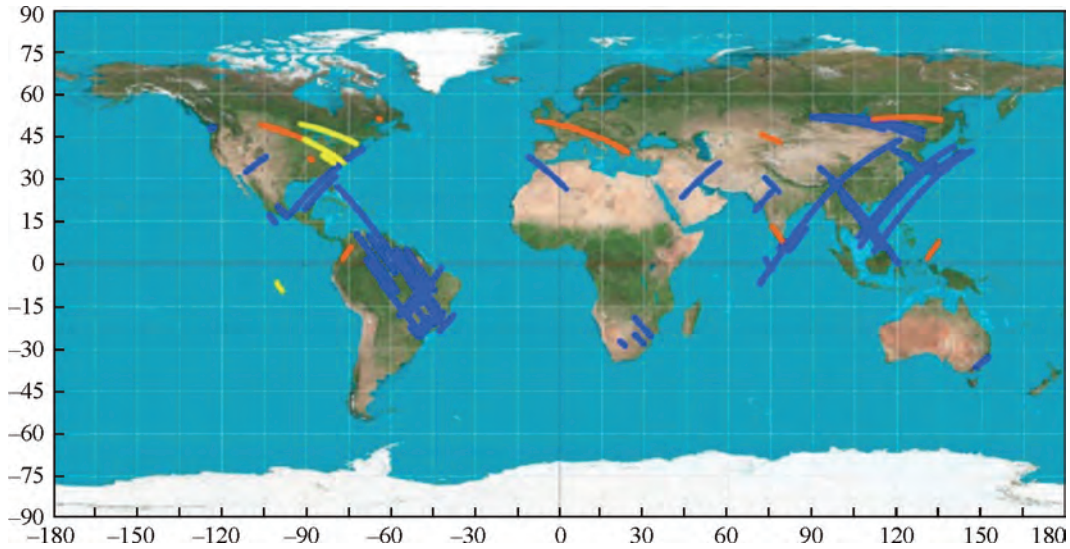

Fig. 3. The parts of Chibis-M orbits where the power line emission 50/60 Hz was detected. See text for details

was over the Pacific equatorial zone (orbit 13495, 22 June 2014, 14:03:10—14:04:01 UTC, altitude 386 km). The closest to MS-extended 50 Hz power line networks are in Chile and Argentina; the distance is over 4000—4500 km.

Here, the attempt to present the possible physical model explaining the mechanism of PLE generation and propagation into the ionosphere is made below.

Physical model of PLE generation and propagation

The theory of PLE, which encompasses the physical model of its generation and propagation, has been proposed in our recent paper [10]. The propagation environment of the PLE exhibits a distinct flat-layered structure consisting of the lithosphere, atmosphere, ionosphere, and magnetosphere space, as schematically shown in Fig. 5. This structure can be conditionally divided into several altitude layers with varying electrodynamic properties. The quantitative parameters of these layers depend on geographical coordinates, solar time, and solar activity. It is important to note that this structure only approximately corresponds to the generally accepted division of the ionosphere into layers with different electron concentrations. Fig. 5 also depicts the PLE wave fronts; however, it does not accurately represent the significant difference between the vertical and horizontal scales of the wave process. In reality, the horizontal wavelength is approximately 6000 km, while the vertical wavelength is on the order of tens of kilometers or less in layers I, III, IV, and V.

Following [10], let us describe the physical picture of PLE propagation. The actual source of emission generation is a magnetic dipole formed by the power line current and by

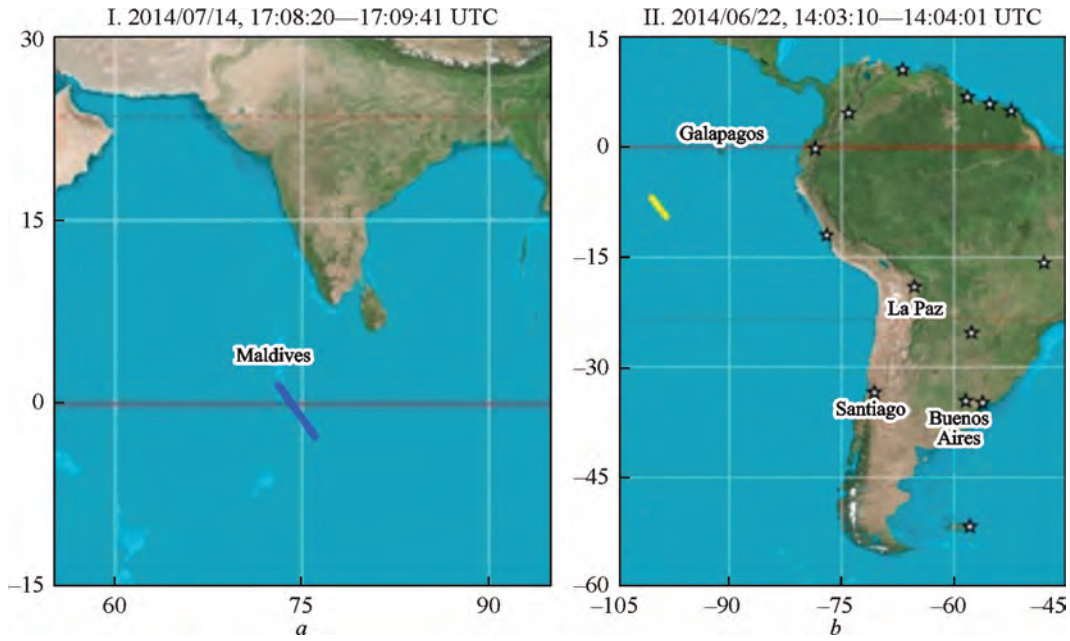

Fig. 4. Two examples of very long-distance propagation of power line emission: *a* — over Maldives, Indian Ocean, and *c* — in the equatorial zone of Pacific Ocean

the secondary image current in the ground, which has the opposite sign. The dipole arm is determined by the skin layer depth of the Earth's crust depending on its conductivity.

In the neutral atmosphere, the PLE wave front expands according to the directional pattern of the dipole source. When PLE reaches the lower boundary of the ionosphere, typically at around 80—90 km altitude, a major portion of it is reflected, however some portion of the energy (a few percent) penetrates into the ionosphere. There it is transformed into a quasi-flat whistler wave. The characteristic horizontal profile of PLE beam at these altitudes is presented in Fig. 6. Image current generation in ground and reflection from the lower bottom of the ionosphere are the main factors that reduce the electromagnetic emission into space. The reflected energy propagates further in the waveguide "Earth surface — ionosphere" similarly to the Schuman oscillations.

In the ionosphere, the PLE wave front propagates approximately vertically, while the energy propagates at an angle, which depends on geomagnetic field inclination. In a wide range of geomagnetic latitudes, from about 20° up to the magnetic poles, the emission is directed by the geomagnetic field according to the whistler propagation law, with the group velocity direction roughly bisecting the angle between the vertical and the geomagnetic field vector. As a result, the ionosphere acts as a focusing system that collects PLE into a unidirectional beam as shown in Fig. 5.

In the equatorial region, the magnetosonic mode of PLE propagation is observed. In this mode, the group velocity aligns with the wave vector, approximately oriented vertically across the geomagnetic field lines. The PLE intensity does not change with altitude over the entire range of ionospheric heights. However, the amplitudes of the electric and magnetic fields changes according to the laws of geometric optics, corresponding to variations in the refractive index.

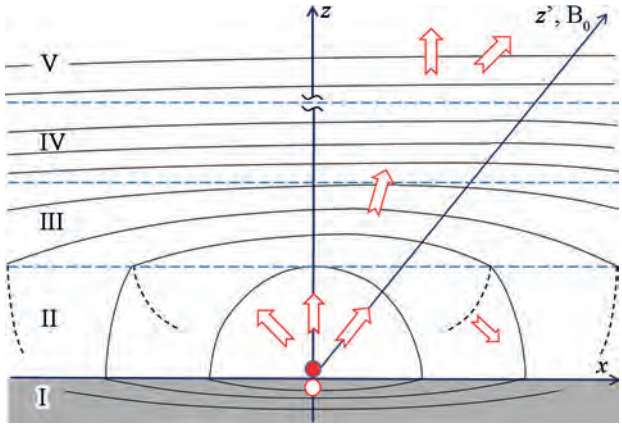

Fig. 5. Theoretical problem definition: I — lithosphere, II — atmosphere, III — dynamo region, IV — *F*-region, V — magnetosphere. Circles indicate the power line current (along the Y axis, filled) and the image current in the ground (empty). Solid lines show the pattern of phase fronts of emission, dashed lines show the phase fronts of the energy flow reflected from the ionosphere. The arrows indicate the directions of PLE energy propagation

In the magnetosphere PLE is transformed to both magnetosonic and Alfvén waves and the emission splits into two rays: one is directed along the wave vector (upwards) and the other one — along the geomagnetic field lines.

To confirm such an evolution of the PLE wave-packet along the propagation path, calculations were performed to determine the horizontal distribution of the electric field at different heights. The results are presented in Fig. 7.

Discussion

Let us compare the theoretical results [10] with the experimental data obtained from satellites such as Chibis-M (orbit altitude ~500 km) [5, 7], C/NOFS (400—850 km) [6]

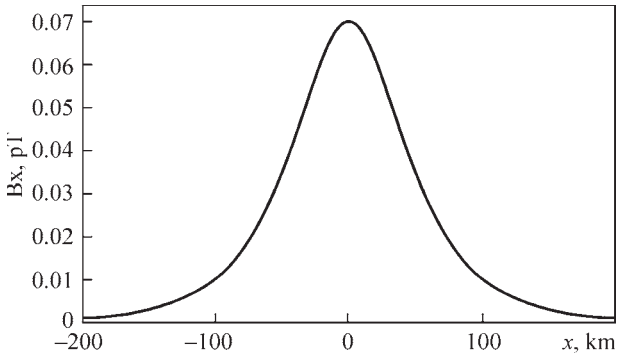

Fig. 6. Horizontal distribution of the magnetic tangential component at 80 km altitude above a power line with the unbalanced current of 1 A and at the crustal conductivity of 10^{-3} S/m

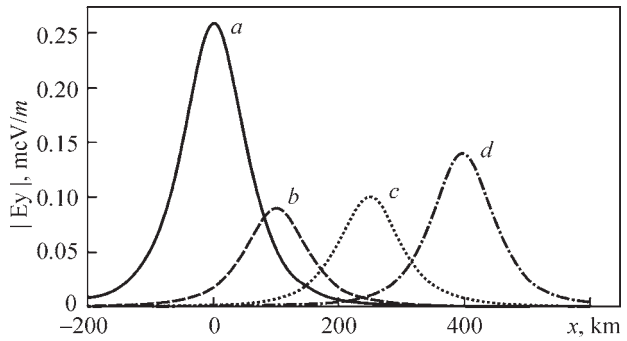

Fig. 7. Horizontal distribution of the electric field horizontal component above a power line with an unbalanced current of 1 A for the location with geomagnetic field inclination of 45° in night conditions at different altitudes: *a*) 100 km, *b*) 300 km, *c*) 600 km, *d*) 900 km

and DEMETER (660 km) [8]. Note that due to the high level of interference, only the data of the electrical component of PLE was published, with the amplitude typically in the range E ~ 0.5—1.0 μV/m, occasionally exceeding these values. For instance, the Chibis-M satellite recorded 0.35 μV/m over Japan and 1.2 μV/m over Brazil [7]. Referring to the theory [10], we can conclude that observed emission amplitudes correspond to the source current 10—20 A. Specifically, these source currents are associated with unbalanced current, which is typically on the order of several percent of the three-phase current transmitted through the high-voltage power line. So, we may note that the power line imbalance, which leads to such unbalanced currents, is generally lower in Japan compared to Brazil. These results demonstrate the fundamental possibility of utilizing satellite-based PLE measurements for remote diagnostics of terrestrial power grid parameters. As the obtained data processing showed, by analyzing the PLE signals detected by satellites, we can infer valuable information about the power line characteristics, such as unbalanced current values, frequency deviation of the generated current from basic 50/60 Hz frequency, and even power lines locations where direct monitoring might be challenging.

In summary, the agreement between the theoretical framework and numerical simulations, along with the correspondence with experimental data, confirms the validity of the assumptions and approximations made in the course of analytical theory development. This alignment enhances our understanding of the physical processes involved in PLE propagation and supports the potential applications of PLE measurements for practical purposes.

Acknowledgment

We would like to express our heartfelt gratitude and appreciation to our dear colleague, Dr. Fedir Dudkin, who played a vital role in the initiation of this study but passed away. His contributions and dedication to this work are greatly acknowledged and will be remembered.

REFERENCES

1. Helliwell R.A., Katsufrakis J.P., Bell T.F., Raghuram R. VLF line radiation in the Earth's magnetosphere and its association with power system radiation. *Journal of Geophysical Research*. 1975. 80. P. 4249—4258. https://doi.org/10.1029/JA080i031p04249

2. Park C.G., Helliwell R.A. Power line radiation in the magnetosphere. *Advances in Space Research*. 1981. 1(2). P. 423—437. https://doi.org/10.1016/0273-1177(81)90317-3

3. Tomizawa I., Yoshino T. Power line radiation observed by the satellite OHZORA. *Journal of Geomagnetism and Geoelectricity.* 1985. 37. P. 309—327. https://doi.org/10.5636/jgg.37.309

4. Rodger C.J., Thomson N.R., Dowden R.L. VLF line radiation observed by satellite. *Journal of Geophysical Research: Space Physics.* 1995. 100. P. 5681—5689. https://doi.org/10.1029/94JA02865

5. Dudkin D., Pilipenko V., Korepanov V., Klimov S., Holzworth R. Electric field signatures of the IAR and Schumann resonance in the upper ionosphere detected by Chibis-M microsatellite. *Journal of Atmospheric and Solar-Terrestrial Physics*. 2014. 117. P. 81—87. https://doi.org/10.1016/j.jastp.2014.05.013

6. Pfaff R., Freudenreich H., Simões F., Liebrecht M. C., Farrell W. Observations of 50/60 Hz power line radiation in the low latitude ionosphere detected by the electric field instrument on the C/NOFS satellite. Paper presented at 2014 XXXIth URSI General Assembly and Scientific Symposium (URSI GASS), Beijing, China. 2014. https://doi.org/10.1109/URSIGASS.2014.6929584

7. Dudkin F., Korepanov V., Dudkin D., Pilipenko V., Pronenko V., Klimov, S. Electric field of the power terrestrial sources observed by microsatellite Chibis-M in the Earth's ionosphere in frequency range 1—60 Hz. *Geophysical Research Letters*. 2015. 42(14). P. 5686—5693. https://doi.org/10.1002/2015gl064595

8. Němec F., Parrot M., Santolík O. Power line harmonic radiation observed by the DEMETER spacecraft at 50/60 Hz and low harmonics. *Journal of Geophysical Research: Space Physics*. 2015. 120. P. 8954—8967. https://doi.org/10.1002/2015JA021682

9. Dudkin F., Korepanov V., Lizunov G. Experiment VARIANT — First results from wave probe. *Adv. Space Res.* 2009. 43(12). P. 1904—1909. https://doi.org/10.1016/j.asr.2009.03.018

10. Lizunov G., Korepanov V., Piankova O. Regarding the theory of power lines emission propagation to the space. *Journal of Geophysical Research: Space Physics*, 2023. 128, e2023JA031668. https://doi.org/10.1029/2023JA031668

RESULTS OF EXPERIMENTAL AND THEORETICAL STUDIES OF PHYSICAL PROCESSES IN THE IONOSPHERE OVER UKRAINE IN THE YEARS 2021—2023

I. Domnin, L. Emelyanov, D. Kotov, S. Panasenko, O. Bogomaz, S. Katsko, V. Pulyaev, A. Miroshnikov, V. Kolodyazhnyi

Institute of Ionosphere of the NAS of Ukraine and MES of Ukraine

Ionospheric Observatory of the Institute of Ionosphere is located in 50 kilometers to the south-east from Kharkiv city (49.6° N, 36.3° E; Φ = 45.7°, Λ = 117.8°). The Ionospheric Observatory facilities include the 158 MHz VHF incoherent scatter (IS) radar equipped with the zenith parabolic Cassegrain antenna of 100 m diameter; the 158 MHz VHF IS radar equipped with the fully steerable parabolic antenna of 25 m diameter and ionosonde VISRC-2.

Incoherent scatter radar with zenith-directed antenna allows measuring with high accuracy (usually error is 1—10%) and acceptable altitude resolution (10—100 km) the following ionospheric parameters: electron density N, electron T_e and ion T_i temperatures, vertical component of the plasma drift velocity V_z, and ion composition. The investigated altitude range is usually 100—700 km, but can reach 100—1500 km in high solar activity period.

The aim of this paper is a brief overview of the investigation results of ionospheric processes over Ukraine, obtained in the years 2021—2023. During this period, we conducted monitoring of ionospheric processes in quiet and disturbed conditions, modernization of measuring systems, improving of geophysical data measurement and processing techniques [1—28].

Regular processes in the ionosphere over Ukraine

Variations of the main parameters of the ionospheric plasma [1—5]. During the period of 2021—2023, observations of diurnal and seasonal variations of the electron density (N_e), electron (T_e) and ion (T_i) temperatures, ionospheric plasma drift velocity (V_z), ion composition over a wide range of altitudes (100—750 km), as well as the critical frequency of the F2 layer (f_0F2), ionospheric F2 peak electron density (N_mF2), peak height (h_mF2) of the ionosphere over Kharkiv and the total electron content were carried out. An analysis of variations in the parameters of the ionosphere and processes in it over previous years was also carried out to obtain new knowledge about the ionosphere and compare the behavior of these parameters under different solar activity.

Variations in the ionospheric parameters during the maximum phase of the 25th cycle of solar activity. The f_0F2, N_mF2, and h_mF2 data were obtained using the VISRC-2t ionosonde of the Institute of Ionosphere. Temporal variations of f_0F2 obtained under conditions of low geomagnetic activity for typical geophysical periods (spring and autumn equinoxes, summer and winter solstices) are shown in Fig. 1.

The repeatability of variations from day to day is observed for each season with the exception of certain periods (in particular, 22 March). The difference in variations for different seasons is explained by different levels of solar activity, characterized by the $F_{10.7}$ index, the position of the Sun relative to the measurement site and other geophysical factors. Significant differences between summer and winter variations are caused, in particular, by the presence of solar illumination of the ionosphere at the height of maximum ionization throughout the day in summer and the winter anomaly.

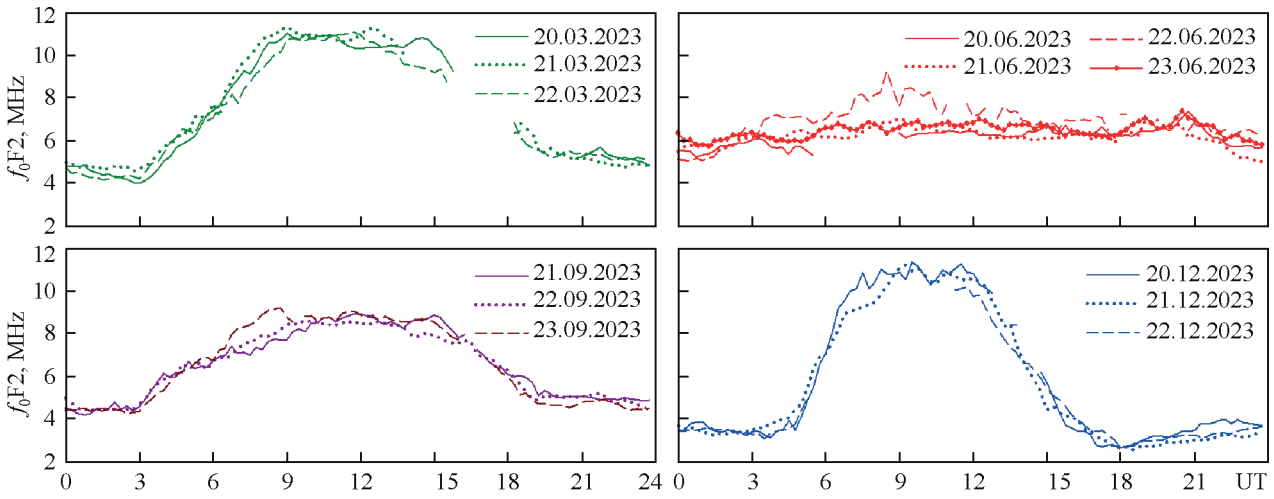

Fig. 1. Diurnal-seasonal variations in the critical frequency of the F2 layer

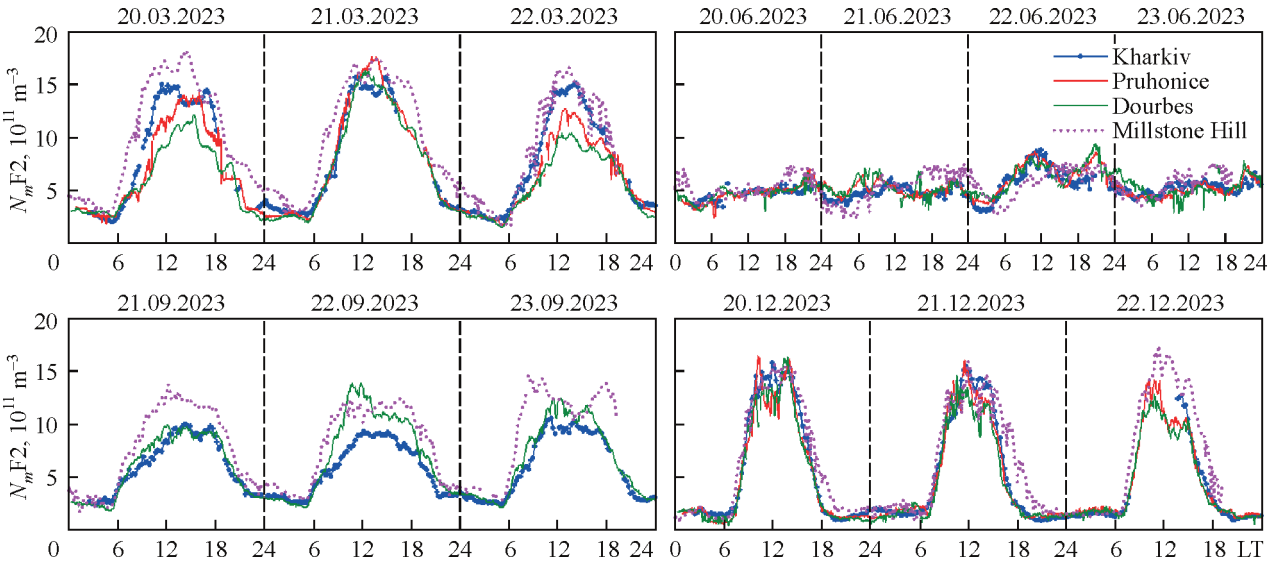

Fig. 2. Comparison of N_mF2 variations obtained using the Kharkiv ionosonde and other mid-latitude stations

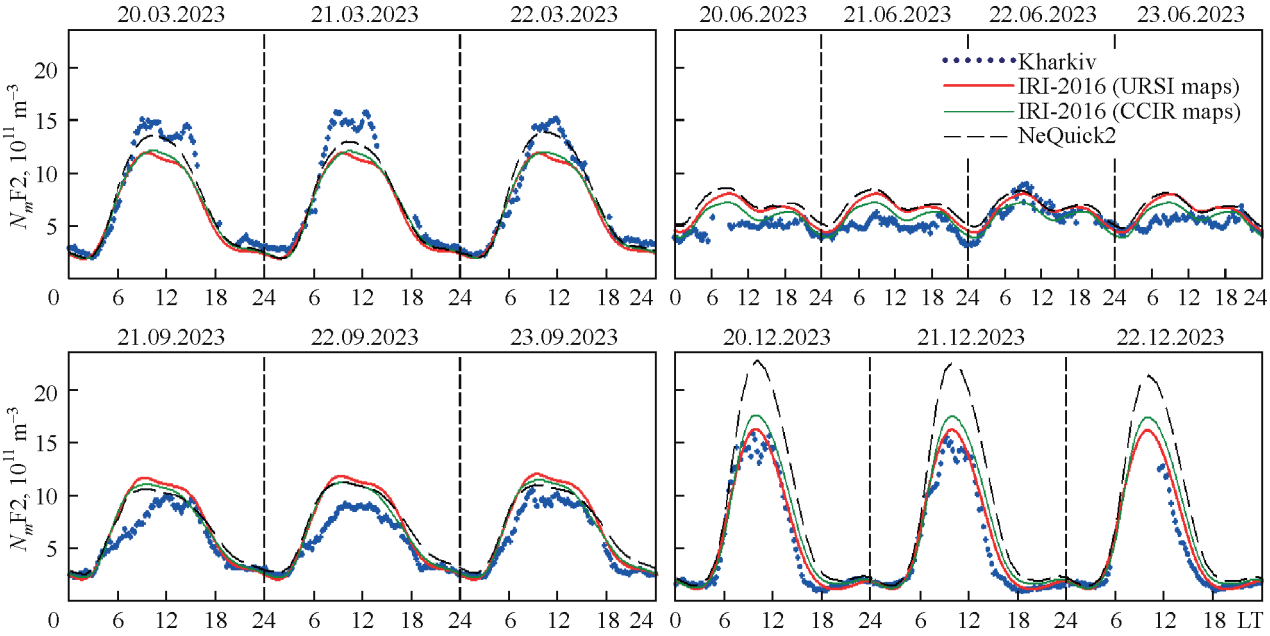

Fig. 3. Comparison of N_mF2 variations obtained using the Kharkiv ionosonde with forecasts of the IRI-2016 and NeQuick2 ionospheric models

For all seasons, a comparative analysis of variations in N m F2 and h m F2 of the Kharkiv ionosonde was carried out with variations obtained using stations located at close latitudes to the Kharkiv ionosonde in the eastern and western hemispheres: Pruhonice, Durbes, and Millstone Hill. Fig. 2 shows temporal variations of N m F2 for all four seasons as a function of local time (LT). The Pruhonice data turned out to be the closest to the Kharkiv data. The variations at Millstone Hill have the greatest difference, which indicates longitudinal effects in the ionosphere associated with the mismatch of geographic and geomagnetic poles.

The h_mF2 variations for all stations under consideration are quite similar, with the exception of some short periods of time. Values of h_mF2 in Millstone Hill are smaller at night in spring and autumn and larger during the day in autumn compared to those in Kharkiv, Pruhonice and Durbes.

A comparative analysis of N_mF2 and h_mF2 diurnal variations of the mid-latitude ionosphere over Kharkiv with the same variations calculated using various options of the International Reference Ionosphere (IRI) model and the ionospheric electron density model (NeQuick2) was also carried out. For the IRI-2016 model, data were considered using three h_mF2 models and two maps for N_mF2. The results for N_mF2 are shown in Fig. 3.

Both options of the IRI-2016 model and the NeQuick2 model give underestimated N_mF2 values for the spring equinox and summer solstice (except for 22 June) and overestimated values for the autumn equinox. The N_mF2

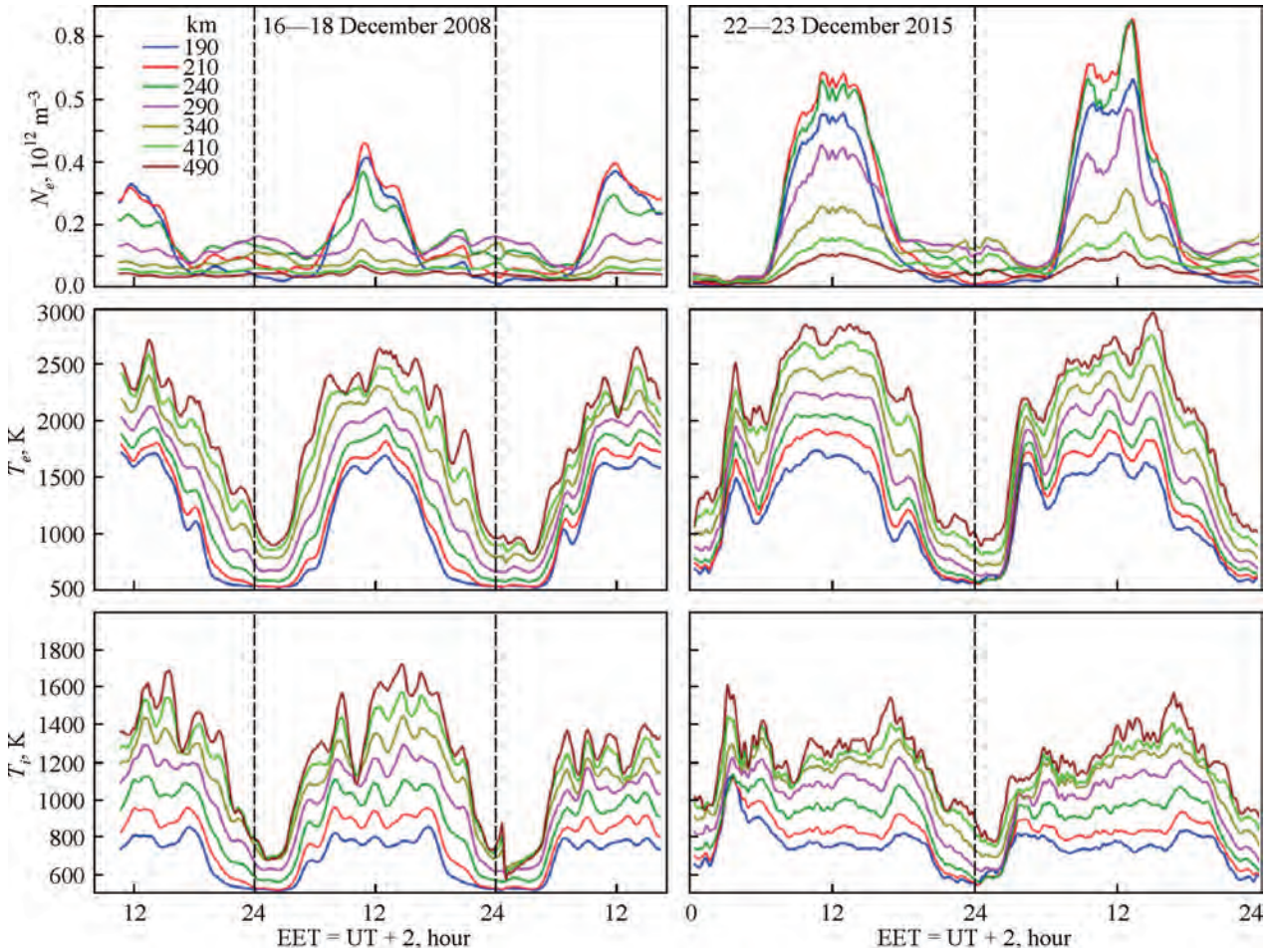

Fig. 4. Temporal variations in the electron density, electron and ion temperatures at fixed altitudes on 16—18 December 2008 and 22—23 December 2015

variations obtained from the IRI-2016 model are in good agreement with the experimental winter solstice data, and the NeQuick2 model significantly overestimates N_mF2 values.

The results of comparison of h_mF2 variations are as follows. The closest model to the Kharkiv results is the IRI-2016 (AMTB-2013) model. The IRI-2016 (CCIR-M2000) and IRI-2016 (Shubin) models describe h_mF2 variations somewhat worse. Autumn and winter daytime variations and summer nighttime variations are best described by the IRI-2016 model (Shubin). The results of calculating daily h_mF2 values using the NeQuick2 model for all seasons are the most distant from h_mF2 values in Kharkiv.

Comparison of ionospheric plasma drift velocity measurement results obtained at middle latitudes of the Earth's eastern and western hemispheres using incoherent scatter radar data [2]. For this purpose, we used the data acquired by Kharkiv incoherent scatter radar and Millstone Hill incoherent scatter radar (USA). Data analysis shows that the daily dependences of the plasma velocity V_z in the ionosphere over Kharkiv and Millstone Hill are mostly close. The identified individual differences in V_z variations can be explained by the longitude effect. The volumes of magnetic force tubes for Kharkiv and Millstone Hill differ significantly (2.14 times). The latitude positions of the magnetically conjugate regions in the Earth's southern hemisphere for Kharkiv and Millstone Hill also differ significantly, and, as a consequence, the exchange processes between the ionosphere and the protonosphere can differ.

Modeling and analysis of spatial-temporal variations of physical process parameters in the ionospheric plasma over Ukraine during the 24-th solar activity cycle have been performed using the experimental data obtained by the incoherent scatter radar [3, 4]. The diurnal dependences of parameters of dynamic and thermal processes were constructed for typical geophysical periods (vernal and autumn equinoxes, summer and winter solstices) on the phases of the minima (2009 and 2019) and maximum (2012—2015) of the 24-th solar activity cycle. The obtained results can be used in basic studies of geospace and solar-terrestrial relations.

Incoherent scatter radar data for calculation of the ionospheric cross-section [5]. For calculation of the ionospheric cross-section and its comparison with the predictions of the IRI model, variations in ionospheric parameters were obtained with the incoherent scatter radar for periods corresponding to the phases of the minimum and the declining of the 24th solar activity cycle. Fig. 4 show temporal variations of ionospheric parameters at discrete heights for one of the seasons.

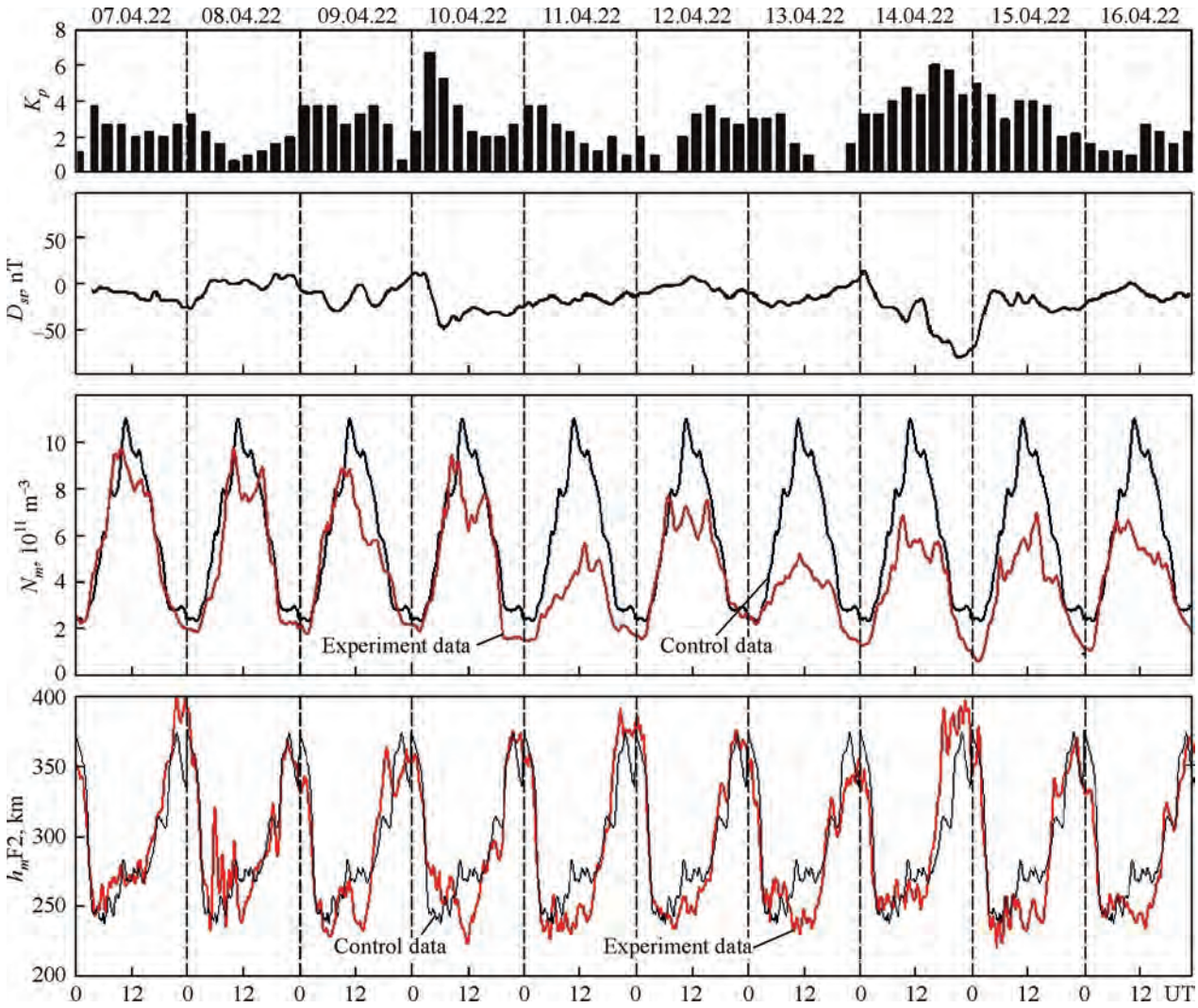

Fig. 5. Diurnal variations of K_p and D_{st} indeses, h_mF2 and N_mF2 (obtained using the digital ionosonde) during 7—16 April 2022

Irregular processes in the ionosphere over Ukraine

Irregular processes in the ionosphere are associated with ionospheric storms [6—12], solar eclipses [13—15], *traveling ionospheric disturbances* [16], etc.

Ionospheric storms

Ionospheric storm on 25 September 2016 [6]. It is found that the weak geospace storm on 25 September 2016 was accompanied by a moderate magnetic storm (the geomagnetic activity index K_p reached 4+) and caused a three-phase ionospheric storm as the variations of electron density indicated. The first phase of ionospheric storm was negative, and its intensity was moderate. The second phase was positive, and the ionospheric storm intensity varied from weak to strong. The third phase was negative, and the ionospheric storm was moderate. The F2 peak electron density value decreased by a factor of 1.3—1.5 during the first (negative) phase of the ionospheric storm, increased by a factor of 1.4—2.2 during the second (positive) phase, and decreased by a factor of 1.5 during the third (negative) phase of the storm. The first negative phase of the ionospheric storm was accompanied by an increase in the electron temperature by 100—200 K, and the positive phase was accompanied by T_e decrease by 520—400 K. During the second negative phase, T_e practically did not change. The ion temperature variations were within ±100 K.

During the negative phases of the ionospheric storm, individual deviations in the vertical plasma drift velocity from those on a geomagnetically quiet day were observed both in the direction of decreasing the downward drift velocity (increasing the upward drift velocity at high altitudes) and vice versa. During the positive phase, the increase in the velocity of downward plasma drift reached 9—20 m/s at altitudes above 450 km. The phases of the ionospheric storm were accompanied by significant variations in the dynamic and thermal processes in the ionosphere.

Long-term ionospheric disturbances during 7—16 April 2022 [12]. We analyzed a series of negative ionospheric disturbances during long-term disturbed geomagnetic conditions on 7—16 April 2022, caused by coronal mass ejections. During the entire experiment, changes in the diurnal variations of the electron density N_mF2 at the F2

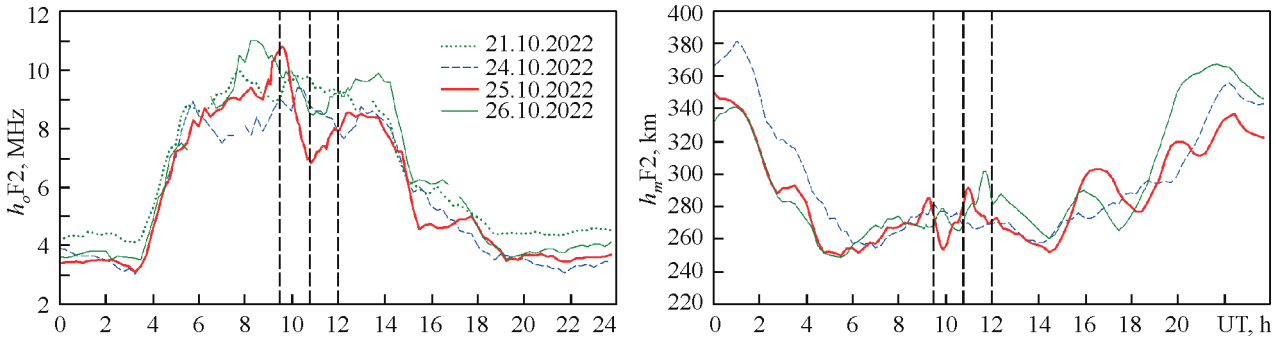

Fig. 6. Temporal variations of f_oF2 and h_mF2 of the ionosphere over Kharkiv on 21—26 October 2022 (vertical lines indicate the beginning, maximum and end of the SE)

layer peak and the height of the F2 layer peak h_mF2 were observed. On 10 April the N_mF2 decreased by 2 times after the end of the main phase of the strong magnetic storm ($K_{p\max}$ = 7–, $D_{st\min}$ = –48 nT) (see Fig. 5). Before that, a decrease in h_mF2 by 35—40 km was observed. But on 11 April changes in N_mF2 were even greater: a decrease in h_mF2 by 50 km was accompanied by a decrease in N_mF2 by 2.3 times. Similar changes took place on 13 April too: a decrease in *hm*F2 by 40 km was accompanied by a decrease in N_mF2 by 2.3 times. Next the minor magnetic storrn ($K_{p\max}$ = 5–, $D_{st\min}$ = –42 nT) caused a decrease in N_mF2 up to 2 times after the end of the main phase of the magnetic storm. Later that day the moderate magnetic storm ($K_{p\max}$ = 6, $D_{st\min}$ = = –81 nT) followed. As a result, we observed such effects: during the main phase of magnetic storm, h_mF2 increased by 75—80 km, after which h_mF2 decreased by 40—45 km and the strongest negative ionospheric disturbance has occurred, N_mF2 decreased by 4.6 times.

As a whole, the chain of successive disturbances of the Earth magnetosphere complicated the mechanisms of ionosphere effects. Thus, on 16 April during the recovery phase of magnetosphere, a significant decrease in N_mF2 by more than 2 times continued to be observed.

Observations of the mid-latitude ionosphere during the solar eclipses

The solar eclipse (SE) on 1 September 2016 [13]. An analysis of the data obtained as a result of measurements of ionospheric parameters over Kharkov on September 1, 2016 was carried out. Changes were identified in the temporal variations of the vertical plasma drift velocity, critical frequency, and F2 peak height, which caused by the solar eclipse in the southern hemisphere and associated with the processes of interaction through the magnetosphere between the ionospheres of the magnetically conjugate regions of the Earth's southern and northern hemispheres. These changes were manifested in a decrease in the absolute value of the velocity of the downward motion of plasma in the ionosphere over Ukraine with an extremum 42 min after the maximum SE in the magnetically conjugate region. The velocity deviation amplitude increased with altitude and amounted to 5—45 m/s at altitudes of 200—580 km. At the same time, foF2 decreased by 0.7 MHz, and hmF2 increased by 30 km.

The solar eclipse on 10 June 2021 started at 10:42:03, ended at 12:12:48, and the maximum eclipse was at 11:28:18. The response of the ionosphere to the partial SE on 10 June 2021 with a small obscuration of the Sun (0.112 in diameter, 0.044 in area) at the studied altitudes of 180—500 km was very weak or absent at all, in contrast to results of previous observations of solar eclipses over Kharkiv with greater obscuration of the Sun's disk area (0.31 and more) [13].

The solar eclipse on 25 October 2022 [14, 15]. The results of observations of f_oF2, N_mF2 and h_mF2 of the ionosphere over Kharkiv during a partial SE on 25 October 2022 have been obtained using the digital ionosonde. The beginning, maximum, and end of the SE were at 09:29, 10:45, and 11:59 UT, respectively; the obscuration of the solar disk area was 57.2%, and the magnitude was 0.66. This experiment is unique because the days before the SE (from 22 October to the beginning of 24 October), a geomagnetic storm was observed, and the consequences of its influence could remain; a temporary decline in the diurnal variation of f_oF2 (and N_mF2, respectively) was observed, which coincided in time with the SE; and fluctuations in f_oF2 and h_mF2 diurnal variations were also detected (Fig. 6).

To study longitudinal effects and clarify contributions of different factors to the observed temporal variations of the ionospheric parameters, the results of observations of the ionosphere over Kharkiv were compared with the data obtained by the ionosonde in Pruhonice. In Pruhonice, the start of the SE was at 09:13 UT and the end was at 11:23 UT. The maximum eclipse was at 10:17 UT (the obscuration of the solar disk area was 30.2%, and the magnitude was 0.42). The comparison was carried out for the universal coordinated time (UT) to take into account the global factors influencing the ionospheric parameters, for the local time (LT) to take into account diurnal variations, and when the moments of the maximum phase of the SE in Kharkiv and Pruhonice were superposed to highlight the direct effect of the SE. A comparative analysis of variations in the ionospheric parameters over Kharkiv and Pruhonice showed that the SE effect in Pruhonice was similar, but less than in Kharkiv, which is explained by a smaller solar obscuration in

Pruhonice (by 1.58 times in eclipse magnitude and 1.89 times in obscuration of the solar disk area). To separate the effect of the solar eclipse from the usual diurnal f_oF2 variation, the data of measurements in Pruhonice on 25 October were used. The calculation of the effect caused directly by a solar eclipse is presented in [14]. Assuming that on 25 October the critical frequency decreased in Kharkiv due to the diurnal factor by the same factor as in Pruhonice (1.24), we determined that the f_oF2 frequency decreased due to the SE in Kharkiv by the factor of 1.23, in contrast to 1.15 times in Pruhonice. Accordingly, the N_mF2 electron density decreased due to SE by the factor of 1.51 in Kharkiv, in contrast to 1.33 times in Pruhonice. Similar results were obtained using data from the Kharkiv ionosonde on 26 October.

The new data obtained will complement the existing understanding of solar eclipse effects and can be used in fundamental studies of solar-terrestrial interaction.

Traveling ionospheric disturbances

Characteristics of traveling ionospheric disturbances during 23—24 September 2020 magnetic storm [16]. We employed three ionosondes and Kharkiv incoherent scatter radar located in Europe to investigate the ionospheric processes during the moderate magnetic storm. Observations showed that a positive ionospheric storm developed during 23—24 September 2020. We detected, characterized and discriminated the large scale traveling ionospheric disturbances (LSTIDs) passed over Kharkiv, Juliusruh and Pruhonice. The key results provided during these coordinated observations are summarized as follows [13].

We revealed several time intervals where the LSTIDs occurred propagating equatorward from higher latitudes and generated during the enhanced auroral activity. There were observed concurrent uplifts of the F2 layer over Juliusruh and Pruhonice, indicating that the traveling atmospheric disturbances (TADs) propagated equatorward with a velocity of about 600 m/s. The relative amplitudes were less over Kharkiv (0.05—0.08) than over Juliusruh and Pruhonice (0.14—0.19). Such LSTIDs were observed almost simultaneously over all three sites and had very comparable dominant periods of 135—150 min and 165—180 min for the first and the second time interval, respectively. They propagated with the horizontal phase velocities of 546 m/s and 576 m/s. Due to the close TAD and LSTID velocities, we can conclude that these ionospheric disturbances were imposed by acoustic gravity waves (AGWs) propagated from high latitudes.

The ionosphere-plasmasphere system

The impact of the exosphere hydrogen (H) density on the entire ionosphere-plasmasphere system was explored [17] using a model whose key inputs were constrained by ionosphere observations at both ends of the magnetic field line with an L-value of 1.75 in the American longitudinal sector during a period with low solar and magnetic activities. This study is the first to be validated by ground-based (digisondes) and satellite (DMSP, Arase) data in the plasmasphere and both hemispheres. The main findings are the following:

1) The entire ionosphere-plasmasphere system is highly sensitive to the neutral hydrogen density in the lower exosphere. Increasing the H density by a factor of 2.75 from the standard NRLMSISE-00 values increases the simulated plasma density in the afternoon plasmasphere up to ~80% and in the nighttime topside ionosphere up to ~100%, bringing the simulated densities into agreement with the Arase and DMSP satellite observations. The last point indicates that using the NRLMSISE-00 H density causes unacceptable errors in the simulated plasma density of the near-Earth plasma shells. We alert the space science community of this problem.

2) The high sensitivity obtained for the American longitudinal sector for L = 1.75 agrees well with the high sensitivity previously seen in the simulations in the European sector at L = 2.1.

The concept of the hot hydrogen exobase [18] was refuted [19] using observational data by incoherent scatter radar of Institute of Ionosphere, exospheric satellite missions (Dynamics Explorer 1 and TWINS), and ground based spectrometer (WHAM). It was concluded that the existence of large amounts of hot H atoms near the exobase is not supported either by independent observations of H atom temperature and density or by numerous observations of hydrogen ion and electron densities conducted with different independent techniques. Conducted near the exobase, in the exosphere, ionosphere, and plasmasphere for various levels of solar activity, seasons, and geographical regions, these independent observations provide comprehensive support for the classic cold hydrogen concept.

Modernization of measuring systems, improvement of measurement and processing methods

In 2021—2023, the modernization of analog and digital components of radar systems continued, as well as the further improvement of methods of obtaining and processing ionospheric data [1, 20—25]. On key issues, Ukraine patents were obtained [26—28].

REFERENCES

1. Emelyanov L.Ya., Chernogor L.F., Lyashenko M.V., Miroshnikov A.E., Aksonova K.D. Plasma motion in the ionosphere: a study by the incoherent scatter technique. Kharkiv: PLANETA-PRINT LLC, 2021. 460 p.

2. Emelyanov L.Ya., Panasenko S.V. Comparison of ionospheric plasma drift velocity measurement results obtained at middle latitudes of the Earth's eastern and western hemispheres using incoherent scatter radar data. *International Conference Astronomy and Space Physics,* October 18 — October 21, 2022. Kyiv, Ukraine. Book of Abstracts. Kyiv, 2022. P. 91—92.

3. Kolodyazhnyi V.V., Lyashenko M.V., Emelyanov L.Ya., Dzyubanov D.A. Modeling of spatial-temporal variations of dynamic and thermal process parameters in geospace over Ukraine during the minimum of 24-th cycle of solar activity (2009, 2019). *Space Science and Technology*. 2023. 29, No. 1(140). P. 15—35. https://doi.org/10.15407/knit2023.01.015

4. Kolodyazhnyi V.V., Lyashenko M.V., Emelyanov L.Ya., Dziubanov D.A. Modeling of spatial-temporal variations of physical process parameters in the ionospheric plasma over Ukraine during the maximum phase of the 24-th solar activity cycle (2012—2015). *Space Science and Technology.* 2024. 30, No. 1. P. 44—65. https://doi.org/10.15407/knit2024.01.044

5. Yasar M., Sagir S., Emelyanov L., Lyashenko M., Korlaelci S., Atici R. Calculation of the Ionospheric Cross-Section with the Incoherent Scattering Radar and Its Comparison with the Predictions of the IRI Model. *Wireless Pers Commun*. 2023. 132. P. 487—503. https://doi.org/10.1007/s11277-023-10619-6

6 Emelyanov L.Ya., Katsko S.V., Lyashenko M.V., Chernogor L.F., Ionosphere response to geospace storm on 25 September 2016 over Kharkiv (Ukraine). *Advances in Space Research.* 2023. 71, Is. 8. P. 3323—3345. https://doi.org/10.1016/j.asr.2023.02.004

7. Katsko S.V., Emelyanov L.Ya., Chernogor L.F. Features of the ionospheric storm on December 21—24, 2016. *Kinematics and Physics of Celestial Bodies*. 2021. 37, No. 2, P. 85—95. https://doi.org/10.3103/S0884591321020045

8. Katsko S.V., Emelyanov L.Ya., Chernogor L.F. Ionosphere response to space weather events on 21—23 March 2017 in the central region of Europe. *URSI GASS 2021, Rome, Italy, 28 August — 4 September 2021. Conference Proceedings*. 2021. https://doi.org/10.23919/URSIGASS51995.2021.9560587

9. Emelyanov L.Ya., Katsko S.V. The reaction of the ionosphere over Kharkiv to the geospace storm of September 23—24, 2020, during the period of low solar activity. *XXIX International scientific and practical conference: Information technologies: science, engineering, technology, education, health (MicroCAD-2021)*, May 18—20, 2021, Kharkiv: abstracts. Part III. Kharkiv, 2021. P. 250.

10. Katsko S.V., Emelyanov L.Ya. Variations in the Middle-Latitude Ionosphere Parameters over Ukraine during the Very Moderate Magnetic Storm on December 18, 2019. *Kinematics and Physics of Celestial Bodies*. 2023. 39, No. 2. P. 78—89. https://doi.org/10.3103/s0884591323020034

11. Katsko S.V., Emelyanov L.Ya., Kolodyazhnyi V.V., Domnin I.F. Ionospheric positive storm phase on 18 December 2019 observed by the Kharkiv incoherent scatter radar. *URSI GASS 2023, Sapporo, Japan, 19—26 August 2023. Conference Proceedings*. 2023. https://doi.org/10.23919/URSIGASS57860.2023.10265568

12. Emelyanov L.Ya., Katsko S.V. Variations of the critical frequency of the F2 ionospheric layer over Kharkiv during long-term disturbed geomagnetic conditions in April 2022. *Information technologies: science, technology, technology, education, health: abstracts of reports of the XXXI international scientific and practical conference MicroCAD-2022*, May 17—20, 2023. Kharkiv, 2023. P. 1251.

13. Emelyanov L. Observation of ionospheric plasma motion over Kharkiv during solar eclipses on September 1, 2016, and June 10, 2021. *2022 IEEE 2nd Ukrainian Microwave Week (IEEE UkrMW-2022), "Microwaves, Radar and Remote Sensing" (MRRS),* 14—18 November 2022. Conference Proceedings. 2022. P. 604—609, https://doi.org/10.1109/UkrMW58013.2022.10037144

14. Emelyanov L.Ya, Bogomaz O.V, Chernogor L.F., Domnin I.F. Response of the mid-latitude ionosphere to the solar eclipse on 25 October 2022: results of F2-layer vertical sounding. *Advances in Space Research*. 2024. 73, Is. 5. P. 2338—2354. https://doi.org/10.1016/j.asr.2023.12.034

15. Emelyanov L.Ya., Bogomaz O.V. Observations of the mid-latitude ionosphere during the solar eclipse of October 25, 2022. *International Conference "Astronomy and Space Physics in the Kyiv University"*, May 23—May 26, 2023, Book of Abstracts. Kyiv, 2023. P. 93.

16. Panasenko S.V., Aksonova K.D., Burešová D., Bogomaz O.V., Zhivolup T.G., & Koloskov O.V. Large-scale traveling ionospheric disturbances over central and eastern Europe during moderate magnetic storm period on 22—24 September 2020. *Advances in Space Research*. 2023. 72, No. 10. P. 4364—4378. https://doi.org/10.1016/j.asr.2023.09.035

17. Kotov D., Richards P., Reznychenko M., Bogomaz O., Truhlík V., Nossal S., Mierkiewicz E., Zhivolup T., Domnin I., Miyoshi Y., Tsuchiya F., Kumamoto A., Kasahara Y., Kitahara M., Nakamura S., Matsuoka A., Shinohara I. and Hairston M. Interhemispheric ionosphere-plasmasphere system shows a high sensitivity to the exospheric neutral hydrogen density: a caution of the global reference atmospheric model hydrogen density. *Front. Astron. Space Sci*. 2023. 10. https://doi.org/10.3389/fspas.2023.1113706

18. Qin J., Waldrop L. Non-thermal hydrogen atoms in the terrestrial upper thermosphere. *Nat. Commun*. 2016. 7, No. 13655. https://doi.org/10.1038/ncomms13655

19. Kotov D., Bogomaz O. Hydrogen atoms near the exobase are cold: independent observations do not support the hot exosphere concept. *Front. Astron. Space Sci.* 2023. 10. https://doi.org/10.3389/fspas.2023.1200959

20. Pulyaev V.O., Rogozhkin E.V., Emelyanov L.Ya., Bogomaz O.V., Katsko S.V., Shulga M.O. Calculation of statistical characteristics of the incoherent scattering signal. Kharkiv: PLANETA-PRINT LLC, 2021. 236 p.

21. Emelyanov L., Rogozhkin E., Pulyayev V. Features of Reception of Signals with Linear and Circular Polarization in the Incoherent Scatter Technique. *2022 IEEE 41th International Conference on Electronics and Nanotechnology (ELNANO).* Kyiv, October 10—14, Ukraine. Conference Proceedings. 2022. P. 529—534. https://doi.org/10.1109/ELNANO54667.2022.9927099

22. Rogozhkin Ye.V., Emelyanov L.Ya., Pulyayev V.O., Domnin I.F., Miroshnikov A.Ye., and Kuzmenko N.O. Hardware and algorithmic features of radiation, reception and processing of signals using incoherent scatter technique. *Radioelectronics and Communications Systems*. 2022. 65, No. 11. P. 609—620. https://doi.org/10.3103/s0735272722120056

23. Emelyanov L., Miroshnikov A. Development of methodological, hardware, and software of the incoherent scatter radar of Institute of Ionosphere (Kharkiv, Ukraine). *International Journal of Electronics and Telecommunications*. 2023. 69, No. 3. P. 579—586. https://doi.org/10.24425/ijet.2023.146510

24. Rogozhkin E., Pulyayev V., Kuzmenko N. Peculiarities of Using the Digital Format in Computational Processing of Coherent Radar Signals. *2022 IEEE 3th KhPI Week on Advanced Technology (KhPI Week).* Kharkiv, October 03—07, 2022, Ukraine, Conference Proceedings. 2022. P. 196—200. https://doi.org/10.1109/KhPIWeek57572.2022.9916377

25. Pulyayev V., Emelyanov L., Rogozhkin E., Kuzmenko N. Hardware Methods for Determination of the Characteristics of Incoherent Scatter Signals in Radar Remote Sensing. *2023 IEEE 4th KhPI Week on Advanced Technology (KhPI Week).* Kharkiv, Ukraine, October 02—06, 2023, Conference Proceedings. 2023. P. 227—232. https://doi.org/10.1109/KhPIWeek61412.2023.10312897

26. *Patent of Ukraine* No. 148777. The method of statistical analysis of solutions of the inverse scattering problem when determining the kinetic temperatures of the ionospheric plasma / Pulyaev V.O., Yemelyanov L.Ya., Panasenko S.V., Bogomaz O.V.; published 15.09.2021. Bull. No. 37 [in Ukrainian].

27. *Patent of Ukraine* No. 151831. The method of calculating the altitudinal distribution of the electron concentration of the ionospheric plasma / Rogozhkin E.V., Pulyaev V.O.; published 21.09.2022. Bull. No. 38 [in Ukrainian].

28. *Patent of Ukraine* No. 153522. The method of calculating kinetic temperatures of ionospheric plasma using the method of incoherent scattering / Pulyaev V.O., Lyashenko M.V., Kotov D.V.; published 19.07.2203. Bull. No. 29 [in Ukrainian].

EXTRACELLULAR MEMBRANE VESICLES AS POSTBIOTICS AND MUCOSA VACCINE IN PREVENTING HUMAN HEALTH DISORDERS ASSOCIATED WITH SPACEFLIGHT

O. Podolich, G. Zubova, H. Melnyk, I. Zaets, N. Kozyrovska

Intitute of Molecular Biology and Genetics of the NAS of Ukraine

Innovative strategies are developing to mitigate the profound physiological effects of spaceflight-related factors on the human body. The new-generation postbiotics, are non-living products of microorganisms, which do not alter under unfavorable or harsh conditions, unlike probiotics, and perform the same health-promoting function more effectively and safely than parental probiotic microbial cells. Here, we underscore the promising role of postbiotics derived from fermenting beneficial microorganisms for the prevention of health disorders during space missions. We pioneered the concept that microbial extracellular vesicles (MEV) as postbiotics may significantly contribute to astronauts' health, potentially serving as a temporary substitute for living microbial cells until more is known about the microbial cell behavior in the space environment.

The spaceflight-related factors affect not only human cells but also host microbiomes

The *human microbiome* can be defined as an organized assemblage of microbial communities inhabiting a specific niche in the body and physiologically responding to the host. In particular, the *gut* microbiome (GM) plays a crucial role in maintaining the overall health of astronauts during space travel. It affects the general immune system, metabolism, and mental strength. Microgravity, radiation exposure, and altered diet can disrupt the balance of microbiome. Using murine/rodent models, the authors hypothesized that microgravity alters more the metabolic environment of the gut microbes than microbes *per se* [1, 2]. Space factors affect fluid shear dynamics, the gut peristaltic, and microbes' physiological and behavioral responses to the host. The gut microbiota adapts to these changes by altering community structure, diversity, and richness, which can substantially impact the host's biological functions. Human microorganisms adapt quickly by rapidly acquiring needed genes to survive harsh conditions [3]. Changes in the GM composition can cause infection due to the overgrowth of pathogens and a weakening immune system. In short-term space travel, it was discovered that alterations in the composition and functionality of the gut microbiome could be induced. Liu et al. [4] reported shifts between dominant genera in the microbiome during space missions of up to 35 days that led to an increased abundance of unwanted *Bacteroides* and a decrease of the beneficial taxa *Lactobacillus* and *Bifidobacterium.* Under long-term space travel, the crew GM composition changed with a specific increase in the *Firmicutes*-to-*Bacteroidetes* ratio and became more similar between astronauts, as well as comparable to the microbiome composition of skin, nose, and tongue [5]. Moreover, the authors have reported an increase in genera associated with chronic intestinal inflammation and a reduction in the relative abundance of the genera with anti-inflammatory properties. At the same time, the experiment tracking the astronaut's microbiome, compared with the ground-staying twin, showed no changes in the richness; nonetheless, the composition of the infight microbiota samples significantly changed [6]. This could result from the flight's imposed conditions, including the absence of live products and decreased dietary fiber in the astronaut's diet. Supplementing live microbial foods may reduce the impact of space-related factors on the gut microbiota. Innovative technologies such as "smart toilets" for monitoring astronauts' gut microbiome will invest in maintaining their health [7]; however, microbial therapeutics should be envisioned along with the correcting therapy.

The gut microbiota modifying therapeutics to treat spaceflight-related health disorders

Maintaining healthy GM during interplanetary journeys to Mars or other celestial bodies will be challenging in the context of the abovementioned factors. The gut-brain axis, immunity, and gut health can be improved by ensuring the gut microbes' normality. Several approaches to mitigating dysbiosis in crews are in progress for elaborating: 1) probiotics supplement; 2) fecal microbiota transplantation (FMT); 3) a genome-guided design of microbial consortium, *i.e.,* a rationally selected collection of defined microbes for the GM engineering, etc.; 4) reconstruction of an Earth-like biosphere and interrelationships with the surrounding biota through a bioregenerative life support system described by [8]. As the human gut microbiota is sensitive to orbital spaceflight, physiological adaptation to the new environment in future exploration missions will be more complicated than in the International Space Station (ISS), leading to more changes in different body systems, including the gut microbiome. Numerous recommendations have been formulated on correcting gut microbiota to keep the crew healthy and brains sharp [9]. Here, we emphasize measures

that include microbial therapeutics and postbiotics instead of antibiotics or at least their combinations.

Probiotics perspectives on therapeutic microbes

Correction of astronauts' gut microbiome with microbial life therapeutics could be appropriate in analogy to ground practice. However, considered a peculiarity of spaceflight missions, therapeutic microbes have limitations in spaceflight practice because of insufficient knowledge about their nature and safety or the reinsurance of officials responsible for flight safety. Among therapeutic microbial organisms, probiotics are considered "a live microorganism(s) which, when administered in adequate amounts, confer a health benefit on the host" (according to the Food and Agriculture Organization of the United Nations [10]. The most studied probiotics are the lactic acid bacteria, particularly Lactobacillus and Bifidobacterium, which are normal inhabitants of the human and animal intestine; their presence is essential for maintaining the intestinal microbial ecosystem. Probiotics are necessary to maintain optimal immunity [11]. Direct effects of probiotics on other microbes convey two primary mechanisms of action: inducing their antimicrobial effects by producing bacteriocins (peptides naturally synthesized by ribosomes) and secreting bile acids; both destroy pathogenic bacterial membranes [12], so maintaining a balanced microbiota by administering probiotics and probiotic-based foods and beverages reduces antibiotic-resistant bacterial infections [13, 14].

It should be noted that probiotics are effective if there are indigestible foods in the diet. That is why prebiotics (food components that selectively stimulate the growth and/or activity of beneficial microorganisms directly in the human intestine) are recommended in the diet, and together with probiotics, these supplements form synbiotics. Synbiotics are often defined as 'synergistic mixtures of probiotics and prebiotics that beneficially affect the host by improving the survival and colonization of live beneficial microorganisms in the host's gastrointestinal tract' (FAO/WHO). Certain dietary fibers may preserve the probiotic efficacy by serving as the scaffold, *e.g.,* for probiotic Bacilli [15]. Synbiotics can modulate gut microbiota composition and microbial metabolite production [16].

Limitations of probiotics use

The criteria used for probiotics selection are highly stringent:

- be Generally Recognized As Safe (GRAS);
- survive through the gastrointestinal tract and colonize it;
- tolerate low pH and bile salts;
- produce antimicrobials and inhibit pathogens;
- do not possess transferable antibiotic-resistance genes;
- be of human origin (summarized in [17].

Some of these traits, e.g., the efficacy of probiotics to integrate into the host gut ecosystem, are variable [18]. One of the shortcomings of wild-type probiotics is their non-specificity. However, a given probiotic could be engineered to exhibit species-specific inhibition of the pathogen and its associated infection [19]. The long-term stability of lactic acid bacteria starters for probiotics production during extended space missions could be problematic because of the impact of radiation. Probably, spores of bacilli and cells of probiotics naturally incorporated into cellulose fibers might be used for in-flight probiotic/synbiotic food production in future missions [20—22]. Kombucha, as a probiotic-like fermented product, possesses excellent potential to be a therapeutic target in microbiota-related diseases such as colitis, metabolic syndrome, and immune diseases due to normalizing the GM [23—25], and its robustness under space/Mars-like conditions has been proven [26].

According to professionals and decision-makers, the use of living microbes for the prevention or correction of disorders in astronauts will require conducting research that meets all required norms known in national regulations for probiotic microbes design, including genetic level (genes for pathogenicity and toxicity, mobile genetic elements, viruses, and known molecular mechanisms that improve human health [27]. The next level is to screen the crew for immunological tolerance against the probiotics and to prove the predicted beneficial effects. Then, a viable probiotics library for the crew should be built, and a personalized in-fight probiotics administration protocol should be established.

Despite progress in researching various microbiomes as candidates for microbial therapeutics, technologies exploiting a microbial structure and function remain limited and need to be enhanced by significant interdisciplinary collaborative efforts. The design of efficient living therapeutics is considered revolutionary [28]. However, humankind will spend a long time in labs and debates for these discoveries, but we need more time before traveling to Mars. In the meantime, astronauts cannot be on a long-distance mission without the support of their gut microbiome by biologicals [22]. Postbiotics as non-alive biologicals can be considered the interim stage of probiotics usage in the prophylaxis of health disorders of crewmembers during spaceflights. The term "postbiotics" as a promising inanimate MEV-based means for astronauts has been coined in our research [26].

Postbiotics based on extracellular membrane vesicles as an interim solution before the microbial therapy era in astromedicine

According to the International Scientific Association for Probiotics and Prebiotics, a postbiotic is "a preparation of inanimate microorganisms and/or their components that confers a health benefit on the host" [29]. Postbiotics refer to probiotic-derived products obtained from food-grade microorganisms that confer health benefits when administered in adequate amounts: secreted by viable cells metabolites, its by-products, the products of cell lysis [30], and cell nanostructures such as extracellular membrane vesicles [26, 31—33]. Recent research indicates that postbiotics / MEVs can have direct immunomodulatory and clinically relevant effects [32, 33]. In Fig. 1, postbiotics / MEVs are represented graphically.

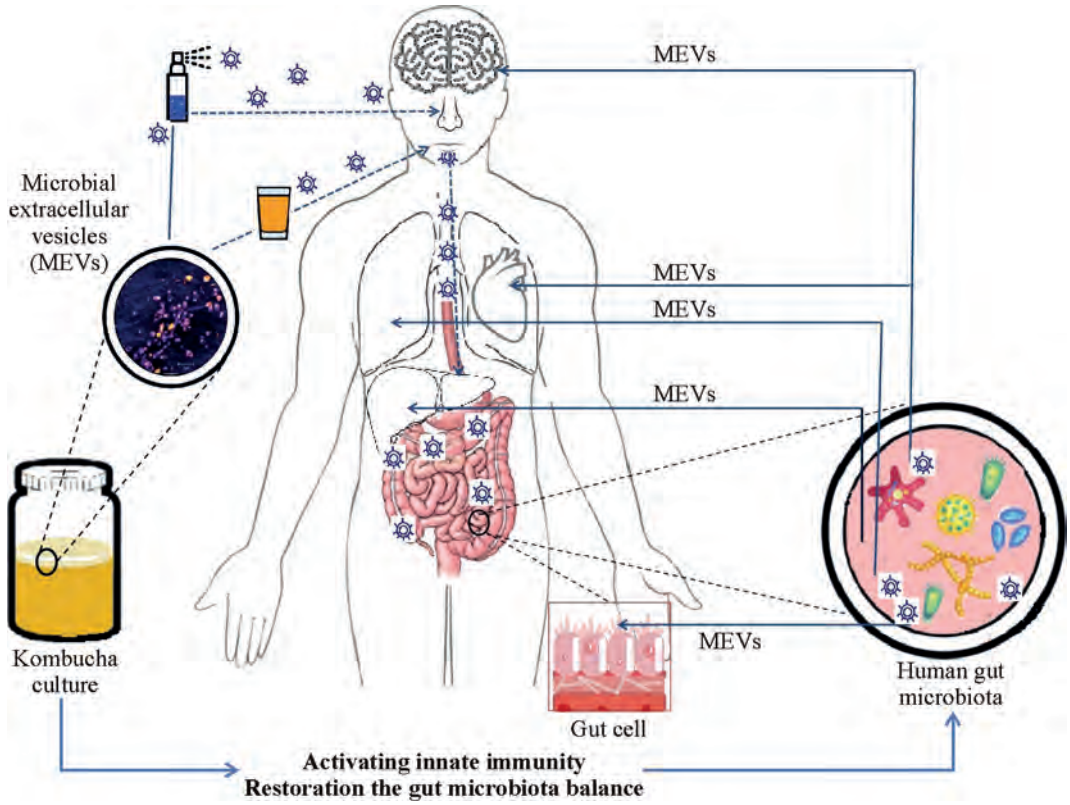

Fig. 1. Schematic presentation of microbial extracellular vesicle (MEV) postbiotics as products of food-grade bacteria, using the kombucha multimicrobial culture as an example. MEVs are a component of the kombucha secretome. The first way of entering the human body for MEVs is the consumption of a kombucha drink. Another way is when the isolated vesicles are used as a spray

Microbiota-secreted membrane vesicles are critical players in microbe-host communication

MEVs are nanoscale structures formed by a living cell and released into the extracellular space to perform biological functions [34, 35]. MEVs carry membrane and cytoplasmic proteins, DNA, various classes of RNA, lipids, ATP, and other bioactive molecules between cells of all three domains of life that secrete several types of nanosized membrane vesicles with different physiological properties. Although their biogenesis is different, they are all formed by phospholipid membranes and excreted by cells externally. All types of MEVs are incapable of self-reproduction and have no metabolism. However, they transfer bioactive molecules from one cell to another over long distances, overcoming the blood-brain barrier in a host body. Due to their unique properties, MEVs have become an attractive object of host-microbial research. More and more evidence appears that host-microbial crosstalk is mediated by MEVs released by gut microbiota [36—38]. In the gut ecosystem, bidirectional microbiota-host communication does not always depend on direct cellular contact, and it is performed by secreted microbial factors, *e.g.,* MEVs, that can penetrate the mucous layer and gain access to intestinal mucosa cells. In regenerative medicine, MEVs are a promising method of treating various diseases and non-healing wounds [33, 35, 39].

Biological functions of bacterial extracellular vesicles in host-microbe interactions

The functions and effects of MEVs on host physiology depend on the diversity of their cargo and the bacterial species, growth, and environmental factors that influence the latter. Bacteria package small molecules, proteins, and genetic material into MEVs to provide a supportive environment under interaction with the host, *e.g.,* enzymes that aid polysaccharide digestion in the gut or host-indigestible glycans and host mucins [40]. MEVs released by lactic acid bacteria deliver bacteriocins and thus kill pathogenic bacteria [41]. Non-coding small RNAs (sRNA) have important implications for regulating the host immune system and other cellular processes [42]. Probiotic beneficial effects, such as preventing pathogen expansion by transferring antimicrobials and modulating host innate and adaptive immunity, are summarized in [17]. MEVs produced by probiotic bacteria reduce the increased expression of pro-inflammatory cytokines and down-regulate enzymes associated with injury and inflammation [43]; activate dendritic cells and subsequent T-cell responses and protect the intestinal epithelial barrier function [44]; facilitate the delivery of signaling and fragile molecules, that could not survive under transportation, and regulate host-microbial communications though, *e.g.*, small non-coding RNAs in host [45].

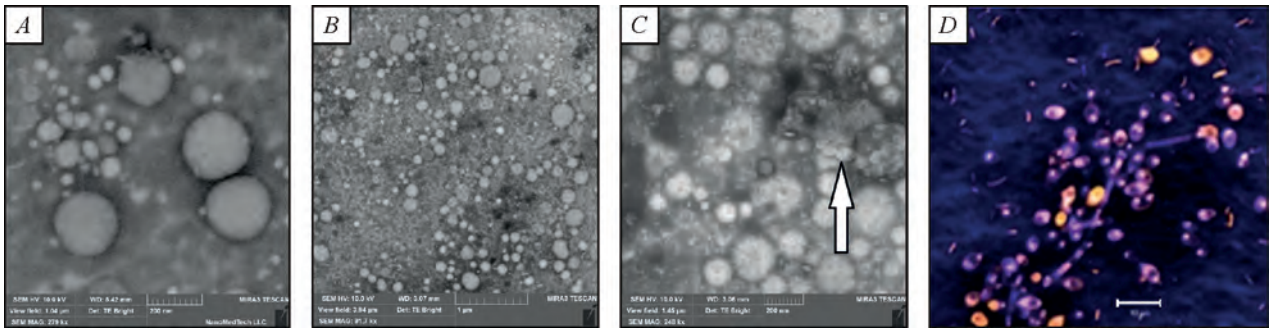

Fig. 2. Scanning electron micrographs of extracellular membrane vesicles (MEV) (*a*, *b*, *c*) generated from the kombucha multimicrobial community (KMC). MEV populations of the native (reference) KMC (*a*); the MEV populations of KMC samples, which were exposed on the the International Space Station in the astrobiological experiment BIOMEX (*b*, *c*) (an arrow indicates MEV aggregation). Kombucha's microbiome in confocal laser scanning microscopy (D). Scale bar: *a* — 200 nm; *b* — 1 μm; *c* — 200 nm; *d* — 10 μm [26]

MEVs as mediators of probiotic beneficial effects could be a safe free of bacteria strategy to preserve astronauts' health

A new generation of postbiotics, the MEV-based products, are expected to avoid the risks associated with the administration of living bacteria. Microbiota-derived vesicles play a role in many of the same activities as parent bacteria, but they have the advantage of access to blood circulation and the central nervous system. MEVs from beneficial bacteria can independently influence the host [40] and could be used concurrently with antibiotics and other antimicrobial agents. Nanosized MEVs also have a set of advantages over both alive and non-viable bacterial cells: they are quite safe, with reduced risk for adverse effects in vulnerable individuals with an impaired immune system (1); they have no risk for mutations (2); MEVs are not alive and cannot proliferate (3).

Extracellular membrane vesicles as a component of the KMC secretome

Production of spherical protein-lipid MEVs (20—500 nm) by KMC microbial cells is observed in bacteria and yeasts, covering both prokaryotes (gram-negative and gram-positive bacteria) and eukaryotes (yeasts). Fig. 2 shows MEVs of bacteria and yeast originating from the kombucha community. The KMC produces six to seven MEV populations composed of 50% of metavesicleome, with two significant populations of MEVs of a diameter of 141 and 164 nm, and the rest of the populations deviate in size. After the revival, the MEVs of exposed KMCs were characterized by different sizes and fraction numbers, depending on the nature of the stressors influenced. For example, MEVs from post-UV-protected KMC samples did not possess small-size fraction vesicles. However, they contained two significant populations with MEVs diameters of 164 and 190 nm, demonstrating a shift in the MEV average sizes.

In contrast, MEVs from unprotected samples produced smaller MEV populations. Most tested vesicle populations appeared to be of single membrane; however, outer-inner bacterial vesicles were also detected. Some deformations in vesicles and aggregations were observed in the KMC-exposed samples, exhibiting changes in the membrane lipidome. Membrane lipids such as sterols, fatty acids (FAs), and phospholipids (PLs) were modulated under the Mars-like stressors, and a level of saturated FAs increased, as well as both short-chain saturated and trans FAs appeared in the membranes of MEVs shed by both post-UV-illuminated and protected on the ISS bacteria. The relative content of zwitterionic and anionic PLs was altered and produced a change in the surface properties of outer membranes (summarized in [31]).

KMC MEVs do not acquire the toxicity under Mars-like stressors simulated on the low Earth orbit

Changes in microbial membranes inevitably affect their communications with hosts. Studying the impact of altered bionanostructures on the host *in vitro* and *in vivo* scenarios will be a vital task of aerospace medicine in developing new solutions for the intestinal microbiota health in astronauts' bodies. In our project, we show that, despite the change in the structure of cell membranes, MEVs isolated from the exposed ISS KMC samples in the BIOMEX project did not show endotoxicity, cytotoxicity, and possibly neuromodulation [31]. Treatment of murine embryonal fibroblasts and macrophages by MEVs/KMC at 0.05—50.0 μg/L concentrations did not affect cell growth [31]. The level of metavesicleome endotoxin activity from post-flight unprotected KMC samples was six times lower than in *E. coli*. The levels of endotoxin activity of MEV/*K. oboediens* from protected and unprotected KMC samples were almost the same as the activity of the reference KMC MEVs. Membrane vesicles of post-flight KMCs did not increase the L-[^{14}C] glutamate neurotransmitter level in synaptosome suspensions in the nerve terminals of the rat brains, *i.e.,* they do not acquire neuromodulation capacity [26].

The changed composition of cell membranes promoted changes in the MEV fitness

Biochemical characterization of the MEV-associated enzymes revealed increased activity (DNAses, dehydrogenases) when exposed to the space/Mars-like stressors

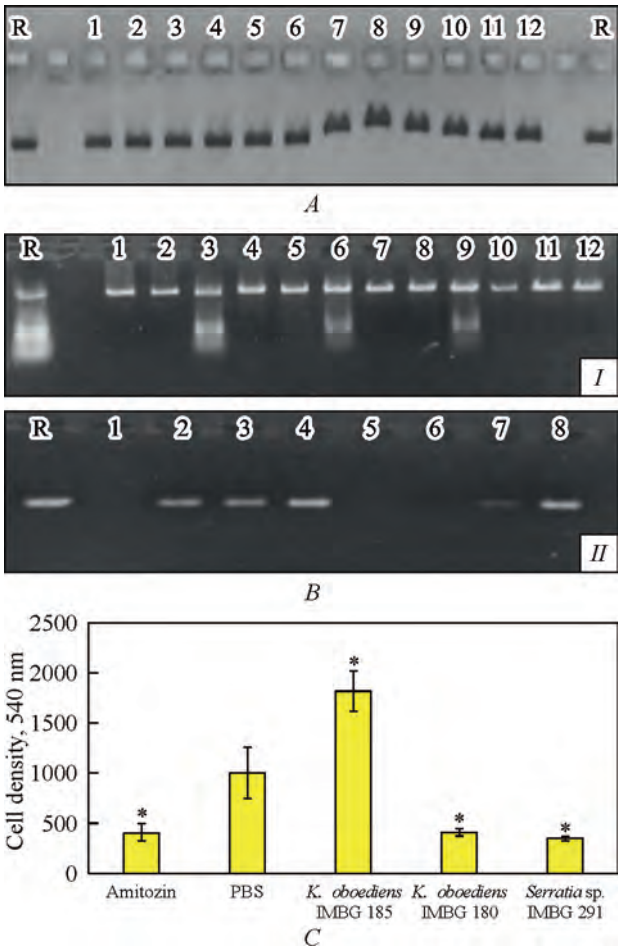

Fig. 3. Effects of membrane vesicles of *Komagataeibacter* spp. isolated from the post-flight kombucha microbial community (KMC) pellicle samples on the *in vitro* interactions with biomolecules: *a* — polynucleotide complexes generated after interacting *Komagataeibacter oboediens* vesicles with a linearized plasmid DNA. Vesicles of *K. oboediens* IMBG185 exposed to space / Mars-like factors do not interact with DNA in contrast to vesicles from reference strain *K. oboediens* IMBG180, as seen in the difference of DNA fragments mobility in agarose gel; *b* — I, II, the T7 bacteriophage RNA polymerase and *Taq* DNA polymerase were inhibited by higher vesicle concentration for exposed bacteria; *c* — a survival rate of human *in vitro* cells K-562 of chronic myeloid leukemia after co-cultivation with different concentrations of vesicles from exposed *K. oboediens* IMBG185 in comparison with ground reference strain IMBG180 and *Serratia marcescens* IMBG291 vesicles [46]

simulated on the ISS (E-MEV)s compared to wild-type MEVs. The role of the enzyme-associated MEVs from food-grade bacteria in human health and disease is not completely clear, particularly after stressful factors (changed gravity and atmosphere, UV-radiation) in the context of astronauts' diet. We researched E-MEVs of *K. oboediens* isolated from exposed KMC samples to know more about their behavior with biomolecules and mammalian cells. A proteogenomic approach predicted membrane translocation by the Sec translocon for RNase I and a periplasm location in the *K. oboediens* MEVs, and it was experimentally approved [46] (Fig. 3, *a*).

A series of *in vitro* experiments on the RNA cleavage, DNA and RNA transcription inhibition and cytotoxic assay with MEVs/Komagataeibacter were conducted. We concluded that the behavior of MEVs in bacteria before and after an impact of stressful conditions differed, relying on differences in associated nucleolytic activity, the inhibitory capabilities against the T7 bacteriophage RNA polymerase and Taq DNA polymerase, and in a cytotoxic effect, despite just minor changes in genomes (Fig. 3, *b*, I, II). The *in vitro* inhibition of RNA and DNA transcriptions was less pronounced in E-MEVs than in vesicles of the ground-based strain. It correlated with a lower RNase activity and a loss of cytotoxicity towards human malignant cells, even five years after the spaceflight. The general conclusion was that Komagataeibacter's MEV-associated activities were modified after exposure to the ISS and inherited in a non-genetic manner, relying on the comparative genomic data [47] (Fig. 3, *c*).

Vesicles exposed to space / Mars-like factors acquired the capacity to fuse with eukaryotic-like membranes

After long-term exposure to the harsh environment, the membranes of bacteria within the KMC were changed as they were the first line in stress resistance. In the study by [48], we describe the acquired capacity of E-MEVs from *K. oboediens* to fuse to different types of model planar bilayer lipid membranes simulating eukaryotic ones in comparison with the unchanged MEVs of the ground-based reference strain. The most reliable fusion was achieved with PC:PE:ergosterol or sterol-free PC:PE bilayers [48]. Separate step-like increases in its conductance confirmed the fusion of E-MEVs with planar bilayer lipid membranes. In contrast, the ground-based reference *K. oboediens* MEVs never induced the fusion event. In our study, except membrane lipidome perturbations, we showed increased protein aggregation in the exposed samples when the outer membranes of *K. oboediens* acquired fusion capability, possibly by altered membrane fluidity and the pore-forming capability (Fig. 4). These data can be used to design vehicles for efficient delivery of drugs/biologicals to host cells.

In vivo interaction of *K. oboediens* MEVs with murine cells

The next step in the study of the effect of modified E-MEVs on the host was the labeling and introduction of them into the mouse body to observe the fate of bacterial vesicles *in vitro* murine cells and *in vivo* in the mouse body. The purified E-MEVs of *K. oboediens* were stained with the lipophilic dye DIO (Benzoxazolium, 3-octadecyl-2-[3-(3-octadecyl-2(3H)-benzoxazolylidene)-1-propenyl]-perchlorate, λEx/λEm (MeOH) = 484/501 nm (488/530) (Fig. 5, *a*), and stained washed MEVs were introduced first into murine fibroblasts. Stained vesicles almost wholly filled the contents of the cells, except nuclei (Fig. 5, *b*).

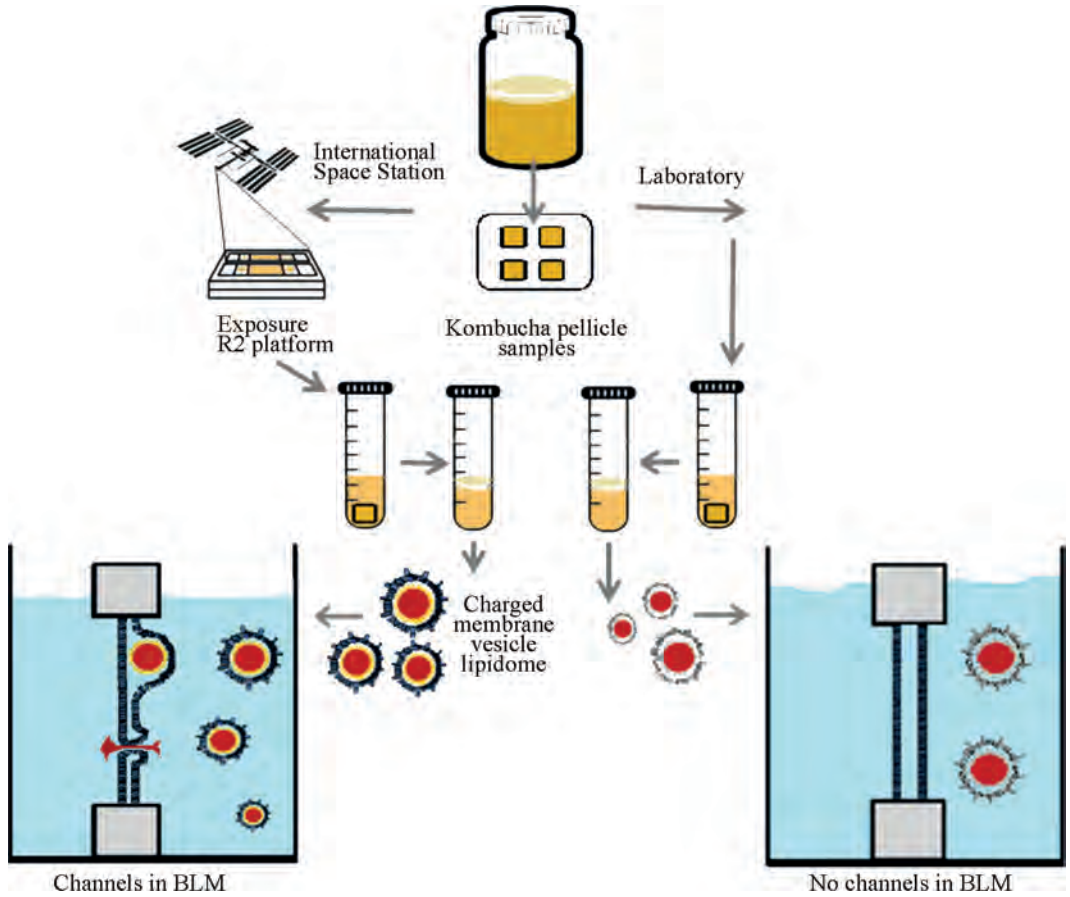

Fig. 4. Schema describes the acquired capacity of vesicles generated from bacteria exposed to space/Mars-like stressors simulated on the International Space Station to fuse to model planar bilayer lipid membrane [48]

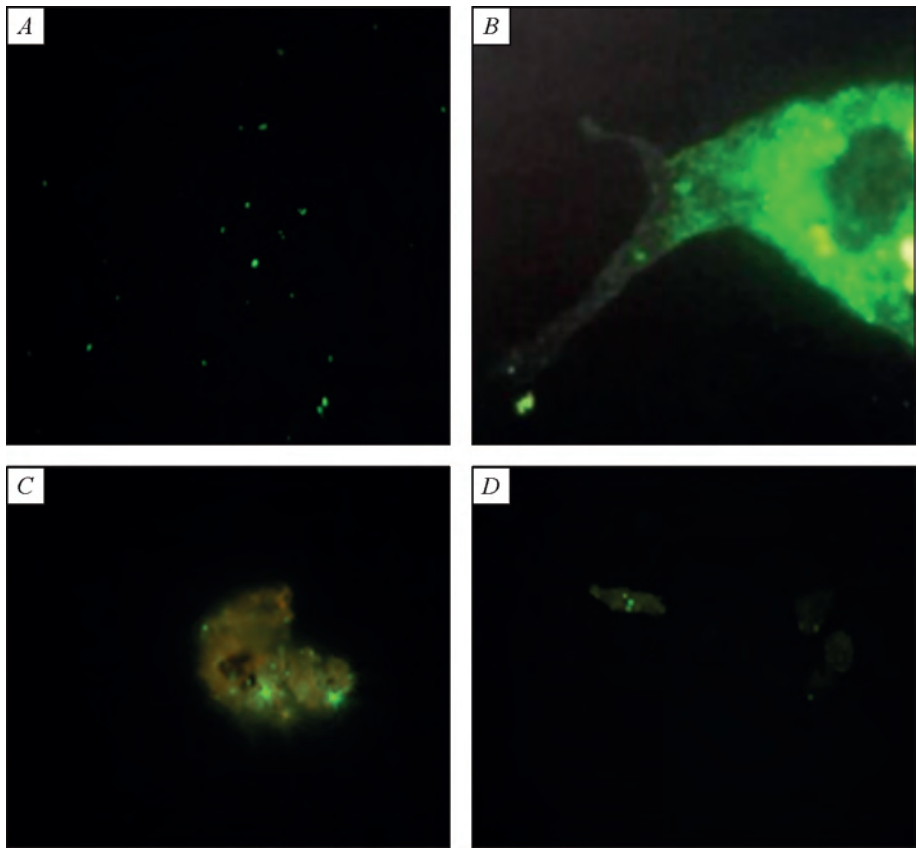

Fig. 5. Interaction of *Komagataeibacter oboediens* E-MEVs with mouse cell cultures *in vitro* (*a*, *b*) and *in vivo* (*c*, *d*). Labeled with lyophilic dye E-MEVs (*a*) enter murine *in vitro* fibroblasts (*b*), peritoneal macrophages (*c*), and fibroblasts (*d*). Scale x 100

Marked vesicles were injected into the mouse peritoneal cavity, and the prints within the entire surface area of the abdominal cavity were made after two hours in euthanized animals. The introduced E-MEVs were densely distributed not only at the injection site but over the entire surface of the cavity, as seen in prints under a fluorescent microscope. In addition, macrophage and fibroblast cells were isolated, and green fluorescence was observed inside them using the microscope's blue filter (Fig. 5, *c*, *d*). In summary, modified under spaceflight vesicles densely colonize the abdomen after the intraabdominal injection; however, macrophages clean up the cavity from alien nanostructures. Future research on GRAS microbe-derived MEVs is needed to understand their systemic spread in animal's body and their fate there.

Conclusion

While the use of live microbial organisms during spaceflights is being debated, MEVs from probiotic and gut commensal bacteria or GRAS communities like kombucha could be efficient in protective mucosal immunization through various routes, as well as in the restoration of the gut microbiota. The mucosal vaccine can be produced *in situ* using MEVs generated from safe, rationally selected microbial organisms for microbiome targeting. Studies with KMC/Komagataeibacter's MEVs have shown that there is a reason to believe that they are safe, and the use of these MEVs might be beneficial in training the nascent immune system and downregulating inflammations. MEV-based products are expected to avoid the risks associated with administering live bacteria. They can be considered the interim stage of the probiotic use to prevent crewmember health disorders until probiotics safety is proven. Furthermore, bacterial MEVs could also be used as suitable drug/gene delivery vectors for the *in situ* production and applications in aerospace medicine. Future research on GRAS microbe-derived MEVs is needed to open new possibilities for crews using bioactive therapeutic molecules in space missions.

Funding this work was supported by the National Academy of Sciences of Ukraine (grant 49/1).

REFERENCES

1. Jiang P., Green S.J., Chlipala G.E., Turek F.W., Vitaterna M.H. Reproducible changes in the gut microbiome suggest a shift in microbial and host metabolism during spaceflight. *Microbiome.* 2019. 7. P. 113. https://doi.org/10.1186/s40168-019-0724-4

2. Siddiqui R., Qaisar R., Khan N.A., Alharbi A.M., Alfahemi H., Elmoselhi A. Effect of microgravity on the gut microbiota bacterial composition in a Hindlimb unloading model. *Life.* 2022. 12. P. 1865. https://doi.org/10.3390/life12111865

3. Rosenberg E. Rapid acquisition of microorganisms and microbial genes can help explain punctuated evolution. *Front. Ecol. Evol*. 2022. 10. P. 10. https://doi.org/10.3389/fevo.2022.957708

4. Liu Z., Luo G., Du R., Sun W., Li J., Lan H. et al. Effects of spaceflight on the composition and function of the human gut microbiota. *Gut Microbes*. 2020. 11(4) . P. 807—819. https://doi.org/10.1080/19490976.2019.1710091

5. Voorhies A.A., Mark Ott C., Mehta S., Pierson D.L., Crucian B.E., Feiveson A., Oubre C.M. et al. Study of the impact of long-duration space missions at the International Space Station on the astronaut microbiome. *Scientific Reports.* 2019. 9. P. 9911. https://doi.org/10.1038/s41598-019-46303-8

6. Garrett-Bakelman F.E., Darshi M., Green S.J., Gur R.C., Lin L., Macias B.R. et al. The NASA Twins Study: A multidimensional analysis of a year-long human spaceflight. *Science*. 2019. 364(6436), eaau8650. https://doi.org/10.1126/science.aau8650

7. Krittanawong C., Singh N.K., Scheuring R.A., Urquieta E., Bershad E.M., Macaulay T.R., Kaplin S., Dunn C., Kry S.F., Russomano T., Shepanek M., Stowe R..P, Kirkpatrick A.W., Broderick T.J., Sibonga J.D., Lee A.G., Crucian B.E. Human Health during Space Travel: State-of-the-Art Review. *Cells.* 2023. 12(1). P. 40. https://doi.org/10.3390/cells12010040. PMID: 36611835; PMCID: PMC9818606.

8. Hao Z., Li L., Fu F., Liu C. The influence of bioregenerative life-support system dietary structure and lifestyle on the gut microbiota: a 105-day ground-based space simulation in Lunar Palace 1. *Environ Microbiol*. 2018. 20. P. 3643—3656. https://doi.org/10.1111/1462-2920.14358.

9. Al K.F., Chmiel J.A., Stuivenberg G.A., Reid G., Burton J.P. Long-Duration Space Travel Support Must Consider Wider Influences to Conserve Microbiota Composition and Function. *Life*. 2022. 12(8). P. 1163. https://doi.org/10.3390/life12081163

10. Food and Agriculture Organization. Probiotics in food: health and nutritional properties and guidelines for evaluation. *Food and Agriculture Organization*, Rome, Italy. 2006.

11. Maldonado G.C., Cazorla S.I., Lemme Dumit J.M., Vélez E., Perdigón G. Beneficial effects of probiotic consumption on the immune system. *Ann Nutr Metab*. 2019. 74(2). P. 115—124. https://doi.org/10.1159/000496426

12. Elshaghabee F.M.F., Rokana N. Mitigation of antibiotic resistance using probiotics, prebiotics and synbiotics. A review. *Environmental Chemistry Lett*. 2022. 20(2). P. 1295—1308. https://doi.org/10.1007/s10311-021-01382-w

13. Thapa S. P., Koirala S., Anal A.K. Potential of probiotics as alternative sources for antibiotics in food production systems. Eds Parmjit Singh Panesar, Anil Kumar Anal. 2022. https://doi.org/10.1002/9781119702160.ch8

14. Wieërs G., Verbelen V., Van Den Driessche M., Melnik E., Vanheule G., Marot J.-C., Cani P.D. Do probiotics during in-hospital antibiotic treatment prevent colonization of gut microbiota with multi-drug-resistant bacteria? A randomized placebo-controlled trial comparing saccharomyces to a mixture of lactobacillus, bifidobacterium, and saccharomyces. *Frontiers in Public Health.* 2021. 8, 578089. https://doi.org/10.3389/fpubh.2020.578089

15. Szlufman C., Shemesh M. Role of probiotic bacilli in developing synbiotic food: Challenges and opportunities. *Frontiers in Microbiology*. 2021. 12, 638830. https://doi.org/10.3389/fmicb.2021.638830

16. Zawistowska-Rojek A., Tyski S. How to improve health with biological agents — Narrative review. *Nutrients*. 2022. 14(9), 1700. https://doi.org/10.3390/nu14091700

17. Domínguez Rubio A.P., D'Antoni C.L., Piuri M., Pérez O.E. Probiotics, their extracellular vesicles and infectious diseases. *Frontiers in Microbiology*. 2022. 13, 864720. https://doi.org/10.3389/fmicb.2022.864720

18. Han S., Lu Y., Xie J., Fei Y., Zheng G., Wang Z. et al. Probiotic gastrointestinal transit and colonization after oral administration: A long journey. Frontiers in cellular and infection. *Microbiology*. 2021. 11, 609722. https://doi.org/10.3389/ fcimb.2021.609722

19. Mathipa-Mdakane M.G., Thantsha M.S. Lacticaseibacillus rhamnosus: A suitable candidate for the construction of novel bioengineered probiotic strains for targeted pathogen control. *Foods*. 2022. 11(6), 785. https://doi.org/10.3390/ foods11060785

20. Fajardo-Cavazos P., Nicholson W.L. Shelf life and simulated gastrointestinal tract survival of selected commercial probiotics during a simulated round-trip journey to Mars. *Frontiers in Microbiology*. 2021. 12, 748950. https://doi.org/10.3389/fmicb.2021. 748950

21. Kozyrovska N., Reva O., Podolich O., Kukharenko O., Orlovska I., Terzova V. et al. To other planets with upgraded millennial kombucha in rhythms of sustainability and health support. *Frontiers in Astron. and Space Sci*. 2021. 8, 701158. https:// doi.org/10.3389/ fspas.2021.701158

22. Bharindwal S., Goswami N., Jha P., Pandey S., Jobby R. Prospective Use of Probiotics to Maintain Astronaut Health during Spaceflight. *Life*. 2023. 13(3). P. 727. https://doi.org/10.3390/life13030727

23. Xu S., Wang Y., Wang J., Geng W. Kombucha Reduces Hyperglycemia in Type 2 Diabetes of Mice by Regulating Gut Microbiota and Its Metabolites. *Foods*. 2022. 11(5). P. 754. https://doi.org/10.3390/foods11050754

24. Permatasari H.K., Nurkolis F., Gunawan W.B., Yusuf V.M., Yusuf M., Kusuma R.J., Sabrina N., Muharram F.R., Taslim N.A., Mayulu N., Batubara S.C., Samtiya M., Hardinsyah H., Tsopmo A. (2022) Modulation of gut microbiota and markers of metabolic syndrome in mice on cholesterol and fat enriched diet by butterfly pea flower kombucha. *Curr Res Food Sci*, 5:1251—1265. https://doi. org/10.1016/j.crfs.2022.08.005.

25. Bergström H. (2018) The effect of the fermented tea beverage kombucha on the gut microflora A double-blind placebo-controlled study. Lund University, Food Technology and Nutrition (M.Sc.), http://lup.lub.lu.se/student-papers/record/8954225.

26. Podolich O., Kukharenko O., Haidak A., Zaets I., Zaika L., Storozhuk O., et al.(2019). Multimicrobial kombucha culture tolerates Mars-like conditions simulated on low Earth orbit. *Astrobiology*, 19(2), 183—196. https://doi.org/10.1089/ast.2017.174627

27. Cunningham M., Azcarate-Peril M.A., Barnard A., Benoit V., Grimaldi R., Guyonnet D., Holscher H.D., Hunter K., Manurung S., Obis D., Petrova M.I., Steinert R.E., Swanson K.S., van Sinderen D., Vulevic J., Gibson G.R. (2021). Shaping the future of probiotics and prebiotics. *Trends in Microbiology*, 29(8), 667—685. https://doi.org/10.1016/j.tim.2021.01.003

28. Cruz N., Abernathy G.A., Dichosa A.E.K., Kumar A. (2022). The age of next-generation therapeutic-microbe discovery: Exploiting microbe-microbe and host-microbe interactions for disease prevention. *Infection and Immunity*, 90, № 5. https:// doi.org/10.1128/iai.00589-21

29. Salminen S., Collado M.C., Endo A., Hill C., Lebeer S., Quigley E.M.M., et al. (2021). The International Scientific Association of Probiotics and Prebiotics (ISAPP) consensus statement on the definition and scope of postbiotics. *Nature Revs Gastroenterology Hepatology*, 18(9), 649—667. https://doi.org/10.1038/s41575-021-00440-6

30. Wegh C.A.M., Geerlings S. Y., Knol J., Roeselers G., Belzer C. (2019). Postbiotics and their potential applications in early life nutrition and beyond. *Int. J. Molecular Sci*., 20(19), 4673. https://doi.org/10.3390/ijms20194673

31. Podolich O., Kukharenko O., Zaets I., Orlovska I., Palchykovska L., Zaika L., et al. (2020). Fitness of outer membrane vesicles from Komagataeibacter intermedius is altered under the impact of simulated Mars-like stressors outside the International Space Station. *Frontiers in Microbiology*, 11, 1268. https://doi.org/10.3389/fmicb.2020.01268

32. Martínez-Ruiz S., Olivo-Martínez Y., Cordero C., Rodríguez-Lagunas M.J., Pérez-Cano F.J., Badia J., Baldoma L. (2024) Microbiota-Derived Extracellular Vesicles as a Postbiotic Strategy to Alleviate Diarrhea and Enhance Immunity in Rotavirus-Infected Neonatal Rats. International *Journal of Molecular Sciences*, 25(2):1184. https://doi.org/10.3390/ijms25021184

33. Junhua Xie, Qiqiong Li, Shaoping Nie. (2024) Bacterial extracellular vesicles: An emerging postbiotic. *Trends in Food Science & Technology*, Volume 143, 104275, https://doi.org/10.1016/j.tifs.2023.104275

34. Fang Y., Wang Z., Liu X., Tyler B.M. (2022). Biogenesis and biological functions of extracellular vesicles in cellular and organismal communication with microbes. *Frontiers in Microbiology*, 13, 817844. https://doi.org/10.3389/fmicb.2022.817844

35. Effah C.Y., Ding X., Drokow E.K., Li X., Tong R. and Sun T. (2024) Bacteria-derived extracellular vesicles: endogenous roles, therapeutic potentials and their biomimetics for the treatment and prevention of sepsis. *Front. Immunol*., 15:1296061. https://doi. org/10.3389/fimmu.2024.1296061

36. Diaz-Garrido N., Cordero C., Olivo-Martinez Y., Badia J., Baldomà L. (2021). Cell-to-cell communication by host-released extracellular vesicles in the gut: Implications in health and disease. *Int. J. Molecular Sci*., 22(4), 2213. https://doi.org/10.3390/ ijms22042213

37. Diaz-Garrido N., Badia J., Baldomà L. (2022). Modulation of dendritic cells by microbiota extracellular vesicles influences the cytokine profile and exosome cargo. *Nutrients*, 14(2), 344. https://doi.org/10.3390/nu14020344

38. Wang S., Luo J., Wang H., Chen T., Sun J., Xi Q., Zhang Y. (2024) Extracellular Vesicles: A Crucial Player in the Intestinal Microenvironment and Beyond. International Journal of *Molecular Sciences*, 25(6):3478. https://doi.org/10.3390/ijms25063478

39. Aytar Çelik P., Derkuş B., Erdoğan K., Barut D., Blaise Manga E., Yıldırım Y., Pecha S., Çabuk A. (2022). Bacterial membrane vesicle functions, laboratory methods, and applications. *Biotechnology Advs*, 54, 107869. https://doi.org/10.1016/j.biotechadv.2021.107869

40. Haas-Neill S., Forsythe P. (2020). A budding relationship: Bacterial extracellular vesicles in the microbiota-gut-brain axis. *Int. J. Molecular Sci*., 21(23), 8899. https://doi.org/10.3390/ijms21238899

41. Dean S.N., Rimmer M.A., Turner K.B., Phillips D.A., Caruana J.C., Hervey W.J., Leary D.H., Walper S.A. (2020). Lactobacillus acidophilus membrane vesicles as a vehicle of bacteriocin delivery. *Front. Microbiol*., 11, 710. https://doi.org/10.3389/fmicb.2020.00710

42. Joshi B., Singh B., Nadeem A., Askarian F., Wai S.N., Johannessen M., Hegstad K. (2021). Transcriptome profiling of staphylococcus aureus associated extracellular vesicles reveals presence of small RNA-Cargo. *Frontiers in Molecular Biosciences*, 7, 566207. https://doi.org/10.3389/fmolb.2020.566207

43. Yamasaki-Yashiki S., Kawashima F., Saika A., Hosomi R., Kunisawa J., Katakura Y. (2024) RNA-Based Anti-Inflammatory Effects of Membrane Vesicles Derived from Lactiplantibacillus plantarum. *Foods*, 13(6):967. https://doi.org/10.3390/foods13060967

44. Olivo-Martínez, Y.; Bosch, M.; Badia, J.; Baldomà, L. (2023) Modulation of the Intestinal Barrier Integrity and Repair by Microbiota Extracellular Vesicles through the Differential Regulation of Trefoil Factor 3 in LS174T Goblet Cells. *Nutrients*, 15, 2437. HTTPS://DOI.ORG/10.3390/nu15112437

45. Yu S., Zhao Z., Hao P., Qiu Y., Zhao M., Zhou G., Zhang C., Kang J. and Li P. (2022) Biological Functions and Cross-Kingdom Host Gene Regulation of Small RNAs in Lactobacillus plantarum-Derived Extracellular Vesicles. *Front. Microbiol*., 13:944361. https://doi.org/10.3389/fmicb.2022.944361

46. Podolich O.V., Zubova G.V., Orlovska I.V., Kukharenko O.E., Shyryna T.V., Palchykovska L.G., Zaika L.A., Zaets I.E., Kozyrovska N.O. (2023) *Komagataeibacter oboediens* changes outer membrane vesicle-associated activities after exposure on the International Space Station. *Biopolymers and Cell*, 39(2):131—145. http://dx.doi.org/10.7124/bc.000A8D

47. Santana de Carvalho D., Kukharenko O., Orlovska I., Podolich et al (2022). The Space-Exposed Kombucha Microbial Community Member Komagataeibacter oboediens Showed Only Minor Changes in Its Genome After Reactivation on Earth. *Front. Microbiol*., 13:782175. https://doi.org/10.3389/fmicb.2022.782175

48. Orlovska I., Zubova G., Shatursky O., Kukharenko O., Podolich O., Gorid'ko T., Kosyakova H., Borisova T., Kozyrovska N. (2024) Extracellular membrane vesicles derived from *Komagataeibacter oboediens* exposed on the International Space Station fuse with artificial eukaryotic membranes in contrast to vesicles of reference bacterium. *Biochim Biophys Acta Biomembr.*, 1866(3):184290. https://doi.org/10.1016/j.bbamem.2024.184290.

THE PLANT CELL SIGNALLING SYSTEMS INVOLVED IN ADAPTATION TO MICROGRAVITY

A. Yemets, S. Plokhovska, R. Shadrina, O. Kravets, Ya. Blume

Institute of Food Biotechnology and Genomics of the NAS of Ukraine

As plants are essential components of bioregenerative life support systems for astronauts in spacecraft, understanding their response to microgravity and their ability to develop stress resistance and adapt to spaceflight factors is crucial for the advancement of space biology. Furthermore, within the confined environment of a spacecraft cabin, plants are exposed not only to microgravity but also to another significant stressor: ionizing radiation. Given the additional stress of ionizing radiation in spacecraft cabins, we investigated its effect on plants as a separate factor, as well as its combined effects with simulated microgravity using a clinostat. Building on our previous studies that established the importance of autophagy for plant adaptation to microgravity, we aimed to further explore this process under combined radiation and microgravity stress [1—3]. Our research demonstrated that simulated microgravity induces autophagy, a cellular recycling process involving the reorganization of microtubules during autophagosome

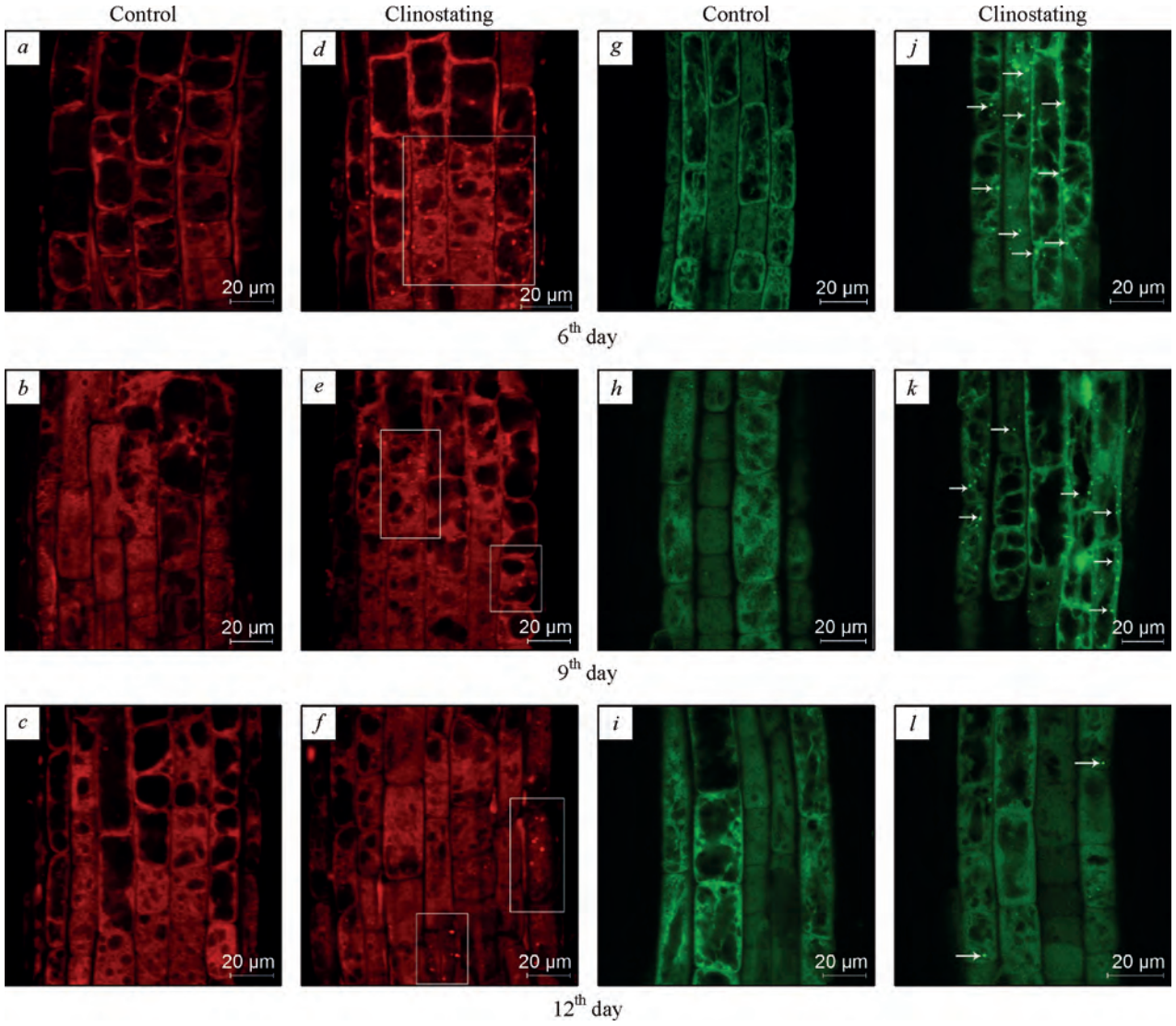

Fig. 1. Induction of autophagy by clinostating conditions on *A. thaliana* root cells: *a—f* roots treated with LysoTracker™ Red for visualization of autophagosomes in epidermal cells of the transition zone; *g* — l cells of the transition zone *A. thaliana* transgenic line with GFP-ATG8a-labeled autophagosomes (indicated by arrows). Bar — 20 μm

formation. To investigate this process further, we analysed α-tubulins, the expression of β-tubulins, and the ATG8 gene [3, 5, 7]. Given the critical role of autophagy in stress resistance and adaptation, studying this process becomes especially relevant for developing methods to enhance plant resilience to microgravity conditions, which was the goal of our further research. While modifications to signalling pathways, particularly those involving nitric oxide (NO), have been shown to enhance plant stress resistance [5, 7, 8], the role of NO in microgravity adaptation, including its potential involvement in autophagy induction, remains unexplored. Therefore, our study aimed to further investigate the role of autophagy in plant stress tolerance mechanisms under microgravity and explore methods to enhance plant resilience to these conditions. The main results of these studies are presented in the papers [3, 5, 7, 8].

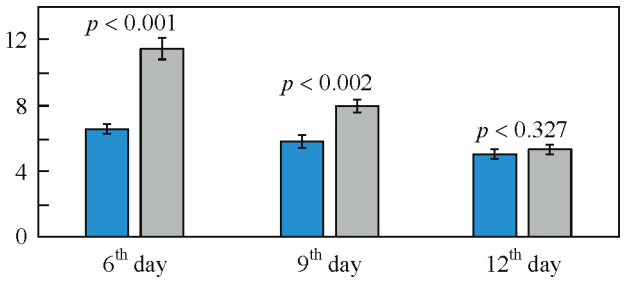

Fig. 2. Number of autophagosomes in plants of the transgenic GFP-ATG8a *A. thaliana* line after 12th day cultivation under clinostating condition. The significance level of the observed differences (p) in the number of autophagosomes per cell (n = 30) is indicated above the error bars (STD)

Clinostat-induced development of autophagy as an adaptive and cell homeostatic factor for strengthening stress resistance

Clinostat-induced development of autophagy was studied in wild-type and transgenic (GFP-ATG8a) *A. thaliana* root cells. A combination of methods was used to more accurately detect the development of autophagy in *A. thaliana* roots induced by simulated microgravity. For this, 6-, 9-, and 12-day-old WT seedlings were treated with LysoTracker™ Red (LTR) dye, and plants of the GFP-ATG8a line grown under the same conditions were used for parallel screening for the induction of clinostat-mediated autophagy (Fig. 1), as LTR can also stain different types of acidic organelles. It should be noted that individual autophagosomes were observed in root cells even in control plants, although their number increased during clinostating. On the 6th and 9th days of simulated microgravity (Fig. 1, *a*, *d*), the epidermal cells of the root transition zone showed an increase in autophagosome numbers compared to control conditions (Fig. 1, *b*, *e*), where autophagosomes were scarce. By the 12th day (Fig. 1, *f*), only a small number of autophagosomes remained in the root transition zone. These observations suggest that plants may be adapting to the stress of microgravity.

Similar dynamics of autophagy development were confirmed in the transgenic *A. thaliana* (GFP-ATG8a) line

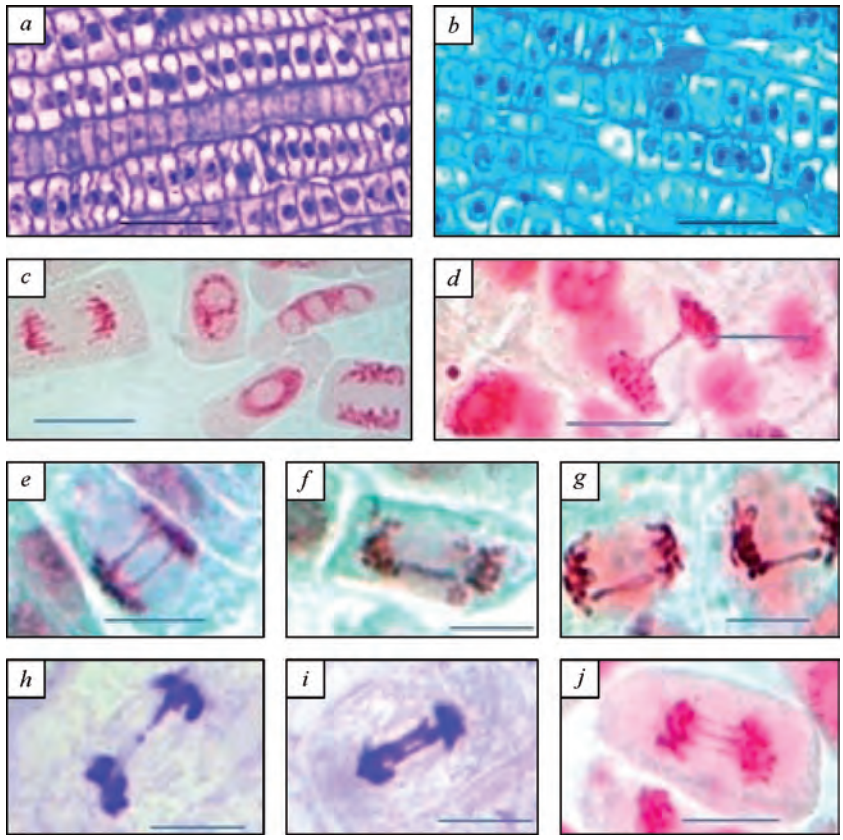

Fig. 3. Changes like cell packaging (*a*, *b*) and the spectrum of chromosomal aberrations in the root meristem of *P. sativum* seedlings irradiated at doses from 2 to 6 Gy: *a*, *c* — control, *d*—*k* — single and double chromosomal bridges as well as multi-aberrant telophases mitosis *Staining*: acetic carmine (*c*, *d*, *g*, *j*), methylene blue (*a*, *b*, *e*, *f*, *h*, *i*). *Scale*: 30 μm (*a*, *b*), 10 μm (*c*—*j*)

(Fig. 1, *g—l*), and these results were further corroborated statistically (Fig. 2). The number of autophagosomes (per cell) in clinostated plants increased by nearly 100% on the 6th day compared to the control. This density then decreased, and by the 12th day, the number of autophagosomes in clinostated and control plants became statistically indistinguishable (Fig. 2). These findings support the observed gradual adaptation of plants to simulated microgravity, evidenced by the decrease in root cell autophagosomes during later growth stages.

The impact of ionizing radiation as a concomitant factor of space flights. Induction of homeostatic mechanisms in plant meristematic tissues

This study investigated the combined effects of simulated microgravity (clinostating) and gamma irradiation on autophagy induction in pea (*Pisum sativum*) seedlings, potentially mimicking an additional stress factor experienced during spaceflight. The effects of gamma radiation doses relevant to spacecraft cabins (1 to 6 Gy) were studied on plant development and root apical meristem cytogenetics. Gamma irradiation caused dose-dependent changes in plant growth and the topology and cytogenetic state of the root apical meristem. (Fig. 3). Pea seedling apical meristems exhibited increased cell line heterogeneity after 2 Gy gamma irradiation. This heterogeneity became more pronounced at higher doses (4—6 Gy), coinciding with an increased burden of chromosomal aberrations (single / double bridges, fragments) and programmed cell death (PCD) indicators in cells and tissues (Fig. 3). Multi-aberrant cells and micronuclei were less frequent. (Fig. 3, *g—j*). Proliferative death of multi-aberrant cells emerged as the dominant form of PCD (programmed cell death) following irradiation. The frequency of chromosomal aberrations increased linearly up to 4 Gy radiation exposure. However, at higher doses (4—6 Gy), this increase plateaued at around 30% aberrant anaphases, likely due to a combined cytostatic effect (inhibition of cell division) and PCD.

While the combined exposure of 2 Gy radiation and clinostating did not significantly impact the growth and morphogenesis of Arabidopsis thaliana main roots, reorientation of cortical microtubules in the distal growth zone was observed in seedlings of the AtGFP-MAP4 line. Interestingly, the combined exposure initially triggered a significant increase in autophagosome numbers in the root tips of 7-day-old seedlings (24 hours after irradiation). However, this increase was followed by a decrease in autophagosomes in 10-day-old seedlings (4 days after irradiation) compared to the non-irradiated control group. Gamma radiation exposure triggers dose-dependent changes in the root apical meristem, impacting its topology, cytogenetics, and physiology. These changes include increased heterogeneity of cell populations, a higher burden of chromosomal aberrations and programmed cell death (PCD) in cells and tissues, and enhanced autophagy activity. Notably, the frequency of chromosomal aberrations plateaus at higher radiation doses due to a combined cytostatic effect and PCB. This plateau could indicate the activation of homeostatic mechanisms and adaptation processes within plant meristematic tissues.

Development of ways to increase plant stress resistance to microgravity conditions. The involvement of nitric oxide in the regulation of root system morphogenesis and the development of autophagy

Nitric oxide (NO) exhibits diverse effects in plants due to its interaction with various molecular targets and the formation of physiologically active metabolites [8]. It can act as both a protector (through antioxidant activity) and a free radical generator and plays a key role as a signalling molecule under various stress conditions. However, the involvement of NO in plant adaptation to microgravity, particularly its potential role in regulating autophagy, remains unexplored. Therefore, this study aimed to investigate the role of NO in regulating seedling growth and autophagy development under simulated microgravity using exogenous NO donors

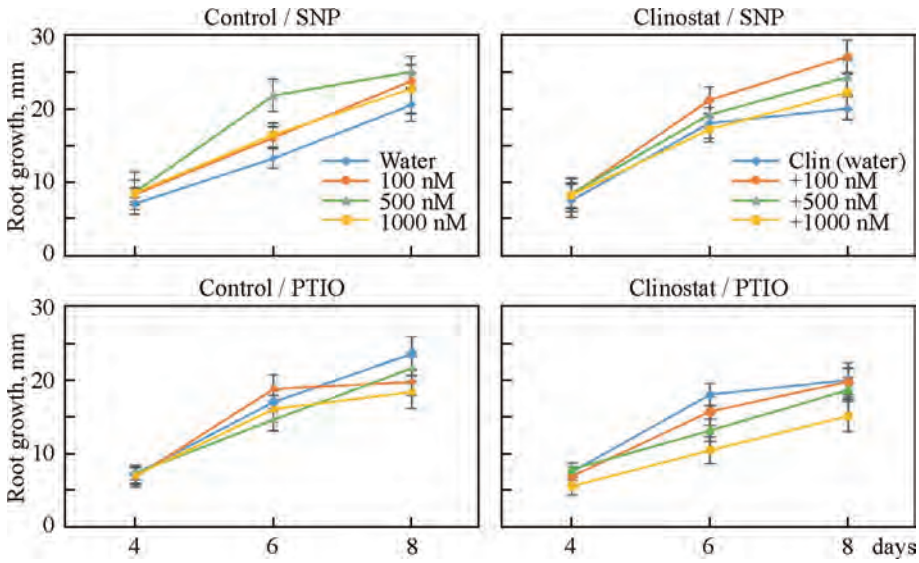

Fig. 4. Effect of SNP/cPTIO on the growth of the main root of *A. thaliana* seedlings under control and clinostating conditions

Fig. 5. Effect of SNP/cPTIO seed treatment (1000 μM) on the formation of root hairs of the root apex of A. thaliana seedlings: *a* — control, *b* — clinostating, *c* — control + SNP, *d* — clinostating + SNP, *e* — control + cPTIO, *e* — clinostating + cPTIO. Scale bar: 100 μm

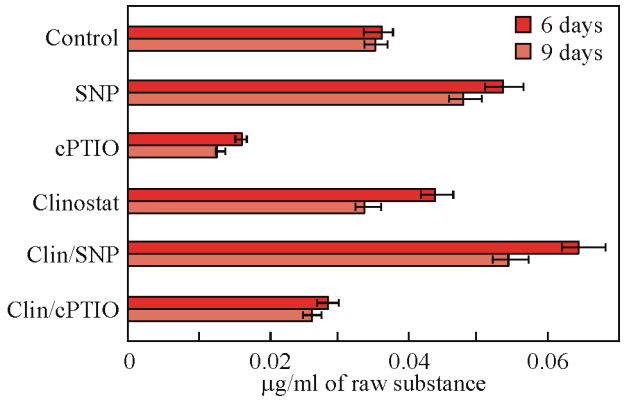

Fig. 6. Endogenous NO content in *A. thaliana* seedlings under the conditions of clinostating and SNP/cPTIO treatment

and scavengers. The main results of these studies were published by us in works [5, 8, 9].

In particular, sodium nitroprusside (SNP), a nitric oxide (NO) donor, in the concentration range of 100 to 1000 μM, had a stimulating effect on seedling growth and enhanced their tolerance to simulated microgravity conditions (clinostating) (Fig. 4). Interestingly, the optimal concentration of NO for growth under clinostating (100 μM) was lower compared to the horizontal control (500 μM), potentially caused by NO's contribution to the formation of reactive oxygen species (ROS). Conversely, seed treatment with PTIO, a nitric oxide scavenger, had a concentration-dependent negative effect, retarding root growth (Fig. 4). Seedlings treated with SNP (a nitric oxide donor) exhibited an increased abundance of root hairs in the differentiation zone of the root apex compared to the control (Fig. 5). Conversely, treatment with cyclopropyl-[(isothiocyanate)-aminocarbonyl]methyl ester (cPTIO), a nitric oxide scavenger, inhibited the initiation and growth of root hair primordia in both control and clinostated seedlings. These results suggest that nitric oxide plays a role in root hair formation.

One possible mechanism involves NO interaction with other hormones, such as auxin. The balance between these signalling molecules might be crucial for processes like root gravitropic bending.

The intracellular content of nitrites (NO_2^-) and localization of NO in root apex tissues

The NO content was determined according to standard methods with modifications [8]. The method is based on the quantitative determination of nitrites using the Griess reagent after the formation of nitrite from endogenous NO. The concentration of nitrites (μg/ml crude substance) was determined in 6- and 9-day-old seedlings of *A. thaliana,* the seeds of which were treated with 500 μM SNP or cPTIO. Our results showed that endogenous NO levels increased by 1.5-fold in control plants and by 1.8-fold in clinostatic plants treated with SNP compared to controls (Fig. 6). This NO level increase was transient, gradually decreasing by day 9. This decline could be due to the depletion of the stimulated NO pool or indicate plant adaptation to altered gravity. Furthermore, cPTIO treatment significantly reduced endogenous NO levels in both control and clinostatic plants. Moreover, clinostat-induced NO production was suppressed by the NO scavenger treatment, highlighting its role in the response to simulated microgravity. DAF-FM DA staining revealed stronger fluorescence in epidermal cells and root hairs of plants grown under simulated microgravity (Fig. 7), suggesting elevated NO levels. SNP seed treatment, which increases NO levels, resulted in further enhanced fluorescence intensity, particularly under clinostating conditions (statistically significant). Conversely, cPTIO treatment (an NO scavenger) caused a decrease in fluorescence intensity in epidermal tissues and root hairs. These results, along with the observed changes in endogenous NO levels, support the involvement of NO in plant responses to altered gravity.

The stimulating effect of NO is likely linked to its interaction with reactive oxygen species (ROS). This interaction may enhance redox homeostasis, a balanced cellular state crucial

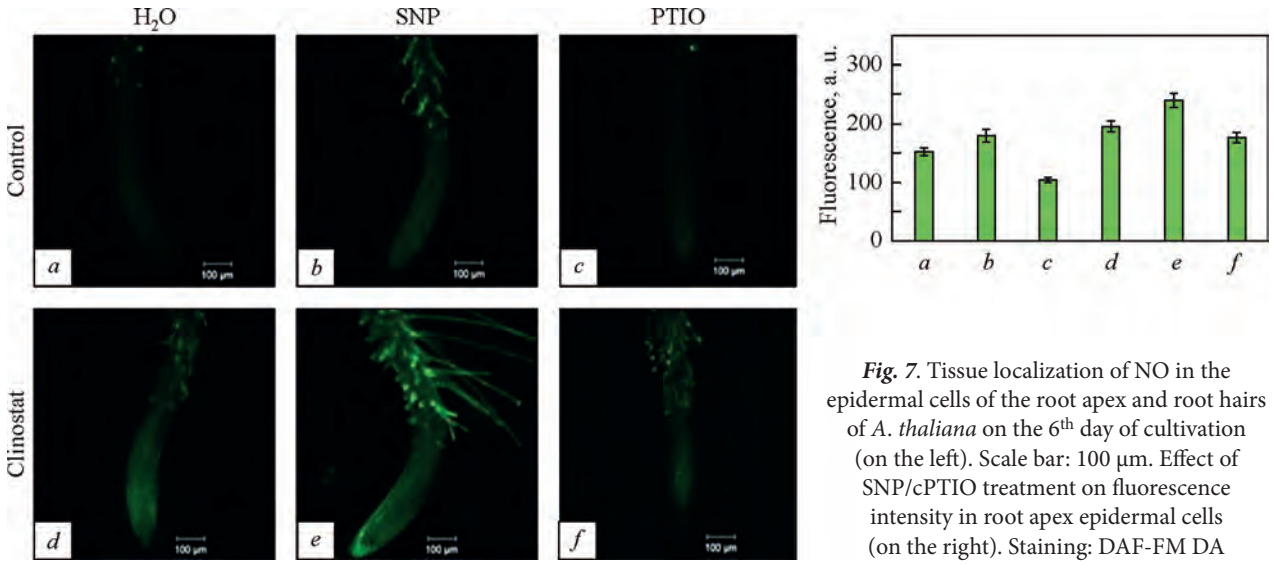

Fig. 7. Tissue localization of NO in the epidermal cells of the root apex and root hairs of *A. thaliana* on the 6th day of cultivation (on the left). Scale bar: 100 μm. Effect of SNP/cPTIO treatment on fluorescence intensity in root apex epidermal cells (on the right). Staining: DAF-FM DA

for plant health. Under simulated microgravity, plants may activate antioxidant defence mechanisms, including increased activity of antioxidant enzymes and glutathione content. However, microgravity can also disrupt this balance by increasing NO production and reducing its buffering capacity, potentially harming cells.

The influence of nitric oxide on the development of autophagy in the cells of the root apex *A. thaliana*

Autophagosome visualization in root tip cells began with 6-day-old seedlings, coinciding with the observed induction of autophagy (Fig. 8). As previously noted, plants grown under simulated microgravity (clinostating) exhibited an initial increase in the number of autophagosomes within root cells, followed by a gradual decrease during further growth. To elucidate the role of NO in autophagy development, we employed an NO donor and scavenger. NO donor treatment led to enhanced autophagy development in epidermal cells of clinostat-grown plants. Treatment with the NO scavenger cPTIO slightly inhibited seedling growth, particularly under clinostating conditions. Interestingly, this coincided with an increased accumulation of autophagosomes in root epidermal cells.

Our findings suggest a potential molecular link between NO signalling and autophagy under stress conditions. In plants, the main biologically active form of NO, S-nitroso glutathione (GSNO), is regulated by GSNO reductase (GSNOR), a key enzyme controlling NO signalling. NO can modify proteins through a process called S-nitrosylation. In Arabidopsis thaliana, NO-mediated S-nitrosylation of GSNOR1 at a specific site (Cys-10) triggers a conformational change that allows it to interact with a protein called ATG8, which is crucial for autophagy. This interaction leads to GSNOR1 being targeted to autophagosomes for degradation [8]. Therefore, this mechanism suggests how NO signalling, through S-nitrosylation of GSNOR1, regulates selective autophagy under stress conditions.

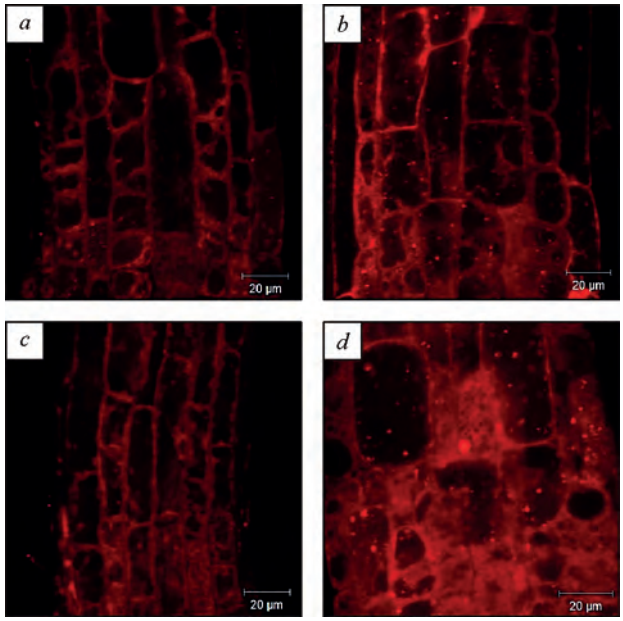

Fig. 8. Visualization of autophagosomes in cells of the root of *A. thaliana* on the 6th day of cultivation under clinostating conditions: *a* — control; *b* — clinostat; *c* — clinostat/SNP; *d* — clinostat/cPTIO. Staining: LysoTracker™ Red DND-99. Scale bar: 20 μm

Study of the effect of melatonin and the combined action of melatonin and NSP on plant development under clinostating conditions

Melatonin (N-[2-(5-methoxy-1H-indol-3-yl)ethyl] ethanamide), a versatile bioregulator and antioxidant, safeguards plants against abiotic stress by scavenging free radicals, maintaining cellular redox balance, and regulating stress-response genes. Interestingly, melatonin's effects on ROS generation appear complex, with reports of suppression and enhancement. This study investigated melatonin's stress-protective properties under simulated microgravity conditions (clinostating) to understand its role in plant responses to spaceflight-like environments [10]. Arabidopsis

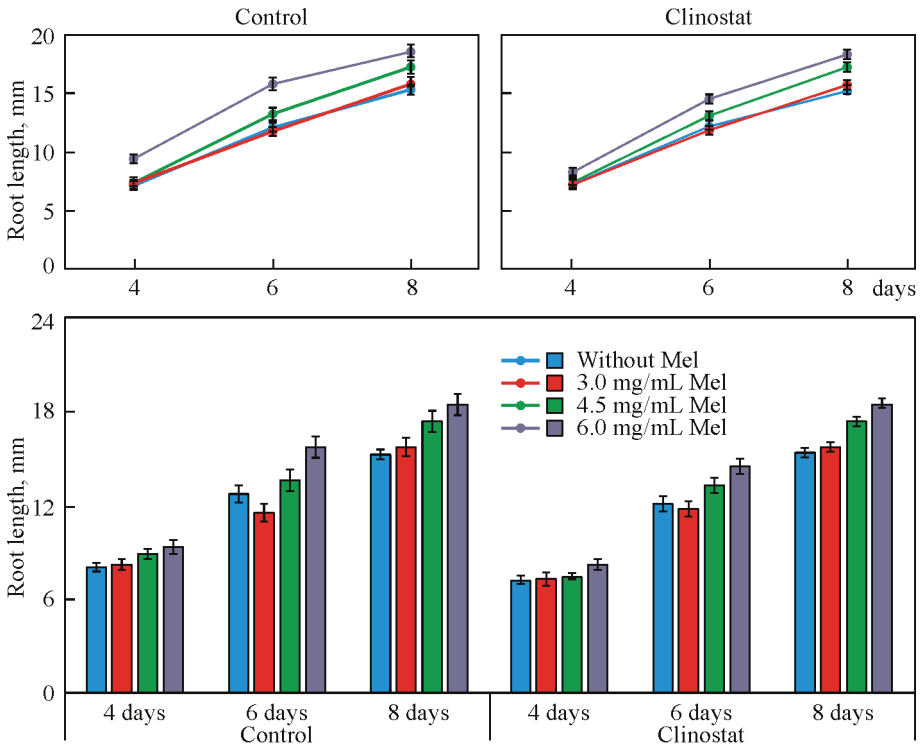

Fig. 9. The effect of melatonin treatment on the growth of the main root of *A. thaliana* seedlings under clinostating and control conditions. Abbreviation: Mel — melatonin

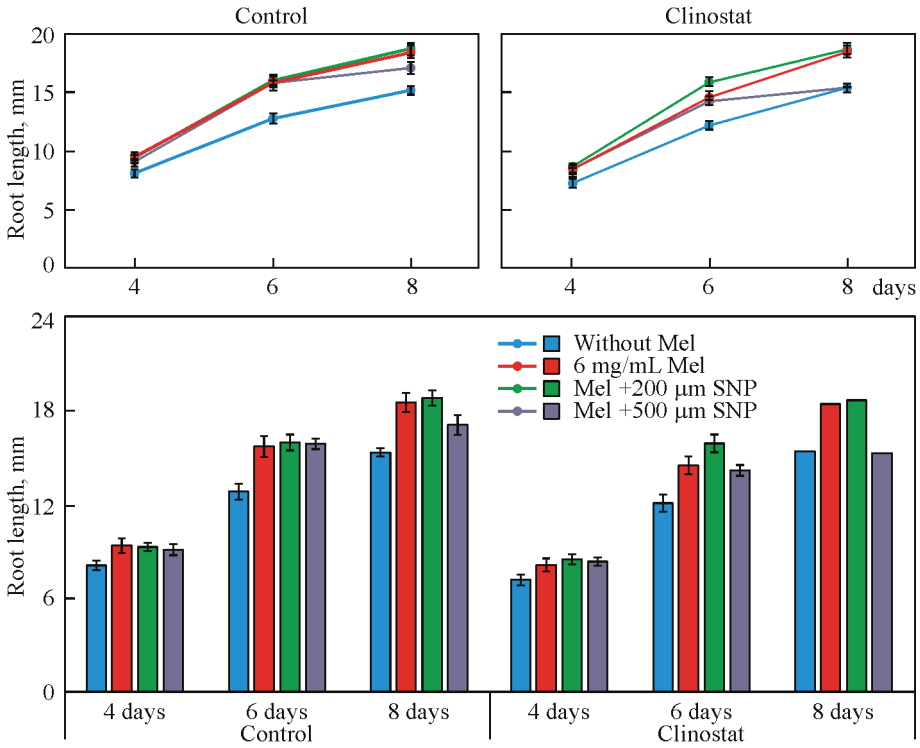

Fig. 10. Combined effect of melatonin and NO (SNP) on plant growth under clinostating and control conditions

seeds were germinated on a horizontal clinostat (simulating microgravity) or under stationary conditions (control) for 10—12 days at 22 °C after a 24-hour treatment with melatonin solutions at concentrations of 3, 4.5, and 6 mg/ml. Melatonin treatment at all investigated concentrations (3, 4.5, and 6 mg/ml) significantly promoted the growth and development of Arabidopsis thaliana roots in both control and clinostatic conditions (Fig. 9). Seedlings also exhibited increased vegetative biomass accumulation.

Melatonin and NO are known to interact in plants, influencing responses to abiotic stress [11]. Melatonin's protective effects include scavenging NO and other free radicals, along with inhibiting NO production. However, the mechanisms underlying their interaction during simulated microgravity (clinostating) are unclear. This study investigated the combined effects of melatonin and NO on plant growth under clinostating conditions. Melatonin treatment (6 mg/ml) combined with NO donor (SNP) at

200 μM stimulated root growth in both control and clinostat conditions (Fig. 10). Interestingly, a higher SNP concentration (500 μM) inhibited growth in clinostat plants compared to controls and melatonin treatment alone (Fig. 10).

Our findings suggest melatonin acts as a potential stress protectant in plants by acting as a direct scavenger of hydroxyl radicals and other reactive oxygen species (ROS), while also regulating endogenous nitric oxide (NO) levels, a key signalling molecule in stress responses. Melatonin's protective effects seem to involve two opposing mechanisms affecting NO. It can act as a scavenger of NO and peroxynitrite, while also potentially suppressing NO production and NO synthase activity. However, melatonin can also stimulate the arginine pathway, leading to NO accumulation and increased NO synthase activity.

Our findings highlight the importance of regulating endogenous nitric oxide (NO) in plant responses to simulated microgravity, suggesting the potential for manipulating plant development using melatonin and NO signalling for enhanced adaptation and stress resistance [10]. This data paves the way for further research on improving plant resilience during spaceflight conditions.

Conclusion

This study has significantly advanced our understanding of the cellular and molecular mechanisms underlying stress-induced autophagy in plants. Autophagy, a self-recycling process, emerges as a critical adaptation mechanism for plants under stress conditions like simulated microgravity. These findings provide a valuable foundation for further research exploring the potential of induced autophagy to enhance plant stress resistance during spaceflight.

The research also highlights the potential of melatonin as a stress protectant. Melatonin acts as a direct scavenger of harmful free radicals and regulates endogenous nitric oxide (NO) levels, a key player in plant stress signalling. Our results demonstrate that melatonin treatment can enhance plant adaptation capabilities under simulated microgravity.

Furthermore, by employing efficient NO donors and scavengers, the study clarifies the role of NO in mediating plant responses to microgravity stress. This knowledge will be instrumental in developing strategies to improve plant adaptation during spaceflight. Ultimately, this research has the potential to solve challenges associated with growing plants in closed life support systems for long-duration space missions.

The work was carried out with the financial support of the project "Development of the concept of regulation of development and stress resistance of plants for their adaptation to the conditions of space flights by involving cell-biological resources" of the target complex program of the National Academy of Sciences of Ukraine on scientific space research for 2018—2022 (state registration № 01118U003742).

Acknowledgements. *We acknowledge the suggestions by Dr. V. Kyrylenko (Institute of Food Biotechnology and Genomics), aimed to improve the manuscript language.*

REFERENCES

1. Shadrina R.Yu., Yemets A.I., Blume Ya. B. Development of autophagy as an adaptive response of *Arabidopsis thaliana* plants to microgravity conditions. *Factors Exp. Evol. Organisms.* 2019. 25. P. 327—332. https://doi.org/10.7124/FEEO.v25.1186.

2. Shadrina R.Y., Goryunova I.I., Blume Ya.B., Yemets A.I. Autophagosome formation and transcriptional activity of *atg8* genes in Arabidopsis root cells during the development of autophagy under microgravity conditions. *Reports Natl. Acad. Sci. Ukraine.* 2020. No. 9. P. 77—85. https://doi.org/10.15407/dopovidi2020.09.077

3. Yemets A., Shadrina R., Horyunova I., Plokhovska S., Kravets O., Blume Ya. Development of autophagy in plant cells under microgravity: the role of microtubules and ATG8 proteins in autophagosome formation. In: *Space Research in Ukraine*. 2019—2020. Ed. O. Fedorov. Kyiv: Akademperiodyka, 2021. P. 79—84.

4. Shadrina R.Yu., Plokhovska S.H., Goryunova I.I., Kravets O.A., Yemets A.I., Blume Ya.B. Development of stress-induced autophagy in the response of plants to microgravity conditions and radiation exposure. *Int. Conference "Stress and Adaptation of Plants"*, February 25—26, 2021, Kharkiv, Ukraine. Kharkiv Natl. Univ. Bulletin: Biol. Series. P. 71.

5. Yemets A.I., Plokhovska S.H., Shadrina R.Yu., Kravets O.A., Blume Ya.B. Elucidation of cellular mechanisms of autophagy involvement in plant adaptation to microgravity conditions. *Space Sci. Technol.* 2023, 29(2). P. 22—31. https: //doi.org/10.15407/knit2023.02.000

6. Yemets A.I., Shadrina R.Yu., Plokhovska S.H., Kravets E.A., Blume Ya.B. Autophagy as key element of plant adaptation to microgravity. *Second Int. Sci. Conference "Plant Stress and Adaptation"*. June 7—8, 2023. P. 20—21.

7. Yemets A., Shadrina R., Blume R.Y., Plokhovska S., Blume Ya. Autophagy formation, microtubule disorientation, and alteration of ATG8 and tubulin gene expression under simulated microgravity in *Arabidopsis thaliana*. *npj Microgravity*. 2024. 10. P. 31. https://doi.org/10.1038/s41526-024-00381-9.

8. Plokhovska S.H., Shadrina R.Yu., Kravets O.A., Yemets A.I., Blume Ya.B. The role of nitric oxide in the *Arabidopsis thaliana* response to simulated microgravity and the involvement of autophagy in this process. *Cytol. Genetics*. 2022. 56(3). P. 244—252. https://doi.org/10.3103/S0095452722030100.

9. Blume Ya.B., Plokhovska S.H., Shadrina R.Yu., Kravets O.A., Yemets A.I. The role of nitric oxide in *Arabidopsis thaliana* response to simulated microgravity and the participation of autophagy in the mediation of this process. *44th COSPAR Sci. Assembly*. July 16—24, 2022, Athens, Greece. Abstracts. 2022. P. 2902. https://ui.adsabs.harvard.edu/abs/2022cosp...44.2902B/abstract

10. Plokhovska S.H., Kravets O.A., Shadrina R.Yu., Yemets A.I., Blume Ya.B. Crosstalk between nitric oxide and melatonin signalling molecules in Arabidopsis under of simulated microgravity. *Int. Sci. Conference "Breeding, genetics and biotechnology of agricultural plants: Achievements, innovations and prospects"*. October 26, 2022, Odesa, Ukraine. Abstracts of the Reports, 2022. P. 144—145.

11. Plokhovska, S.H., Kravets, E.A., Yemets, A.I., Blume, Y.B. Crosstalk between melatonin and nitric oxide in plant development and UV-B stress response. In: *UV-B Radiation and Crop Growth.* Eds Kataria S., Singh V.P. Springer: Singapore, 2023. P. 319—339. https://doi.org/10.1007/978-981-19-3620-3_15.

THE NEUROTOXICITY RISK ASSESSMENT OF PLANETARY DUST COMPONENT FULLERENE C60

N. Pozdnyakova, N. Krisanova, M. Dudarenko, A. Pastukhov, R. Sivko, L. Kalynovska, M. Driuk, A. Nazarova, V. Shliakhovyi, T. Borisova

Palladin Institute of Biochemistry of the NAS of Ukraine

Introduction

Over the past decades, a number of molecules and various signatures of interstellar dust have been discovered in different environments with the help of astronomical observations. Most of the dust that determines the physical and chemical characteristics of the interstellar medium is formed in the outflows of asymptotic giant stars and is further processed when these objects become planetary nebulae. In 2010, a study of the infrared spectrum of the environment of the planetary nebula Tc 1 revealed the radiation of cold and neutral fullerenes C60 and C70. These two molecules accounted for several percent of the available space carbon in this region, indicating that under certain conditions fullerenes can be efficiently formed in space [1]. Data obtained in 2012 using the infrared spectrograph on the Spitzer Space Telescope first provided evidence for the presence of fullerene C60 in the solid phase of a XX Oph binary system consisting of a late (M7III) giant and an early (B0V) star. The hot star of this system is a sub dwarf B, which is surrounded by an ionized shell and a fullerene C60-containing shell, presumably in the shape of a disk [2]. At the end of 2015, a group of Swiss and German researchers, led by John Mayer from the University of Basel, managed to prove in laboratory conditions the presence of fullerene C60+, which had a positive charge, in interstellar space. fullerene C60+ ions were analysed in the gas phase at a temperature of 5.8 K. The obtained spectra in the infrared region exactly coincided with two diffuse interstellar lines. According to the study, up to 0.9% of cosmic carbon can exist in this form [3]. In 2019, the results of the analysis of infrared spectra obtained with the help of the Hubble space telescope conclusively proved the existence of fullerene C60+ in the interstellar medium. The ratios of wavelengths and band strengths were found to be quite similar to those determined in the laboratory experiments. This confirmed the hypothesis that large carbon-containing molecules can form and exist in the interstellar medium, and are also candidates for explaining many diffuse interstellar absorption bands [4].

Since its discovery, fullerene C60 has attracted the attention of biologists due to its unique chemistry and potential biological applications. It has relatively large size (~0.7 nm), hollow sphere architecture, wide electrical conjugation, electrophilicity, symmetry and ability to accumulate in biological tissues. All these facts create unique opportunities for fullerene C60 applications in a wide range of fields from materials science to medicine.

Fullerene C60 has also attracted considerable attention due to its potential as an antioxidant and scavenger of ROS (reactive oxygen species) [5]. Fullerene C60 derivatives have been shown to scavenge a number of free radicals, including superoxide and hydroxyl radicals [6]. It has also been shown that various fullerene C60 derivatives can localize in the mitochondrial membrane and so fullerene C60 can affect mitochondrial function *in vitro* [7], and it has been suggested that fullerene C60 can localize in the mitochondrial membrane *in vivo* and detoxify mitochondrial ROS. Hypothetically, this should prevent cellular damage and mitigate the long-term toxicity of mitochondrial ROS, perhaps even extending healthy life spans. The latter according to the mitochondrial and free radical theories of aging proved to be significant contributors to human longevity.

One of the most striking results regarding the *in vivo* effects of fullerene C60 was a study that showed that a group of rats which were injected with fullerene C60 dissolved in olive oil (C60-OO) from a young age had an extended average life span (a 90% increase) compared to rats injected with olive oil (OO) or control ones without any injected compounds [8]. However, another study provided evidence of deleterious effects of fullerene C60 on mouse embryos *in vitro* and *in vivo* [9], while a number of studies focused on the protective properties of fullerene C60 in specific injury models [10, 11]. Rodent lifespan studies were also conducted using fullerene derivatives, carboxyfullerenes, which have important physical and chemical differences from fullerene C60. Mice treated with carboxyfullerene lived 11% longer than control mice with improved cognitive performance [12].

Thus, studies have revealed diverse effects of fullerene C60 *in vitro* and *in vivo*. The potential ability to extend life, and the discrepancy in the results obtained, possible toxic effects under certain conditions, especially under the conditions of long-duration space missions, require further research which is extremely valuable.

It should be emphasized that during long-term manned space missions, one of the possible causes of brain dysfunction may be the influence of planetary and interstellar dust, the composition and properties of which, as well as the impact on human health, in particular, the neurotoxic effect, have not been sufficiently studied [13, 14]. It has been shown that lunar dust particles were absorbed by spacesuits and entered space stations [15, 16]. As a result of direct contact with lunar dust particles during several Apollo missions, irritation of the eyes, respiratory tract and skin of astronauts

were observed. Lunar dust as well as nanoparticles have been shown to cause inflammation [17], which is known to alter the permeability of the blood-brain barrier [18]. The neurotoxic effect of nanoparticles can be realized by inhibiting neurotransmitter synthesis, changing the flow of ions through cell membranes, blocking the transport of neurotransmitters in the nerve terminals of the brain.

The aim of our study was to assess the acute neurotoxicity of component of planetary dust fullerene C60 (the commercial compound from Sigma, USA). This goal was realized by evaluating one of the key characteristics of synaptic neurotransmission using presynaptic nerve terminals (synaptosomes) isolated from the cortex regions of the rat brain. The extracellular level of radioactively labelled neurotransmitters L-[^{14}C]glutamate and gamma-aminobutyric acid ([^{3}H]GABA) was studied in nerve terminals. It should be noted that glutamate and GABA are key fast excitatory and inhibitory, respectively, neurotransmitters in the central nervous system. Impaired transport and homeostasis of glutamate and GABA contributes to neuronal dysfunction and the pathogenesis of major neurological disorders.

Materials and Methods

Materials

The following reagents were used in the work: HEPES (N-2-hydroxyethylpiperazine-n-2-ethanesulfonic acid), EGTA, EDTA, Ficoll-400, aminooxyacetic acid, glutamate, fullerene C60, scintillation fluid Sigma-Fluor® High Performance LSC Cocktail, components of the incubation medium for nerve terminals — "Sigma", USA; [^{3}H]GABA, L-[^{14}C]glutamate, Perkin Elmer (USA).

Ethical norms

All experiments were performed in accordance with the "Rules for Conducting Work Using Experimental Animals" approved by the Commission for the Care, Maintenance and Use of Experimental Animals of the Palladin Institute of Biochemistry of the National Academy of Sciences of Ukraine (Protocol No. 1 dated January 14, 2020). The research was conducted on white male Wistar rats. Rats were kept on a standard vivarium diet.

Isolation of the purified fraction of synaptosomes from the brain of rats

Synaptosomes were isolated according to the Cotman method [19]. Rats weighing 150—200 g were used in the experiments. The cortex region of the brain was taken from decapitated animals. To obtain the fraction of synaptosomes, a 20% homogenate was prepared using a glass Potter homogenizer (gap 0.2 mm). The isolation medium contained 0.32 M sucrose, 5 mM HEPES-NaOH pH 7.4, 0.2 mM EDTA. The homogenate was centrifuged at 2 500 g for 5 min for separating nuclei, blood vessels, and destroyed nerve cells. Further centrifugation of the supernatant at 12 000 g for 10 min made it possible to obtain a "coarse" mitochondrial fraction containing mitochondria, synaptosomes, and myelinated remnants. The pellet was resuspended in isolation medium and applied to a Ficoll gradient containing 13%, 6%, 4% Ficoll prepared in isolation medium and centrifuged at 70 000 g for 45 min on the bucket rotor. The fraction of synaptosomes obtained in the interphase between 13% and 6% Ficoll solutions was collected, diluted with isolation medium 1:4 and centrifuged at 15 000 g for 20 min. The resulting sediment was suspended in a medium containing in mM: NaCl 126, KC1 5, $MgCl_2$ 1.4, NaH_2PO 1.0, HEPES 20, pH 7.4, D-glucose 10. All operations were carried out at 0—4 °C.

Determination of the extracellular level of L-[^{14}C] glutamate in the preparation of synaptosomes

The suspension of synaptosomes was diluted with standard saline up to 1 mg of protein/ml, and after 10 min of preincubation at 37°C, it was loaded with L-[^{14}C]glutamate (500 nM, 238 mCi/mmol) in the standard saline for 10 min. After that, the suspension of synaptosomes was washed with 10 volumes of the standard saline solution and diluted to a concentration of 1 mg protein/ml and immediately used to determine the release of L-[^{14}C]glutamate from synaptosomes. Aliquots (120 μl; 25—30 μg of synaptosomes loaded with L-[^{14}C]glutamate) were preincubated for 10 min at 37 °C, then an aqueous suspension of fullerene C60 was added at concentrations of 0.05—1.00 mg/ml. The extracellular level of L-[^{14}C]glutamate was determined as the unstimulated release of L-[^{14}C]glutamate from synaptosomes in a calcium-free media in 6 min. The suspension of synaptosomes was rapidly precipitated in an Eppendorf microcentrifuge at 10 000 g for 20 s. Aliquots of the supernatant (90 μl) and sodium dodecyl sulfate-solubilized precipitate (90 μl) were mixed with Sigma-Fluor® High Performance LSC Cocktail scintillation liquid (1.5 ml) and radioactivity was determined using a Hidex 600SL scintillation counter (Finland). The extracellular level of L-[^{14}C]glutamate was calculated as % of the total content of radioactively labelled L-[^{14}C]glutamate accumulated in synaptosomes [20].

Determination of the extracellular level of [^{3}H]GABA in the preparation of synaptosomes

Synaptosomes (2 mg protein/ml) in the standard saline solution containing 10 μM aminooxyacetic acid were incubated for 5 minutes at 37 °C in the presence of $5 \cdot 10^{-7}$ M (0.1 Ci/ml) [^{3}H]GABA. After cooling on ice, the suspension was diluted three times with the saline and centrifuged at 4000 g for 5 minutes. The precipitate was suspended at a temperature of 4°C and a protein concentration of 1 mg/ml in a saline solution containing 10 μM of aminooxyacetic acid. Synaptosomes accumulating [^{3}H]GABA (1 mg protein/ml) were immediately used to study the processes of GABA release. Aliquots (120 μl; 25—30 μg of loaded [^{3}H]GABA synaptosomes) were preincubated for 10 min at 37 °C, then an aqueous suspension of fullerene C60 was added at concentrations of 0.05—1.00 mg/ml. The extracellular

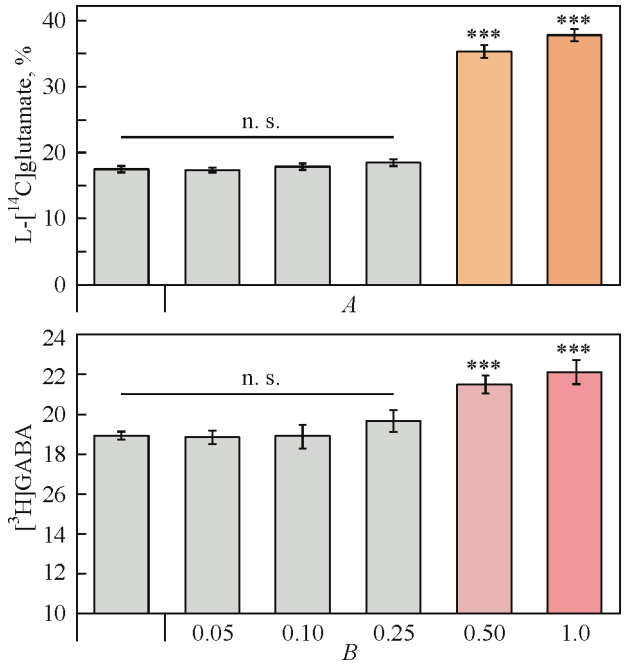

Fig. 1. Extracellular levels of L-[^{14}C]glutamate (*a*) and [^{3}H]GABA (*b*) in preparations of synaptosomes in the presence of fullerene C60 at concentrations of 0.05—1.00 mg/ml. Data are presented as mean ± SEM; ***, $p < 0.001$; n.s., no significant difference compared to control, $n = 12$

level of [^{3}H]GABA was determined as the unstimulated release of [^{3}H]GABA from synaptosomes in 6 min. The suspension of synaptosomes was rapidly precipitated in an Eppendorf microcentrifuge at 10 000 g for 20 s. Aliquots of the supernatant (90 μl) and sodium dodecyl sulfate-solubilized precipitate (90 μl) were mixed with Sigma-Fluor® High Performance LSC Cocktail scintillation liquid (1.5 ml) and radioactivity was determined using a Hidex 600SL scintillation counter (Finland). The extracellular level of [^{3}H]GABA was calculated as % of the total content of radioactively labelled [^{3}H]GABA accumulated in synaptosomes.

Statistics

Results are presented as mean ± SEM of n independent experiments. The difference between the two groups was compared using one-way ANOVA. The difference was considered significant at $p < 0.05$. Statistical data processing, graphing and function calculations were performed using the Excel program.

Results and discussion

Na^+-dependent glutamate and GABA transporters are key players in the termination of synaptic neurotransmission and mediate the transportation of neurotransmitters into the cytoplasm and the establishment of the definite extracellular level of neurotransmitters. These transporters use the Na^+/K^+ electrochemical gradient across the plasma membrane as a driving force. An increase in the extracellular glutamate concentration in the synaptic cleft leads to neurotoxicity and death of postsynaptic neurons due to excessive excitation of glutamate receptors on their membrane. An increase in the extracellular level of GABA can lead to a violation of the excitation-inhibition balance in the nervous system.

In our experiments, it was shown that fullerene C60 in the concentration range from 0.05 to 0.25 mg/ml did not change the extracellular level of L-[^{14}C]glutamate in preparations of synaptosomes.

As shown in Figure 1, *A*, the extracellular level of L-[^{14}C]glutamate in preparations of synaptosomes was equal to 17.51 ± 0.46% of the total amount of radioactively labelled L-[^{14}C]glutamate accumulated by synaptosomes in the control, 17.36 ± 0.39% in the presence of 0.05 mg/ml fullerene C60 [$F_{(1,22)} = 0.06$; $p = 0.79$; $n = 12$]; 17.88 ± 0.51% in the presence of 0.10 mg/ml fullerene C60 [$F_{(1,22)} = 0.31$; $p = 0.57$; $n = 12$], 18.58 ± 0.42% in the presence of 0.25 mg/ml fullerene C60 [$F_{(1,22)} = 3.24$; $p = 0.08$; $n = 12$].

However, an increase in the concentration of fullerene C60 to 0.50 mg/ml and 1.00 mg/ml, resulted in an increase in the extracellular level of L-[^{14}C]glutamate in synaptosome preparations, which was 35.21 ± 1.18% of the total amount of radioactively labelled L-[^{14}C]glutamate accumulated by synaptosomes at a fullerene C60 concentration of 0.50 mg/ml [$F_{(1,22)} = 212.49$; $p < 0.001$; $n = 12$], and 37.84 ± 0.85% at fullerene C60 concentration of 1.00 mg/ml [$F_{(1,22)} = 483.39$; $p < 0.001$; $n = 12$] (Fig. 1, *a*).

The extracellular level of [^{3}H]GABA in the preparation of synaptosomes also did not change in the presence of fullerene C60 in the concentration range from 0.05 to 0.25 mg/ml and was 18.94 ± 0.29% of the total amount of radioactively labelled [^{3}H]GABA accumulated by synaptosomes in the control, 18.89 ± 0.37% in the presence of 0.05 mg/ml fullerene C60 [$F_{(1,22)} = 0.01$; $p = 0.91$; $n = 12$]; 18.96 ± 0.62% in the presence of 0.10 mg/ml fullerene C60 [$F_{(1.22)} = 0.0007$; $p = 0.97$; $n = 12$], 19.68 ± 0.61% in the presence of 0.25 mg/ml fullerene C60 [$F_{(1,22)} = 1.29$; $p = 0.26$; $n = 12$] (Fig. 1, *b*).

Increasing the concentration of fullerene C60 in the suspension of synaptosomes loaded with [^{3}H]GABA to 0.50 mg/ml and 1.00 mg/ml, as in the experiments with L-[^{14}C]glutamate, led to an increase in the extracellular level of [^{3}H]GABA, which was equal to, respectively, 21.55 ± ± 0.46% of the total amount of radioactively labelled [^{3}H]GABA accumulated by synaptosomes at a concentration of fullerene C60 0.50 mg/ml [$F_{(1,22)} = 25.52$; $p < 0.001$; $n = 12$], and 22.17 ± 0.65% at fullerene C60 concentration of 1.00 mg/ml [$F_{(1,22)} = 22.63$; $p < 0.001$; $n = 12$] (Fig. 1, *b*).

Thus, it was shown that the component of planetary dust fullerene C60 in the unirradiated state at concentrations of 0.05—0.25 mg/ml did not change the extracellular levels of L-[^{14}C]glutamate and [^{3}H]GABA in preparations of nerve terminals. Therefore, fullerene C60 did not have signs of acute neurotoxicity in nerve terminals at these concentrations. In the concentration range 0.5—1.0 mg/ml, an increase in the extracellular level of both neurotransmitters was registered that may result in excitotoxicity and a violation of the excitation-inhibition balance in nerve terminals.

Data from the literature indicate that fullerene C60 is destroyed under the influence of UV radiation. Polymerization and aggregation of fullerene after exposure to light were also reported, which indicates that multiple transformations can occur with fullerene C60 under these conditions [21].

Functionalized fullerene C60 derivatives have been investigated as antitumor photosensitizers in photodynamic therapy, antiviral molecules as HIV protease inhibitors, drug delivery vectors for peptides, genes and other large molecules, as well as diagnostic imaging agents as metal conjugates [22].

Given that fullerene C60 undergoes photooxidation, it can be expected that it can acquire neurotoxic properties *in situ* even at low concentrations. This question needs to be further investigated in model experiments.

Acknowledgements. *The work was carried out with the support of the Target Program of Scientific Research of the National Academy of Sciences of Ukraine "Aerospace Observations of the Environment in the Interest of Sustainable Development and Security" (ERA-PLANET/UA) for 2021—2023 and the Target Comprehensive Program of the National Academy of Sciences of Ukraine for Scientific Space Research for 2018—2022.*

REFERENCES

1. Cami J., Bernard-Salas J., Peeters E. et al. Detection of C60 and C70 in a young planetary nebula *Science*. 2010. 329, No. 5996. P. 1180—1182. https://doi.org/10.1126/SCIENCE.1192035

2. Evans A., Loon J.T. van, Woodward C.E. et al. Solid-phase C60 in the peculiar binary XX Oph *Mon. Not. R. Astron. Soc. Lett.* 2012. 421, No. 1 P. L92—L96. https://doi.org/10.1111/J.1745-3933.2012.01213.X

3. Campbell E.K., Holz M., Gerlich D. et al. Laboratory confirmation of C60(+) as the carrier of two diffuse interstellar bands *Nature*. 2015. 523, No. 7560. P. 322—323. https://doi.org/10.1038/NATURE14566

4. Cordiner M.A., Linnartz H., Cox N.L.J. et al. Confirming Interstellar C60+ Using the Hubble Space Telescope *Astrophys. J. Lett.* 2019. 875, No. 2. P. L28. https://doi.org/10.3847/2041-8213/AB14E5

5. Markovic Z., Trajkovic V. Biomedical potential of the reactive oxygen species generation and quenching by fullerenes (C60) *Biomaterials*. 2008. 29, No. 26. P. 3561—3573. https://doi.org/10.1016/J.BIOMATERIALS.2008.05.005

6. Yin J.J., Lao F., Fu P.P. et al. The scavenging of reactive oxygen species and the potential for cell protection by functionalized fullerene materials *Biomaterials*. 2009. 30, No. 4. P. 611. https://doi.org/10.1016/J.BIOMATERIALS.2008.09.061

7. Santos S.M., Dinis A.M., Peixoto F. et al. Interaction of fullerene nanoparticles with biomembranes: from the partition in lipid membranes to effects on mitochondrial bioenergetics *Toxicol. Sci.* 2014. 138, No. 1. P. 117—129. https://doi.org/10.1093/TOXSCI/KFT327

8. Baati T., Bourasset F., Gharbi N. et al. The prolongation of the lifespan of rats by repeated oral administration of [60]fullerene *Biomaterials*. 2012. 33, No. 19. P. 4936—4946. https://doi.org/10.1016/J.BIOMATERIALS.2012.03.036

9. Tsuchiya T., Oguri I., Yamakoshi Y.N. et al. Novel harmful effects of [60]fullerene on mouse embryos in vitro and in vivo *FEBS Lett.* 1996. 393, No. 1. P. 139—145. https://doi.org/10.1016/0014-5793(96)00812-5

10. Aly F.M., Othman A., Haridy M.A.M. Protective Effects of Fullerene C60 Nanoparticles and Virgin Olive Oil against Genotoxicity Induced by Cyclophosphamide in Rats *Oxid. Med. Cell. Longev.* 2018. https://doi.org/10.1155/2018/1261356

11. Shershakova N., Baraboshkina E., Andreev S. et al. Anti-inflammatory effect of fullerene C60 in a mice model of atopic dermatitis *J. Nanobiotechnology*. 2016. 14, No. 1. P. 1—11. https://doi.org/10.1186/S12951-016-0159-Z/TABLES/2

12. Quick K.L., Ali S.S., Arch R. et al. A carboxyfullerene SOD mimetic improves cognition and extends the lifespan of mice *Neurobiol. Aging*. 2008. 29, No. 1. P. 117—128. https://doi.org/10.1016/J.NEUROBIOLAGING.2006.09.014

13. Borisova T. Nervous System Injury in Response to Contact With Environmental, Engineered and Planetary Micro- and Nano-Sized Particles *Front. Physiol.* 2018. 9. P. 728. https://doi.org/10.3389/fphys.2018.00728

14. Borisova T. Express assessment of neurotoxicity of particles of planetary and interstellar dust *npj Microgravity*. 2019. 5, No. 1. P. 2. https://doi.org/10.1038/s41526-019-0062-7

15. Rehders M., Grosshäuser B.B., Smarandache A. et al. Effects of lunar and mars dust simulants on HaCaT keratinocytes and CHO–K1 fibroblasts *Adv. Sp. Res.* 2011. 47, No. 7. P. 1200—1213. https://doi.org/10.1016/j.asr.2010.11.033

16. Wallace W.T., Taylor L.A., Liu Y. et al. Lunar dust and lunar simulant activation and monitoring *Meteorit. Planet. Sci.* 2009. 44, No. 7. P. 961—970.

17. Chatterjee A., Wang A., Lera M. et al. Lunar Soil Simulant Uptake Produces a Concentration-Dependent Increase in Inducible Nitric Oxide Synthase Expression in Murine RAW 264.7 Macrophage Cells *J. Toxicol. Environ. Heal. Part A*. 2010. 73, No. 9. P. 623—626. https://doi.org/10.1080/15287390903578182

18. Abbott N.J. Inflammatory mediators and modulation of blood-brain barrier permeability. *Cell. Mol. Neurobiol.* 2000. 20, No. 2. P. 131—147. https://doi.org/10.1023/A:1007074420772/METRICS

19. Cotman C.W. Isolation of synaptosomal and synaptic plasma membrane fractions. *Methods Enzymol.* 1974. 31. P. 445—452.

20. Krisanova N.V., Dudarenko M. V., Pastukhov A.O., Sivko R.V., Kalynovska L.M., Driuk M.M., Nazarova A.G., Shliakhovyi V.V., Pozdnyakova N.G. Evaluation of the potential neuroactivity in the brain nerve terminals of the c60 fullerene planetary dust component. *Space Science and Technology*. 2023. 29, No. 5 (144). P. 60—68. https://doi.org/10.15407/knit2023.05.060

21. Sun Y.P., Ma B., Bunker C.E. et al. All-carbon polymers (polyfullerenes) from photochemical reactions of fullerene clusters in room-temperature solvent mixtures *J. Am. Chem. Soc.* 1995. 117, No. 51. P. 12705—12711. https://doi.org/10.1021/JA00156A007

22. Huang Y.Y., Sharma S.K., Yin R. et al. Functionalized Fullerenes in Photodynamic Therapy *J. Biomed. Nanotechnol.* 2014. 10, No. 9. P. 1918. https://doi.org/10.1166/JBN.2014.1963

REMOTE SENSING RESEARCH AND APPLICATIONS AT THE UKRAINIAN HYDROMETEOROLOGICAL INSTITUTE

V. Osadchyi, Yu. Ilyin, O. Kryvobok, O. Kryvoshein, A. Oreshchenko, M. Savenets, O. Shcheglov, V. Shpyg

Ukrainian Hydrometeorological Institute of the State Emergency Service of Ukraine and the NAS of Ukraine

Introduction

The Ukrainian Hydrometeorological Institute (UHMI) of the State Emergency Service of Ukraine and the National Academy of Sciences of Ukraine is a leading Ukrainian research institution in the fields of meteorology, climatology, terrestrial and marine hydrology, hydrochemistry and environmental radiation monitoring. Encompassing a broad variety of tasks, studies and activities, UHMI processes and analyzes a huge amount of data, including those derived from satellite missions launched to help overcome hydrometeorological issues.

Despite the critical importance of satellite data use during extreme hydrological and meteorological events, UHMI experts significantly widened the role of remote sensing from just simple monitoring in Ukraine and prompt data processing during emergencies towards continuous research at different spatial and time scales (including implementation in climatological studies), developing more understandable tools for public usage, and providing technologically complex tasks for remote sensing incorporation into modern NWP models and integrity with national ground-based measurements. The full-scale russian invasion started in 2022, following the devastating consequences for the environment, resulting in more active and precise remote sensing implementation in UHMI's usual activity.

We are presenting the recent UHMI work directions and developments concerning satellite data use in Ukraine. Firstly, we are focusing on a brief introduction to the establishment of the satellite data reception system and its consequent meteorological applications. Then we describe the most relevant implementations of remote sensing in agricultural meteorology, numerical modeling, the atmospheric domain, and wildfire monitoring. The last part of the paper is dedicated to some hydrological and marine studies, showing the importance of satellite data during war emergency situations.

Establishment of the satellite data reception system and the crop classification system

In 1994, the Laboratory of Remote Research Methods (now the Satellite Application Laboratory) was created at UHMI on the basis of the remote research group of the Agrometeorological Department. The main goal of the laboratory was to develop new methods of satellite data processing with further implementation into the operational activities of the Ukrainian Hydrometeorological Service (UHS). In 2006, the laboratory's specialists suggested using the newest technology for obtaining satellite data — EUMETCast, which was developed at the end of 2003 by the European Organization for the Operation of Meteorological Satellites (EUMETSAT). It is a technology for the quasi-operational dissemination of digital meteorological data through a system of telecommunication satellites, which is an alternative to the traditional facility of obtaining data. It is based on the transmission of a digital video signal, for the reception of which standard, inexpensive equipment is used. Thus, it was possible to improve satellite data availability and, as a result, their effectiveness in use. On the basis of the license obtained by the UHS from EUMETSAT, EUMETCast data reception stations were installed in regional forecasting centers of Ukraine (Kyiv, L'viv, Odesa, Simferopol and Donetsk, Fig. 1). UHMI was the initiator of this work (installation of equipment and a minimum set of software for receiving and processing data). Operational data received by the EUMETCast reception station at UHMI are available at the following link https://dat.uhmi.org.ua/map.

Traditionally, obtained satellite data are used to retrieve meteorological characteristics (surface temperature and cloud parameters, vertical profiles of air temperature and humidity) and control a dynamic of synoptic processes; therefore, a significant part of the laboratory's research is related to the development of methods for obtaining meteorological parameters of cloudiness, land surface and atmosphere. Based on the developed methods, the accuracy of the obtained parameters was assessed: the accuracy of the retrieval of the cloudiness is 81—96%; stratus cloudiness can be identified with an accuracy of 85%. Retrieval of the temperature of the cirrus clouds using satellite data is possible with an accuracy of more than 90%, and their height — 85%.

Since 2008, the research in the laboratory has concentrated on the study of the spatial-temporal variability of the spectral characteristics of the main types of natural objects: water surface, forests, meadows, bushes, etc. A quantitative estimation of error classification on satellite images for major crops in Ukraine was obtained. The results of the study showed the possibility of crops detection and natural vegetation in different growing seasons using high-resolution multispectral images that can be used to scientifically justify

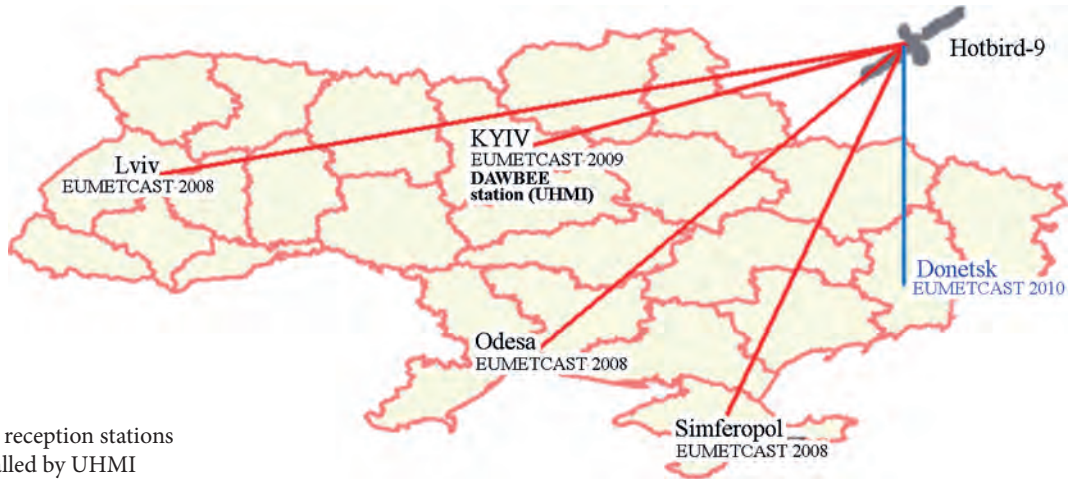

Fig. 1. EUMETCast reception stations in Ukraine installed by UHMI

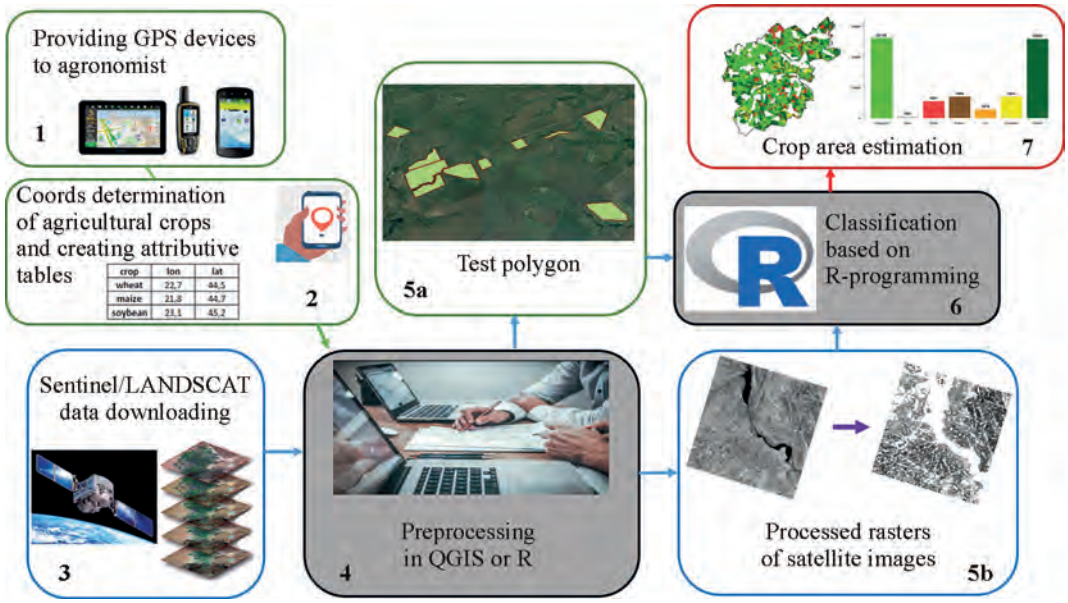

Fig. 2. Flow chart of crop classification system developed by UHMI

the timing of effective satellite imaging in solving the problems of monitoring agricultural crops and the environment. It has been proven that in most cases, the probability of crops detection of individual arable fields in Ukraine by spectral features on space images is very low, but at the same time, there is a high probability of winter crops classification on images (the accuracy of winter crops classification until the middle of May is no less than 80%).

An analysis of the accuracy of crop area estimation within the administrative district using high spatial resolution satellite data during the growing season was performed on the experimental data. An increase in the error in determining the structure and area of crops was noted from 10—15% in the spring period to 35—40% in the summer.

Based on the results, the semi-automatic crop area estimation system for individual agricultural crops was developed (Fig. 2), in which the following tasks are solved step by step: development of the method of obtaining geo-informational data for individual agricultural crops; development of classification methods; determination of crop areas.

The method for classification of multispectral satellite images to determine individual sowings of agricultural crops based on the analysis of spectral channels responses of satellite images was used in the developed system. The method consists of different applications: Random Forest (RF), Support Vector Machine (SVM) and Neural Networks (NN) classifiers, where the values of all spectral channels of cloud-free satellite images during the vegetation period are used as input features, followed by the determination of the most accurate result. The tools for classification of agricultural crops were developed in the R environment (version 3.5.1) using maptools, raster, rgdal, random forest and caret libraries. The tools consistently perform the following tasks: loading raster images in .tiff format; adjusting of all rasters to one calculation area; creating a "stack" of rasters; an extract of the "stack" values within the test fields (the .shp files of the test fields are loaded beforehand); training of classifiers; and construction of the error matrix.

The verification of the results obtained from the crop area estimation system was carried out (Fig. 3): the

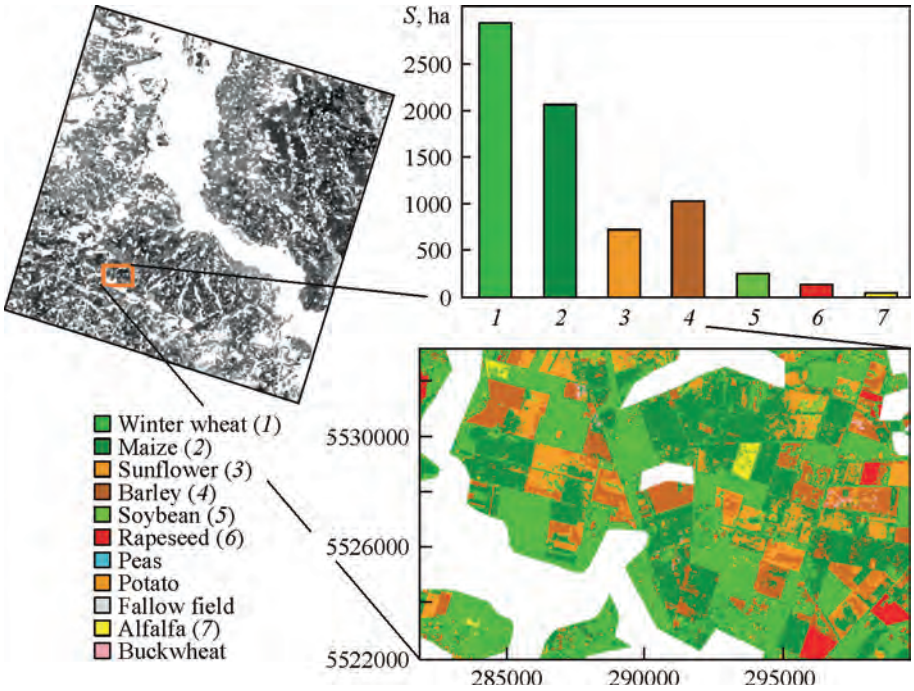

Fig. 3. Crop classification results in the Kyiv region (example)

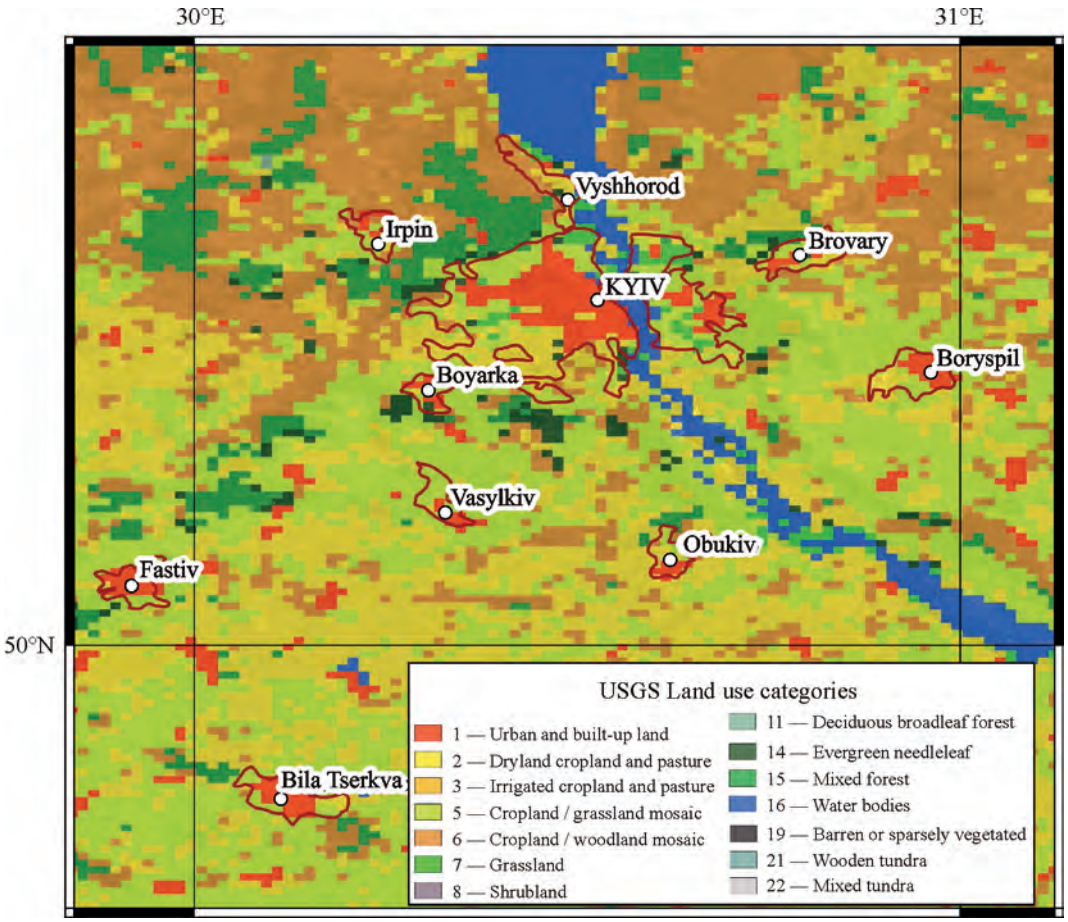

Fig. 4. USGS Land Use Categories in Kyiv Region [11]

lowest accuracy is observed for corn crops; the classification accuracy of soybeans and spring barley is low for most test areas; and the most acceptable accuracy is typical for sunflower, winter wheat and rapeseed crops.

Satellite data usage for numerical weather prediction tasks

Satellite data that reflect the physical state of the Earth's atmosphere and surface, the spatial distribution of cloudiness and precipitation are important sources of input data for

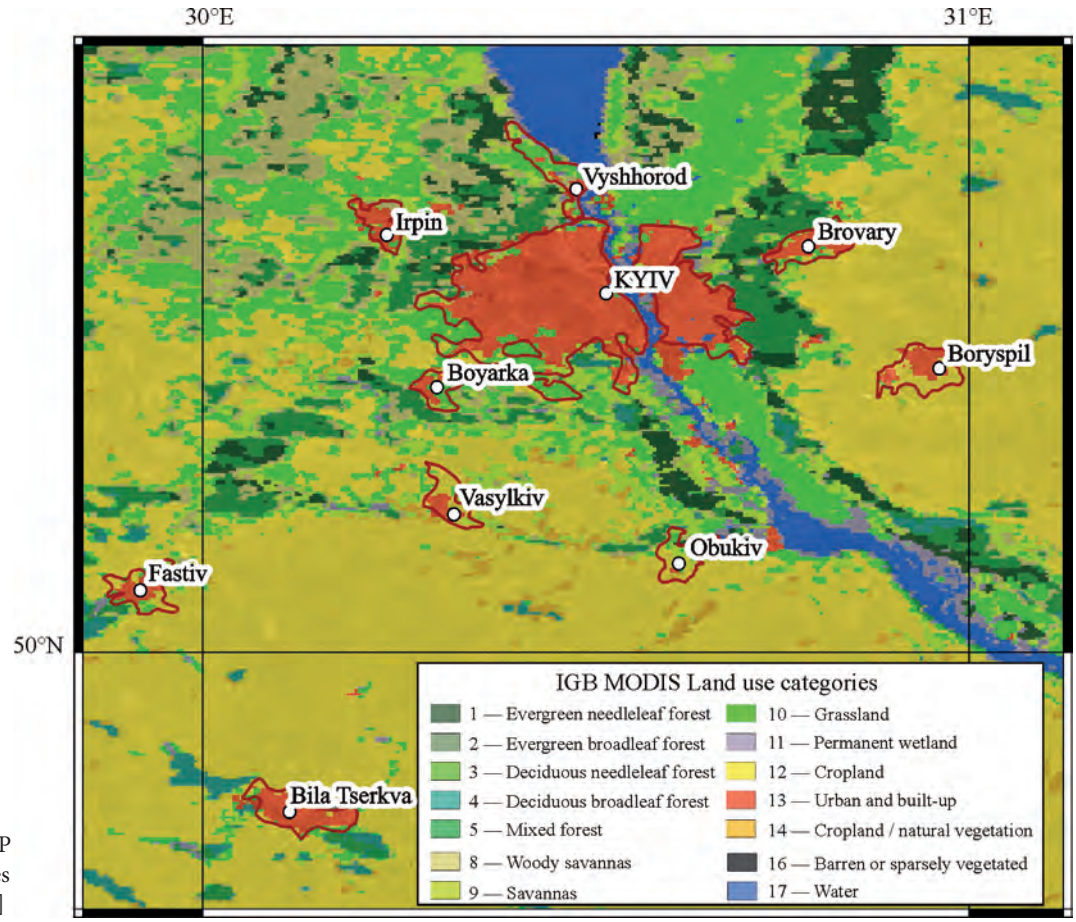

Fig. 5. MODIS IGBP Land Use Categories in Kyiv Region [11]

numerical weather prediction, its refinement and verification. The Earth's surface features significantly affect air circulation in the atmosphere, micro- and mesoscale meteorological processes and phenomena [1]. Therefore, taking into account land surface properties is an important aspect of mesoscale atmospheric modeling. The description of land surface features in atmospheric models is implemented by splitting them into small areas and conducting a subsequent classification of these areas. Modern LULC (land use and land cover) databases are built on the principle of a surface classification within geometrically equal areas of certain spatial resolution. The LULC definition includes two concepts — the type of land cover (LC) and the type of land use (LU) [2, 3].

UHMI has been working on the adaptation of the Weather Research and Forecasting (WRF) mesoscale meteorological models [4] for various purposes and improvement for a long time [5—7]. Together with the use of other methods and models, it makes it possible to create specialized forecasting systems (forecasting of atmospheric phenomena, hydrological forecasting, forecasting of wind waves on the seawater area, etc.) and provides a modern level of hydrometeorological service [8].

The standard LULC database for all versions of the WRF model is the USGS dataset named after the developing institution — The United States Geological Survey [9]. The second standard LU database for WRF is the Collection 5 MODIS Global Land Cover Type [10].

An analysis of the LU USGS's and the MODIS IGBP's categories spatial distribution over the Kyiv region was carried out. An overlay of the USGS and MODIS categories and the current borders of urbanized areas is carried out using QGIS v. 3.22 and Google Maps shown in the Fig. 4 and Fig. 5 respectively. In [11] it was shown that the default WRF LULC datasets are not ideal and contain various types of inaccuracies. Thus, compared to USGS, MODIS IGBP is characterized by a better spatial resolution, more correctly describing the urban built-up territories, forest areas and the Dnipro riverbed, but MODIS IGBP does not display small settlements.

Numerical experiments were carried out using the WRF ARW v. 4.1.3 model in a 2-D configuration (horizontal steps on the main grid and on the nested grid were 10 km and 3.3 km, respectively). For this purpose, the precipitation that fell during the warm and cold half-year in 2020 and 2021 was selected. The data of surface observations, which are carried out on the Ukrainian state meteorological stations network, and the meteorological radar, which was located at Boryspil International Airport were used to evaluate the obtained results.

It is shown that the change of input static data regarding the types of land use (LULC) does not influence the general configuration of the precipitation field and the time of their fall, but there is a redistribution of cells inside the precipitation field and a change in their intensity (Fig. 6).

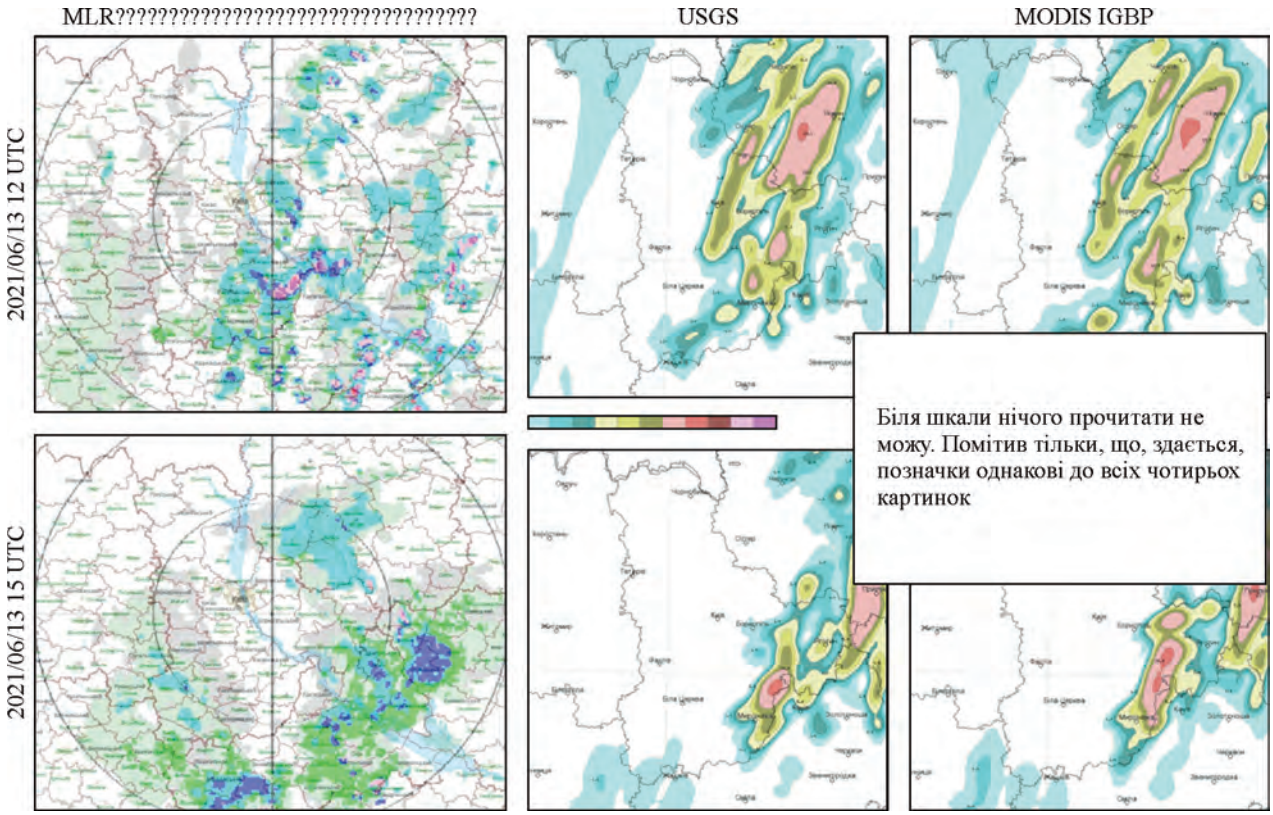

Fig. 6. Observations of the weather radar and results of WRF ARW v. 4.1.3 modeling for the Kyiv Oblast (Region)

Remote Sensing of Atmospheric Composition

Remote sensing data are actively used in UHMI for research and monitoring of atmospheric composition. Over the last years, gaseous pollutants have been studied mainly using the TROPOspheric Monitoring Instrument (TROPOMI), aerosols using the Moderate Resolution Imaging Spectroradiometer (MODIS), and total ozone content using the Ozone Monitoring Instrument (OMI) and TROPOMI.

The first detailed results of air quality over Ukrainian territory based on the Sentinel-5P satellite data were obtained by implementing the Google Earth Engine [12]. However, numerous limitations and inapplicability for operational tasks showed the necessity to use our own fully automated system for near-real-time air quality monitoring in Ukraine, which was successfully developed at the Laboratory of Air Monitoring, UHMI. This system utilizes TROPOMI Level-2 data for nitrogen dioxide (NO_2), carbon monoxide (CO), sulfur dioxide (SO_2), formaldehyde (CH_2O), ozone (O_3), absorbing aerosol index (AAI), and cloudiness. After filtering and binning, it creates Level-3 data files that are stored internally and visualizes results for the entire Ukrainian territory as well as for the biggest cities after downscaling to 2 × 2 km horizontal resolution (Fig. 7).

Being upgraded to use offline (OFFL) data in addition to near-real-time (NRTI), the system helped to study the main features of the spatio-temporal distribution of pollutants in Ukraine, detect emission sources, and analyze elevated pollution content during wildfires, dust storms, and other natural and anthropogenic hazards. All the research was summarized in the monograph [13].

After a three-year period of the Sentinel-5P operation, the TROPOMI data were compared against Ukrainian ground-level observations [14]. This study filled the gap on understanding how TROPOMI can reflect air pollution in highly polluted local urban areas. It became possible to assess because Ukrainian monitoring sites were established for detecting maximum air pollution from specific emission sources. TROPOMI and ground-level data did not correlate at all due to two processes: (1) remote sensing at a particular time might not catch the elevated pollution levels after air mass transportation (hourly-to-daily scale), and (2) because of differences in seasonality between near-surface and column pollutants' content (seasonal scale).

Started on February 24, 2022, the full-scale russian invasion of Ukraine had devastating consequences for air pollution, resulted in the redistribution of emission sources, and formed new war-originated emissions. The war negatively influenced the ability of ground-based measurements to capture air quality changes and provide operative monitoring in emergency situations. A number of monitoring sites were destroyed; some had interruptions in activity due to the impossibility of observers carrying out measurements under artillery and missile shelling. Under the mentioned circumstances, remote sensing of atmospheric composition became the main source of data and information about air quality during the war. The Laboratory of Air Monitoring at UHMI launched two activities that are crucial for air quality

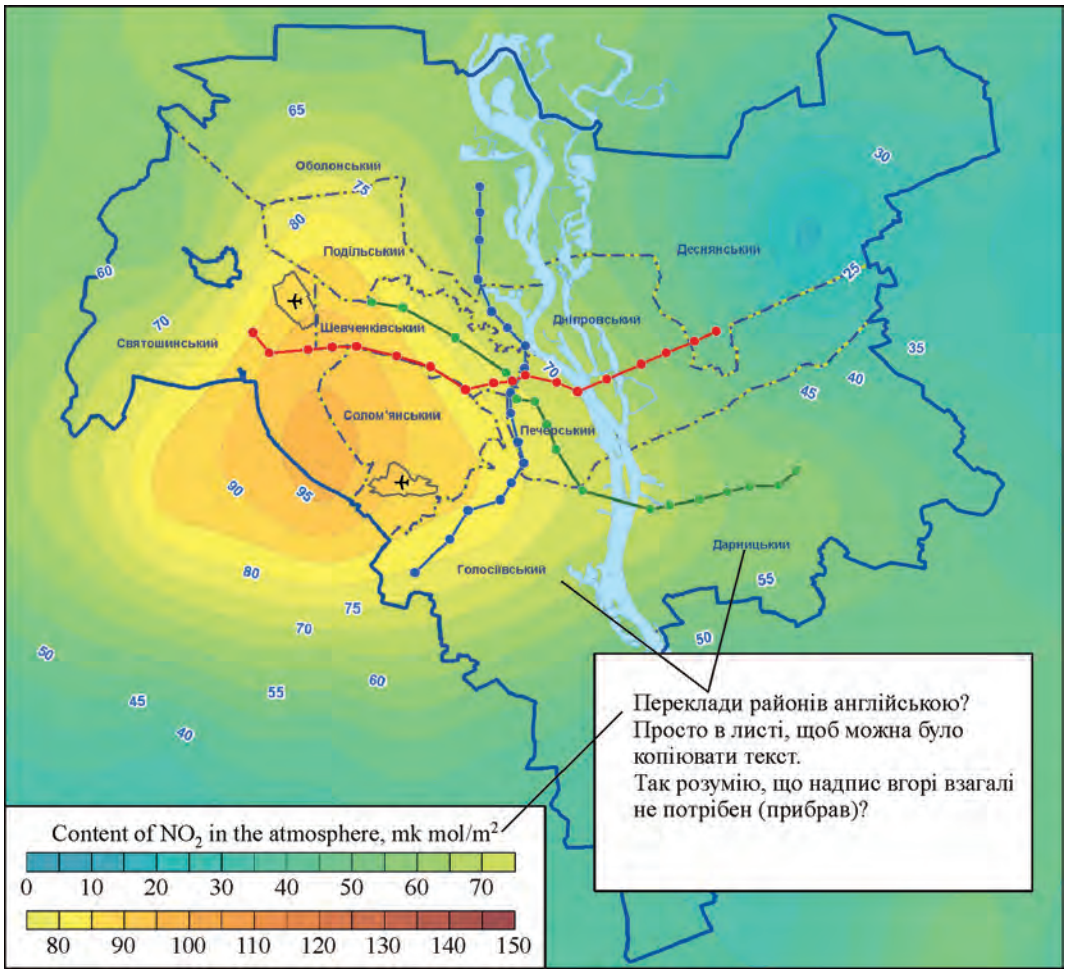

Fig. 7. Near-real time NO_2 content on the example of Kyiv, July 5, 2022, obtained from the developed in UHMI fully automated system (original visualization of the system output)

research and applications during the war. The first activity is the shaping of baseline air pollution needed for future cost estimations, which can be used to claim reparations. The second activity is the permanent monitoring and analysis of air pollution using satellite-based sensors during the war.

Baseline air pollution was described using TROPOMI data after analysis of NO_2, SO_2, CO, and CH_2O total columns for the three-year period prior to the full-scale russian invasion [15]. The study has delineated the most polluted industrial regions with a detailed description of pollutants' variability, including the areas around the biggest thermal power plants. The cleanest ambient air was detected in the mountains and over several national parks. With the support of meteorological data on boundary layer height and wind parameters, the dependencies between air pollution and weather conditions were estimated. The main findings are intended to be used for an assessment of the impact of war on air quality in Ukraine and relevant post-war development measures.

The study of the russian — Ukrainian war impact on air pollution using TROPOMI data was performed after a year-round period [16]. The overall detected changes reflected a NO_2 drop of —35% in big cities after industry damages and a decrease in mobile source emissions; a NO_2 increase of 25% over the regions with the presence of military equipment; and a CO increase of 8% near the front-line because of wildfires caused by artillery shelling (Fig. 8). Numerous other local changes at the urban scale were also found. Consideration of meteorological impact in [16] showed that CO decreased by 15%, mainly caused by changes in regional meteorological conditions and not due to the war.

Remote sensing is actively used for monitoring of the ozone layer over Ukraine and for the prediction of ultraviolet radiation. Using satellite data for several decades, it was calculated total ozone climate normals considering the recommended 30-year climate period of 1991—2020 [17]. These normals are used to estimate ozone anomalies and study the role of stratospheric circulation in ozone variability in the region.

Detection of potentially dangerous fires using thermal anomalies

Ukraine has always been remarkable by a large number of fires on its territory. Incineration of waste from the production of agriculture in the fields, cleaning of the land from dried vegetation and landscape fires lead to the

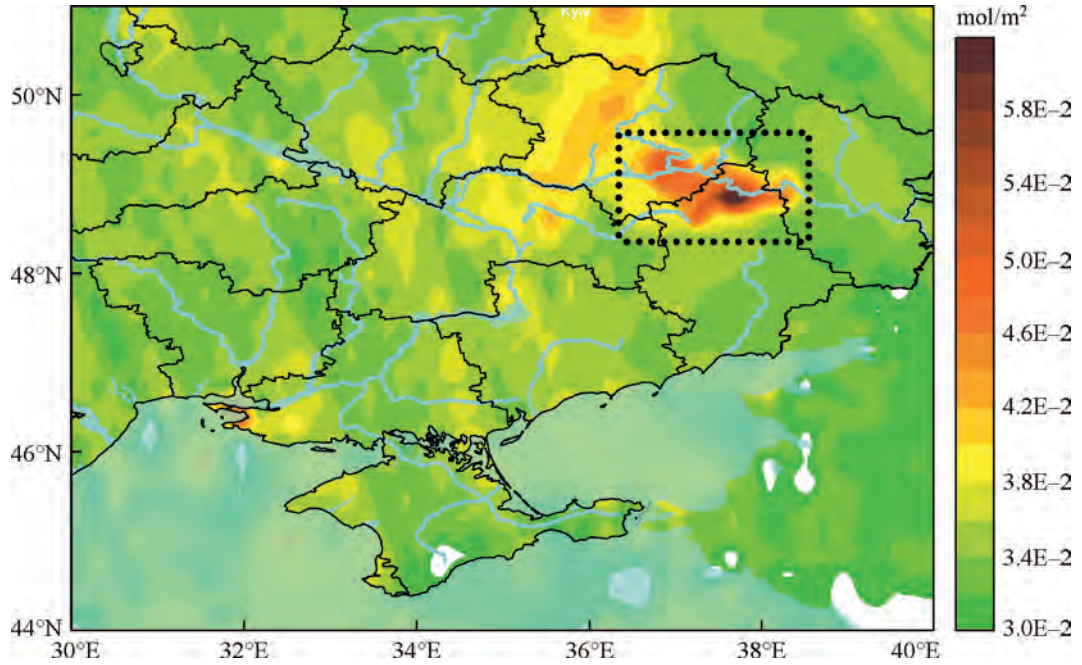

Fig. 8. CO content on May 5, 2022, with maximum values near the front-line along the Siverskyi Donets River (figure published in [16])

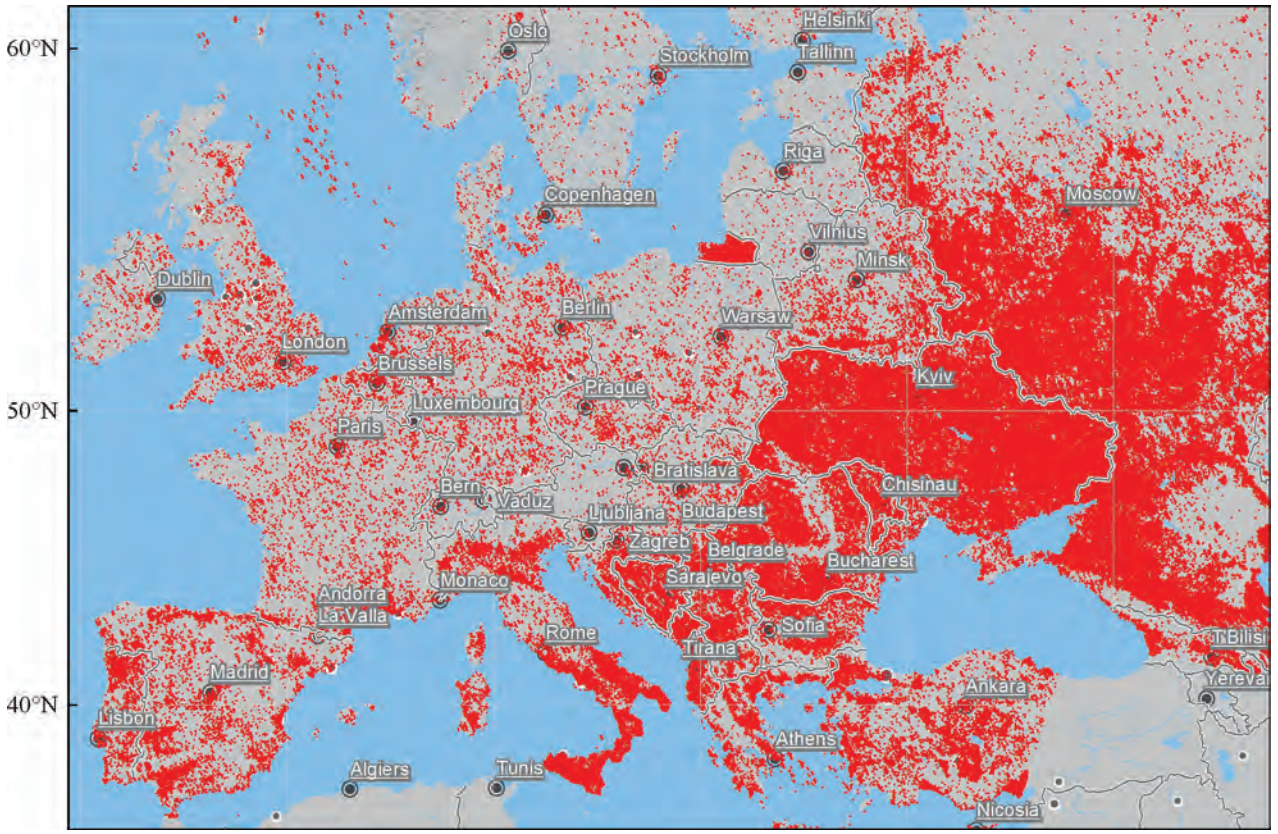

Fig. 9. Thermal anomalies collected for the year

fixation of thousands of thermal anomalies throughout the territory of Ukraine (Fig. 9). However, in addition to fires controlled by farmers, some catastrophic fires have occurred in forest areas. In particular, enormous forest fires covered large areas within the Zhytomyr and Kyiv regions in April 2020. The same year in July, similar fires occurred in the Luhansk region. In response to these challenges, we elaborated the Automatic System for monitoring thermal anomalies and searching for potentially dangerous fires.

The System of fires monitoring represents heat emissions in cartographic view and searches for potentially dangerous fires using these anomalies. This software uses the data from the

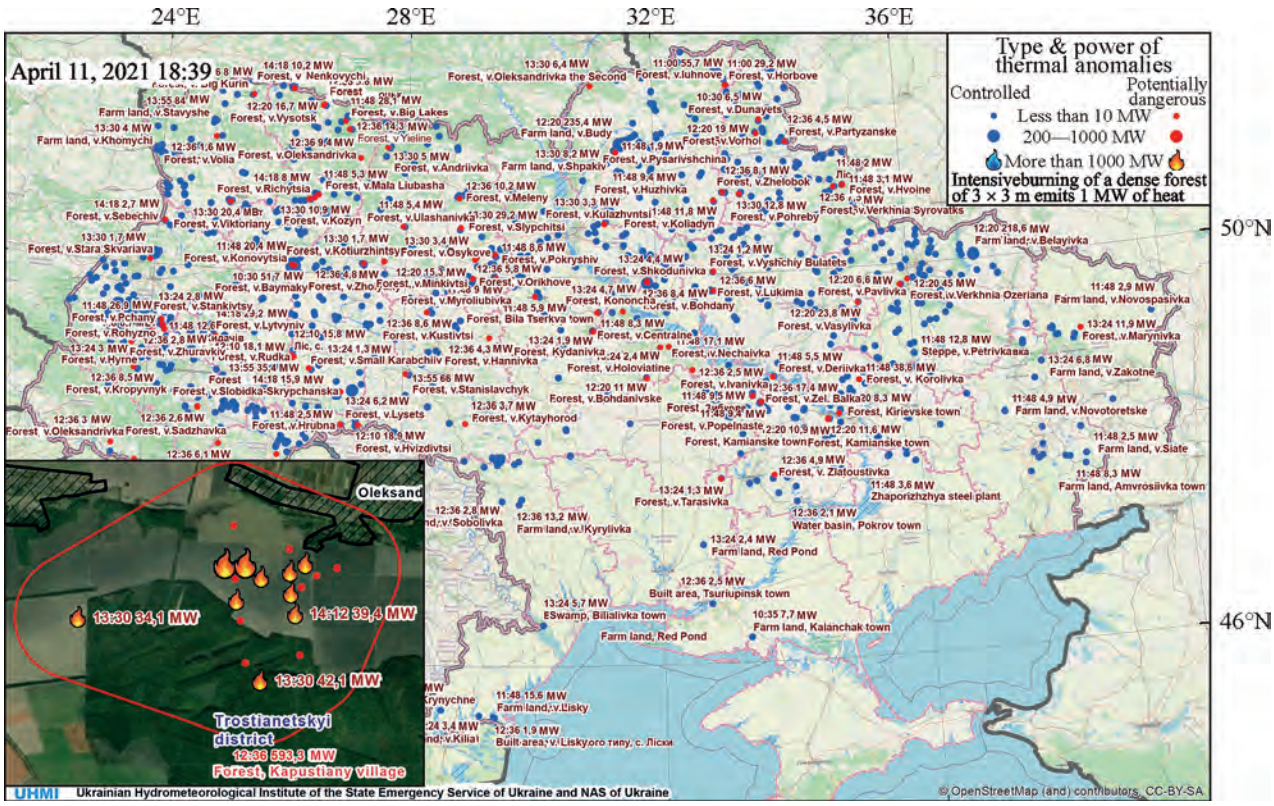

Fig. 10. Heat emissions on the territory of Ukraine on April 11, 2021 (Sunday)

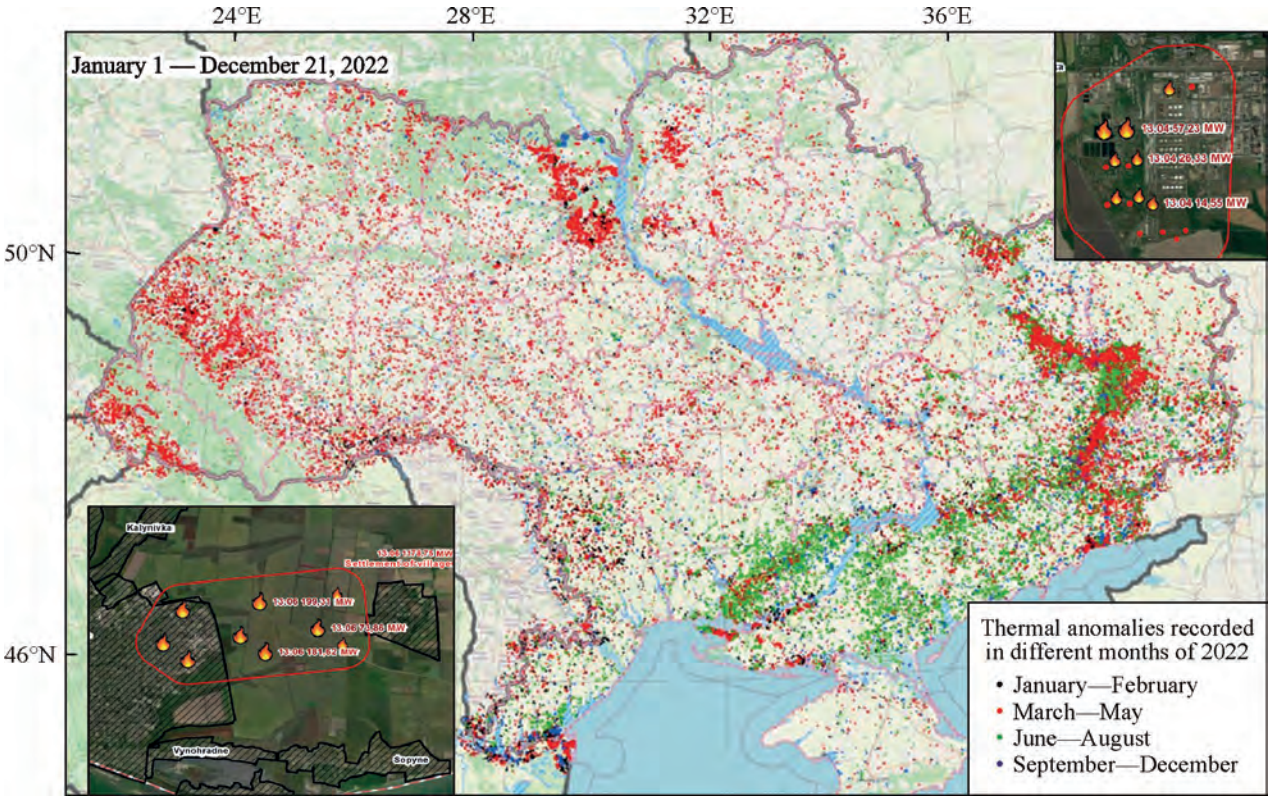

Fig. 11. Spatial and temporal distribution of thermal anomalies on the territory of Ukraine in 2022

FIRMS service [18], which provides open access to thermal scanners' data obtained from four NASA satellites. The geographical name of the object where the ignition occurred was determined by means of geocoding of thermal anomalies. A number of geospatial operations allow us to determine the exact contour of the fire and calculate its power and area.

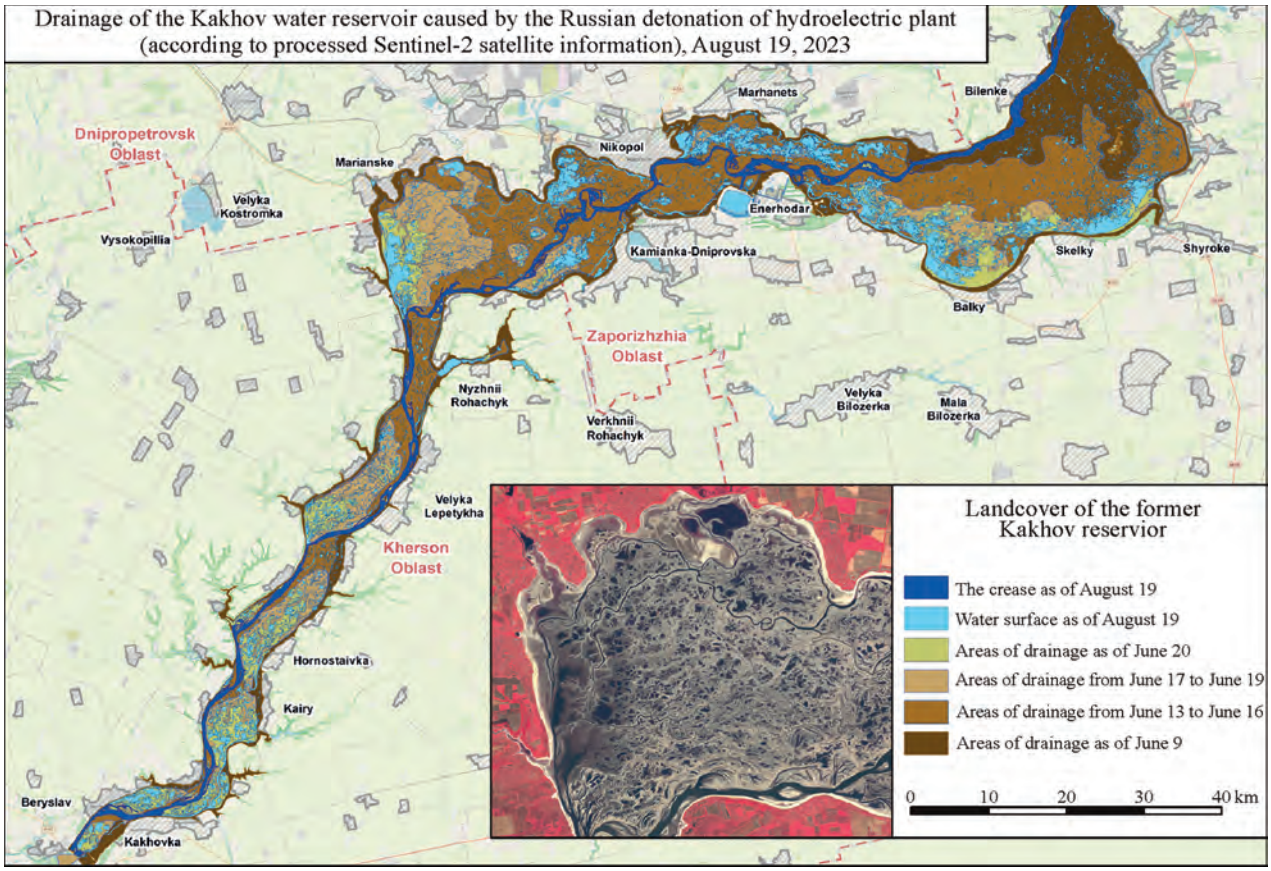

Fig. 12. The stages of drainage of the Kakhovka reservoir

To classify a fire as potentially dangerous, the program takes into account the total power and area of the fire. If the total power of thermal anomalies from the fire exceeds 300 MW or the fire area is more than 10.000 hectares, then we can consider this fire as potentially dangerous. For forest fires, these criteria are smaller. The power of forest burning must exceed 40 MW, or there is heat emission with power over 10 MW in the forest. At last, the total burning power must be more than 200 MW, including fire units near the forest and the burning area exceeding 3,000 hectares to classify this fire as potentially dangerous.

The inset space map in Fig. 10 shows a potentially dangerous forest fire. Fig. 10 generally shows the fires that occurred on April 11, 2021. It was a day off and most of the inflammations (blue dots) originated from burnings of dry grass by farmers and unextinguished bonfires after recreation in nature. Fires near or on the territory of forest areas are shown in red.

Since the beginning of russian aggression against Ukraine, the number of fires has increased in the territories where hostilities are taking place, but not limited to them (Fig. 11). The locations of these fires indicate dangerous areas for civilians and for specialists of the State Emergency Service of Ukraine who are responsible for their extinguishing. However, the separation of fires from combat operations among the rest of the fires that have an economic origin is a scientific problem. Based on the results of the analysis of thermal anomalies and their location, we determined a number of fire characteristics of non-economic origin. These are fires in atypical areas (build-up, industrial areas), the irregular shape of ignition contours, large fires in territories with different types of land use, too powerful fires, and fires at an atypical time. These signs can also include the location of thermal anomalies on critically important objects (upper inset) and their clear structure, as in the city of Mariupol (lower inset in Fig. 11).

Drainage of the Kakhovka Reservoir and deciphering the land cover types of its territory

On June 6, 2023, the occupying forces of the russian federation blew up the engine room of the Kakhovka hydroelectric power station. This environmental crime provided an opportunity for UHMI specialists and for the world scientific community to observe the draining of one of the world's largest reservoirs with an area of 2155 km^2 and a water volume of 18.2 km^3, which was built 67 years ago.

We have monitored the general condition of the reservoir daily using satellite images in the visible spectrum from NASA satellites [19] (Terra, Aqua and NOAA-20) and spectrozonal photos from the satellites of the Sentinel series (especially Sentinel-2A) [20]. It made it possible to compute the degree of its dehydration more accurately and to make a detailed soil map.

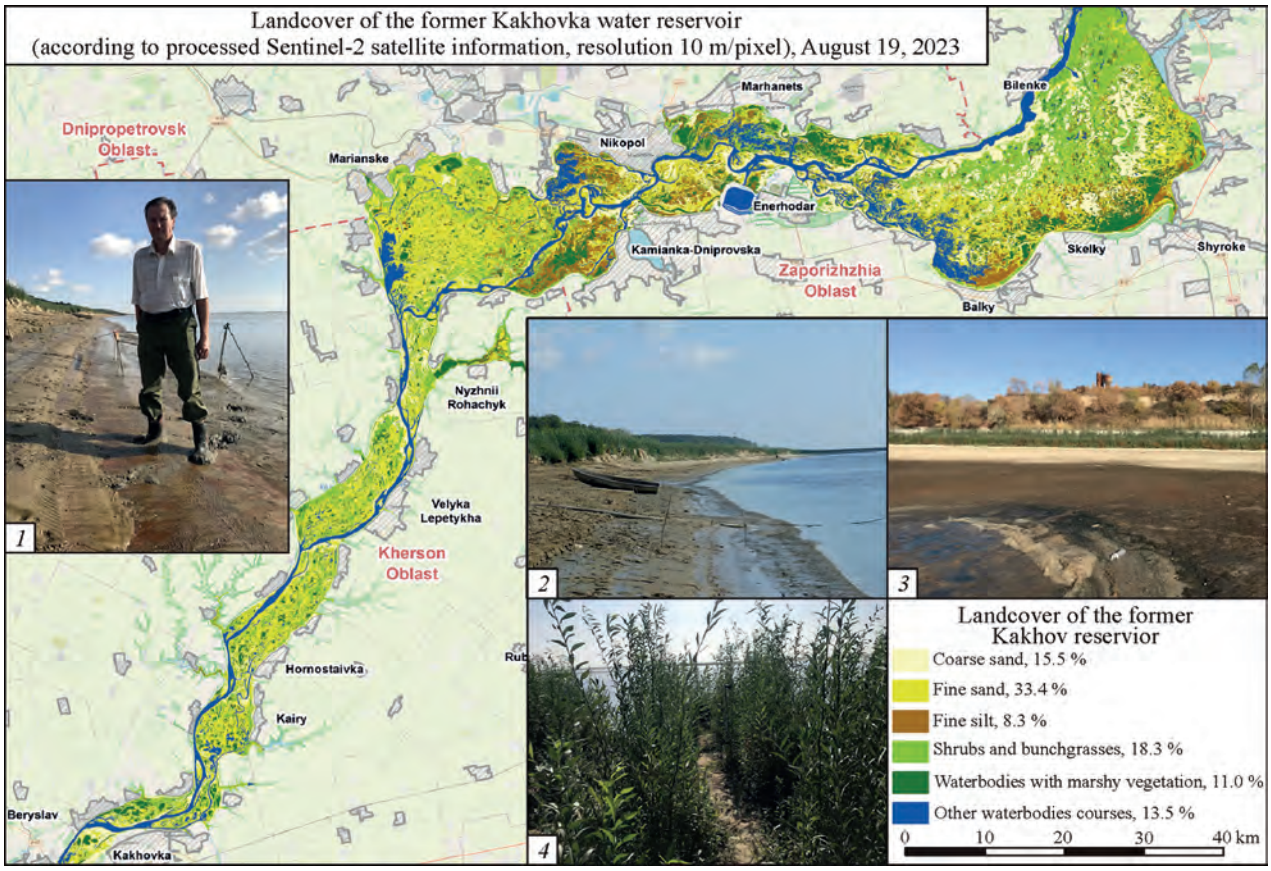

Fig. 13. Land cover types of the Kakhovka Reservoir.
Photos 1—3 show the shore of the reservoir, covered with sand, silty sand and sandy silt. Photo 4 — white willow shoots

The reservoir lost up to 30—40 thousand m^3 of water per second after the dam was blown up and became shallow by 2—3 m in the first 3 days. As of June 13, the depth of the Kakhovka reservoir decreased by 4—5 meters, and the bottom of the reservoir began to be exposed (Fig. 12). Two channels of the Dnipro River were formed in the north of the reservoir. One of the channels has passed near the town of Nikopol and the next one — near the town of Energodar.

On June 17—18, the reservoir split into a series of basins, some of which were no longer connected to the main channel of the Dnipro River. These separated basins can no longer be used for water supply. Their total area became less than a third (31.8%) of the initial area of the reservoir. From that moment, the restoration of the Dnipro riverbed began in the contours that they were before the flooding of this territory in 1953.

Numerous temporary watercourses were formed on the territory of the reservoir at the same time. They were similar to a dense river network. The small watercourses disappeared gradually during the 40—50th days after their appearance. A space photo of this area as of August 19 is shown in the insertion of Fig. 12. The large ones remain filled with water to this day. The total area of residual reservoirs was equal to 140.16 km^2 on July 10. If we add the area of the Dnipro riverbed (120.89 km^2) to that number, we will get the total area of the drained reservoir (261 km^2). That is 12.66% of the initial area of Kahovka reservoir. The decrease in water level led to the drainage of the water intakes of the settlements located around the reservoir. That occurrence also led to the drainage of the water intake in the North Crimean Channel.

The second stage of the research was the analysis of the changes in its territory after the drainage. A month after the dam breach (on July 10—15) some lakes began to turn green due to the development of aquatic vegetation. Once more month later, on August 10, the appearance of vegetation was recorded in drained areas.

Automated decoding of space images showed that the surface of the reservoir consists of sediments (Fig. 13): sand covers an area of 331 square km (15.5%); silty sand — 716 sq. km (33.4%); sandy silt — 178 sq. km (8.33%); vegetation — 391.6 sq. km (18.3%); reservoirs with swamp vegetation — 235.7 sq. km (11.0%); deep reservoirs and riverbed — 288.3 sq. km (13.5%).

On 5th of October, an UHMI expedition to the shores of the reservoir showed that the latter were covered mainly with willow (presumably white) and possibly poplar and several types of herbaceous plants. In other words, herbaceous vegetation was not the first to populate the drained area. As we will know later, the detonation of the dam on 6th of June coincided with the beginning of the sowing of poplar and willow seeds. There were the seeds that could be carried

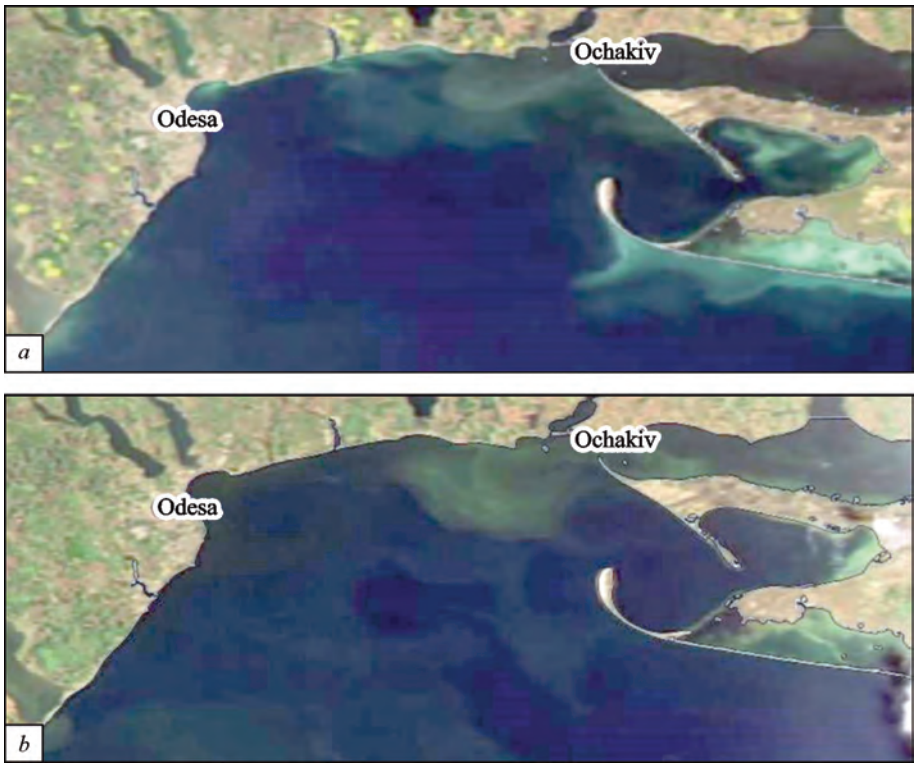

Fig. 14. Enhanced natural color images of the NW Black Sea obtained by MODIS/Aqua 04.05.2007 (*a*) and MODIS/Terra 20.05.2007 (*b*)

by the wind, and they were sown over the entire territory of the reservoir. In addition to this, these two species grew in large numbers on the shores of the former reservoir, resulting in the formation of several million shoots. A well-moistened, silty substrate with the remains of mussels and bottom dwellers, without grass cover, turned out to be ideal to inhabit for these types of trees. As a conclusion, we can point to the unsuitability of this territory for agriculture.

Marine shelf and coastal zone water dynamics

Since 2022, research on the dynamics of transitional waters (transformed riverine waters) spreading on the northwestern shelf of the Black Sea from the estuarine areas of the Dnipro, Southern Buh and Dniester rivers has been initiated in UHMI [21]. Satellite images in the visible range play an important part in these studies due to the fact that the color of marine and transitional waters differs significantly correlating with water salinity in the region [22]. In addition, satellite images show other dynamical processes affecting the structure of the shelf waters, in particular, coastal upwelling and advection of relatively clean water from the deep-sea area.

Table 1

Parameters of medium resolution satellite instruments' visible channels

Satellites	Aqua, Terra		NOAA-20, Suomi NPP	
Instrument	MODIS		VIIRS	
Channels:	Wavelength, nm	Resolution, m	Wavelength, nm	Resolution, m
Red	620—670	250	600—680	375
Green	545—565	500	545—565	750
Blue	459—479	500	478—498	750

Convenient sources of information are series of low-cloud or cloud-free images in true (natural) colors obtained from MODIS (Terra, Aqua satellites) and VIIRS (NOAA-20, Suomi-NPP satellites) scanners, which have similar spectral characteristics and spatial resolution of visible channels (Table 1, URL: https://worldview.earthdata.nasa.gov/).

The following examples of satellite data analysis concern typical and extraordinary cases of transient water from the Dnipro-Buh estuary (DBE) expansion to the NW shelf of the Black Sea.

The first two scenes (4 and 20 May, 2007) were taken after and during the different riverine discharge conditions: from 20 April to 13 May it was less than 1000 m^3/s, and then it increased significantly to more than 1650 m^3/s by 19 May. Image for 04 May demonstrates rather contrast plume of gray-brown water (that is rich with terrigenous suspended matter) surrounded by light-green patches of previously delivered estuarine water (Fig. 14, *a*). The latter obviously contributed to the active blooming of phytoplankton due to the increased content of nutrients. Other manifestations of phytoplankton (and chlorophyll) content rise can be seen along the Tendra Spit (south-eastern corner of the image), but they have another origin — most probably coastal upwelling driven by north-eastern wind delivers nutrients with the bottom water to the warmed and enlightened sea surface. Under the sharply enlarged freshwater supply from the Dnipro and Southern Buh rivers, to 20 May the plume from DBE was intensified and extended to the west and south (Fig. 14, *b*). Generally, the described situation is close

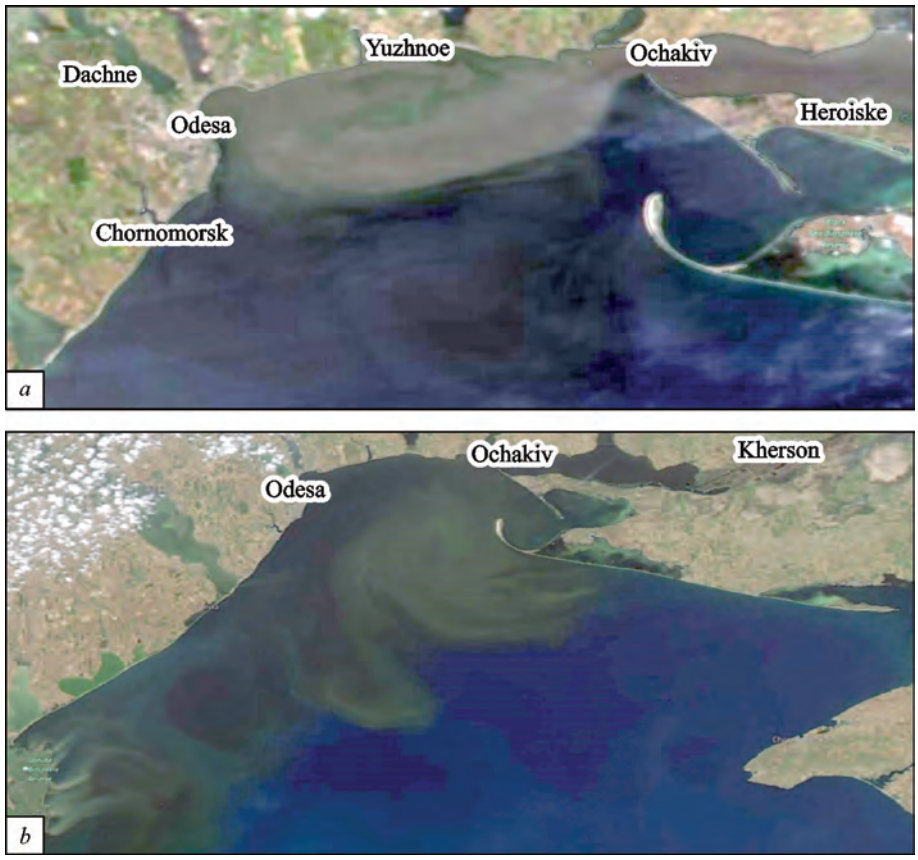

Fig. 15. Enhanced natural color images of the NW Black Sea obtained by VIIRS/NOAA-20 09.06.2023 (*a*) and MODIS/Aqua 24.06.2023 (*b*)

to the average conditions of the DBE water expansion [21].

The next example demonstrates the consequences of the extreme riverine water discharge after the explosion of Kakhovka reservoir dam by russian troops on June 6, 2023. According to the analysis of the high-resolution images obtained from the Sentinel-2A satellite carried out by UHMI [23], the change in the area of the Kakhovka Reservoir from June 6 to June 9 corresponded to an average volumetric water flow of about 20,5 thousand m^3/s, which came in the DBE and on the adjacent sea shelf. This discharge is 14,4 times more than the average monthly long-term value for the years 1960—2010 (1424 m^3/s); 10,5 times — the average monthly long-term maximum in the seasonal rate (for May, 1958 m^3/s); finally, 2,2 times more than the maximum daily flow registered on May 6, 1970 (9440 m^3/s).

The abnormally powerful flow of riverine water led to the fact that in 1—2 days the DBE was filled with practically fresh water, which then quickly reached the Odesa Bay. On June 9, the VIIRS/NOAA-20 image showed (due to the high content of dissolved and suspended substances in water) an anomalous plume of turbid waters with a width of 17—27 km, stretching from DBE to Odesa (Fig. 15, *a*). Moreover, within this plume, one can distinguish an anticyclonic eddy structure, which was formed by the westward water flow and the compensating alongshore current, which returned the accumulated water mass to the east again. The front of this return flow reaches the traverse of the Tyligul liman, and the total distance traveled by the front of desalinated turbid waters to the Odesa Bay and back along the coast reached ~100 km. That is, the average current speed on the sea surface at the front of the muddy plume was about 55 cm/s in low-wind weather!

The bulk of the Dnieper water continued to spread along the coast to the southwest, and by the middle of June, a continuous and wide strip of transformed riverine waters was formed between the DBE and the Kiliya delta of the Danube River. After that, the south, south-westerly wind intensified, which formed a system of currents of anticyclonic vorticity on the north-western shelf of the Black Sea, as can be noted by the jets direction flowing from the arms of the Danube delta (south-western corner in Fig. 15, *b*). Under these conditions, the main features of the riverine water influence (RWI) zone moved from June 22 to 24 by 30—40 km in the general direction to the southeast, with an average speed of 16—22 cm/s. In the last week of June, this process continued, and on July 1, the RWI zone in the form of intense phytoplankton bloom spots stretched eastward, to the Crimea peninsula. According to contact and satellite observations, such a surface water structure was previously formed only in August [22].

Conclusions

The implementation of remote sensing in hydrological, marine and meteorological studies has gained momentum in recent years in Ukraine. A full-scale russian invasion following the destruction of the national hydrometeorological network and decreasing the capabilities of in-situ monitoring resulted in the indispensability of satellite data use. These

caused UHMI to enhance its capacities and develop new applications for remote sensing in hydrometeorological research and monitoring. UHMI continues their usual tasks for studying spatio-temporal variability of cloudiness and its parameters, retrieval of vertical profiles of meteorological variables, monitoring of crops and other vegetation, detecting and analyzing hydrometeorological hazards, improving NWP models considering land cover changes, tracking air pollution, ozone layer monitoring, wildfire detection, studying marine water dynamics, especially in coastal regions. Since the full-scale war started, the initial focus was also shifted towards emergency tasks: land cover changes, war-originated air pollution and wildfires near the frontline, the consequences of the Kakhovka dam destruction, and enhancing the ability to integrate and incorporate remote sensing data with ground-level measurements and NWP modeling at different time and spatial scales, considering the necessity of a quick response to unpredicted environmental hazards.

REFERENCES

1. Manual on the Global Observing System (WMO No. 544). 2015. I. 92 p. URL: https://library.wmo.int/viewer/58672/?offset=1#page=1&viewer=picture&o=bookmark&n=0&q= (Accessed: 08 April 2024)

2. Liping C., Yujun S., Saeed S. Monitoring and predicting land use and land cover changes using remote sensing and GIS techniques — A case study of a hilly area, Jiangle, China. *PLoS ONE*. 2018. 13(7). e0200493. https://doi.org/10.1371/journal.pone.0200493

3. Rawat J.S., Kumar M. Monitoring land use/cover change using remote sensing and GIS techniques: A case study of Hawalbagh block, district Almora, Uttarakhand, India. *The Egyptian Journal of Remote Sensing and Space Science*. 2015. 18(1). P. 77—84. https://doi.org/10.1016/j.ejrs.2015.02.002

4. Skamarock W.C. et al. A description of the Advanced Research WRF version 3. NCAR Tech. Note NCAR/TN-475+STR. 2008. 113 p. https://doi.org/10.5065/D68S4MVH

5. Shpyg V. et al. The application of regional NWP models to operational weather forecasting in Ukraine. *CAS Technical Conference on "Responding to the Environmental Stressors of the 21st Century"*, 18—19 November 2013: Conf. Materials. 2013. URL: https://www.researchgate.net/publication/312488806_The_Application_of_Regional_NWP_Models_to_Operational_Weather_Forecasting_in_Ukraine (Accessed: 08 April 2024).

6. Shpyg V., Budak I. WRF reflectivity simulation and verification of thunderstorm forecast by radar and surface observation. *16th International Radar Symposium*, 24—26 June 2015. Symposium Materials. Dresden. P. 610—615. https://doi.org/10.1109/IRS.2015.7226388

7. Shpyg V., Budak I. Estimation of effectiveness of thunderstorms observation and their forecast by the instability indices. *7th International Verification Methods Workshop*. 03—11 May 2017. Berlin, Germany. *Annalen der Meteorologie*. 2017. 51. P. 81.

8. Numerical atmospheric models and their application in different areas of economics / Anatoliy Doroshenko, Vitalii Shpyg, Igor Budak, Kateryna Huda. In: Kvasniy L. And Tatomyr I. (eds) Ukraine in the context of global and national modern servisation processes and digital economy. Praha: Oktan Print, 2020. P. 155—171. https://doi.org/10.46489/UITCOG0909

9. USGS EROS Archive — Land Cover Products — Global Land Cover Characterization (GLCC). https://doi.org/10.5066/7GB230D

10. Friedl Mark A., Sulla-Menashe Damien, Tan Bin, Schneider Annemarie, Ramankutty Navin, Sibley Adam, Huang Xiaoman. MODIS Collection 5 global land cover: Algorithm refinements and characterization of new datasets. *Remote Sensing of Environment*. 2010. 114, Iss. 1. P. 168—182. https://doi.org/10.1016/j.rse.2009.08.016

11. Shpyg V.M., Shchehlov O.A. Influence of land use categories on WRF forecast and its accuracy. *Hydrology, Hydrochemistry and Hydroecology*. 2022. No. 3(65). P. 68—78. https://doi.org/10.17721/2306-5680.2022.3.5

12. Savenets M. Air pollution in Ukraine: a view from the Sentinel-5P satellite. *Idojaras*. 2021, 125(2). P. 271—290. https://doi.org/10.28974/idojaras.2021.2.6

13. Osadchyi, V., Orechshenko, A., Savenets, M. Satellite monitoring of fires and air pollution. Kyiv, 2023. 256 p. https://doi.org/10.15407/uhmi.2023_1

14. Savenets M., Dvoretska I., Nadtochii L., Zhemera N. Comparison of TROPOMI NO_2, CO, HCHO, and SO_2 data against ground-level measurements in close proximity to large anthropogenic emission sources in the example of Ukraine. *Meteorological Applications*. 2022, 29(6). e2108. https://doi.org/10.1002/met.2108

15. Savenets M.V., Nadtochii L.M., Kozlenko T.V., Komisar K.M., Zhemera N.S. Status of atmospheric air pollution in Ukraine prior to the full-scale russian invasion. Part 2: Pollutants total content according to the satellite data. *Ukrainian Hydrometeorological Journal*. 2023. 32. P. 130—143. https://doi.org/10.31481/uhmj.32.2023.09 (In Ukrainian).

16. Savenets M., Osadchyi V., Komisar K., Zhemera N., Oreshchenko A. Remotely visible impacts on air quality after a year-round full-scale Russian invasion of Ukraine. *Atmospheric Pollution Research*. 2023. 14(11). 101912. https://doi.org/10.1016/j.apr.2023.101912

17. Dvoretska I.V., Savenets M.V., Umanets A.P. Updated total ozone climate normals over the territory of Ukraine. *Ukrainian Hydrometeorological Journal*. 2021. 28. P. 5—15. https://doi.org/10.31481/uhmj.28.2021.01 (In Ukrainian).

18. Providing Active Fire Data for Near-Real Time Monitoring and Applications. *FIRMS*. URL: https://firms.modaps.eosdis.nasa.gov/ (Accessed: 12.04.2024).

19. Worldview Start Page. URL: https://worldview.earthdata.nasa.gov/ (Accessed: 12.04.2024).

20. Copernicus Browser. URL: https://browser.dataspace.copernicus.eu/ (Accessed: 12.04.2024).

21. Ilyin Yu.P. Average condition and seasonal variability of the structure and dynamics of transitional waters in the Dnieper-Bug estuary region. Ukrainian *Hydrometeorological Journal*. 2023. 32. P. 63—79. https://doi.org/10.31481/uhmj.32.2023.05 (In Ukrainian).

22. Ilyin Y.P., Grishin G.A. Summer desalination of the northwestern part of the Black Sea and the possibility of its control by satellite video data. *Geographical interpretation of aerospace information*. 1998. Moscow. P. 119—125 (In Russian).

23. Oreshchenko A. Draining of the Kahovka Water Reservoir Caused by the Russian Blowing of the Hydroelectric Plant Dam. *International Conference of Young Scientists on Meteorology, Hydrology and Environmental Monitoring*. November 1516, 2023. Kyiv. P. 34. https://doi.org/10.15407/icys-mhem.2023.034

APPLICATION OF SPACE TECHNOLOGIES TO ASSESS THE ECOLOGICAL STATE AND CONSEQUENCES OF MILITARY OPERATIONS ON THE MARINE ECOSYSTEMS OF UKRAINE

G. Minicheva, E. Sokolov
Institute on Marine Biology of the NAS of Ukraine

After signing the Association with the European Union [1], Ukraine assumed a large range of obligations, including those in the area of the natural environment. Two of the 6 Water Directives in this document are related to transit, coastal and offshore zones of marine ecosystems, it is the Water Framework Directive [2] and the Marine Strategy Framework Directive [3]. In accordance with the standards and requirements of these Directives, Ukraine should perform state monitoring and strive to achieve Good Ecological Status in national waters of marine ecosystems. In this regard, remote assessment of the ecological condition of marine areas with the usage of satellite data has become extremely relevant, due to the need for performing continuous monitoring of marine areas, which requires significant technical and economic costs in the collection of field material. Data received from satellite carriers [4, 5] allows remount monitoring of numerous indicators such as: temperature regime, suspended matter, transparency, chlorophyll "a" concentration, oil pollution, etc., with the help of which it is possible to monitor and estimate with minimal costs MSFD Descriptors such as: D5 — Eutrophication, D7 — Hydrographic Condition, D8 — Contaminants, D10 — Marine Litter.

The full-scale military invasion of russian federation to Ukraine, which began on February 22, 2022, has not only catastrophic humanitarian but very profound negative ecological consequences, which are taking over marine ecosystems inclusively. With the onset of active hostilities over the marine water areas of the Black and the Azov seas, and also as a result of the military's mining of the coastal sea strip, researchers no longer have the opportunity to assess contact indicators. Starting from March 2022, remote technologies of satellite data remained the only tool enabling rapid assessment for the environmental situation, related to warships sinking, aircraft destruction over the water areas, oil spills and reaction to extensive environmental disasters.

Thus, taking into account the strategic tasks of Ukraine on monitoring of national marine waters, as well as the operational situation, related to the consequences of hostilities on marine ecosystems and the limited possibility of ecological indicators contacting measurement — technologies, related to the space information receiving, have become the main, effective tool for the Ukrainian marine water areas assessment. These circumstances became the reason for operational methodological developments of satellite information methods application to the regional conditions of the Sea of Azov and the North-Western part of the Black Sea, as well as for oil spill scale direct assessment in marine water areas, including Marine Protected Areas (MPA), as a result of military actions. The results of these methodological developments, and also the scale of hostilities consequences assessment on marine ecosystems of Ukraine, are outlined in this work.

Methodological developments of satellite technologies application to regional conditions of marine ecosystems of Ukraine

For oil spills detection on the water surface, the great importance has a combination of various satellite technologies. In the oil spills research the data of radar and optical modes were used, which are publicly available. The usage of radiolocational satellites, such as Sentinel-1 [4], ensures spill monitoring even at cloudy weather conditions and at night [6]. This makes it possible to react quickly to ecological events and take quick measures to eliminate them. The usage of optical technologies such as Landsat 8 [5] and Sentinel-2 [4] allows to receive multispectral data for more detailed spills analysis, even, even including their thickness and different physical and chemical characteristics [7].

The radiolocational data was received from the Sentinel-1 satellite with synthetic aperture radar (SAR) in the mode of interferometric wide swath (IW), which plays an important role and is the most spread in the tasks of oil spills detecting in marine water areas. The radar sensors (SAR), on the board the Sentinel1 satellite, use long wavelengths in the radio frequency range, with an active signal reception type and are sensitive to sequential radio wave pulses with a resolution capacity of 10 m [8]. The presence of oil products leads to reduction of the interaction between waves and wind, and forms smoothed areas on the ocean surface (slicks). These areas show up on radiolocational images as areas with low scattering and thus serve as indicators of the pollutive films presence on the sea surface [9, 10]. However, one of the main problems in oil slicks detection is "false targets". Areas of reduced backscattering values are not always caused by mineral oil spills (natural biogenic films, areas of localized wind attenuation, wind shadow from land, rain cells, internal waves, fresh ice, algal blooms, wastewater from onshore industrial or municipal enterprises, hydrological fronts, upwelling zones) [6].

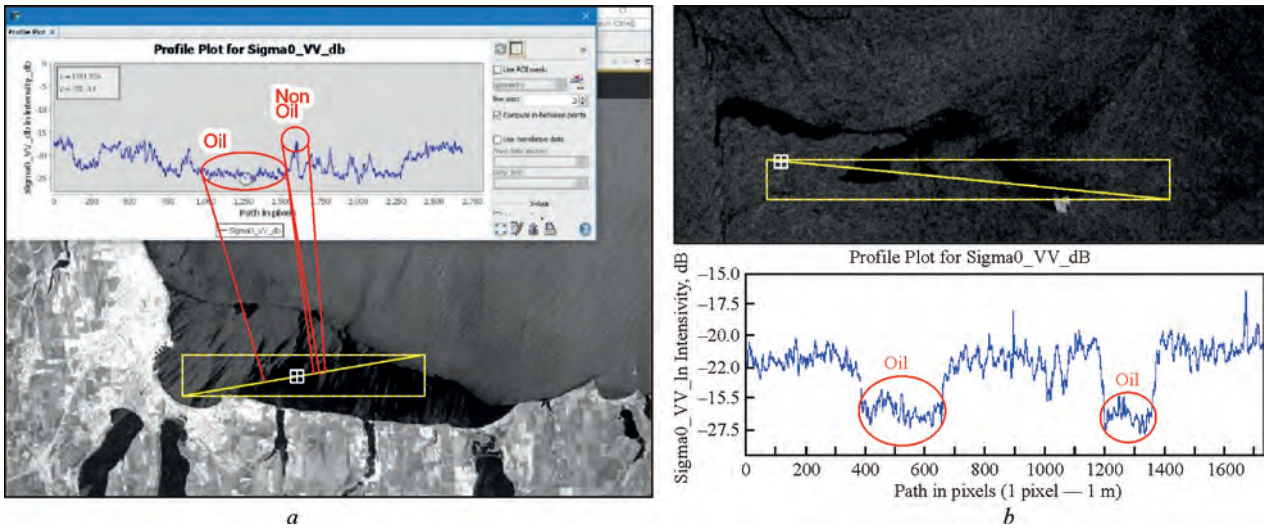

Fig. 1. Histogram of Sigma dB values in oil spill places and in their absence: *a* — 15.03.2022, area of Gulf of Odesa; *b* — 07.05.2022, Snake Island area (NWBS)

For solving this problem were applied: object-oriented and discriminant analysis methods (statistical analysis, texture features, dark spots — slicks shape and geometry) [12, 13]; the usage of multispectral satellite imagery in the optical and thermal shooting ranges; hydrodynamic data and atmospheric phenomena data from the international services Eumetsat [14] and Copernicus Marine Service — CMEMS [15] geodatabases. The limitation in such an approach is that not all hydro-meteorological and satellite data in optical shooting modes coincide in time with radiolocational images, or interfere with a cloudy atmosphere.

Multispectral satellite sensors were used separately or in conjunction with radiolocational imagery in the regional oil spills research: Landsat 8 (Operational Land Imager, OLI), Sentinel 2 (Multispectral Instrument, MSI) and Sentinel 3 (Ocean and Land Colour Instrument, OLCI), which collect data in the short-wave and infrared parts of the electromagnetic spectrum. A quantitative characteristic that allows to identify oil products by optical satellite data is "normalised water leaving reflectances" in different spectral ranges bands of satellite imagery — was calculated using the optical processor of atmospheric correction for coastal waters C2RCC [16]. For the calculation of oil spills square in the optical footage mode were used both — the satellite channels spectral signatures classification (automatic clustering of spectral and semi-automatic with training) [17] and their stable combination in the form of the spectral index OSI — Oil Spill Index [18].

Pre-processing (preparation) of satellite imagery for spill detection analysis was implemented on the basis of methodological guidelines developed by the European Space Agency [8].

The processing and calculation of potential places of oil spills in the region were carried out using software: ESA SNAP (European Space Agency, The Sentinel Application Platform) developed by the European Space Agency, and in the geoinformational package QGIS. Both software are freely available. In order to quantify the density of oil spills in the water area of the Black Sea North-Western part (NWBS), overlay grid computations were performed based on the geoprocessing tools of the platform QGIS — the water area was covered with the grid with cell area of 1 sq km.

After radiometric calibration of the satellite imagery in the radio frequency range, which means leading the signal to well-known and standard quality values, radio signal scattering intensity in decibels (Sigma, dB) corrected data was received.

Oil spill objects, which are characterized by low value of backscatter, show up as dark spots in comparison with the surrounding water, because they dampen short surface waves generated by the wind (Fig. 1).

However, not all ecological factors distribution geodata coincide in time, and there are situations where, even after the comparison with oceanographic and production factors, it is difficult to draw an unambiguous conclusion, for example, on 11 June 2022 (Fig. 2), the large dark spot is likely to represent a biogenic film and phytoplankton bloom.

The return signal (Sigma dB) value of the Sentinel 1 satellite radar for oil spills objects is the same low (Fig. 3), as in case of phytoplankton blooms biogenic films, even in terms of intensity, the values are almost identical [6].

Thus, expert conclusion with the engagement of oceanographic, meteorological and bioproductive information is a crucial element in oil spills monitoring systems, which allows to exclude cases with other oceanographic phenomena that have similar slick-forming and spectral-signature characteristics. In addition, solving this task includes the analysis of a wide range of characteristics, such as texture features, shape and geometry of dark spots (slicks), which can significantly increase the efficiency of spill detection.

In comparison with the radiowave range of waves length, physical and optical (spectral) spills characteristics

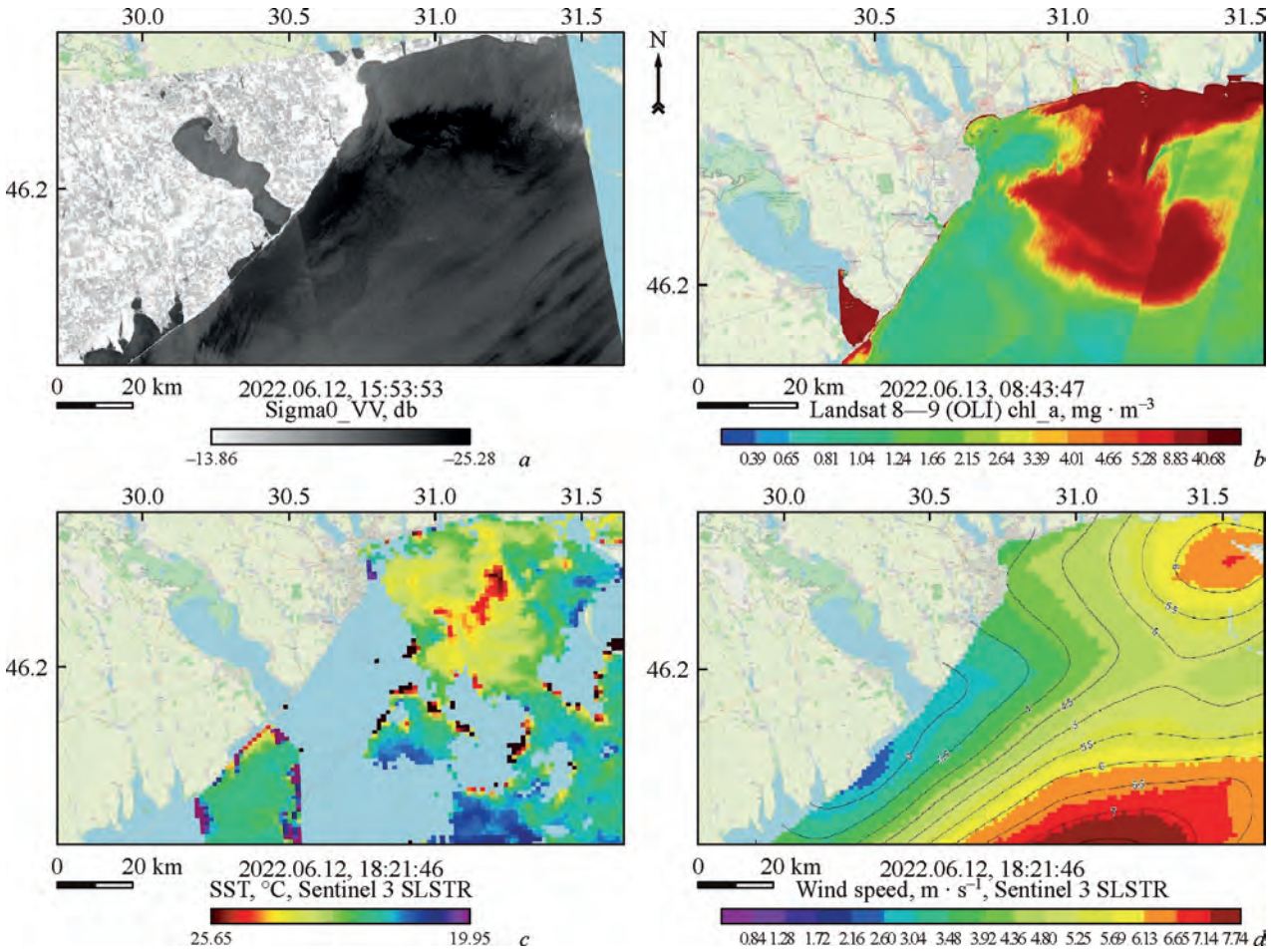

Fig. 2. Radiolocational satellite image Sentinel1 and Sentinel 3 satellite sensor products during 12—13 June 2022:
a — Sentinel1 radar satellite image, *b* — chlorophyll "a" concentration, *c* — surface temperature distribution, *d* — wind speed

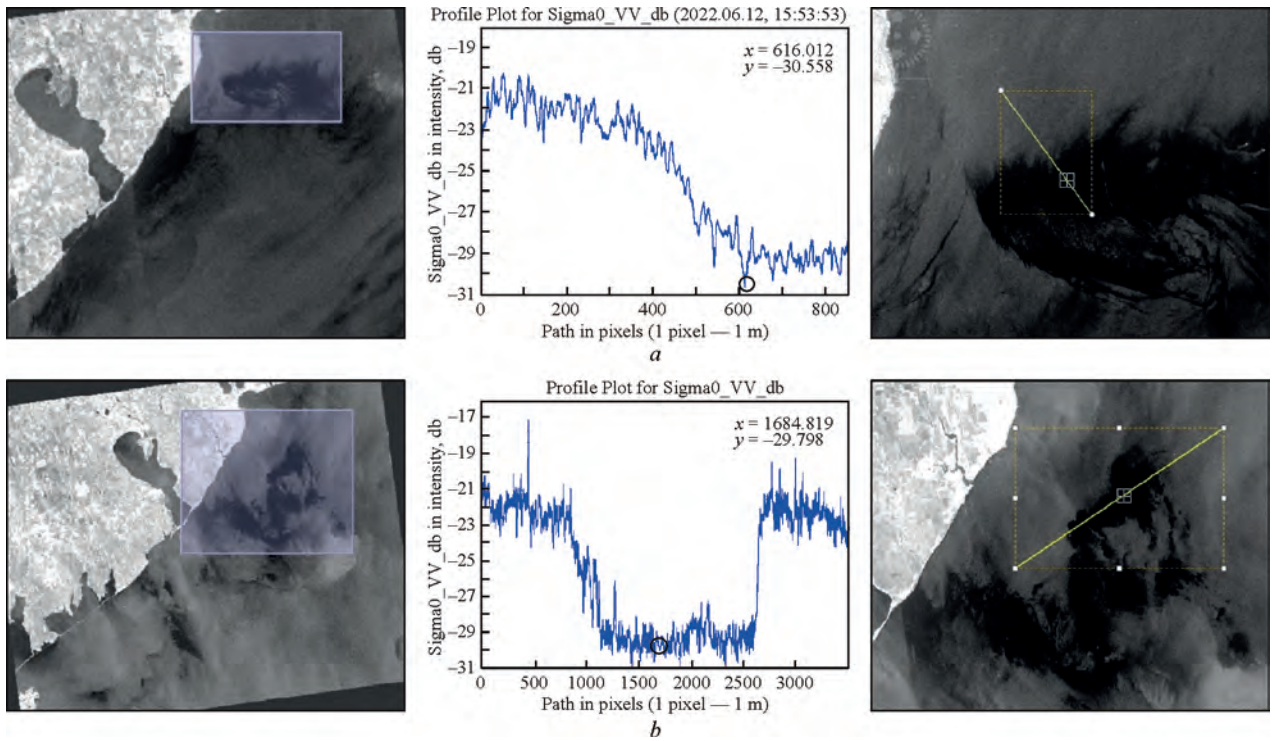

Fig. 3. Histogram of Sigma dB values of satellite Sentinel 1 (IW), in places of dark spots and in their absence:
a — 2022.06.12, probable concentration of biogenic and algal films); *b* — 2022.03.08, probable oil spill

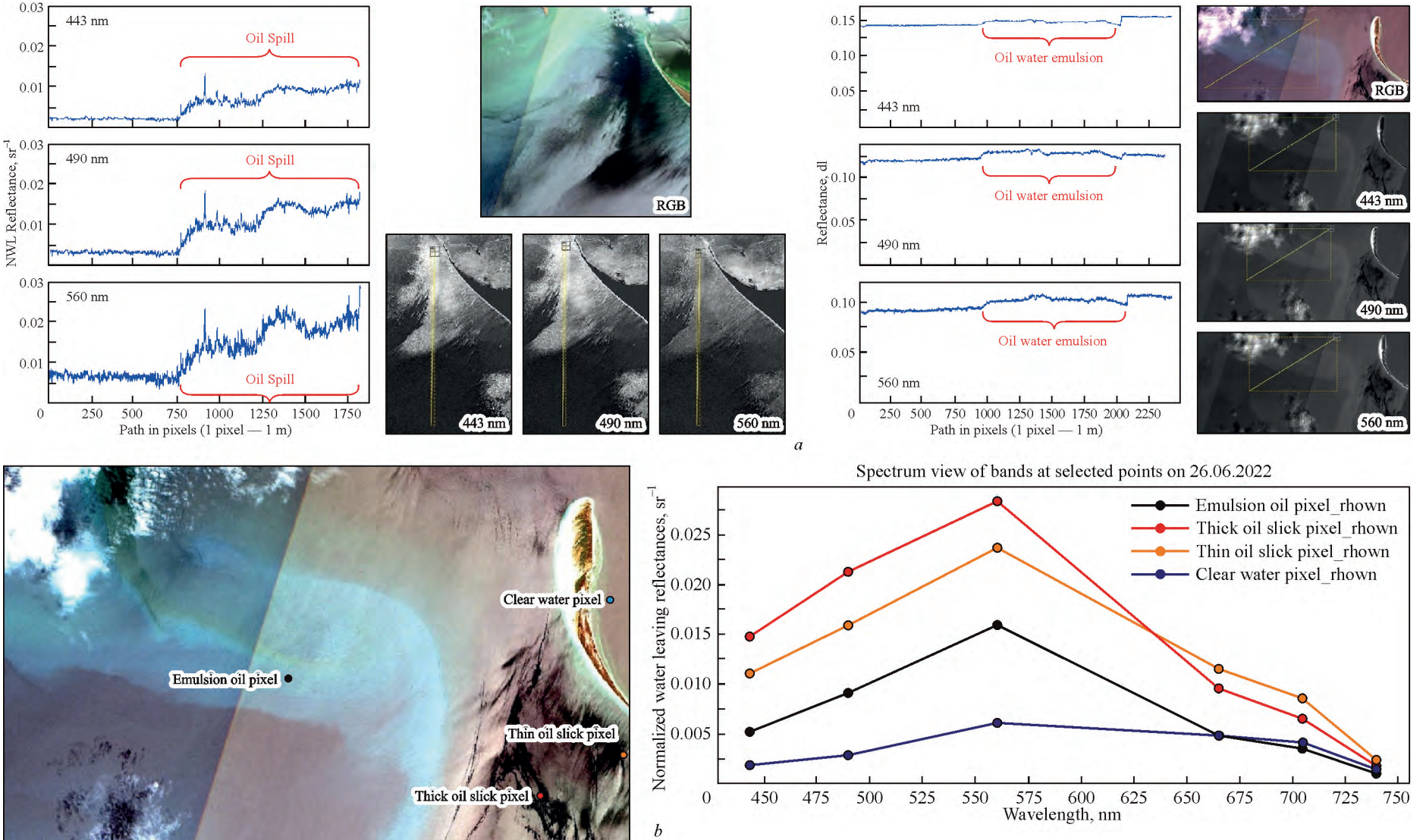

Fig. 4. Histogram (spectral profiles) of coefficient water reflectances values of different spectral bands of the Sentinel2 satellite, in places of oil spills with a different layer thicknesses, and in their absence during 26.06.2022: *a* — along the lines; *b* — at points of different pollution degrees

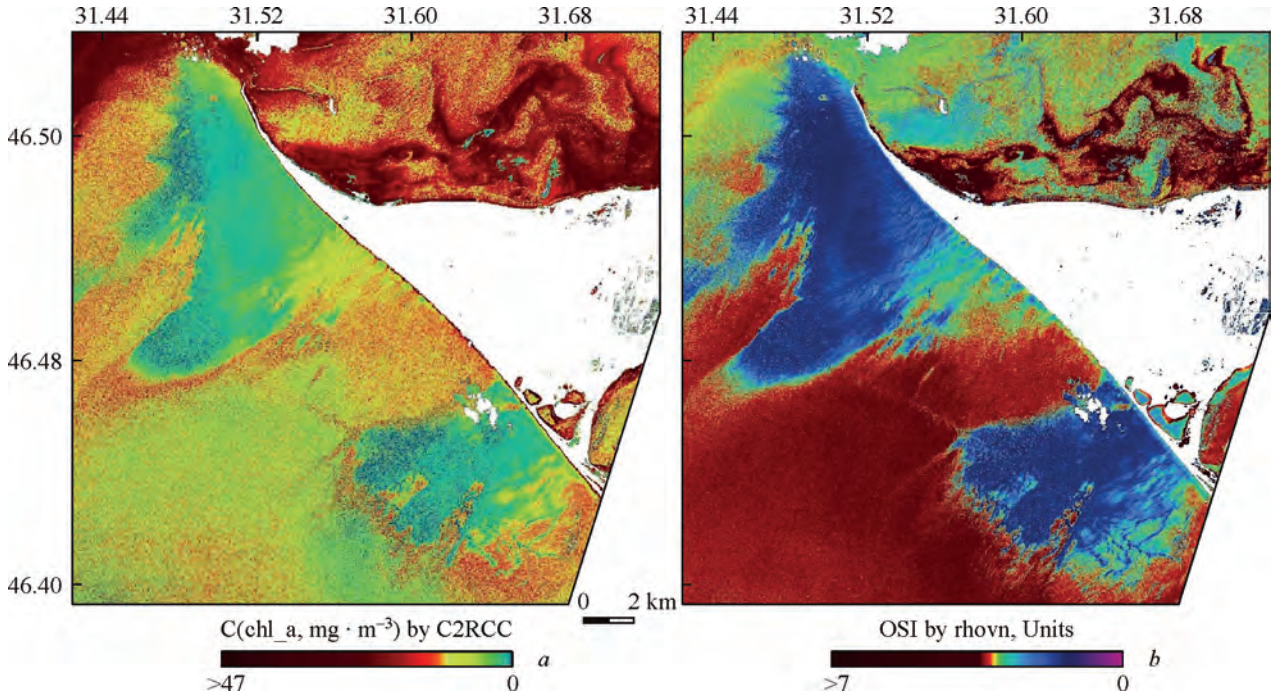

Fig. 5. Distribution of oil spills characteristics:
a — chlorophyll "a" concentrations; *b* — Oil Spill Index in the Kinburn Spit area (NWBS)

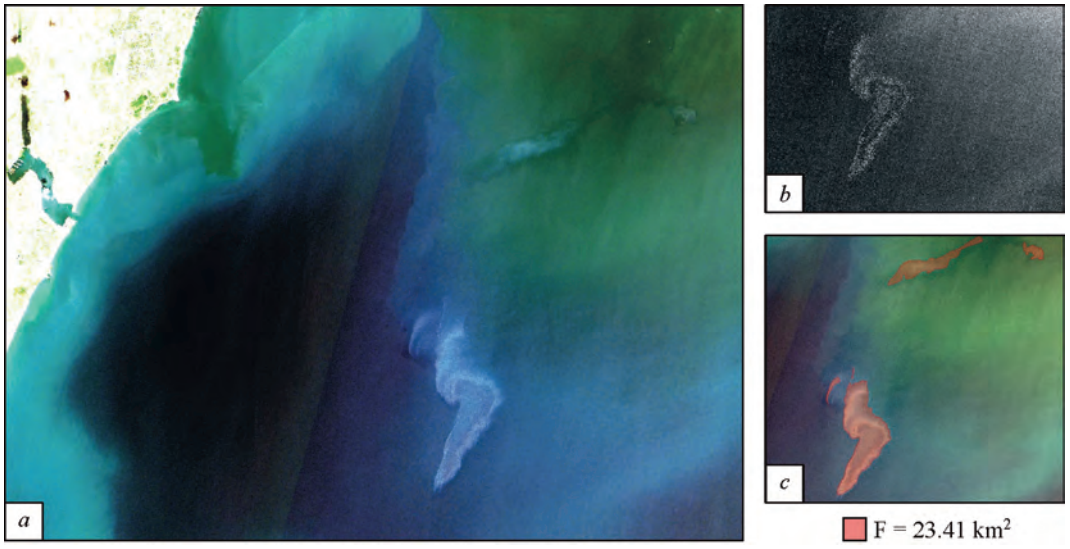

Fig. 6. Oil spills emulsion traces on the water area of NWBS opposite the Sukhyi liman according to Sentinel2 satellite (MSI_L1C) data during 2022.07.08: *a* — full-colour image; *b* — "Oil Spill Index" — spectral coefficients ratio of sea surface reflectances in the form of: $(Rrs_{560\ nm} + Rrs_{665\ nm}) / Rrs_{490\ nm}$; *c* — spills mask with the area calculation

in the optical satellite images mode on the basis of the coefficient of water reflectances (Rrs, sr-1), on the contrary, were characterized by higher values of the corresponding characteristic, and in a single-channel black-and-white image looked like more lighted areas. Thus, according to the Sentinel2 satellite (MSI) in the optical range of waves length on June 26, a probable accumulation of oil products in the form of films and emulsion traces was recorded in the area of the Karkinitska and Tendrovskaa Bays (Fig. 4).

Oil spills extent assessment resulting from hostilities, including marine protected areas (MPAs)

According to Sentinel2 (MSI) data, oil products spills differed on chlorophyll "a" concentration values and the OSI (Oil Spill Index) spectral index from primary productive processes (Fig. 5).

According to the MSI optical instrument of the Sentinel2 satellite, emulsion spills were recorded in the beginning of July 2022, which were well identified by the coefficients

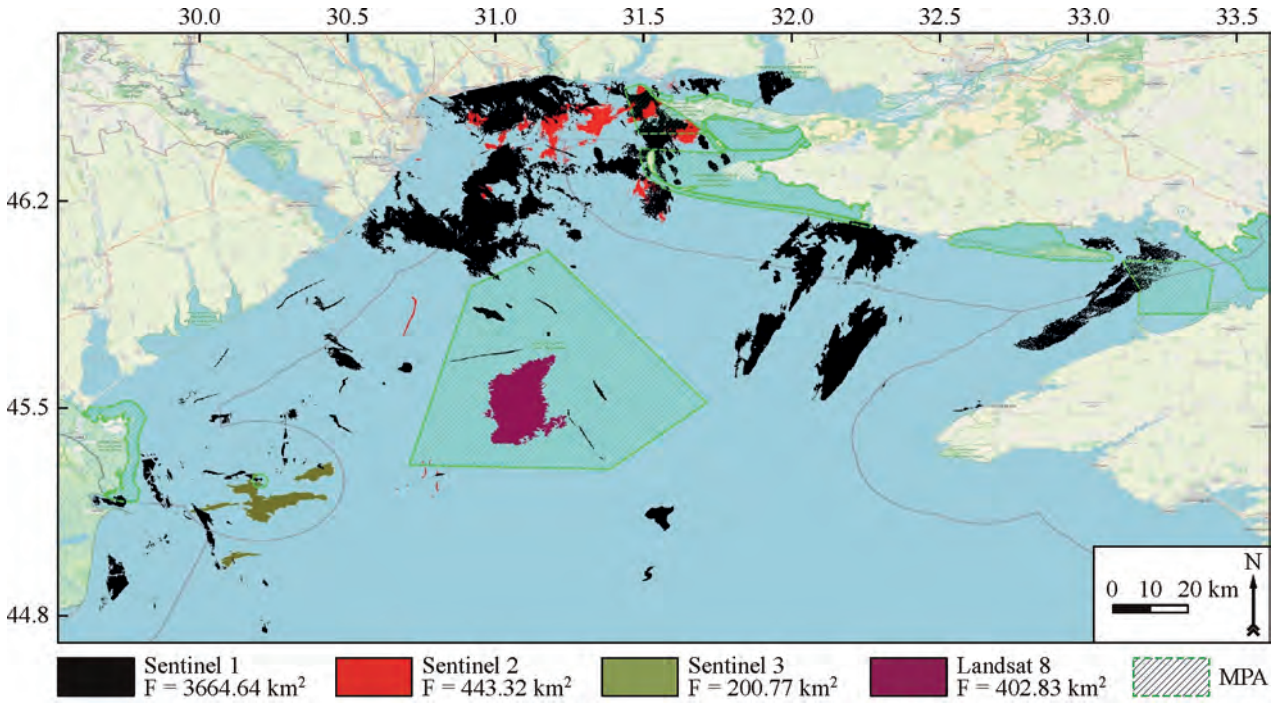

Fig. 7. Identified oil spills in 2022, within the boundaries of the Ukrainian sector of the NWBS, based on satellite imagery in optical and radar

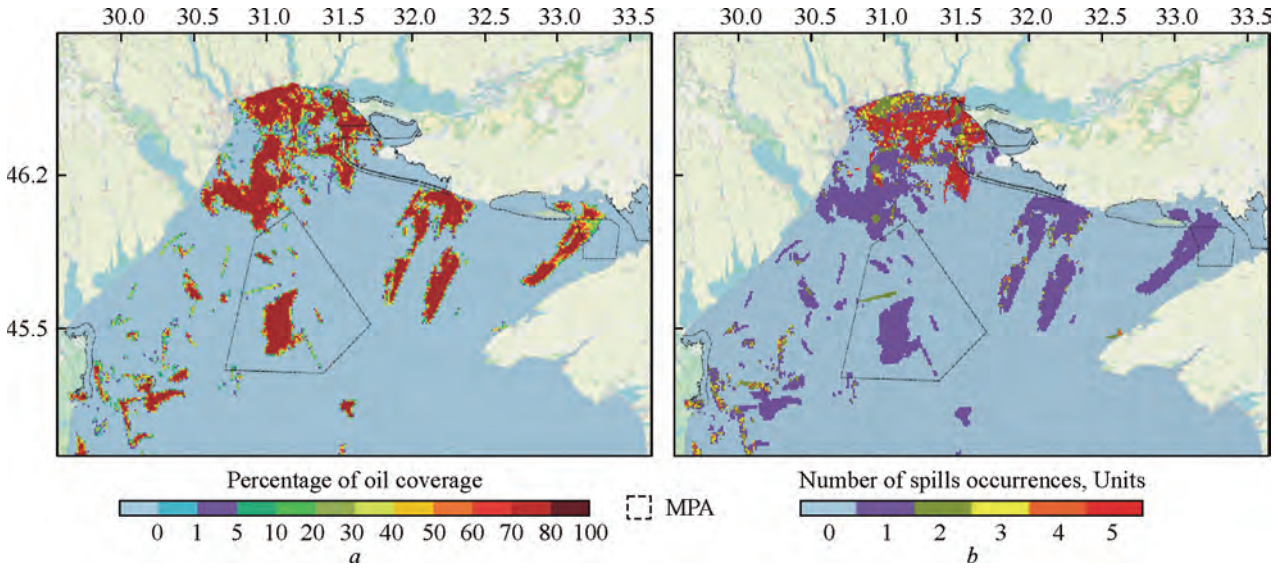

Fig. 8. "Grid-computations" of coverage percentage and amount of oil spills overlays in 1sq m cells: *a* — the percentage of oil pruducts coverage; *b* — the amount of spillage repeats

ratio of sea water surface reflectances in the form of the Oil Spill Index [18] (Fig. 6).

Based on the developed regional algorithm for oil spills indetification, the database of satellite imagery in radiolocational — Sentinel1 (GRD) and optical modes — Sentinel2 (MSI), Sentinel3 (OLCI), Landsat8—9 (OLI) was analyzed during the hostilities. The analysis excluded cases and areas with weather hydroecological conditions which introduce uncertainty and do not ensure the possibility of oil spills detection. 31 cases (images) of oil spills were detected on the water areas of the North-Western Black Sea (NWBS) in total, with a total area of 4711.6 sq km (including overlaps for different dates), which is 16.2% of the NWBS area. The total area without overlays for different dates was 4354.98 sq km, which is 14.9% (Fig. 7).

According to the visual features of spills distribution spatial structure, the most dense is the northern part of the region — Odesa and Dnipro-Bug districts. In order to assess the spatial damage scale of the most valuable

marine protected areas (MPAs) as a result of hostilities, a spatial "overlay" (multi-layered) analysis of the planar intersection between MPAs and oil spills was carried out. The number of cases which characterize the oil spills overlay in space and time was 9.9% of the total. The square of corresponding areas, based on the "Grid-computation", was 1756 sq km. The largest number of repeats was recorded in the Dnipro-Bug district and near Zmeiny Island.

The percentage of the oil spills covering of marine protected water areas squares of the NWBS during February-September 2022 was as following, %:

- Beloberezhe Svyatoslava National Nature Park — 67;
- Botanical Reserve of the National Significance "Zernov's Phyllophora Field" — 21;
- Zoological Reserve of the National Significance "Zmeiny Island" — 62;
- Black Sea Biosphere Reserve — 16;
- Karkinitskiy Reserve — 25;
- Danube Biosphere Reserve — 5.

In order of the density distribution quantitative evaluation of oil spills on the NWBS water area overlay "Grid-computations" were carried out, and the percentage of oil spills coverage and the spatial frequency intersection of oil spills pollution coverage of the NWBS were calculated for each cell (Fig. 8).

Geoinformational assessment of the density of oil pollution distribution based on the "Overlay Grid-computation", allowed to receive the information on the oil products coverage intensity of the NWBS areas, including protected water areas in the period of 2022—2023.

The square of cells affected by oil products amounted to 6762.5 sq km, what is 23.3% of the total square of the NWBS, the square of cells affected by more than 5% amounted to 6140.1 sq km, what is 21% of the total square of the NWBS, affected by more than 50% cells amounted to 3086.7 sq km and 10.6% accordingly, affection of cells >80% amounted to 2473.9 sq km and 8.5%. The square of completely covered on 100% by oil products cells amounted to 1396.5 sq m, or 4.8% of the total square of the NWBS.

REFERENCES

1. Association Agreement between the European Union and its Member States, of the one part, and Ukraine, of the other part. *OJ L*. 29.5.2014. 161. P. 3—2137. https://eur-lex.europa.eu/legal-content/EN/ALL/?uri=CELEX:22014A0529(01)

2. DIRECTIVE 2000/60/EC of the European Parliament and of the Council establishing a framework for the Community action in the field of water policy, 23 October 2000. (WFD, 2000/60/EC).

3. DIRECTIVE 2008/56/EC of the European Parliament and of the Council establishing a framework for Community action in the field of marine environmental policy, 17 June 2008. (MSFD, 2008/56/EC).

4. Copernicus Data Space Ecosystem. URL: https://dataspace.copernicus.eu/ (accessed on 05 July 2023).

5. USGS Global Visualization Viewer. 2013. URL: http://glovis.usgs.gov (accessed: 06 June 2022)

6. Alpers W., Espedal H.A. Oils and surfactants. Synthetic aperture radar marine user's manual. 2004. 25. P. 263.

7. Leifer I., Lehr W.J., Simecek-Beatty D., Bradley E., Clark R., Dennison P., Wozencraft J. State of the art satellite and airborne marine oil spill remote sensing: Application to the BP Deepwater Horizon oil spill. *Remote Sensing of Environment*. 2012. 124. P. 185—209.

8. Chaturvedi S.K., Banerjee S., Lele S. An assessment of oil spill detection using Sentinel 1 SAR-C images. *Journal of Ocean Engineering and Science*. 2020. 5(2). P. 116—135.

9. Lombardini P.P., Fiscella B., Trivero P., Cappa C., Garrett W.D. Modulation of the spectra of short gravity waves by sea surface films: slick detection and characterization with a microwave probe. *Journal of Atmospheric and Oceanic Technology*. 1989. 6(6). P. 882—890.

10. Topouzelis, Konstantinos N. Oil spill detection by SAR images: dark formation detection, feature extraction and classification algorithms. *Sensors*. 2008. 8.10. P. 6642—6659.

11. Alpers W., Holt B., Zeng K. Oil spill detection by imaging radars: Challenges and pitfalls. *Remote sensing of environment*. 2017. 201. P. 133—147.

12. Konik M., Bradtke K. Object-oriented approach to oil spill detection using ENVISAT ASAR images. *ISPRS Journal of Photogrammetry and Remote Sensing*. 2016. 118. P. 37—52.

13. Kolokoussis P., Karathanassi V. Oil spill detection and mapping using sentinel 2 imagery. *Journal of Marine Science and Engineering*. 2018. 6(1). P. 4.

14. EUMETSAT. Meteosat-8/MSG 1-Channel Spectral Bands. URL: https://www.eumetsat.int/ (accessed on 05 July 2023).

15. Copernicus Marine Service. URL: https://marine.copernicus.eu/ (accessed on 23 June 2023).

16. Brockmann C., Doerffer R., Peters M., Kerstin S., Embacher S., Ruescas A. Evolution of the C2RCC neural network for Sentinel 2 and 3 for the retrieval of ocean colour products in normal and extreme optically complex waters. *Living Planet Symposium*. 2016. 740. P. 54.

17. Corucci L., Nardelli F., Cococcioni M. Oil spill classification from multi-spectral satellite images: exploring different machine learning techniques. In: Remote Sensing of the Ocean, Sea Ice, and Large Water Regions. 2010. 7825. P. 73—87.

18. Rajendran S., Fahad A.S., Sadooni F.N., Al-Kuwari H.A.S., Vethamony P. et al. Oil Spill Index (OSI) to Sentinel-2 satellite data: QU in International Contribution. 2021.

DESERTIFICATION INDICATORS MONITORING BASED ON MULTISPECTRAL SATELLITE IMAGERY: CASE STUDY FOR OLESHKY SAND REGION

A. Khyzhniak, I. Piestova, M. Lybskyi, A. Lysenko, A. Andreiev, T. Orlenko, S. Golubov

State Institution "Scientific Centre for Aerospace Research
of the Earth of the Institute of Geological Sciences of the NAS of Ukraine"

Desertification is a complex phenomenon simultaneously considered as a process of landscape transformations and ecosystems' transition to the final degradation stage — a desert. Desertification includes a combination of anthropogenic, biophysical, and climatic factors [1] that negatively affect arid and semi-arid ecosystems decreasing its sustainability with further expanding with increasing aridity. Desertification manifests due to the bioproductivity loss, decrease in soil fertility and decrease vegetation recovery, further aggravated by a reduction in soil moisture, transpiration and a surface temperature increment.

According to various UNEP estimates, arid ecosystems covers from 41% [2] to 47% [3] of the Earth's surface, making these regions the World's largest biome. Key features of these regions are aridity, high surface and air temperatures, lack of moisture.

According to the World Resources Institute, Ukraine is one of the countries with a high risk of droughts on par with the Middle East, North Africa and Asia, and the Southern Ukraine is very vulnerable to desertification. A study of the aridity index for the territory of Ukraine carried out in the period 2000—2021 based on the data of the MODIS data demonstrated its growth for most of Ukraine, especially for the South [4, 5].

The driest region of Ukraine is the western part of the Kherson region, on the left—bank Dniepro River. Here are situated dry sandy plains, called Oleshky Sands, is the most recognizable Ukrainian arid area. The total area is estimated at 219.9 thousand hectares, 80% are sand arenas where bare sands are the dominant land surface [6]. The main aim of the study — reveal the long-term spatial dynamics of the key desertification indicators within the study area.

This study covers the period 1986—2020, before the full-scale invasion of Russia. Fig. 1 presents a Landsat optical image covering the arenas of the Oleshky Sands based on Landsat-5 satellite image from August 14, 1986, and Fig. 2 represents Landsat-8 data from July 26, 2020.

After a full-scale invasion in 2022 and the long-term occupation of the southern regions of Ukraine, the risks

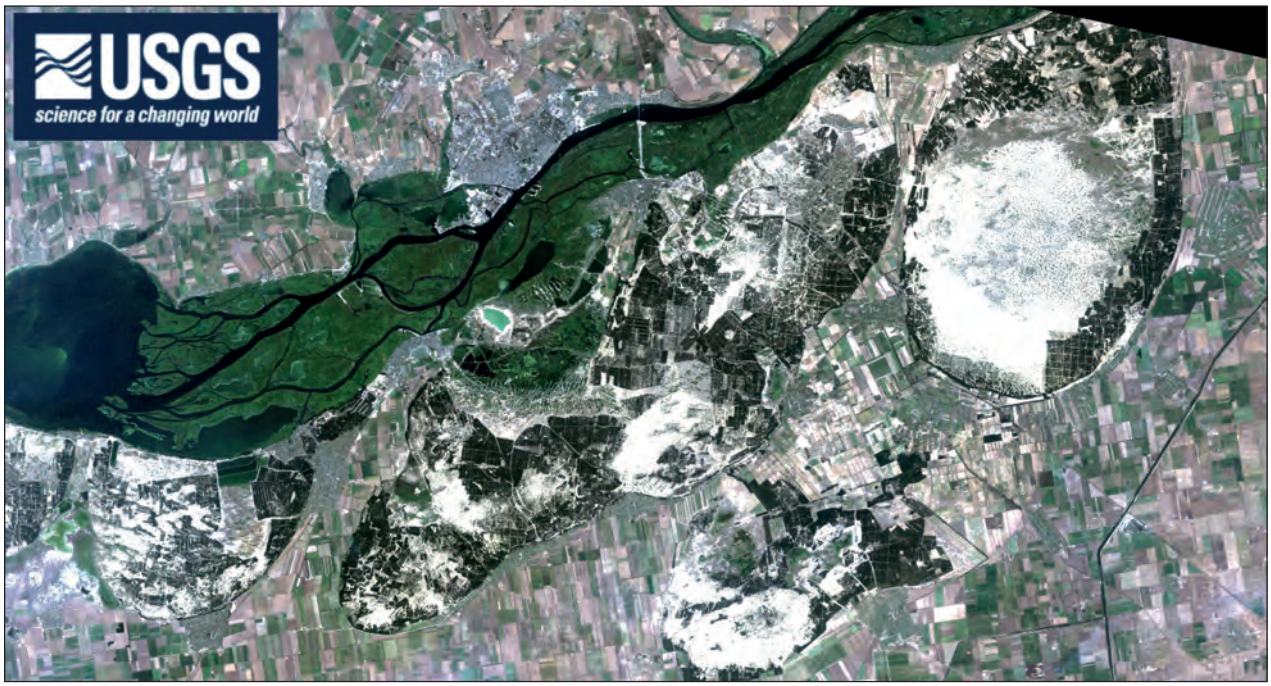

Fig. 1. Oleshky Sands image received byLandsat-5 satellite, August 14, 1986

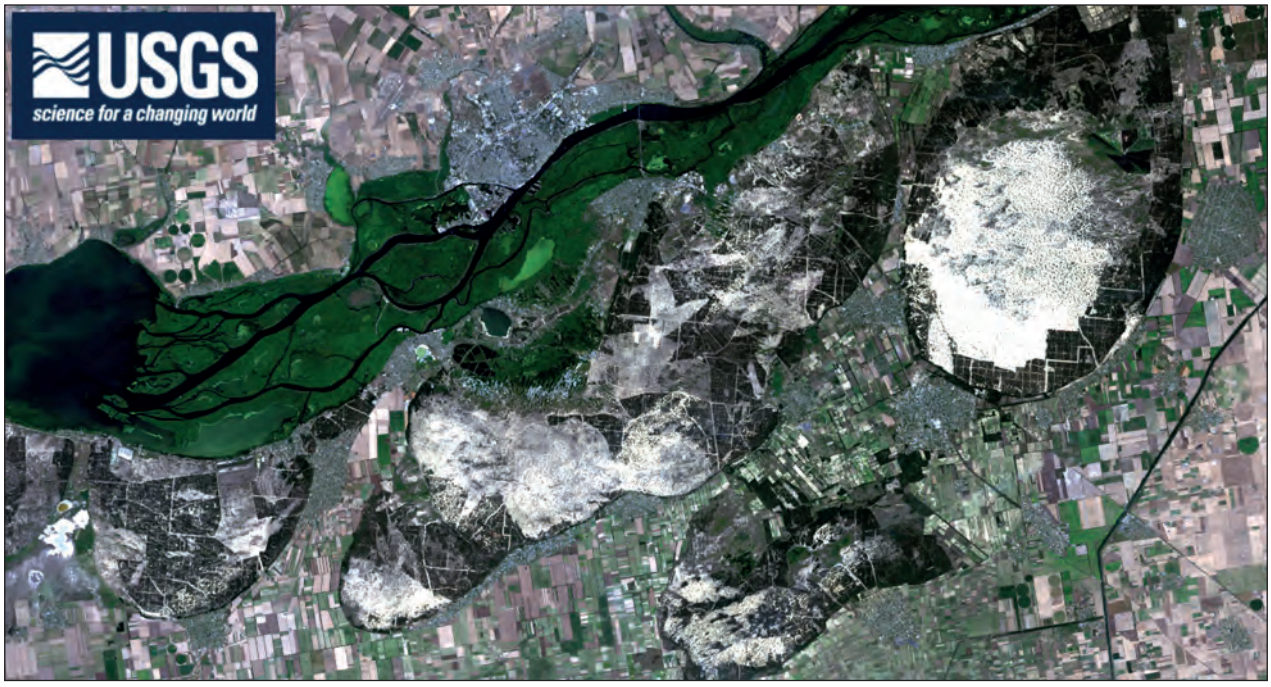

Fig. 2. Oleshky Sands image received byLandsat-8 satellite, July 26, 2020

of desertification significantly increased due to destruction of the existing forests, wildfires, and soil cover destruction.

Matherials and methods

Study area

Oleshky Sands are one of the largest natural deserts in Europe. A large variety of biotopes is concentrated within this area: semi-desert and desert areas, sandy steppe, fresh and saltwater bodies, deciduous groves, and coniferous forests. The uniqueness of these sands is it is drifting. In the 20th century, desertification hazzard became acute because sand masses began to spread closely to the surrounding villages. Many hectares of artificial forests has been grown to detain sand spreading.

The territory of the Lower Dnipro sands belongs to the southeastern climatic zone of Ukraine, which is characterized by the predominance of eastern and northeastern winds, relatively low air humidity, low cloud cover, a precipitation shortage, and relatively large daily and annual air temperature amplitudes. These main features make the climate arid and continentality. Critical temperatures of the sand surface (more than 50 °C), which can cause wildfires, are repeated in during whole vegetation period, including September [7]. Area of interest includes five arenas of the Oleshky Sands: Ivanivska, Zburyivska, Kelegeyska, Chalbasska and Kozachelagerska (Fig. 3).

Methodology

For long-term landscape dynamics research, it is relevant to utilize Landsat satellite data, which have provided multispectral images since 1972 with 80 m spatial resolution and starting from 1982 with 30 m spatial resolution [8]. This study used imagery obtained during the period July 1986 — July 2020, obtained during the vegetation period (May—September).

The methodology for evaluating the dynamics of desertification based on remote sensing data includes following steps:

- formation of a Landsat satellite imagery serise from 27 multispectral Landsat images;
- determination of the area of interest and vector layer formation for delineating study areas of the Oleshky Sands;
- selection and estimation of desertification indicators spatial distribution;
- regression analysis and mapping of each indicator's spatial and temporal dynamics.

Selection of the desertification indicators

The Oleshky Sands are typical arid landscapes characterized by a lack of the soil moisture. To estimate distribution of the Earth's surface moisture the NDMI (normalized difference moisture index) has been chosen, which is estimated according to the further formula:

$$(NIR - SWIR_1) / (NIR + SWIR_1) \quad (1)$$

where NIR is spectral reflectance data in the near-infrared region (4th band of Landsat-4, Landsat-5 and Landsat-7 satellites, and 5th band of Landsat-8 and Landsat-9 satellites), SWIR1 is spectral reflectance data in the first band of the short-wave infrared range (5th band of Landsat-4, Landsat-5 and Landsat-7 satellites, and data 6th band of Landsat-8 and Landsat-9 satellites).

Combining NIR with SWIR removes changes induced by internal leaf structure and dry matter content, increasing the accuracy of determining plant moisture content. The

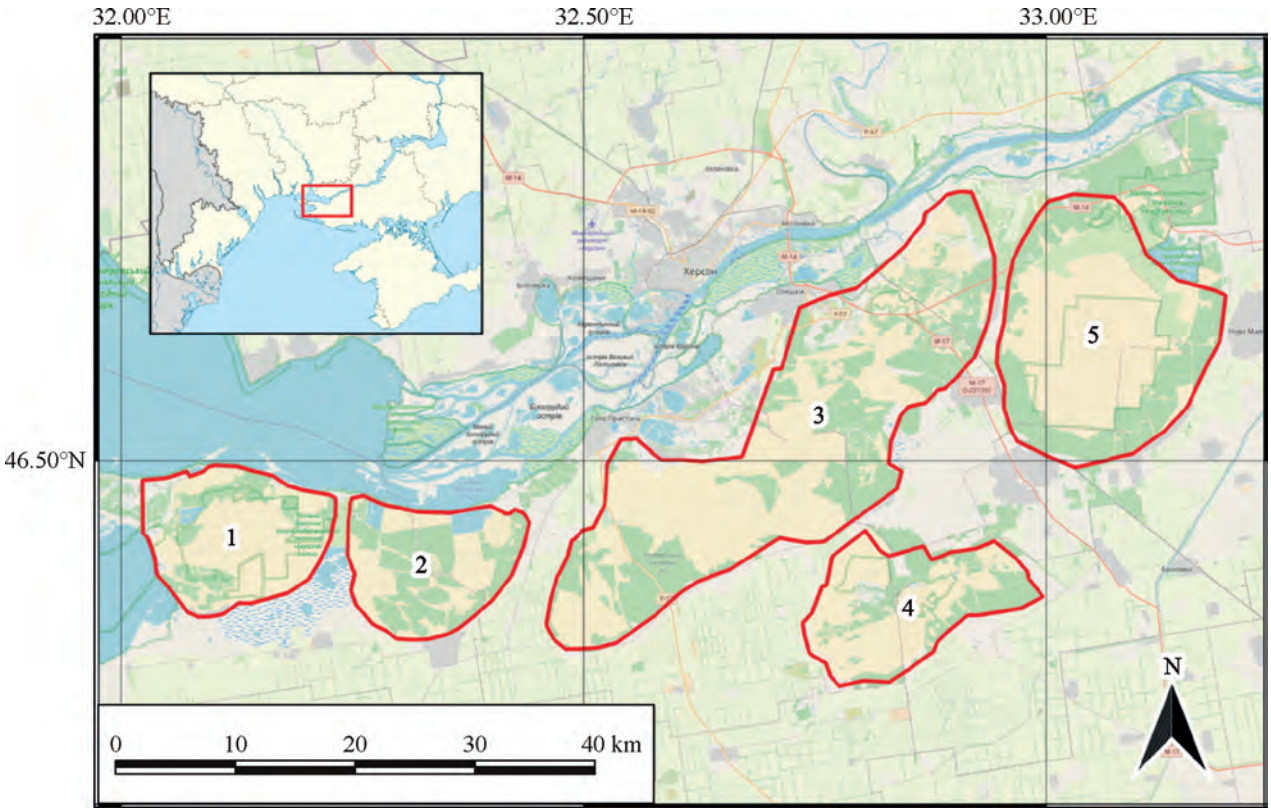

Fig. 3. Study area map with delineated sand arenas: 1 — Ivanivska, 2 — Zburyivska, 3 — Kelegeyska, 4 — Chalbasska, 5 — Kozachelagerska

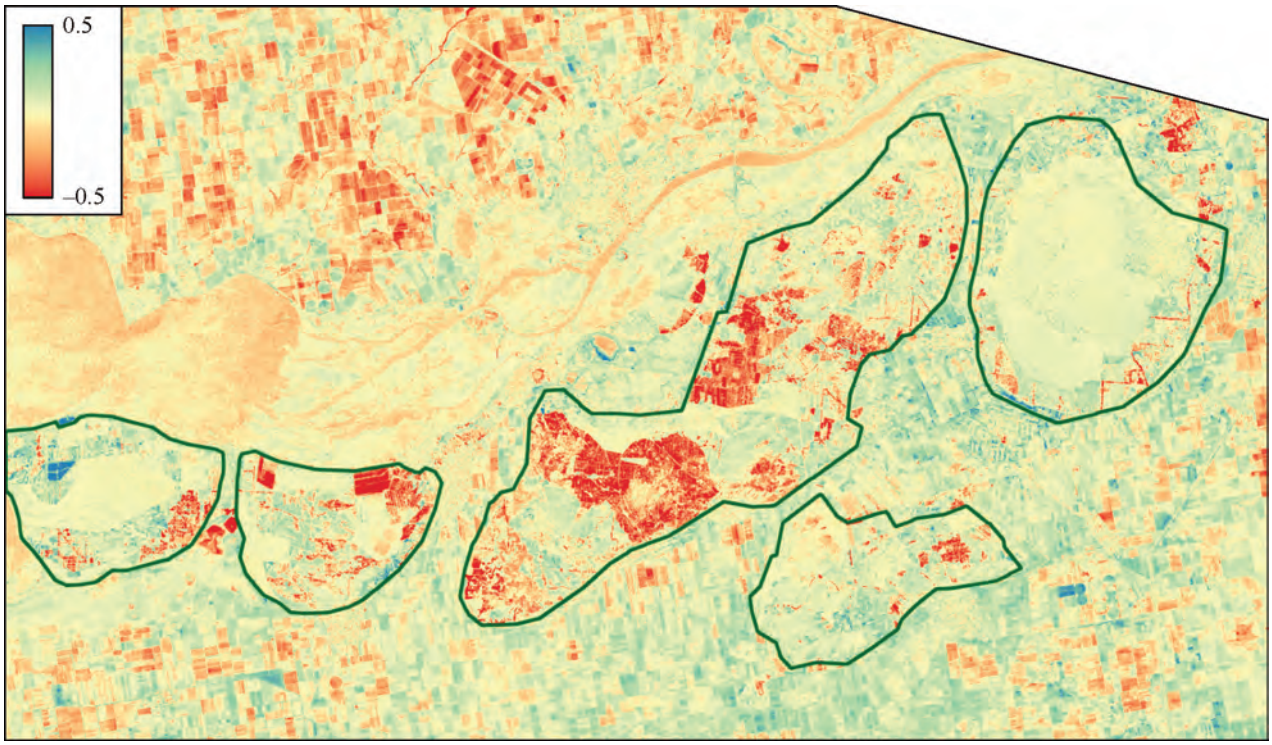

Fig. 4. Spatial distribution of the NDMI index based on the results of processing a long-term series of Landsat satellite data data with the studied arenas boundaries

amount of water present in leaves essentially controls the spectral reflectance in the infrared range of the electromagnetic spectrum [9].

The next landscape degradation indicator is distribution of green vegetation density. At the same time, it is an indicator of moisture, potential transpiration, and the

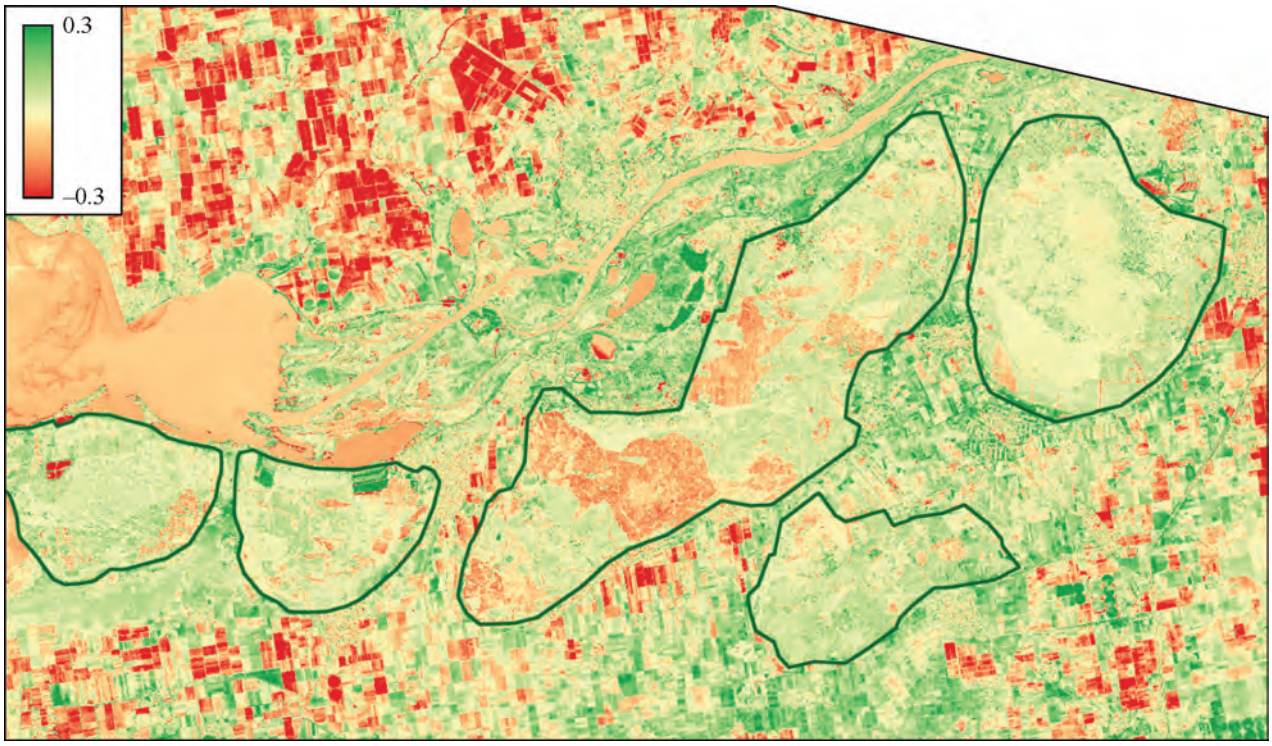

Fig. 5. Spatial distribution of the EVI index based on the results of processing a long-term series of Landsat satellite data data with the studied arenas boundaries

ability to anchor the soil with turf and root systems of tree vegetation. For determination of the vegetation cover density, the EVI index (Enhanced vegetation index) is used, which is calculated according to the formula:

$$\frac{2.5\cdot(NIR-\mathrm{Re}d)}{(NIR+6\cdot\mathrm{Re}d-7.5\cdot Blue+1)}, \qquad (2)$$

where Red — spectral reflectance in 3rd band of Landsat-4, Landsat-5 and Landsat-7 satellites, and 4th band of Landsat-8, Landsat-9 satellites), Blue — spectral reflectance data in the blue spectral range (3rd band of Landsat-4, Landsat-5 and Landsat-7 satellites, and 4th band of Landsat-8, and Landsat-9 satellites).

The sand cover itself is the main indicator of the final stage of soil degradation, is estimated according to one of the equations of the weighted accumulation of spectral reflectance Tasseled Cap [10], particularly, Earth's surface brightness, since sand has a very high reflectivity in all spectral ranges:

$$0.3037\cdot Blue + 0.2793\cdot Green + 0.4743\cdot Red + 0.5585\times \\ \times NIR + 0.5082\cdot SWIR1 + 0.1863\cdot SWIR2 \qquad (3)$$

where Green is spectral reflectance in the green spectral range (2nd band of the Landsat-4, Landsat-5 and Landsat-7 satellites, and 3rd band of the Landsat-8 and Landsat-9 satellites), SWIR2 — spectral reflectance in the second band of the short-wave infrared range (6th band of the Landsat-4, Landsat-5 and Landsat-7, and 7th data channel of Landsat-8 and Landsat-9 satellites).

After forming a long-term series of each desertification indicator, the analysis of their spatial and temporal dynamics has been carried out. For this purpose the linear regression has been selected. Through the 27 images of each indicator in each pixel temporal changes has been determined. The most common method of calculating the regression dependence is the method of least squares, the task of which is reduced to finding coefficients of linear dependence, where the function of two variables a and b represented as

$$F(a,b)=\sum_{i=1}^{n}(y_i-(ax_i+b))^2 \qquad (4)$$

takes the lowest value.

To determine the spatial of the long-term dynamics of the obtained desertification indicators distribution, the estimated value of the regression gradient or the angular coefficient is taken, which represents the average annual increase in the indicator's value.

Determination of the desertification indicators dynamic

The NDMI distribution (Fig. 3) has changed significantly in most arenas. NDMI reduction are observed on the territory of the Ivanivska and Zburyivska arenas. The largest decrease has been determined in the Kelegeyska arena, with clearly defined borders, which may indicate an intense anthropogenic influence on vegetation cover. There are also pockets of slight index increase within the Ivanivska, Chalbaska, and Kozachelagerska arenas.

The EVI dynamics (Fig. 5) is mainly positive for all arenas, especially for Chalbaska and Kozachelagerska, where the formation of forest protection strips are being carried out most intensively. On the territory of the Kozachelagerska

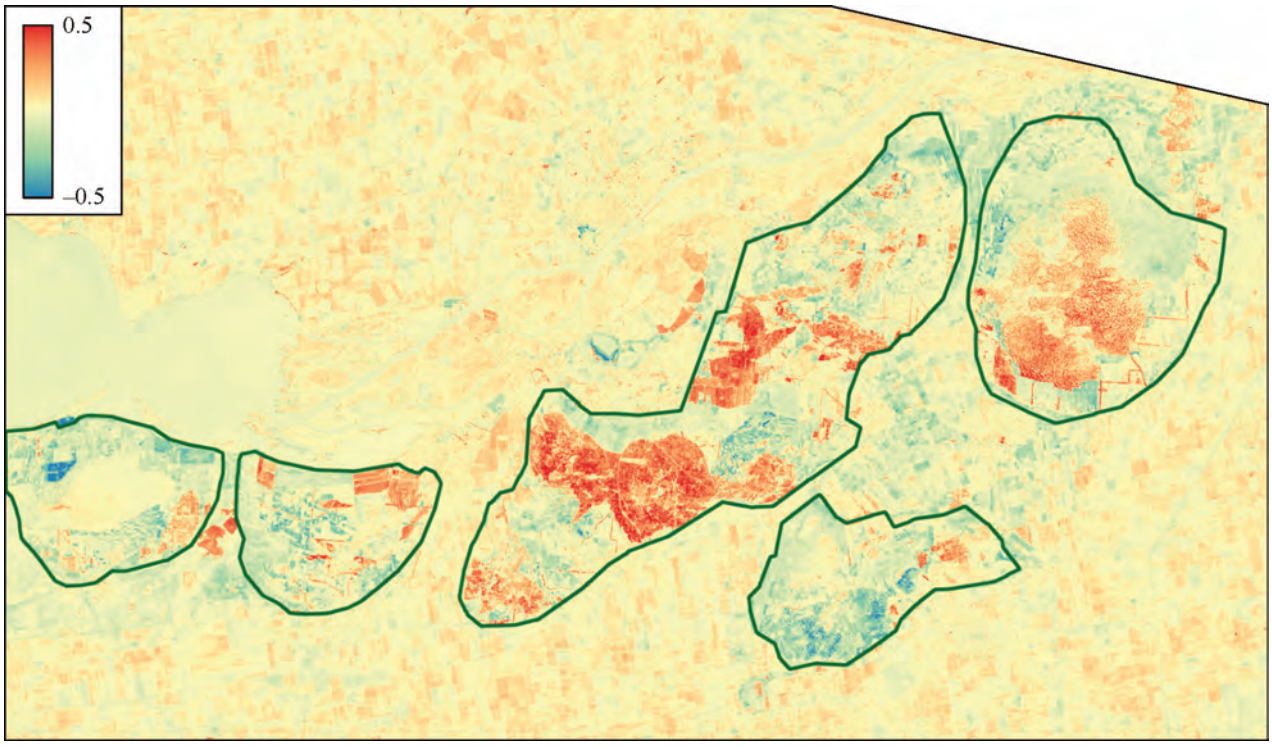

Fig. 6. Spatial distribution of the Tasseled Cap Brightness based on the results of processing a long-term series of Landsat satellite data with the studied arenas boundaries

arena, a gradual increase in grass vegetation increment has been indicated.

The dynamics of the Earth's surface brightness has an inverse correlation with the NDMI dynamics due to decrease in the soil water content. Even though an increase in green vegetation within the boundaries of the Kozachelagerska arena has been observed, at the same time, a significant increase in albedo has been determined, which could potentially indicate the degradation of the remaining soil cover. Fig. 6 shows the distribution of the long-term dynamics of the brightness value.

The analysis of the averaged increments of desertification indicators showed that the lowest threat of desertification is in the Ivanivska and Chalbaska arenas. They are characterized by increment in moisture index, vegetation cover, and a decrease in albedo. It should be noted that part of the Ivanivka Arena belongs to the Black Sea Biosphere Reserve. Within the boundaries of the Kozachelagerska arena, increases in vegetation cover and moisture were also detected, including increment in vegetation cover area. However, a significant increase in albedo was also admitted, which may indicate soil cover degradation and sand spreading.

For most of the studied areas, trends towards a decrease in bioproductivity were found, which is associated with the loss of vegetation cover in large areas, mainly coniferous trees, which were planted to detain the sands expansion. On the territory of most of the arenas, a significant reconfiguration of the landscapes has been revealed. The most significant loss of vegetation cover was found in the largest Kelegeyska arena, and the shape of the vegetation cover loss area may indicate an anthropogenic factor of influence (cutting the trees).

Positive trends related to the increase in the tree cover area were observed in several arenas, notably the Kozachelagerska and Ivanivka arenas, which are part of the natural reserve. This underscores the potential for successful nature protection measures and the importance of these areas in the overall conservation strategy for the Oleshky Sands.

However, a full-scale invasion of Russia in 2022 contributes to a significant increase in the degradation of these vulnerable areas through wildfires and spontaneous deforestation and halting the restoration of forest cover in the most vulnerable areas, and it requires further research.

REFERENCES

1. Zeng N., Yoon, J. Expansion of the world's deserts due to vegetation-albedo feedback under global warming. *Geophys. Res. Lett.* 2009. 36(17). L17401. https://doi.org/10.1029/2009GL039699

2. Safriel U., Adeel Z. Dryland systems. *In Millennium Ecosystem Assessment.* Ch. 22. World Resources Institute, Island Press, Washington, DC. 2005.

3. Middleton N., Thomas D. World atlas of desertification. London, New York, Sydney, Auckland, Arnold, UNEP. 1997.

4. Lyalko V.I., Romanciuc I.F., Yelistratova L.A., Apostolov A., Chekhniy V. Detection of Changes in Terrestrial Ecosystems of Ukraine Using Remote Sensing Data. *Journal of Geology, Geography and Geoecology*. 2020. 1(29). P. 102—110. https://doi.org/10.15421/112010

5. Apostolov O., Yelistratova L., Romanciuc I., Chekhniy V. Identification of deserted areas in Ukraine based on calculations of water indices based on remote sensing of the Earth. *Ukrainian Geographical Journal*. 2020. 1. P. 16—25. https://doi.org/10.15407/ugz2020.01.016 (In Ukrainian).

6. Kryvulchenko A. Oleshky sands as a hierarchically constructed natural system. *Bulletin of Lviv University. The Geographical Series.* 2019. 53. P. 197—209.

7. Granovska L.M. Hydrological and hydrogeological features of formation and use of Nizhny Dnieper sands. *Ecological Sciences*. 2019. 3(26). P. 40—45. https://doi.org/10.32846/2306-9716-2019-3-26-8

8. Markham B.L., Storey J.C., Williams D.L., Irons J.R. Landsat sensor performance: history and current status. *IEEE Trans. Geosci. Remote Sens.* 2004. 42(12). P. 2691—2694. https://doi.org/10.1109/TGRS.2004.840720

9. Gao B.C. NDWI-A normalized difference water index for remote sensing of vegetation liquid water from space. *Remote Sens. Environ.* 1996. 58. P. 257—266. https://doi.org/10.1016/S0034-4257(96)00067-3

10. Zanchetta A., Bitelli G., Karnieli A. Monitoring desertification by remote sensing using the Tasselled Cap transform for long-term change detection. *Natural Hazards*. 2016. 83. P. 223—237. https://doi.org/ 10.1007/s11069-016-2342-9

MONITORING AND ASSESSMENT OF THE SUSCEPTIBILITY OF THE TERRITORY TO LANDSLIDES ON THE EXAMPLE OF THE RIGHT BANK OF THE KANEVSKY RESERVOIR

T. Orlenko, O. Sedlerova, A. Khyzhniak

State Institution "Scientific Centre for Aerospace Research
of the Earth of the Institute of Geological Sciences of the NAS of Ukraine"

The constant denudation of slopes, a natural process-involving landslide, shifting, collapse, and erosion, is a pressing issue. The active development of landslides on Ukraine's territory results from various factors, including geological, geographical, geomorphological, tectonic, and neotectonic. Monitoring of exogenous geological processes based on remote sensing data is a source of obtaining reliable data about objects on Earth's surface with a wide range of coverage of territories in short time intervals.

Landslides, mudslides, and crumbling are dangerous geological phenomena that can be observed in any region with ravines, steep banks, hills, and mountains. Landslides form in various rocks due to their imbalance and weakening of strength caused by natural and anthropogenic factors [1]. The natural causes of landslides include an increase in the steepness of slopes and their washing away, weathering processes and earthquakes, and anthropogenic causes include construction and blasting works, destruction of slopes by excessive removal of soil, felling of forests, destruction of vegetation on slopes or their ploughing, increased irrigation of agricultural lands located on slopes, clogging of groundwater outlets, etc. Landslides can rise at a steepness of the slope of 10° or more, but on clay foundations, with their high moisture, they can also occur at a steepness of the slope of 5—7°.

Landslides on the banks of reservoirs can be caused by over-wetting of the soil by rain and snow, slope washing, climate change, and over-anthropogenic influence. The activation of landslides depends on the intensity of the destruction of soil cover. Landslides are often caused by the lack of vegetation and changes in the region's topography. The volume of soil mas in a landslide can range from several hundred to thousands of cubic meters, and the speed varies from several meters per year to several meters per second. The right-bank slopes of the Dnipro River valley and the slopes of the right-hand tributaries, sides of streams and ravines are the most prone to landslides [2]. The activation of gravity processes, which began in the second half of the 20th century in the Kaniv region (now the territory of the Rzhyshchiv United Territorial Community of the Kyiv Region), was caused, among other things, by an artificial change in the hydrological regime of the Dnipro River, intensive slopes development and the construction of relevant communications (Fig. 1).

The research aims to increase the efficiency and reliability of forecasting the occurrence of new or intensified stabilised coastal landslides by developing a technique for remote geoecological monitoring of landslide-prone areas. It creates a forecasting algorithm based on a comprehensive analysis of radar interferometry data, optical images of the Earth, and terrestrial climatological, lithological, and landscape data.

Scientifically study based on conclusions of the influence of geological and geophysical factors on landslide activation, biophysical factors, and the influence of climatic change. High-level soil moisture on landslide processes was carried out; it is shown how it is possible to fix areas of increased susceptibility to landslides. The technique of remote geoecological monitoring of landslide processes is based on these theoretical and practical results.

Remote sensing data plays a crucial role in our study of exogenous processes, particularly in understanding the processes of landslide formation. In this article, we propose a methodology with a direct practical implementation of comprehensive landslide hazard assessment analysis. These methodologies are based on selecting optimal remote sensing data and their processing methods.

Remote sensing data should possess high spatial and temporal resolution to delineate areas of landslide process activation. Satellite surveys allow timely monitoring of landslides in the optical and radar ranges to detect changes in the relief of territory and the state of the soil cover. However, the use of optical data has significant limitations compared to radar data. In contrast to optical imaging systems, radar systems provide imaging of the Earth's surface during periods of substantial cloudiness and at night.

Sentinel-1 radar data (Fig. 2, *b*) with a spatial resolution of 10 m were used to calculate the Earth's surface displacements and establish the region's landslide susceptibility. Radar images containing discrete integer value (DNSAR) data were processed in the Sentinel Application Platform (SNAP) open-source software environment. Multispectral data from the Sentinel-2 satellite, with a spatial resolution of 10 m, were used to study the region's vegetation and soil moisture state. The remote geoecological monitoring technique, developed within this study's framework, considers the influence of the area's topographic features using SRTM-30 m DEM, geological, geographical, and historical maps.

Fig. 1. Illustrarion of the study area: Staiky, Ukraine. 50° 5'46.75»N 30°54'2.06»E

Monitoring vertical displacements of the Earth's surface on the right bank of the Kaniv Reservoir in the Vytachiv — Stajky region, conducted using the differential radar interferometry (DinSAR) technique, has yielded significant results. Over the spring of 2015 to 2023, we successfully mapped active landslide-prone areas. Importantly, our findings have shown a high level of correlation with the data obtained by previous researchers, further validating the results of this study. This confirms the presence of active displacement zones on the right bank of the Kaniv Reservoir, a crucial discovery in landslide processes.

The main stage of creating a map of the territory's susceptibility to landslides is calculating the vertical displacements of the Earth's surface and constructing a mapping scheme of their distribution within the study area, according to the DinSAR technique.

The spread and intensity of landslide manifestations are intricately linked to the geological and geomorphological structure of the territory, its tectonic, neotectonic and seismic activity, and hydrological and climatic conditions. The method's limitations, such as temporal decorrelation of the radar signal in areas with a large amount of vegetation, have been carefully considered.

The process of creating a displacement map is a full-phase representation of topographic variations, as shown in Fig. 2.

The unwrapped phase is geocoded and translated into a geophysical unit, representing the calculated surface's height over the spherical Earth. This can be done by integrating the height of either surveyed reference points or extracted from an external DEM, but across-track approaches, which are independent of a reference, also exist.

Finally, the retrieved heights are referenced to an ellipsoid (e.g., WGS84), projected into a coordinate reference system based on either geographical or UTM coordinates, and resampled to a uniform pixel spacing (Fig. 3).

A comprehensive technique was developed to overcome the significant correlation between the obtained results in forested and watered areas. This methodology combines the DinSAR method, the analysis of a digital relief model (DEM), the study of base surface maps, and the results of calculating spectral indices [3]. This approach has proven

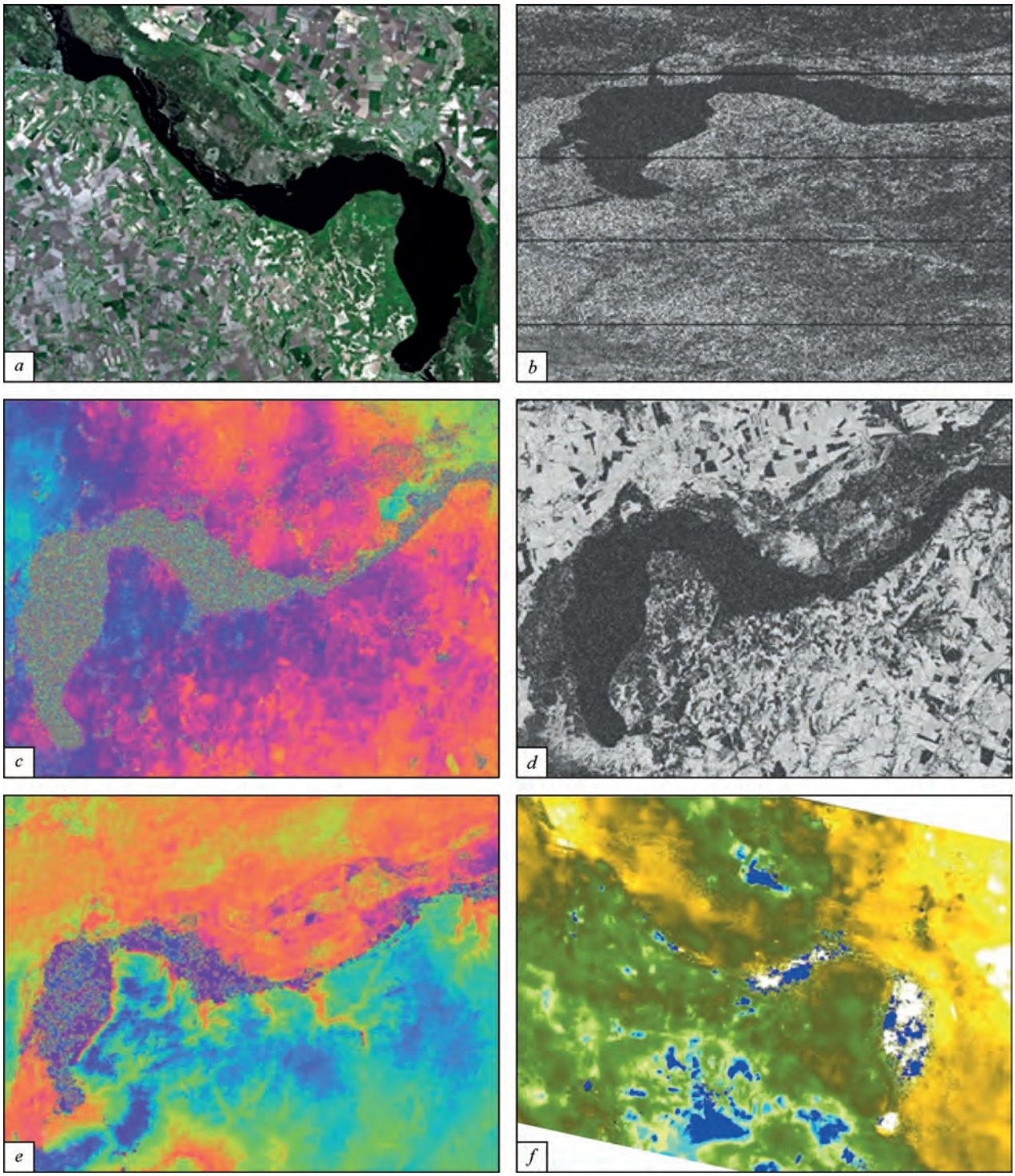

Fig. 2. Steps of DEM generation with Sentinel-1: *a* — Sentinel-2 image from 15.03.2023 (for visual reference), *b* — Sentinel-1 image from 21.03.2023, *c* — interferogram from 21.03.2023 and 03.04.2023, *d* — coherence image, *e* — unwrapped interferogram, and *f* — phase to displacement calculated based on derived unwrapped interferogram

effective in remote geoecological monitoring of landslide processes, particularly in identifying areas of active landslides caused by the overwetting of rock complexes on the Dnieper slopes.

One of the study's results is the creation of a susceptibility landslide map of the territory at the regional level for the Rzhyshchiv United Territorial Community of the Kyiv Region. Eight factors that affect the development of landslides or can be defined as indicators of landslide processes were selected for this analysis.

In the Kyiv region, landslides manifest in various characteristics and stages of development. The severity of landslide development intensifies under conditions of high relief energy, steep and high slopes, fluctuating reservoir levels,

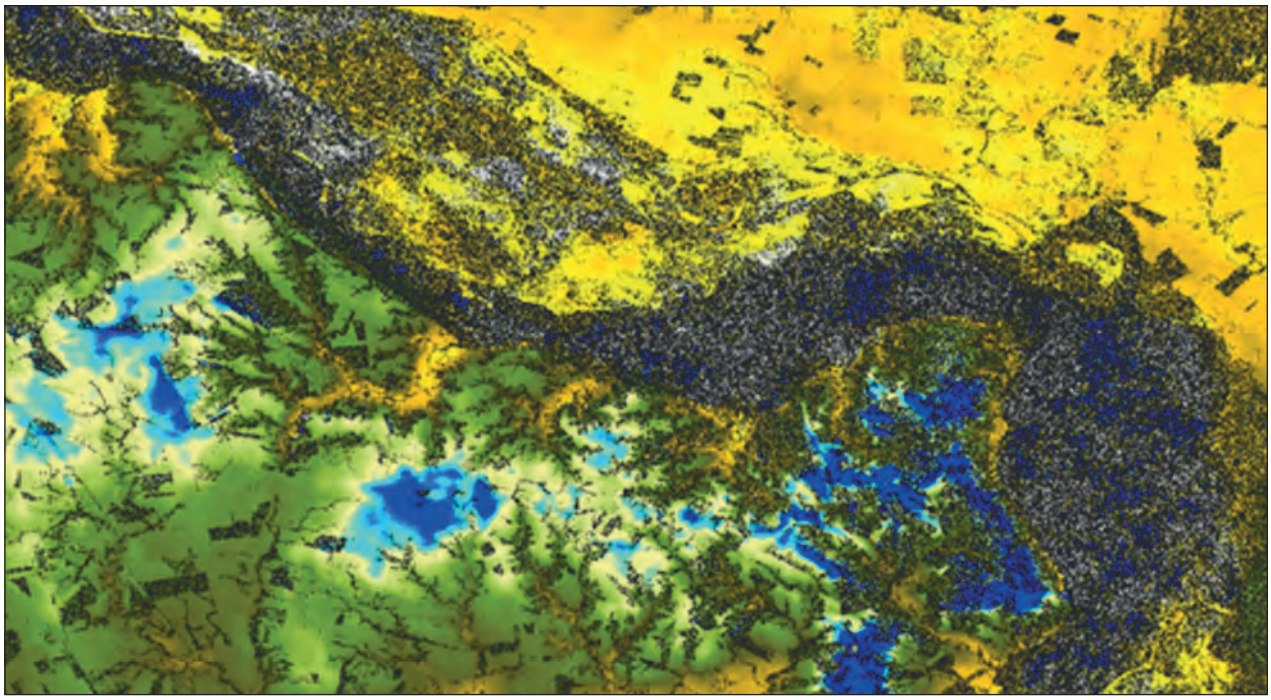

Fig. 3. Fragment of the displacement map result with masked areas of low coherence for the Kaniv Reservoir

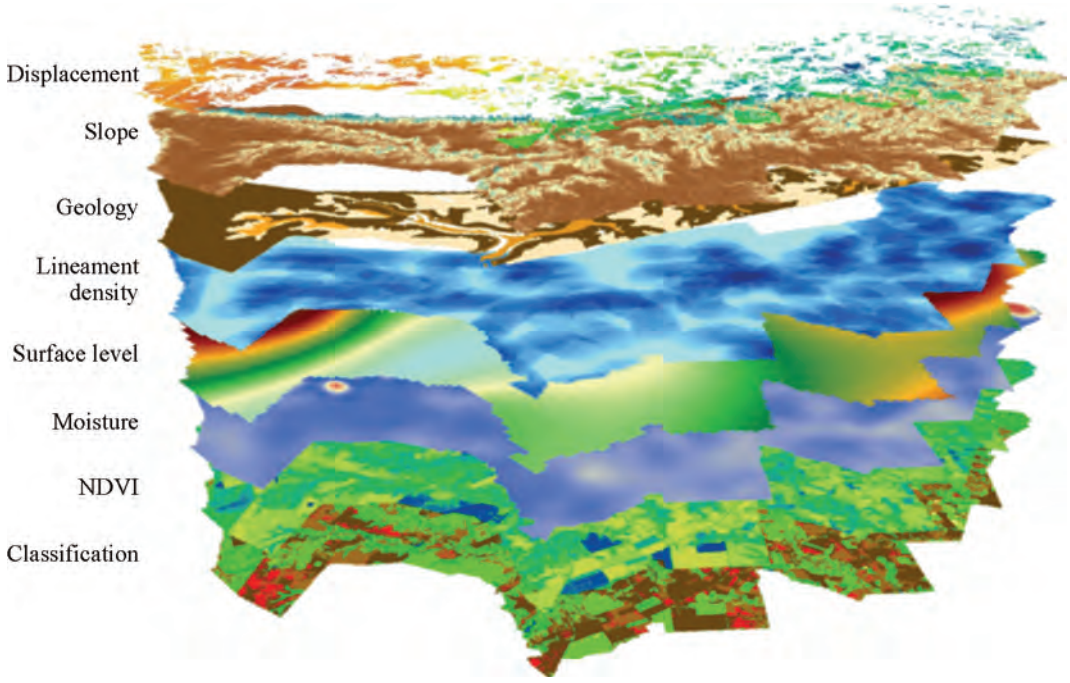

Fig. 4. 3D model of the resulting maps of the geological, geographical and geophysical state of the study region

and proximity to sub-parallel faults. The hydrometeorological factor significantly triggered the heightened landslide activity in 2013, particularly excessive precipitation and soil oversaturation. Vegetation, notably trees, conceals a substantial portion of the right bank of the Kaniv Reservoir, rendering stabilised landslide bodies invisible on optical images. Vertical walls of landslides with outcrops are only visible from lower terraces or floodplains. Our study leveraged remote sensing data to depart from conventional landslide research methods. This data offers a unique advantage regarding remote accessibility, observation visibility, and the ability to monitor geological processes with high periodicity, thereby enhancing our understanding of landslide activity [2].

In the frame of this study, we developed an algorithm and described the technique for creating a landslide sus-

ceptibility map using the hierarchy analysis method. This is the final stage of the developed methodology for remote geoecological monitoring of landslides, applied to the right bank of the Kaniv Reservoir in the Vytachiv — Stayka region. The technique is generally based on algorithms for obtaining data, mainly the algorithm for creating a mapping scheme of vertical displacements of the earth's surface using radar interferometry (Fig. 4).

The analytic hierarchy process (AHP), a well-established approach introduced by Saaty in 1980, was used to determine the factors' relative weight [4]. This method allowed us to establish the priority of factors and subfactors that cause landslides on the right bank of the Kaniv Reservoir. The factors found to be significant for assessing landslide hazards as indicators grouped according to the genesis or the method of obtaining information. Our team of experts, who used a nine-point ordinal "relative importance" scale, carried out the pairwise comparisons, which were crucial in this process.

The AHP tool in our study enables us to construct an objective function and evaluate the influence of each system characteristic. The analysis of factors affecting landslides is a step-by-step process involving the development of a hierarchical structure, binary comparisons of criteria, establishment of a comparative matrix, calculation of priority vectors, evaluation of the consistency index, creation of a table of importance, and final decision making based on a generalised criterion.

Using the AHP, we determined two potential scenarios for the study area: stable and unstable. We also created maps of the area's susceptibility to landslides under these conditions. Our findings revealed that vertical displacements, slope steepness, lithology, and soil moisture are the most influential factors in landslide activation. Using maps of base surfaces and lineament density, we also identified the zones at the highest risk for new landslide formation. Interestingly, the biophysical parameters of the study area allowed us to identify regions unaffected by landslides, underscoring the practical value of our research [5].

The result is significant as it explains the varying susceptibility of different areas in the studied region to developing landslide processes. This understanding is crucial as it helps us identify the areas with the most significant threats, thereby paving the way for the rational adoption of management decisions.

One of the meticulous stages in the method of remote geoecological monitoring involves conducting field research at nine carefully selected test sites. Here, we observe manifestations of exogenous geological processes, such as landslides and erosion, which significantly impact the topography of the slopes. We also study the influence of natural factors, such as precipitation, water flows, and wind, which are common in the study area. To ensure the accuracy of our findings, we chose control plots that serve as ideal examples for measuring the stable level of the Earth's surface. These plots are untouched by agriculture, remain unprocessed, and are free from anthropogenic influence, ensuring their relief remains unchanged.

We delve into the region's current geoecological issues, investigating the factors that trigger the formation or stabilisation of landslides. It introduces a novel technique for remote geoecological monitoring of landslides, enabling the analysis of the present state and prediction of landslide development in a specific area. This innovative approach is founded on using remote sensing data and geoinformation systems. The application of up-to-date remote sensing data processing and analysis technologies facilitates the efficient identification of potential landslide risk regions and their environmental impact.

Remote geoecological monitoring technique of landslides consists of the following stages:

– determination of the potential risk of danger — identification of the area's most susceptible to landslides;

– determination of the structural features of the study area — the main characteristics of the structure, including geological formations and natural landscape complexes;

– determination of the topographic features of the study area — the relief of the territory, including the difference in heights, the presence of reservoirs, valleys, ravines and streams;

– creating a map of the territory's susceptibility to landslides (Fig. 5), analysing the geological structure of the study area and its topographic and biophysical properties to determine the degree of susceptibility to landslides; analyzing the reliability of the constructed susceptibility map using the available information of the study region.

Active landslide areas occupy the reservoir bank, spread within all settlements and in truss-beam systems. Within the field research route, the landslide areas have a very high level of danger under favourable and unfavourable scenarios of the development of events. According to the magnitude of the vertical displacements of experimental sites 5—9 during the entire study period, the landslide susceptibility map has a very high level of danger. At the same time, sites 1—4, which were almost inactive during the entire study, also have a very high level of danger.

This is explained using the AHP software module, according to which all data have a spatial resolution of 10 m. Accordingly, the result of the analysis is more generalized. In the study area, landslides are most common in areas with grassy cover and open soils; the most stable regions are forests. The most significant amount of moisture and landslides is characteristic of the right bank of the Kaniv Reservoir. The value of the earth's surface displacements is the primary evaluation criterion, demonstrating the correlation between vertical displacements of the surface and the territory's susceptibility to landslides.

The accuracy and reliability of forecasts of the territory's susceptibility to landslides depend on the quality, type, and volume of input information and the choice of the optimal combination of factors for activating landslide processes, which directly depend on the characteristics of the studied territory.

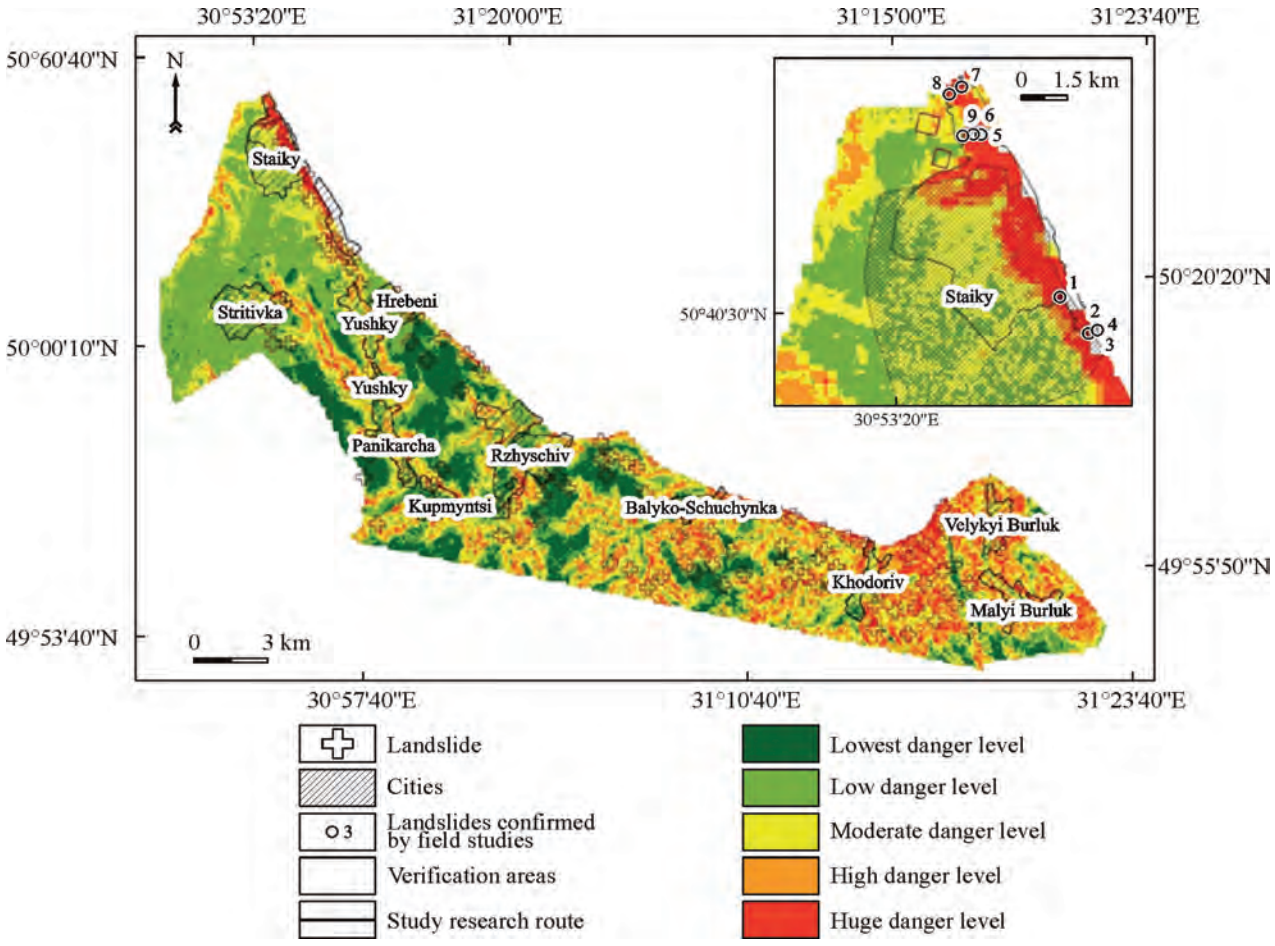

Fig. 5. Map of landslide susceptibility level

The advantage of using remote sensing data to assess the susceptibility of the territory to landslides is their promptness and availability. Since field geological studies require detailed preliminary planning of works and a significant period of time for their implementation from two months to six months, at the same time, the use of remote data allows monitoring of landslide-prone areas with a frequency of 12 days [6].

Another significant advantage of using remote sensing data with a mathematical apparatus for processing many criteria to obtain a result is visibility and flatness. When planning and establishing engineering-geological studies, as a rule, attention is paid to areas already known with a particular history of observations. During the planar assessment of the territory, it is possible to assess those areas where previous studies were not conducted. Still, according to the data of remote geoecological monitoring, there is a high or very high level of danger, and prior studies have yet to reveal such facts, or these areas were not studied.

Landslide susceptibility mapping using remote geoecological monitoring techniques can provide decision-makers with frequent information on infrastructure development and land use planning at the local and regional levels.

REFERENCES

1. Yelistratova L.O., Apostolov A.A., Romanciuc I.F., Orlenko T.A., Tymchyshyn M.A. Application of remote sensing data for detection the landslide areas in Ukraine. Conference Proceedings *Third EAGE Workshop on Assessment of Landslide Hazards and Impact on Communities,* Sep 2021. 2021. P. 1—5. https://doi.org/10.3997/2214-4609.20215k1017

2. Orlenko T.A. Monitoring of vertical displacements of the earth surface of the right bank of the Kaniv reservoir. *Visnyk of Taras Shevchenko National University of Kyiv. Geology.* 2023. 4(103). P. 5—13. https://doi.org/10.17721/1728-2713.103.01 (In Ukrainian).

3. Orlenko T.A. Vertical displacement monitoring technique using radar interferometry data. *Ukrainian journal of remote sensing.* 2023. 10(3). P. 16—20. https://doi.org/10.36023/ujrs.2023.10.3.247 (In Ukrainian).

4. Saaty T.L. A scaling method for priorities in hierarchical structures. *Journal of Mathematical Psychology.* 1980. 15. P. 234—281.

5. Orlenko T.A., Sedlerova O.V., Lybskyi M.S., Golubov S.I., Khyzhniak A.V. Mapping of landslide susceptibility using analytical hierarchy process on the example of the right bank of the Kaniv Reservoir. *Ukrainian journal of remote sensing.* 2023. 10(4). P. 17—21. https://doi.org/10.36023/ujrs.2023.10.4.251 (In Ukrainian).

6. Orlenko T.A., Tomchenko O.V., Lischenko L.P., Sedlerova O.V. Landslide Hazard Assessment Using Radar Data in the Staiky, Rzhyshchiv Urban Hromada Ukraine. Conference Proceedings *Fourth EAGE Workshop on Assessment of Landslide Hazards and impact on communities,* Sep 2023. 2023. P. 1—5. https://doi.org/10.3997/2214-4609.2023500027

INNOVATIVE APPROACHES FOR FOREST MONITORING USING REMOTE SENSING AND CLOUD COMPUTING

N. Kussul [1, 2, 3], A. Shelestov [1, 2], B. Yailymov [1], H. Yailymova [1, 2], M. Lavreniuk [1], L. Shumilo [3], S. Skakun [3], V. Kuzin [2], N. Salii [1, 2], A. Kolotii [1, 2]

[1] Space Research Institute of the NAS of Ukraine and the State Space Agency of Ukraine
[2] National Technical University of Ukraine "Igor Sikorsky Kyiv Polytechnic Institute"
[3] University of Maryland, College Park, USA

Introduction

This article presents advanced methods for forest monitoring using remote sensing data, computational machine learning techniques, and cloud computing platforms. The work focuses on three main research directions: 1) Intelligent feature engineering for semantic segmentation of damaged forest areas from satellite imagery using genetic algorithms [1—5]; 2) Intelligent analysis of forest cover change dynamics in conflict zones based on time-series satellite imagery [6]; 3) Semi-automated mapping of European forest types with high resolution using the Google Earth Engine cloud platform [7—9]. The results demonstrate the effectiveness of the developed approaches in detecting damaged forest areas, assessing the impact of military actions on forest vegetation, and creating up-to-date maps of forest vegetation types across Europe.

The first part of the study introduces an automated feature selection method using genetic algorithms for semantic segmentation of forest diseases from satellite imagery. This approach includes numerical evaluation of individual features and their combinations, along with a simplified representation of vegetation indices to facilitate feature set optimization. The framework enhances feature engineering for earth observation, enabling precise identification of forest health degradation with minimal labeled data.

The second part aims to explore the impact of militarized occupation of natural protected areas and the subsequent interruption of conservation efforts on ecosystem sustainability. By analyzing time-series satellite imagery before, during, and after the conflict, the study quantifies and evaluates policies and processes underlying the establishment of the Emerald Network in the Luhansk region of Ukraine. The results indicate that the separation of ecosystems from environmental protection institutions and policies through the occupation of territory led to dramatic deforestation and loss of ecosystem sustainability.

The third part focuses on mapping European forest types by harnessing the power of high-resolution Sentinel-1 and Sentinel-2 satellite data from the Copernicus program. The novelty lies in the integration of various data sources for training dataset creation and the utilization of the Random Forest classifier on the Google Earth Engine cloud computing platform. The resulting forest type map for 2022 has a fine spatial resolution of 10 meters and distinguishes between broadleaved, coniferous, and mixed forests, with an impressive overall accuracy of 93%.

This research demonstrates the potential of synergizing cutting-edge remote sensing, machine learning, and cloud computing technologies to tackle complex environmental challenges at a continental scale. The developed methodologies pave the way for future advancements in forest disease monitoring, fire danger, conservation efforts, and environmental impact assessment, empowering informed decision-making in sustainable forest management.

Feature Engineering for Semantic Segmentation of Forest Diseases

Remote sensing techniques leveraging satellite imagery are increasingly utilized for environmental monitoring tasks such as land use classification and assessment of vegetation health. In particular, semantic segmentation methods based on machine learning have recently attracted much attention for their ability to delineate geographical regions of interest in satellite imagery. However, while these techniques have been extensively studied for various applications, such as land cover mapping and urban development analysis, the task of forest health monitoring [5], particularly the fire danger monitoring [11, 12], identification of bark beetle-induced damage, remains relatively novel.

Our study aims to address the following research questions:

1) How to effectively define and optimize feature informativeness and independence for semantic segmentation of forest diseases?

2) Does computational feature engineering improve segmentation accuracy and increase model robustness compared to utilizing spectral bands of satellite imagery?

To deal with the research questions we introduce an automated feature selection method using genetic algorithms that eliminates the need for model training. This approach includes a numerical evaluation of individual features and their combinations, alongside a simplified representation of vegetation indices for easier feature set optimization. Our framework enhances feature engineering for earth observation, especially in identifying forest diseases.

We have defined two key study areas for our investigation. The primary area, located in the Grand Est region of France, includes satellite images and corresponding stress

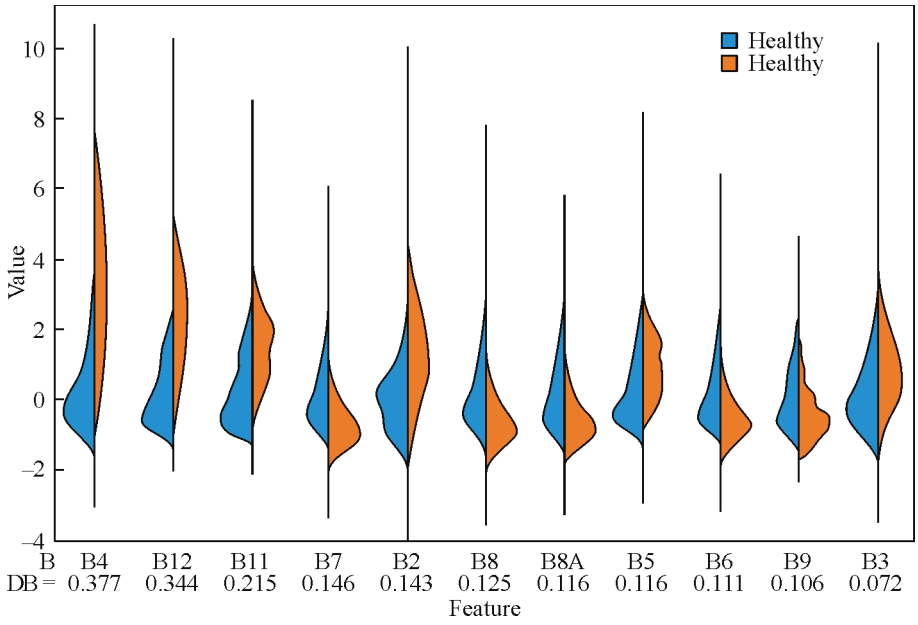

Fig. 1. Violin plot of spectral bands used and their individual informativeness (DB)

masks that delineate areas of forest under stress. The project provided us with the Dataset 1, which comprises 60 sites of damaged forests, totaling 385,637 coniferous forest pixels, of which 7% exhibit signs of stress. For the purposes of model training and validation, we divided these sites so that both the training and validation datasets contained a nearly equal proportion of stressed pixels. The training set includes 28 sites, featuring 13,017 stressed and 189,608 healthy pixels, whereas the validation set encompasses 32 sites, with 13,868 stressed and 169,144 healthy pixels.

To assess the robustness and general applicability of our models, we also incorporated a second study area located in the Chornobyl Exclusion Zone, Ukraine, utilizing 2018 satellite imagery. This area serves as an additional dataset for visual analysis to evaluate model performance (Dataset 2), although it is important to note that comprehensive labelling of stressed coniferous areas is not available for this dataset.

We use Sentinel-2 multispectral images as input data. As is known, such images contain information about the Earth's surface in different spectral bands, which allows us to use them for various purposes, such as land cover monitoring, vegetation measurement, and detection of environmental changes. Also, we have used vegetation indices — quantitative indicators used to measure and analyze plant growth and health based on the spectral properties of vegetation. As well as vegetation indices are quantitative state estimates and can be designed to distinguish objects from others, they serve (along with spectral bands) as features for segmentation. Since vegetation indices are mathematical functions, we propose to use a more generalized concept — a class of vegetation indices — to facilitate work with them. A detailed description of the methodology for the formation of informative features using the Bhattacharya distance is described in detail in the works [1—3].

Violin plots (Fig. 1) for features from the top-performing BANDS, MCARIbased, FRAC3, and HUESIMP models show the distribution across healthy and stressed labels, with feature values normalized using RobustScaler trained on healthy forest data. Fig. 1 suggests the most discriminative bands are Red (B4) and SWIR (B11-B12), while other bands are less informative. Fig. 1 indicates that selected features are more informative, albeit with some decreasing trends.

The segmentations by the models based on MCARIbased (Fig. 2, *b*), FRAC3 (Fig. 3, *a*), and HUE (Fig. 3, *b*) were largely consistent, with MCARIbased occasionally identifying non-forest areas as stressed. The segmented areas, viewed against the ground truth in Fig. 4, *b*, tended to overestimate stressed regions. Yet, comparing the RGB image in Fig. 4, *a* with the segmentations in Fig. 3, it's noticeable that areas classified as stressed have a distinct, lighter, and more brownish hue, potentially signaling imminent stress. This suggests a mild over-sensitivity in the models, possibly stemming from inaccuracies in the training data or a need for finer threshold adjustments for classifying forest health.

The segmentation outcomes (Fig. 2, 3) suggest the need for suitable augmentation during model training, favoring complex convolutional networks over pixel-based approaches, or relying on vegetation indices like HUE that are resistant to constant noise.

Model robustness was tested on Dataset 2 (Ukraine), with segmentation results shown in Fig. 6. The images in Fig. 5, normalized like in Fig. 4, *a*, display significant brightness variations, emphasizing the importance of accounting for brightness differences in feature selection and model training. Segmentation analysis (Fig. 6) suggests a high stress level across the coniferous forest. However, BANDS (Fig. 6, *a*) and MCARIbased (Fig. 6, *b*) models yielded noisy outcomes, while FRAC3 (Fig. 6, *c*) and HUE (Fig. 6, *d*) models were less noisy but HUE misclassified many non-coniferous areas as stressed. This was expected since the models were trained solely on coniferous forest data without a forest type mask. The models' sensitivity led to most forests being marked as

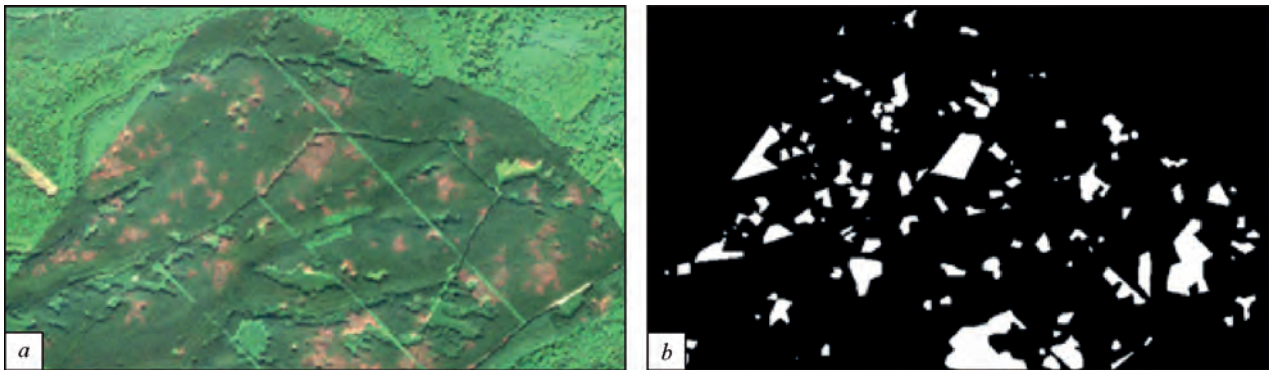

Fig. 2. Results of segmentation of test site of Dataset 1 by *a* — BANDS, *b* — MCARIbased models

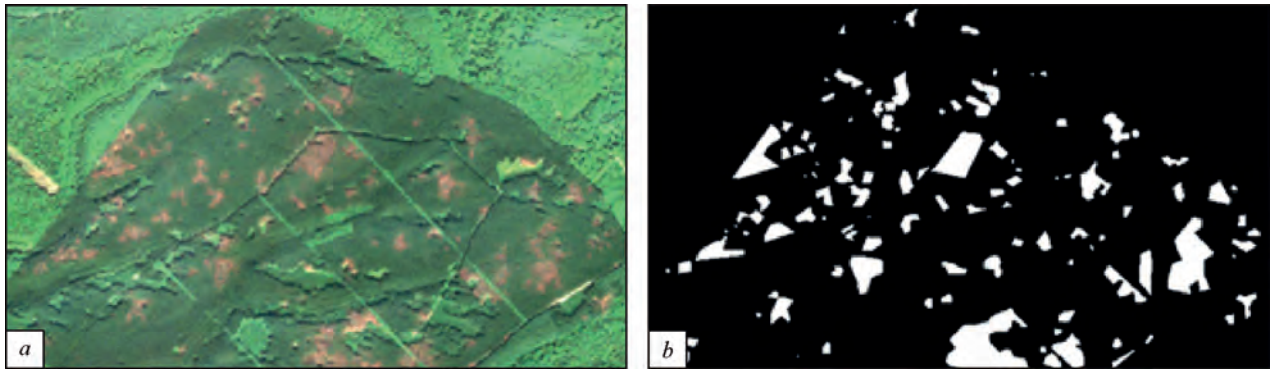

Fig. 3. Results of segmentation of test site of Dataset 1 by constant noise independent *a* — FRAC3, *b* — HUE models

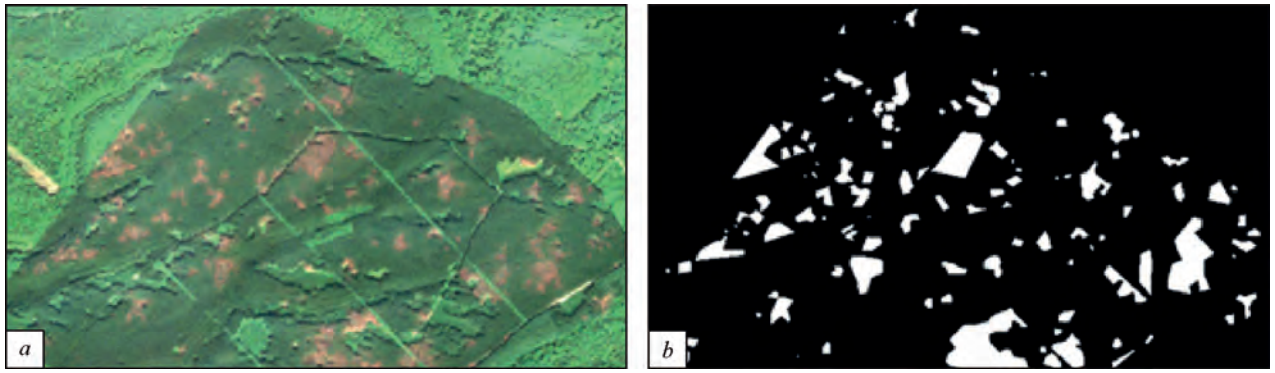

Fig. 4. Dataset 1 test area: *a* — RGB Sentinel-2 image, *b* — ground truth mask

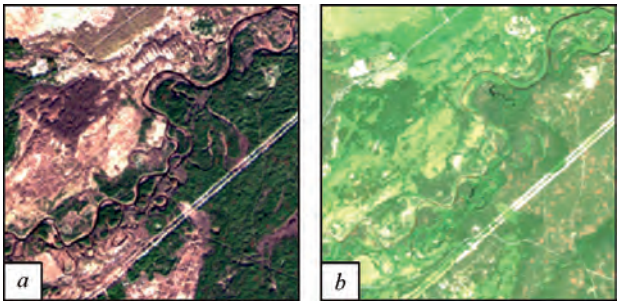

Fig. 5. Sentinel-2 images for Dataset 2 test area during winter (*a*) and summer (*b*) of 2018

stressed, which was later confirmed by experts, especially visible in the light brown tint of the forest in Fig. 5, *b*.

This research illustrates that leveraging optimized feature engineering with vegetation indices can notably enhance the semantic segmentation of satellite forest imagery over traditional spectral band usage [1—3]. By employing specialized informativeness and independence functions along with genetic algorithms for feature selection, we achieved high-quality models without compromising accuracy. Vegetation indices resilient to brightness variations proved especially effective in maintaining segmentation quality despite significant differences in image brightness between

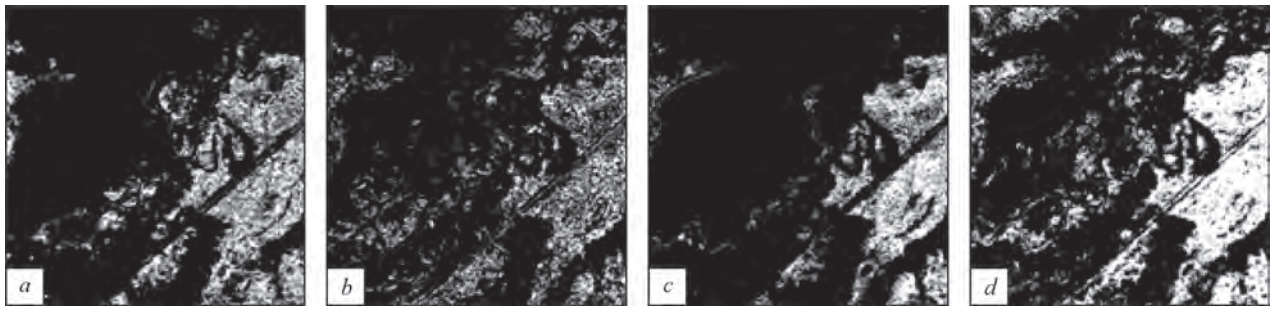

Fig. 6. Results of Dataset 2 test area segmentation by BANDS (*a*), MCARIbased (*b*), FRAC3 (*c*), HUE (*d*)

training and test datasets, addressing a common challenge with spectral bands and conventional indices [4]. We introduced novel approaches to feature engineering in remote sensing, such as mathematical definitions for feature informativeness and independence that facilitate numerical feature set optimization, and the use of generative classes for vegetation indices to bypass the need for manual index enumeration. These methodologies, particularly the introduction of brightness-invariant index classes, demonstrated consistent segmentation results across varying image conditions. These techniques can significantly aid in large-scale forest monitoring, enabling precise detection of health degradation with minimal labelled data [5]. To expand the research area and detailed analysis of forest health, we created a data set for machine learning for the territory of Ukraine [13].

Methods of intellectual analysis of the dynamics of forest cover change in Ukraine

The war has inflicted a range of harms on the socio-ecological system which are very likely to have lasting socio-ecological impacts. Assessing the environmental consequences of these events is nearly impossible due to the lack of physical access to these areas. To these ends, we aimed to explore the impact of the militarized occupation of natural protected areas and the subsequent interruption of conservation efforts on ecosystem sustainability. Such research can be conducted only using long-term observations before the military conflict and after the hot phase of the conflict and the establishment of a stable demarcation line. Due to the active warfare in 2022 and 2023, it is premature to quantify ecosystem conservation consequences. Thus, we focused on the progress of the Emerald Network establishment in the Luhansk region (Fig. 7) in terms of land cover changes in the environmental protection zones from 1996 to 2020 [6].

Quantification and evaluation of policies and processes underlying the establishment of Emerald Network in the Luhansk region was conducted by analyzing forest cover changes trends in the territories on both sides of the conflict demarcation line established after the "Minsk-2" and "Misnk-3" agreements in 2014 and 2015. Utilizing the principles of deforestation pressure-based management regime comparison, we evaluated the effectiveness of the Bern Convention's conservation policies and examined the

Fig. 7. Emerald Network sites in Luhansk region separated by demarcation line. The gray hashed area represents territory under Russian control after 2014 with an established demarcation line in 2015. The hashed area represents Emerald Network sites established on the blanks of Siverskyi Donets river

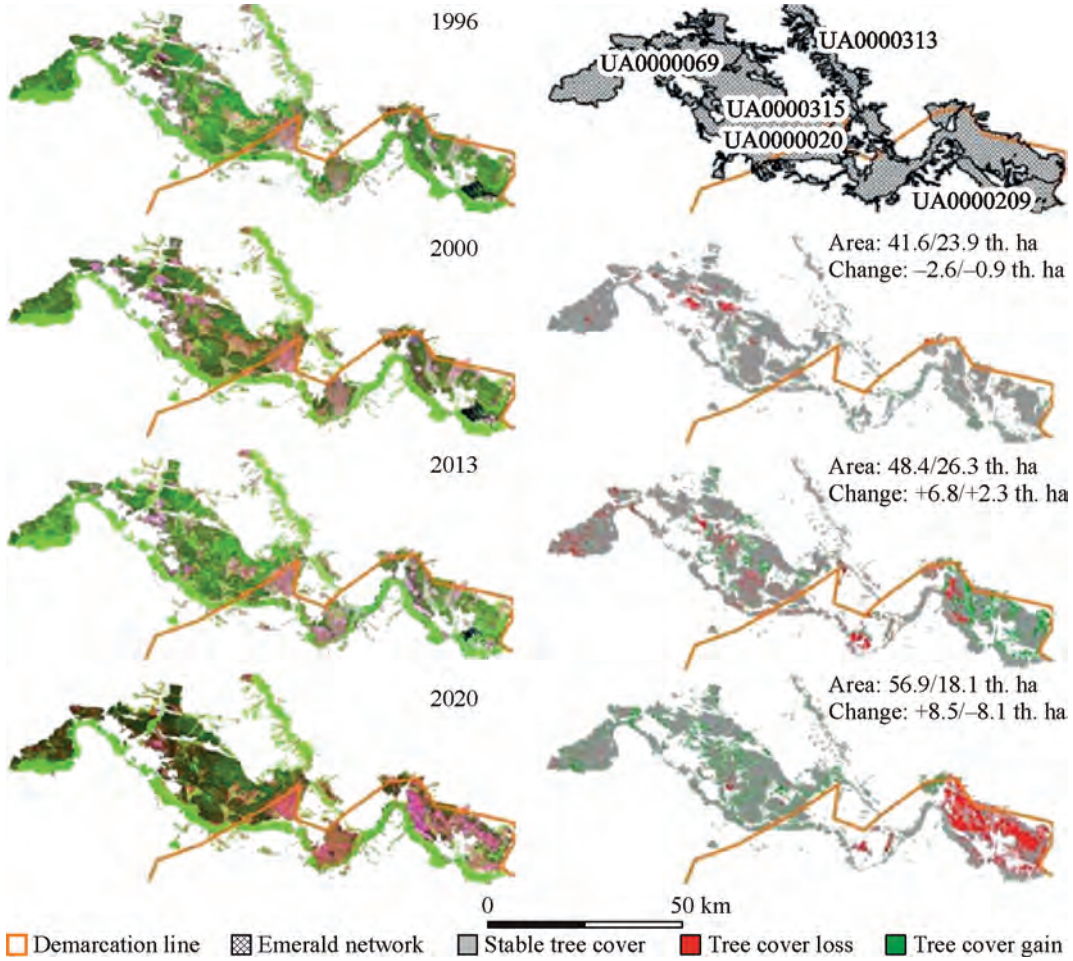

Fig. 8. Emerald Network sites established on the blanks of Siverskyi Donets river in Luhansk region. The map represents Emerald Network sites with IDs UA0000069, UA0000315, UA0000209, UA0000078, and the southern portion of UA000031377. The left images show Landsat images for 1996 to 2013 and Sentinel-2 images for 2020 in false color with short wave infrared 1 (~1.6 ^m), near-infrared (~0.8 ^m), and blue (~0.4 ^m) band combinations. The right images show the stable, gained, and lost tree cover for respective years and time periods. Areas and changes represent tree cover changes and net gains for territories under Ukraine and Russia's control, respectively

impact of the territory's separation on the environment by comparing forest area changes in territories under Ukrainian and Russian control. Gathering ground-referenced data in active conflict zones is impossible because of the high risks to security. Consequently, we employed remote sensing-based approaches, commonly used for assessing areas affected by warfare, to analyze changes in land cover and land use before, during, and after the conflict. We chose 1996 to 2020 as a research time period for the analysis because during these years Ukraine joined The Bern Convention, and the planned final year for Emerald Network establishment (excluding time after the catastrophic wildfire). This time period is further divided into three parts. The first (from 1996 to 2000) shows the trend before the creation of the Emerald Network. The second (from 2000 to 2013) shows the progress of the Emerald Network establishment before the conflict. The third (from 2013 to 2020) shows the progress of conservation after the beginning of the conflict. After the end of the Russian-Ukrainian war, the establishment of a stable demarcation line, and ecosystem's restoration process beginning, the methodology presented in this article can be extended to other regions of Ukraine for the post-war ecosystem conservation damage assessment.

We carried out a land-cover change assessment with the use of generated maps of the Luhansk region for 1996, 2000, 2013, and 2020. The accuracy values of tree cover maps in terms of F1 score (which is the harmonic mean of the user's accuracy and producer's accuracy68) were 0.9, 0.9, 0.84, and 0.88, correspondingly.

Between 1996 and 2000, the annual deforestation rate on the territories under Ukrainian control was –0.86 ± ± 0.22 th. ha per year or overall –3.42 ± 0.86 th. ha. A similar rate was observed in territories taken under Russian control after 2014 at an annual rate of –0.28 ± 0.1 th. ha per year or overall –1.1 ± 0.4 th. ha. Since 2000 Ukrainian government considered the creation of Emerald Network sites as a priority for the short- and long-term environmental-protection strategies. After work began on establishing Emerald Network sites and implementing EU sustainable development policies, changes in trends on both parts of the Emerald Network are

evident. Between 2000 and 2013, annual reforestation rates in territories under Ukraine control were +0.67 ± 0.09 th. ha per year with +8.7 ± 1.2 th. ha total forest area growth. At the same time, territories that were to be under Russian control had an annual rate of +0.19 ± 0.06 th. ha per year and total +2.48 ± 0.79 th. ha growth. The military conflict in 2014, and the subsequent segmentation of territory on the occupied and non-occupied by demarcation line, changed trend's patterns during 2013—2020. During this time period, we found that territories that remained under Ukraine's control kept in place reforestation and conservation processes with +1.19 ± 0.18 th. ha per year annual rate and total area in an increase of +8.3 ± 1.25 th. ha. However, territories that were taken by the Russian control experienced rapid deforestation of –1.23 ± 0.15 th. ha per year annual rate and –8.6 ± ± 1 th. ha total forest area loss. Results (Supplementary Tables 2 and 3) indicate that territories remained under Ukraine's control even under the conditions of military conflict with increased vulnerability and consequent ecological problems in the region continued progression of conservation while territories under Russian control lost 20 years of sustainable development progress with 25% of forest loss (compared the 2013 estimates).

The majority of forest area in the Luhansk region is concentrated in the floodplains of the Siverskyi Donets River site (Fig. 8) and was divided into two parts by a demarcation line. Both parts have the same ecological communities of flora and fauna and are equally vulnerable to ecological problems due to post-military action damage. Before the conflict in 2014, this area was entirely under Ukrainian government control and not segmented; this is reflected by the uniform and consistent land-cover change trends before the war. However, after the partial separation of the region, we observed severe deforestation. Between 2013 and 2020, Ukraine-controlled territories gained 18% of forest area, while Russia controlled lost 31%.

Our analysis indicates that Ukraine achieved a total reforestation area of 11.17 ± 1.45 th. ha before the beginning of the conflict and 17 ± 1.74 th. ha from 2000 to 2020 on the Ukraine-controlled territories. At the same time, deforestation rates of territories under Russian control with similar bio-physical characteristics and the same war-related vulnerability factors indicate that the separation of ecosystems from environmental protection institutions and policies through the occupation of territory led to dramatic degradation of the environment and loss of ecosystem sustainability.

European forest types mapping using high-fidelity satellite data

Accurate and up-to-date forest type maps are crucial for effective monitoring and management of forest ecosystems across Europe. However, the availability of up to date high-resolution forest type maps has been limited. This study introduces an innovative semi-supervised approach for mapping European forest types by harnessing the power of high-resolution Sentinel-1 and Sentinel-2 satellite data from the Copernicus program. The novelty of the approach lies in the integration of various data sources for training dataset creation and the utilization of the Random Forest classifier on the Google Earth Engine cloud computing platform. This innovative combination enables efficient processing and classification of vast amounts of satellite imagery for large-scale forest type mapping. In particular, the LUCAS Copernicus 2018 and 2022 datasets were employed for training and validation, ensuring the robustness of the classification model. The resulting forest type map for 2022 has a fine spatial resolution of 10 meters and distinguishes between three key classes: broadleaved, coniferous, and mixed forests. Accuracy assessment using independent validation data demonstrated the reliability of the proposed approach, yielding an impressive overall accuracy of 93%. Comparative analysis with existing forest products revealed both consistencies and differences, underscoring the dynamic nature of forest ecosystems. The generated map fills a gap in up to date geospatial information on European forest types, empowering informed decision-making in forest management, conservation efforts, and environmental impact assessment. This study demonstrates the potential of synergizing cutting-edge remote sensing, cloud computing, and machine learning technologies to tackle complex environmental challenges at a continental scale, paving the way for future advancements in forest monitoring and management.

For forest type classification we have used 12-day mean composites of SAR Sentinel-1 satellite data with VV, VH bands with 10-meters spatial resolution and Sentinel-2 data with preprocessing Level-2A and a spatial resolution of 10 meters are employed in Google Earth Engine cloud platform [14, 15]. The revisit time of Sentinel-2 is every 5 days; however, due to significant cloud cover, three composites are generated and used.

For training and testing the creation of forest type maps for Europe, the LUCAS Copernicus 2018 open dataset serves as the primary resource. Despite being based on 2018 data, this dataset remains suitable for forest type classification due to the relatively slow change in forest types over time. A five-year span is not considered extensive for a land cover type like forests. To update this dataset for 2022, the global land cover data from WorldCover 2021 was utilized. Samples that exhibited a change in class between 2018 and 2021 were subsequently excluded from consideration. The great advantage of LUCAS Copernicus 2018 data set is that for each sample there were 5 photos that confirm the correctness of the class that is entered for this sample. Fig. 9 illustrates the geospatial distribution of the resulting dataset for three types of forests (broadleaved, coniferous, and mixed). To train the model and validate the resulting product, the dataset was divided into an 80:20 ratio within each distinct group of countries.

The prepared stack of satellite Sentinel-1 and Sentinel-2 composites together with prepared pre-filtered LUCAS

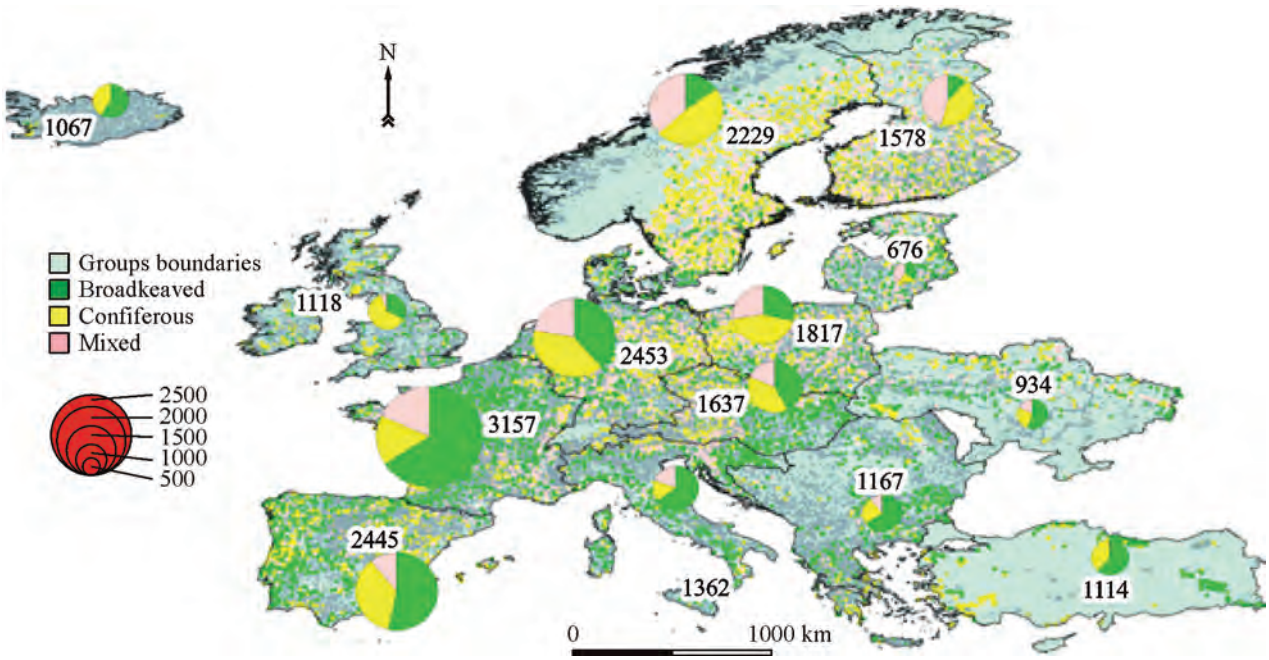

Fig. 9. The geospatial distribution of the prepared data set for 3 types of forests (broadleaved, coniferous and mixed) by selected groups

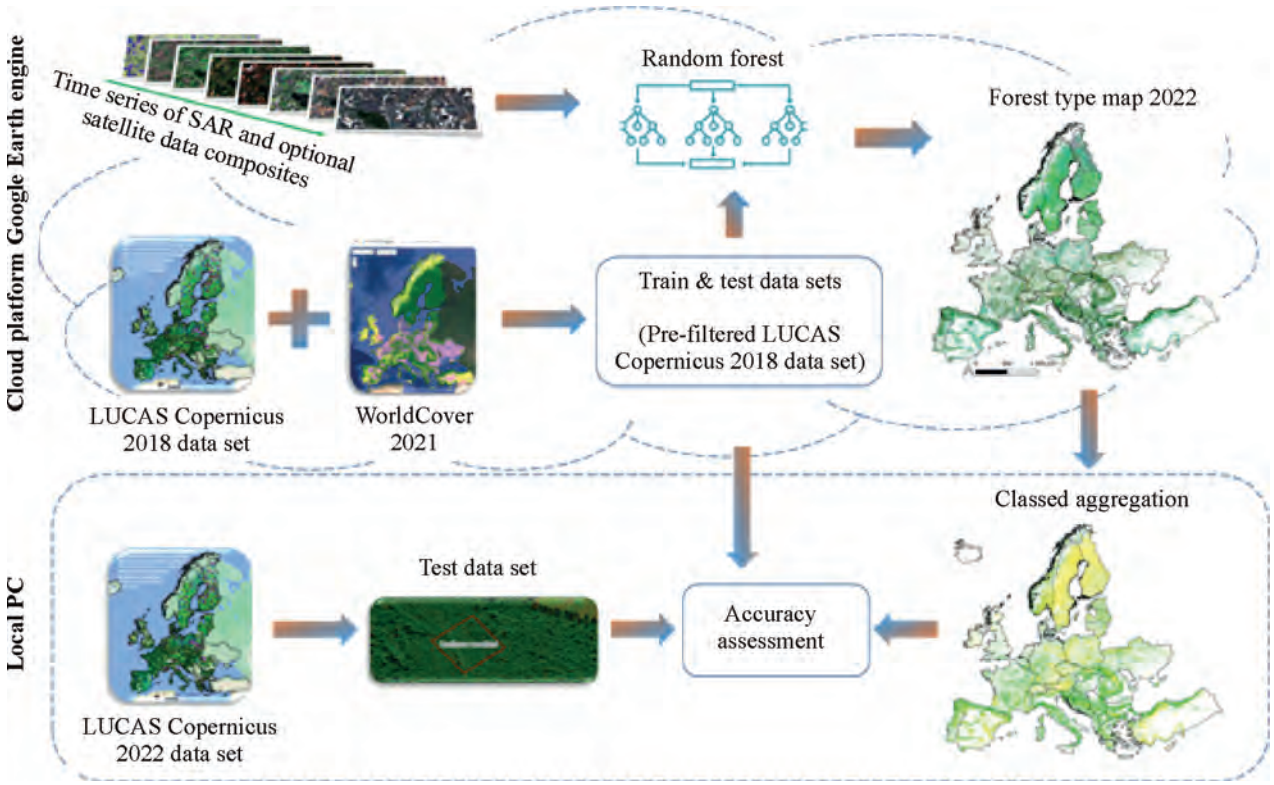

Fig. 10. Workflow of forest type map creation

Copernicus 2018 train data were used as input data for forest type classification. All data (satellite and train data set) is contained in cloud and we don't need extra resource to train the classifier. For each separate group of countries, we trained different Random Forest models due to GEE capacity with 100 number of trees. Leveraging the cloud platform Google Earth Engine facilitates seamless scalability and utilization of the model across extensive areas, particularly throughout Europe, as demonstrated by previous studies [7, 15]. The developed methodology for obtaining a classification map of forest types for Europe [8, 16] is schematically presented in the Fig. 10.

The main outcome of this study is the forest type classification map for the year 2022 covering the European territory, featuring a spatial resolution of 10 meters. The overall accuracy of created map is more than 90%. The resulting map includes 3 forest type classes (broadleaved, coniferous and mixed) and available for visualization by the link https://ee-swiftt.projects.earthengine.app/view/foresttype [9].

Conclusions

This article has demonstrated the immense potential of integrating advanced remote sensing data, computational machine learning techniques, and cloud computing platforms for addressing complex challenges in forest ecosystem monitoring and management. The developed approaches have yielded promising results across three main areas of investigation.

Firstly, the proposed automated feature engineering framework based on genetic algorithms has showcased remarkable performance in identifying informative features for semantic segmentation of damaged forest areas from satellite imagery. By numerically evaluating feature informativeness and independence, and leveraging a simplified representation of vegetation indices, this method has proven effective in optimizing feature sets for accurate segmentation. The elimination of manual feature selection and model training processes represents a significant advancement, enabling efficient analysis of vast satellite data repositories with minimal labeled data requirements.

Secondly, the intellectual analysis of forest cover change dynamics in conflict zones has provided insights into the detrimental impact of militarized occupation on ecosystem sustainability. Through the analysis of time-series satellite imagery, this study has quantitatively demonstrated the stark contrast in deforestation rates between areas under Ukrainian control, where conservation efforts were maintained, and those under Russian occupation, which experienced rapid and severe deforestation. These findings underscore the critical importance of environmental protection policies and institutions in preserving forest ecosystems, even amidst challenging circumstances such as armed conflicts.

Thirdly, the innovative semi-automated approach for mapping European forest types has yielded highly accurate and up-to-date geospatial information on a continental scale. By harnessing the power of high-resolution Sentinel-1 and Sentinel-2 satellite data, in conjunction with the Random Forest classifier and the Google Earth Engine cloud computing platform, this methodology has overcome the limitations of traditional mapping techniques. The resulting 10-meter resolution forest type map for 2022, distinguishing broadleaved, coniferous, and mixed forests, with an overall accuracy of 93%, represents a significant contribution to informed decision-making in forest management and conservation efforts across Europe.

The successful integration of cutting-edge technologies, including remote sensing, machine learning, and cloud computing, has opened new frontiers in the field of forest monitoring and management. By leveraging the synergies between these domains, researchers and practitioners can overcome the challenges posed by the vast scales and complexities of forest ecosystems, enabling more comprehensive, accurate, and timely assessments.

Future research endeavors should focus on further refining and enhancing these methodologies, exploring the incorporation of additional data sources such as ground-based observations and climate models, and expanding their applications to diverse forest ecosystems worldwide. Collaborative efforts between researchers, policymakers, and stakeholders will be crucial in translating these technological advancements into tangible impacts on sustainable forest management, biodiversity conservation, and climate change mitigation efforts.

Acknowledgement. *This work is supported from the European Commission through the HORIZON Europe project SWIFTT "Satellites for Wilderness Inspection and Forest Threat Tracking" (101082732) (https://swiftt.eu/).*

REFERENCES

1. Салій Є.В., Лавренюк А.М. Пошук значущих ознак для виявлення захворювань лісу на основі супутникових знімків. *Теоретичні і прикладні проблеми фізики, математики та інформатики: матеріали XXI Всеукраїнської науково-практичної конференції студентів, аспірантів та молодих вчених* (11—12 травня 2023 р., м. Київ, Україна). Київ, 2023. С. 401—404.

2. Salii Y., Kuzin V., Lavreniuk A., Kussul N. Features' Selection for Forest State Classification Using Machine Learning on Satellite Data. *Proceedings of 2024 IEEE International Geoscience and Remote Sensing Symposium*. 7—12 July, 2024, Athens, Greece (accepted).

3. Salii Y., Kuzin V., Kussul N., Lavreniuk A. Optimized Feature Engineering for Semantic Segmentation of Satellite Imagery. Computers and Geosciences (under review).

4. Гордійко Н., Яйлимова Г. Аналіз часових рядів супутникових даних для моніторингу стану лісів. *Проблеми керування та інформатики*. 2023. 68(4). С. 96—104. https://doi.org/10.34229/1028-0979-2023-4-8

5. Salii Y., Kuzin V., Lavreniuk A., Kussul N., Features' selection for forest state classification using machine learning on satellite data. *2024 IEEE International Geoscience and Remote Sensing Symposium*, 7—12 July, 2024, Athens, Greece (accepted).

6. Shumilo L., Skakun S., Gore M.L., Shelestov A., Kussul N., Hurtt G., Karabchuk D., Yarotskiy V. Conservation policies and management in the Ukrainian Emerald Network have maintained reforestation rate despite the war. Accepted in Communication Earth and Environment. *Nature*. 2023. 4, 443. https://doi.org/10.1038/s43247-023-01099-4

7. Kussul N., Shelestov A., Yailymov B., Yailymova H. Semi-Supervised Forest Type Mapping in Europe on Satellite Data. *2023 IEEE 12th International Conference on Intelligent Data Acquisition and Advanced Computing Systems: Technology and Applications* (IDAACS). 2023, September. 1. P. 454—458. https://doi.org/10.1109/IDAACS58523.2023.10348948

8. Salii Y., Kuzin V., Hohol A., Kussul N., Yailymova H. Machine learning models and technology for classification of forest on satellite data. *IEEE EUROCON 2023-20th International Conference on Smart Technologies*. 2023. P. 93—98. https://doi.org/10.1109/EUROCON56442.2023.10199006

9. Yailymov B., Yailymova H., Kussul N., Shelestov A. Semi-Supervised European Forest Types Mapping Using High-Fidelity Satellite Data. *Computers and Geosciences*. 2024 (under review).

10. Yailymov B., Yailymova H., Shelestov A., Shumilo L. Monitoring of Fires Caused by War in Ukraine Based on Satellite Data. *13th International Conference Dependable Systems, Services and Technologies* (DESSERT 2023), Greece, Athens, October 13—15. 2023. P. 1—5. https://doi.org/10.1109/DESSERT61349.2023.10416520

11. Kussul N., Fedorov O., Yailymov B., Pidgorodetska L., Kolos L., Yailymova H., Shelestov A. Fire danger assessment using moderate-spatial resolution satellite data. *Fire*. 2023. 6(2). P. 72. https://doi.org/10.3390/fire6020072

12. Kussul N., Yailymov B., Shelestov A., Yailymova H. Fire danger assessment based on the improved fire weather index. *IGARSS 2022—2022 IEEE International Geoscience and Remote Sensing Symposium*. 2022, July. P. 1584—1587. https://doi.org/10.1109/IGARSS46834.2022.9884378

13. Yailymova H., Yailymov B., Salii Y., Kuzin V., Odruzhenko A., Sydorenko S., Shelestov A., Kussul N. A multimodal dataset for forest damage detection and machine learning. *2024 IEEE International Geoscience and Remote Sensing Symposium*. 7—12 July, 2024, Athens, Greece (accepted).

14. Kussul N., Shelestov A., Yailymov B. Cloud Platforms and Technologies for Big Satellite Data Processing, International scientific and practical conference Information and communication technologies and sustainable development. Cham: Springer Nature Switzerland. 2022. P. 303—321. https://doi.org/10.1007/978-3-031-46880-3_19

15. Yailymov B., Shelestov A., Yailymova H., Shumilo L. Google Earth Engine framework for satellite data-driven wildfire monitoring in Ukraine. *Fire*. 2023. 6(11). P. 411. https://doi.org/10.3390/fire6110411

16. Shelestov A., Salii Y., Hordiiko N., Yailymova H. Current Advances on Cloud-Based Distributed Computing for Forest Monitoring in Ukraine. Lecture Notes in Networks and Systems. Springer, 2023. P. 322—336. https://doi.org/10.1007/978-3-031-46880-3_20

APPLICATION OF SATELLITE REMOTE SENSING FOR SURFACE WATER QUALITY ASSESSMENT IN UKRAINE; INTEGRATING SUPERVISED LEARNING AND A SPECTRO-TEMPORAL CONVOLUTIONAL NEURAL NETWORK

O. Polishchuk [1], T. Kazantsev [2], O. Bilous [3], I. Nezbrytska [3], O. Burova [1], S. Stepanov [1], K. Zolotareva [1]

[1] M.G. Kholodny Institute of Botany of the NAS of Ukraine
[2] Spatiolab Private Company
[3] Institute of Hydrobiology of the NAS of Ukraine

Introduction

Water quality indicators of surface reservoirs are important for obtaining drinking water, recreation, agriculture and industry. Finally, but not least, the quality of surface water is important for the maintenance of biodiversity in aquatic and terrestrial ecosystems, so its monitoring is necessary. From an ecological point of view, the term "water quality" corresponds to the most important biotic and abiotic characteristics, among which the concentration of chlorophyll and suspended solids are the most important. The concentration of chlorophyll is an integral indicator of the number of algae, and therefore of the inflow of energy and biomass into the reservoir due to photosynthesis. Since phytoplankton development depends on the availability of micro- and macronutrients, a high chlorophyll concentration is a reliable indicator of pollution by return water of water channels or washing off fertilizers used in agriculture. Suspended solids are direct pollution due to the lifting of silt by turbulent currents or brought from tributaries with high linear current velocity. Since they increase turbidity and make it difficult to correctly determine the concentration of chlorophyll, their remote determination is needed also for making the corresponding corrections.

Different approaches and algorithms exist for determining and monitoring various parameters of water quality, in particular: suspended matter [1, 2], chlorophyll [3—6], concentration of cyanobacteria, colored dissolved organic matter, dissolved organic carbon and water color [7, 8]. Such algorithms are developed by creating models based on spatio-temporal data bases on *in situ* water quality and their corresponding combinations of light reflectance coefficients of various spectral bands received remotely by satellites. The implementation of such algorithms in a new water area, depending on the characteristics of watercourses, requires at least adaptation based on *in situ* data, and in some cases, it may be necessary to modify existing or develop new algorithms. Simulated, or synthetic, data on surface water pollution derived from satellite data, despite lower accuracy and unavailability for narrow watercourses, can be a valuable addition, as they provide an assessment of pollution over large areas, in places where ground monitoring is not carried out or is not possible. Thanks to the wider and detailed spatial coverage, in particular, it is possible to localize potential sources of pollution and carry out integral assessments of watercourse pollution levels.

The purpose of our research was to develop and test the concept of surface water quality modeling based on the spectro-temporal data of the Sentinel-2 satellite (level L2A).

Methodology

General workflow. 1. Analyze the open monitoring data of the State Water Agency for 2016—2021 to create a concept of their modeling and initial research points sampling. The choice of research points and dates is determined by the possibility of obtaining relevant satellite data and reliably different levels of pollution with a similar general structure of pollution. 2. Develop scripts for downloading and preprocessing data using Python and Google Earth Engine. 3. Using the sample of spectral data for selected points (potential predictor variables) and State Water Agency data (ground truth data on the actual state of water bodies), conduct preprocessing, analysis and implement the modeling conception using deep learning algorithms at selected points on data for 2019, 2021, 2022 and 2023, and the prediction on the Dnipro River for 2021—2023. 4. Perform the analysis of the predictions and their possible relationships with the "blooming" of water and hostilities.

Data

Ground truth data. The data were obtained from an open source at the link https://data.gov.ua/dataset/surface-water-monitoring. We analyzed the general availability of data for all parameters and chose for analysis those that were present in the vast majority of measurements: BOD-5 (biochemical oxygen consumption for 5 days), suspended matter content (mg/l), sulfate content (mg/l), chloride content (mg/l),

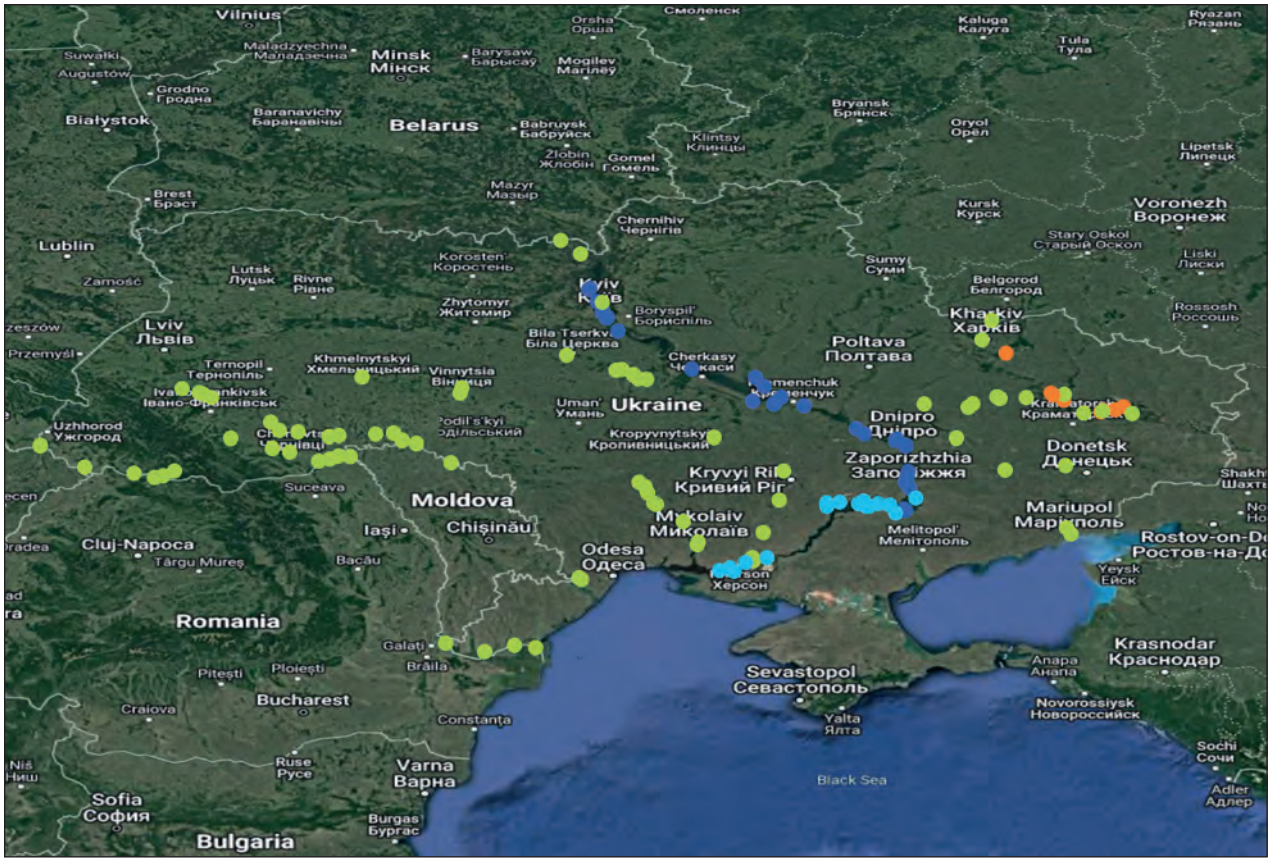

Fig. 1. Spatial distribution of test points by groups: the "Other" group is marked in green, "Siverskyi Donets" in orange, "Dnipro-1" in blue, and "Dnipro-2" in light blue

ammonium ion content (mg/l), nitrate content (mg/l), nitrite content (mg/l), phosphate content (mg/l), COD (chemical oxygen consumption).

An exploratory analysis was performed, including comparing average annual dynamics, a correlation analysis between various pollution parameters, and a principal component analysis to assess the differences in the structure of pollution between river basins. Based on this analysis, it was concluded that different points and different years are generally characterized by consistent differences in pollution levels, and variations within one point and year are significantly lower. Also, basins were consistently different by the pollution structure.

All records from 2016 to 2021 were used to analyze the pollution structure, and only from 2019 to 2023 were used for modeling, as there were not enough cloud-free Sentinel-2 images in earlier years.

The test points were selected manually in such a way that the riverbed in the corresponding places was wide enough for the correct interpretation of the Sentinel-2 data, that is, at least 60 m. Polygons were created at the level of the corresponding points (Fig. 1). A total of 133 plots were created. For spatial cross-validation and the study of the possible impact of the war, all stations were divided into 4 groups: "Siverskyi Donets", "Dnipro-1", "Dnipro-2", "Others". The "Dnipro-1" group included stations above the Kakhovka Reservoir, and the "Dnipro-2" group — at the level and below the Kakhovka Reservoir (Fig. 1).

For the "Siverskyi Donets" group, data from the State Water Agency are available only until 2021. The "Dnipro-1" group includes stations more than 300 km upstream, data are available until 2023 inclusive. Group "Dnipro-2" includes stations below 300 km downstream, data are available until 2023. Group "Other" — other rivers, except Kalchik, Kalmius, Danube and its tributaries.

Sentinel-2 data. The data were downloaded using Google Earth Engine through the appropriate application program interface (API) in Google collaboratory. Collections "COPERNICUS/S2_SR" and "'COPERNICUS/S2_CLOUD_PROBABILITY" were used.

Starting in 2022, in some images of the Sentinel-2 L2A collection a value of 1000 have been added to all channels to harmonize the data. We detected and corrected this so that all data are in a single domain and suitable for direct comparison. To detect this shift, a 1 percentile was calculated for the B2 (blue) channel and compared to 1000.

For modeling, the spectral bands B2, B3, B4, B5, B6, B7, B8, B8A, B11, B12 and the vegetation indexes (VIs) NDVI, NDWI, SAVI, and ARVI were used. To mask out clouds and shadows, we used the algorithm recommended by the Google Earth Engine. We used a cloudiness filter threshold at 60%, and masked out all pixels with a probability of

Fig. 2. The view of the Kakhovka Reservoir on the Sentinel-2 image as of 2023-08-05 (*a*) and the updated contour of the main channel of the Dnipro River shown in purple on top of the old contour shown in green (*b*)

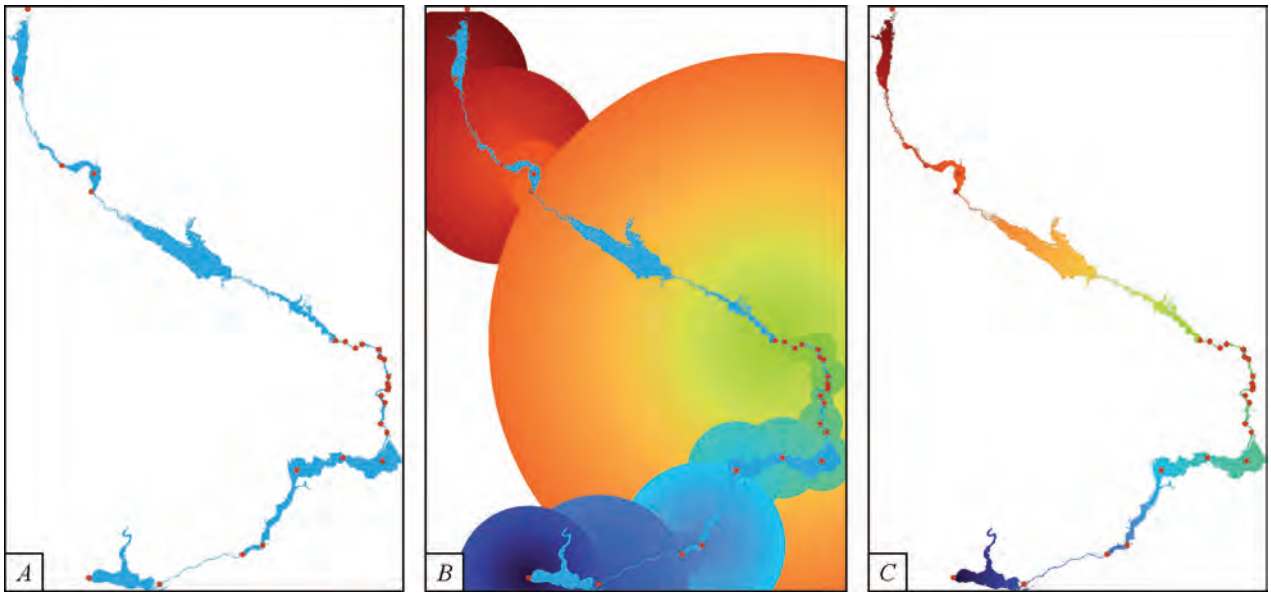

Fig. 3. The procedure for preparing a gradient raster to determine the distance downstream

cloud or cloud shadow greater than 10% plus a buffer of 80 m out of them. After data exporting, a further pixelwise filtering and processing was performed according to the number of unique dates and linear resampling of the corresponding spectral data to equal intervals of 15 days from May 1 to September 30. The "interp1d" function of the "scipy" software package was used for resampling. For this dataset, the global 2nd and 98th percentiles were calculated for each year and the data were normalized to these percentiles using the formula:

$$\text{Normalized data} = (\text{Data} - P2) / (P98 - P2), \quad (1)$$

where P2 is the 2nd percentile, P98 is the 98th percentile. Thus, 96% of the data range on all channels was reduced to the 0—1 range.

Since the selected polygons varied greatly in size, from 15 to 2000 pixels, the training data were regularized by randomly taking no more than 20 pixels from each polygon.

For making predictions, the spectral data for the entire Dnipro River was employed. In 2023, the geometry of the watercourse at the level of Kakhovka Reservoir was manually corrected considering changes after the explosion of the Kakhovka hydroelectric power station (Fig. 2).

To assess the dynamics of "water bloom" the ABDI index [9] was used, which was calculated according to the formula:

$$ABDI = RRE2 - RRed - ((RNIRn - RRed) \cdot (\lambda RE2 - \lambda Red)) / (\lambda NIRn - \lambda Red) - [RRed - 0.5xRGreen], \quad (2)$$

where λ and *R* are the wavelength and spectral reflectance index, and the marks *RE2, Red, NIRn* and *Green* correspond to channels B6, B4, B8A, and B3, respectively.

For ease of further analysis and interpretation, all the rasters with predictions and water «blooming» were converted to plots of dependence on the distance upstream. To generate the respective distance raster, a special algorithm was developed and employed: 1) along the entire course of the river, points were placed in the direction from the confluence with the sea and upstream in such a way that a circle could be drawn from each previous point and none of the following points fell into it, except for the first

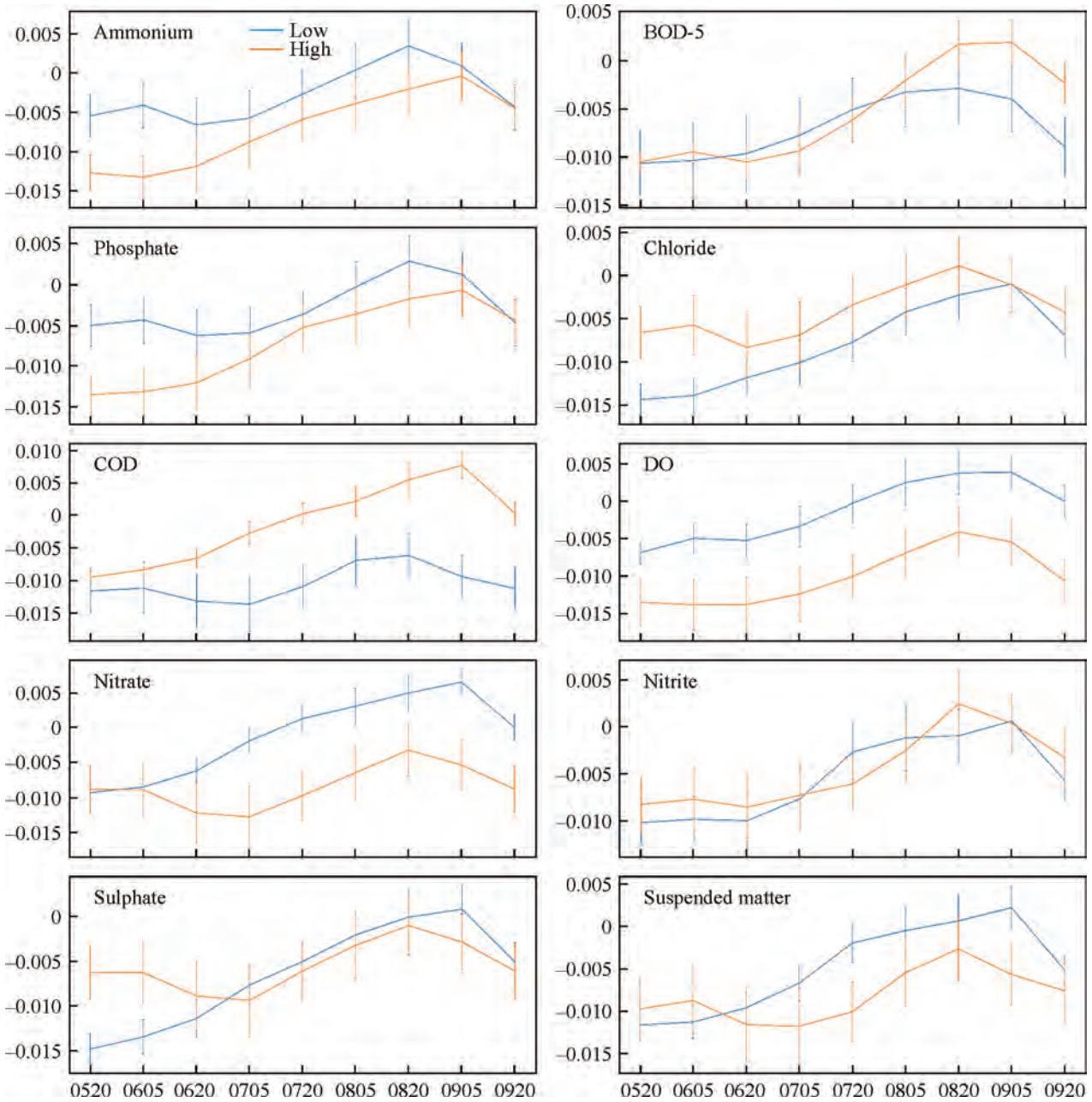

Fig. 4. Seasonal dynamics of water "blooming" at different levels of water pollution according to various parameters

following one (Fig. 3, *a*); 2) from each point to the next, a gradient circular raster was generated by the gdal.proximity function (Fig. 3, *b*) in order from the point of entry into the sea, where the gradient values corresponded to the distance from the center (previous point) in meters; 3) merged all rasters in reverse order; 4) cut the obtained raster along the contours of the river (Fig. 3, *c*).

Modeling

Considering generally low intraseasonal pollution variability and the high inherent parasitic variability of spectral reflectance of water bodies caused by currents and winds, training a supervised model for monitoring and fast-tracking pollution changes seems impossible. However, a more integral approach can be used, adopting generalized time-series spectral data throughout a season and averaged yearly pollution data. The modeling was based on the assumption that the dynamics of complex changes in the spectral characteristics of water in the May—September period is related to the average level of pollution in the February—August period. Each point in time and space was validated for compliance with a given area of the water surface (masking of clouds, shadows from clouds, haze, boats, etc.). The available data on water quality parameters for the period February—August were averaged for each point-year combination. Thus, satellite and ground data were combined into one training dataset. Each pixel was regarded as a single-channel image with a size of $14 \cdot 10 \cdot 1$ (14 spectral channels for 10 dates). For training, we used a spectro-temporal convolutional neural network architecture for

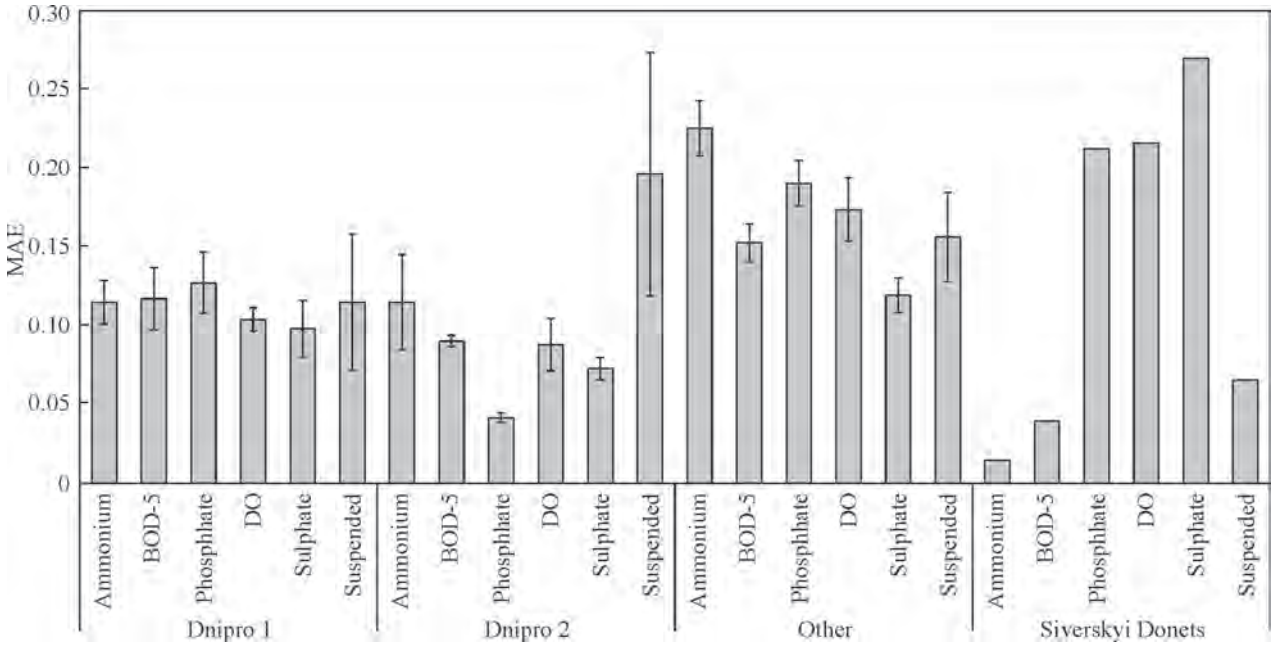

Fig. 5. Spatial cross-validation results, MAE ± SE where applicable

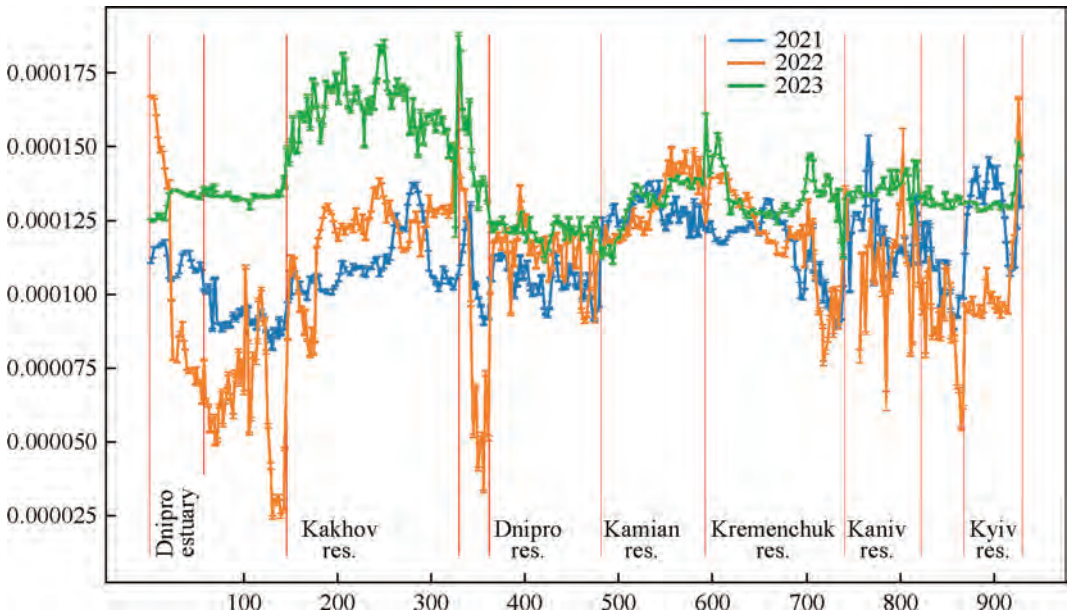

Fig. 6. Distribution of simulated BOD-5 by distance downstream of the Dnipro River

regression problems, adapted from the source [10], where a similar topology was used, but for the classification problem.

Spatial validation. Using data from years before 2022, when the State Water Agency had full access to the monitoring stations, the suitability for spatial extrapolation was assessed. That is necessary for modeling water pollution in areas that became inaccessible after 2022 due to hostilities and occupation. To reduce the uneven distribution of values and the impact of outliers, all pollution indicators were logarithmized and the obtained result was normalized to the range 0—1. For each pollution indicator, a separate model was trained, using all available records in the State Water Agency database for each indicator. Thus, the amount of available data was different for different indicators and, accordingly, different amounts of spectro-temporal data were used.

For model performance evaluation and as a loss function, a "mean absolute error" (MAE) metric was used.

Results

Relationships between water "blooming" and pollution level. For each pollution parameter, all stations were divided into "low" and "high" groups based on a comparison of the value with its median in the entire dataset. In each of the groups, the averaged seasonal dynamics of water "blooming"

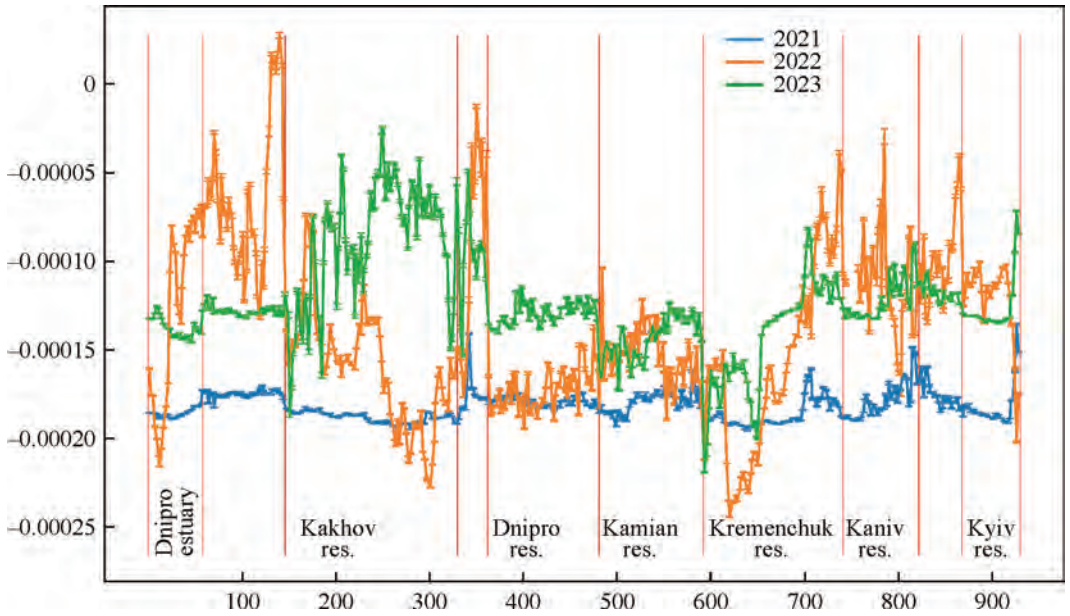

Fig. 7. Distribution of simulated Phosphate by distance downstream of the Dnipro River

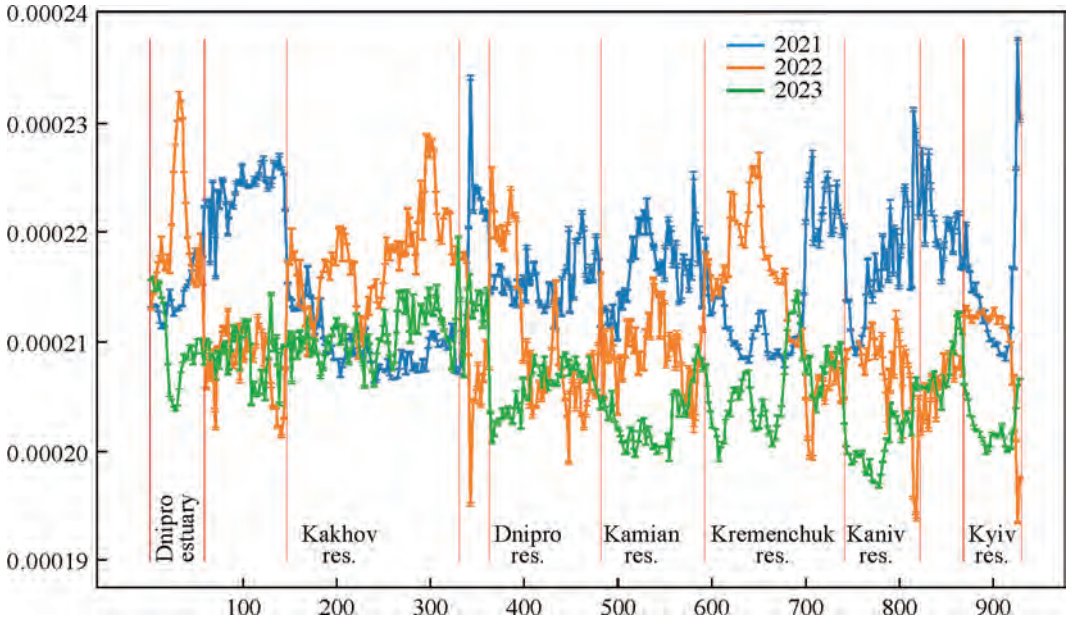

Fig. 8. Distribution of simulated DO by distance downstream of the Dnipro River

were constructed and compared (Fig. 4). The content of biogenic ions (ammonium, phosphate, nitrate) was lower in water with a higher level of "bloom", so other factors such as temperature and flow velocity were the main cause. Another explanation is the decrease in the content of biogenic elements due to their consumption by microalgae during their active growth. A decrease in the content of suspended matter was accompanied by an increase in the level of "blooming", which is probably related to more efficient photosynthesis in clearer water. The relationship with oxygen-related parameters was predictable — increased levels of BOD-5 and COD decreased oxygen concentration with a more pronounced "bloom", which is associated with intensive respiration of phytoplankton and increased concentrations of organic substances. Therefore, the seasonal dynamics of water "blooming" is strongly related to different water pollution parameters, and its use as a predictor not only for chlorophyll concentration but also for other parameters makes sense.

Cross-validation. Spatial cross-validation was carried out separately for years (2019, 2021 — 2023) for ammonium, BOD-5, phosphate, dissolved oxygen (DO), sulfate and suspended matter, and MAE was averaged (Fig. 5). In the "Dnipro-1" group, MAE was lower than 0.1 only for the DO and sulfate; in "Dnipro-2", for BOD-5, phosphate, DO, and

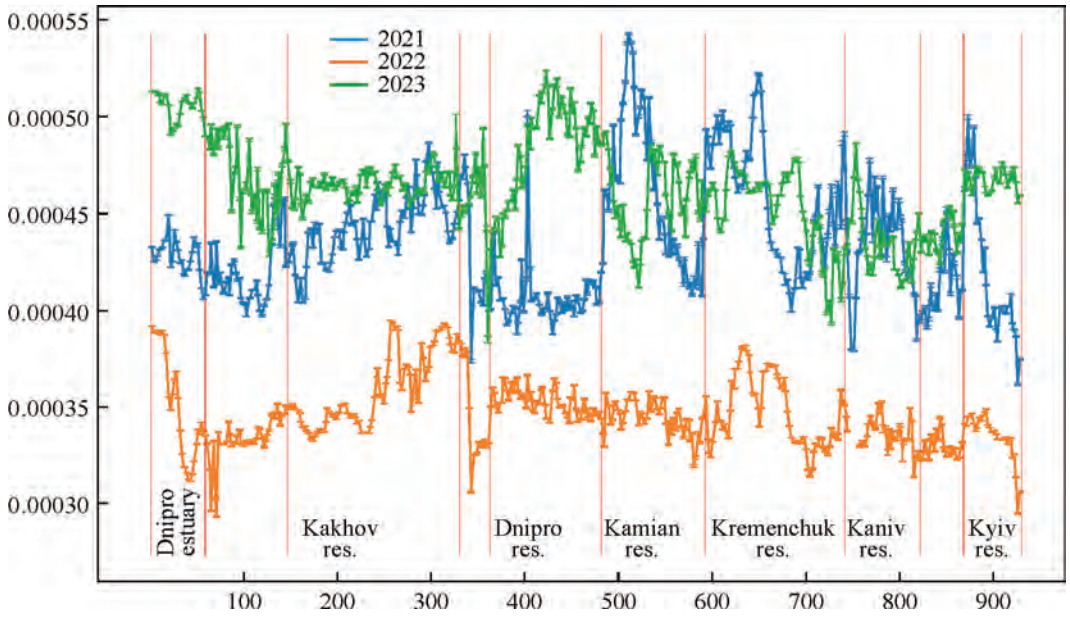

Fig. 9. Distribution of simulated Sulfate by distance downstream of the Dnipro River

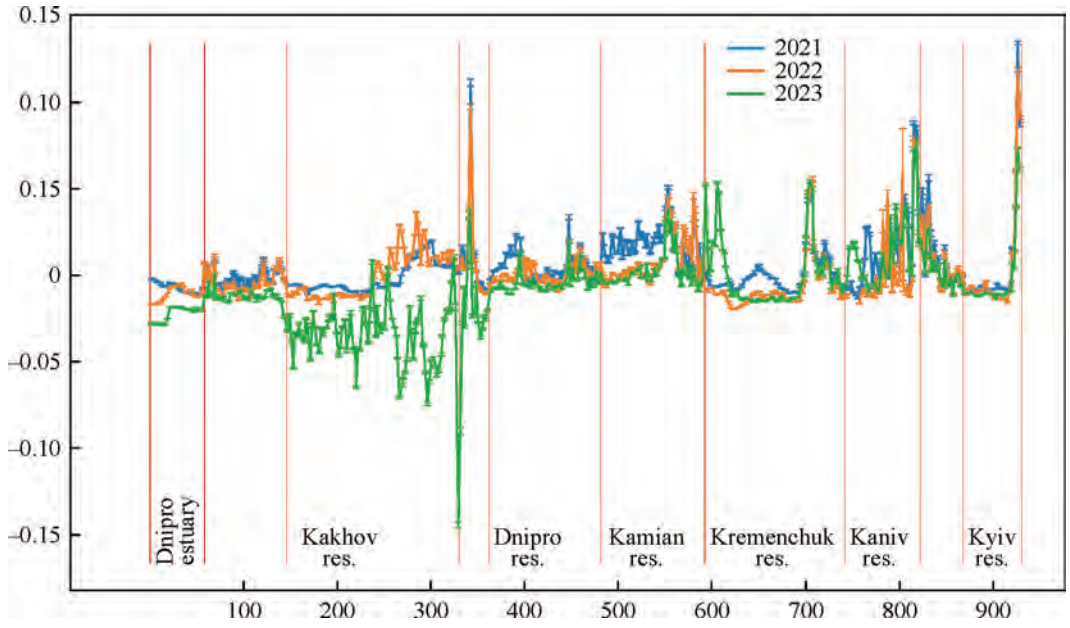

Fig. 10. Distribution of the water "blooming" level according to the ABDI index by distance downstream of the Dnipro River

sulfate; in the "Other" the extrapolation was unsuccessful; in the "Siverskyi Donets" group, the error was lower than 0.1 for ammonium, BOD-5 and suspended matter, but the reliability of the extrapolation is questionable, since the data for this group were available only in 2019.

Analysis of predictions on the example of the Dnipro River. In the simulated BOD-5, an increase was observed in 2023 compared to 2021—2022 at the level of the Kyiv, Kaniv, Kremenchuk, and Kakhovka reservoirs, as well as in the area below the Kakhovka Reservoir (Fig. 6). The most pronounced difference was precisely at the level and below the Kakhovka Reservoir, which may be a consequence of the undermining of the Kakhovka Hydroelectric Power Plant dam and the change in the hydrological regime of the Dnipro River in 2023.

In the simulated phosphate, an increase was mostly observed in 2022—2023 compared to 2021 at the level of Kyiv, Kaniv, in the upper part of the Kremenchuk and the lower part of the Kamianske reservoirs. An increase was observed at the level of the Dnipro and Kakhovka reservoirs only in 2023, and below the Kakhovka Reservoir — in 2022—2023 (Fig. 7). Such changes can also be associated with hostilities. DO showed a weak downward trend observed in 2022—2023 compared to 2021, except in the Kakhovka region, where the trend was the opposite (Fig. 8). The simulated sulfate in 2022 was significantly lower than in 2021 and 2023 (Fig. 9).

According to the ABDI index, there was a decrease in the level of water "blooming" in the lower part of the Kremenchuk, Kamianske and Dnipro reservoirs in 2022—2023 compared to 2021 and a significant decrease in the level of the Kakhovka Reservoir in 2023 compared to 2021—2022. This trend also continued below downstream from the Kakhovka Reservoir.

Conclusions

The developed approach is in essence an extrapolation of ground truth information water quality with the use of Sentinel-2 spectral reflectance as auxiliary data. The performance of the trained models may be questionable when applied to different water areas or vegetation seasons. However, the validation results on the scale of Ukraine are reasonably good, corresponding to 10% error on average, and allow extrapolation and further analyzes of the state of reservoirs, based on which management decisions can be made in the future.

One of the important stages in the preparation of such extrapolations for large-scale calculations will be the identification of centers of growth of higher aquatic plants, since in these places the prediction of various indicators of pollution is incorrect, and the water "blooming" index acquires high values, although "blooming" may actually be absent.

REFERENCES

1. Domínguez Gómez J.A., Chuvieco Salinero E., Sastre Merlín A. Monitoring transparency in inland water bodies using multispectral images. *International Journal of Remote Sensing*. 2009. 30, Iss. 6. P. 1567—1586. https://doi.org/10.1080/01431160802513811
2. Nechad B., Ruddick K.G., Park Y. Calibration and validation of a generic multisensor algorithm for mapping of total suspended matter in turbid waters. *Remote Sensing of Environment*. 2010. 114, Iss. 4. P. 854—866. https://doi.org/10.1016/j.rse.2009.11.022
3. Gitelson A., Mayo M., Yacobi Y.Z., Parparov A., Berman T. The use of high-spectral-resolution radiometer data for detection of low chlorophyll concentrations in Lake Kinneret. *Journal of Plankton Research*. 1994. 16, Iss. 8. P. 993—1002.
4. Yacobi Y.Z., Gitelson A., Mayo M. Remote sensing of chlorophyll in Lake Kinneret using highspectral-resolution radiometer and Landsat TM: spectral features of reflectance and algorithm development. *Journal of Plankton Research*. 1995. 17, Iss. 11. P. 2155—2173.
5. Gower J., King S., Borstad G., Brown L. Detection of intense plankton blooms using the 709 nm band of the MERIS imaging spectrometer. *International Journal of Remote Sensing*. 2005. 26, Iss. 9. P. 2005—2012. https://doi.org/10.1080/01431160500075857
6. Zlinszky A., Padányi-Gulyás G. Ulyssys water quality viewer technical description supplementary. Preprints 2020, 2020010386 (https://doi.org/10.20944/preprints202001.0386.v1).
7. Toming K., Kutser T., Laas A., Sepp M., Paavel B., Niges T. First experiences in mapping lake water quality parameters with Sentinel-2 MSI Imagery. *Remote Sensing*. 2016. 8, Iss. 8. P. 640. https://doi.org/10.3390/rs8080640
8. Potes M., Rodrigues G., Penha A.M., Novais M.H., Costa M.J., Salgado R., Morais M.M. Use of Sentinel 2-MSI for water quality monitoring at Alqueva reservoir, Portugal. *Proceedings of IAHS*. 2018. 380. P. 73—79. https://doi.org/10.5194/piahs-380-73-2018
9. Cao M., Qing S., Jin E., Hao Y., Zhao W. A spectral index for the detection of algal blooms using Sentinel-2 Multispectral Instrument (MSI) imagery: a case study of Hulun Lake, China. *International Journal of Remote Sensing.* 2021. 42, Iss. 12. P. 4514—4535. https://doi.org/10.1080/01431161.2021.1897186
10. Pelletier Ch., Webb G.I., Petitjean F. Temporal convolutional neural network for the classification of satellite image time series. *Remote Sensing*. 2019. 11, Iss. 5. P. 523. https://doi.org/10.3390/rs11050523

INNOVATIVE MODELS AND APPLICATIONS OF SATELLITE INTELLIGENCE

N. Kussul [1, 2, 3], A. Shelestov [1, 2], S. Drozd [1, 2], B. Yailymov [1], H. Yailymova [1, 2], M. Lavreniuk [1], L. Shumilo [3], S. Skakun [3]

[1] Space Research Institute of the NAS of Ukraine and the State Space Agency of Ukraine
[2] National Technical University of Ukraine "Igor Sikorsky Kyiv Polytechnic Institute"
[3] University of Maryland, College Park, USA

Introduction

The ongoing military conflict in Ukraine has had devastating impacts on the country's environmental monitoring [1], as well as agricultural lands, posing a severe threat to global food security [2]. Accurate and timely monitoring of crop production losses and field damages is crucial for guiding recovery policies, quantifying economic impacts, and ensuring food availability worldwide [3—21]. This study aims to leverage the power of satellite imagery and advanced machine learning techniques to address two critical tasks related to the war's effects on Ukrainian agriculture [22—30].

The first task focuses on developing an innovative data augmentation approach to enhance crop classification models' performance. Crop classification maps are vital for various agricultural applications, including yield estimation, risk assessment, and sustainable land management. However, the real-world distribution of crop types and land cover classes is often imbalanced, hindering the scalability and transferability of traditional machine learning models. To overcome this challenge, the study proposes a novel data augmentation method that employs Generative Adversarial Neural Networks (GANs) with pixel-to-pixel transformation [31—35]. This approach generates realistic synthetic satellite images and corresponding segmentation masks, capturing underrepresented crop type distributions and enabling better representation of minority classes during model training.

The second task addresses the quantification of war-induced crop losses in Ukraine and their impact on global food security [22—30]. By analyzing a multi-year panel of village councils across Ukraine, the study estimates the reduction in winter crop area and yield caused by the conflict. This analysis provides crucial insights into the direct and indirect effects of military activities on agricultural production, highlighting the need for targeted support and recovery efforts.

Furthermore, the study presents a robust methodology for near real-time monitoring and assessment of agricultural land damage caused by military actions [23—24]. Leveraging freely available Sentinel-2 satellite data, the proposed approach combines machine learning techniques with spectral band and vegetation index anomaly detection to accurately identify and delineate damaged fields. This automated monitoring system can aid in documenting war crimes, informing recovery analyses, and supporting targeted food security policies at local and global levels.

By addressing these critical tasks, this study aims to contribute to the advancement of satellite intelligence for agricultural monitoring, damage assessment, and the development of effective strategies to mitigate the severe consequences of armed conflicts on global food security. Since Ukraine is an associate member before joining Europe, currently active implementation of the Land Parcel Identification System practice has been initiated in Ukraine with the support of the World Bank.

The Training Data Imbalance Problem in Crop Classification

An efficient GAN architecture enables the generation of realistic synthetic satellite images for training data augmentation [31—36]. The relationship between satellite images and segmentation masks hinges on textural and multispectral features within the images. We trained a model capable of producing realistic satellite images for any artificially generated segmentation mask. This method allows for the creation of synthetic pairs of satellite images and masks, capturing unobservable crop type distributions and providing control over class balance in the dataset. We used 256 × 256 pixel sparse segmentation masks to generate 4-bands synthetic satellite images. The resulting augmentation algorithm shown on Fig. 1. First, we trained pix-2-pix GAN model to generate realistic satellite image based on the segmentation map. Then, we modified real segmentation maps to generate artificial masks with better representation of minority classes. After this, we combined original satellite data and generated into the joint training data collection that was used to train segmentation model with higher accuracy of minority classes separation [32, 33].

As a result, we created 2,384 synthetic satellite images with artificial masks using both GAN and statistical methods. We then trained four models: (I) using real satellite data; (II) combining real satellite data with synthetic images from the statistical method; (III) with synthetic images from the sampling method; (IV) with synthetic images from the GAN method. We applied standard augmentations like

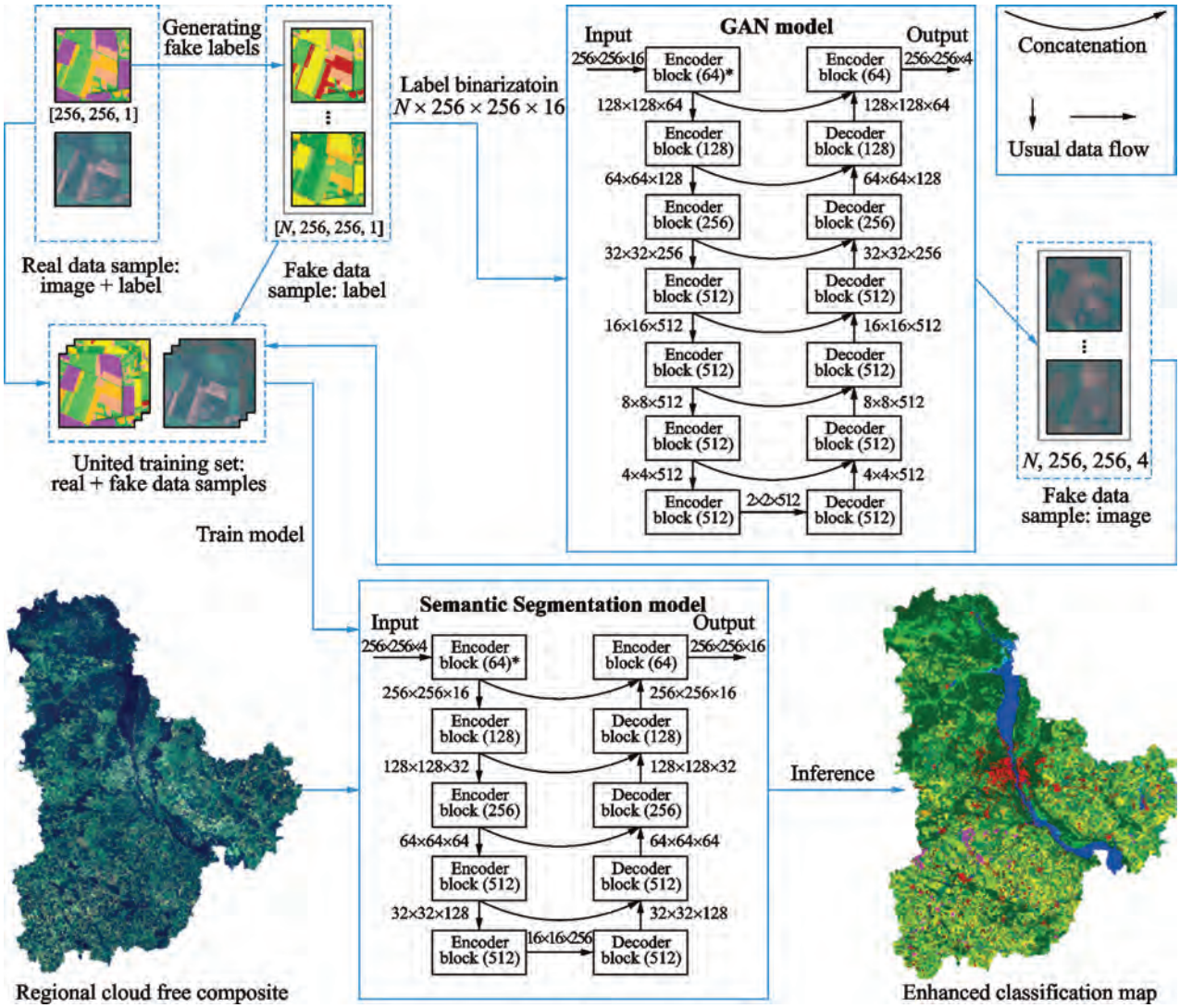

Fig. 1. Proposed GAN augmentation approach scheme for crop type mapping with use of deep learning segmentation model

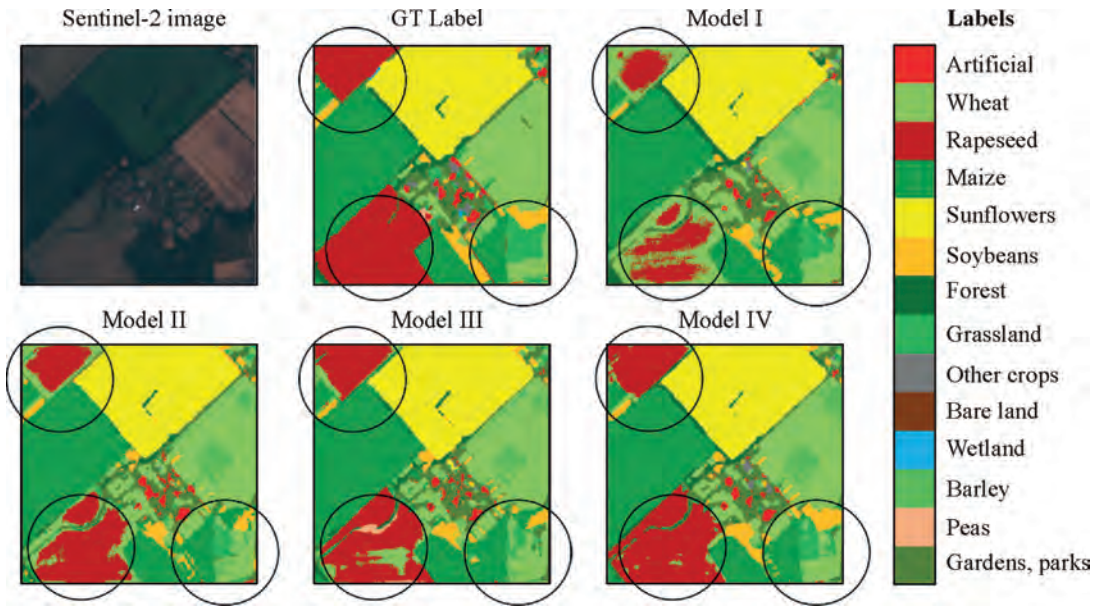

Fig. 2. Comparison of ground truth labels (GT Label) with classification results obtained using only real Sentinel-2 image (Model I), with generated by the statistical method data (Model II), with generated by the sampling method data (Model III), and with generated by the GAN method data (Model IV)

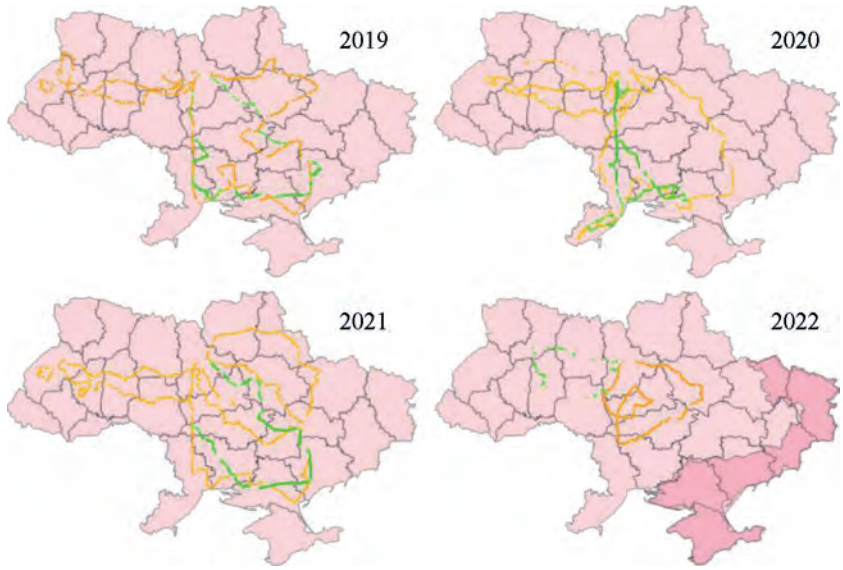

Fig. 3. Routes for in-situ training data collection, 2019—2022. Green and orange refer to the paths of ground data collection for winter and summer crops, respectively

rotations and flips and used the focal loss function to address class imbalance, incorporating established techniques. Subsequently, we evaluated the performance of these four methods on an independent testing dataset consisting of 2,125 real images. The model (I) achieved 77.3% Overall accuracy (OA) and 64.1% of Intersection over Union (IoU), however the average accuracies of cropland (AAC) for User Accuracy (UA), Producer Accuracy (PA) and IoU are very low, due to the high imbalance of real representation of crop classes. The model (IV), trained with use of proposed GAN augmentation methodology, overperformed model (I), model (II) and model (III). In comparison with model (II), average UA raised by 2.7%, PA by 1.1% and IoU by1.2%. In the same the OA accuracy and overall IoU increased by 1.4% and 1.6% relatively.

The Fig. 2 shows the visualization of obtained classification maps based on the models (I)—(IV). It is possible to mention that majoritarian classes like maize, wheat and sunflower have high quality on both maps. However, the minority class rapeseed (dark red) obtained by model (I) have defects and artefacts and much smaller quality in comparison with model (IV). This result can be explained precisely by the fact that GAN, unlike classical statistical methods of generation, allows retrieval of artificial examples that will preserve the similarity of not only the pointwise statistical characteristics of the classes, but also their textures.

The proposed new approach for the data augmentation in the task of crop classification is based on the GAN pix2pix model for realistic, in terms of multi-spectral and textural characteristics, image generation that provides the possibility to eliminate the problem of data set disbalance for deep learning semantic segmentation methods. The proposed method was compared with classical image generation approaches based on the statistical characteristics of multispectral features of crop type classes and has been tested upon basic augmentations and loss function applicable in a case of class imbalance. As a result, the proposed method outperformed models trained based on the real only data and classical approaches for most of cropland classes with significant improvement of accuracies for all minority classes.

Quantifying war-induced crop losses in Ukraine in near real time to strengthen local and global food security

While many studies investigate effects of conflict on food security, they focus on the demand rather than the supply side. To assess how the war is likely to affect Ukraine's production and thus global food security, we use Sentinel-2 imagery to construct outcome variables and indicators for the location and extent of conflict activity at different points in time. Although data used for winter crops, results point towards a reduction of up to 4.84 million tons of wheat only a small portion of which is attributable to direct field damages associated with the war and a reltively large effect on small farmers. This evidence already prompted several donors to establish cash transfers or investment grants targeted specifically at small farmers.

To provide training data for generation of crop cover estimates using machine learning techniques, in-situ data collection along main roads following JECAM guidelines was undertaken yearly from 2019 to 2021. In each year, two extended field trips, one for the winter and one for summer crops, were conducted (Fig. 3 presented the route maps in each year) [37—45].

Cloud-free satellite imagery from the period during which ground data were collected was then used to hand-label contiguous blocks of clearly identifiable crop cover that were used to train the machine learning model. While conflict conditions prevented in situ data collection during the spring, a ground survey for the 2022 crop was eventually organized in June 2022. Crop maps for 2019—21 build on analysis performed in [40, 41] who used optical data from Sentinel-2 and SAR data from Sentinel-1 during the vegetation period using a convolutional neural network

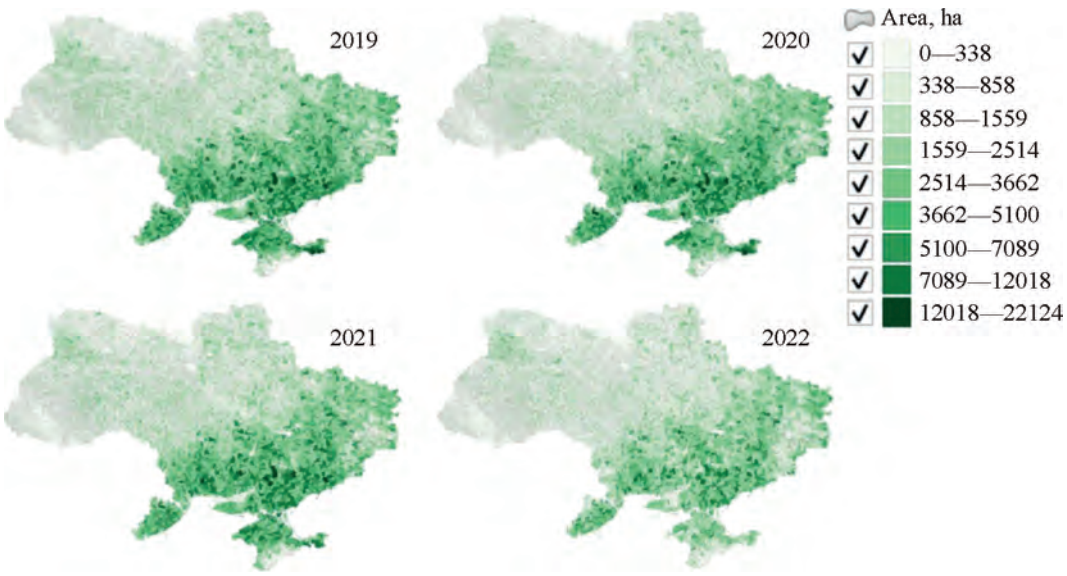

Fig. 4. Map of winter crop cover for 2019 to 2022 growing seasons

on the Amazon Web Services cloud computing platform as well as a random forests classifier on the Google Earth Engine (GEE) platform [46—49]. A winter crop mask for 2022 was created by computing the maximum NDVI for all of Ukraine in any two-week interval between February 1 to May 31 on GEE and applying threshold segmentation. Maps of the estimated winter cereal area by VC generated on this basis as displayed in Fig. 4 illustrate a concentration of winter cereals in the country's South and East and suggest a much lower level of winter cereal cover in 2022 and to some extent in 2020 than in 2021 and 2019.

We use a 4-year panel (2019—2022) of 10,125 village councils in Ukraine to estimate effects of the war started by Russia on area and expected yield of winter crops aggregated up from the field level. Satellite imagery is used to provide information on direct damage to agricultural fields; classify crop cover using machine learning; and compute the Normalized Difference Vegetation Index (NDVI) for winter cereal fields as a proxy for yield. Without conflict, winter crop area would have been 9.35 rather than 8.38 million ha, a 0.97 million ha reduction, only 14% of which can be attributed to direct conflict effects. The estimated drop associated with the conflict in NDVI for winter wheat, which is particularly pronounced for small farms, translates into an additional reduction of output by about 1.9 million tons for a total of 4.84 million tons. Taking area and yield reduction together suggests a war-induced loss of winter wheat output of up to 17% assuming the 2022 winter wheat crop was fully harvested.

Assessing Damage to Agricultural Fields from Military Actions in Ukraine

This study presents a robust methodology to automatically identify agricultural areas damaged by wartime ground activities using free Sentinel-2 satellite data [22]. The 10 meters resolution spectral bands and vegetation indices are leveraged, alongside their statistical metrics over time, as inputs to a Random Forest (RF) classifier. The algorithm efficiently pinpoints damaged fields, with accuracy metrics around 0.85. Subsequent anomaly detection delineates damages within the fields by combining spectral bands and indices. Applying the methodology over 22 biweekly periods in 2022, approximately 500 thousand ha of cropland across 10 regions of Ukraine were classified as damaged, with the most significant impacts occurring from March to September. The algorithm provides updated damage information despite cloud cover and vegetation shifts. The approach demonstrates the efficacy of automated satellite monitoring to assess agricultural impacts of military actions, supporting recovery analysis and documentation of war crimes.

The algorithm identifies direct damages on the fields as anomalies in Sentinel-2 images. The algorithm is structured into three primary steps, as illustrated in the level-0 dataflow diagram in Fig. 5:

1. Experts manually identify damaged fields to create training and test datasets.

2. The machine learning model, specifically RF classification, is employed to recognize damaged fields.

3. Damaged areas within these fields are further identified using threshold segmentation for anomaly detection.

According to satellite bands and vegetation indexes analysis the B2 (Blue) and B3 (Green) spectral bands are especially effective for pinpointing damage in fields with sparse vegetation. On the other hand, vegetation indexes NDVI and GCI are more efficient at detecting damage in fields with dense vegetation. As a Machine Learning model, we have chosen the RF classifier with binary output, classifying fields as either damaged or undamaged. The inputs for this model will be the statistical attributes of the most pertinent spectral bands and vegetation indices. To evaluate the accuracy of the model efficacy, we use widely accepted metrics, including user's accuracy (precision), producer's accuracy (recall), and the F1-score.

To ensure the validity of the experiment, considering vegetation shifts, we construct distinct classification models for each study period. We adopt the 5-fold cross-

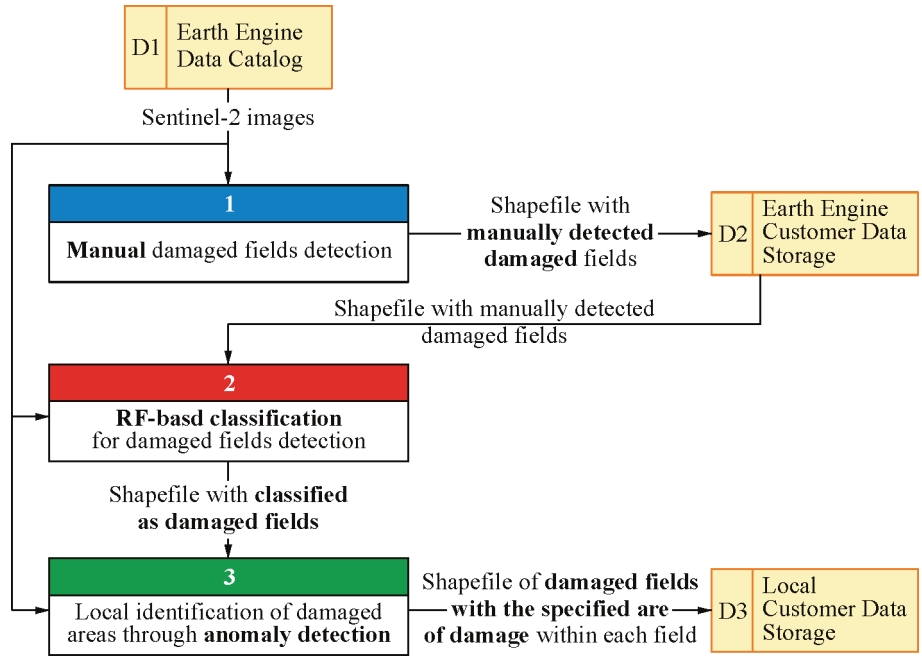

Fig. 5. Level-0 Dataflow Diagram for Damage Detection

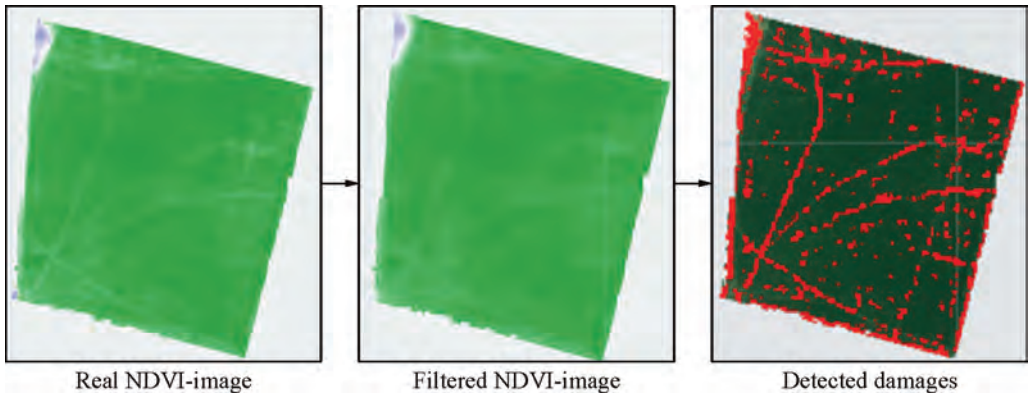

Fig. 6. Damages identification using vegetation indexes filtering

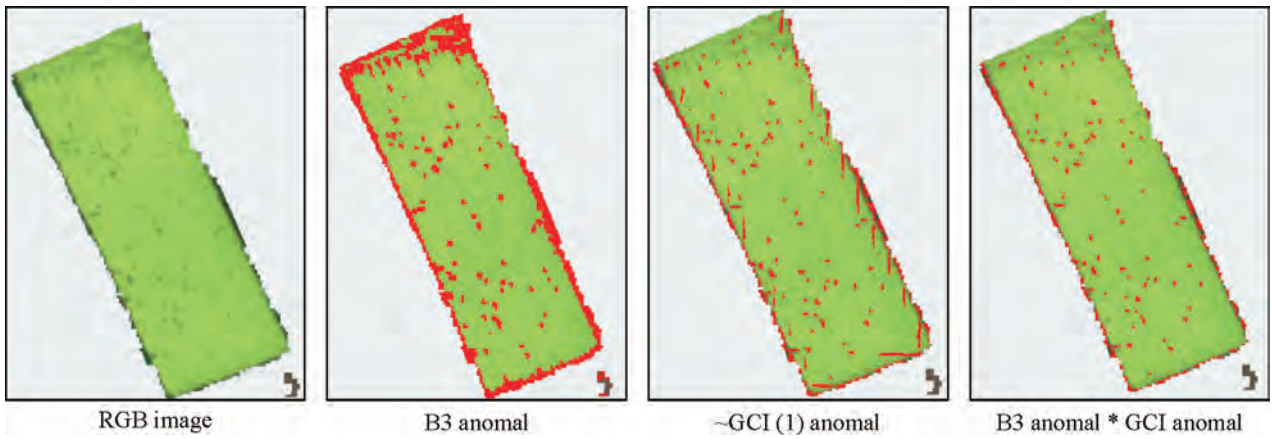

Fig. 7. Damage detection using the Green band B3 and the GCI index, NDVI = 0.63 < 0.65, May 9—23, Zaporizhzhia region

validation method (allocating 80% for training and 20% for validation). During this process, we evaluate accuracy metrics for each iteration and compute their mean, providing accuracy estimates for each period. Finally, we aggregate these metrics across periods to determine the overall classification accuracy.

To detect anomalies with vegetation indices we implement smoothing, applying a 5 × 5 mean filter to the raster

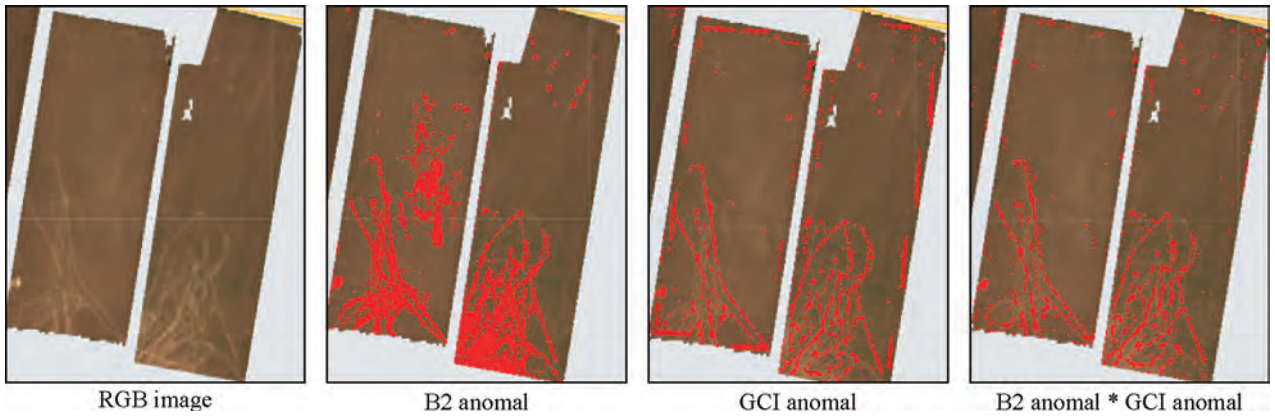

Fig. 8. Damage detection using the Blue band B2 and the GCI index, NDVI = 0.43 < 0.65, June 20 — July 4, Zaporizhzhia region

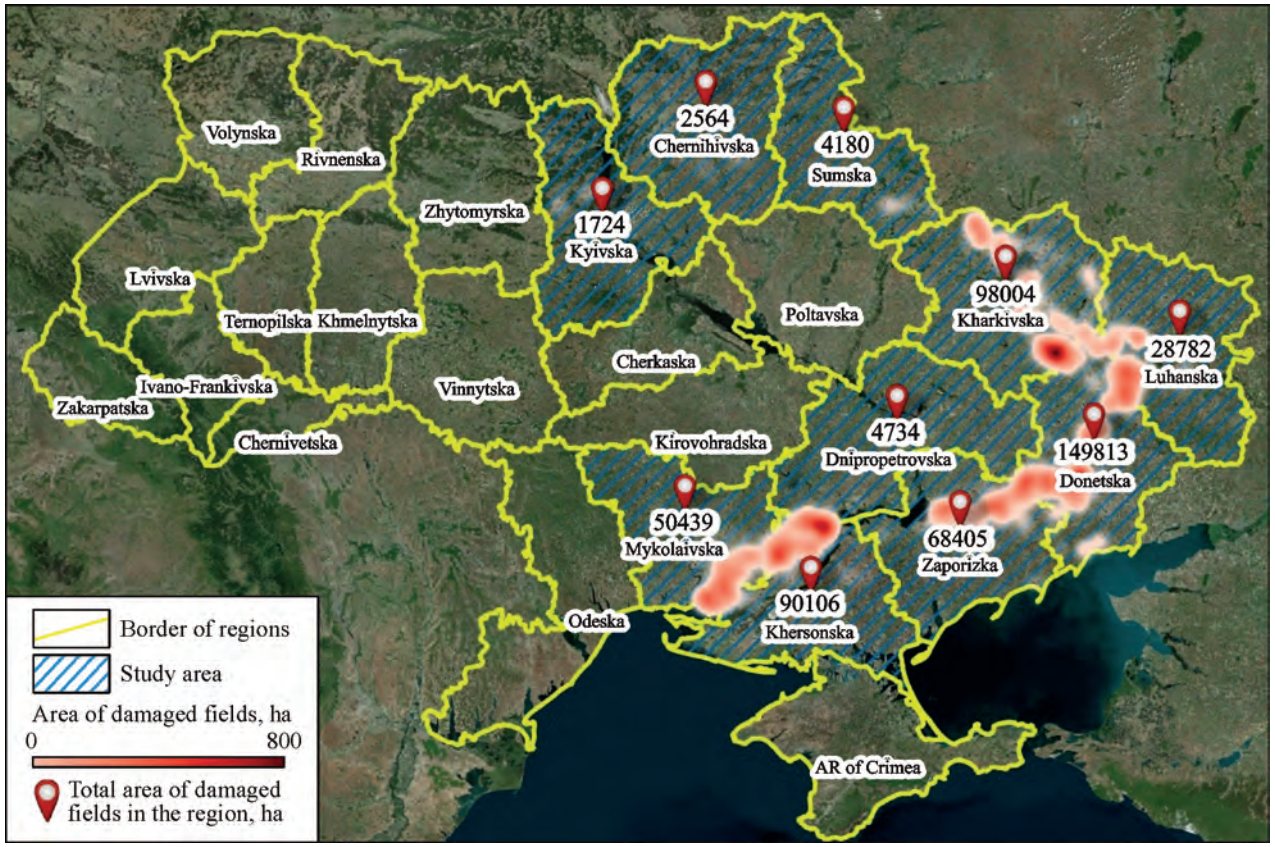

Fig. 9. Heat map of damaged agricultural fields and total areas of damage by region

maps of the vegetation indices. Then we compute the difference between the actual vegetation index values and the smoothed values at each pixel. This differential analysis aids in spotting anomalies or deviations, signaling potential field damage. Fig. 6 illustrates the results of the proposed algorithm.

Similarly, the concurrent anomalies in the GCI index and the Blue band B2 facilitate the identification of craters from bomb detonations on both highly and sparse vegetated fields. To delineate these damages, we intersect anomalous pixels from GCI and B2 (for NDVI < 0.65, Fig. 7). Concurrent anomalies in the inverse GCI index and the Green band B3 help to identify anomalies with moderate to low vegetation (NDVI < 0.65, Fig. 8).

We run RF classification models for each region and for every individual 2-weeks period separately (started from 24 February, 2022). Then we calculated the accuracy metrics for these models and averaged the results by region and by period. The period-wise results demonstrate relatively consistent accuracy levels across the board.

The analysis by regions reveals that the most significant damage occurred in the Donetsk region, where approximately 149 th. ha or 30% of the total damaged agricultural area were affected by the war. Following that, the Kharkiv region

experienced damage to approximately 98 th. ha (19.65%). The Kherson and Zaporizhzhia regions recorded damages on 90 th. ha (18.1%) and 68 th. ha (13.72%) respectively (Fig. 9).

Overall, considering all regions over the entire evaluation duration, the war has impacted a cumulative area of 499 th. ha of agricultural land.

This work presents a robust methodology to automatically identify approximately 500,000 ha of cropland damaged by wartime ground activities across 10 regions of Ukraine using free Sentinel-2 satellite data. The 10 meters resolution spectral bands and vegetation indices are leveraged, alongside their statistical metrics over time, as inputs to a RF classifier.

The algorithm efficiently pinpoints damaged fields, with producer and user accuracy metrics consistently around 0.85. Subsequent anomaly detection combining spectral bands and indices delineates localized damages within the fields. The approach is applied over 22 biweekly periods in 2022, revealing heightened impacts from March to September.

Conclusions

This study presents an innovative approach to near real-time monitoring of agricultural land damage caused by military activities in Ukraine, utilizing freely available Sentinel-2 satellite data and advanced machine learning techniques. The proposed methodology effectively addresses several critical challenges, including the imbalanced distribution of crop types and land cover classes in real-world data, which hinders the scalability and transferability of traditional classification models.

To overcome the data imbalance problem, a novel data augmentation method employing Generative Adversarial Neural Networks (GANs) with pixel-to-pixel transformation (pix2pix) is introduced. This approach generates realistic synthetic satellite images and corresponding segmentation masks, capturing unobservable crop type distributions and enabling better representation of minority classes during model training. The GAN-based augmentation technique outperformed classical statistical methods, significantly improving the accuracy of crop classification, particularly for minority classes.

Furthermore, the study quantifies the war-induced crop losses in Ukraine, highlighting the severe impact on global food security. By analyzing a 4-year panel (2019—2022) of village councils across Ukraine, the study estimates a reduction of up to 4.84 million tons of winter wheat output, representing a staggering 17% decrease. This loss is attributed not only to direct field damages but also to the indirect effects of the conflict on small farmers, emphasizing the need for targeted support and recovery policies.

The proposed damage detection algorithm, which combines machine learning techniques with spectral band and vegetation index anomaly detection, has proven highly effective in identifying and delineating damaged agricultural fields. With overall accuracy metrics consistently around 0.85, the algorithm has successfully identified approximately 500,000 hectares of cropland damaged across 10 regions of Ukraine during the 2022 growing season.

The study's findings underscore the critical importance of near real-time monitoring and assessment of agricultural land damage during armed conflicts. The developed methodology can aid in documenting war crimes, quantifying production losses, and informing targeted recovery efforts and food security policies at both local and global levels.

In conclusion, this research contributes significantly to the advancement of satellite intelligence for agricultural monitoring and damage assessment, while also highlighting the pressing need for international cooperation and support to mitigate the severe consequences of the ongoing conflict on global food security.

REFERENCES

1. Shumilo L., Skakun S., Gore M.L., Shelestov A., Kussul N., Hurtt G., ... Yarotskiy V. Conservation policies and management in the Ukrainian Emerald Network have maintained reforestation rate despite the war. Communications *Earth Environment*. 2023. 4(1). P. 443. https://doi.org/10.1038/s43247-023-01099-4

2. Kussul N., Drozd S., Yailymova H. Forecast of Yield of Major Crops in Ukraine in War Conditions 2022 Based on MODIS and Sentinel-2 Satellite Data. *Proceedings of the 11th International Conference on Applied Innovations in IT* (ICAIIT). 2023. P. 89—95. https://doi.org/10.25673/101923.

3. Yailymova H., Yailymov B., Kussul N., Shelestov A., Shumilo, L. Geospatial monitoring of sustainable and degraded agricultural land. *IGARSS 2023 — 2023 IEEE International Geoscience and Remote Sensing Symposium*. 2023, July. P. 2446—2449. https://doi.org/10.1109/IGARSS52108.2023.10283189

4. Fedorov O., Kussul N., Shelestov A. Monitoring of sustainable development goals using satellite data. Kyiv, Naukova Dumka. 2023. 164 p. https://doi.org/10.15407/978-966-00-1865-5 (in Ukrainian).

5. Куссуль Н., Шелестов А., Яйлимов Б., Федоров О., Яйлимова Г., Скакун С., ... Дякун О. 2023). Оцінка цілей сталого розвитку в межах Європейської дослідницької мережі (ERA-PLANET). *Проблеми керування та інформатики*. 2023. № 1.

6. Yailymova H., Yailymov B., Mazur Y., Kussul N., Shelestov A. Sustainable Development Goal 2.4. 1 for Ukraine Based on Geospatial Data. *Proceedings of the 11th International Conference on Applied Innovations in IT* (ICAIIT). 2023. P. 67—73. https://doi.org/10.25673/101915

7. Kussul N., Shumilo L., Yailymova H., Shelestov A., Krasilnikova T. Complex method for land degradation estimation. *IOP Conference Series: Earth and Environmental Science*. 2023. 1126, No. 1. P. 012032. https://doi.org/10.1088/1755-1315/1126/1/012032

8. Куссуль Н.М., Шелестов А.Ю., Яйлимов Б.Я., Лавренюк М.С., Яйлимова Г.О., Колотій А.В., ... Пархомчук О.М. Методологія оцінки індикатора цілей сталого розвитку 11.3. 1. *Problems of Control and Informatics*. 2022. 67(5). P. 51—60.

9. Lehmann A., Mazzetti P., Santoro M., Nativi S., Maso J., Serral I., ... Giuliani G. Essential earth observation variables for high-level multi-scale indicators and policies. *Environmental Science Policy*. 2022. 131. P. 105—117. https://doi.org/10.1016/j.envsci.2021.12.024

10. Kussul N., Shelestov A., Shumilo L., Titkov D., Yailymova H. Information Technology for Land Degradation Assessment Based on Remote Sensing. *Proceedings of International Conference on Applied Innovation in IT*. 2022. 10, Iss. 1. P. 113—117. https://doi.org/10.25673/76941.

11. Яйлимов Б.Я., Яйлимова Г.О., Шелестов А.Ю., Лавренюк А.М. Використання супутникових продуктів для аналізу змін територій природно-заповідного фонду України. *Problems of Control and Informatics*. 2022. 67(3). P. 135—150.

12. Яйлимов Б.Я., Шелестов А.Ю., Ємельянов М.О., Пархомчук О.М. Валідація карт деградації земель на основі геопросторових даних. *Проблеми керування та інформатики*. 2022. С. 112—125. https://doi.org/0.34229/1028-0979-2022-1-10

13. Ємельянов М., Шелестов А., Яйлимова Г., Шуміло Л. Вплив зміни клімату на площі основних сільськогосподарських культур. *Космічна наука і технологія*. 2022. 28, № 2(135). С. 30—38. https://doi.org/10.15407/knit2022.02.030

14. Yailymova H., Mikava P., Kussul N., Krasilnikova T., Shelestov A., Yailymov B., Titkov D. Neural network model for monitoring of landfills using remote sensing data. *2022 IEEE 3rd International Conference on System Analysis Intelligent Computing* (SAIC). 2022. P. 1—4. https://doi.org/10.1109/SAIC57818.2022.9923013

15. Yailymova H., Yailymov B., Shelestov A., Krasilnikova T. Інтелектуальні методи та моделі обробки супутникових даних у задачі моніторингу звалищ. *Проблеми керування та інформатики*. 2022. С. 128—140. https://doi.org/10.34229/1028-0979-2022-2-9

16. Kussul N., Drozd S. Assessing Ukrainian Territory Suitability for Solar Power Station Placement Using Satellite Data on Climate and Topography. *2023 13th International Conference on Dependable Systems, Services and Technologies* (DESSERT). 2023. P. 1—5. https://doi.org/10.1109/DESSERT61349.2023.10416483

17. Yailymova H., Yailymov B., Kussul N., Shelestov A. Geospatial Analysis of Life Quality in Ukrainian Rural Areas. *2023 13th International Conference on Dependable Systems, Services and Technologies* (DESSERT). 2023. P. 1—5. https://doi.org/10.1109/DESSERT61349.2023.10416517

18. Yailymova H., Kolotii A., Kussul N., Shelestov A. Air quality as proxy for assessment of economic activity. *IEEE EUROCON 2023-20th International Conference on Smart Technologies*. 2023. P. 89—92. https://doi.org/10.1109/EUROCON56442.2023.10198882

19. Gerasopoulos E., Bailey J., Athanasopoulou E., Speyer O., Kocman D., Raudner A., ... Paasonen P. Earth observation: An integral part of a smart and sustainable city. *Environmental Science Policy*. 2022. 132. P. 296—307. https://doi.org/10.1016/j.envsci.2022.02.033

20. Хайдуров В.В., Яйлимов Б.Я., Шелестов А.Ю. Модель оцінки якості повітря за супутниковими даними на основі методу групового урахування аргументів. *Problems of Control and Informatics*. 2023. 68(5). P. 93—106.

21. Khaidurov V., Yailymov B., Shelestov A. Mathematical Model for Determining the Geometric Location of the Environmental Pollutant Based on Sensor Data. *2023 IEEE 12th International Conference on Intelligent Data Acquisition and Advanced Computing Systems: Technology and Applications* (IDAACS). 2023. 1. P. 703—707. https://doi.org/10.1109/IDAACS58523.2023.10348700

22. Kussul N., Drozd S., Yailymova H., Shelestov A., Lemoine G., Deininger K. Assessing damage to agricultural fields from military actions in Ukraine: An integrated approach using statistical indicators and machine learning. *International Journal of Applied Earth Observation and Geoinformation*. 2023. 125. 103562.

23. Deininger K., Ali D.A., Kussul N., Shelestov A., LemoineG., Yailimova H. Quantifying war-induced crop losses in Ukraine in near real time to strengthen local and global food security. *Food policy*. 2023. 115, 102418. https://doi.org/10.1016/j.foodpol.2023.102418

24. Kussul N., Drozd S., Skakun S., Duncan E., Becker-Reshef I. Fusion of very high and moderate spatial resolution satellite data for detection and mapping of damages in agricultural fields. *2023 13th International Conference on Dependable Systems, Services and Technologies* 2023. (DESSERT). P. 1—7.

25. Kussul N., Yailymova, H., Drozd, S. Detection of War-Damaged Agricultural Fields of Ukraine Based on Vegetation Indices Using Sentinel-2 Data. *2022 12th International Conference on Dependable Systems, Services and Technologies* (DESSERT). 2022. P. 1—5. https://doi.org/10.1109/DESSERT58054.2022.10018739

26. Shelestov A., Drozd S., Mikava P., Barabash I., Yailymova H. War damage detection based on satellite data. *Proceedings of the 11th International Conference on Applied Innovations in IT* (ICAIIT). 2023. P. 97—103. https://doi.org/10.25673/101924

27. Мікава П.В., Дрозд С.Ю. Метод виявлення пошкоджень земної поверхні внаслідок воєнних дій за допомогою супутникових даних. *Проблеми керування та інформатики*. 2023. 68(6). С. 83—93. https://doi.org/10.34229/1028-0979-2023-6-6

28. Kussul N., Shelestov A., Yailymov B., Yailymova H. Analysis of Cultivated Areas in Ukraine During the War. *12th International Conference on Dependable Systems, Services and Technologies* (DESSERT). 2022. P. 1—4. https://doi.org/10.1109/DESSERT58054.2022.10018813

29. Skakun S., Abys C., Adegbenro M., Becker-Reshef I., Duncan, E. Eun J., ... Shelestov A., Kussul N., … Prishchepov A. High-Impact Hot Spots of Land Cover Land Use Change in Ukraine. *2022 12th International Conference on Dependable Systems, Services and Technologies* (DESSERT). P. 1—5. https://doi.org/10.1109/DESSERT58054.2022.10018657

30. Kussul N., Shelestov A., Yailymova H., Shumilo L., Drozd S. Agriculture land appraisal with use of remote sensing and infrastructure data. *IGARSS 2022—2022 IEEE International Geoscience and Remote Sensing Symposium*. 2022. P. 2785—2788. https://doi.org/10.1109/IGARSS46834.2022.9884045

31. Lavreniuk M., Shumilo L., Lavreniuk A. Generative Adversarial Networks for the Satellite Data Super Resolution Based on the Transformers with Attention. *IGARSS 2023 — 2023 IEEE International Geoscience and Remote Sensing Symposium*. 2023. P. 6294—6297.

32. Shumilo L., Okhrimenko A., Kussul N., Drozd S., Shkalikov O. Generative adversarial network augmentation for solving the training data imbalance problem in crop classification. *Remote Sensing Letters*. 2023. 14(11). P. 1129—1138.

33. Охріменко А.О., Куссуль Н.М. Метод виявлення складних для розпізнавання зразків у наборах даних для задач класифікації у машинному навчанні. *Problems of Control and Informatics*. 2023. 68(4). P. 84—95.

34. Kussul N., Okhrimenko A., Shkalikov O., Shumilo L. Crop classification synthetic training data generation with use of generative adversarial network. Leaving Planet Symposium. 2022.

35. Lavreniuk M., Kussul N., Shelestov A., Lavrenyuk A., Shumilo L. Super resolution approach for the satellite data based on the generative adversarial networks. *IGARSS 2022—2022 IEEE International Geoscience and Remote Sensing Symposium*. 2022. P. 1095—1098. https://doi.org/ 10.1109/IGARSS46834.2022.9884460

36. Okhrimenko A., Kussul N. KNN-based algorithm of hard case detection in datasets for classification. *Proceedings of International Conference on Applied Innovation in IT*. 2023. P. 113—118. https://doi.org/10.25673/101926

37. Qadir A., Skakun S., Kussul N., Shelestov A., Becker-Reshef I. A generalized model for mapping sunflower areas using Sentinel-1 SAR data. *Remote Sensing of Environment*. 2024. 306, 114132. https://doi.org/10.1016/j.rse.2024.114132

38. Lavreniuk M., Shumilo L., Yailymov B., Kussul N. Reviewing Deep Learning Methods in the Applied Problems of Economic Monitoring Based on Geospatial Data. *Cybernetics and Systems Analysis*. 2022. 58(6). P. 1008—1020. https://doi.org/10.1007/s10559-023-00535-9

39. Лавренюк М.С., Шуміло Л.Л., Яйлимов Б.Я., Куссуль Н.М. Огляд методів глибинного навчання у прикладних задачах економічного моніторингу на основі геопросторових даних. *Кібернетика та системний аналіз*. 2022. 58, № 6. С. 177—192.

40. Shelestov A., Yailymov B., Yailymova H., Shumilo L., Lavreniuk M., Lavreniuk A., ... Kussul N. Advanced Method of Land Cover Classification Based on High Spatial Resolution Data and Convolutional Neural Network. *Proceedings of International Conference on Applied Innovation in IT*. 2022. 10, Iss. 1. P. 125—132. https://doi.org/10.25673/76943.

41. Kussul N., Deininger K., Shumilo L., Lavreniuk M., Ali D.A., Nivievskyi O. Biophysical impact of sunflower crop rotation on agricultural fields. *Sustainability*. 2022. 14(7). P. 3965. https://doi.org/10.3390/su14073965

42. Khan M.A.Q., Skakun S., Shumilo L., Prashnani M., Kussul N. Evaluating the generalization capability of spatio-temporal classifiers for crop mapping using Sentinel-1 data. *Fall Meeting 2022*. AGU. 2022.

43. Яворський О., Куссуль Н. Дослідження представлення багаточасткових графів за допомогою топологічного аналізу даних. 2023. https://doi.org/10.34229/1028-0979-2023-5-9

44. Yavorskyi O., Asseko-Nkili A., Kussul N. Persistent Homology in Machine Learning: Applied Sciences Review. *Proceedings of the 11th International Conference on Applied Innovations in IT* (ICAIIT). 2023. P. 61—66. https://doi.org/10.25673/101914

45. Kolodiazhna O., Savin V., Uss M., Kussul N. 3D scene reconstruction with neural radiance fields (NeRF) considering dynamic illumination conditions. *Proceedings of the 11th International Conference on Applied Innovations in IT* (ICAIIT). 2023. P. 233—238. https://doi.org/10.25673/101943

46. Kussul N., Shelestov, A., Yailymov, B. Cloud Platforms and Technologies for Big Satellite Data Processing. Cham: Springer Nature Switzerland. 2022. P. 303—321. https://doi.org/10.1007/978-3-031-46880-3_19

47. Shelestov A., Yailymov B., Yailymova H., Nosok S., Piven O. Cloud-Based Technologies for Data Processing in Ukraine: International Context. Cham: Springer International Publishing. 2021. P. 101—118. https://doi.org/ 10.1007/978-3-031-16368-5_5

48. Kuzin V., Musial J., Shelestov A. EO4ua initiative: Scientific european support of ukrainian scientific community. 2022 *12th International Conference on Dependable Systems, Services and Technologies* (DESSERT). 2022, December. P. 1—5. https://doi.org/10.1109/DESSERT58054.2022.10018706

49. Shelestov A., Siemens E. OCRE project: consortium, main goals, approaches and opportunities. *2022 12th International Conference on Dependable Systems, Services and Technologies* (DESSERT). 2022. P. 1—4. https://doi.org/10.1109/DESSERT58054.2022.10018772

MULTY-POLARIZATION RADAR SATELLITE DATA SPATIAL RESOLUTION ENHANCEMENT

S. Stankevich, A. Lysenko

State Institution "Scientific Centre for Aerospace Research of the Earth of the Institute of Geological Sciences of the National Academy of Sciences of Ukraine"

Introduction

Satellite data quality is the one of the key properties that stand for remote sensing tasks problem solving. One of the main satellite's data quality characteristics is its spatial resolution. Due to hardware limitations and satellite's orbit height, land object's distinguishability may not be sufficient for scientific needs. Thus, spatial resolution enhancement is a relevant topic today.

There are two possible ways to increase satellite data spatial resolution: hardware and software. Hardware requires significantly more expensive sensor manufacturing and, as a rule, dispositioning such sensor on lower orbits, which increases satellite's revisit time, decreases sensing area and so on. On top of that, it may not be possible, yet, to manufacture a sensor with a satisfactory spatial resolution. Software methods, on the other hand, do not require any hardware adjustments. They simply process available data to produce a new one.

There are several well-known approaches for spatial resolution enhancement: filtering [1], special-purpose artificial neural networks (ANN) [2] and super-resolution [3]. Filtering methods can improve image spatial resolution using sharpening, denoising techniques and others. They usually operate with a single image, thus, it is not possible for them to provide any new information. The ANN-based methods can give remarkable results; however, they tend to require intensive training and adjustments before they are applied to the different set of tasks or, even, within the same set. Usually, such adjustments require some additional training, which in turn requires an appropriate training dataset. Creating such dataset can be a challenge, not to mention the debugging difficulty: problem identification may become obscure if something goes wrong. On the other hand, super-resolution techniques are easy to debug, because they are strictly driven through a single clear mathematical model. The main super-resolution paradigm is to fuse high-resolution output image from several low-resolution input ones; thus, it becomes possible to provide new information.

Super-resolution approach, generally, has several source data requirements. Firstly, each input image pair should have some distinct shift between them, otherwise, there will be no new information that can be combined in the fusion process. Secondly, each image pair should be shifted with a subpixel precision, in other words, any two images should represent the same region of interest (ROI) with a precision less than a pixel size. Thirdly, there should be little to none fast moving objects present on the images, e.g. clouds, otherwise it can lead to image smearing. Fourthly, data should represent the same physical property; otherwise, it will be not possible to fuse the data in a unified way. Lastly, of course ideally, there should be no geometric distortions between images (which in practice is almost impossible).

Recently, Earth's remote sensing with a radar has become popular. That is due to radar's benefits, comparing to the optics: bigger wavelength, which allows to penetrate the clouds, thus, gather data despite the cloudiness conditions, as well as the time of the day. Thus, development of methods for satellite radar spatial resolution enhancement is necessary.

Radar data

Synthetic aperture radar (SAR) imagery can be considered to be much more attractive for the super-resolution techniques, because it is much more convenient to create a set of images that are independent of cloudiness. Thus, it is easier to get images that are close enough to a single date, meaning there should be fewer changes between image pairs. Furthermore, as a rule, SAR images come in a set of at least two images, that were taken in a different polarization modes. For example, Sentinel-1 *C*-band SAR data, usually, consists of two images taken in VV and VH modes, where the first letter denotes polarization of the sent towards land surface signal and the second one denotes the polarization of the recorded by the satellite sensor signal. Therefore, there is already one image pair that is taken with a subpixel and neglectable time shift (less than ten millisecond). Nonetheless, such image pair comes with a problem — data that differ in acquisition mode also differ in the physical nature of the data. Thus, before spatial resolution enhancement becomes possible, radar data need to be converted into unified physical property. Such unified physical property can be land's surface dielectric permittivity. To convert multi-polarization radar data into dielectric permittivity any well-known radar backscattering model, that takes into account dielectric permittivity, can be used. For example, the Oh model [4]:

$$q \triangleq \sigma^0_{vh}/\sigma^0_{vv} = 0.23\sqrt{\Gamma_0}\ [1 - e^{-ks}],$$

$$\Gamma_0 = \left|\frac{1-\sqrt{\varepsilon_r}}{1+\sqrt{\varepsilon_r}}\right|^2,$$

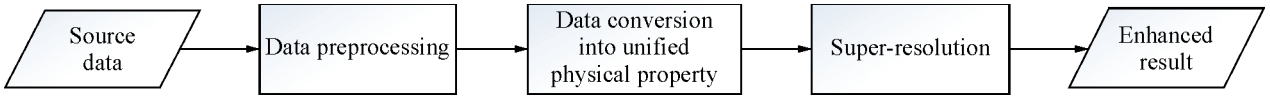

Fig. 1. Brief multi-polarization radar data spatial resolution enhancement framework

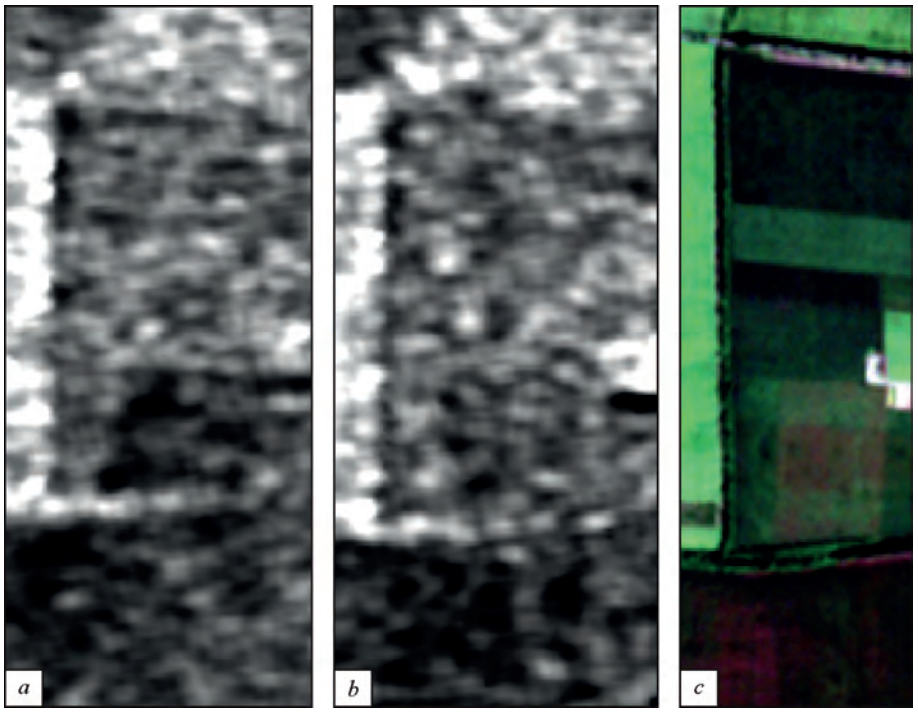

Fig. 2. Preprocessed radar images: *a* — Sigma nought for VV, *b* — Sigma naught for VH, *c* — Sentinel-2 optical satellite image of the test site

where σ^0_{pp} — sigma nought (calibrated backscattering coefficient) for *pp* acquisition mode, ε_r — land surface dielectric permittivity, k — wave number and s — surface roughness.

After all data was converted into the dielectric permittivity, it becomes possible to apply super-resolution techniques for its spatial resolution enhancement. For example, the model that fuses two images in order to produce a twice upscaled image with an enhanced spatial resolution [5]:

$$Y(y, x) = G(\Delta y, \Delta x) \otimes X(y, x),$$
$$-0.5 \le \Delta y \le 0.5, -0.5 \le \Delta x \le 0.5,$$

where Y — is the enhanced image, X — is the source image, Δy and Δx are subpixel vertical and horizontal shifts accordingly and $G(\cdot)$ — is the general convolution matrix of the super-resolution transform:

$$G(\Delta y, \Delta x) = \begin{pmatrix} (0.5-\Delta y)(0.5-\Delta x) & (0.5-\Delta y) & (0.5-\Delta y)(0.5+\Delta x) \\ (0.5-\Delta x) & 1 & (0.5-\Delta x) \\ (0.5+\Delta y)(0.5-\Delta x) & (0.5+\Delta y) & (0.5+\Delta y)(0.5+\Delta x) \end{pmatrix}.$$

The general super-resolution model can be written as:

$$4\hat{Y}_k = T_k(\eta,\xi)\cdot\hat{X}(\eta,\xi) + T_k(\eta \pm m,\xi)\cdot\hat{X}(\eta \pm m,\xi) + T_k(\eta,\xi \pm n)\cdot\hat{X}(\eta,\xi \pm n) + T_k(\eta \pm m,\xi \pm n)\cdot\hat{X}(\eta \pm m,\xi \pm n) + 4\hat{E}_k(\eta,\xi),$$

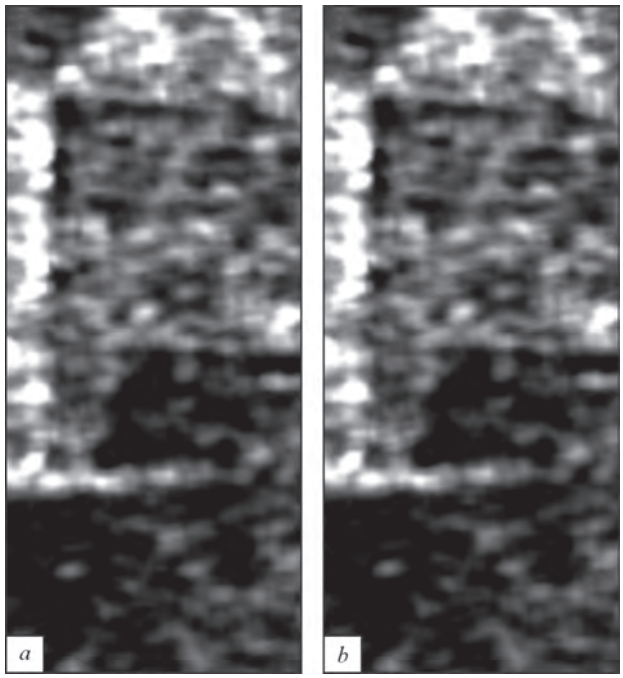

Fig. 3. Radar data converted into land surface dielectric permittivity: *a* — VV polarization, *b* — VH polarization

where $T(\eta,\xi) = \left((0.5-\Delta y)e^{\frac{-2i\pi\eta}{m}} + 1 + (0.5-\Delta y)e^{\frac{2i\pi\eta}{m}}\right) \times \left((0.5-\Delta x)e^{\frac{-2i\pi\xi}{n}} + 1 + (0.5-\Delta x)e^{\frac{2i\pi\xi}{n}}\right)$

Table 1

Sentinel-1 source data

№	Satellite data segment name	Test plot location (longitude, latitude), °
1	S1B_IW_GRDH_1SDV_20200815T155324 _20200815T155349_022936_02B88F_6C09	POLYGON((30.131 49.759,30.136 49.759,30.136 49.761,30.131 49.761,30.131 49.759))
2	S1A_IW_GRDH_1SDV_20230725T155405 _20230725T155430_049582_05F647_F242	POLYGON((30.083 49.780,30.096 49.780,30.096 49.789,30.083 49.789,30.083 49.78))
3	S1B_IW_GRDH_1SDV_20200729T154520 _20200729T154545_022688_02B102_7A81	POLYGON((30.483 50.378,30.490 50.378,30.490 50.382,30.483 50.382,30.483 50.378))
4	S1A_IW_GRDH_1SDV_20200728T155348 _20200728T155413_033657_03E698_B348	POLYGON((28.415 49.225,28.426 49.225,28.426 49.233,28.415 49.233,28.415 49.225))
5	S1A_IW_GRDH_1SDV_20190831T152101 _20190831T152126_028815_0343B4_6530	POLYGON((36.163 49.879,36.179 49.879,36.179 49.888,36.163 49.888,36.163 49.879))
6	S1A_IW_GRDH_1SDV_20190530T154445 _20190530T154510_027459_031913_134A	POLYGON((31.897 46.888,31.932 46.888,31.932 46.905,31.897 46.905,31.897 46.888))
7	S1A_IW_GRDH_1SDV_20200828T154547 _20200828T154612_034109_03F5F4_CEF5	POLYGON((29.806 49.736,29.827 49.736,29.827 49.743,29.806 49.743,29.806 49.736))
8	S1A_IW_GRDH_1SDV_20190627T040445 _20190627T040510_027860_032534_F2F5	POLYGON((30.517 46.559,30.535 46.559,30.535 46.569,30.517 46.569,30.517 46.559))
9	S1A_IW_GRDH_1SDV_20190618T042832 _20190618T042857_027729_03213D_711D	POLYGON((24.126 49.748,24.146 49.748,24.146 49.756,24.126 49.756,24.126 49.748))
10	S1B_IW_GRDH_1SDV_20200829T042801 _20200829T042826_023133_02BEC4_BEC0	POLYGON((25.538 49.543,25.554 49.543,25.554 49.551,25.538 49.551,25.538 49.543))
11	S1A_IW_GRDH_1SDV_20200831T161028 _20200831T161053_034153_03F793_D074	POLYGON((26.237 50.612,26.259 50.612,26.259 50.624,26.237 50.624,26.237 50.612))
12	S1B_IW_GRDH_1SDV_20190730T153723 _20190730T153748_017365_020A74_C9BA	POLYGON((31.284 51.485,31.312 51.485,31.312 51.500,31.284 51.500,31.284 51.485))
13	S1A_IW_GRDH_1SDV_20200711T154544 _20200711T154609_033409_03DEFD_2FD4	POLYGON((30.784 49.830,30.806 49.830,30.806 49.841,30.784 49.841,30.784 49.830))
14	S1A_IW_GRDH_1SDV_20200728T155413 _20200728T155438_033657_03E698_7C3D	POLYGON((28.986 50.032,29.007 50.032,29.007 50.042,28.986 50.042,28.986 50.032))
15	S1A_IW_GRDH_1SDV_20200830T042022 _20200830T042047_034131_03F6C6_65AE	POLYGON((26.862 49.388,26.873 49.388,26.873 49.396,26.862 49.396,26.862 49.388))
16	S1A_IW_GRDH_1SDV_20200821T155350 _20200821T155415_034007_03F264_BAD5	POLYGON((28.088 49.019,28.096 49.0196,28.096 49.024,28.088 49.024,28.088 49.019))
17	S1A_IW_GRDH_1SDV_20190625T042011 _20190625T042036_027831_032454_3886	POLYGON((28.804 49.701,28.813 49.701,28.813 49.705,28.804 49.705,28.804 49.701))
18	S1B_IW_GRDH_1SDV_20190622T155314 _20190622T155339_016811_01FA2F_4B2A	POLYGON((30.096 49.826,30.100 49.826,30.100 49.829,30.096 49.829,30.096 49.826))
19	S1A_IW_GRDH_1SDV_20190726T041204 _20190726T041229_028283_0331F4_EB6B	POLYGON((29.961 50.173,29.969 50.173,29.969 50.178,29.961 50.178,29.961 50.173))
20	S1A_IW_GRDH_1SDV_20190729T154538 _20190729T154603_028334_033394_A78B	POLYGON((30.920 49.630,30.942 49.630,30.942 49.641,30.920 49.641,30.920 49.630))
21	S1B_IW_GRDH_1SDV_20190828T154450 _20190828T154515_017788_02179A_1258	POLYGON((30.363 49.482,30.373 49.482,30.373 49.489,30.363 49.489,30.363 49.482))
22	S1B_IW_GRDH_1SDV_20190828T154450 _20190828T154515_017788_02179A_1258	POLYGON((29.645 49.728,29.668 49.728,29.668 49.736,29.645 49.736,29.645 49.728))
23	S1A_IW_GRDH_1SDV_20200626T041209 _20200626T041234_033183_03D816_7063	POLYGON((30.108 50.010,30.120 50.010,30.120 50.015,30.108 50.0155,30.108 50.010))
24	S1A_IW_GRDH_1SDV_20200626T041209 _20200626T041234_033183_03D816_7063	POLYGON((30.314 50.169,30.327 50.169,30.327 50.174,30.314 50.174,30.314 50.169))
25	S1B_IW_GRDH_1SDV_20200729T154520 _20200729T154545_022688_02B102_7A81	POLYGON((30.772 50.510,30.797 50.510,30.797 50.519,30.772 50.519,30.772 50.510))
26	S1A_IW_GRDH_1SDV_20200728T155348 _20200728T155413_033657_03E698_B348	POLYGON((28.667 49.106,28.683 49.106,28.683 49.115,28.667 49.115,28.667 49.106))
27	S1A_IW_GRDH_1SDV_20200828T154457 _20200828T154522_034109_03F5F4_9B75	POLYGON((30.435 46.403,30.443 46.403,30.443 46.408,30.435 46.408,30.435 46.403))
28	S1B_IW_GRDH_1SDV_20200824T152851 _20200824T152916_023067_02BCC0_8107	POLYGON((35.936 49.991,35.949 49.991,35.949 49.997,35.936 49.997,35.936 49.991))
29	S1B_IW_GRDH_1SDV_20200831T041125 _20200831T041159_023162_02BFAB_8D5B	POLYGON((30.325 50.399,30.466 50.399,30.466 50.466,30.325 50.466,30.325 50.399))
30	S1B_IW_GRDH_1SDV_20200824T041934 _20200824T042002_023060_02BC91_02AC	POLYGON((28.505 50.211,28.659 50.211,28.659 50.285,28.505 50.285,28.505 50.211))
31	S1A_IW_GRDH_1SDV_20200830T042022 _20200830T042047_034131_03F6C6_65AE	POLYGON((28.028 50.254,28.267 50.254,28.267 50.378,28.028 50.378,28.028 50.254))

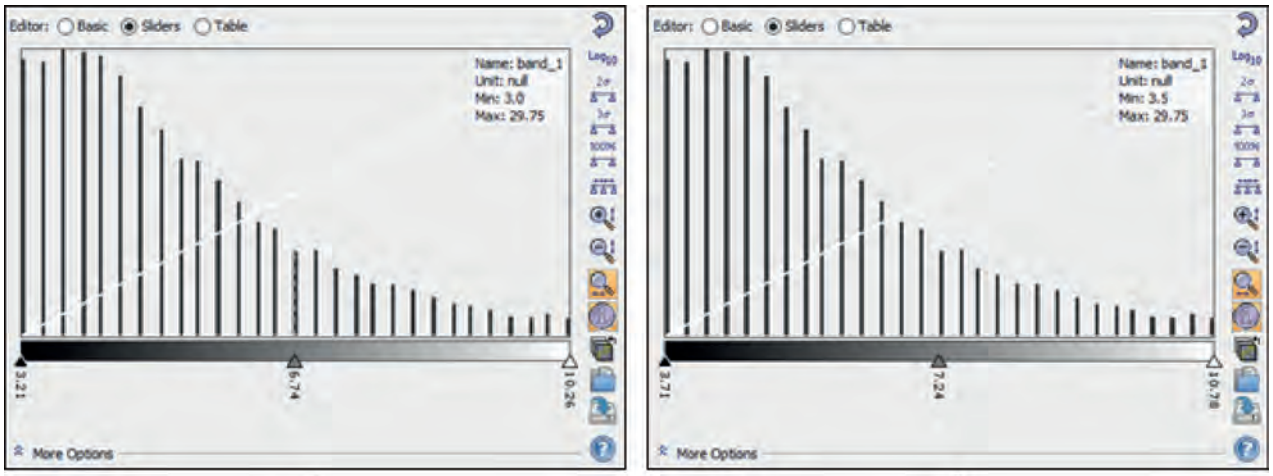

Fig 4. Histograms of converted into dielectric permittivity images:
a — VH-derived dielectric permittivity, *b* — VV-derived dielectric permittivity

is the image transfer function, $(\cdot)$ — is the Fourier transform operator, E — is the noise matrix and source image size is $m \times n$.

Thus, the general radar data spatial resolution enhancement framework is explained by Fig. 1 flowchart.

Now, the mentioned framework is to be tested.

Source data

The source data used for the testing purposes was taken from the Copernicus Open Access Hub [6] and consists of 31 Sentinel-1 radar satellite image pairs. Each image pair was taken from the Ukraine territory with a mix of pure agro, agro-urban, or pure urban ROIs. The territories selection was arbitrary with a focus for each image pair to be somewhat unique. The full list of input radar data is provided in the Table 1 below.

As such, this input set may be not enough representative for special cases, but is sufficient to study the general behavior of super-resolution technique.

Results

The described technique was tested on a series of 31 images. Firstly, each radar image was preprocessed according to the typical Sentinel-1 radar image preprocessing algorithm [7] using free open-source Sentinel Application Platform (SNAP) software [8]. The example of preprocessed image pair is shown in the Fig. 2.

Next, each image pair was converted to the land surface dielectric permittivity using the specially developed software. The model used for conversion was the Oh semi-empirical radar backscattering model. The result is presented by Fig. 3.

The histograms of the corresponding dielectric permittivity data are shown in Fig. 4.

And finally, converted radar images were used in the super-resolution technique. The super-resolution process was carried out using the, author developed, dedicated satellite data super-resolution software. The result is given by Fig. 5.

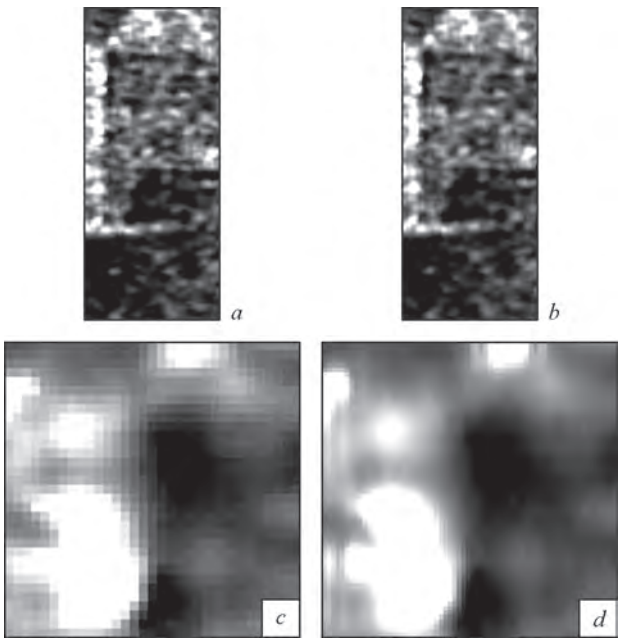

Fig. 5. Enhanced resolution radar images: *a* — VV-derived input dielectric permittivity, *b* — enhanced resolution dielectric permittivity, *c* — high-zoomed VV-derived dielectric permittivity image fragment, *d* — high-zoomed enhanced resolution dielectric permittivity image fragment

Having acquired the result with enhanced spatial resolution it is appropriate to measure the enhancement gain. The result can be quantitatively evaluated using the modulation transfer function (MTF) approach. The main principle here is to find such a limit spatial resolution value, which corresponds to the level, where two different objects become indistinguishable. The result was evaluated using the specific spatial resolution evaluation [9] script, which interface is shown in Fig. 6.

$$G_{ain} = (K_{enh} \cdot r_{base} / r_{enh} - 1) \cdot 100\%,$$

where K_{enh} — is the upscale coefficient, r_{base} — mean source spatial resolution, r_{enh} — enhanced result spatial resolution.

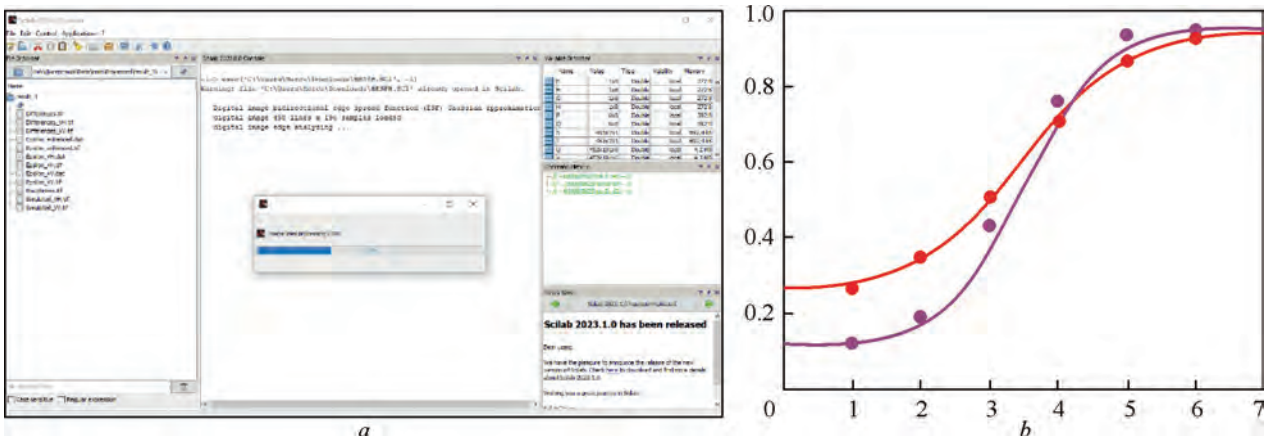

Fig. 6. Spatial resolution evaluation: *a* — SciLab script execution, *b* — edge-spread function

Table 2

Spatial resolution enhancement results

Data №	Spatial resolution, pixels			Spatial resolution gain, %
	ε_{vv}	ε_{vh}	$\varepsilon_{enhanced}$	
1	2.846	2.821	4.068	39.30%
2	2.193	2.139	3.307	30.99%
3	1.871	1.881	3.334	12.53%
4	2.173	2.168	3.948	9.95%
5	3.426	3.345	4.537	49.23%
6	2.304	2.309	3.793	21.61%
7	3.819	3.814	4.629	64.89%
8	3.111	3.151	4.087	53.21%
9	2.302	2.328	3.708	24.86%
10	1.992	2.005	3.862	3.49%
11	1.712	1.706	3.562	–4.04%
12	1.879	1.853	3.597	3.75%
13	2.314	2.302	3.808	21.21%
14	3.667	3.694	3.908	88.35%
15	3.576	3.565	4.754	50.21%
16	4.587	4.569	4.816	90.11%
17	3.644	3.614	4.771	52.12%
18	4.661	4.579	4.268	116.49%
19	3.578	3.610	4.497	59.83%
20	2.727	3.117	4.002	46.02%
21	2.018	2.011	3.911	3.01%
22	1.941	1.927	3.550	8.95%
23	2.644	2.649	3.869	36.8%
24	2.167	2.313	3.808	17.64%
25	1.977	2.160	3.637	13.74%
26	2.203	2.227	3.996	10.86%
27	2.149	2.157	4.141	3.98%
28	3.544	3.506	4.368	61.40%
29	1.716	1.727	3.625	–5.02%
30	1.932	2.030	3.889	1.87%
31	2.997	3.021	4.596	30.93%
Average				**32.84%**

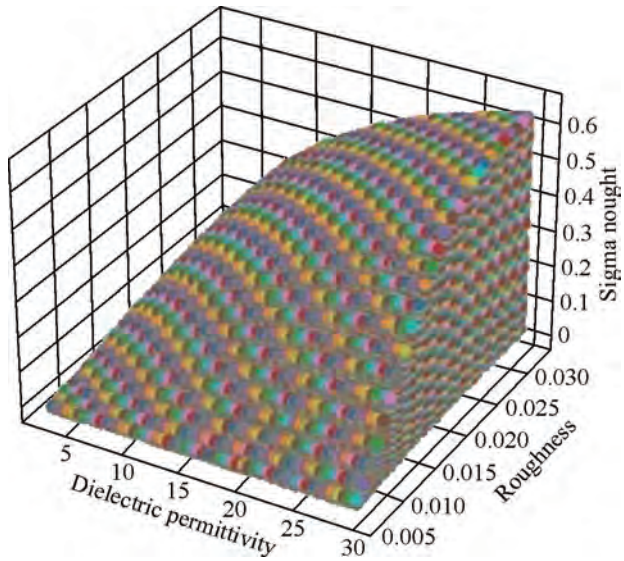

Fig. 7. Oh's model backscattering values simulation range

The results of spatial resolution gain are listed in Table 2.

As one can see, the average spatial resolution gain is 32.84%.

For the test samples with negative or small spatial resolution gain, it was discovered to be related to the Oh's radar backscattering model inability to simulate large backscattering values, which is shown in Fig. 7.

The described procedure was repeated for every image from the input set. The spatial resolution gain was evaluated using the following expression:

Thus, it is not recommended to apply Oh backscattering model to urban areas in order to convert radar data into the dielectric permittivity.

Conclusion

In this paper a multi-polarization radar satellite data spatial resolution enhancement technique was described. The multi-polarization radar data physical heterogeneity was dealt with by conversion to the unified physical land surface value, namely — dielectric permittivity, through

the well-known Oh's radar backscattering model. The spatial resolution enhancement technique has shown 32.84% average spatial resolution gain for the test dataset. The inability of Oh's radar backscattering model to simulate large backscattering values led to a significant drop in the effectiveness of the described approach. Thus, it is best to use the presented method for scenes with low to none presence of high-reflectance objects, which, as a rule, appear due to anthropogenic activity and are mostly present in urban-like areas. Nonetheless, given technique can be useful for many scientific tasks, especially those that consist of processing homogenous non-urban areas. In order to enhance radar data with high-reflective objects, a more appropriate radar backscattering model is needed.

REFERENCES

1. Fahnestock M., Scambos T., Moon T., Gardner A., Haran T., Klinger M. Rapid large-area mapping of ice flow using Landsat 8. *Remote Sensing of Environment*. 2016. 185. P. 84—94. https://doi.org/10.1016/j.rse.2015.11.023

2. Moustafa M.S., Sayed, S.A. Satellite Imagery Super-Resolution Using Squeeze-and-Excitation-Based GAN. *International Journal of Aeronautical and Space Sciences*. 2021. 22(6). P. 1481—1492. https://doi.org/10.1007/s42405-021-00396-6

3. Stankevich S., Popov M., Shklyar S., Lysenko A., Andreiev A., Xing K., Cao S., Tao R. Satellite Imagery Superresolution Based on Optimal Frame Accumulation. *Springer Proceedings in Physics*. 2023. P. 395—412. https://doi.org/10.1007/978-981-99-4098-1_35

4. Oh Y.D., Kamal Sarabandi, Ulaby F.T. An empirical model and an inversion technique for radar scattering from bare soil surfaces. *IEEE Transactions on Geoscience and Remote Sensing*. 1992. 30(2). P. 370—381. https://doi.org/10.1109/36.134086

5. Stankevich S., Popov M., Shklyar S., Sukhanov K., Andreiev A., Lysenko A., Kun X., Shixiang C., Yupan S., Xing Z., Boya S. Subpixel-shifted satellite images superresolution: software implementation. *WSEAS TRANSACTIONS on COMPUTERS*. 2020. 19. P. 31—37. https://doi.org/10.37394/23205.2020.19.5

6. Ecosystem C.D.S. *Data collections. Copernicus Data Space Ecosystem*. URL: https://dataspace.copernicus.eu/explore-data/data-collections (April 18, 2024).

7. Filipponi F. Sentinel-1 GRD Preprocessing Workflow. *Proceedings*. 2019. 18(1). P. 11. https://doi.org/10.3390/ecrs-3-06201

8. SNAP Download — STEP. URL: https://step.esa.int/main/download/snap-download/

9. Stankevich S.A. Evaluation of the Spatial Resolution of Digital Aerospace Image by the Bidirectional Point Spread Function Parameterization. *Advances in Intelligent Systems and Computing*. 2020. P. 317—327. https://doi.org/10.1007/978-3-030-58124-4_31

YUZHNNNOY'S RESEARCH ACTIVITIES ON MOON EXPLORATION

M. Degtiarov, I. Husarova, Ye. Yermolenko, D. Kalynychenko, G. Osinovyy, Yu. Lysenko

Yuzhnoye State Design Office

Introduction

The Moon is currently drawing more and more attention in many countries.

As ADASTRA Analytical Center states: "The astropolitics, where space exploration and geopolitics meet, is a political tool that develops as countries admit the potential of celestial bodies to be levers for global influence intensification. The policy of countries concerning Moon exploration demonstrates this most, turning rapidly into a new milestone for human research efforts" [1].

The leading space countries are coming back to the idea of expeditions to the Moon, intensively developing, and building the components of lunar settlements. Staying on the Moon for long and building temporary or permanent settlements are part of the paradigm of future space exploration. The nearest celestial body to Earth, the Moon is regarded as a component of Earth's space infrastructure and is the first celestial body to which humanity connects its plans of satisfying the demand for resources and establishing a site for future exploration of the solar system planets.

It is planned to establish a lunar research and manufacturing base in several phases. First, global cooperation on Moon exploration should be established with the principal functions of developing the strategy and the joint program of lunar base construction and operation as well as managing and supervising the ongoing work. Besides, it is necessary to explore the Moon using unmanned vehicles for the detailed mapping and 3D modeling of the surface, lunar soil survey and composition analysis, selection of potential regions for the lunar base, landing of a mobile survey vehicle (a rover) at the selected spot, site reconnaissance, and installation of landing beacons. An Earth — Moon — Earth space transportation system (a super-heavy launch vehicle, boosters, a landing-and-take-off pad) and lunar base infrastructure components (lunar base modules, lunar transport vehicles, power plants, and a system to maintain uninterruptible connection with Earth) should be built.

Moon exploration market

The market of lunar projects appeared and became growing in the last decade.

In its report *Space Exploration Perspectives* [2], Euroconsult states that Moon exploration efforts turned out to be the catalyst of an unprecedented boom that has led to public investment in space exploration rising to 26 billion USD in 2023. It is expected that public investment in space exploration will reach 33 billion USD by 2032, of which 17 billion will be the share of Moon exploration investment. Currently, 235 missions of Moon exploration are planned for the next decade, and the cost of these missions will take second place after the manned flights to a low Earth orbit.

According to the report *Space Investment Quarterly* 2023 [3], the amount of non-public investment in the lunar industry reached 1 billion USD overall in 2014—2023. The first five investment recipients in 2014—2023 were the United States (65%), Japan (21%), Singapore (10%), the United Kingdom (10%), and Israel (1%).

In 2023, the total investment exceeded 173 million USD, which was 52% more than in 2022. From the results of 2023, only four countries received investment: Singapore (58%), the United States (40%), Canada (2%), and Israel (0.63%).

The reports *Lunar Market Assessment: Market Trends and Challenges in the Development of a Lunar Economy (PriceWaterhouseCoopers)* and *NSR 2022* predict that the payload weight (total) on the global lunar transportation market will rise to 187 tons from 2020 to 2040 in the nominal scenario (to 128 and 230 tons in the conservative and optimistic scenarios, respectively). It will lead to the total market value of the Moon transport services reaching 79 billion USD in 20 years in the nominal scenario, 55 billion USD in the conservative scenario, and 102 billion USD in the optimistic scenario.

The mentioned financial data and expectations indicate the significant promise of Moon exploration projects for taking a share in this new market. It is clear that the state order market has far more potential than the commercial market.

Ongoing programs and present-day technologies for Moon research and exploration in the world

United States

The United States aims to play the leading role in the global efforts to colonize our nearest neighbor in space using new technologies and strategic plans.

For coming back to the Moon, the United States started the Artemis program in 2017, an ambitious plan of NASA

to return astronauts to the Moon. The principal objective of this program is to send people to the Moon by 2025, including a woman for the first time [4].

The primary milestones of the Artemis program are the development of the international lunar station Gateway and the super-heavy launch vehicle Space Launch System (SLS) for manned expeditions to a lunar orbit and cargo supply flights to the lunar station. The SLS rocket is the development of Boeing in cooperation with ULA and other prominent American companies. Overall, it is planned to invest up to 93 billion USD in the Artemis program. The cost of the SLS development is estimated to reach 35 billion USD, and the launch price is evaluated at up to 500 million USD.

The lunar station will be the base for missions to the Moon's surface, supporting the astronauts' lives and further space research activities. In the framework of Artemis, the United States is gathering its allies to beat China in the race for being the first in the exploration of Moon resources. The United States has intense interaction with other space countries, such as the European Space Agency (ESA) and Japan Aerospace Exploration Agency (JAXA), to involve global cooperation in the construction and servicing of Gateway. Currently, overall 33 countries take part in the Artemis program. As many as nine of them joined the Artemis Accords in 2023. They were the Czech Republic, Spain, India, Germany, the Netherlands, Iceland, Bulgaria, and Angola [5].

The Artemis-1 mission included an unmanned spacecraft Orion ascended to the Moon aboard the SLS launch vehicle. This mission was successfully finished on 11.12.2022. According to NASA's schedule, Artemis-2 will be launched in September 2025 to deliver four astronauts to the Moon. It is expected that in Artemis-3 scheduled for September 2026, American astronauts will land on the Moon's surface. For landing on the Moon's surface, NASA is considering the Starship developed by SpaceX, a giant space rocket system to deliver astronauts from Earth to a lunar orbit and then from that orbit to the south pole of Earth's natural satellite. It is also planned to use ULA's Vulcan Centaur launch vehicle to deliver research payloads to the Moon.

At the same time, the Defense Advanced Research Projects Agency (DARPA) of the United States started its 10-year lunar program LunA-10 aiming to establish infrastructure on the Moon with the necessary outfit to support human living and implement commercial projects on natural resource extraction.

The United States is carrying out active investigations concerning the establishment of the lunar economy and the development of techniques of natural resource extraction on the Moon (ISRU), especially hydrogen and helium-3, potentially the principal resources for the future of the power generation industry on Earth [6].

The specificity of the United States' lunar programs is the intensive involvement of commercial companies. Commercial companies and startups take up their own commercial lunar initiatives to participate in the lunar programs of state agencies and earn profit in the future from the exploitation of lunar resources, particularly from helium-3 extraction on the Moon.

In February 2024, the Odysseus vehicle made by the private company Intuitive Machines had a successful landing on the Moon. This vehicle went in history for good: Odysseus was the first private lander to appear on the Moon and the first US-made lander to do this after Apollo astronauts who the last time were to the Moon in December 1972.

European Union

The European Space Agency (ESA) confirms its interest in the Moon. The agency is implementing an integrated lunar program aiming to join the efforts of the European Union and the United States. Together with the United States, the European Space Agency is taking part in the development of the Orion spacecraft. ESA suggests establishing a broad international cooperation, far more extensive than the existing one in the ISS program, to create a permanent settlement on the backside of the Moon.

Furthermore, ESA suggested the Moonlight program, within which it is planned to launch three or four satellites to orbit around the Moon and provide stable coverage for the telecommunication and navigation services and connection with Earth. Implementing its technological innovations and strategic vision, the EU has become an important player in the global activities on Moon exploration. The up-to-date research activities and development efforts prove that the EU is ready to contribute to the future of space exploration and Moon colonization. ESA may use a new European launch vehicle Ariane 64 in its lunar projects. The development cost of Ariane 6 is roughly 3.6 billion USD. The launch cost is expected to reach 75 million USD for Ariane 62 and up to 115 million USD for Ariane 64.

Presently, ESA is preparing a mission to the Moon's surface to demonstrate the ISRU techniques on the Moon [7].

The global non-governmental organization Moon Village Association (www.moonvillageassociation.org) was established in Vienna in 2017. The aim of this association is to form a platform for nonofficial communication between the public and governmental entities, companies, and scientists, concerning the implementation of the Moon village concept, Moon exploration, and making it possible for people to stay on the Moon permanently. Currently, MVA is a community of experts and organizations from over 40 countries.

China

So far, China remains the only country that has implemented expensive space programs for Moon exploration. At the same time, China is actively making efforts to gather allies to get their support in the Moon race. China is doing this within the framework of the project, initially Chinese-Russian, on the construction of the International Lunar Research Station. In 2023, the UAE, Venezuela, South Africa, Azerbaijan, Pakistan, Belorussia, and

Egypt joined the agreement on the construction of this station. As of early 2024, nine countries are taking part in this project. The lunar base to be built by 2035 will be used for scientific investigations and exploration of the Moon's surface. From 2031 to 2035, China and its allies are planning to build great infrastructure both on the Moon's surface and on a lunar orbit. This infrastructure will include communication systems, power generation plants, research equipment, and many others.

The core element of China's lunar project is the heavy-lift launch vehicle Changzheng 6.9 that can deliver spacecraft with large scientific research equipment to the Moon. Besides, China is working on the launch vehicles Changzheng 9 and Changzheng 10 in this Moon exploration program. Changzheng 9 is a concept of a super-heavy launch vehicle suggested in 2018 in the course of preparation for the landing on the Moon somewhere in the 2030s. Changzheng 10 is being designed for manned missions to the Moon. Changzheng 10 will be about 90 meters high and will have three boosters on the first stage 5 meters in diameter. As of 2024, the maiden flight of this launch vehicle is scheduled for 2027.

So far, four independent projects of Moon exploration by automatic stations have been implemented, including the lunar rover landing on the Moon's surface. An outstanding achievement was the successful launch and return of Chang'e 5 with lunar soil samples. That historical event emphasized China's technological maturity and scientific potential in the field of Moon exploration.

China is intensively developing technologies for the extraction of lunar resources. One of the core directions of research activities is the search for water that could be a valuable resource for life support and fuel production.

As the research company Euroconsult estimates, China invested 12 billion USD in this program in 2022 [8—10].

India

India's space program also includes Moon exploration, and India implements its lunar projects by itself. A mission of launching an automatic explorer to the Moon was accomplished, and the full-scale model of the spacecraft's recovering vehicle was flight-tested.

On July 14, 2023, India launched its Chandrayaan-3 spacecraft (carrying a Pragyan rover aboard) that soft-landed on the Moon's surface on 23.08.2023. The Chandrayaan-3 mission is designed to test the entire capability of landing on and traveling over the Moon's surface. This Indian lander and lunar rover worked throughout a lunar day and completed their task successfully. After that, the lander Chandrayaan-3 performed a maneuver to return to Earth. For its lunar projects, India uses its launch vehicle GSLV Mark III.

India became the fourth country that managed to implement such a mission (after the USSR, the United States, and China) and the first country to land on the Moon's South Pole. The cost of the mission was estimated at roughly 73 million USD. The success of this mission proves India to be a serious rival to China in the lunar race.

India is investigating the possibility of delivering a research station to the Moon in the long-term perspective and carrying out manned flights to the Moon and Mars on its own or through participation in international programs.

Japan

Japan has launched an automatic explorer to the Moon and an unmanned lander to the Moon's surface. Currently, Japan is designing a future multifunctional manned spacecraft [11].

Japan's space industry is the most advanced on the globe. This country has up-to-date launch vehicles of any class, from lightweight to heavy-lift, the own ISS module Kibo (the largest module of the station), and the cargo spaceship HTV Kounotori to deliver supplies to the ISS.

Japan is negotiating with its partners in the International Space Station (the United States, Canada, and ESA) about the project of a joint lunar orbital station that will be derived from the ISS and will be used as the first interplanetary spaceship.

Japan's space agency JAXA intends to develop robots and other equipment to assist in the construction and servicing of settlements on the Moon and Mars. Another mission of JAXA is to develop technologies that enable the mining of the necessary construction materials, such as aluminum and iron, directly on the Moon and Mars and to find a technique to produce drinking water from ice. JAXA is investigating the possibility of implementing the offer of the Japanese company Kajima concerning the development of automatic in-space building equipment to be used in the project of constructing a dwelling (Space Exploration Innovation Hub) for six people on the Moon in roughly 2030 and Mars in 2040.

In August 2023, JAXA ascended its Smart Lander for Investigating Moon (SLIM) aboard the H-2A launch vehicle and successfully delivered this lander to the Moon's surface. Despite certain problems in spacecraft power supply, the successful landing on the Moon allowed Japan to join the exclusive club of the countries that have managed to do this.

A new Japanese launch vehicle H3 that successfully flew in 2024 is to substitute the currently operating H2A. It will be used to deliver cargo to the ISS and the future orbital outpost Gateway on a lunar orbit, the construction of which is planned within the framework of the space program Artemis on advancing the manned space flights under the supervision by the United States.

Other countries

Russia defines two directions of Moon exploration in its federal space program: unmanned and manned flights. However, the implementation periods of the projects changed continuously, and the financing was reduced several times. After the breakup of the USSR, Russia never implemented any of its few interplanetary missions

(Mars-96, Fobos-Grunt) and paid zero attention to Moon exploration. A second attempt to fly to the Moon (the Luna-25 interplanetary station) was made in August 2023, forty-seven years after the Luna-24 expedition, but it failed [8].

Ukraine

Ukraine joined the international program Artemis but was not able to introduce its projects into the program because of the war and lack of funds.

At the same time, Ukraine has its lunar base concept (Fig. 1) devised by the team of Yuzhnoye State Design Office headed by O.V. Degtiarev, General Designer — General Director during 2010—2019.

Yuzhnoye's team framed a concept of the lunar base design, defined the lunar base construction strategy, configuration, and infrastructure in different service life phases, outlined the schedule of project implementation, studied the space transportation system for unmanned and manned missions, the typical structure of the lunar base modules and various residential modules based on this typical structure, outlined the unloading, assembly, and installation sequence for the lunar modules, investigated lunar orbital vehicles and those for traveling over the Moon's surface, and evaluated the preliminary cost-performance indexes and economic efficiency of the project.

Yuzhnoye's concept of the lunar base was presented at various international events and earned many positive comments, including approvals of the wide range of addressed issues.

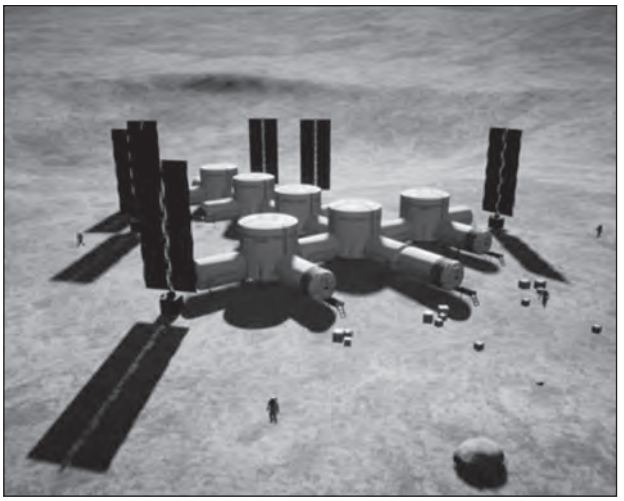

Fig. 1. Concept of a lunar research and manufacture base by Yuzhnoye State Design Office. The ideas of creating a settlement on the Moon and carrying out interplanetary missions were Alexander Degtiarev's cherished dreams that defined the course of Yuzhnoye's development

Yuzhnoye's lunar technologies

Yuzhnoye is the leading enterprise in Ukraine's space industry with its own concept of Moon exploration, including the construction of a lunar base. Naturally, Yuzhnoye cannot stand aside in the research and engineering challenges concerning Moon exploration. It is clear that Ukraine can work in this field only in cooperation with other countries because the cost of building all the systems and equipment necessary for Moon exploration is extremely high. For instance, NASA is planning to invest about 93 billion USD to return to the Moon by 2025 [1].

A lunar base is one of the global and most expensive, science, and labor-intense projects humanity is going to implement in the near future. Building the base should be a gradual and step-by-step process where each step and mission is checked and confirmed to ensure the super reliable functioning of all the lunar base components.

Yuzhnoye's team framed the concepts of a wide spectrum of technologies necessary for Moon exploration. The principal system for lunar infrastructure establishment is a space transportation system for lunar expeditions, both manned and cargo supply. From the analysis of Yuzhnoye's efforts in the development of heavy-lift and super-heavy launch vehicles, it was decided to use an asymmetrical two-launch profile in lunar expeditions with launch vehicles of different classes was selected: the medium-lift Mayak-S3.9 and the super heavy-lift Mayak-ST6. The medium-lift launch vehicle is planned for manned missions, and the super heavy-lift is expected to deliver heavy cargo ships, lunar base modules, etc. to the Moon. This profile makes it possible to use launch vehicles of lower payload capacity that are more cost-saving in manufacture but can be involved in a wide range of commercial flights in addition to missions to the Moon. It is planned to develop the medium-lift Mayak-S3.9 first to operate on the commercial market of launch services. Afterward, it is planned to use this launch vehicle as the basis for rockets of higher payload capacity with tandem staging using the existing equipment, test, and ground facilities. Besides the economic advantages, this approach makes it possible to pass certification for manned flights during the commercial operation of the medium-lift launch vehicle, i.e., with minimum expenses. Furthermore, certification for manned flights will not be necessary for the super heavy-lift launch vehicle.

The Moon Flight System (MFS) designed by Yuzhnoye comprises the Lunar Expedition Complex (LEC) for the manned flights to the Moon's surface and the Lunar Transport Complex (LTC) to deliver heavy supplies to the Moon (Figs 2, *a*, *b*).

The Moon Flight System comprises the following:

- Spaceflight facility with the medium-lift launch vehicle Mayak-S3.9,
- Spaceflight facility with the super-heavy launch vehicle Mayak-ST6,
- Manned spacecraft,
- Lunar spacecraft,
- Lander based on a universal heavy-lift lander,
- Lunar booster,
- Universal heavy-lift lander,
- Lunar orbital tug.

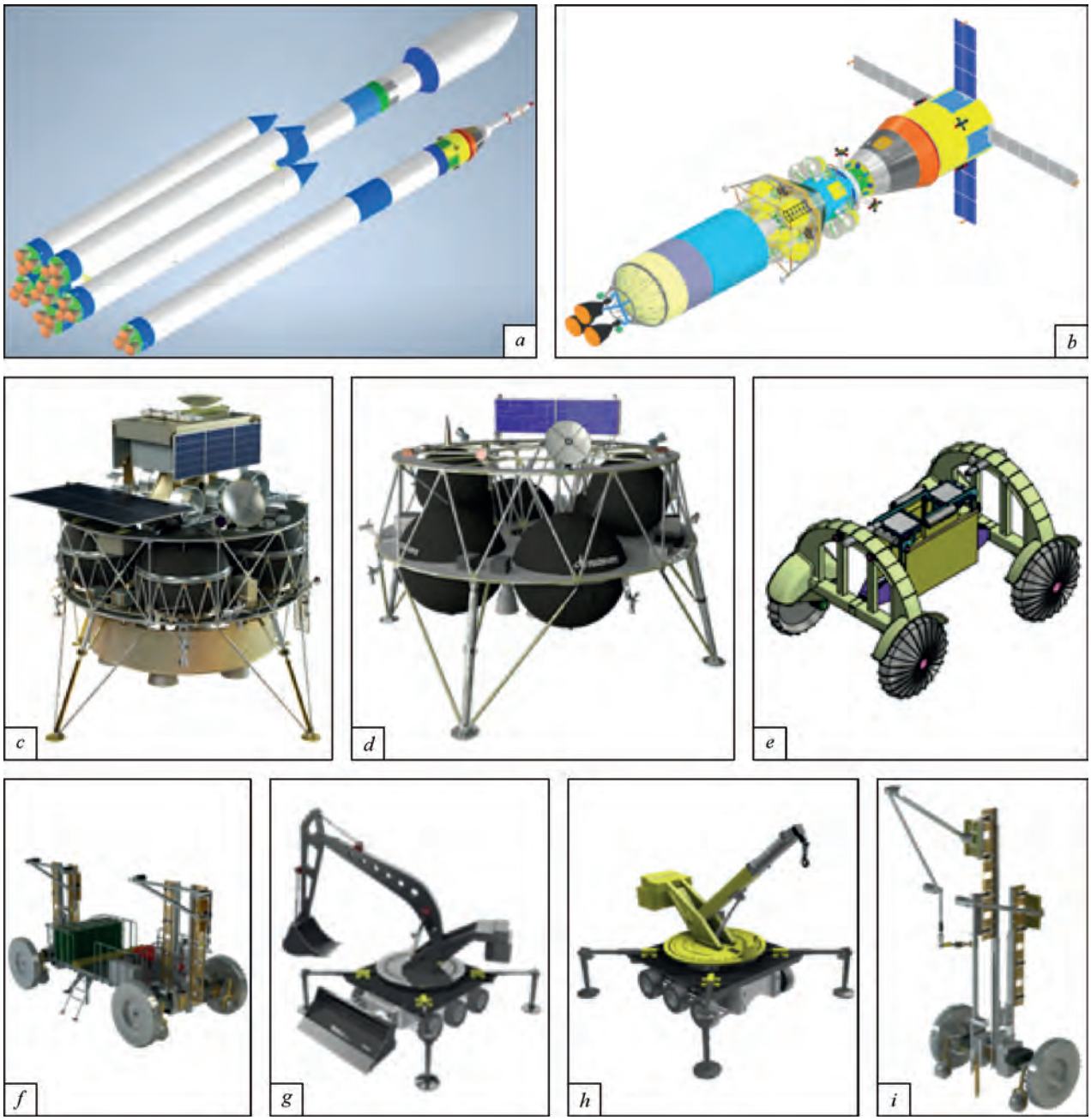

Fig. 2. Primary elements of the Moon Flight System (*a*, *b*) and the infrastructure of the research and manufacturing base (*c*—*f*). Yuzhnoye's concept: *a* — Mayak-S3.9 medium-lift launch vehicle and Mayak-ST6 super-heavy launch vehicle; *b* — Lunar Expedition Complex at the beginning of its flight to the Moon; *c* — lander for the Moon's surface exploration; *d* — lander to deliver supplies; *e* — surveying rover; *f* — transport vehicles for the hoisting and transportation, assembly and construction, manufacture and processing, and soil excavation operations on the Moon's surface

Furthermore, the conceptual design of the lunar base includes ideas concerning landers to deliver supplies to the Moon's surface (a hopping lunar lander for the Moon's surface exploration at several spots per expedition, see Fig. 2, *c*), a lunar lander to deliver research equipment, mobile laboratories, or supplies for the lunar base to the Moon's surface (Fig. 2, *d*), a surveying rover for reconnaissance operations on the Moon's surface, transport vehicles for the hoisting and transportation, assembly and construction, manufacture and processing, and soil excavation operations on the Moon's surface (Fig. 2, *e*), vertical and horizontal living modules, and other elements of lunar infrastructure (Fig. 1).

The long list of studied lunar infrastructure elements indicates Ukraine's significant potential and readiness for participation in a global project on Moon exploration using advanced technologies and scientific achievements.

The present-day shows that international cooperation is the only way for Yuzhnoye to take part in Moon colonization.

Fig. 3. RD840 rocket engine

Fig. 4. RD860 rocket engine

Yuzhnoye has developed innovative technologies and equipment with a readiness level of TRL 6—7, having no or surpassing the comparable articles on the globe in the performance parameters and cost-effectiveness indexes.

From the analysis of the conceptual design of a lunar research and manufacturing base, these technologies include rocket engines, assemblies, and units of rocket jet engines (TRL 6—7) together with promising developments such as a hydrogen energy accumulator and inert anodes from ultra-high temperature ceramics for melted regolith electrolysis.

Propulsion systems, their assemblies, and equipment

Yuzhnoye has developed rocket jet engines for various applications and certain elements of the propellant feed systems for these engines, particularly the following:

- sustainer engine RD840 for apogee rocket stages and spacecraft (Fig. 3). It is a single-chamber single-mode restartable engine with a pressure feed system (TRL-7);
- single-chamber restartable engine RD860 with a pneumatic pump feed system. This engine is designed for boost stages, space tugs, and unmanned landing and take-off modules (Fig. 4). Most of the engine's assemblies and systems (including the combustion chamber and the pneumatic pump assembly) have passed the development tests (TRL-7);
- units of various turbopump and pump assemblies;
- automatic equipment assemblies for cryogenic and hypergolic propellants, high-temperature, and high-pressure gases;
- assemblies of high-pressure cylinders and propellant tanks for liquid-propellant rocket engines with the pressure feed system;
- assemblies of gas generators and combustion chambers of liquid-propellant rocket engines.

The above-mentioned structures are comparable to the world-class developments. Making these structures at the facilities of Yuzhnoye State Design Office (in cooperation with Ukrainian partners) has the following significant advantages:

- complete cycle of development (design, detailed design documents, fabrication, development tests) for various engines;
- competitive cost of development;
- own manufacturing and test facilities.

The engine assemblies and the elements of propellant feed systems may be used in spacecraft and landers intended to deliver supplied to the Moon and Mars, including those of NASA's Artemis program.

The potential customers include governmental institutions and private companies in the United States, Europe, Japan, and other countries, including the participants of Artemis (NASA, Lockheed Martin, Venturi Astrolab,

Fig. 5. Laboratory model of hydrogen energy accumulator for this, it is necessary to increase the voltage drop on the electrodes from the current 1—1.5 V to 30—40 V

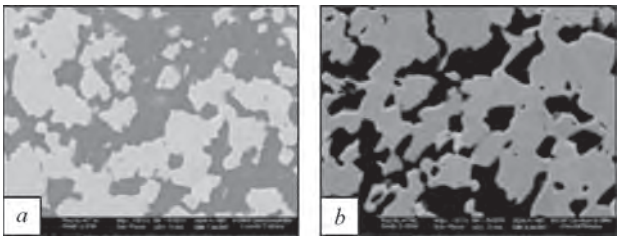

Fig. 6. Microstructure of ZrB_2—$SiC(ZrSi_2)$ ceramics with different compositions

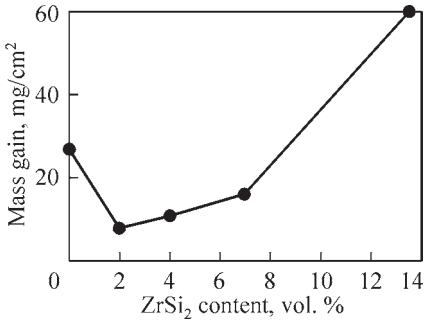

Fig. 7. Mass gain versus $ZrSi_2$ content (vol%) in an oxidation furnace charge at 1500 °C for 50 hours in oxygen

Northrop Grumman, Firefly Aerospace, Moon Express, Sierra Nevada Corp., and others).

Hydrogen energy accumulator

The best option for providing the lunar base with power during a lunar night is to use the accumulated excessive solar energy in the form of hydrogen and oxygen produced by water electrolysis during a lunar day. Ukrainian experts developed an innovative technique for water electrolysis that uses a high-pressure membraneless electrolyzer with its power efficiency 10—20% higher than the best traditional electrolyzers because of no membranes used. This technique was tested on laboratory models (Fig. 5). Adapting a high-pressure membraneless electrolyzer for operation in the space environment requires a drastic reduction of the amount of working currents and a consequential reduction of ohmic loss in current-conducting buses.

The conducted theoretical work and experiments on the parallel and successive starts of electrode assemblies in a membranelss electrolyzer show that the only method to increase the working voltage is to use a hybrid starting system, where the monopolar sources of electrode assemblies are connected in succession and the electrolysis amount of each source is isolated. The primary specific feature of the suggested innovative technology of the electrolyzer is the separation of the hydrogen and oxygen production processes in time, which prevents the gases in the electrolyte from mixing and producing an explosive compound. This innovative technique makes it possible, in fact, to avoid and prevent the primary problems in using the existing methods to generate oxygen and hydrogen on the Moon's surface: the huge size, large weight, the high cost of delivering compression equipment to the Moon's surface, and the complicated maintenance of this equipment on the Moon's surface.

The potential customers of this technique are the governmental and private developers of the power generation and living infrastructure for the colonization of other planets, including the participants of the Artemis program (NASA, Lockheed Martin, Lunar Resource, and others).

The results of the research efforts of Ukrainian experts open the way for making prototypes to try out this technique in space equipment and high-power industrial plants.

Ultra-high temperature ceramics for anodes

Lunar soil, regolith, is the primary raw resource for oxygen generation and the production of various construction materials. The generation of them by the electrolysis of oxides occurring in most planetary rocks and soils is one of the promising techniques under development to determine the level of its suitability for space missions.

The most attractive is the electrolysis of melted regolith that offers a one-stage single process of separating oxygen from metals by the direct electrolysis of melted oxides and requires almost zero import of consumable materials from Earth. The topical problem of such separating systems is that the anode material loses its physical parameters through oxygen release, which results in the relatively short life of a plant.

It is the first time when it is suggested that this problem can be solved by using anodes from ultra-high temperature ceramics that are resistant to active oxygen at the operating temperatures and have an adequate electrical conductivity.

Ukrainian engineers have developed and tested such ultra-high temperature composite ceramics (UHTCs) ZrB_2—SiC($ZrSi_2$) and ZrB_2—($MoSi_2$) for anodes [12, 13].

The structure of the obtained UHTCs is heterophase (Fig. 6). The residual porosity does not exceed 5%.

The ZrB_2—SiC and ZrB_2—SiC—$ZrSi_2$ ceramics were tested for resistance to high-temperature oxidation in a pure oxygen environment at a temperature of 1500 °C for 50 hours.

It was demonstrated that adding $ZrSi_2$ to ZrB_2—SiC increases the oxidation resistance of the latter (Fig. 7). The maximum oxidation resistance occurs at the $ZrSi_2$ content of 2 vol%.

Ukraine has developed a technique to make structures from ZrB_2 ceramics, including the following: processes to hot-press plates from ceramic materials were tried out; experimental and industrial facility was set up to manufacture articles from SiC—ZrB_2—$ZrSi_2$ and ZrB_2— $MoSi_2$ ceramics. This facility can be used to make inert anodes for the electrolysis of melted regolith on the Moon.

The advantages of this technique are as follows:

- it enables the direct electrolysis of melted regolith at temperatures of up to 1600 °C for long periods, requiring no consumable materials;
- enhanced life of the system;
- competitive cost;
- own manufacture and test facilities.

The potential customers of this technique are the governmental and private developers of the living and power generation infrastructure for the colonization of other planets, including the participants of the Artemis program (NASA, Lockheed Martin, Lunar Resource, and others).

Conclusions

Yuzhnoye State Design Office studied a wide range of techniques and technologies necessary for Moon exploration and framed their concepts.

It is the first time when it is suggested, considering the high level of developments of potential partners, that promoting Yuzhnoye's technologies is reasonable since they have been successfully tried out and demonstrated the readiness level of TRL 6—9, as well as it is sensible to promote Yuzhnoye's innovative developments that are unique or surpass other world-class technologies in the performance parameters and cost-effectiveness indexes.

From the analysis of the conceptual design of the lunar research and manufacturing base, these technologies and developments include rocket engines, the assemblies and units of rocket jet engines (TRL 6—7), and promising developments, such as a hydrogen energy accumulator and inert anodes from ultra-high temperature ceramics for melted regolith electrolysis.

REFERENCES

1. Місячна програма Індії та провал рф: як космічні перегони стають новою реальністю. *Аналітичний центр ADASTRA*. 20.08.2023. URL: https://adastra.org.ua/blog/misyachna-programa-indiyi-ta-proval-rf-yak-kosmichni-peregoni-stayut-novoyu-realnistyu

2. Euroconsult & SpaceTec Partners Merge to Form Novaspace — The Global Leading Consulting Firm in the Space Sector. *Euroconsult*. URL: https://www.euroconsult-ec.com

3. Report of the consulting company Space Capital. URL: https://www.spacecapital.com/quarterly

4. Creech S., Guidi J., Elburn D. Artemis: An overview of NASA's activities to return humans to the Moon. *Paper presented at: 2022 IEEE Aerospace Conference* (AERO). 2022 Mar 05—12. Big Sky, Montana.

5. Німеччина приєдналась до програми вивчення Місяця Artemis. 15.09.2023. URL: https://www.dw.com/uk/nimeccina-priednalas-do-programi-vivcenna-misaca-artemis/a-66826693

6. In-Situ Resource Utilisation (ISRU) Demonstration Mission. 2019. URL: https://exploration.esa.int/web/moon/-/60127-in-situ-resource-utilisation-demonstration-mission

7. Peng Z., Wei D., Ran N., Guang Z. et al. Overview of the Lunar In-Situ Resource Utilization Techniques for Future Lunar Missions. *Journal Space: Science & Technology*. 2023. 3. P. 1—18. Article ID: 0037. https://doi.org/10.34133/space.0037

8. Росія втратила «Луну-25», Індія успішно завершила місію. Чому країни поновили гонку за ресурси Місяця? *Економічна правда*. 23.08.2023. https://www.epravda.com.ua/publications/2023/08/23/703510

9. Lin X., Hui L., Pei Z., Zou Y., Wang C.A brief introduction to the International Lunar Research Station Program and the Interstellar Express Mission. *Chinese J Space Sci*. 2022. 42(4). P. 511—513.

10. Li C., Wang C., Wei Y., Lin Y. China's present and future lunar exploration program. *Science*. 2019. 365(6450). P. 238—239.

11. Японський зонд увійшов до орбіти Місяця перед посадкою. *Укрінформ*. 25.12.2023. URL: https://www.ukrinform.ua/rubric-technology/3804665-aponskij-zond-uvijsov-do-orbiti-misaca-pered-posadkou.html

12. Григорьев О.Н., Фролов Г.А., Евдокименко Ю.И., Кисель В.М., Панасюк А.Д., Мелах Л.М., Котенко В.А., Коротеев А.В. Ультравысокотемпературная керамика для авиационно-космической техники. *Авиационно-космическая техника и технология*. 2012. № 8 (95). С. 119—128.

13. Grigoriev O.N. et al. Oxidation of ZrB_2—SiC—$ZrSi_2$ ceramics in oxygen. *Journal of the European Ceramic Society*. 2010. 30. P. 2397—2405.

DEVELOPMENT OF EQUIPMENT AND TECHNOLOGY OF ELECTRON BEAM WELDING OF ALUMINUM ALLOYS IN SPACE CONDITIONS

N. Piskun, Y. Ternovyi, S. Glushak, V. Zakorko, I. Statkevych, V. Shulym

E.O. Paton Electric Welding Institute of the NAS of Ukraine

Hardware complex for application of electron beam technologies in space and on the lunar surface

Severe physical conditions on the lunar surface have a significant influence of the specific features of performance of mounting and repair-restoration operations such as welding, cutting, brazing and coating deposition. This, in its turn, requires ensuring specific characteristics of the hardware designed for realization of various technological processes under the lunar conditions.

Results of experiments on manual electron beam welding conducted in open space show that the hardware developed earlier allows performing welding of stainless steels, titanium and aluminium alloys of up to 1.5 mm thickness. At the same time, thickness of material used at manufacture of manned space vehicle skins can be up to 4—6 mm, and the weld length can be up to several meters.

An electron beam gun which is the main tool of the welding hardware complex was proposed and manufactured. This gun uses a triode optical system and it has the power of up to 2.0 kW that is 2 times greater than the earlier developed guns. The new generation gun allows producing more focused electron beams, which enables conducting the technological operations at the distance of 80—120 mm instead of 40—50 mm. The performed theoretical calculations with application of the procedure of path analysis and synthesis allowed development of a more efficient optical system of the gun and improvement of the electron beam geometry, which promoted increase of electron beam specific power density to 12 kW/mm^2 and performance of sound welding of up to 8 mm aluminium alloys [1—3]. Here, monolithic combination of the gun with the high-voltage power source was eliminated, that contributed to more comfortable working conditions of the welding operator during observation of the welding process, and also allowed two times reduction of the tool weight. Operating life of the cathode assembly was extended by almost an order, compared to previous guns with directly heated cathodes.

New generation gun can operate both in the manual (during work performance by welding operator), and in the automatic mode as part of a robot or artificial intelligence. At operation in space, situations can develop, which require involvement of the cosmonaut-welder, for instance to assess the scale of an emergency situation and its liquidation methods, which necessitates performance of such work with manual tools.

Fig. 1, *a*, *b* shows the appearance of a new generation gun for manual electron beam welding. Fig. 1, *b* demonstrates how the welder-tester conducts ergonomic testing of the developed manual tool in a special vacuum test facility KC-4015.

A new generation tool has been developed for operation in the automatic mode as part of a robot or manipulator.

The gun (Fig. 2, *a*) for automatic welding uses a triode emission system of short-focus modification, unlike the long-focus one, which was applied in the manual version of the gun [4]. When creating this gun, the following functional blocks were developed: the cathode block of the gun with a high-voltage supply; anode block and focusing electromagnetic system. The small-sized gun is connected to the power source by a high-voltage flexible cable with a connector, and it allows generating a sharp electron beam of not more than 1.0 mm diameter (at 10 kV accelerating voltage), using a double electromagnetic focusing system.

The gun cathode has the operating life of 10 hours. The monolithic combination of the electron beam gun with the high-voltage power source is eliminated, which ensures convenient observation at a sufficient distance from the object processing location.

A special manipulator with five degrees of freedom (Fig. 2, *b*) was developed for operation in the automatic mode.

When developing the gun electron-optical system, theoretical calculations with application of the path analysis procedure were used.

The developed emission system forms an electron beam sufficient for performance of electron beam welding of up to 6 mm metals, and it can be used in the gun for mounting operations in open space and on the lunar surface.

For work in space, for the first time in the world, using modern components, a set of equipment has been developed, which includes: a small-sized power source operating in a high vacuum and a control panel (Fig. 3).

The developed welding tool when operating as part of a robot or artificial intelligence will allow manufacturing different load-carrying truss structures directly in space, also for fastening the solar batteries, which is very important for space solar power generation. Availability of space

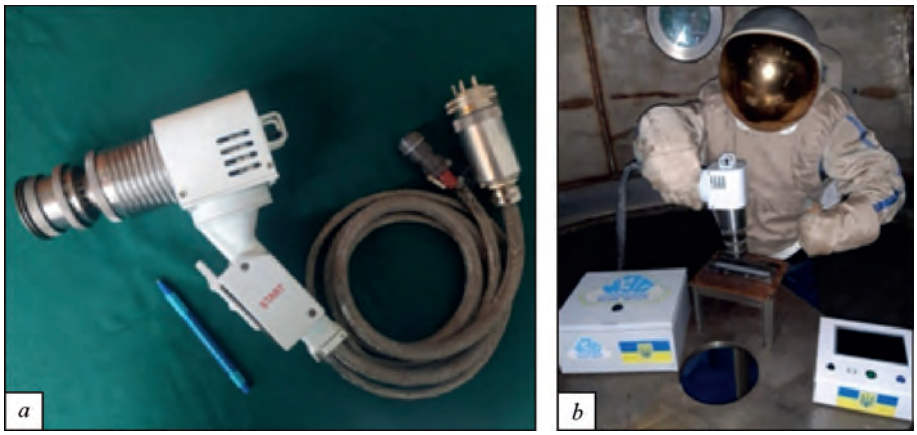

Fig. 1. Electron beam gun for manual electron beam welding in space and on the lunar surface: *a* — New generation electron beam gun for manual welding; *b* — Welder-tester performs ergonomic testing of the manual tool in KC-4015 facility

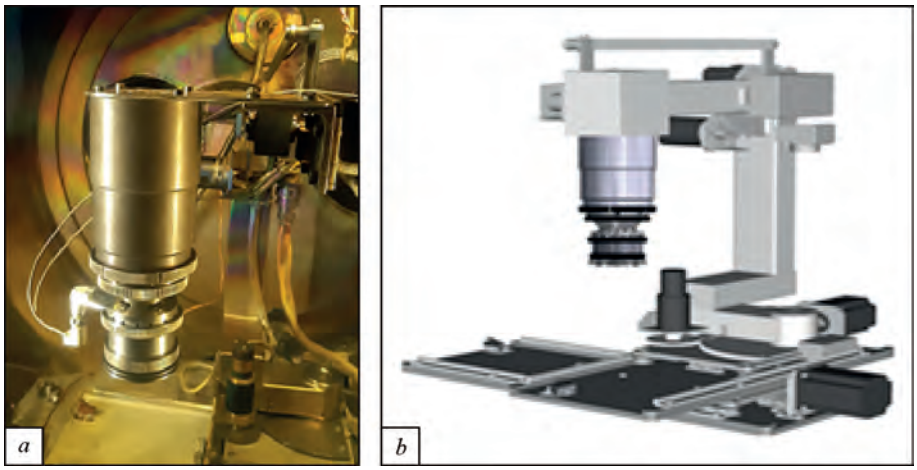

Fig. 2. Equipment for automatic welding in space and on the lunar surface: *a* — Electron beam gun for automatic welding in space as part of the manipulator; *b* — Manipulator for electron beam gun operation in the automatic mode

transformable reusable solar batteries enables conducting energy-intensive experiments and research.

Moreover, it is rational to use this tool at construction of long-term lunar bases for mounting pipelines and other facilities, as well as during performance of repair-restoration operations in high vacuum.

Work on creation of hardware for welding in space and on the lunar surface will promote development of space sector of Ukraine which will have a positive impact on the prestige of our State in the world.

Features of electron beam welding in space

Application of welding processes in space is required primarily for manufacture, mounting and repair of large-sized structures of space stations, both in the Earth orbit and when exploring the Moon, where it is planned to create long-term lunar bases. These can be mounting-assembling operations at construction of pressurized structures for residential and industrial premises, as well as structures for storing energy resources, space complex pipelines, or repair and preventive operations, related to ensuring the operating life of existing systems.

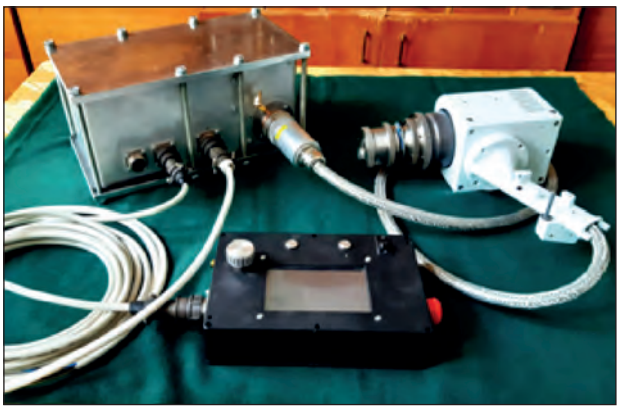

Fig. 3. Complex of hand-held electron beam equipment for technological work in space conditions

Electron beam welding (EBW) is an optimal and more technological process for performance of this work, compared to other welding methods.

During EBW performance in ultra high vacuum, reduced gravity and low temperatures, this process becomes more complicated [5], and the quality of welded joints

Fig. 4. Roentgenogram of a butt joint of 5456 alloy produced by electron beam welding in the flying laboratory in the mode of reduced gravity of 1/6 g (Lunar surface)

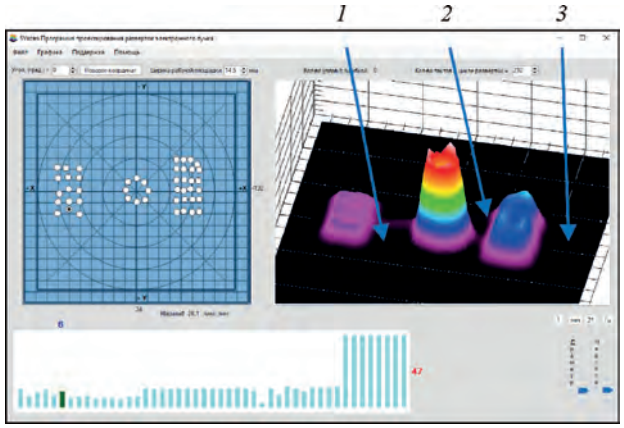

Fig. 5. Scanning with periodical deflection of the electron beam and preheating and further heat treatment of the weld (1 — preheating; 2 — welding by a circular reverse scan, 3 — further heat treatment)

(WJ) can deteriorate. In his work aluminium alloys 2219 and 5456 for space applications were studied.

Obtained results of the conducted experiments under reduced gravity and low temperatures in space, as well as in the flying laboratory, showed an increased quantity of pores in aluminium alloy welds (Fig. 4).

Investigations also showed that one of the causes for porosity in welding aluminium and its alloys is hydrogen present in the base metal, as well as in the oxide film on the edges of the metal being welded [6].

Considering these circumstances, a welding process was proposed with preheating and postweld heat treatment of the weld, with molten pool metal stirring by reverse circular scanning of the electron beam with programmed thermal intensity in each zone of the technological process.

Technological work was conducted in vacuum facility OB1469m, in which the manipulator with PL104 electron beam gun was mounted. Power to the electron beam gun was supplied from laboratory source IUN-5 with 10 kV accelerating voltage. Sample welding was performed with periodical deflection of the electron beam along a reverse circular path, as well as with beam deflection for preheating and further heat treatment at the speed of 25 m/h (Fig. 5). Roentgenograms and macrosections of aluminium alloy welded joints produced by electron beam welding with periodical deflection of the electron beam are shown in Table 1.

X-ray testing was conducted to detect hidden defects in the joints along their entire length (pores, blowholes, cracks, lacks-of-penetration, etc.), and it was performed in RAP-150/300 X-ray unit. Control method sensitivity was equal to 0.05 mm.

Analysis of control WJ images produced by a static electron beam without periodical deflection during welding revealed presence of pores of 0.3 to 1.0 mm size, but no internal defects were found in joints produced with periodical deflection. Results of mechanical tests of WJ produced with periodical deflection for all the alloys, show that all of them demonstrate high stability of ultimate strength values and high values of strength coefficients (Table 2).

Analysis of elemental composition (Table 3) in WJ produced by EBW with periodical scanning showed a uniform distribution of all the elements from the base metal to weld metal.

Table 1

Roentgenograms and macrosections of aluminium alloy welded joints produced by electron beam welding with periodical deflection of the electron beam

Alloy	Thick-ness, mm	Roentgenogram	Macrosection
5456 No scan.	6.0	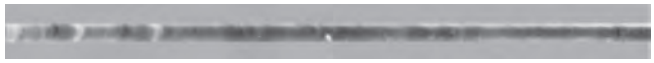	
5456 With period. defl.	6.0	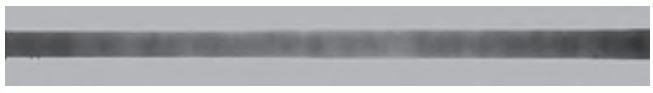	
5456 With period. defl.	4.0		
2219 With period. defl.	5.0		

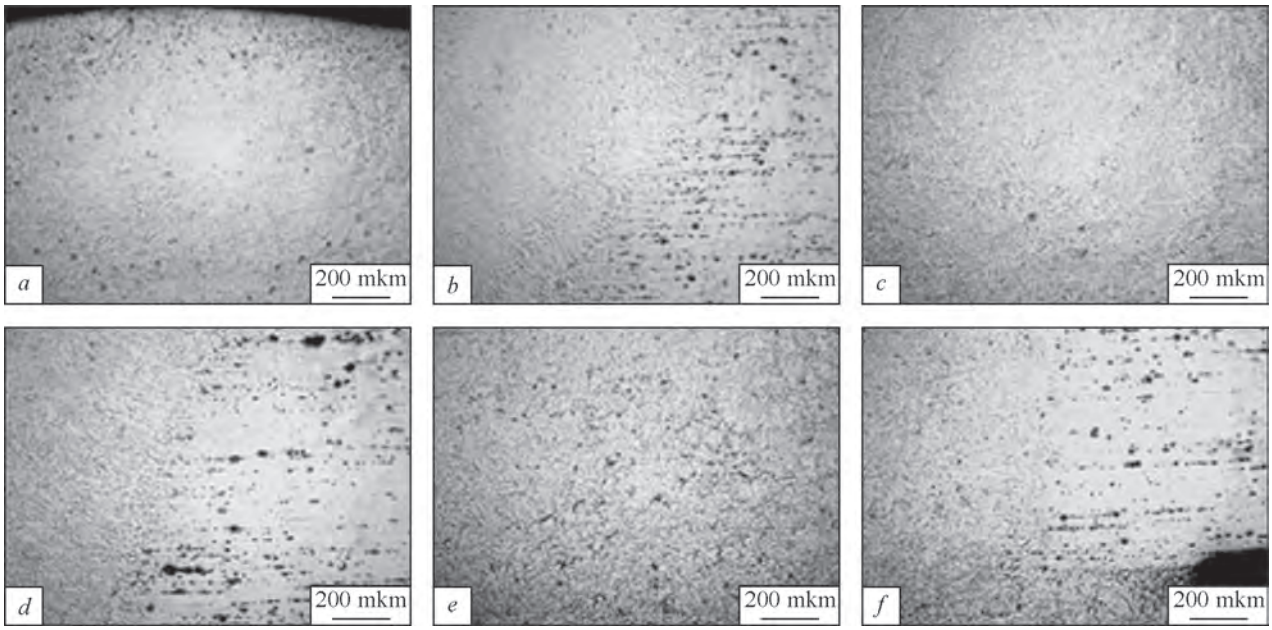

Fig. 6. Microstructure of a welded joint of 5456 alloy 6.0 mm thick produced by electron beam welding with periodical deflection of the electron beam: *a* — weld metal in the upper part; *b* — zone of weld metal fusion with base metal in the upper part; *c* — weld metal in the central part; *d* — zone of weld metal fusion with base metal in the middle part; *e* — weld metal in the root part; *f* — zone of weld metal fusion with base metal in the root part

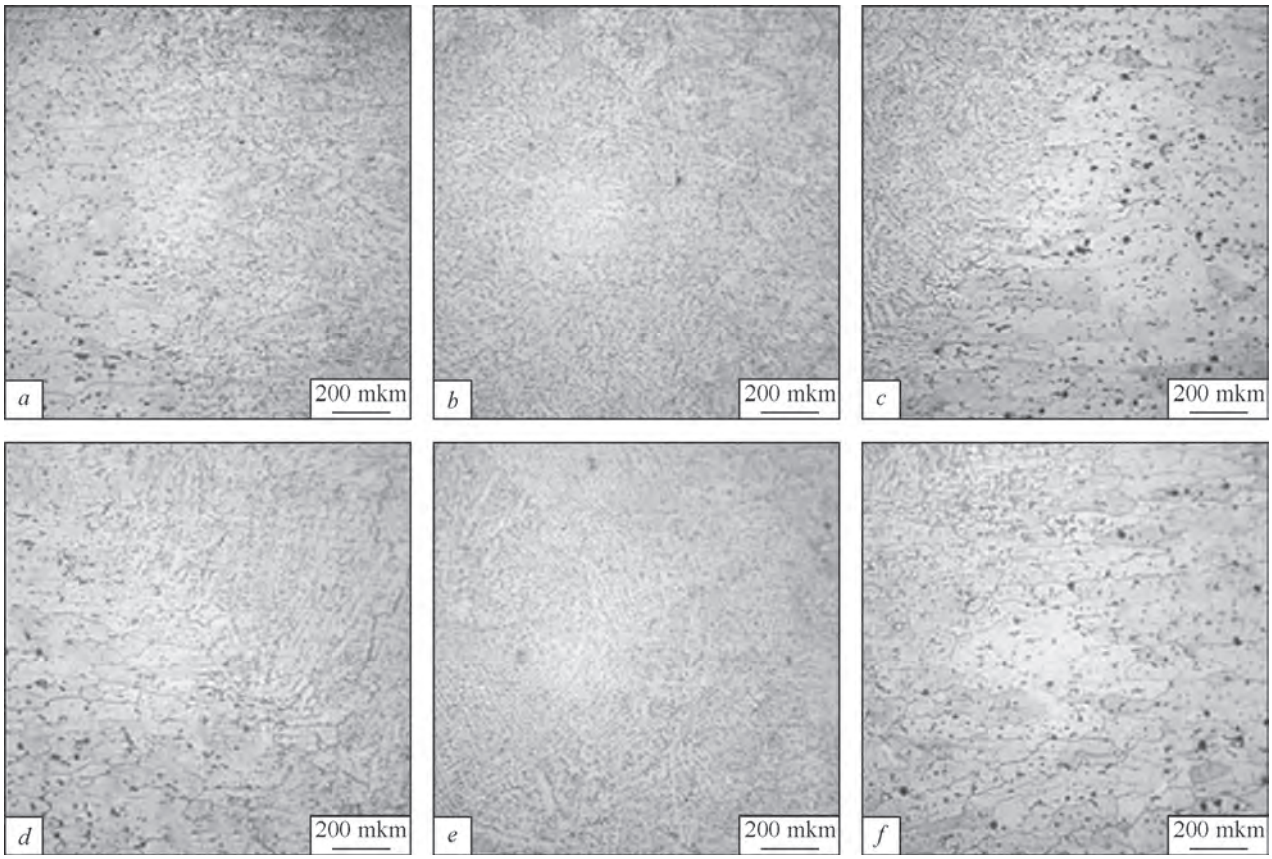

Fig. 7. Microstructure of a welded joint of 2219 alloy 5.0 mm thick produced by electron beam welding with periodical scanning: *a* — zone of weld metal fusion with base metal (upper part on the left); *b* — base metal (upper part in the middle); *c* — zone of weld metal fusion with base metal (upper part on the right); *d* — zone of weld metal fusion with base metal (lower part on the left); *e* — base metal (lower part in the middle); *f* — zone of weld metal fusion with base metal (lower part on the right)

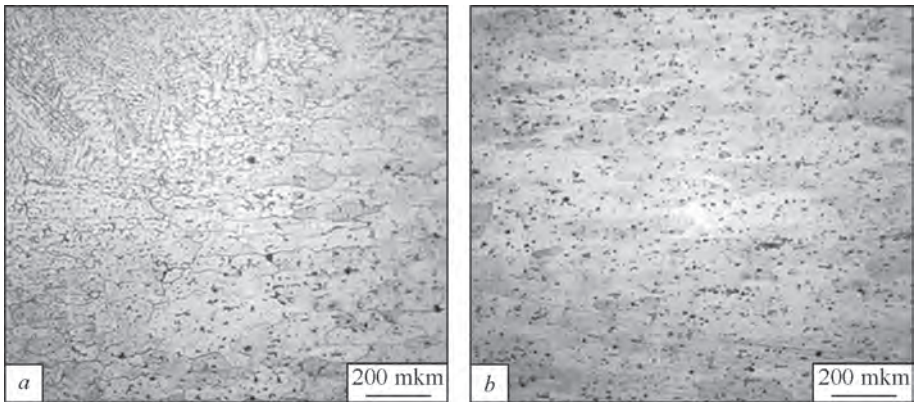

Fig. 8. Microstructure of fusion zone and HAZ (*a*) and of base metal (*b*)

Table 2

Values of ultimate strength σ_t (ranges and average) and strength coefficient *n* of welded samples from AMg6 and 1201 aluminium alloys produced by EBW with periodical deflection

Sample number	Alloy type	Thickness, mm	σ_t w.j, MPa	σ_t b.m, MPa	Strength coefficient, N
1	5456	6.0	304…310 (306)	335…340 (338)	0.9
2	2219	5.0	368…377 (370)	413…424 (417)	0.89

Table 3

The elemental composition of the welded joint from different alloys obtained by discrete-scan EEP

Spectrum No	Elemental composition, %			
	Mg/Cu	Al	Mn	Cr
Alloy 5456, thickness 6 mm				
S1	5,2	92.4	0.3	0.1
S3	5.15	94.45	0.28	0,12
S3	5.16	94.44	0.29	0.11
S4	4.98	94.63	0.3	0.09
S5	4.99	94.63	0.3	0.08
S6	4.98	94.64	0.29	0.09
S7	4.97	94,67	0.28	0.07
S8	4.96	94.68	0.29	0.07
S9	4.98	94.69	0.1	0.09
Alloy 2219, thickness 6 mm				
S1	6.2	93.50	0.3	—
S3	6,15	93.56	0.29	—
S4	6.14	93.57	0.3	—
S5	6.19	93.52	0.3	—
S6	6.15	93.56	0.3	—
S9	6.18	93.53	0.3	—

Determination of the local elemental composition of welded joints from aluminum alloys obtained by EPZ was carried out using a Tescan Mira3 LMU scanning electron microscope. The assessment of the local elemental composition was carried out with an Oxford X-max 80 mm EMF detector mounted on a scanning electron microscope.

Figures 6—5 show the microstructure of welded joints of 5456 and 2219 alloys produced by electron beam welding with periodical deflection of the electron beam.

Metallographic investigations revealed that a dense structure of weld metal (WM) is observed in the main volume. The weld structure is dendritic, and the dendrite parameter does not essentially change along the weld height, i.e. WM structure is stable by volume. Isolated pores of up to 30 μm size are observed in the weld root. Fine pores of up to 40 μm size are present in the fusion zone and in the heat-affected zone (HAZ). Pores are observed to the depth of 1000 μm from the fusion line into the weld metal. Such a pattern is characteristic for all WJ of 2219 alloy produced by fusion welding irrespective of the method. No defects in the form of cracks were found.

Analysis of elemental composition in WJ produced by EBW with periodical scanning showed a uniform distribution of all the elements from the base metal to weld metal.

Conclusions

1. A hardware complex was developed for performance of electron beam welding and related technologies in space and on the lunar surface

2. A gun was proposed with a triode emission system, electron bombardment of the cathode and long operating life of the cathode assembly due to combined cooling.

3. The developed new generation hardware complex is capable of operation both in the manual and automatic variant as part of a robot or artificial intelligence.

4. A small-sized power source, functioning in high vacuum environment was created for the first time in the world, using modern components.

5. The proposed variant of distribution of the power of electron beam thermal impact allows synthesizing

control of electron beam deflection to create the specified temperature field at EBW with simultaneous preheating and further heat treatment.

6. Developed elements of the technology of aluminium alloy EBW by single-pass method with preheating and further heat treatment of the weld with molten pool metal stirring by reverse circular scanning and periodical deflection of the electron beam open up new possibilities for creation of structures under the conditions of the lunar surface.

7. Mechanical property tests, metallographic investigations and WJ elemental composition showed the high quality of the joints produced by the method of periodical deflection of the beam in welding with preheating and further heat treatment.

8. Availability of such hardware will allow Ukraine becoming a participant of US NASA "Artemis" Program for conducting work on the lunar surface at construction of long-term lunar bases. It will allow Ukraine taking a worthy place among the space powers of the world.

REFERENCES

1. Paton B.E., Lobanov L.M., Naidich Y.U., Asnis Yu.A., Zubchenko Yu.V., Ternovyi E.G. New electron beam gun for welding in space. *Sci. and Technology of Welding and Joining*. 2019. 24(4). P. 320—326. https://doi.org/10.1080/13621718.2018.1534794
2. Patent of Ukraine for invention № 118896. Paton B.E., Lobanov L.M., Ternovyi E.G., Zubchenko Yu.V. A device for manual electron beam welding and related technologies in open space. Publ. 25.03.2019, Bul. № 6.
3. Lobanov L.M., Piskun N.V., Ternovyi E.G., Glushak S.O., Kryukov V.A., Kharkivska T.M., Statkevich I.I., Shulym V.F., Zakorko V.O. Electron beam gun for manual electron beam welding on the lunar surface. *Space Science and Technology*. 2024. 30 (1). No. 1. P. 80—91. https://doi.org/10.15407/knit2024.01.080
4. Lobanov L.M., Asnis E.A., Ternovy Ye.G., Zubchenko Yu.V., Statkevich I.I., Volkov V.S. Some issues of repairing manned space vehicles in outer space using electron beam welding. *Solid State Phenomena*. 2021. 315. P. 101—105. https://doi.org/10.4028/www.scientific.net/SSP.315.101
5. Bondarev A.A., Ternovoj E.G. Features of weld formation and properties of aluminium and magnesium joints under the space simulation conditions. *The Paton Welding Journal*. 2010. No. 11. P. 22—27.
6. Ishchenko A.Ya., Labur T.M. Welding modern structures from aluminium alloys. Kyiv: Nauk. Dumka, 2013. 414 p. (In Ukrainian).
7. Solovjov V.G., Lankin Yu.M., Romanova I.Yu. Programming electron beam scan pattern for welding with heat treatment. *The Paton Welding Journal*. 2022. No. 4. P. 1—7.

APPLICATION OF WELDING PROCESSES FOR OBTAINING JOINS FROM LIGHT ALLOYS

Iu. Falchenko, L. Petrushynets, A. Poklyatskyi, V. Fedorchuk
E.O. Paton Electric Welding Institute of the NAS of Ukraine

SECTION 1. Diffusion welding of light three-layer honeycomb panels

Three-layer honeycomb panels are widely used in aircraft construction, shipbuilding, construction and other industries. This structure type has high strength and rigidity at relatively low weight. Load-carrying layers strengthened by the core, are capable of withstanding high compressive stresses, exceeding the material elasticity limit. Such structures have good vibrational and radio technical characteristics, sound and thermal insulation properties [1]. A three-layer panel consists of two covers and the honeycomb core, which differ significantly both by their geometry and by mechanical properties in different planes (Fig. 1). Therefore, when making this type of structure, it is necessary to apply different approaches, both to welding of the profiled strips into a honeycomb core block, and to forming a tee-joint of the covers with the core.

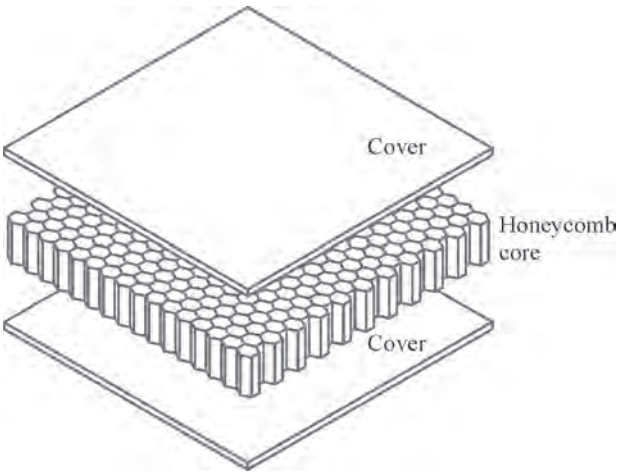

Fig. 1. Scheme of a three-layer honeycomb panel

PWI Department of «Physical-Metallurgical Process of Welding Light Metals and Alloys" developed a technology of manufacturing 150 × 150 mm three-layer honeycomb panels from aluminium alloys (Fig. 2). Honeycomb core from 0.15 mm AD1 aluminium alloy was produced by joining the corrugated strips into blocks by spot welding. As this approach does not guarantee producing a core with plane-parallel end faces, and their presence is one of the main requirements in vacuum diffusion welding (VDW) of the core to the covers, grinding of the contact surfaces was used. VDW of the core to the covers from 1 mm AMg2 aluminium alloy was performed in the device, consisting of the lower and upper flanges and sleeve. The flanges ensure pressing of the covers to the end faces of the honeycomb core over the entire contact area, and the sleeve allows equalizing the temperature field in the product and ensures control of the degree of its deformation during welding [2].

Considering that the modulus of elasticity of aluminium quickly decreases at heating, and already at 250—300 °C it can lead to loss of stability of the structures, further work

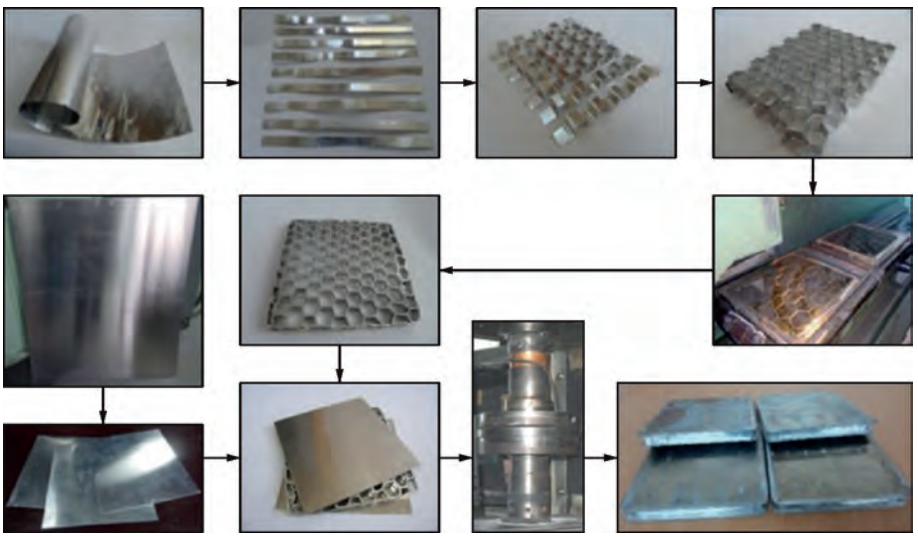

Fig 2. Technology of manufacturing the three-layer honeycomb panel

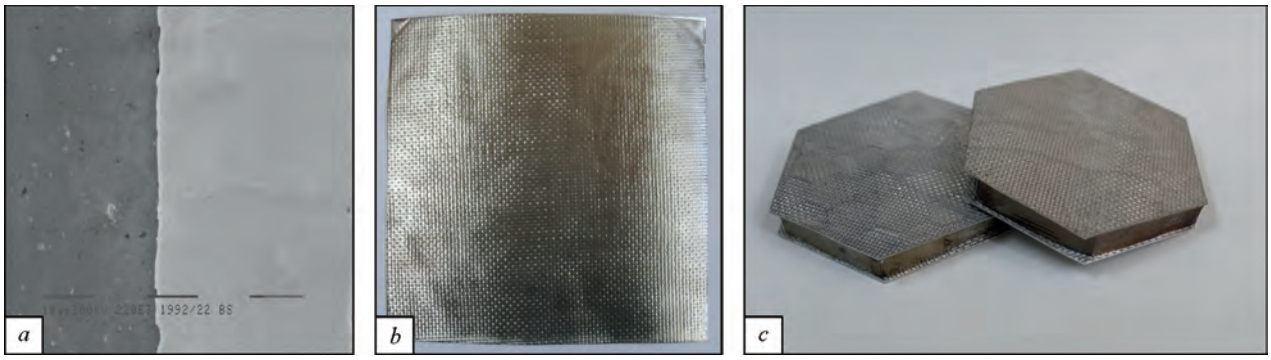

Fig. 3. Microstructure (*a*), general view of the layered composite material produced from AD1 and VT1-0 (*b*) alloys and model sample of a three-layer honeycomb panel made from LCM (*c*)

was aimed at development of a new layered composite material (LCM), which would be able to compete with the traditional aluminium alloys in a wide range of working temperatures. Foil from AD1 aluminium alloy and VT1-0 titanium alloy of 150 and 30 μm thickness, respectively, was used as the research material.

It was established experimentally that VDW of sheet AD1 alloy to VT1-0 alloy should be conducted at high pressures (~20 MPa), because of the limited deformability of the foil, and even in this case defects are observed in the butt joint in the form of individual pores and cracks. Considering that dimensions of the samples should be enough for further manufacturing of honeycomb cores and covers of the three-layer panel from them, application of such pressure values leads to considerable deformation of the welding fixtures and their fast wear. As shown by our research, localization of plastic deformation on the contact surfaces between titanium and aluminium promotes lowering of welding pressure to 5MPa. Such an approach allowed producing defectfree aluminium/titanium joints (Fig. 3, *a*, *b*) of the specified dimensions [3] with different specific weight values, which is achieved due to different ratio of titanium and aluminium layers. A batch of three-layer honeycomb panels was produced using such a layered composite material (Fig. 3, *c*) [4]. It is also shown that the layered material demonstrates higher thermal stability, compared to aluminium alloys, as sample annealing at the temperature of 700 °C for 30 minutes does not lead to their melting or loss of shape.

SECTION 2.
Main advantages of butt joints of AMg5M aluminium alloys produced by friction stir welding

Semi-finished products in the form of sheets, plates, extruded panels, shaped sections, rods, forgings, stampings, etc. from a strong and ductile AMg5M aluminium alloy are widely used in manufacture of welded structures, operating at temperatures from –190 °C to +70 °C [1]. Different fusion welding methods are used in the majority of the cases to produce permanent joints, when the weld forms as a result of melting of a certain volume of the materials being welded and filler wire, and their solidification. It leads to significant structural transformations in the weld metal and regions adjacent to it, as well as frequent occurrence of defects in the form of pores, oxide film macroinclusions and hot cracks, resulting in lower physical-mechanical properties of the welded joints [2—4].

In solid-phase friction stir welding it is possible to avoid metal melting in the weld formation zone and to ensure maximum preservation in the welded assemblies of the properties of semi-finished products used in their manufacture [5]. Metal heating only to the plastic state in the welding zone due to friction, intensive stirring, deformation in a limited space and its densification by the tool working surfaces in the weld result in formation of a fine structure, and base material is softened to a smaller degree in the HAZ than in fusion welding. It leads to an increase of ultimate strength of such joints at uniaxial tension and of their fatigue resistance at cyclic loading, as well as lowering of the level of residual stresses and strains [6—13].

The objective of the work is determination of the main advantages of butt joints of sheet AMg5M aluminium alloy produced by friction stir welding, compared to those made by nonconsumable electrode argon-arc welding.

AMg5M aluminium sheets 1.8 mm thick were used for investigations. Butt joints were produced by mechanized nonconsumable electrode argon-arc (TIG) welding at the speed of 20 m/h at the current of 135—140 A in ASTV-2M unit from MW-450 power source (Fronius, Austria), using SvAMg5 filler wire of 1.6 mm diameter. Friction stir welding (FSW) was performed in a laboratory unit developed at the E.O.Paton Institute, using a special tool with a conical tip and shoulder of 12 mm dia. [14], with the rotation speed of 1420 rpm, and the linear movement speed was 12 m/h. Here, the width of the welds produced by fusion welding was equal to 6.5 mm on average, and of those produced by friction stir welding was 3.5 mm (at the width of the thermomechanical impact zone of approximately 12 mm from the weld face side).

The produced welded joints were used to prepare microsections to study their structure and samples with the working part width of 15 mm to determine their ultimate

strength at uniaxial static tension in keeping with GOST 6996-66. The width of the sample working part for assessment of fatigue resistance characteristics was equal to 25 mm. Mechanical tests of the samples were performed in a universal servohydraulic complex MTS 318.25. Cyclic test were conducted at axial loads by a sinusoidal cycle with coefficient $R_\sigma = 0.1$ and frequency of 15 Hz up to complete fracture of the samples. A series of 5—7 samples of the same type was tested under the same conditions. Experimental data of fatigue testing were processed by the methods of linear regression analysis, commonly accepted for such a kind of investigations. Proceeding from the results of the conducted studies the respective S—N curve — regression line in $2\sigma_a$ — lgN coordinates was plotted for each sample series based on the established limited endurance limits.

Metal hardness was measured on the face surface of the samples of scraped joints. The degree of metal softening in the welding zone was assessed in «ROCKWELL» instrument at load P = 600 N. Evaluation of the structural features of welded joints was performed in optical electron microscope MIM-8.

Residual longitudinal stresses in the welded joints were determined by an experimental method based on metal cutting. The relieved residual stresses caused by heating in welding were calculated by the magnitude of metal deformation, arising as a result of its cutting, using the respective formulas of the theory of elasticity (Hooke's law).

Conducted investigations showed that the weld dimensions in friction stir welding are smaller, and its shape compares favourably with that obtained at nonconsumable electrode argon-arc welding (Fig. 4). It does not have any weld reinforcement, which forms from the filler wire, or the back bead which is due to application of a backing with a groove in fusion welding. This allows avoiding a significant stress concentration in the zone of transition from the weld to the base metal, which has a negative impact on the operational and life characteristics of the joints.

More over, formation of a permanent joint in the solid phase without melting of the edges being welded allows avoiding their oxidation during welding. And deformation and intensive stirring of plasticized metal promote mechanical destruction and dispersion of oxide films, located on its surfaces. Therefore, FSW welds have no defects in the form of oxide film macroinclusions, characteristic for fusion welding. Absence of molten metal, in which hydrogen solubility rises abruptly, allows avoiding additional saturation of the welding zone with it, leading to absence of defects in the form of pores in the welded joints. As at FSW the processes of metal fusion and solidification are absent, it is possible to completely avoid formation of the most hazardous defects — hot cracks, which can arise during molten metal solidification in the area of accumulation of low-melting eutectic inclusions.

The process of permanent joint formation at FSW combines a whole complex of interrelated phenomena, which include intensive local heat evolution on the friction surface, rapid heating and cooling of small metal volumes in a closed space at high pressure, displacement of plasticized metal along a complex trajectory, plastic deformation in metal microvolumes, recrystallization, diffusion, mechanical fragmentation of the components, intensive dislocation movement, instantaneous formation of a permanent joint behind the tool, etc., which accounts for structural features of its different regions. In the weld central part (nugget) a fine-crystalline weld structure forms as a result of intensive dynamic recrystallization. The size of grains having a practically globular shape is not more than 4 μm, and that of dispersed phase precipitates is ≤1 μm, which is 5—7 times smaller than in the base metal. In the thermomechanical impact zone near the boundary of weld transition to base metal, in addition to fine grains, also coarser grains (6—7 μm) are observed, which are elongated in the direction of plasticized metal displacement, and in the HAZ the grain size is 10—15 μm.

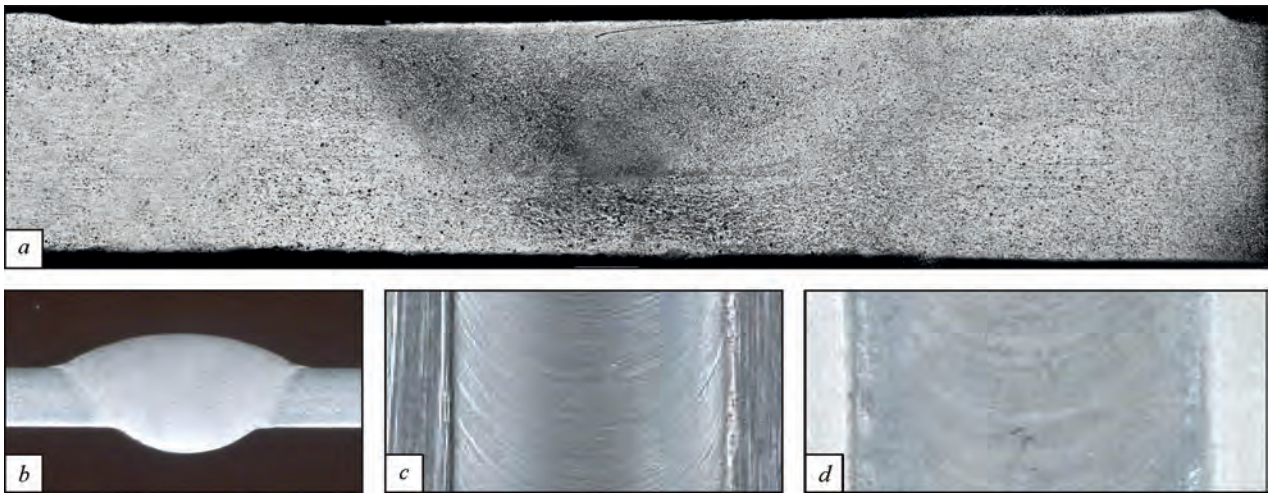

Fig. 4. Transverse sections (*a*, *b*) and appearance of face surfaces of welds (*c*, *d*) of AMg6M alloy 1.8 mm thick, made by FSW (*a*, *c*) and TIG welding (*b*, *d*)

The TIG weld has a mixed dendritic structure, characteristic for aluminium-magnesium alloys in the cast state, which consists of columnar and equiaxed grains. Here, equiaxed dendrites of approximately 25 μm size form in the weld central part. Near the line of its fusion with the base material a layered dendritic structure with extended phase precipitates along these grain boundaries is more pronounced.

Intensive plastic deformation of metal in the zone of permanent joint formation at FSW not only promotes refinement of its structure, but also leads to its strain hardening (Fig. 5). So, in the weld central part metal hardness is at the level of 84 HRB, and in the zones of its transition to base metal it is 83 HRB. Here, minimal metal hardness (78 HRB) is observed in the HAZ, whereas at TIG welding metal hardness is not higher than 76 HRB in the weld central part, and 78 HRB in the zones of its fusion with the base material. Therefore, the samples of joints produced by TIG welding using SvAMg5 filler wire with the removed weld reinforcement and back bead fail through the weld metal at uniaxial tension and have the ultimate strength at the level of 300 MPa. Destruction of joints of such samples with weld reinforcement occurs in the base metal, similar to FSW samples. Here, their ultimate strength is at the level of 320 MPa.

As a result of the conducted investigations, it was established that lowering of metal heating temperature in the zone of permanent joint formation at FSW has a positive influence also on the level of residual stresses, arising in it as a result of nonuniform distribution of the thermal field. So, at TIG welding the maximal value of residual longitudinal tensile stresses at 10 mm distance from the weld axis is at the level of 103 MPa (Fig. 6). In the weld center these stresses are equal to 72 MPa. At the distance of approximately 22 mm from the weld axis they decrease to zero, and furtheron compressive stresses develop with the maximal value of 38 MPa at 35 mm distance from the weld axis. In FSW joints, the maximal value of tensile stresses is just 78 MPa. Here, their value in the weld center is at the level of 36 MPa that is two times smaller than at TIG welding. The maximal value of residual compressive stresses at 35 mm distance from the weld axis also decreases to 23 MPa, accordingly.

Results of experimental studies of fatigue resistance of FSW joints of AMg5M alloy showed that their endurance limit on the base of $2 \cdot 10^6$ cycles of stress alternation is equal to ~90% of the respective values for the base metal and it practically reaches the level of values of conditional endurance limit (Fig. 7). In its turn, the fatigue resistance of TIG welded joints is significantly inferior in the entire fatigue life range based on 10^5—$2 \cdot 10^6$ cycles of stress alternation. Here, the fatigue life of FSW joints is much higher than that of TIG welded joints, and the limited endurance limit based on 10^6 cycles of stress alternation is 15—20% higher. The main cause for lower fatigue life of TIG welded joints mainly is the high concentration of acting stresses, which is due to the weld geometrical parameters.

Conclusions

1. At FSW of AMg5M aluminium alloy intensive plastic deformation of metal in the weld nugget results in formation of a homogenous disoriented structure with grain size of 3—4 μm and disperse (≤1 μm) phase precipitates. In the zones of weld transition to base material elongation of some grains to 6—7 μm and their distortion in the direction of plasticized metal displacement take place.

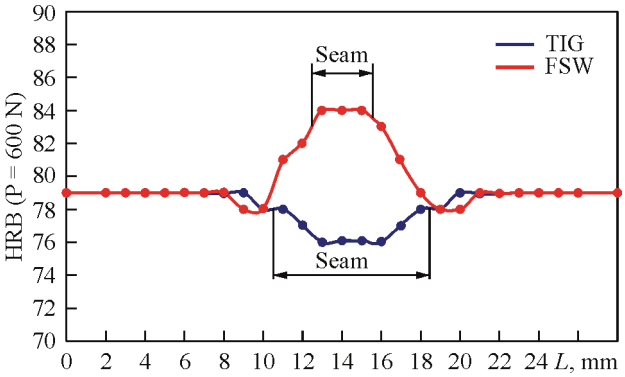

Fig. 5. Hardness distribution in welded joints of AMg5M alloy 1.8 mm thick, produced by TIG welding and FSW

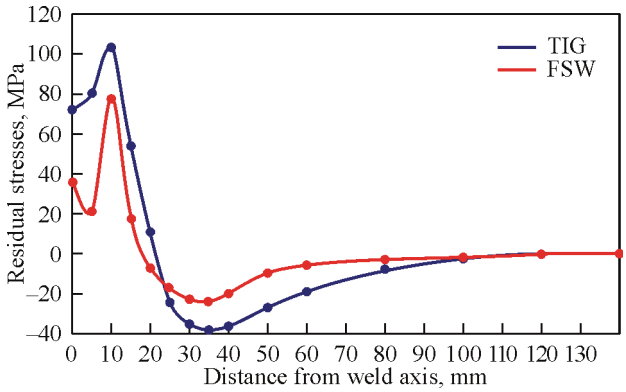

Fig. 6. Residual stresses in welded joints of AMG5M alloy 1.8 mm thick, produced by TIG welding and FSW

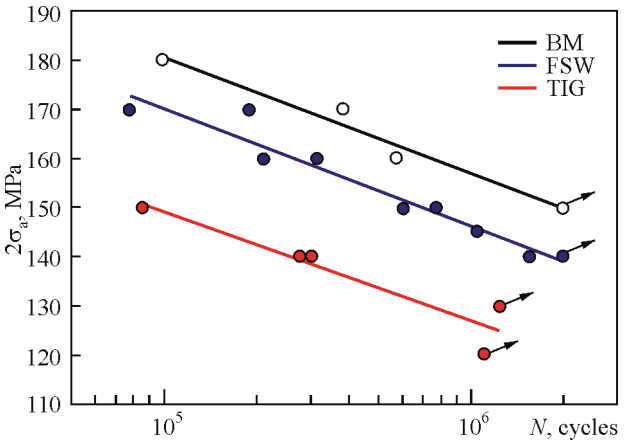

Fig. 7. S-N curves of base material (BM) and welded joints of AMg5M alloy 1.8 mm thick at stress cycle asymmetry $R_\sigma = 0.1$

2. FSW process ensures formation of a permanent joint with minimal level of stress concentration in the zone of transition from the weld to the base material, and it allows avoiding defects in the form of pores, oxide film macroinclusions and hot cracks in welds, caused by metal melting and solidification in fusion welding.

3. At FSW of AMg5M alloy metal hardness in the joint zone becomes higher due to strain hardening of the metal caused by grain refinement, while in TIG welding metal hardness in this zone decreases as a result of formation of cast coarse-grained dendritic structure of the welds. Therefore, the ultimate strength of FSW samples is 20 MPa higher at uniaxial tension than that of samples with the removed reinforcement and back beads of the welds, produced by fusion processes.

4. Owing to weld formation in the solid phase at lower temperatures than those in fusion welding, the maximal level of residual longitudinal tensile stresses in FSW joints of AMg5M alloy is by 25% lower than in TIG welding.

5. The effectiveness of FSW process application instead of TIG welding for fabrication of structures from AMg5M alloy operating at alternating loading was substantiated experimentally by obtaining the fatigue resistance characteristics. It is shown that fatigue life of FSW butt joints is much higher than that of TIG welded joints, and their limited endurance limit based on $2 \cdot 10^6$ cycles of stress alternation practically reaches the level of fatigue life of base metal samples, whereas for TIG welded joints it is 30—40% lower.

REFERENCES

1. Bitzer T. Honeycomb Technology. Materials, Design, Manufacturing, Applications and Testing. Dordrecht, Springer-Science+ Business Media, 1997. 233 p.

2. Petrushinets L.V., Falchenko Yu.V., Fedorchuk V.E., Shinkarenko V.S. Possibilities of manufacturing three-layer welded honeycomb panels from aluminium alloys. *The Paton Welding Journal*. 2018. No. 7. P. 25—29.

3. Falchenko Yu.V., Petrushynets L.V., Polovetskii E.V. Peculiarities of producing Al—Ti bimetal sheet joints by the method of vacuum diffusion welding. *The Paton Welding Journal*. 2020. No. 8. P. 25—28.

4. Petrushinets L.V., Falchenko Yu.V., Novomlynets O.O., Fedorchuk V.E. Application of a layered composite material based on aluminium and titanium alloys to produce welded three-layer honeycomb panels. *The Paton Welding Journal*. 2022. No. 7. P. 17—22.

5. Beleckij V.M., Krivov G.A. Alyuminievye splavy (Sostav, svojstva, tehnologiya, primenenie) Spravochnik. Ed. I.N. Fridlyandera. Kyiv, 2005. 365 p.

6. Rabkin D.M., Lozovskaya A.V., Sklabinskaya I.E. Metallovedenie svarki alyuminiya i ego splavov. Ed. V.N. Zamkov. Kyiv: Nauk. dumka, 1992. 160 p.

7. Mashin V.S., Poklyackij A.G., Fedorchuk V.E. Mehanicheskie svojstva soedinenij alyuminievyh splavov pri svarke plavyashimsya i neplavyashimsya elektrodom. *The Paton Welding Journal*. 2005. No. 9. P. 43—49.

8. Poklyatsky A.G. Peculiarities of formation of macroinclusions of oxide film in weld metal of aluminium alloys (Review). *The Paton Welding Journal*. 2001. No. 3. P. 36—38.

9. Int. Patent Application No. PCT/GB 92/02203; GB Patent Application No. 9125978.8. Friction Stir Butt Welding / Thomas W.M., Nicholas E.D., Needham J.C. et al. Publ. 1991.

10. Shibayanagi T. Microstructural aspects in friction stir welding. *Journal of Japan Institute of Light Metals*. 2007. No. 9. P. 416—423.

11. Pietras A., Zadroga L. Rozwój metody zdrzewania tarciowego z mieszaniem materiału zgrzeiny (FSW) i możliwosci jej zastosowania. *Biuletyn Instytutu Spawalnictwa w Gliwicach*. 2003. No. 5. P. 148—154.

12. Sato Y. Relationship between Mechanical Properties and Microstructure in Friction Stir Welded Al alloys. *Journal of the Japan Welding Society*. 2002. No. 8. P. 33—36.

13. Larsson H., Karlsson L., Svensson L. Friction Stir welding of AA5083 and AA6082 aluminium alloys. *Svetsaren*. 2000. No. 2. P. 6—10.

14. Kluken A., Ranes M. Aluminium bridge constructions — welding technology and fatigue properties. *Svetsaren*. 1995. No. 3. P. 13—15.

15. Ericsson M., Sandstrom R. Influence of melding speed on the fatigue of friction stir welds, and comparison with MIG and TIG. *International Journal of Fatigue*. 2003. No. 25. P. 1379—1387.

16. Lanciotti A., Vitali F. Characterization of friction welded joints in aluminium alloy 6082-T6 plates. *Welding International*. 2003. No. 8. P. 624—630.

17. Jata K.V., Sankaran K.K., Ruschau J.J. Friction Stir Welding Effects on Microstructure and Fatigue of Aluminum Alloy 7050-T7451. *Metallurgical Transactions*. 2000. 31A. P. 2181—2192.

18. Pat. 54096 Ukrayina, MPK V23K 20/12. Instrument dlya zvaryuvannya tertyam z peremishuvannyam alyuminiyevih splaviv / Ishenko A.Ya., Poklyackij A.G.; zayavnik i patentovlasnik IEZ im. Ye.O. Patona NAN Ukrayini. No. U201005315; zayav. 30.04.2010; opubl. 25.10.2010, Byul. No. 20.

REUSABLE LOW-ORBIT SERVICE COMPLEX ORBITAL STRUCTURE SYNTHESIS AND OPERATIONAL SERVICE PLANNING

A. Alpatov, Yu. Holdstein

Institute of Technical Mechanics of the National Academy of Sciences of Ukraine and State Space Agency of Ukraine

At the current stage of the development of space activities, the world's leading space states are actively developing promising on-orbit services (OOS). OOS is turning into a viable space industry, the development of which is determined by the development of new space technologies, which include OOS industrialization and the development of modular spacecraft. It is expected that OOS industrialization and modular satellites will be revolutionary technologies for the satellite industry].

Most of the OOS missions that are planned and executed at this time use disposable OOS spacecraft. The use of disposable OOS spacecraft may be profitable in the near future. However, it is not a reliable solution for OOS in the long term. As an alternative, a more useful concept is the concept of industrialization of OOS due to the deployment of reusable and sustainable OOS complexes. This concept can ensure the timeliness and efficiency of OOS implementation for scheduled and random requests of OOS clients for service. However, despite the potential advantage of using reusable OOS complexes, the design of their orbital structure and operational service planning is much more complex and difficult compared to the traditional concept of OOS organization. This is because when planning the response of the OOS complex to the requests of OOS clients, it is necessary to carry out the distribution of OOS client service operations between spacecrafts of the OOS complex. According to experts, for the effective functioning of the OOS complex, the number of OOS spacecrafts in their structure can vary from several units to tens.

In modern literature, the main attention is given to certain aspects of OOS missions performed by disposable OOS spacecraft. Only a relatively small number of works are devoted to the development of methods for optimal planning of the orbital structure and operational planning of low-orbit reusable OOS complex. In this regard, there is currently a need to improve the existing and develop new methods for solving these problems.

The purpose of the article is to develop a technique for the optimal synthesis of the orbital structure and optimal operational planning of the low-orbit OOS complex in near-Earth orbits with a small eccentricity. Methods for solving the problem are the averaging method, the branch-and-bound method, and the multi-objective optimization method. The novelty of the obtained results lies in the development of a technique for the optimal synthesis of the orbital structure and optimal operational planning of the low-orbit OOS complex in low orbits with a small eccentricity.

Formulation of the problem

It is assumed that the OOS complex, consisting of n reusable OOS spacecrafts, has been deployed. It is designed to fulfill scheduled or random service requests from m OOS clients. In the problem, it is assumed that the base orbits of OOS spacecraft have a small eccentricity and their orbital planes have the same speed of nodal precession. To ensure synchronization of nodal precession, their orbits have the same semi-major axes and inclinations. The planes of the base orbits of the OOS spacecrafts are evenly distributed along the longitudes of the ascending nodes (LAN). One OOS spacecraft is located in each orbital plane. It is assumed that the orbits of OOS clients also have a small eccentricity and differ little in inclination between themselves and the orbits of OOS spacecrafts. In the problem, a significant difference in the orbits of the OOS clients along the major semi-axes and LAN is allowed. The difference in the LAN precession speeds of OOS spacecraft and OOS clients is achieved due to the difference in the semi-major axes of their orbits. It is assumed that interorbital flights are the main factor affecting fuel consumption and the time of execution of the OOS. Any of the OOS spacecrafts can perform any of the OOS execution requests. Each OOS spacecraft can be assigned to perform only one OOS execution request, and each OOS, in turn, must be performed by only one OOS spacecraft. The work does not take into account the effect of gravitational disturbances of a higher order, than those associated with the influence of the second zonal harmonic of the Earth's geopotential. Disturbances due to the influence of the Earth's atmosphere and the gravitation of the Moon and the Sun are not taken into account.

As a result of solving the considered problem, it is necessary to develop methods for the rational synthesis of the orbital structure and optimal operational planning for the low-orbit OOS complex in near-Earth orbits with a small eccentricity. The technique is designed to determine in an acceptable time: the parameters of interorbital flight of OOS spacecrafts, optimal waiting times of OOS spacecrafts on parking orbits, determination of the appropriate

distribution of client service requests of OOS between OOS spacecraft, determination of the appropriate number of OOS spacecrafts and optimal semi-major axis and inclination of their parking orbits.

Orbital clustering of the OOS clients

When planning the OOS, it is necessary to take into account the limited energy possibilities of service spacecraft. In this connection, the problem arises of rationally splitting up a set of orbits of the OOS clients into subsets (clusters) of orbits that are available for utilization by a single service spacecraft. Each orbit of the OOS clients should belong to only one cluster, and the orbits belonging to the cluster should be near in terms of energy consumptions for the interorbital transfer between them.

To date, a sufficiently large number of cluster analysis algorithms have been developed: hierarchical algorithms, non-hierarchical iterative algorithms, graph algorithms, fuzzy clustering algorithms, algorithms using neural networks, and genetic algorithms. To solve the problem of clustering orbits of the OOS clients, it was proposed [1] to use the *k*-means clustering algorithm, which belongs to the group of non-hierarchical methods of cluster analysis. The advantages of the *k*-means algorithm are the simplicity and speed of its use, clarity, and transparency of the algorithm. The disadvantages of the algorithm include the need to specify the number of clusters before clustering.

Let us imagine the elements of the set of the OOS client's orbits $X = \{x_1, x_2, \ldots, x_n\}$ in the form of their characteristic vectors. Later, we will fully identify the orbit with its characteristic vector, which is a set of orbital parameters. It is required to divide this set of orbits into k clusters $S_1, S_2, \ldots, S_k$. Each orbit should belong to one cluster only located at the smallest distance from this orbit. The distribution of the orbits in clusters must satisfy the criterion of optimality, expressed in terms of the distance $\rho(x_i, x_j)$ between any pair of orbits of the considered set. When splitting the original set X of orbits of space debris fragments into k clusters $S_1, S_2, \ldots, S_k$, it is proposed to apply an iteration algorithm of *k*-means that minimizes the sum of squares of distances from each point of the cluster to its center. The advantages of the *k*-means algorithm are the simplicity and speed of its use, clarity and transparency of the algorithm. The disadvantages of the algorithm include the need to specify the number of clusters before clustering. As a distance (metric) between the orbits $\rho(x_i, x_j)$, any non-negative real function can be used that is defined on the set X and satisfies the following conditions:

$$\rho(x_i, x_j) = 0 \text{ only when } x_i = x_j,$$
$$\rho(x_i, x_j) = \rho(x_j, x_i),$$
$$\rho(x_i, x_j) \le \rho(x_i, x_k) + \rho(x_k, x_j).$$

When splitting the original set of orbits X into k clusters $S_1, S_2, \ldots, S_k$, an iterative algorithm *k*-means is used. It minimizes the sum of distances from each point of the cluster to its center.

The action of the *k*-means algorithm comes down to a search:

$$\arg\min_S \sum_{i=1}^{k} \sum_{x \in S_i} \rho(x, \mu_i),$$

where $S = \{S_1, S_2, \ldots, S_k\}$,
μ_i are cluster centers $i = 1, \ldots, k$,
$\rho(x, \mu_i)$ are distances between orbit x and cluster centers μ_i.

In the sequel, a variable t is used to indicate the iteration step number. At the first step of the algorithm *k*-means execution the initial values of the cluster centers μ_i^0 are determined. Arbitrary points of the orbit characteristics are chosen as the initial values of the cluster centers. In the next step, the orbits are distributed among the clusters.

All orbits are grouped into clusters, the distances to the centers of which are minimal

$$\forall x_i \in X, i = 1, \ldots, n : x_i \in S_j \Leftrightarrow j = \arg\min_k \rho(x_i, \mu_k^{(t-1)}).$$

The next step is to recalculate the centers of the changed clusters.

$$\forall i = 1, 2, \ldots, k : \mu_i^{(t)} = \frac{1}{|S_i|} \sum_{x \in S_i} x.$$

The process of calculating the centers and redistributing the orbits continues until one of the conditions is satisfied: the cluster centers have stabilized, i.e. all orbits belong to the cluster to which they belonged before the current iteration or the number of iterations is equal to the maximum number of iterations.

For clustering orbits of the OOS clients, it was proposed [1] to use a non-standard energy metric — delta-velocity of interorbital transfer between these orbits. The introduction of the energy metric made it possible to successfully cluster the orbits of space debris.

Dynamics of interorbital flight of the OOS spacecraft

On the interorbital flight orbit of the *i*-th OOS spacecraft from the parking orbit to the *j*-th destination orbit, the flight control of the OOS spacecraft is performed by the engine of low constant thrust at a zero pitch angle due to a change in the magnitude and direction of the thrust yaw angle β_{ij}. The yaw control angle changes its sign every half-turn of the orbit at values of the latitude argument u equal to $\pi/2$ and $3/2\ \pi$ [2]. For short flights of OOS spacecraft, mass reduction due to fuel outflow can usually be neglected.

Under the assumption of zero eccentricity of the flight orbit and using the results of [2], we consider the system of averaged over the argument of latitude equations (1)—(3) of the OOS spacecraft flight from the parking orbit to the target orbit. This system of equations takes into account the influence of the second zonal harmonic of the Earth's geopotential.

$$\frac{da_{ij}^f}{dt} = 2\sqrt{\frac{(a_{ij}^f)^3}{\mu}}\varepsilon_i \cos\tilde{\beta}_{ij}, \quad (1)$$

$$\frac{di_{ij}^f}{dt} = \frac{2}{\pi}\sqrt{\frac{a_{ij}^f}{\mu}}\varepsilon_i \sin\tilde{\beta}_{ij}, \quad (2)$$

$$\frac{d\Omega_{ij}^{f}}{dt} = -\frac{3}{2} J_2 \sqrt{\frac{\mu}{(a_{ij}^{f})^7}}\, R_e^2 \cos i_{ij}^{f}, \qquad (3)$$

where a_{ij}^{f}, i_{ij}^{f}, Ω_{ij}^{f} are, respectively, the averaged values of the semi-major axis, inclination, and LAN of the flight orbit of the i-th OOS spacecraft from the parking orbit (a^p, i^p, Ω_i^p) to the j-th destination orbit (a_j^d, i_j^d, Ω_j^d), R_e — the equatorial radius of the Earth, μ — the gravitational parameter of the Earth, J_2 — the coefficient at the second zonal harmonic of the Earth's geopotential.

Equations (1) and (2) have analytical solutions (4) and (5), which are given [2].

$$a_{ij}^{f}(t) = a^p \left(1 - \varepsilon_i \cos\tilde{\beta}_{ij} \sqrt{\frac{a^p}{\mu}} t\right)^{-2}, \qquad (4)$$

$$i_{ij}^{f}(t) = i^p - \frac{2}{\pi} \tan\tilde{\beta}_{ij} \log\left(1 - \varepsilon_i \cos\tilde{\beta}_{ij} \sqrt{\frac{a^p}{\mu}} t\right). \qquad (5)$$

Using (4)—(5), we write down the boundary value problem for determining the controlling yaw angle $\tilde{\beta}_{ij}$ and the time of interorbital flight t_{ij}^{f} in the form of a system of transcendental equations.

$$a_j^d = a^p \left(1 - \varepsilon_i \cos\tilde{\beta}_{ij} \sqrt{\frac{a^p}{\mu}} t_{ij}^{f}\right)^{-2}, \qquad (6)$$

$$i_j^d = i^p - \frac{2}{\pi} \tan\tilde{\beta}_{ij} \log\left(1 - \varepsilon_i \cos\tilde{\beta}_{ij} \sqrt{\frac{a^p}{\mu}} t_{ij}^{f}\right). \qquad (7)$$

The system of transcendental equations (6)—(7) has an analytical solution, which is given in [2].

Determination of waiting time for the start of interorbital flights

The use of the waiting of the OOS spacecraft on the parking orbits allows for eliminating the initial (at the time of service start) differences in the LAN of the parking orbit and the destination orbit due to the different angular velocities of nodal precession of these orbits. The duration of the wait depends significantly on the initial difference in the LAN of the parking orbits and the destination orbits of the OOS spacecraft. If the initial differences in the LAN of the parking and destination orbits of the OOS spacecraft are greater than the change in the LAN during the flight of the OOS spacecraft between these orbits, then the OOS spacecraft are waiting for the start of the flight. At the moments when the differences in the LAN of the parking and destination orbits of the OOS spacecraft are equal to the change in the difference in LAN during the flight, the flight between the parking and destination orbits of the OOS spacecraft begins.

Let us consider the angles $\Delta\Omega_{ij}^{0}$, $\Delta\Omega_{ij}^{f}$ and $\Delta\Omega_{ij}^{w}$. The angle $\Delta\Omega_{ij}^{0}$ is equal to the initial difference of the LAN of the parking orbit of the i-th OOS spacecraft and the j-th destination orbit. The angles $\Delta\Omega_{ij}^{f}$ and $\Delta\Omega_{ij}^{w}$, respectively, are equal to the changes in the differences in the LAN of the parking orbit of the i-th OOS spacecraft and j-th the destination orbit during the flight time t_{ij}^{f} from the parking orbit to the destination orbit and during the waiting time t_{ij}^{w} of the OOS spacecraft in the parking orbit. The angle $\Delta\Omega_{ij}^{0}$ is measured in the direction of nodal precession of the parking and the destination orbits from the orbit with a higher angular velocity of nodal precession to an orbit with a lower angular velocity of nodal precession. Its value depends on the ratio of the values of Ω_i^p, Ω_j^d and ω^p, ω_j^d, where Ω_i^p, Ω_j^d and ω^p, ω_j^d are, respectively, the LAN and the angular velocity of nodal precession of the parking orbit of the i-th OOS spacecraft and the j-th destination orbit. Fig. 1 explains the calculation $\Delta\Omega_{ij}^{0}$ for the case ($\Omega_j^d \geq \Omega_i^p$) and ($\omega_j^d > \omega^p$).

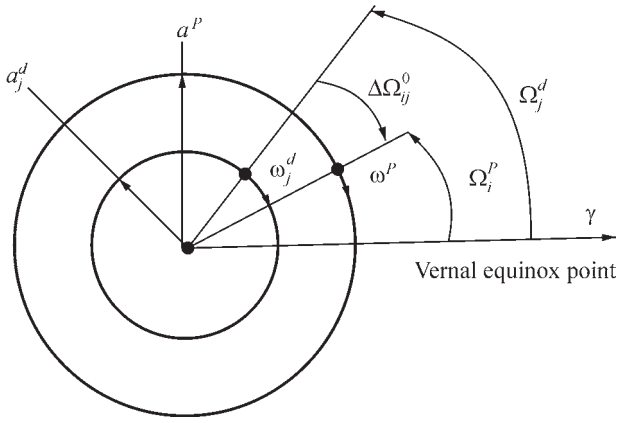

Fig. 1. Scheme for calculation $\Delta\Omega_{ij}^{0}$

Formulas for calculation $\Delta\Omega_{ij}^{0}$ in four possible cases are given in [3].

Operational planning of the OOS complex

According to the problem statement, there are m requests for the execution of OOS. Requests can be performed by n spacecrafts of the OOS complex. m and n are natural numbers. To fulfill requests for OOS, each spacecraft of the OOS complex must fly from the parking orbit to the destination orbit. The waiting time for the i-th spacecraft of the OOS complex to start the flight from the parking orbit to the destination orbit to serve the j-th OOS client is estimated by the matrix t_{ij}^{w}. Let's consider integer variables x_{ij} that take the value 0 or 1. Assume that $x_{ij} = 1$, if i-th spacecraft of the OOS complex is assigned to fulfill the j-th request for execution of OOS and $x_{ij} = 0$ if i-th spacecraft of the OOS complex is not assigned to fulfill the j-th request for execution of OOS. In the problem, it is necessary to distribute the requests for execution of OOS among the spacecraft of the OOS complex in such a way that the total waiting time for the start of flights for the execution of all requests for execution of OOS is minimal. Taking into account the positive waiting times for the start of flights by spacecraft of the OOS complex, the minimum total waiting time for the start of flights by spacecraft of the OOS complex is equivalent to the minimum waiting times for each of the spacecraft of the OOS complex.

The problem of distribution of requests for the execution of OOS between spacecrafts of the OOS complex allows a mathematical formulation in the form of an integer linear programming problem with linear constraints:

$$x_{ij}^{*} = \arg\min_{x_{ij}\in\{0,1\}} \sum_{i=1}^{n}\sum_{j=1}^{m} t_{ij}^{w}\, x_{ij},$$

Where x_{ij}^{*} is the matrix of the optimal distribution of requests for performing OOS between the spacecrafts of the OOS complex. Depending on the ratio of values m and n, in addition to the condition $x_{ij}\in\{0, 1\}$, x_{ij} must satisfy various systems of linear equalities and inequalities. If $m < n$, then it is assumed that all requests for the implementation of the OOS must be fulfilled, and some spacecraft of the OOS complex may not perform the OOS. The mathematical formulation of these conditions has the form:

$$\sum_{j=1}^{m} x_{ij} = 1,\ \forall i \in \{1,2,...,n\},$$

$$\sum_{i=1}^{n} x_{ij} \le 1,\ \forall j \in \{1,2,...,m\}.$$

If $m > n$, then all spacecraft of the OOS complex perform OOS, and some OOS requests may not be fulfilled. The mathematical formulation of these conditions has the form:

$$\sum_{j=1}^{m} x_{ij} \le 1,\ \forall i \in \{1,2,...,n\},$$

$$\sum_{i=1}^{n} x_{ij} = 1,\ \forall j \in \{1,2,...,m\}.$$

If $m = n$ then all spacecrafts of the OOS complex perform OOS and all requests for OOS execution must be fulfilled. The mathematical formulation of these conditions has the form:

$$\sum_{j=1}^{m} x_{ij} = 1,\ \forall i \in \{1,2,...,n\},$$

$$\sum_{i=1}^{n} x_{ij} = 1,\ \forall j \in \{1,2,...,m\}.$$

To solve the considered problem of integer linear programming with linear constraints, the method of branches and bounds was used [3].

Orbital structure synthesis of the OOS complex

Orbital structure synthesis of the OOS complex includes the determination of the rational number of the OOS complex spacecrafts and the parameters of their parking orbits. According to the conditions of the problem, for the OOS complex spacecrafts parking orbits are known Ω_i^p $(\forall i \in\{1,2,\ldots,n\})$. For the OOS complex spacecrafts destination orbits are known a_j^d, i_j^d, Ω_j^d $(\forall j \in\{1,2,\ldots,m\})$. It is necessary to find the optimal values of the semi-major axis a_{opt}^p and the inclination i_{opt}^p of the OOS complex spacecrafts parking orbits. The parameters a^p and i^p must satisfy the following constraints: $a_{\min}^p \le a^p \le a_{\max}^p$ and $i_{\min}^p \le i^p \le i_{\max}^p$. In constraints $a_{\max}^p$, $i_{\max}^p$ and $a_{\min}^p$, $i_{\min}^p$, respectively, are the maximum and minimum allowable values of the semi-major axis and the inclination of the OOS complex spacecrafts parking orbits. The average duration of the maneuver waiting for the start of the flights t_{mid}^w and the average fuel consumption Δm_{mid} for the flights were taken as optimality criteria.

The problem of determining the optimal parameters ($a_{opt}^{\text{баз}}$, $i_{opt}^{\text{баз}}$) of the OOS complex spacecrafts parking orbits allows a mathematical formulation in the form of a be-objective optimization problem:

$$(a_{opt}^p, i_{opt}^p) = \arg\min_{(a^p, i^p)\in\Im} (t_{mid}^w(a^p, i^p),\ \ \Delta m_{mid}(a^p, i^p)),$$

where the set of allowed values $\Im$ is formulated by the following system of constraints

$$a_{\min}^p \le a^p \le a_{\max}^p,$$

$$i_{\min}^p \le i^p \le i_{\max}^p.$$

This problem consists of finding a vector of target variables (a_{opt}^p, i_{opt}^p) satisfying the constraint and optimizing the vector objective function $(t_{mid}^w(a^p, i^p),\ \Delta m_{mid}(a^p, i^p))$, the elements of which $t_{mid}^w(a^p, i^p)$ and $\Delta m_{mid}(a^p, i^p)$ are calculated according to the following formulas:

$$t_{mid}^w(a^p, i^p) = \sum_{i=1}^{n}\sum_{j=1}^{m} t_{ij}^w x_{ij}^* \Big/ \min(n, m),$$

$$\Delta m_{mid}(a^p, i^p) = \sum_{i=1}^{n}\sum_{j=1}^{m} \Delta m_{ij} x_{ij}^* \Big/ \min(n, m).$$

The objective functions $t_{mid}^w(a^p, i^p)$ and $\Delta m_{mid}(a^p, i^p)$ mutually in conflict with each other, because as the difference between a^p and a_j^d of the OOS complex spacecrafts increase, then t_{mid}^w decreases and Δm_{mid} increases. For this bi-objective optimization problem, there is no single solution that would simultaneously optimize both objective functions. Therefore, the Pareto principle was used for optimization. The Pareto principle does not single out a single solution; it only narrows the set of possible alternatives to a representative set of Pareto-optimal solutions (Pareto fronts). For solutions belonging to the Pareto front, none of the objective functions can be improved in value without worsening the other. The Pareto-optimal solution (a_{opt}^p, i_{opt}^p) must be chosen by the decision maker only from the Pareto front P, $(a_{opt}^p, i_{opt}^p) \in P$.

In [3], the computer approximation of the Pareto front is carried out using the genetic algorithm of global optimization. At each optimization step, the distribution problem was solved and the matrix x_{ij}^* of the optimal distribution of requests for the execution of OOS between OOS complex spacecrafts was determined. The advantage of the genetic algorithm is that it generates a set of solutions that allow you to calculate an approximation of the whole Pareto front. In addition, it does not depend on the type of objective functions, the definition area, and the types of optimization variables do not require the setting of initial approximation and have a large number of control parameters.

The article [3] presents computational results of a Pareto optimization example, which are visualized as plots of Pareto fronts (compromise curves). The compromise curves provide complete information on how the improvement of one objective function is related to the deterioration of another when moving along the compromise curve. The decision maker can take this information into account when determining the Pareto-optimal objective point.

The analysis of the performed calculations showed that an increasing the number of of OOS complex spacecrafts usually leads to a decrease in the average waiting time for the start of the interorbital flights by spacecrafts of the OOS complex. To determine the required number of OOS complex spacecrafts, the problem of determining the optimal parameters of the OOS complex spacecrafts parking orbits is solved for a different number of spacecrafts in the OOS complex. Using the obtained plots of the Pareto fronts, the decision maker determines the required number of the OOS complex spacecrafts.

Conclusions

In the paper, the orbital structure of the low-orbit complex OOS in near-Earth orbits with a small eccentricity is proposed. The peculiarity of the proposed orbital structure is the placement of the OOS complex spacecrafts on the orbits with a small eccentricity, and the same nodal precession speed. The planes of the parking orbits of the spacecraft of the OOS complex are evenly distributed by the LAN. The nodal precession speeds of the OOS spacecraft orbits and the orbits of the OOS clients differ significantly due to the difference in the major semiaxes of their orbits. For OOS spacecrafts, the technique for optimal synthesis of the orbital structure and optimal operational planning of the low-orbit OOS space complex in orbits with low eccentricity has been developed. Several ballistic and optimization problems that arose during the development of the technique were formulated and solved. Methods for solving the problems are the averaging method, the branch-and-bound method, and the multi-objective optimization method.

REFERENCES

1. Alpatov A.P., Goldshtein Yu.M. Assessment perspectives for the orbital utilization of space debris. *Space Science and Technology*. 2021. 27. No. 3. P. 3—12.

2. Гольдштейн Ю.М., Фоков О.А. Оптимізація перельотів між низькими орбітами з суттєвою різницею довгот висхідних вузлів. *Технічна механіка*. 2022. № 3. С. 63—74.

3. Goldshtein Yu.M. Orbital structure optimization technique of the low-orbit complex of on-orbit service. *Space Science and Technology*. 2023. 29. No. 4. C. 3—11.

CONCEPTUAL DESIGN OF THE SPACE INDUSTRIAL PLATFORM

A. Alpatov, O. Palii

The Institute of technical mechanics of The National Academy of Sciences of Ukraine
and of The State Space Agency of Ukraine

Mankind is facing the need to solve the problems of global warming and shortage of Earth's resources. One of the constituent ways of solving these problems is the step-by-step industrialization of space, which results in the transfer of high-energy production to space. Space industrial platforms are the technological basis for the transfer of certain types of industrial production [1]. Of particular interest is the production of unique materials and substances with characteristics that can be achieved in weightlessness and vacuum conditions. In some cases, exposure to harsh radioactive radiation may also be necessary. Thus, a whole direction in the field of space technology development has emerged, related to the design of specialized space platforms, oriented to ensure the production of unique materials and products requiring open space conditions.

The state of the art in the development of the key component modules of an orbital industrial platform is analyzed, and it is concluded that space conditions make it possible to produce new materials and substances whose characteristics are improved in comparison with their earth counterparts [2]. The most interest in the development of production processes in vacuum and zero gravity conditions is shown by the USA, Russia, and the EU countries. It is shown that at the initial stage of development of orbital industrial platforms raw materials for the production of unique materials can be supplied from the Earth. With further technological development, it will be possible to use space resources. Orbital industrial platforms are a new class of engineering systems. To develop a mathematical model of an orbital platform and components thereof, its functional diagram with the key functional links between the platform components is presented. The problem of orbital industrial platform development is complex, and thus it has a wide range of different aspects of its solution.

To generate the initial data for calculating the design parameters of the platform, it is necessary to combine the characteristics of technological processes in an appropriate manner [3]. To achieve this goal, it is proposed to cluster the characteristics of technological processes and their subsequent classification based on relevant criteria. The clustering criterion was chosen as "conditions of physical implementation of the technological process". The following criteria are proposed for further classification: "type of aggregate state of raw materials"; "method of crystallization"; "temperature field mobility in the directed crystallization chamber"; "type of process of precipitation of raw materials from steam"; "type of epitaxy"; "form of final space metallurgy products"; 'method of pore formation in the melt". An analysis of the technological processes implemented in outer space is carried out, and a set of their parameters is formed, which must be ensured on the space industrial platform. Using the classifier, the functional diagrams of various technological processes that can be implemented in near space are analyzed. Functional diagrams contain main and auxiliary modules depending on the type of technological process. The relationship between the technological and basic modules of the industrial platform is shown. The cargo flow, communication and control channels, power supply, thermal conditions of the platform, ventilation and vacuum are defined and shown in the form of a diagram.

In general, the industrial platform is equipped with main and auxiliary modules [4]. The main modules include: a hull with a supporting structure, a control module, an energy complex, a thermal management module, an orientation and stabilization module, an onboard transport system, an industrial module, receiving and shipping docks, and a finished product storage module. The industrial module houses the basic equipment for the implementation of technological processes. The set of auxiliary modules is determined by the type of production. In general, the auxiliary modules are characterized by the following list: raw material storage module, raw material primary processing module, raw material supply module to process equipment, module for storing and supplying auxiliary substances (water, gas, solution) to process equipment, auxiliary substance preparation module, heat removal module from equipment to the platform's thermal control system, gas removal module from equipment to the platform's ventilation and gas removal system.

The industrial platform has a number of features, namely [5]:

- significant weight and dimensions of the structure;
- modular construction principle;
- maintainability;
- use of standardized structural elements, such as unified electrical connectors, attachment points and fixing elements for equipment, etc;
- availability of specialized docks that include systems for guidance, docking and fixing the service spacecraft;

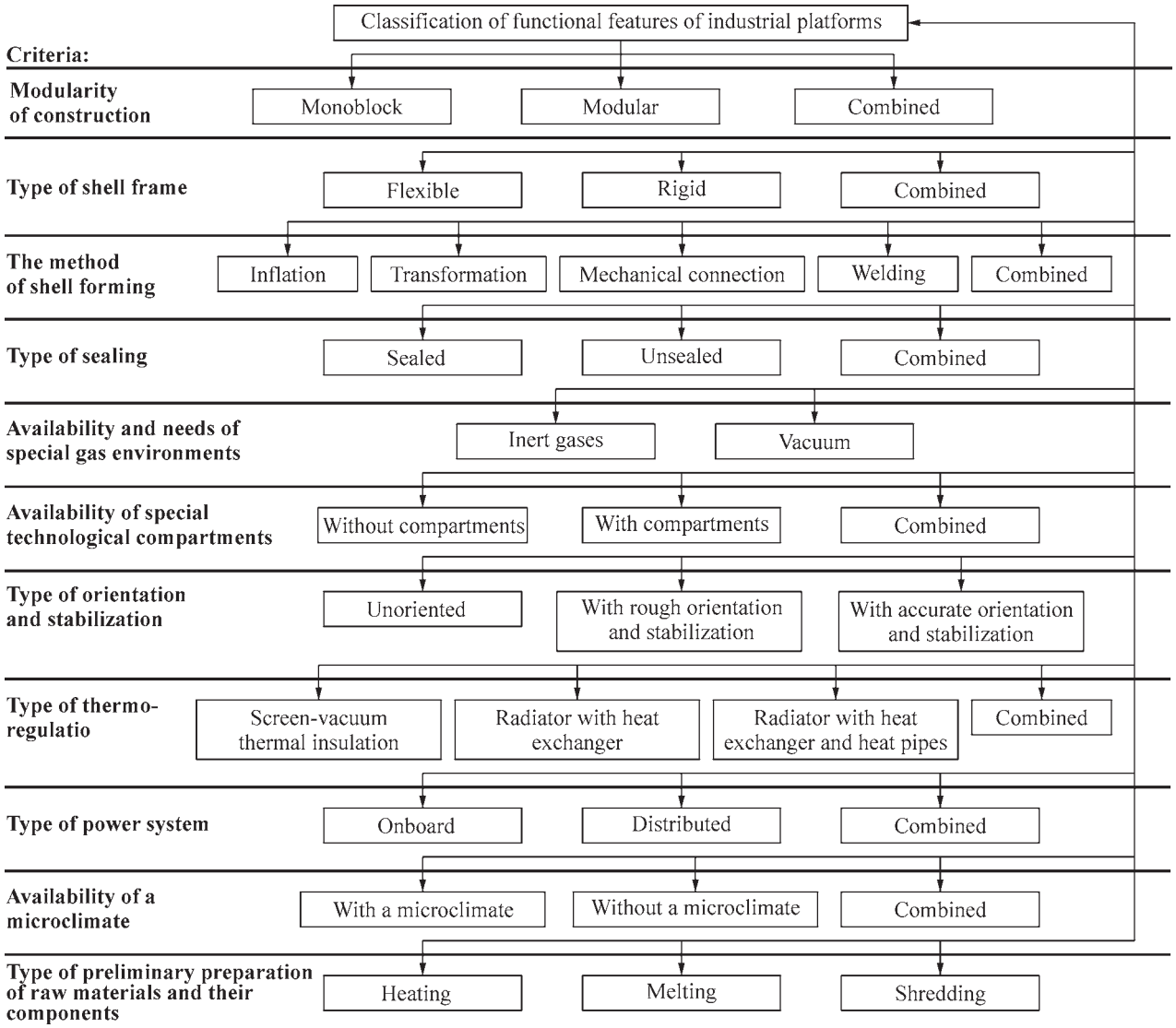

Fig. 1. Structure of classification of functional features of SIP

• availability of the necessary interface for servicing by service space systems.

The design scheme of the space industrial platform (SIP) significantly depends on the requirements of the technological processes implemented on it: The formation of the SIP design depends largely on a number of criteria arising from the functional features of the platform. These are the following criteria [5]: modularity of the structure, type of shell frame, method of shell formation, type of sealing, availability and needs of a special gas environment, availability of special process compartments, type of orientation and stabilization, type of power system, type of thermal control, availability of microclimate, type of preliminary preparation of raw materials and its components. Using these criteria, a classification of the functional features of the SIP shell is proposed, the structure of which is shown in Fig. 1 [5].

Optimization problems of industrial platform parameters were formulated. The stages of optimization are as follows: analysis of technological processes implemented on the SIP; formation of clusters of design parameters that need to be optimized; construction of a matrix of correspondence of parameters of SIP modules to the parameters of technological processes; determination of optimal vectors of parameters of platform modules [5].

A weight model of the industrial platform and its modules was developed, during the development of which the platform and its components were decomposed to the level of system elements [6]. A statistical analysis of the mass fractions of on-board systems of spacecraft was carried out. The average indicators of mass fractions from the researched sample of spacecrafts and their corresponding dispersion indica-tors (dispersion, mean square deviation) were determined. Confidence intervals with a confidence prob-ability of 99.9 percent were determined for the averages and variances. Further studies on the design of space industrial platforms are planned to be carried out taking into account the determined mass

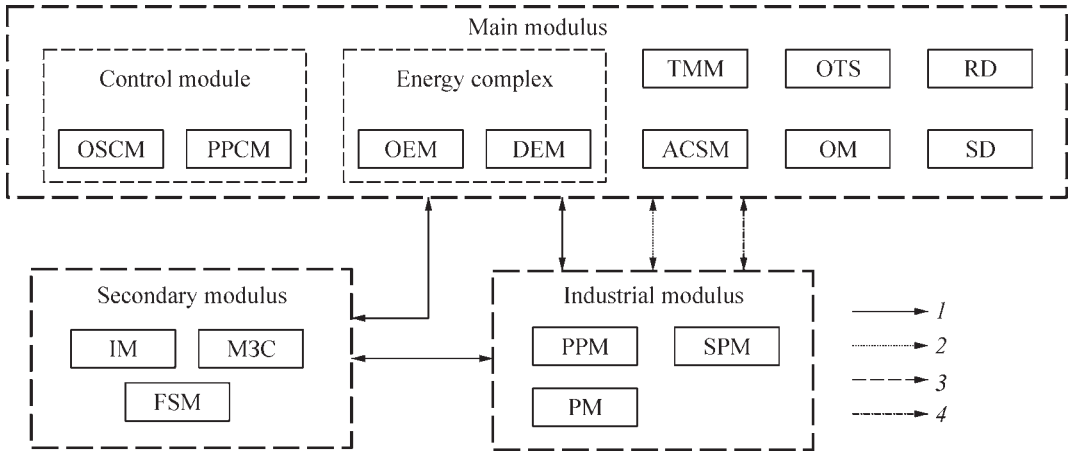

Fig. 2. Functional diagram of the process of obtaining raw materials from space debris at the space industrial platform: 1 — cargo flow; 2 — communication and control channel; 3 — energy supply channel; 4 — thermal control channel; 5 — ventilation and vacuum system channel; CM — control module; OSCM — on-board systems control module; PPCM — production process control module; OEM — on-board energy module; DEM — distributed energy module; TMM — thermal management module; ACSM — attitude control and stabilization module; OTS — on-board transportation system; OM — on-board manipulators; RD — receiving docks; SD — shipping docks; IM — SDF identification module; FSM — SDF fragmentation and sorting module; RSM — raw material storage module; PPM — primary processing module; SPM — secondary processing module; PM — production module; FPSM — finished product storage module

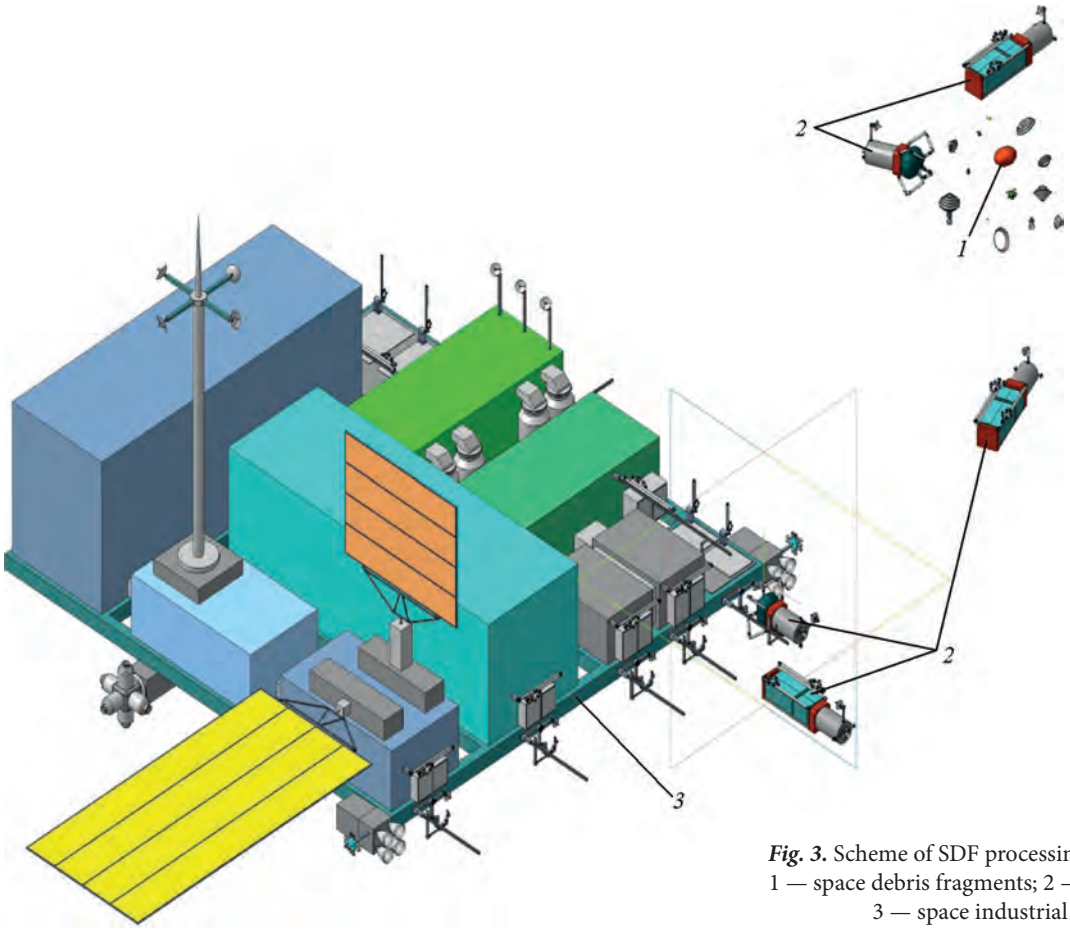

Fig. 3. Scheme of SDF processing into raw material: 1 — space debris fragments; 2 — service spacecraft; 3 — space industrial platform

fractions of satellite systems, taking into account the appropriate confidence intervals, namely the minimum and maximum possible masses for one or another system.

An analysis of the configurations of existing orbital stations as a prototype of space industrial platforms was carried out, and the ranges of the main parameters of

their modules were determined [7]. A set of parameters of technological processes in vacuum and zero gravity conditions that can be implemented on a space industrial platform has been formed. The relationship between technological and basic modules of the industrial platform is shown. The structure of a complex mathematical model of the space industrial platform functioning is developed. For successful work at the conceptual design stage, a general statement of the problem of optimizing the mass of the space industrial platform is formulated. The minimum mass and dimensions of the space platform obtained as a result of the optimization are used in the future to refine the optimal parameters of the platform and, therefore, affect the formation of conditions for the implementation of the technological process. The algorithm of the sequence of operations for solving the problem of optimal design of a space industrial platform is shown in general.

To implement energy-intensive technological processes on an industrial platform, it is proposed to use a distributed energy system [8]. Mathematical models for the analysis of orbital, angular and relative motion of power spacecraft and receiver spacecraft was developed. Algorithms for calculating the parameters of the orientation and stabilization system of powered space vehicles are proposed. A generalized model for determining the maximum distance and the length of the time interval for the transmission of electricity from the power spacecraft to the platform using microwave radiation has been developed. The developed model allows for the selection of design parameters of energy space vehicles at the stage of conceptual design of power systems of the space industrial platform.

A new paradigm for solving the problem of space debris growth in Earth orbits is proposed. Within the framework of this paradigm, a method of processing space debris fragments (SDF) into raw materials for further use is proposed [9]. The method is implemented as follows: after capture, the SDF is placed on a specialized slipway for fixation and transportation; using the onboard propulsion system of the service spacecraft (SSC), an orbital maneuver is performed to approach the SDF; after the SSC and SDF dock, the SDF is placed on a slipway located in the receiving docks, where its primary fragmentation is carried out, using a remote-controlled manipulator. Next, the SDFs are moved to the appropriate primary processing modules, where the SDFs are identified, sorted, and further fragmented to the specified dimensions, and then the latter are moved to the secondary processing module, where they are processed. At the initial stage, man-made space debris from low Earth orbits can be used. Later, fragments of natural space debris (asteroids, comets) can be used as raw materials for the industrial platform.

The functional diagram of the process of obtaining raw materials from space debris at the space industrial platform is shown in Fig. 2.

To implement this process, a three-dimensional model of the SIP was developed, as shown in Fig. 3.

REFERENCES

1. Алпатов А.П., Горбулин В.П. Космические платформы для орбитальных промышленных комплексов: проблемы и перспективы. *Вісник НАН України*. 2013. № 12. С. 26—39.

2. Palii O.S. State of the art in the development of orbital industrial platforms. *Tech. meh*. 2021. No. 3. P. 70— 82.

3. Палій О.С. Класифікація технологічних процесів за їхньою реалізацією на космічній індустріальній платформі. *Технічна механіка*. 2022. № 2. С. 123—136.

4. Палій О. С. Формування проєктного вигляду космічної індустріальної платформи. В: О.С. Палій. Системне проектування та аналіз характеристик аерокосмічної техніки. 2023. XXXII. С. 78—88.

5. Палій О.С. Класифікація функціональних особливостей оболонки космічної індустріальної платформи. *Технічна механіка*. 2023. № 2. С. 3—11.

6. Палій О.С. Моделі для оцінки маси космічної індустріальної платформи та її модулів. *Технічна механіка*. 2022. № 3. С. 75—84.

7. Алпатов А.П., Палій О.С., Сюткіна-Дороніна С.В. Концептуальне проєктування космічної індустріальної платформи. *Постановка задачі*. 13. 2023. 29. № 6. С. 13—25.

8. Палій О.С., Лапханов Е.О., Своробін Д.С. Модель керування рухом космічних розподілених енергетичних систем. *Технічна механіка*. 2022. № 4. С. 35—50.

9. Заявка на патент на винахід України № a202201533, МПК B64G 1/00, B64G 1/64, B23K 9/04. Спосіб переробки фрагментів космічного сміття природнього та штучного походження в елементи конструкції об'єктів космічної техніки та космічна індустріальна платформа для його здійснення / Алпатов А.П., Палій О.С. a202201533; заявл. 13.05.2022.

ON-BOARD NAVIGATION, ATTITUDE DETERMINATION AND CONTROL SYSTEMS FOR MICRO- AND NANO-SATELITES

O. Zbrutskyi, V. Burnashev, Y. Marynych, V. Meleshko, S. Tarnavskyi, S. Pukha, A. Ganzha, O. Bondarenko

National Technical University of Ukraine "Ihor Sikorsky Kyiv Polytechnic Institute"

Actuality. Demand for the use of micro and nano satellites is growing in Ukraine and around the world. In the next 3 years, the number of CubeSat launches is expected to 600—800 per year. After 2027, this figure is expected to exceed 1,000. The cost of manufacturing, launching and ground support of one ordinary specialized satellite weighing several hundred kilograms is $300—700 million, while CubeSat projects are valued at $100,000—300,000. Global and local needs of humanity have necessitated and confirmed the feasibility of developing the young segment of space technology, which consists of micro- and nano-satellites (MNS). The possibility of miniaturizing the spacecrafts to the "nano" size for a wide tasks range created the prerequisites for the construction of satellites in universities and became an attractive factor for the mass young people participation.

For many applications of micro- and nano- satellites (research of near-Earth space, stratosphere, synthesis of new materials, biological experiments, etc.), it is sufficient to determine their position in space. Successes in the miniaturization of optical-electronic and radio equipment have created technical opportunities for expanding the using scope of micro- and nano- satellites (MNS) to the tasks such as Earth remote sensing (ERS), observations of Earth's surface and climate, space debris collection. These applications require, in addition to position location, also the spacecrafts attitude determination and control.

Such systems as separate ready-made modules (such as autopilots for atmospheric unmanned aerial vehicles) in a combination of hardware and software for the MNS are not widespread enough on the market today. As a rule, the developers of the MNS create their own attitude determination and control system (ADCS) for each spacecraft. The need for a unified flight controller for the MNS, which can be adjusted to the satellite being created, is becoming urgent.

Development results (The work was carried out according to the state order)

1. For the first time in Ukraine, an integrated Navigation, Attitude Determination and Control System (NADCS) was developed for low-orbit satellites as part of an electronic module as a unit of on-board equipment and a set of software work algorithms modules. Its main advantage over analogues is its versatility, which includes the ability to automatically take satellite parameters into account and the ability to set the composition of sensors, actuators and operating modes selected by the manufacturer of the MNS. This makes it possible to build the small satellites control systems for various purposes, including for Earth remote sensing, using on board the proposed NADCS development as a basic.

A package of programmed work algorithms allows to control the satellite rotational movement in all typical modes of its operation: detumbling angular rates after deployment stage or an emergency situation; turning in the given direction; pointing working axis to the Earth for the operation of the payload; building an Sun-oriented mode for efficient operation of solar panels; angular stabilization both in the illuminated part of the orbit and in the shadow; work in sun-synchronous orbit.

The developed algorithms and software can use information from a group of sensors (inertial, magnetic, optical, micromechanical, solar) and provide control of variable actuators (electromagnetic coils or electric reaction wheels), which are built on different physical principles, and are functioning in conditions of uncertainty external influences and limited information accuracy.

Operating algorithms have been prepared for typical abnormal situations based on complexing methods with strapdown inertial attitude system algorithms, which ensure the operation of NADCS in the event of magnetometer or solar sensor failures, solar sensor shading, satellite entering in the Earth's shadow, reference vectors collinearity, etc. using GPS receiver information.

Algorithms for adjusting the control system have been developed depending on the composition of sensors and actuators and the technical characteristics of the MNS.

2. The design documentation of the prototype of the NADCS electronic module as a unit of the onboard equipment of the MNS has been developed.

3. A pilot sample of the onboard NADCS module of the MNS was produced (Fig. 1).

4. For the first time in Ukraine, an experimental sample of a mini reaction wheel was developed for the MNS control with technical characteristics and operation accuracy that correspond to world standards. The design documentation

for the experimental sample of the reaction wheel was developed (Fig. 2).

5. Conducted ground tests (Fig. 3—5) and tests on the platform of the micro-satellite of the PolyITAN series of KPI named after I. Sikorskyi (Fig. 6) of the onboard NADCS module and the mini reaction wheel experimental sample confirmed the compliance of their technical characteristics with the specified requirements.

Scientific-technical level and development novelty

1. Integrated NADCS for micro- and nano- satellites was developed and created for the first time in Ukraine. Its main advantage over global analogues is its versatility based on a unique set of algorithms, the ability to automatically take satellite parameters into account, as well as the possibility of own adjustments to the composition of sensors, actuators and operating modes selected by the MNS manufacturer [1, 2].

2. The NADCS work algorithms implement a complex attitude determination system of the MNS, which is based on the generalization and development of modern methods of processing the array of spacecraft orientation vectors and includes the use of onboard magnetometers, solar sensors, angular rate sensors and GPS receiver [3]. The attitude determination accuracy is achieved using specially developed signal filtering methods [4, 5].

3. The algorithms of the on-board NADCS are implemented in the form of software on a modern microcontroller STM32F series. The test results confirmed the efficiency of the developed algorithms and the electronic module, as well as the compliance of the NADCS with its specified technical characteristics (Table 1).

4. The NADCS electronic module is built on the principles of a flexible distributed computing architecture, which allows for the creation of a wide range of low-orbit satellites control systems, which differ in terms of

Table 1

NADCS main technical data

Parameter	Unit of measurement	Numerical value
Mass	kg	<0,3
Accuracy orientation angles measurement (depending on the selected sensors)	degree	0,06…5,0
Angular rate control	degree /s	1,0
Operating temperature range	°C	–20...+45
Interface		RS485
Supply voltage	V	12 (5)
Power consumption	W	0,5...1,0
System dynamic errors by the attitude angles and angular rates:		
– under reaction wheel control	deg / deg/s	<0,5/<0,01
– under electromagnetic coils control	deg / deg/s	<5,0/<0,3

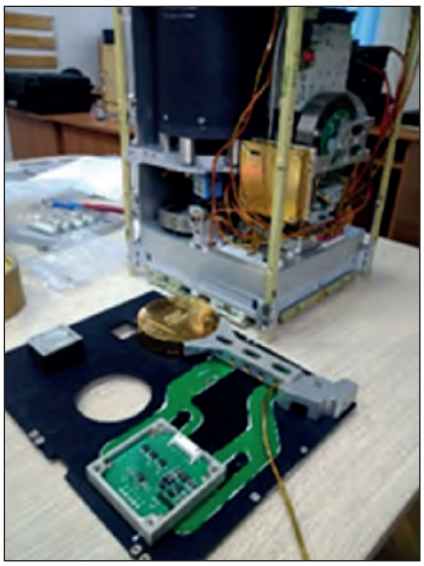

Fig. 1. NADCS pilot sample as part of the micro satellite PolyITAN series engineering model

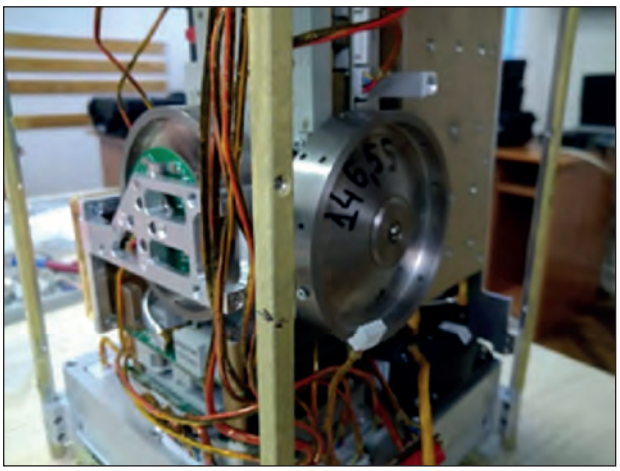

Fig. 2. Mini reaction wheel as part of the PolyITAN micro satellite

Fig. 3. Testing the reaction wheel on a vibrating stand

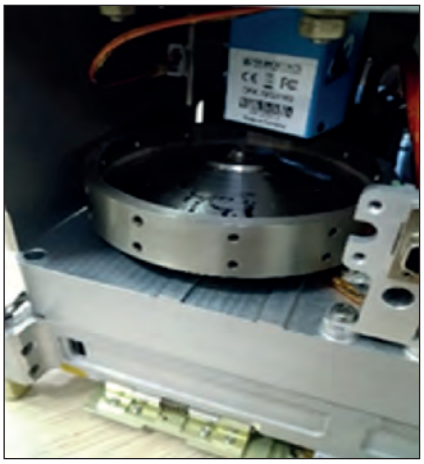

Fig. 4. Testing of the reaction wheel in a thermal chamber

Fig. 5. Checking the reaction wheel parameters

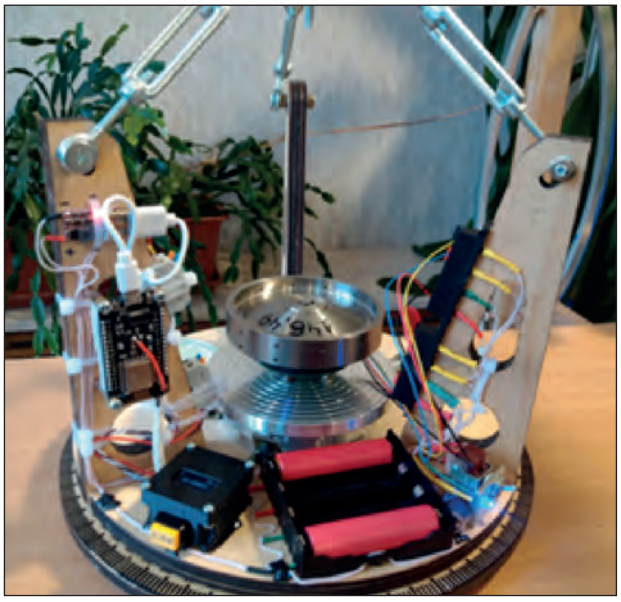

Fig. 6. Testing the NADCS and reaction wheel on a string stand

characteristics and purpose, including ERS; the selected set of adjacent on-board equipment of the spacecraft (sensors and actuators) allows to optimize the cost of components

Table 2

Main technical data of experimental model mini reaction wheel (RW)

Parameter	Unit of measurement	Numerical value
Supply voltage	V	8
Angular momentum, max	N·m·s	0,22
Control torque, max	N·m	0,004
Initial starting torque	mN · m	0,015
Maximum control torque error	mN · m	0,01
Power consumption	W	<9
Dimensions	mm	Ø95 × 30
Mass	kg	<0,3

with the minimum necessary redundancy of functions. The effectiveness of the interaction of the electronic module with the developed experimental reaction wheel sample was confirmed by full-scale tests on a laboratory stand with a string suspension (Fig. 6).

5. The mini reaction wheel (RW) experimental sample as the NADCS actuator for the MNS has technical characteristics and operation accuracy that correspond to modern foreign samples, which is confirmed by autonomous tests (Table 2). The RW advantage is the open design with the possibility of working in two environments (ground and space), which reduces its weight and cost. The novelty RW design is confirmed by the patent [6], and its production will allow Ukraine to become a full-fledged participant in the market of on-board equipment for the MNS.

Conclusions

1. The developed and tested package of algorithms for the navigation, attitude determination and control system provide automatic consideration of satellite parameters and the possibility of settings for the composition of on-board sensors, actuators and operating modes selected by the manufacturer of the low-orbit MNS.

2. Developed and generalized modern methods of the spacecrafts attitude determination using magnetometers, solar sensors, angular velocity sensors, and a GPS receiver combined with an increase in the attitude determination accuracy by new methods of signal filtering.

3. An experimental sample of a mini reaction wheel as an actuator of the NADCS of the MNS has technical characteristics and operation accuracy that correspond to world samples. The advantage of RW is an open design with the possibility of working in two environments (ground and space), which reduces its weight and cost.

4. The development of the navigation, attitude determination and control system of micro and nano satellites with own mini reaction wheel was carried out at a modern scientific and technical level, which corresponds to the world, which is confirmed by scientific publications and patents.

REFERENCES

1. Burnashev V., Zbrutsky O., Marinich Yu. Micro-satellite orientation control system with rotation wheels. *Mechanics of gyroscopic systems*. 2022. No. 43. P. 20—30.

2. Zbrutsky O., Osokin V. Stabilization and control system with guaranteed accuracy for optical axis. *Mechanics of gyroscopic systems*. 2022. No. 43. P. 5—12.

3. Zbrutsky O., Meleshko V., Ganja A., Tarnavskyi S., Bondarenko O., Ponomarenko S., Saurova K. System definition of micro- and nano- satellite orientation. *Mechanics of gyroscopic systems*. 2022. No. 43. P. 46—60.

4. Zbrutsky A., Meleshko V. Filtering a Signal from Noise at a SINS Coarse Initial Alignment, SCIREA. *Journal of Information Science and Systems Science*. 2022. 6, No. 1. P. 1—14.

5. Meleshko V. Algorithm of the autonomous initial alignment of SINS with sequential filtering. *Mechanics of gyroscopic systems*. 2021. No. 41. P. 37—50.

6. Marynych Yu.M., Zbrutskyi O.V., Humenyuk Yu.M. Invention Patent "Flywheel engine". Patent No. 107272. Registered in the State Register of Patents for Inventions of Ukraine on December 10, 2014.

DIRECTIONAL SOLIDIFICATION IN MICROGRAVITY: EFFECT OF DENSITY CHANGE ON INTERFACE STABILITY; PHENOMENOLOGICAL APPROACH

O. Fedorov [1, 2], A. Mashkovsky [1], E. Zhivolub [2]

[1] Space Research Institute of the NAS of Ukraine and State Space Agency of Ukraine
[2] G.V. Kurdyumov Institute for Metal Physics of the NAS of Ukraine

Introduction

The solid-liquid interface stability during directional solidification is of considerable fundamental and practical interest as one of the basic problems of solidification physics [1—3]. This interest is related to the dependence of the crystalline material properties on the morphological features of the crystallization front, as well as to the development of external action technologies on crystallizing melts. The problem of interface stability is of primary important in the development of new methods of space material sciences [4, 5].

An adequate physical description of directional solidification requires a coherent solution of three interrelated problems: three-dimensional hydrodynamic problem, heat and mass transfer and two-dimensional morphological stability one [2]. In general terms, meeting the conditions of these three tasks together is a major challenge, so substantial simplifications are introduced when considering real crystallization [1, 3, 6].

It is known that taking into account real crystallization factors can change the stability areas identified in the theory

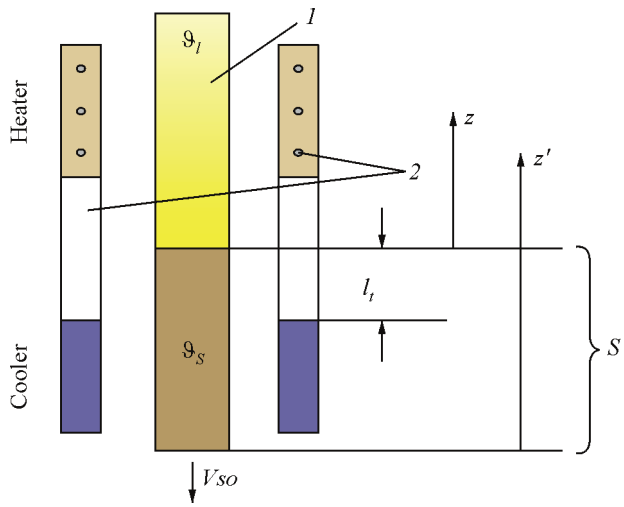

Fig. 1. Scheme of the directional solidification process: *1* — ampoule containing a binary melt; *2* — device consisting of heater and cooler; ϑ_l — heater temperature; ϑ_s — cooler temperature; *S* — interface position; l_t — distance of the interface from the cooler; V_{SO} — velocity vector of the ampoule relative to heater / cooler device

[6]. For example, various effects of melt flow on interface stability have been theoretically and experimentally detected: stimulation and suppression of perturbations by melt flow, coupled convective-morphological instability, traveling waves etc. [7—13]. The analysis of the interface stability in the conditions of lateral melt flow has demonstrated a complicated pattern of alternation of stability areas, which is substantially dependent on the flow rate [13]. It should be noted, however, that the above mentioned works (including the linear model [6] as well as the model [13]) have certain limitations, as they ignore the effect of density change during crystallization and the resulting melt flow as well as the effect of heat transfer through the solid phase. The above—mentioned factors are usually neglected because of their small effect in comparison with the main factor in action — constitutional melt supercooling. However, without proper analysis, this simplification does not appear to be physically justified. For example, a number of works on dendritic growth theory, eutectic crystallization, and crystal growth kinetics have shown the significant role of density change during crystallization [14—18]. Note that under microgravity conditions, when there is no gravitational convection, this effect is inevitable. It seems that the study of its relative contribution is extremely interesting precisely for the problems of space material sciences.

This paper is dedicated to the description a phenomenological theory of stability, in which it is possible to compare above mention acting physical factors during directional crystallization in a two-component system. The study of the morphological stability is carried out using the phenomenological approach in the framework of continuum mechanics in planar geometry. Furthermore, the boundary value problem of directional solidification under stationary conditions is solved, and then the eigenvalues of the boundary value problem, formulated for infinitely small perturbations of the stationary process, are determined. This approach allows to study morphological stability for perturbations with any wave number $k > 0$.

The details of the mathematical formulation of the problem and the basic equations are presented in the article [19]. This review presents the main results of the analysis of the relevant models and the main conclusions of interest to the problem of directed crystallization in microgravity.

Problem statement; hierarchy of considered models

Two-dimensional scheme of a stationary directional solidification of a binary melt is considered, as shown in Fig. 1: positive direction of the coordinate axes: Y — from the reader, X — to the right.

A binary melt is located in the upper half-plane ($Z > 0$), and a solid phase is in the lower one ($Z < [0, \infty]$. The crystallization front lies in the plane X, Y ($Z = 0$) at $\forall t \in \in [0, \infty]$. The laboratory coordinate system (X', Y', Z') is connected to the ampoule and moves in the positive direction of the Z' axis with the interface velocity (solidification rate) w. Coordinate transformations are determined by the following ratios:

$$x = x',\ y = y',\ z = z' - wt.$$

To study the stability of the phase boundary, one considers the infinitesimal perturbation of stationary variables in the system of equations (A1.1)—(A1.13) [18]

The simplest mathematical model of directional solidification includes differential equations of heat transfer in the liquid phase, transfer of impurity in the liquid phase, boundary conditions and a condition for impurity flow continuity when crossing the phase boundary. This model is close to that considered by Mullins and Sekerka [6].

In the next, more complex mathematical model considers the heat transfer in solid phase, equation. This will satisfy the condition of conservation of perturbed energy flux density. Compared to the previous model, the energy exchange at the phase boundary is considered, which includes the latent melting heat Λ. As a result, model #2 increased the order of the obtained dispersion equation, $n = 3$.

Finally, one considers an even more complex model #3 which, in addition to the physical factors included in the models #1and #2 takes into account mass transfer in the liquid phase with the boundary conditions. In this model, the condition of «flowing» across the phase boundary is critical. In the case of $\rho > 1$ (for example, for a system of succinonitrile-acetone $\rho = 1{,}028$) a strong interaction occurs between the dynamic behavior of the liquid phase and the dynamic behavior of the interface. In other words, the boundary condition singularly perturbs the dynamic system, even when the relative density ρ is little different from one.

Then, sequentially executing all the operations as in the models considered above, one obtains a variance equation of order nine

$$\sum_{j=0}^{9} Q_{9-j} \cdot \Omega^{9-j} = 0. \qquad (1)$$

The coefficients Q_i, $i \in \{0,1,...,9\}$ of the dispersion equation (1), due to their bulkiness, are not explicitly represented here. The variance equation (1) describes model #3.

Results of Numerical Calculations

Numerical studies have been carried out for the process of directional solidification of succinonitrile — acetone binary system (SCN-Ac). The main characteristic parameters of the process are as follows: acetone concentration at an infinite distance from the interface $c_0 = 0.2$ mol.%, characteristic solidification rate $W_0 = 10^{-6}$ m/s, characteristic temperature difference $\Theta_0 = 0.259$ °K (chosen such that the dimensionless latent heat of solidification is $\Lambda \sim 1$.

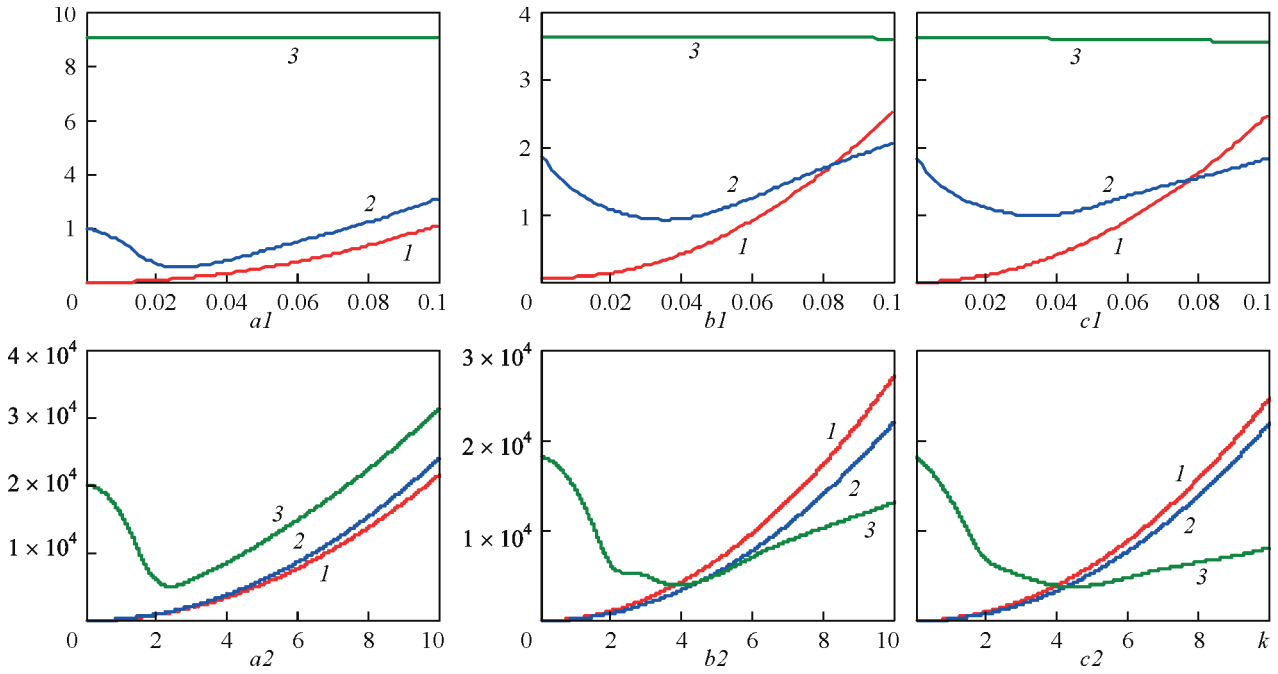

Fig. 2. Spectral characteristics of the increment $\delta_{m,i}(k)$, i ∈{1,…, 3} obtained as a result of solving the second-order dispersion equation: *a* — $\zeta = 0.1291$, *b* — $\zeta = 1.0$, *c* — $\zeta = 1.5$. Curve 1 corresponds to the solidification rate $w = 0.01$; 2 — $w = 1.0$; 3 — $w = 100$. Scale: *a*, curve 1 — $\delta_{m,1}(k) \cdot 10$, 2 — $\delta_{m,3}(k)$; 3 — $\delta_{m,3}(k) \cdot 10^{-2}$; *b*, curve 1 — $\delta_{m,1}(k) \cdot 2$; 2 — $\delta_{m,2}(k) \cdot 2$; 3 — $\delta_{m,3}(k) \cdot 0.5$; *c* — all curves scaled one to one

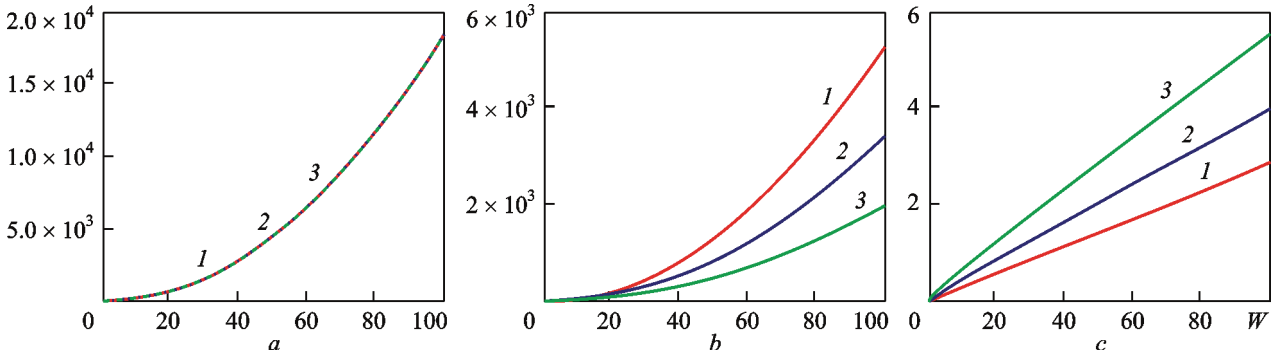

Fig. 3. Spectral characteristics of the generalized increment $\delta_{m,i}(k)$, i ∈{1,…, 3} obtained as a result of solving the ninth-order dispersion equation. Fig. *a*1, *a*2 — ζ = 0.1291; *b*1, *b*2 — ζ = 1.0, *c*1, *c*2 — ζ = 1.5. Curve 1 corresponds to solidification rate $w = 0.01$, 2 — $w = 1.0$, 3 — $w = 100$. Scale: a1 curve 2 — $\delta_{m,2}(k) \cdot 1.1$; 3 — $\delta_{m,3}(k) \cdot 5 \cdot 10^{-4}$; *a*2 curves 2 and 3 — $\delta_{m,i}(k) \cdot 1.1$ for $i = 2, 3$; *b*1 curve 3 — $\delta_{m,3}(k) \cdot 2 \cdot 10^{-4}$; *c*1 curve 3 — $\delta_{m,3}(k) \cdot 2 \cdot 10^{-4}$; *c*2 curve 1 — $\delta_{m,1}(k) \cdot 1.1$

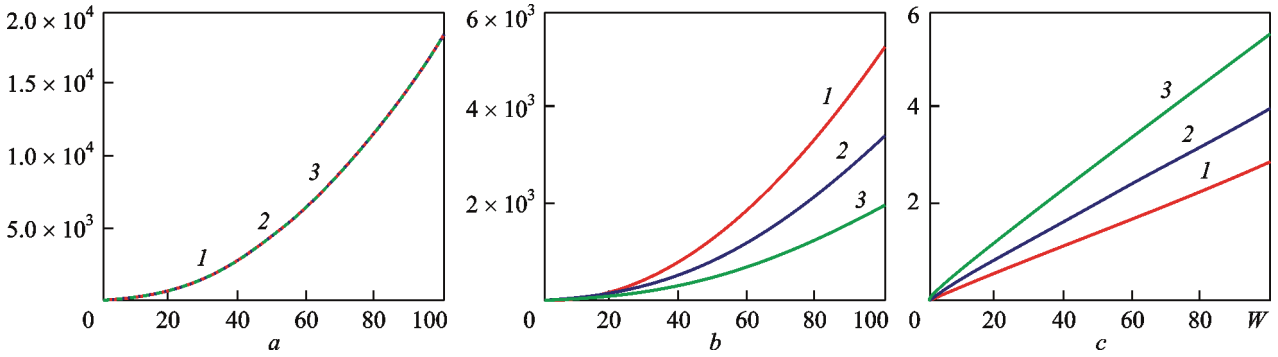

Fig. 4. Dependences of the increment $\delta_{m,i}(w, k)$, and wave numbers $k_{\delta m,i}(w)$ corresponding to the minimum of the increment, on the solidification rate. Curves 1, 2, 3 correspond to ζ ∈ {0.1291; 1.0; 1.5}, respectively: *a* — dependence of the increment $\delta_{m,i}(w; k_0)$, $i \in \{1,\ldots, 3\}$, $k_0 \sim 10^{-6}$; *b* — dependence of minimum values of the increment $\delta_{m,i}(w; k_{\delta m,i}(w))$, i ∈{1,…, 3}; *c* — dependence of the wave numbers $k_{\delta m,i}(w)$, i ∈{1,…, 3}

The roots Ω_j of the dispersion equations (1), were computed by the Laguerre method [19]. Note that these roots are the natural numbers of the considered boundary problem and are related to the eigenfrequencies ω_j by the ratio

$$\omega_j = i\left(\frac{\Omega_j^2}{4} - \frac{\rho^2 w^2}{4} - k^2\right), \quad j = 1,\ldots, n, \qquad (2)$$

where n is the order of the corresponding dispersion equation.

Model #1

Figure 2 shows the results of the spectral characterization of generalized increment $\delta_m(k)$. Three values of parameter ζ ((20)—(22)) ∈ {0.1291; 1.0; 1.5} and three values of solidification rate w ∈ {0.01; 1.0; 100.0} were used. The figure shows that in the vicinity of the $k \sim 10^{-6}$ wavenumbers there is an area of stability ($\delta_m(k) < 0$), which expands as the solidification rate w increases for all ζ < 1 values (Fig. 2, *a*, *b*). At ζ ≥ 1 as the velocity of w increases, the area of stability in the vicinity of small values of k disappears (Fig. 2, *c*, curve 3). In other words, there is instability relative to the long wave perturbations, whereas stability area occurs under large k values. Then, as w increase, this area of stability expands and its borders move towards large values of k (short waves).

Model #2

The results of computing the spectral characteristics of the imaginary part of the roots of the dispersion equation (1) on a set of parameter values {ζ, w}, make it possible to compute the spectral characteristic of the generalized increment $\delta_m(k)$. Calculations show that the spectral characteristic $\delta_m(k)$, at some $k = k_m$ assumes a minimum value of $\delta_m(k_m)$. This value as well as k_m wavenumbers is strongly dependent on the parameter ζ and the solidification rate w.

Model #3

Model #3 assessed the impact of the density change and latent heat of solidification, along with the effect of concentration supercooling on interface stability. The results are shown in Fig. 3, 4. Figure 3 demonstrate that the spectral characteristics of generalized increments $\delta_{m,i}(k)$, $i \in \{1,\ldots, 3\}$ have a minimum which, with the increase of parameters w and ζ shifts towards the higher values of the wave numbers k_m. At the same time for $k > k_m$, there is a monotone increasing of $\delta_{m,i}(k)$, $i \in \{1,\ldots, 3\}$ at $k \to \infty$.

As the solidification rate w increases, the increasing rate of increment decreases $\delta_m(k)$, $k \to \infty$ (Fig. 3, *c*). Figure 4 represents the dependencies on w the increments $\delta_{m,i}(w; k_0)$, $k_0 \sim 10^{-6}$ (Fig. 4, *a*), minimum increments $\delta_{m,i}(w; k_{\delta m,i}(w))$ (fragment *b*) and wave numbers $k_{\delta m,i}(w)$ corresponding to the minimum spectral characteristics of the increments for the three values ζ (Fig. 4, *c*). It can be seen from the figure that with the increasing of w the increment, at a given very small wavelength number $k = k_0$ monotonically grows and does not depend on the parameter ζ.

Discussion

The phenomenological approach developed in this paper allows to study the relative contribution of various physical effects to the loss of stability of a planar solid-liquid interface in microgravity. It is known that the most approaches to this problem ignore such factors as the removal of latent melting heat through solid and density change during crystallization. The description of the latter factor allows to clarify the role of melt flow in the formation of interface morphology. The effect of melt flow caused by convection or forced stirring has been investigated in many studies (see references in [13]. For example, the work [9] shows that the flow can both suppress and stimulate the development of distortions on the interface. The analysis in [13] showed that the fluid flow tangent to the interface significantly reduces the areas of stability. Present paper examines the flux effects associated with a density change. This effect is irreducible because it is related to the internal properties of the substance. It is interesting to compare this effect with others that determine the loss of stability conditions at the interface during directional crystallization in microgravity.

In order to solve the problem, the phenomenological theory of continuous media [19, 20] considers the hierarchy of three mathematical models of different complexity constructed in an infinite region of flat geometry. Furthermore, the stability of the phase boundary during the stationary process of directional solidification was solved numerically. Stability conditions are investigated by introducing infinitely small perturbations followed by the determination of the generalized spectral characteristic (increment) $\delta_m(k, w)$, the sign of which defines areas of stability or instability. That is, the approach is basically the same as in the theory of Mullins and Sekerka [6]. However, a substantial difference is the way of calculation the value of the temperature gradient at the interface. Theory [6] assume the special temperature conditions on the heater and cooler that are necessary to form a stationary temperature gradient at the interface. In the presented model, it is assumed that the temperature of the heater and cooler at infinity have constant values ϑ_l and ϑ_s. The temperature gradient at the crystallization front is described by two dimensionless parameters ζ and τ, whose values are uniquely related to ϑ_l and ϑ_s, which automatically fulfill the stationary condition. In other words, the study of the stability of the crystallization front using ζ and τ is guaranteed for the stationary process.

For ease of comparison of the results of all three models, the calculations were performed using a set of parameter values $\{\zeta, w\}$ common to the models in question. Model #3 provides for the most complete consideration of factors controlling the real solidification process. In this case, the decisive role of the density change in comparison with other factors has been demonstrated, as well as the absence of the area of stable interface morphology. At the same time, it is interesting not only this end result, but also the evolution of the morphological features of the interface, taking into account different approximations. Note also that the present approach gives not only the configuration of the areas of stable interface morphology, but also allows to estimate the relative rates of the development of distortions of different wavelengths.

A comparison of the various approximations makes it possible to analyze the summary of results. Model #1 takes into account the transport of heat and impurity in a liquid phase, continuity equations for impurity flux crossing the phase boundary, and boundary conditions corresponding to the Mullins and Sekerka model. The calculated configurations of the stability areas demonstrate their alternation with the areas of instability in a wide range of solidification parameters. For low k values the model #1 gives an area of stability that is missing when considering models #2 and #3. There is a parameter range where this model gives a picture similar to that considered in Mallins and Secerka theory. On Fig. 2, *b* one can see the emergence of a stability area at mean k values for some growth rate. In this case, numerical values have the same order of magnitude, with estimates made on the basis of the theory [6] for the system of succinonitrile-acetone.

Additional consideration of latent melting heat in model #2 and mass transfer effect due to density change in model #3 (in addition to model #1) results in significant reconfiguration of the stability areas. In particular, model #2 gives a weak instability, which increases rapidly with w and ζ. Model #3 with increasing of w gives an even larger increase of instability at $k = 10^{-6}$ (Fig. 3), which in this model is practically independent of the parameter ζ (Fig. 4, *a*). Thus, in models #2 and #3 (as opposed to model #1), at low values w, the front has a low instability relative to longwave perturbations, which increases rapidly with the solidification rate. Characteristically, the maximum contribution to longwave instability is the effect of a density change on the solidification front.

The configuration of the obtained instability domains is characterized by pronounced extremes in the area of certain values of solidification parameters. For example, for model #1 at $\zeta = 1$ (in model #2 $\zeta = 1.3$), a special point is identified where all regions of stability and instability converge. At this point, the generalized increment $\delta_m(k, w)$ takes the minimum (for models #1 and #2 negative) values, which corresponds to the absence of perturbations

(or their slow development in the case of model #3) for all growth rates. The observed features indicate that in the real spectrum of disturbances one should expect a large set of different frequencies which evolve at different speeds.

In order to compare present results with those of the experimental studies, one took the work [19] as reference one. First, it dedicated to experimental study of the interface dynamics during directional solidification of succinonitrile-acetone binary system, the physical characteristics of which are taken as a basis in present paper. In addition, the parameters of the experimental set-up and the measurement procedure are sufficiently detailed in [21]. To adapt our calculations to [21], in the coordinate system related to the solidification front, one enters the coordinate of the lower edge of the heater (Fig. 1)

$$z_h = l_h - l_t, \tag{3}$$

where l_h is the distance between the top edge of the cooler and the bottom edge of the heater (Fig. 1). Then the temperature on the lower edge of the heater, considering (13), will have the following appearance

$$\theta_l(z_h) = \vartheta_l \cdot [1 - e^{-P_l w(l_h - l_t)}] + \vartheta_0 e^{-P_l w(l_h - l_t)} \tag{4}$$

and the temperature at the top of the cooler

$$\theta_s(-l_t) = \vartheta_s. \tag{5}$$

Solving equation (21) with respect to ζ and taking into account (4), one get

$$\varsigma = \frac{\chi P_l(\theta_h - \vartheta_0) + \Lambda^* [1 - e^{-P_l w(l_h - l_t)}]}{(1-k)\vartheta_0 [1 - e^{-P_l w(l_h - l_t)}]}. \tag{6}$$

Note that in this case (due to fixing the temperatures of the heater and the cooler and therefore the external gradient) parameter ζ becomes dependent on the solidification rate w. After deleting from (22) the parameter ζ, considering (5), and entering the symbol

$$x = e^{P_l w l_t} \tag{7}$$

one gives an equation to determine the position of the solidification front l_t at fixed temperatures of heater $\theta_l(z_h) = \theta_h$ and cooler $\theta_s(-l_t) = \theta_c$

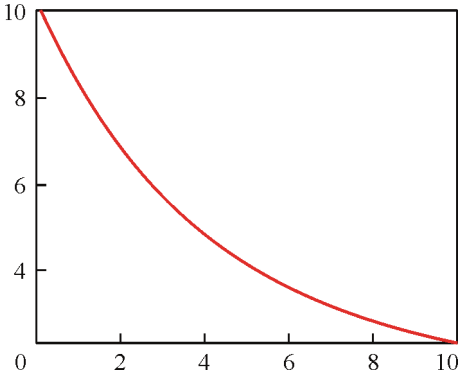

Fig. 5. Spectral characteristic of the increment $\delta_{m,i}(w, k)$ calculated for the experimental conditions given in [10]

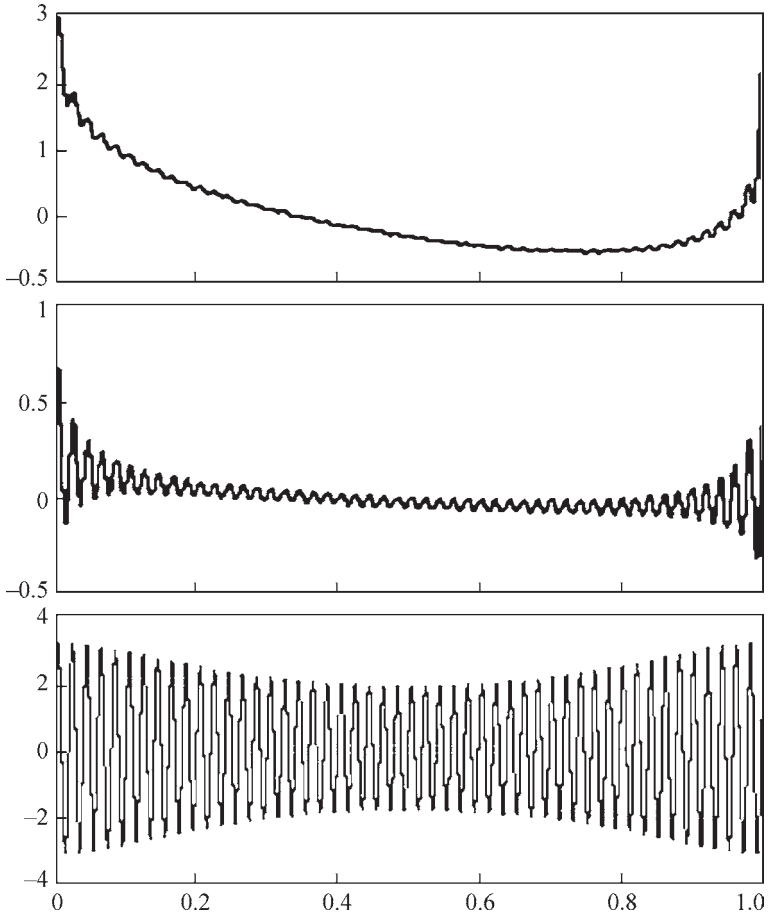

Fig. 6. Spatial structures formed as a result of superposition of 50 eigenfunctions corresponding to a set of unstable eigenvalues $\delta_m(n) = \delta_{m,n}$; $n \in \{0,1,\ldots,49\}$ for time points $t \in \{10^{-4}; 10^{-3}; 3 \cdot 10^{-3}$ c$\}$

$$Ax^{\left(1+\frac{P_s}{P_l}\right)} + B_1 x + B_2 x^{\frac{P_s}{P_l}} + C = 0, \quad (8)$$

where

$$A = \Lambda^* exp(-P_l w l_h),$$

$$B_1 = [P_s/(1-k)\cdot(\theta_c - \vartheta_0) - \Lambda^*] exp((-P_l w l_h),$$

$$B_2 = -\chi P_l(\theta_h - \vartheta_0) - \Lambda^*,$$

$$C = -\chi P_l(\theta_h - \vartheta_0) - P_s/(1-k)\cdot(\theta_c - \vartheta_0) + \Lambda^*.$$

Figure 5 shows the spectral characterization of the increment $\delta_m(k)$, calculated using a model adapted to [21] for the solidification rate of $w = 0.75$ μm/s.

The structures presented in the Fig. 6 are the result of superposition of eigenfunctions. Since a linear model was used, these structures should be considered the beginning of a process that becomes non-linear over time. The structure presented in Fig. 6 is close to the cellular and its period is close to the experimental one, [21]. Therefore, it can be argued that the theory gives a qualitatively consistent with the experiment morphology of the interface. It should be noted that theory consider a linear model, so the coincidence of the order of magnitude of the cellular spacing refers to the linear stage of patter formation. In most experiments known to us, as in the work [21] there is a substantially non-linear process of cell formation, the description of which goes beyond this work.

Conclusions

The phenomenological analysis of the directional solidification of binary alloy which account the influence of a solid-liquid density change and heat removal through solid phase has been developed for the problem of a planar interface stability. The approach is free of some assumptions of Mullins and Sekerka theory, in particular the assignment of special conditions for the formation of a stationary temperature gradient at a crystallization front. The areas of stability and instability are described in terms of the system of parameters ζ and τ, whose range of values is guaranteed to provide the stationarity condition at the interface. They are only related to the temperature values of the heater and cooler ϑ_l и ϑ_s.

The problem of interface stability was studied by introducing infinitesimal perturbations, followed by determination of eigenvalues of the boundary problem formulated for perturbations. The dispersion equation, which relates the wave number k to the complex frequency ω, is obtained in the form of a polynomial of degree n. Polynomial roots make their natural complex frequency ω dependent on the wave number and physical parameters of the solidification process. The sign and numerical value of the imaginary part of the complex frequency ω determines the index of increase ("+" increment) or attenuation ("–" decrement) the amplitude of perturbations over time. The generalized spectral characteristic of the perturbation (increment) $\delta_m(k, w)$, is introduced, the sign of which is guaranteed to determine the areas of stability or instability of an interface.

Within the framework of the general approach, the hierarchy of three particular models, which correspond to different degrees of consideration of physical parameters of solidification process, has been studied. The model #1 (polynomial degree $n = 2$) takes into account of heat and impurity transfer in the liquid phase, condition for impurity flow continuity when crossing the phase boundary and boundary conditions, which correspond to Mullins and Sekerka model. Additional consideration of the latent melting heat in model #2 results in an increase in the order of the dispersion equation to $n = 3$. Model #3 ($n = 9$) takes account of the liquid phase mass transfer, due to the effect of fluid movement due to density change other than the parameters included in models #1 and #2.

Model #1 shows alternating areas of stability and instability over a wide range of solidification parameters. There is an interval of parameters where this model gives a similar behavior as described in Mullins and Sekerka theory (Fig. 2, *b*): the emergence of stability area under mean K values for a certain growth rate value; the numerical values have one order of magnitude with the assessment of the theory [6] for the succinonitrile-acetone system. At the same time, in contrast to the Mullins and Sekerka theory, under relatively high growth rates and small K values an area of stability has been identified.

For all models considered, there is a complex pattern of alternating areas of stability and instability, which is sensitive to the change of parameters w and ζ (dimensionless parameters characterizing the growth rate and temperature gradient at the interface. The configuration of the obtained areas includes pronounced extremes under certain values of solidification process parameters. Thus, for a model #1 at $\zeta = 1$ (in model #2 $\zeta = 1.3$) a special point is identified in which all areas of stability and instability converge. At this point, the generalized increment $\delta_m(k, w)$ adopts minimum (in models #1 and #2 it becomes negative) values, which corresponds to no perturbations (or their slow development in the case of model #3) for all growing rate values. The observed features indicate that in the real picture of perturbations development a large set of different frequencies that develop at different speeds should be expected.

A comparison of the three models shows that the effect of heat dissipation through the solid phase (model #2) and the melt flow due to the density change (model #3) has a significant influence on the occurrence of instability, and neglect of these factors distorts the physical picture of the process.

The most significant factor in comparison with others is the density change at crystallization. When this factor is taken into account, there are no areas of stability, but only slowly developing long-wave distortions at low growth rates.

Under microgravity conditions, gravitational convection is known to be suppressed. It could therefore be assumed that the loss of stability of the flat front is determined only by molecular transfer processes. The results of the calculations in this paper show that the melt flow associated with the density change during crystallization plays a significant role. This effect, which until now was considered negligible, should be taken into account when constructing a description of crystallization in weightlessness.

REFERENCES

1. Flemings M. Solidification Processing. McGraw-Hill, 1974.
2. Chernov A. Modern Crystallography III, P.1. Crystallization Processes. Springer-Verlag, 1984.
3. Fisher D.J. Fundamentals of Solidification, Fourth Edition. CRC Press, 1998.
4. Feuerbacher B., Hamacher H., Naumann R.J. Materials Sciences in Space. A Contribution to the Scientific Basis of Space Processing. Springer-Verlag, 1986.
5. Strelov V.I., Kuranova I.P., Zakharov B.G., Voloshin A.E. *Crystallography Reports*. 2014.59, No. 6. P. 781.
6. Mullins W.W., Sekerka R.F. *J. Appl. Phys.* 1964. 35. P. 444.
7. Caroli B., Caroli C., Misbah C., Roulet B. *J. Physique*. 1985. 46. P. 401.
8. Noel N., Jamgotchian H., Billia B. *J. Cryst. Growth*. 1997. 181. P. 117.
9. Davis S.H., Schulze T.P. *Metall. Mater. Trans. A*. 1996. 27. P. 583.
10. Jiang T., Georgelin M., Pocheau A. *Europhysics Letters*. 2013. 102. P. 54002.
11. Noel N., Jamgotchian H., Billia B. *J. Cryst. Growth*. 1998. 187. P. 516.
12. Jamgotchian H., Bergeon N., Benieli D. *Microscopy.* 2001. 203, Pt. 1. P. 1.
13. Fedorov O., Mashkovskiy A. *Crystallography Reports*. 2015. 60, No. 2. P. 236.
14. Coriell S., McFadden G., Mitchell W.F., Murray B., Andrews J., Arikawa Y. *J. Crystal Growth*. 2001. 224. P. 145.
15. Mori A., Sato M., Suzuki Y. *Japanese Journal of Applied Physics*. 2019. 58. P. 045506.
16. Oxtoby D. *J. Chem. Phys.* 1992. 96. P. 3834.
17. Conti M. *Phys. Rev. E. Stat. Nonlin. Soft Matter.* 2001. 64, No. 5, Pt. 1. P. 051601.
18. Fedorov O.P., Mashkovsky A.G., Zhivolub Ye.L. *Progress in Physics of Metals*. 2023. 24. P. 366—395.
19. Sedov L. *Mechanics of Continuous Media*. 1. World Scientific, 1997.
20. Landau L., Lifshitz E. *Fluid Mechanics*. Pergamon Press, 1987.
21. Lee T.C., Brown R.A. *Phys. Rev.* 1993. B 47:4937.
22. Graham R., Knuth E., Patashnik O. *Concrete Mathematics — A Foundation for Computer Science.* 2nd ed. Addison-Wesley, 1994.

TRANSFORMABLE SHELL METAL STRUCTURES FOR CREATING PROTECTED SPACE CONSTRUCTIONS

L. Lobanov, V. Volkov, Y. Borovyk
E.O. Paton Electric Welding Institute of the NAS of Ukraine

A rapid increase in the rate of space exploration requires a constant resolution of the contradiction between the increasing volume of payload of means of delivery and their own cargo capacity. The number of carriers' launches and the total weight of their payload in recent decades have increased by more than 2.5 times, and the vast majority of spacecrafts are built in the form of shell structures, which is predetermined by the need to maintain the characteristic conditions of the Earth's environment in the limited space of technological and habitat modules. The low specific mass to volume ratio of shell structures stimulates the constant search for technological solutions for their compact assembly during delivery by the carrier, which have a limited efficiency for today due to strict requirements for the load-carrying capacity, stability and density of a folding shell after deploying in a vacuum of outer space. Therefore, the dynamic change in the technological picture of the used materials and methods of compact transformation requires a relevant analysis of their advantages and disadvantages, which should result in a universal method of manufacturing rigid folding shells acceptable for solving most existing problems.

Folding and deployable types of compact transformable structures are used to create variable spatial elements such as antennas, functional elements of satellites, solar panels, as well as capacitive structures, whose construction requires the presence of rigid properties of a load-carrying shell typical for metal materials. The E.O. Paton EWI theoretically justified the problem of transforming the volume of all-welded metal shells and found technological solutions to this problem, which can be divided into two methods. The first method consists in replacing the surface of convex shells with a sequence of plane figures with bending along the lines of their joining, which is known in modern world practice as "z-Folding". The second method is based on isometric bending of shells on the base of deployable linear surfaces and allows creating long-length rigid structures capable of compensating for heavy loads without buckling (Fig. 1).

Welding of structural elements of a multi-section transformable structure is the most effective method for providing the structure with the required complex of properties — structural integrity, sealing, rigidity and long-term reliability. Joining of closed spatial structures of metal foils by the microplasma method requires accurate fixing of billets that do not have sufficient own rigidity, efficient cooling of the joining zone, as well as precision movement of the heating source relative to the fixture for assembly and welding. When developing the technology for joining structural elements of a transformable structure, varying pulsed welding modes allows removing the contradiction between the need for additional weld reinforcement at its sufficient ductility and the requirement to approximate geometric parameters of reinforcement and base metal, which enables the further process of rotation deformation of a thin metal shell. The used equipment usually has a modular design, which allows implementing automatic precision movement of the plasmotron (Fig. 2, *a*) in three coordinates both in welding individual structural elements of the structure on linear keyboard devices (Fig. 2, *b*), as well as during their joining into a single structure on segmented rotary welding-assembly devices (Fig. 2, *c*). Advantages of the implemented technology allow guaranteeing the required vacuum density of the end shell after passing all deformation cycles.

Among the recent most studied concepts of transformable structures of aerospace purpose, projects of long-term extraterrestrial constructions occupy a special

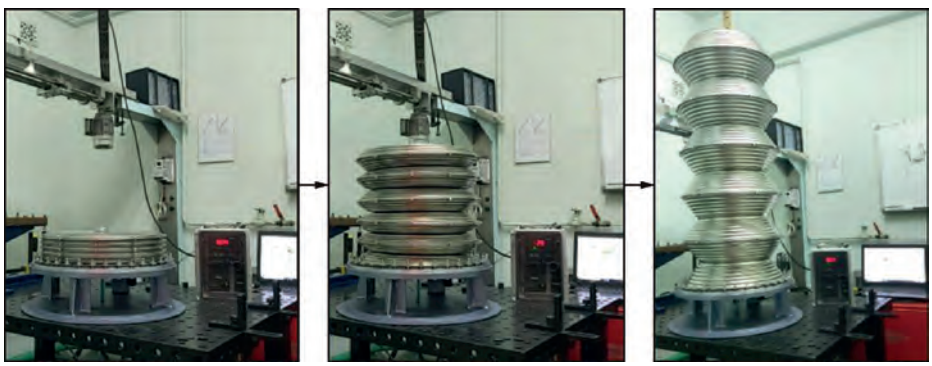

Fig. 1. Process of deploying a metal load-carrying transformable structure of a periodic profile constructed on the base of a folded conical surface

place. The extraordinary cost of lunar missions, which in perspective are longer and more complex compared, for example, to the Apollo historical mission, requires radical solutions for reduced costs. These solutions can be implemented in two ways: this is modernization of delivery means or improvement of mass-size indices of a payload. Compact assembly of large-sized shell structures of lunar bases for the delivery period allows reducing the number of launches, other things being equal, but requires solving the problem of placing loads and preliminary installed equipment in them. Probably, the main disadvantage of known deployable and pneumatic shell structures is the lack of spatial rigidity in them, comparable to traditional ISS-type modules. In some concepts of resemble constructions developed at the E.O. Paton EWI jointly with the SE «DB «Pivdenne»», the so-called hybrid approach has been used, which consists in the joint use of rigid and deployable, as well as folding structures. A membrane-frame structure depicted in Fig. 2 [1] for the so-called greenhouse modules has a rigid base of rods (*F*) from porous aluminium assembled in-situ into a single frame using electron beam welding [2]. The outer shell is formed from several multilayer deployed membranes with separate functions of radiation, ballistic and thermal barriers. The principle of membranes assembly is based on the method of isometric shells' bending similar to the variant in Fig. 1. The fields of distribution of equivalent displacements S_e (Von Mises) in the material of the membrane layers at the stage of assembly, shown in Fig. 3, *e*, which corresponds to the maximum compactness, demonstrate the possibility

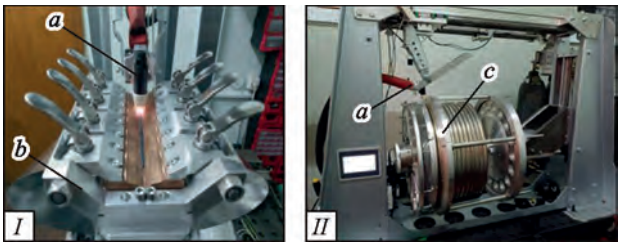

Fig. 2. Modular equipment for assembly and welding of structural elements of a transformable structure (I) and their subsequent joining into a single structure of a periodic profile (II)

of non-destructive deformation of the protective shell based on the Whipple shield with a filler and additional layers of thermal and radiation protection.

Another example of a hybrid approach to the creation of planetary constructions is the concept of inflatable self-carrying shell with an alignment device, which can be used in the creation of habitat modules of various purposes, as well as gateway and technological modules for protected storage of products, etc. A load-carrying shell with the maximum length L = 6 m and diameter D = 3 m (Fig. 4, *a*) after deploying is formed of eight metal truncated-conical shells with a double wall and can be the base of both a separate module, as well as its deployable part (Fig. 4, *b*). The gap between the metal walls, as well as the outer surface of the shell are equipped with multilayered flexible coatings of known materials, the efficiency of which for radiation, ballistic and thermal protection is well confirmed by the experience of practical use in aerospace engineering. The main

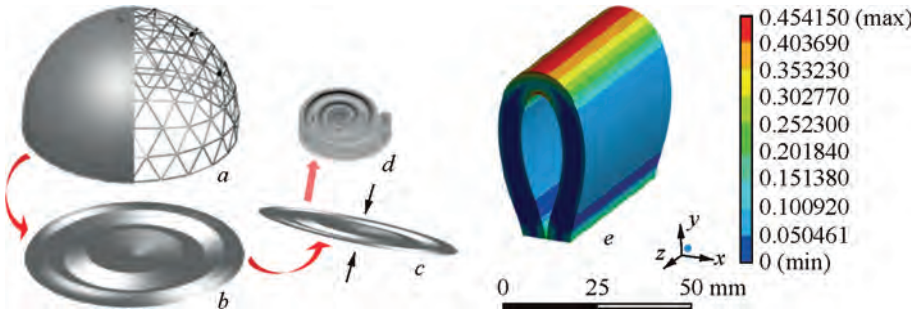

Fig. 3. General appearance of membrane-frame structures of planetary constructions (*a*) and algorithm of compact assembly of the outer shell membrane (*b*—*d*) with fields of equivalent displacements' distribution in the material of its layers at the stage of assembly

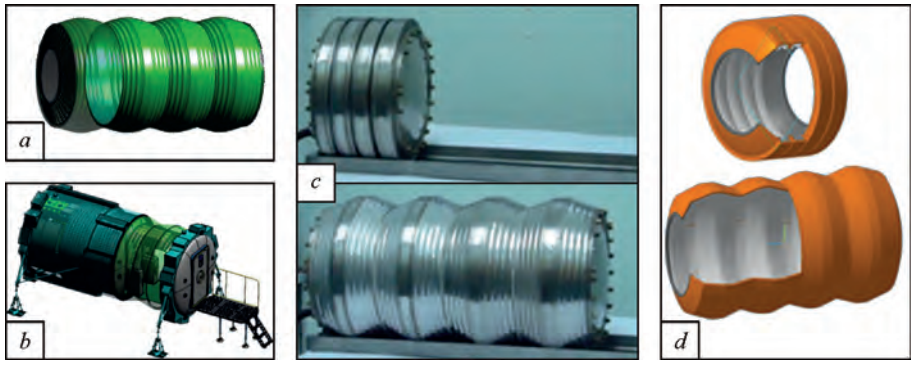

Fig. 4. Concept of using double-walled transformable shell as a base of protected habitat module [1]

idea of a multilayered shell consists in the practical isometricity of each pair of its adjacent metal or synthetic layers.

Fig. 4, *c* illustrates the process of deploying a large-scale (1:10) model of a module with a double load-carrying wall of aluminium (δ = 1.5 mm) depicted in Fig. 4, *d* with an outer anti-meteorite (MMOD) and a thermal control coating (MLI), where a multilayered radiation protection is placed between the metal walls of the shell. It should be noted that the ratios of geometric parameters of inflatable shells are limited only by specific conditions of their use and the required compactness [3]. Therefore, based on the spatial orientation, dimensions and configuration of modules (Fig. 4), branched spatial structures of different functional purpose and degree of protection can be created.

REFERENCES

1. Degtyarev A.V., Lobanov L.M., Kushnar'ov A.P., Baranov Ie.Yu., Volkov V.S., Perepichay A.O., … Kaliapin M.D. On possibilities for development of the common-sense concept of habitats beyond the Earth. *Acta Astronautica*. 2020. 170. P. 487—498. https://doi.org/10.1016/j.actaastro.2020.02.014

2. Paton B.E., Lobanov L.M., Naidich Y.V., Asnis Y.A., Zubchenko Y.V., Ternovyi E.G., … Umanskii V.P. New electron beam gun for welding in space. *Science and Technology of Welding and Joining*. 2019. 24(4). P. 320—326. https://doi.org/10.1080/13621718.2018.1534794

3. Lobanov L., Volkov V., Yakimkin A. Construction methods and comparative evaluation of metal deployable load-carrying shell structures. *Journal of Aerospace Technology and Management*. 2018. 10 (e3818). https://doi.org/10.5028/jatm.v10.959

Звіт для COSPAR узагальнює результати космічних досліджень, проведених протягом 2022—2024 років. У цьому виданні представлено сучасний стан української космічної науки за такими напрямами: космічна астрономія та астрофізика, спостереження Землі та навколоземні космічні дослідження, науки про життя, космічні технології та науки про матеріали. Низку робіт присвячено створенню наукового обладнання для перспективних космічних місій. Значну увагу приділено прикладним дослідженням космічного моніторингу Землі. Видання може бути корисним для широкого кола читачів, які цікавляться космічними дослідженнями.

Наукове видання

НАЦІОНАЛЬНА АКАДЕМІЯ НАУК УКРАЇНИ

КОСМІЧНІ ДОСЛІДЖЕННЯ В УКРАЇНІ 2022—2024

Звіт підготовлений Інститутом космічних досліджень НАН України та ДКА України

Англійською мовою

В авторській редакції

Художнє оформлення
С.А. Горбаненка

Технічне редагування і комп'ютерна верстка
С.С. Думанецької

Підписано до друку 17.06.2024. Формат 60 × 84/8.
Ум. друк. арк. 20,00. Обл.-вид. арк. 26,85. Зам. № 7312е

Видавець і виготовлювач
Видавничий дім «Академперіодика» НАН України
01024, Київ, вул. Терещенківська, 4

Свідоцтво про внесення до державного реєстру суб'єктів
видавничої справи серії ДК № 544 від 27.07.2001 р.


ВИДАВНИЧИЙ ДІМ
АКАДЕМ ПЕРІОДИКА